Lecture Notes in Nanoscale Science and Technology 32

Nashaat N. Nassar
Farid B. Cortés
Camilo A. Franco *Editors*

Nanoparticles: An Emerging Technology for Oil Production and Processing Applications

Springer

Lecture Notes in Nanoscale Science and Technology

Lecture Notes in Nanoscale Science and Technology (LNNST) aims to report latest developments in nanoscale science and technology research and teaching – quickly, informally and at a high level. Through publication, LNNST commits to serve the open communication of scientific and technological advances in the creation and use of objects at the nanometer scale, crossing the boundaries of physics, materials science, biology, chemistry, and engineering. Certainly, while historically the mysteries in each of the sciences have been very different, they have all required a relentless step-by-step pursuit to uncover the answer to a challenging scientific question, but recently many of the answers have brought questions that lie at the boundaries between the life sciences and the physical sciences and between what is fundamental and what is application. This is no accident since recent research in the physical and life sciences have each independently cut a path to the edge of their disciplines. As both paths intersect one may ask if transport of material in a cell is biology or is it physics? This intersection of curiosity makes us realize that nanoscience and technology crosses many if not all disciplines. It is this market that the proposed series of lecture notes targets.

More information about this series at http://www.springer.com/series/7544

Nashaat N. Nassar • Farid B. Cortés
Camilo A. Franco
Editors

Nanoparticles: An Emerging Technology for Oil Production and Processing Applications

Springer

Editors
Nashaat N. Nassar
Department of Chemical and Petroleum Engineering
University of Calgary
Calgary, AB, Canada

Camilo A. Franco
Grupo de Investigación en Fenómenos de Superficie–Michael Polanyi
Departamento de Química y Petróleos
Facultad de Minas
Universidad Nacional de Colombia Sede Medellín
Medellín, Colombia

Farid B. Cortés
Grupo de Investigación en Fenómenos de Superficie–Michael Polanyi
Departamento de Química y Petróleos
Facultad de Minas
Universidad Nacional de Colombia Sede Medellín
Medellín, Colombia

ISSN 2195-2159 ISSN 2195-2167 (electronic)
Lecture Notes in Nanoscale Science and Technology
ISBN 978-3-319-12050-8 ISBN 978-3-319-12051-5 (eBook)
https://doi.org/10.1007/978-3-319-12051-5

This Springer imprint is published by the registered company Springer Nature Switzerland AG
The registered company address is: Gewerbestrasse 11, 6330 Cham, Switzerland

Contents

Chapter 1
Nanoparticles: Preparation, Stabilization, and Control Over Particle Size

Maryam Razi, Maria Contreras-Mateus, Kotaybah W. Hashlamoun, and Nashaat N. Nassar

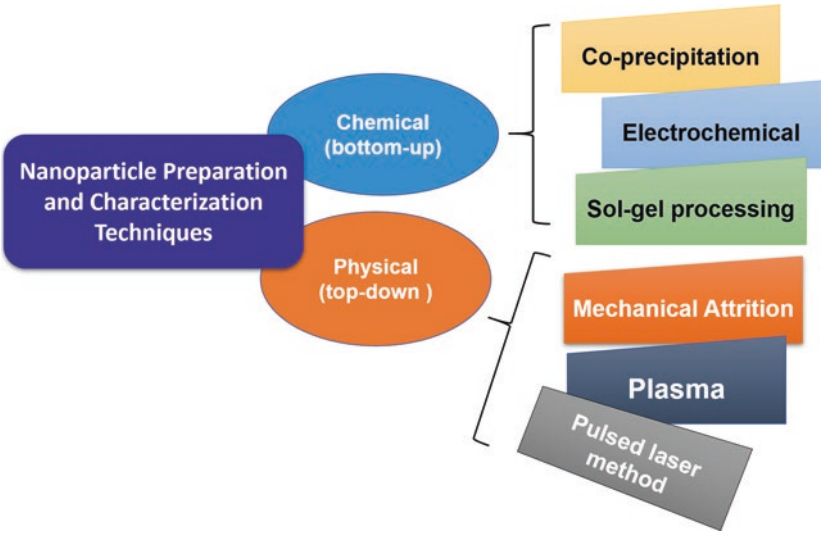

Graphical Abstract

1.1 Introduction

Human dreams often give rise to new science and technology. Nanotechnology, a twenty-first-century technology, was born out of these dreams. Nanotechnology is defined as the control and understanding of materials at scale between 1 and 100 nm,

M. Razi · M. Contreras-Mateus · K. W. Hashlamoun · N. N. Nassar (✉)
Department of Chemical and Petroleum Engineering, University of Calgary, Calgary, AB, Canada
e-mail: nassar@ucalgary.ca

N. N. Nassar et al. (eds.), *Nanoparticles: An Emerging Technology for Oil Production and Processing Applications*, Lecture Notes in Nanoscale Science and Technology, https://doi.org/10.1007/978-3-319-12051-5_1

at least in one dimension, where unique phenomena enable novel applications [1]. Nanotechnology has emerged during the industrial revolution, although human exposure to nanoparticles has occurred throughout human history. The study of nanoparticles dates back to 1925, when the concept of nanometer was first proposed by Richard Zsigmondy, the 1925 Nobel Prize Laureate in chemistry. He explicitly used the term nanometer for the first time for characterizing particle size, and he was the first to measure the size of particles such as gold colloids using a microscope. Although he was the first in using the term, what we know now as "modern nanotechnology" was the brainchild of Richard Feynman, the 1965 Nobel Prize Laureate in physics. It was during the 1959 American Physical Society meeting at Caltech that he presented his well-known lecture, entitled as "There's Plenty of Room at the Bottom", in which he introduced the concept of matter manipulation at atomic levels.

This is from that time in history that our understanding of the modern nanotechnology has been born and developed over the decades. Now, we know him as the father of "modern nanotechnology". Norio Taniguchi, a Japanese scientist, was the first to use the term "nanotechnology" to describe semiconductor processes happening at nanoscale, almost 15 years after Feynman's memorable lecture at Caltech. The golden era of nanotechnology arrived in the 1980s when Smalley, Kroto and Curl discovered fullerenes and Eric Drexler of Massachusetts Institute of Technology (MIT) adopted ideas from Feynman's "There is Plenty of Room at the Bottom". Taniguchi's use of "nanotechnology" in his 1986 book entitled "Engines of Creation: The Coming Era of Nanotechnology" was one of the first definition of nanotechnology as "processing, separation, consolidation, and deformation of materials by one atom or one molecule". Afterward, Drexler suggested the idea of a "nano-assembler" which can build a copy of itself and of other items of arbitrary complexity, which later was known as "molecular nanotechnology". By developing carbon nanotubes by Iijima, another Japanese scientist, the science of nanotechnology was further advanced to a new level [2].

Nanoparticles have novel physical properties distinct from both molecular and solid-state matter due to their significant fraction of surface atoms. Study of these physical properties provides a unique way to learn how nanoparticles can be prepared and characterized. Knowledge of application of nanoparticles in different industrial settings dictates nanoparticles' preparation techniques and characterization. There are surface atoms in nanoparticles by which the nanoparticle "communicates" with its environment. Appropriate preparation techniques can lead to the formation of different types of nanoparticles which can be used as adsorbents and catalysts for different applications in energy and the environment. Different preparation techniques can result in different types of structures. These techniques, developed using appropriate experiments may give insights into complex issues in adsorption and catalysis, such as selectivity of binding of substrates to vertex, edge, or face sites on a nanoparticle. For example, nanosized metal, pharmaceutical, semiconductor, and simple or complex ceramic particles have numerous applications in the development of sensors, thermal barrier coatings, catalysts, pigments, drugs, etc. Considering diverse application, there are different techniques of nanoparticles'

preparations each associated with challenges. The challenges can range from controlling the particle size and size distribution to particle crystallinity, morphology, shape, being able to use the nanoparticles for a given application, and to produce them from a variety of precursors of choice. Different techniques of nanoparticles preparation are chosen according to being suitable for a range of applications and minimizing the challenges associated with such preparation methods. A general nanoparticle synthesis combines the advantages of low toxicity and cost of precursors and high yield of traditional aqueous-based colloidal chemistry with the size dispersion control. It was with this goal in mind that Boutonnet, Kizling, and Stenius first used aqueous pools of water in oil-continuous microemulsions to solubilize simple ionic metal salts of Au, Pd, Pt, and Rh, which was followed by chemical reduction using hydrazine or hydrogen gas to produce metal nanoparticles dispersed in oils [3]. Such novel nanomaterials are shown to have good catalytic activity for hydrogenation reactions.

Another industrially important nanoparticles can be categorized as polymeric nanoparticles (PNPs). Polymeric nanoparticles (PNPs) have gained considerable attention in numerous research activities and have been employed in encouraging number of domains during the last few years. They have been speculated as nanosized solid colloidal particles generated from polymers. Nanoparticles, which are originating from polymers, possess novel properties. PNPs' preparation techniques impose novel properties attached to them without the need for making new compounds. It is in their sizing that refashioning of their physicochemical characteristics happens, which is related to the magic which happens at nanoscale as is the subject in nanoscience and nanotechnology. The factors causing PNPs to attain relatively unique properties than bulk materials are connected to their reduced particle size. As already known, at nanoscale, quantum effects predominate, and the exposed surface area to volume ratio increases. Considering a crystal with many atoms, each atom will have different properties relative to those of bulk material. As seen in Fig. 1.1a, b, large surface area favors enhanced interaction with the surrounding material, specifically with the intermixed materials like composites as well as the performance of products like batteries, and reduces resource usage in catalytic processes, decreasing the amount of waste. This figure also demonstrates the transition effect from macro to nanoscale which causes the large surface area with reduced particle size (Fig. 1.1c) [4, 5]. Interaction of polymer confined to nanoscale with surrounding material makes them an ideal candidate for industrial application as high surface area is considerably a critical factor in the fabrication of new materials [6]. The PNPs' size and size distributions are remarkably interesting as they make for features such as surface area, packing density, viscosity, compact structure, and defined shape [7]. In this regard, Wang et al. [8] have developed variety of novel PNPs of different sizes and shapes using different preparation techniques.

PNPs' preparation techniques can differ to achieve different property optimization. PNPs can be prepared using two major categories named as chemical and physical preparation techniques. Chemical methods are used when monomer has been used as precursor, while physical techniques are implied when preformed polymers are used initially. If monomer is used as precursor, the PNPs' preparation

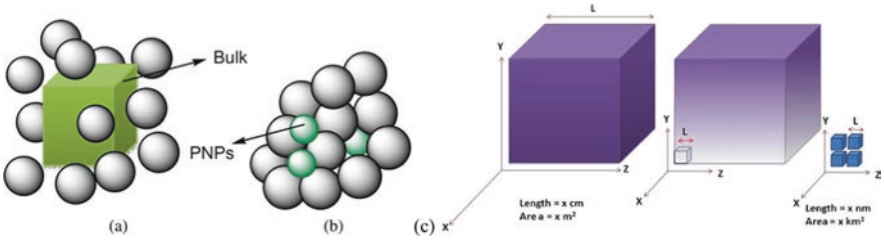

Fig. 1.1 Interaction with the surrounding (**a**) bulk polymer and (**b**) PNPs. (**c**). Large surface area with reduced particle size. Adapted from reference [4] after permission

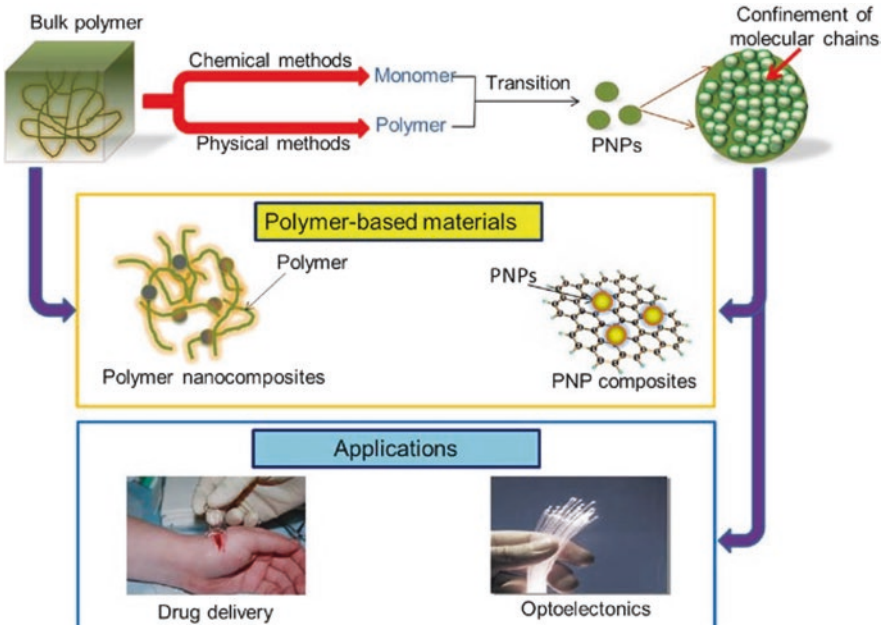

Fig. 1.2 From PNP's preparation to PNP's application. (Adapted from [4]) after permission)

techniques can be categorized as microemulsion, interfacial, conventional emulsions, mini emulsion, controlled radical, and surfactant-free emulsions. If a polymer is used as precursor, the nanoparticles' preparation techniques can be as diverse as freeze drying, solvent evaporation, salting out, spreading evaporation, nano-precipitation, dialysis, freeze extracting, fast evaporation, spray drying, etc. The diverse application of PNPs has been depicted in Fig. 1.2.

Several preparation techniques have been reported for nanoparticles manufacturing. This chapter is aimed at providing a summary of the two general techniques of nanoparticles' preparation, namely physical and chemical preparation techniques, and their characterization methods. These methods can be categorized into

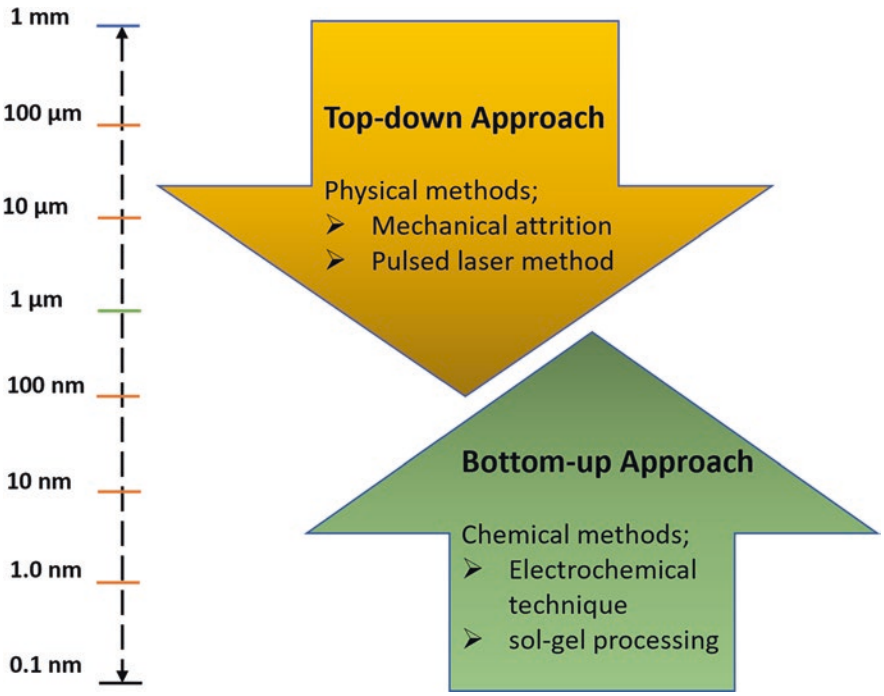

Fig. 1.3 Schematic representation illustrating the bottom-up and top-down approaches for nanoparticles preparation

bottom-up (chemical) and top-down (physical) techniques as shown in Fig. 1.3 [9]. The topics covered in this chapter include (1) the main bottom-up synthesis and top-down methods and its characterization; (2) importance of controlling nanoparticle size and shape; and (3) health and risk issue facing nanoparticles scaling up and applications at industrial level. The chapter also presents various factors and experimental conditions affecting the synthesis of nanomaterials in general.

1.2 Chemical Preparation Techniques

This preparation technique, also known as bottom-up, involves molecular components as starting materials linked with chemical reactions, nucleation, and growth processes to promote the formation of nanoparticles [10–14]. Six main techniques fall under the chemical preparation techniques category, namely: (1) chemical coprecipitation, (2) electrochemical, (3) sonochemical, (4) sol-gel processing, (5) chemical vapor deposition (CVD) and chemical vapor condensation (CVC), and (6) microemulsions.

Typically, in most of the aforementioned methods, a stabilizing agent is required during the synthesis to prevent aggregation of the resultant nanoparticles. A brief discussion on each technique with more focus on advantages and drawbacks, as well as suitability for field application is addressed.

1.2.1 Nanoparticle Synthesis by Chemical Coprecipitation

Coprecipitation is a well-established liquid phase synthesis approach that stands out for its ease of implementation at laboratory and industrial scale, rapid processing, low cost, and energy efficiency [15–17]. The precipitation/coprecipitation method requires the occurrence of supersaturation, nucleation, and growth steps, complemented by secondary steps such as aging (coarsening or Ostwald ripening) and/or agglomeration processes [17]. Figure 1.4 represents the overall steps of precipitation. Fundamentally, the coprecipitation method follows the principles of fast crystallization processes, although the former involves high initial supersaturation conditions and irreversibility or sparingly solubility of the products. The most prevalent and practical route to induce precipitation for nanoparticle synthesis is through chemical reactions, which are typically carried out by the rapid mixing of two concentrated solutions (>2000 rpm) [17, 18]. Addition/exchange, reduction, hydrolysis, and oxidation are the most distinguished of these chemical routes [19, 20]. Additionally, changes in temperature and fractionation of the solvent (through evaporation or crystallization) could also be used as approaches to induce supersaturation [17]. Such thermodynamic conditions promote fast nucleation and, thus, the successive growth of these resulting nuclei to form large numbers of visible crystallites. In parallel, these crystallites can either stabilize or coagulate/agglomerate in the solution [17, 19, 21]. In this final step, the coagulated nanoclusters can continue to grow until promoting sedimentation.

Although precipitation is a straightforward experimental technique feasible at moderate temperatures (<100 °C [16]), its thermodynamic and kinetic understanding is quite complex, especially in systems that involve tertiary and quaternary products given that multiple species precipitate simultaneously (hence, the term coprecipitation) [17, 19].

As shown in Fig. 1.4, nucleation is stated as the initial stage in coprecipitation. In general, this thermodynamic step involves the formation of a solid phase, hence requires overcoming an energy barrier for producing an interface between the bulk solution and the newly developed nuclei [20]. This barrier is determined by the total Gibbs free energy of the system (ΔG) and is driven by the supersaturation, temperature, and surface free energy conditions [20]. According to the fundamental theory, the nucleation ways that arise simultaneously in synthesis processes are classified into heterogeneous, homogeneous, and secondary nucleation. Heterogeneous nucleation is an inherent process that implies the presence of previous stable nucleating sites in the bulk solution [15]. According to Nielsen [21], the presence of solid impurities is a natural phenomenon, even in high-quality solvents, an average of 100

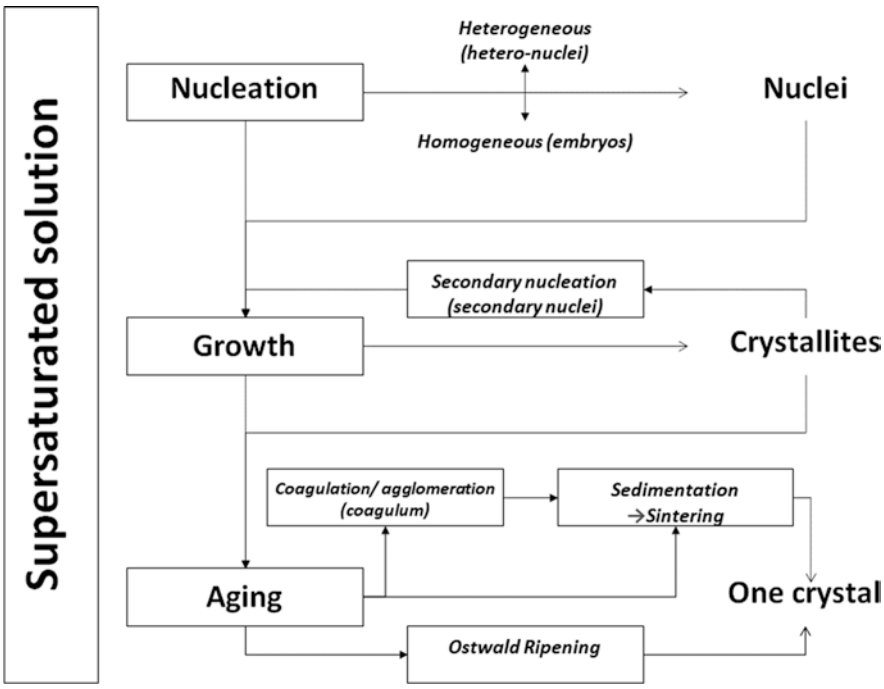

Fig. 1.4 Coprecipitation steps for nanoparticle synthesis. Idea adapted from reference [21] after some modifications

particles per mm^3 are present. These solid particles act as heteronuclei or catalysts for the initiation of precipitated crystals by the adsorption of elemental units that form a layer on the face of the crystal until it reaches sizes above the critical value, and thus, it can grow in the solution. The secondary nucleation is at some point analogous, since it refers to an intermediate state in the growth process from which the smallest crystallites serve as the "catalysts" for (secondary) nucleation. Meanwhile, in homogenous nucleation, there is a significant number of subcritical associates of crystal-like structure (embryos) in equilibrium with the bulk solution that spontaneously reach the critical size because of thermal fluctuations; these phenomena increase the probability of association above redissolution [19]. Therefore, this way of nucleation requires higher energetic barrier.

After the nuclei have been formed, they grow by the continued addition of new layers of elemental/molecular units (molecules, atoms, or ions) onto the surface of the nanocrystal. The transport phenomena involved are diffusion through the bulk solution (sometimes diffusion and convection combined) and one or more processes in the crystal solution interface (surface reactions) [19–21]. Therefore, the process can be either diffusion-limited or reaction limited, which depends on the precursor concentration; the limiting phenomenon is fundamental for the shape and size control of the nanoparticles. For instance, during the synthesis of monodisperse nanoparticles, diffusion-limited growth is the desirable process, although the final

shape of the nanoparticles will be closely linked to the surface reactions [19, 20]. Literature also recommends that for further increase monodispersity, capping ligands (surfactants or polymers) should be added to the system to promote steric repulsion between particles, as well as the induction of electrostatic repulsion by chemisorbed charged species (usually by changing the pH) [19]. Complementary, the secondary processes are also relevant in coprecipitation due to their fundamental contribution to thermodynamic stability. They involve minimization of the total surface free energy by reducing the interfacial area of the precipitates through processes known as aging. According to Nielsen [7], they include recrystallization of the primary particles to more compact shapes; the transformation of a crystal from a metastable modification into a stable modification by dissolution and reprecipitation; aggregation of primary particles followed by sintering (intergrowth); and Ostwald ripening, i.e., growth of the larger particles at the expense of the smaller ones.

Based on the above, this technique, from the experimental point of view, poses important theoretical challenges. Control of morphology, size, and dispersibility of the nanoparticles are linked to the interplay of nucleation and aggregation processes. Some authors have grouped the most relevant experimental parameters that play fundamental roles in controlling the thermodynamic and kinetics of these steps [15, 19, 20, 22], besides the concentration of precursors and temperature; pH and ionic strength, nature of the solvent, heteronuclei/seeds and templates, and capping ligands are recommended to be included and/or modified during the synthesis. To illustrate, the solubility product constant, Ksp, which is a very useful parameter for calculating the solubility of sparingly soluble compounds, tends to be very low in hydroxides, carbonates, phosphates, oxalates, and chalcogenides, which make them suitable precipitants [18, 19, 23]. Furthermore, remarkable experimental works, such as the presented by Jia et al. [24], showed the effect of pH on the growth rate of α-Fe_2O_3. At pH ≥ 6, 2D snowflake-like α-Fe_2O_3 dendrites were formed; while at pH ≤ 5, 3D houseleek-like α-Fe_2O_3 NPs were generated. Several other reports have focused on the capping ligands, such as polymers (which are the most popular ligands) like polyvinylpyrrolidone (povidone, PVP) [25–27], polyacrylic acid (PAA) [28], polyetherimide (PEI) [29], polyvinyl alcohol (PVA) [30, 31], and poly(ethylene glycol) (PEG) [32], and surfactants such as cetyltrimethylammonium bromide (CTAB) [26, 33, 34] and sodium dodecyl sulfate (SDS) [35], among others.

1.2.2 Nanoparticle Synthesis by Electrochemical Methods

Electrochemical deposition or electrodeposition methods have been categorized as a potential alternative, environmentally friendly/low emission (since electrons are used as a reagent, the use of hazardous reagents can be avoided [36]), easily controlled (by switching on/off the power supply [36]), and economical competitive technique for the synthesis of a wide variety of nanostructured materials, including semiconductors, superconductors, electrically conductive polymers, and biomaterials, for different kind of industrial applications such as catalysis, sensing and

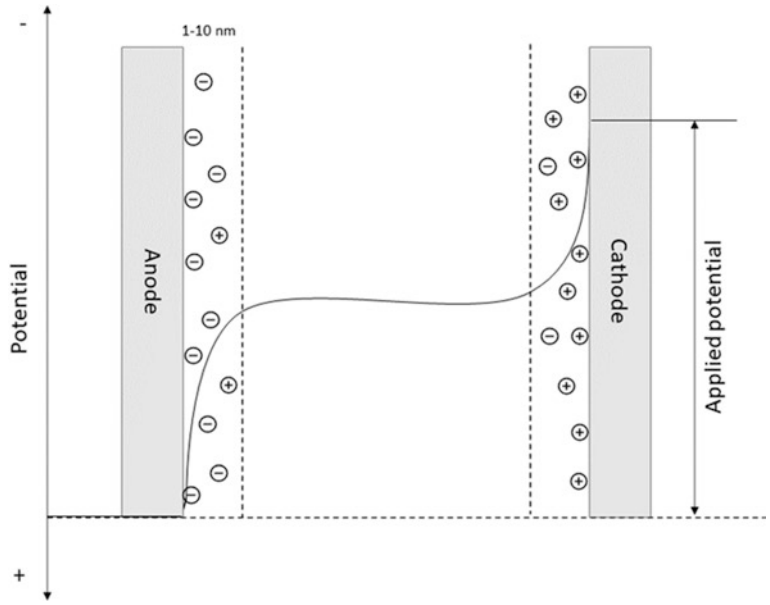

Fig. 1.5 Electrical double-layer model [36]

biosensing, medicine, optics, environmental remediation, nanorobotics, and microelectronics, among others [37–40]. In general, electrodeposition consists of the formation of solid or condensed matter deposits on conducting surfaces through electrochemical reactions that are driven by an external source of current or voltage [37, 38, 41]. A basic explanation of electrodeposition arises by the fundamental understanding of the simple two-electrode electrolytic electrochemical cell, as shown in Fig. 1.5. When the electrodes submerged in an electrolyte solution (usually aqueous-based formed from either simple salts or complexes) are polarized, it implies the appearance of a charge imbalance across the electrode–electrolyte interface that is neutralized by the migration of the nearest charged species (electrons or ions [42]) in the solution to the electrode surface within a few hundredths of a second. The interaction between the adsorbed species and the electrode surface promotes the appearance and growth of an electrical double layer (Fig. 1.5). The induced potential gradient is no longer represented by the gradient observed in the bulk solution (which is in the order of 1 or more volts), it is gathered in the thickness of the double layer, which implies an extremely steep gradient (~106 V/cm) and, thus, a high-intensity electrical field [36] (see the potential curve in Fig. 1.5). Therefore, the electromotive force supplied by an external source in this method represents the driving force, as mentioned before. In this regard, increases in the polarization intensify the electron transfer reaction at the electrodes and the consequent phenomena of charge imbalance/neutralization (a continued Faradaic current is observed) [36].

On the other hand, as the potential drop across the working electrode–electrolyte interface must be controlled, it is practical to consider the conventional three-electrode system in which the functions of the counter electrode are divided between a reference electrode (with negligible polarization, being the most popular, the standard hydrogen electrode (SHE), saturated calomel electrode, or mercury chloride (SCE), and silver/silver chloride (Ag/AgCl) [43]) and an auxiliary electrode (that carries the current, such as carbon or graphite, platinum, gold, lead, and titanium [36, 43].). Thus, the potential is controlled between the reference and working electrodes, while the current passes between the auxiliary and working electrodes [36]. The auxiliary electrode usually has a bigger surface area in comparison with the working electrode, to guarantee that the half-reaction occurring at its surface occurs faster, avoiding limitations of the process at the working electrode.

Against this background, the electrodeposition can be controlled by either an applied potential or current, being classified as potentiostatic and galvanostatic, respectively [36–38]. The control of the potential/current input allows that the reacting species overcome an energy barrier (activation energy) to make thermodynamically feasible the reduction/oxidation couple. In that sense, the spotlights are the energy of the electrons of the working electrode and those of the electroactive species. In the former, the Fermi-level (E_F), which refers to the energy of the highest occupied orbitals (HOMO) in metals, can be controlled by the external potential (when a negative potential is applied, E_F moves to higher energy; when a positive potential is applied, E_F moves to lower energy [36]) until it reaches a lower level than the HOMO of the active molecules in solution, allowing the electron-transfer processes to the electrode. The critical potential at which this electron-transfer process occurs is known as the standard/equilibrium potential (E_0) of the reduction/oxidation couple. Therefore, the difference between the applied positive potential (E_i) and E_0 is known as overpotential (OPD) [36].

Once the current density is increased in the cell or the OPD condition is reached, the adsorption of the active species on the surface of the substrate is promoted until the final development of nanostructures. The overall process is analogous to that explained in coprecipitation, i.e., it comprises the fundamental steps of nucleation and growth, which are grouped in two major processes, deposition and electrocrystallization [38]. Figure 1.6 is a schematic representation of the overall electrodeposition process. In brief, the initial step is the mass transportation (immigration, diffusion, and convection) of solvated ions (in aqueous electrolytes, hydrated ions) from the bulk toward the cathode. At the border of the electrical double-layer OHP occurs the charge-transfer reaction, i.e., the ions partially desolvate/dehydrate until their attachment onto the substrate cathode surface. Finally, the ad-ions and the consequent ad-atoms are formed. Surface diffusional phenomena appear until the completed lattice incorporation of the ad-atoms that results in nucleation of stable atomic clusters and, eventually, their growth [38]. In parallel, depending on the magnitude of the difference between the applied and standard potentials (E_i and E_o), the kinetics of the process can be activation (charge transfer) controlled, mixed controlled, or diffusion controlled. Initially, electron transfer rates are dramatically increased, and the potential–current density (voltammetric curve) grows

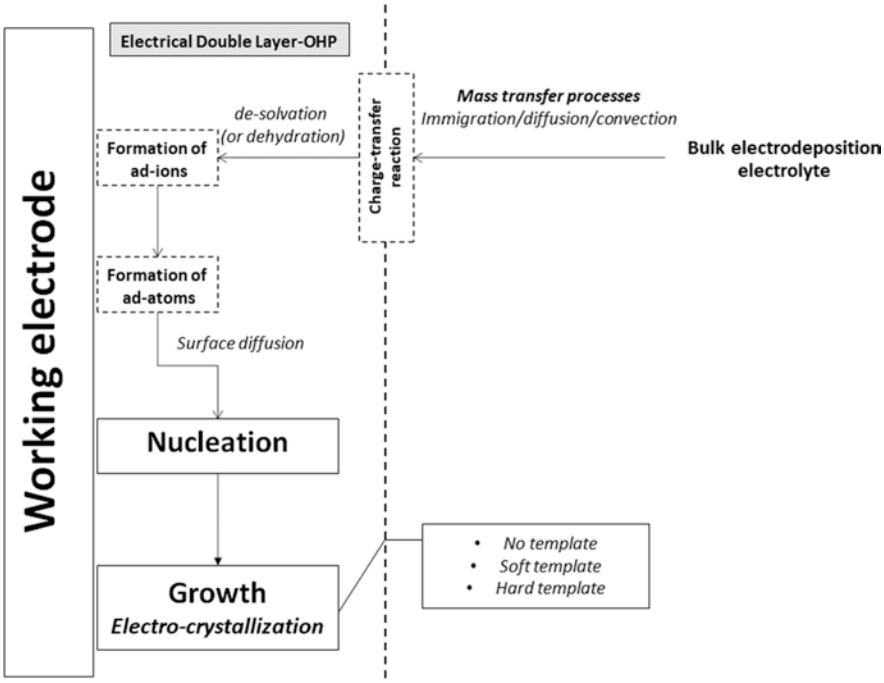

Fig. 1.6 Electrodeposition steps for nanoparticle synthesis [38]

exponentially (Butler–Volmer model); then, the voltammetric curve reaches the mixed region in which the diffusion and activation rates both limit the electrolysis current. Finally, the currents are purely diffusion limited, and peak or plateau currents are observed in quiet and stirred solutions, respectively [36, 38].

Analogously, several experimental parameters can be modified/applied for controlling the thermodynamic and kinetics of the process, besides the input potential/current; the following factors should be considered: nature of the substrate (crystal structure, specific free surface energy, and lattice orientation, among other); type of electrolyte (aqueous or ionic); pH; the use of templates; agitation; stabilizing agents; area of the electrodes; and time of exposition; among others. To illustrate, the synthesis of shape-controlled nanostructures (mainly nanowires and nanorods) is significantly improved when soft and hard templates are used. Among the most popular soft templates are surfactants and polymers [44–48]; as well as microemulsions [37, 49, 50]. Likewise, the most common and available hard templates are anodized alumina (AAM), as wells as inorganic and polymeric membranes [40, 51, 52]. Furthermore, potentiodynamic or pulsed electrodeposition is also used, mainly to improve the control in the growth step, allowing the system to experience periods in which electrodeposition occurs and others in which the nearest electroactive species recover [37].

1.2.3 Nanoparticle Synthesis by Sonochemical Methods

In the direction of reaching important technological developments at the nanoscale that, at the same time, are in synchrony with ecofriendly chemical synthesis processes, the use of alternative energy sources, such as electromagnetic and mechanical waves, has been widely contemplated for the activation of chemical reactions in recent years, avoiding excessive consumption of hazardous reagents and generation of waste [53]. Among these techniques, sonochemistry is one of the most relevant due to its superiority at certain fundamental aspects in comparison to all other nanoparticle synthesis techniques. Gedanken [54] highlighted the advantages of sonochemistry in the following areas: preparation of amorphous products, insertion of nanomaterials into mesoporous matrices, deposition of nanoparticles on ceramic and polymeric surfaces, and formation of proteinaceous micro- and nanospheres. Other positive aspects of sonochemistry are the short time of reaction, high purity of products, and narrow size distribution with large surface area of the nanoparticles [53, 55].

The fundamentals of sonochemistry arise from the application of powerful ultrasound radiation (20 kHz–15 MHz [54, 56–58]) to stimulate chemical reactions in a liquid solution. These chemical effects proceed from nonlinear acoustic phenomena, primarily acoustic cavitation, i.e., formation, growth, and implosive collapse of bubbles [57, 58]. As a result of the collapsing phenomena that occur in less than a nanosecond, a huge amount of energy is released into the liquid; therefore, local heating, high pressures, and high-speed jets (with speeds >100 m/s [55, 56]) are produced. Such localized hot spots that reach very high temperature (5000–25,000 K [58]), pressure (>100 MPa [54, 57, 58]), and high cooling rates (1011 K/s [54, 57]) are responsible for the appearance of turbulence in the flow of the liquid and an improved mass transfer, causing the thermomechanical conditions capable of cleaving the intermolecular bonds of the precursors [53]. Likewise, the mechanisms of product generation depend on the quality of the reagents (mainly volatility) and the conditions of the reaction, which classifies the sonochemistry as primary (gas phase chemistry occurring inside collapsing bubbles) and secondary (solution phase chemistry occurring outside the bubbles) [55, 57, 59]. In the former case, a volatile precursor produces free metal atoms generated by bond dissociation (e.g., metal–carbon bonds in organometallic compounds [60]) due to the intense thermodynamic conditions reached during bubble collapse; these newly formed atoms nucleate to form nanostructured materials [57]. Additionally, because of high cooling rates, the organization and crystallization of the products are inhibited and, thus, amorphous nanoparticles are developed [54, 59]. In the case of nonvolatile precursors, the sonochemical reactions occur in the solvent phase. After the bubble collapse, the surrounding liquid also experiences transient heating within a ring region of 200 nm, reaching temperatures above 1900 °C [54, 56, 59]. The resultant high-energy species (e.g., radicals) diffuse into the liquid phase and react, leading to the formation of nanoparticles [57]. In this case, the products are sometimes amorphous nanomaterials or, in other cases, nanocrystalline. The final structural organization will depend on the temperature of the ring region [54].

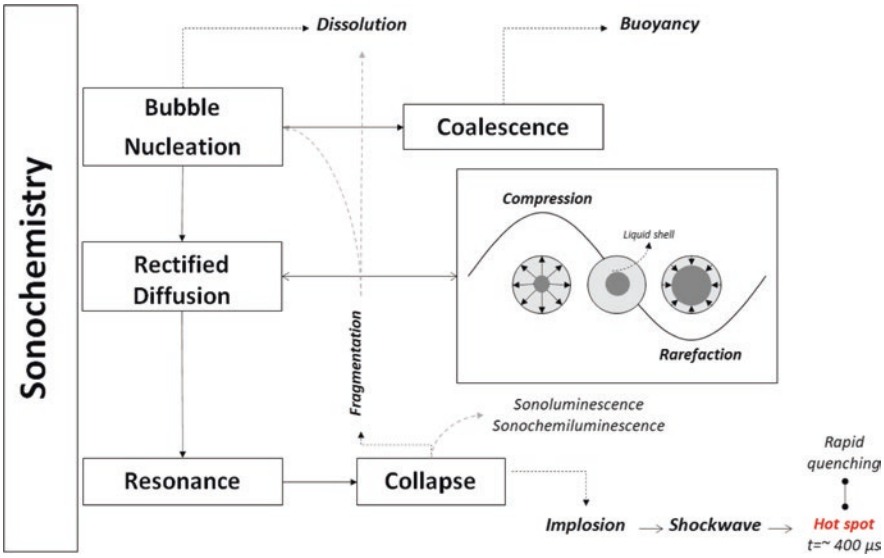

Fig. 1.7 Sonochemistry steps for nanoparticle synthesis. Part of figure is adapted from reference [61] with permission

From a fundamental point of view, acoustic cavitation stimulates several complex processes in the generated bubbles; thus, a theoretical understanding of these phenomena can lead to enhanced control of the method. Figure 1.7 summarizes schematically the distinct stages that the bubbles can go through. In general, the initiation step corresponds to the bubble nucleation that arises because of preexisting impurities in the solvent phase (small gas bubbles protected by a skin of organic impurities, bubbles trapped in motes or crevices in solid surfaces [57, 61]). Sequentially, when the applied acoustic pressure is above a certain threshold, the growth step begins. The pathways of this step are coalescence and, mainly, rectified diffusion [61]; this latter process is fundamental for describing the interlink between growing and mass diffusion across the air–liquid interface: as the acoustic cycle alternates between the compression and rarefaction (see Fig. 1.4), gas is forced to diffuse in and out of the bubbles [56]. The changing area and liquid shell are considered the two main contributors to rectified diffusion; when the bubbles shrink, the surrounding gas will be concentrated near the interface (Henry's Law), and the liquid shell will become thicker, reducing the driving force for the diffusion of gas out of the bubble. By contrast, the expansion of the bubbles will reduce the liquid shell; thus, the driving force for the inlet diffusion will increase [56, 61]. Therefore, the area and shell effects synergistically contribute to a net mass diffusion into the bubble over time or growth ($t < 100$ µs, bubble ratio < 50 µm) that finishes with an adiabatic implosive collapse, and the subsequent formation of nanostructures. According to Gedanken [54], these nanostructured products are the consequence of the fast kinetics that inhibit the nuclei growth. Because of the described physicochemical effects, several experimental parameters can be modified/controlled

during the overall process to improve the quality of the nanoproducts, including acoustic power, frequency, hydrostatic pressure, properties of the solvents and reagents (mainly boiling temperature and ratio), the inclusion of templates and their nature, process temperature, and sonication time, among others [53]. To illustrate, in the synthesis of nanostructured noble metals, the use of nonvolatile precursors dissolved in volatile solvents such as water is a common practice, considering that sonolysis of the water vapor produces chemical intermediates (specifically H radicals and $e(aq)^-$) that act as strong reducers species in redox reactions. Thus, chemical-reducing agents can be avoided, although alcohols (e.g., 2-propanol, ethanol [62]) and surfactants (e.g., SDBS, SDS, PVP, PEG, CTAB [62]) are also recommended to generate secondary radicals, which can dramatically promote the reduction rate [67, 71]. On the other hand, the use of volatile organometallic precursors (e.g., $Fe(CO)_5$, $Ni(CO)_4$, $Co(CO)_3NO$, $Mo(CO)_6$, $W(CO)_6$ [57, 60]) dissolved in nonvolatile solvents (e.g., silicone oil, polyethylene glycol, ethylene glycol [57, 62, 63]) has the particular advantage of achieving more secure conditions, due to the capacity of the solvents of absorbing the energy (via rotational and vibrational molecular modes, ionization, and competing bond dissociation [57]).

1.2.4 Nanoparticle Synthesis by Sol-Gel Processing

Sol-gel processing is a well-documented and cost-competitive wet chemical method that stands out for its low-temperature reaction, good composition control (high purity products and stoichiometry level), production of shaped and homogeneous nanomaterials (e.g., bulk monoliths, fibers, powders, sheets, coatings, films), large-scale industrial production, and broad applicability, mainly in material science and ceramic engineering [64–67]. From a general perspective, the sol-gel method involves the preparation and subsequent transformation of a sol (which refers to a dispersion of colloidal particles in a liquid medium with diameters between 1 and 100 nm [68]) into a gel-like intermediate (an oxide or alcohol-bridged network) because of the simultaneous hydrolysis and polycondensation of a precursor (either inorganic metal salt or metal–organic) that promote dramatic increases in the viscosity of the dispersion (syneresis) until the final transformation into a functional solid nanomaterial; complementary processes such as thermal treatment are essential for the remotion of the solvent from the interconnected gel network (drying) and the calcination of this gel (dehydration) [19, 68]. Due to the resultant drying stress, monolithic gel bodies are often destroyed, and powders are obtained [69]. Figure 1.8 represents the overall steps of sol-gel processing.

In principle, the precursors, either alkoxide or solvated metals, are dispersed into an aqueous solution to induce hydrolysis and simultaneous (competitive/complementary) condensation reactions. However, it is important to highlight that the reaction routes differ substantially as a function of the precursors; therefore, a specific description of the processing in virtue of their nature is fundamental and discussed below.

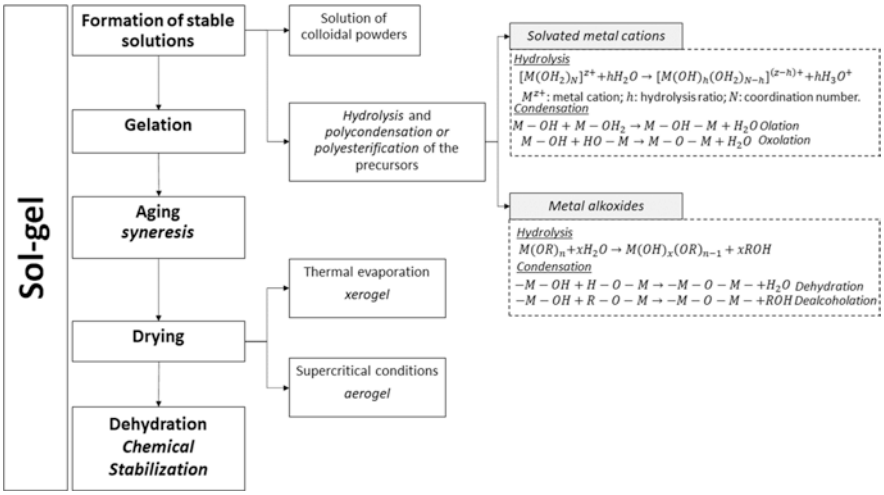

Fig. 1.8 Sol gel method's steps for nanoparticle synthesis [19, 65, 70, 73]

Solvated Metal Cations In an aqueous medium, metal cations (M^{z+}) are solvated by dipolar water molecules, giving rise to aquo ions ($[M(OH_2)_N]^{z+}$). This electron transfer process occurs from the bonding orbitals of coordinated water molecules toward empty orbitals of the metal cation, $M^{z+} + NH_2O \rightarrow [M(OH_2)_N]^{z+}$, where N is the coordination number of the cation [70]. Likewise, the transfer process also results in weakening the O–H interactions of bounded water that becomes more acidic. The resultant hydrolysis (deprotonation) reaction is as follows:

$[M(OH_2)_N]^{z+} + hH_2O \rightarrow [M(OH)_h(OH_2)_{N-h}]^{(z-h)+} + hH_3O^+$, where h is the hydrolysis ratio.

In dilute solutions, the reaction can produce monomeric species ranging from aquo cations ($[M(OH_2)_N]^{z+}$), hydroxy species ($[M(OH)_z]^0$), and oxo anions ($[MO_m]^{(2m-z)-}$), when all the protons have been removed from the coordination sphere of the metal cation [70]. These equilibria depend mainly on the pH, and, in a lesser extent, temperature and concentration. The theoretically analysis of this reaction is generally based on the electronegativity equalization principle or Partial Charge Model (PCM) [19, 70]. Thus, the proton exchange between the precursor ($[M(OH)_h(OH_2)_{N-h}]^{(z-h)+}$) of mean electronegativity χ_h and the aqueous solution of mean electronegativity χ_w proceeds until they reach equal values ($\chi_h = \chi_w$) Parallelly, χ_h depends on the metal cation (M^{z+}) and the hydrolysis ratio (h) at a given pH. The charge-pH diagram (refer to [19, 69, 70]) is a useful guide because it is possible to predict the parameters that favor condensation reactions, as they are only possible when the system is brought from the aquo (low-valent cations) or oxo (high-valent cations) domains to the hydroxy domain, i.e., OH groups must be present in the precursor [19, 70]. Based on the above, the condensation reactions are promoted mainly by pH variations. According to Henry et al. [70], condensation is initiated by adding a base to low-valent metal ions (e.g., Cu^{2+}, Al^{3+}, Zr^{4+}) or an acid to

high-valent metal ions (e.g., W^{6+}, V^{5+}). Redox reactions are also initiators [70]. Furthermore, the condensation of hydrolyzed metal ions follows two main mechanisms: *olation* when $N = z$, i.e., nucleophilic attack (substitution) of a negatively charged OH group ($[\delta(OH^-)]$) to a positively charged metal cation ($[\delta(OH_2)]$), that produces "*ol*" bridges ($M - OH - M$, see the reactions in Fig. 1.8); and *oxolation* when $N - z > 0$, i.e., nucleophilic addition of OH groups onto metal ions, followed by the formation of an "*oxo*" bridge ($M - O - M$, see the reactions in Fig. 1.5) [70].

Metal Alkoxides In this case, hydrolysis is induced because of the introduction of water or water alcohol mixture into the system. The reaction is initiated through nucleophilic attack (substitution) of H_2O molecule to a positively charged metal atom, generating the insertion of hydroxide groups into the coordination sphere of the metal atom ($[M(OH)_x(OR)_{n-1}]$). Analogously, the rate of substitution depends on the coordination instauration of the metal atom ($N - z$); higher values of ($N - z$) require lower activation energy of the nucleophilic attack [71]. Equally important, the alkoxide/water ratio $\left(\frac{M(OR)_n}{H_2O} = x\right)$ determines the number of substituted alkoxy groups. Thus, variation and control of x has profound consequences in the morphology and structure of the resulting gel [19]. Simultaneously, after the insertion of hydroxide groups, condensation occurs in the following ways [65]: *dehydration* or *dealcoholation* (see the reactions in Fig. 1.8).

The second step of the overall process is gelation, which appears because of the hydrolysis and polycondensation reactions by the random collision of polymeric species in solution, leading to crosslinking bridges (oxide or alcohol) that eventually become a three-dimensional network [65]. As already mentioned, the main characteristic of this step is the sharp increase of the viscosity. Casting is also common to stimulate the formation of specific shapes, which can be easily recovered at the end of the process, by just ejecting the product out of the mold. Complementary, this developed network is further subjected to polycondensation for a period of time (hours to days), leading to decreases in the porosity of the interconnected system in a process known as aging (syneresis); thus, the aged gel must reach high strength to avoid any cracking during drying. In this last process, the solvent is removed from the crosslinked network by either thermal evaporation (xerogel) or supercritical solvent extraction (aerogel) [68, 72]. In the former case, large capillary stresses appear (in small pores <20 nm [68]) due to increases in the coordination numbers of the particles that result in the formation of additional linkages and the consequential collapse of the network; therefore, considerable shrinkage and reduction in the surface area and pore volume are the main consequences observed in thermal evaporation [19, 72]. A practical solution is the use of surfactants that decrease the surface energy of the solvent or supercritical extraction (capillary stresses disappear due to the lack of solvent–vapor interfaces [19]). The most common method is removing the pore fluid above its critical point, although an alternative route is replacing the solvent with CO2 and then removing it above its critical point [72]. As discussed, aerogels are low-density materials with high surface area (200–1000 m^2/g [73]) and controlled pore size distribution. Finally, the gel is dehydrated to desorb the

hydroxyls, avoiding rehydration processes. To get this stabilized gel, the sample is calcinated at a temperature in the range of 500–800 °C [19, 68].

Analogously to the other methods, there are critical experimental parameters that can be controlled to increase the efficiency of the process. Particularly, in this method, these aspects are well differentiated: pH of the solution (acid- or base-catalyzed hydrolysis of metal alkoxides [74–77]), the molar ratio of water to alkoxide [78], and temperature [79].

1.2.5 Nanoparticle Synthesis by Chemical Vapor Deposition (CVD) and Chemical Vapor Condensation (CVC)

Chemical vapor deposition (CVD) and chemical vapor condensation (CVC) are distinctive material processing techniques that are characterized for their capability of producing highly dense and pure materials, as wells as nanoparticles with narrow size and homogeneous films with good reproducibility and adhesion as they can coat complex-shaped substrates uniformly [80]. Their fields of applicability include electronics, optoelectronics, surface modification, and biomedicine [81]. In these methods, vapor phase precursors are convectively transported into a high-temperature reaction chamber to promote thermal dissociation and/or chemical reactions on or near the vicinity of a substrate to form stable solid products [80–82]. In this regard, when the nucleation step is favored in the vapor phase and ultrafine clusters or nanoparticles are formed, the approach is defined as vapor synthesis or CVC (thus, it requires activation energy to proceed) [83, 84]. Analogously, when the nucleation step is favored onto the surface of a heated substrate (which acts as the activation energy source), deposition and adsorption of the active gas species and reaction intermediates are stimulated, and the method is differentiated as CVD [80–82]. Regardless of these variations, which are mostly associated to the hierarchy of the experimental systems and equipment, the physicochemical principles of both methods are equivalent. According to Choy [80], the chemical reactions that proceed can be classified as: thermal decomposition (pyrolysis), oxidation, reduction, hydrolysis, nitridation, deprotonation, photolysis, and/or combined reactions.

On the one hand, the CVC setup mainly consists of a feed system and a reaction chamber that is maintained under vacuum. The injected precursors flow through a tubular reactor where gas-phase homogeneous reactions take place within a short residence time (<0.1 s), driving to the fundamental steps of nucleation and growth. At the outlet, the two-phase stream (gas and nanostructures) is subjected to a rapid expansion that serves to mitigate undesired agglomeration processes. Finally, the nanoparticles are deposited on a rotating nitrogen-cooled substrate. Figure 1.6 represents schematically the steps of CVC [83, 84]. A relevant aspect of this technique is its linkage with some Physical Vapor Deposition (PVD) methods; according to Chang et al. [83], this technique takes the advantages of the significant energy provided by laser beam, combustion flame, and plasma in the thermal decomposition of

organometallic precursors, as well as the Inert Gas Condensation (IGC) synthesis methods, that lead to the evaporation and condensation of volatile species in a reduced pressure environment. Therefore, CVC is useful in processing almost all kind of precursors. The main experimental aspects that must be rigorously controlled were summarized by Tavakoli et al. [84] and involved low concentration of precursor in the carrier gas to minimize the collision frequency of the formed nanoclusters, expansion of the ejecting gas stream, and rapid quenching of the gas-phase nucleated clusters.

On the other hand, as CVD is more thermodynamically feasible (e.g., it does not require high vacuum working environments), scientific literature has extensively focused on this method [85–87]. The overall processes involved are summarized in Fig. 1.9. First, the reactant gases are transported into the chamber to induce, either gas-phase homogenous reactions that generate byproducts and intermediates, or the eventual diffusion of these gaseous precursors to the boundary layer of the substrate. Both the precursors and intermediates adsorb onto the substrate surface; and phenomena such as heterogeneous chemical reactions and surface diffusion are promoted, which contribute to the induction of nucleation and the subsequent growth steps. Alongside, some byproducts and unreacted species desorb from the surface and are directed to the effluent gas treatment system [80–82]. According to Choy [80], the most relevant experimental parameters to control in the process are deposition temperature, pressure, input gas ratio, and flow rate, the temperature being the dominant parameter. This deposition rate–temperature correlation generally fitted an Arrhenius model, i.e., high surface temperatures increase thermally activated reactions, which induce higher deposition rates and thus enhanced surface diffusion processes of the atomic species and growth rates. This region is defined as the

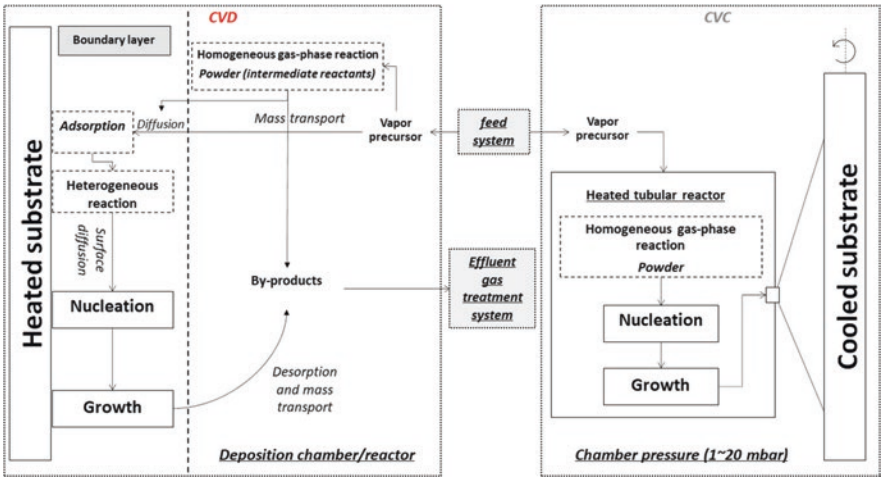

Fig. 1.9 Chemical Vapor Deposition (CVD) and Chemical Vapor Condensation (CVC) steps for nanoparticle synthesis [80, 81, 83]

chemical kinetics limited zone [80, 82]. The main characteristic is the homogeneity of the formed films that is reached by controlling the temperature over the substrate surface. Nevertheless, if the temperature further increases, the growth rate becomes almost independent, and the process is controlled by the mass transport of the precursors through the boundary layer, and this region is known as mass transport limited [80, 82]. Besides the operation temperature, pressure is also considered a relevant parameter in this method. Although CVD processes are viable at atmospheric pressures, some subdivisions have been stipulated regarding the working pressure ranges as atmospheric-pressure CVD (APCVD) or low-pressure CVD (LPCVD, ~0.1 10 torr). The particularity of the LPCVD condition is that the process is mass transport limited [80]. Furthermore, there have been developed some advanced technological variants of CVD systems, mainly focused on the type of energy sources, such as plasma enhanced CVD [88–90], photo-assisted CVD [91], and laser-assisted CVD [92, 93].

1.2.6 Nanoparticle Synthesis by Microemulsions

Microemulsion-based (ME) synthesis is a low-temperature powerful method for the preparation of high-quality colloidal nanoparticles, characterized by comprising low-cost instrumentation and good control of stoichiometry, size, homogeneity, and morphology of the products due to its ability to mix reactants efficiently at the molecular level [94, 95]. It is widely used in sensing, catalysis, and biomedicine for drug-delivery systems involving mainly polymeric nanoparticles [96]. Essentially, this approach embraces surfactant-stabilized droplets phase that acts as the "nanoreactors" (diameters varying between 2 and 50 nm [96, 97]), leading to flexibility, accessibility, and adaptability of the precursors and reactions. Therefore, nanoparticles can be synthesized in water-in-oil (w/o), oil-in-water (o/w), and/or bicontinuous microemulsions, i.e., polar/hydrophilic- (w/o-ME) or nonpolar/hydrophobic- (o/w-ME [97]) droplets/nanoreactors. The complete microemulsions schemes in virtue of the dispersed phase (w/o-ME or o/w-ME) are schematically represented in Fig. 1.10. In general, the synthesis of nanoparticles in o/w-MEs has the advantages of low environmental impact (since the continuous phase is water) and stable phase behavior (interactions between the organometallic precursors and surfactants are weaker) [97]; while the w/o-MEs have been categorized as the most important and widely implemented technique because of their easy formulation and affinity with the abundant water-soluble metallic salt precursors [94].

According to Sanchez-Dominguez et al. [97], two strategies have been identified for the synthesis of inorganic nanoparticles in o/w-MEs: oil–water interface controlled microemulsions, in which the precursor is an ionic salt dissolved in the water continuous phase; and single microemulsion, in which the precursor is an organometallic salt dissolved in the oil droplets of the microemulsion (see the detailed schemes in Fig. 1.10). In the former, the precipitant agent and the metallic precursor (A and B) dissolved in the continuous phase are transferred and adsorbed on the

oil–water interface. Initially, the diffusion of the metallic cations is driven by the electrostatic attraction with the anionic part of the surfactant to increase the stability of the system. After a while, the precipitant agent is added and the balance is destroyed, which leads to the occurrence of the reaction at the interface and the subsequent fundamental nucleation and growth steps that proceed until the final formed nanostructures [97, 98]. The two pathways of these steps are intramicellar and/or intermicellar nucleation and growth. For the first one, the reactions are located close to a droplet interface, and electrically neutral nanoclusters are formed. Eventually, the surfactant encapsulates them, as they are unstable at the interface, and promotes phase-transfer processes. On the other hand, reactions can also occur at the shared interfaces of two collapsing micelles, and the process is termed as

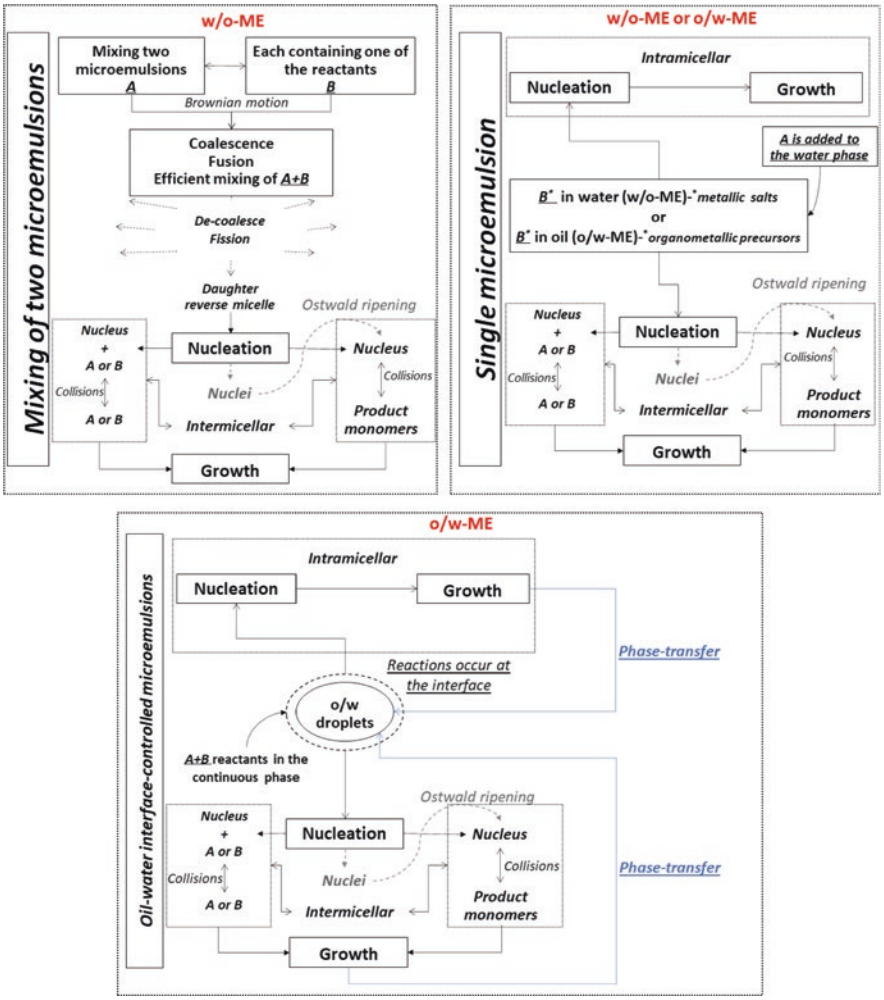

Fig. 1.10 W/O and O/W microemulsion schemes for nanoparticle synthesis [94, 97]

intermicellar [97, 98]. The consequent steps are analogous to the explained above, as they involve phase transfer of the hydrophobic nanoparticles. In both cases, the hydrophobic nanoparticles can be precipitated, or the system can be subjected to hydrothermal treatment for increasing crystallinity [97]. Furthermore, the single microemulsion synthesis route is a straightforward approach, considering that the organometallic precursors are dispersed in the oil droplets of the o/w-ME; thus, the only action required is the incorporation of the precipitating agent (typically water soluble) at a delayed time to promote intramicellar and/or intermicellar nucleation and growth steps.

In a similar way, Husein and Nassar [94] identified two strategies for the synthesis of nanoparticles in w/o-MEs: mixing of two microemulsions, in which each of the mixed w/o microemulsions contains one of the reactants; and single microemulsion, in which the precursor is dissolved in the water droplets (see the detailed schemes in Fig. 1.10). In the former, intermicellar nucleation and growth is the synthesis route, because of fusion and subsequent fission processes of micelles that are driven by Brownian motions. Initially, the collisions promote coalescence, fusion, and efficient mixing of reactants. Sequentially, the chemical reactions proceed at their intrinsic rate of reaction; for instance, in fast reaction scenario, the rate is controlled by the collisions between reverse micelles (which in turn is governed by the rigidity of the surfactant layer); in contrast, for slow reactions, the rate depends on the statistical distribution of the reaction species among the reverse micelles (they are typically well described by Pseudo continuous models). The final step is decoalesce/fission into daughter reverse micelles where the reactions occur, and the following nucleation and growth steps. The possibilities of growing scenarios are represented in Fig. 1.10, e.g., a micelle carrying a nucleus collapse with another one carrying product monomers. Furthermore, the single microemulsion route follows the same principles explained above; after the incorporation of the second reactant, the process is controlled by one or more of the following mechanisms: reaction kinetics, particle aggregation, and intramicellar and/or intermicellar nucleation and growth. For instance, intramicellar routes will dominate when high reactant occupancy numbers are coupled with rigid surfactant layer, which is the desired condition to avoid particle aggregation. According to the literature [94, 99, 100], the use of surfactants with reactive counterions favors intermicellar nucleation and growth.

Similarly, there are several operation variables widely analyzed in the literature that can be controlled/modified to improve the reaction schemes of these approaches [94–98, 101–104], including dispersed phase/surfactant ratio, nature and concentration of surfactants, cosurfactants and reactive species, volume fraction and type of the dispersed and continuous phases, mixing, and temperature, among others.

1.3 Physical Preparation Techniques

Other preparation methods of nanoparticles are the top-down methods where nanoparticles are prepared directly from bulk materials via the generation of isolated atoms by using various distribution techniques that involve physical methods, such as milling or grinding, laser beam processing, repeated quenching, and photolithography [105]. Different nanoparticles preparation and characterization techniques and their effects on nanoparticles stability have been generously discussed by other researchers [106-119].

To name a few of these technologies, we can categorize these techniques as:

(i) Mechanical attrition, like attrition ball mill, planetary ball mill, vibrating ball mill, low energy tumbling mill, and high energy ball mill
(ii) Plasma
(iii) Microwave irradiation
(iv) Pulsed laser method
(v) Gamma radiation

A discussion on the first two techniques, as they are important ones, is addressed below.

1.3.1 Mechanical Attrition

Mechanical attrition, or "milling", is a process in which a device is used to apply energy to a coarse-grained structure, resulting in the reduction in particle size. Under certain conditions, mechanical attrition may result in nanoparticles which also exhibit nanostructural behavior due to the nanocrystallinity of the resulting material [120]. In the attrition process, the media is usually placed between two colliding balls, where the media is then subjected to an impact process reducing its size. During the process of attrition, the material, which usually contains large spaces compared to the particle size, undergoes three stages: The first stage is rearrangement of the particles, as particles slide past each one another with minimum fracture, followed by second stage of elastic and plastic deformation, and finally particle fracture.

There are several devices that can be used for mechanical alloying, which can be used for different applications (e.g., sample sizes, milled materials, etc.). These devices include the followings.

1.3.1.1 Shaker Mills

The sample is deposited in a vial that contains a grinding media, which are hard spheres. The shaking of the vial is accompanied by a lateral movement, both at several thousand times per minute. Due to the high speed of the hard spheres, the method is classified under the high-energy methods. These devices are usually used in laboratories, and for small amount of powder samples [120].

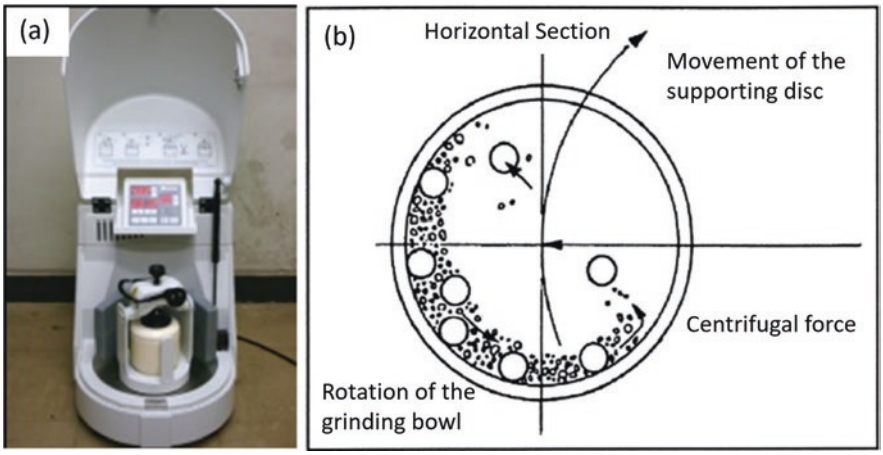

Fig. 1.11 (**a**) Planetary ball mill and (**b**) schematic showing motion of ball motion inside the grinding jar. (Adapted from [121] with permission)

1.3.1.2 Planetary Ball Mills

In this setup, shown schematically in Fig. 1.11, grinding jars or vials, which contain grinding hard spheres and the sample, are attached to a rotating disk (sun wheel). The vials rotate around their own axis and are subjected to the rotation of the sun wheel, which rotates in an opposite direction. This motion results in impact and friction forces on the hard spheres, causing a high degree of sample size reduction. These mills are also used in laboratories, but for larger sample sizes compared to shaker mills [121].

1.3.1.3 Attritor Mills

The mill consists of a drum filled with hard spheres, the powder sample, and an agitator. The milling is produced by the rotation of an agitator, which is a rotating vertical shaft with arm (impellers) attached at right angles. This rotation results in various impacts within the drum, including impacts among the hard spheres, the spheres, and the impellers and the walls, which finally lead to grinding the powder and reducing its size [120].

1.3.2 Plasma

One of the most common techniques for the preparation of supported metal/metal oxide nanoparticles as catalysts is wet process (including impregnation and precipitation), which is usually employed for economic and practical reasons. In contrast to these techniques, dry processes (including chemical/physical vapor deposition,

sputtering, and ion implantation) remain limited as catalytic nanoparticles preparation techniques. These methods specifically are applied in the emerging field of semiconductor technology. Although the science behind dry processes is important from a fundamental point of view, dry processes that enable the use of powdered catalyst nanomaterials for practical applications are not well-known.

Plasma has been used for catalyst nanomaterials preparation [122–125]. Various types of thermal and cold plasmas, including not limited to plasma jets, DC coronas, arcs, glow discharges, radio frequencies, and microwaves, have been employed for preparation of ultrafine particles including nanoparticles, supported catalysts, and/or catalyst surfaces modification. The potential advantages of using plasmas are (1) preparation of highly dispersed active species, (2) enhanced catalyst activation, selectivities, and lifetimes, (3) reduced energy requirements, and (4) shortened preparation times [124]. One of the promising techniques in this category can be named as pulsed cathodic arc plasma technique, which is a simple and innovative approach toward preparation of nanoparticles. This method enables the deposition of metal nanoparticles or nanofilms from bulk metals or other electronic conducting materials [126–142]. One of the most important applications of pulsed cathodic arc plasma technique is preparation of powdered-supported catalysts and photocatalysts. This method enables the one-step deposition of catalyst nanoparticles on various support powders, in contrary to the multistep preparation needed for conventional wet impregnation processes. A schematic and a photograph of the experimental setup for nanoparticle catalyst preparation using pulsed arc plasma deposition have been depicted in Fig. 1.12. This apparatus consists of arc discharge sources, a vacuum chamber with a turbomolecular pumping system, and a powder container with a rotating stirring mechanism. In the arc discharge source unit, an insulator tube, a columnar cathode, a trigger electrode, and a cylindrical anode are arranged coaxially. Cathode is a 10-mm-diameter and 17 -mm-long metal rod of the target material connected to a DC supply, while cylindrical anode is connected to the ground [143]. Trigger electrode in this case is connected to a pulsed power supply.

For the sake of charge and discharge, an electrolytic capacitor is connected between the cathode and the ground. An electronic breakdown between the trigger and cathode electrodes is caused by the application of a 3 kV pulse to the trigger electrode. This electronic breakdown ignites pulsed arc discharges with a period of 0.1 to 0.2 ms between the cathode and the anode.

Transmission electron microscopy (TEM) images and energy-dispersive X-ray spectroscopy (EDX) spectra of unsupported Pd–Fe nanoparticles prepared by (left) synchronous (syn) and (right) asynchronous (asyn) pulsing have been demonstrated in Fig. 1.13. As seen in this picture, each EDX spectrum was taken from a circular region containing one nanoparticle. In synchronous pulsing, the as-deposited single nanoparticles contained both Pd and Fe (Fe: 67 wt%, Pd: 33 wt%), whereas the single nanoparticles prepared via asynchronous pulsing contained only Fe (Fe: 100 wt%, Pd: 0 wt%) [143].

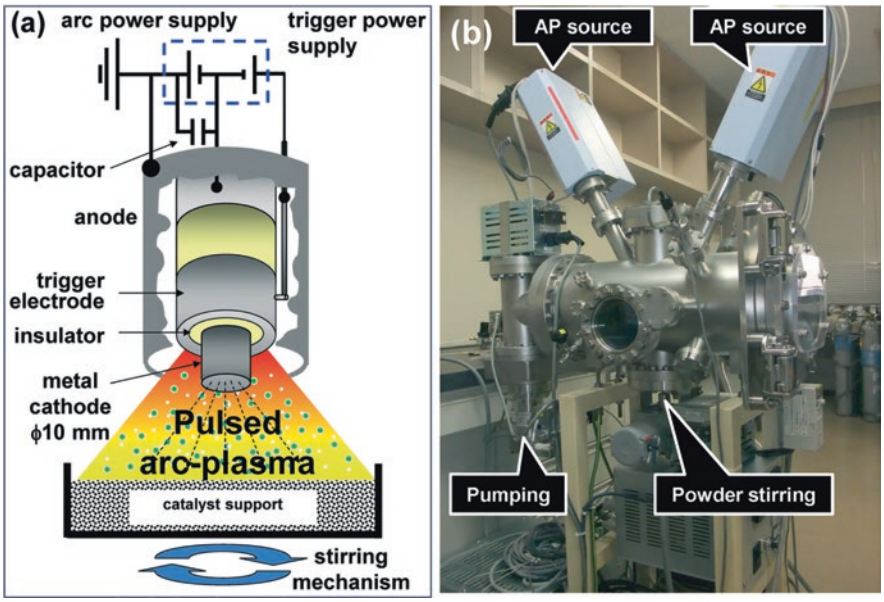

Fig. 1.12 (**a**) Schematic of the pulsed arc plasma process for the deposition of metal nanoparticles and (**b**) experimental setup with dual arc plasma sources. (Reproduced from [143] with permission from The Royal Society of Chemistry)

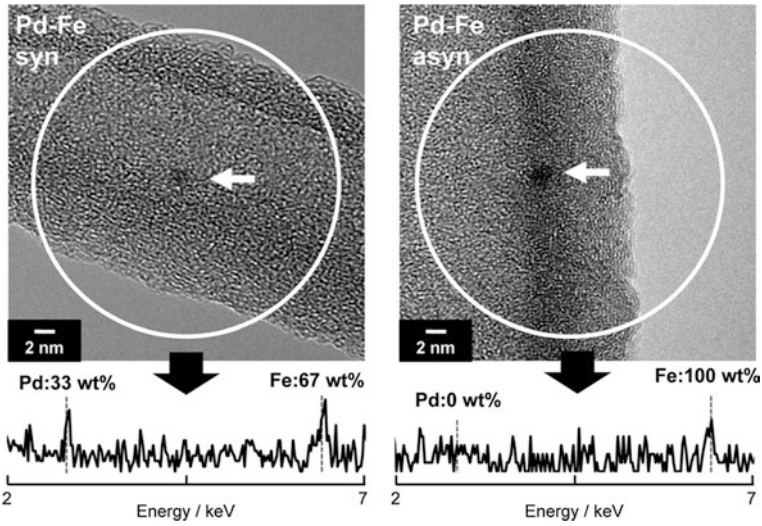

Fig. 1.13 TEM images and EDX spectra of unsupported Pd–Fe nanoparticles prepared by (left) synchronous (syn) and (right) asynchronous (asyn) pulsing. Each EDX spectrum was taken from a circular region containing one nanoparticle. (Reproduced from [143] with permission from The Royal Society of Chemistry)

1.4 Application: Importance of Controlling the Shape and Size of Nanoparticles

Nanotechnology is concerned with understanding the correlation between the chemical, optical, electrical, and magnetic properties of nanomaterials with respect to their size, shape, and surface chemistry [144]. The importance of the size is highlighted in the very definition of nanotechnology which, according to the National Nanotechnology Initiative (NNI), is the "*science, engineering, and technology conducted at the nanoscale, which is about 1 to 100 nm*" [145]. Once we are in the nanoparticle size range, the function of the nanoparticle size plays an equally important role as material properties (e.g., chemical and magnetic) become size-dependent and, therefore, a desired nanoparticle function is closely related to the nanoparticle size. To highlight the size and shape effects, we briefly go over a selected few field applications, but we emphasize that size and shape effects are present in all applications.

1.4.1 Metallurgy

Following observations regarding the effect of the size of small particle on melting temperature, Buffat and Borel [146] studied the melting temperature of gold particles of various sizes and found, using scanning electron-diffraction, that melting temperature increases with increasing particle size (see Fig. 1.14). Later, [147] highlighted what is known as *cluster size equations*, which included energetic, quantum, electronic, and electrodynamic size effects of the clusters.

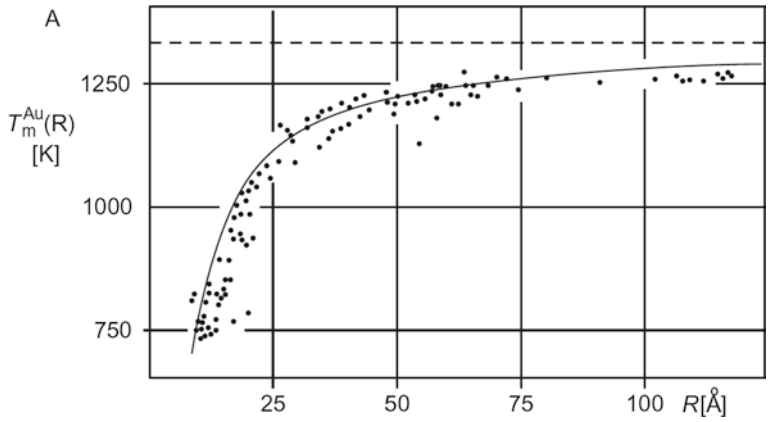

Fig. 1.14 Effect of gold nanoparticle size on the melting temperature. Adapted from [146, 147] with permission

1.4.2 Biological Systems

One way to explore the size and shape effects of nanoparticles is to look at these effects in naturally occurring biological nanostructures. Viruses, which are nanosized entities, exist in different shapes such as filamentous, isometric (or icosahedral), head and tail, and enveloped, and their ability to infect a certain cell type and their residence time in the infected cell are impacted by their shape [144]. The combined effect of shape and size can be noticed in the therapeutics used for degenerated (e.g., osteoarthritic) cartilage, where the molecule's size is the most important factor in the design of therapeutics, as the effective pore size in the matrix of the cartilage is very small (~6 nm). Surprisingly, certain molecules of larger hydrodynamic radius (e.g., 500 kDa dextran with ~16 nm) can penetrate and diffuse through cartilage. It is hypothesized that the linear shape of the dextran molecule enables it to penetrate and diffuse within pores of smaller size, while spherical molecules of similar hydrodynamic radius cannot penetrate cartilage [148]. Currently, therapies of degenerated cartilage are based on drugs of small hydrodynamic radius, which have limited long-term efficacy, and thus, the ability to inject cartilage with drugs of larger molecules that can penetrate the tissue could substantially improve the health of the degenerated tissue, but would also require knowing the size and shape, among other factors. Antigens and proteins are other examples of nanostructures whose functions are impacted by size and shape [144]. These examples of naturally occurring nanostructures demonstrate the importance of both size and shape, and that for designing synthetic nanoparticles for biological applications, e.g., detecting and repairing infected cells, tumor diagnosis, or drug delivery, physical properties play a detrimental role in the application, as they impact the interaction between nanoparticle and the cell surface (see Fig. 1.15). For instance, for tumor targeting nanoparticles, Perrault et al. [149] have shown that the permeation of the nanoparticles within a tumor, as well as their tumor accumulation capacity, is highly influenced by the nanoparticle's diameter, where smaller nanoparticles are able to diffuse throughout the tumor matrix.

1.4.3 Oil Well Construction

In oil well construction, cements experience volume shrinkage, which impacts the long-term stability of the wells and leads to gas leakage [150]. To reduce the effect of the shrinkage, certain additives, including nanoparticles, can be used. For instance, nanoscale magnesium oxide (MgO) is used as an additive in the cement slurry, expanding as it is converted to magnesium hydroxide once it is exposed to the water in the slurry and thus, reducing the shrinkage. The expansion properties are influenced by the surface area of the MgO particles, i.e., MgO particle size [151]. In the same topic, cements experience what is known as "waiting on cement" (WOC), which is the amount of time it takes the slurry to solidify. This waiting time

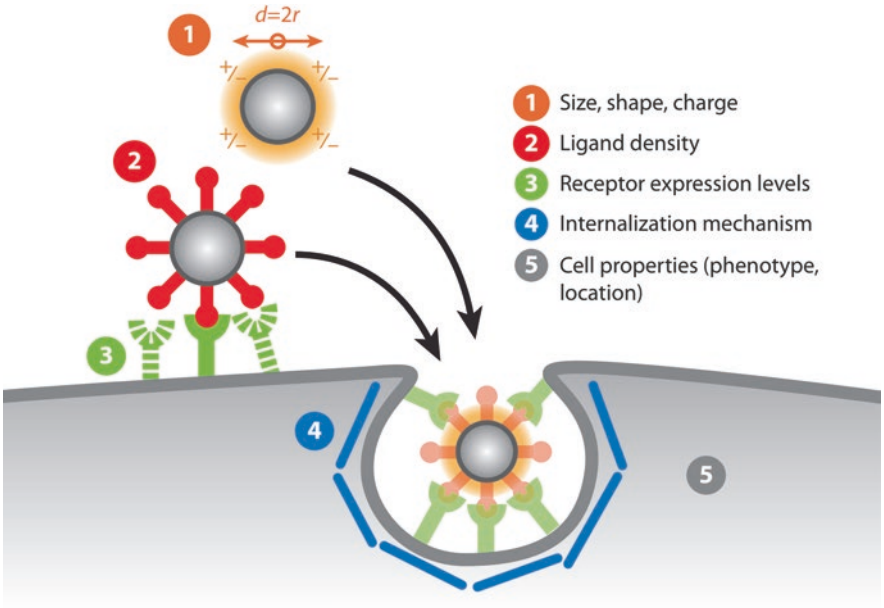

Fig. 1.15 Factors that impact nanoparticle and cell surface interaction. Adapted from reference [144] after permission

can be costly and is generally minimized by additives, or *cement accelerators*. Nanosilica has been shown to increase strength of the cement and decrease porosity, making it a favorable additive over other accelerators [152, 153]. Different sizes and shapes of nanosilica lead to different results [154]. For instance, the smallest nanosilica (5 nm in diameter), and the rod-shaped nanosilica exhibited the fastest rates of cement setting [151].

Tough well conditions and cement material issues can lead to debonding of the cement from the casing or the rock formation in the wellbore and the fracturing of the bulk cement, as has been proven with previous studies [151], as depicted in Figs. 1.16 and 1.17. Nanoparticles which have shown substantial promise in improving the properties of oil and gas well cement can be named as nanosilicas, calcium-silicate-hydrate (C-S-H) nanofoils, and nanomagnesia [151].

It should be noted that several other factors, besides size and shape, play significant roles on the function and kinetics of nanoparticles, such as magnetic field, mechanical properties, and pH effect, considering their applications.

1.4.4 Nanotechnology: Industrial Applications and Risk Factors

Over the past few decades, nanotechnology has infiltrated almost all research fields and introduced unconventional solutions to the current industrial problems. However, most of these solutions have not fully transitioned from the experimental

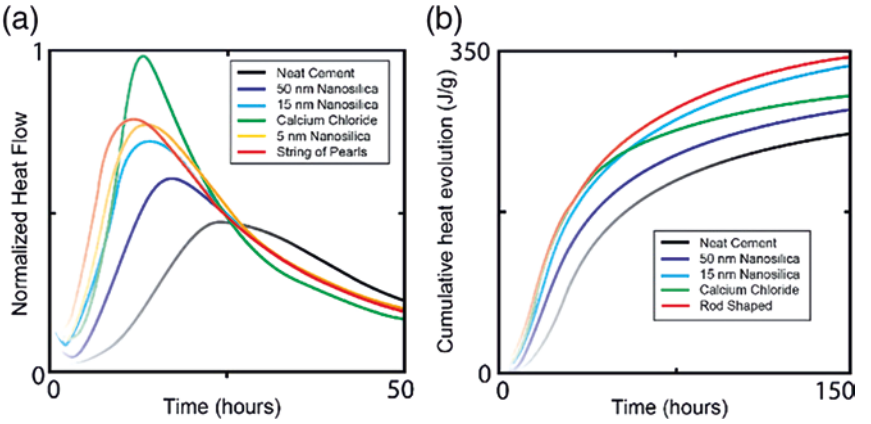

Fig. 1.16 Hydration kinetics of class H cement (**a**) heat flow and (**b**) cumulative heat, showing the effect of shape and size. (Adapted from [151] with permission)

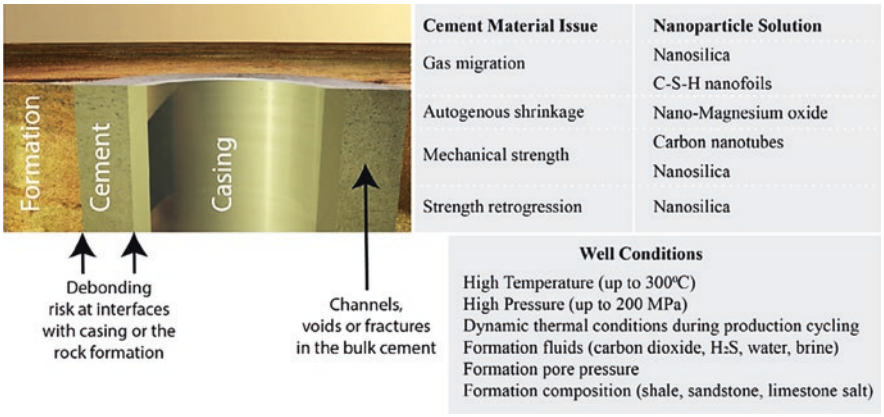

Fig. 1.17 Oil well construction materials and nanosolutions. (Adapted from [151] with permission)

laboratory stage to the industrial stage. With the rapid increase in the applications of nanotechnology in the industry, there are risks, concerns, and challenges attached to its use. In the following, we address some of the applications of nanotechnology along with potential risks. While we focus on two sectors, food industry and oil and gas, similar risks are also present in the other sectors.

1.4.4.1 Food Industry

Nanotechnology has recently attracted much attention in the food and beverage packaging industry, where there are several benefits of using engineered nanoparticles (ENP) in food-contact applications. However, such applications are also

accompanied by health concerns. While traditional packaging is mainly concerned with product preservation, nanotechnology is involved in *active* packaging, which extends the roles of packaging from the *inert* containment of the product to the *active* containment, which targets the improvement of nutrient and flavor delivery, and extends its shelf life [155]. According to the European regulation (EC) No 450/2009, active packaging technologies are designed to deliberately incorporate components that would release or absorb substances into or from the packaged food or the environment surrounding the food. Active packaging technologies include releasing systems (e.g., carbon dioxide) and absorbing systems such as oxygen scavengers, which can be used for products like cooked meat, or bakery products, and prevent them from discoloration and mold growth, as well as moisture scavengers, which extend shelf life by preserving moisture in products like fresh meat and certain fruits. For instance, Mu et al. [156] introduced an oxygen scavenging technology based on iron nanoparticles blended with active carbon, calcium chloride, and sodium chloride, which showed superior performance to its counterpart technology that utilizes microsized iron powder, in terms of both scavenging rate and capacity. Although there has been active packaging products (e.g., sachets and absorbent pads), the primary challenge in the commercialization of these technologies is the health risk they pose as the active additives, e.g., nanoparticles, could migrate from the packaging into the product by means of diffusion from higher concentration (package) into lower concentration (food) [157]. A schematic of absorbent pad architecture has been depicted in Fig. 1.18 [159].

Moreover, due to their size, nanoparticles can navigate the body (cells, tissues, and organs) much more easily compared to microsized particles. As a result, there

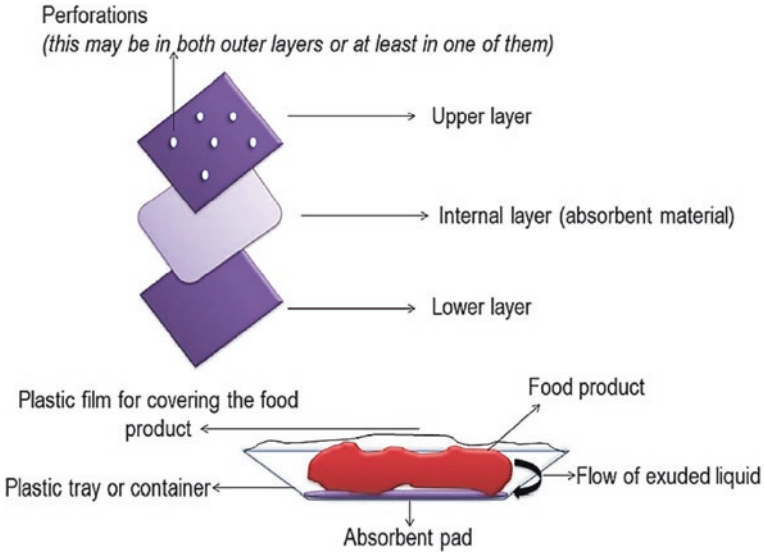

Fig. 1.18 Architecture of absorbent pad. (Adapted from [159] with permission)

has been a tendency for studying the interaction between the food matrix and the engineered nanoparticles. To address this issue, the conditions under which nanoparticles migrate need to be studied. Zhang et al. [158] introduced a standardized food model for the evaluation of the effect of food matrix on the toxicity and fate of ingested nanoparticles, and the study looked into titanium dioxide nanoparticles, a common food additive.

1.4.4.2 Oil and Gas

Recently, there has been extensive research on using nanotechnology in different aspects of the oilfield industry, including drilling, reservoir completion, enhanced oil upgrading and recovery, and produced water treatment, to name a few. The need for new technologies is fueled by the fact that the current resources are diminishing quickly, and therefore, such resources need to be well utilized. However, many of the proposed technologies, which are in their experimental stage, face many challenges, which hinder their applicability to the industry. Two of the main challenges are listed below.

1.4.5 Upscaling from Laboratory to Industry

When scaling up to meet the industrial demand, the level of control over the nanoparticle size, which would be feasible at the nanoscale, becomes more difficult to achieve, which is reflected on the properties of the synthesized matter [160]. This also is accompanied by the high cost and time that come with using nanoparticles at the industrial level, in addition to the inconsistent performance which may result from using several batches. As a result, processes for synthesizing nanoparticles at an industrial scale need to be developed, which is another challenge as this would require having the industry invest in developing such processes. In oil and gas industry, different additional challenges depend on the application. A summary of some of the key challenges is provided in Table 1.1 [160].

1.4.6 Health and Safety Risks

The nature of the nanostructure plays an important role in risk assessment. Nanoparticles that are incorporated into a substance (e.g., nanocomposite and nanocomponents) are referred to as *fixed* nanoparticles and pose lower risk than *free* nanoparticles, which are individual nanoparticles. For instance, in oil and gas applications, free nanoparticles could be injected into the wellbore with the enhanced-oil-recovery fluids. Although the effect of nanoparticles on the body is still to be studied, if they enter the body, e.g., by inhaling, absorption, or skin contact, they

Table 1.1 Nanotechnology applications in oilfield and attached challenges adopted with permission from [160]

Nanotechnology	Nano tool	Oilfield application	Key challenges
Nano electronics	Nano sensors	Reservoir and flood front imaging	Long battery life under reservoir conditions
Nano optics	Quantum dots	Logging	Transport through reservoir
Nano magnetism	Ferrofluids	Reservoir/ fracture imaging	Development of MNP, EM sources and receivers, data acquisition and signal processing software
	Magnetic nanoparticles	Produced water (PW) treatment	Scale up from lab to field
Nano composites and fibers	Single wall carbon tube, fullerenes, multiwall carbon tube	New casing and tubing materials, drill bits, proppants	Constructing and testing prototype
Surface active nanoparticles	Functionalized nanoparticles	EOR	Transport through reservoir
Nanoencapsulation	Chemical-laden nanoparticles, Biodegradable polymeric nanoparticles, phase inversion nanoencapsulation	Acid stimulation, profile control, gas mobility control	Scale up from lab to field
Nano thin film	Nanocomposite coatings	Drill bits, drilling fluids, completion fluids, shale inhibition	Construction and testing prototype
Nanocatalyst	Nickel nanoparticles	Catalyst for *in situ* thermal upgrading of heavy oil	Transport through reservoir, scale up

trigger an immune response and cause an overload of phagocytes (cells that destroy and devour pathogens). Moreover, they may interfere with the biological processes, which is made worse due to their large surface-area-to-volume ratio posing higher risk than their counterpart microsized particles [161]. In addition to the safety risks, there are several environmental risks of using nanoparticles at an industrial scale. A thorough review of challenges and uncertainties of using nanoparticles in oil and gas applications and associated risk factors will be addressed in detail in Chap. 15 of this book.

1.5 Conclusion

Nanoparticles, being a byproduct of industrial revolution, have great potential in changing the way humans connect to the world in the modern era. Nanoparticles have special physical properties distinct from both molecular and solid-state matter due to their significant fraction of surface atoms. Study of these physical properties provides us a unique way to learn how nanoparticles can be prepared and characterized. Knowledge of the application of nanoparticles in different industrial settings dictates nanoparticle preparation techniques and characterization. Knowledge of diverse application of these nanomaterials in the oil and gas industry from exploration and production to refinery, dictates urgent need for advanced preparation techniques and characterization.

Nanoparticle preparation techniques can be categorized into two main categories of chemical and physical techniques. Chemical pathway, also known as bottom-up technique, involves molecular components as starting materials linked with chemical reactions, nucleation, and growth processes to promote the formation of nanoparticles. Chemical coprecipitation, electrochemical, sonochemical, sol-gel processing, chemical vapor deposition, chemical vapor condensation, and (w/o) microemulsions are only a few of these methods. On the other hand, physical preparation methods, known as top-down methods, imply the preparation of nanoparticles via generation of isolated atoms by using various distribution techniques that involve physical methods, such as milling or grinding, laser beam processing, repeated quenching, photolithography, pulsed laser techniques, and plasma techniques, whose recent advances have been reviewed briefly in this chapter. Later, importance of controlling the shape and size of nanoparticles considering their application has been generally reviewed. In the last part of this chapter, industrial applications and risks/challenges associated with the advancements of nanotechnology have been briefly discussed.

Over the past few decades, nanotechnology has found its way in almost all research fields, and introduced unconventional solutions to the current industrial problems; however, most of these solutions have not fully transitioned from the experimental laboratory stage to the industrial stage. With the rapid enhanced applications of nanotechnology in the industry, there are risks, concerns, and challenges attached to its use, which are still somehow not known or under investigation. In the last section, we addressed some of the applications of nanotechnology along with its potential risks/challenges. While we focus on two sectors, food industry and oil and gas, similar risks are also present in the other sectors. Facing the fast-paced advancement of nanotechnology in almost every industry, we need to be aware and adopt ourselves in unconventional and out of the box thinking methods toward novel solutions, as modern problems solutions dictate a novel way of thinking.

References

1. National Nanotechnology Initiative (NNI). National Science and Technology Council. Committee on Technology, Subcommittee on Nanoscale Science, National Technology Initiative Strategic Plan, www.nano.gov (2011, Accessed 25 Aug 2015)
2. S. Iijima, Helical microtubules of graphitic carbon. Nature **354**, 56–58 (1991)
3. M. Boutonnet, J. Kizling, P. Stenius, Colloids Surf. **5**, 209 (1982)
4. A. Nasir, A. Kausar, A. Younus, A review on preparation, properties and applications of polymeric nanoparticle-based materials. Polym. Plastics Technol. Eng. **54**(4), 325–341 (2015). https://doi.org/10.1080/03602559.2014.958780
5. R. Francis, N. Joy, E.P. Aparna, R. Vijayan, Polymer grafted inorganic nanoparticles, preparation, properties, and applications: A review. Polym. Rev. **54**, 268–347 (2014)
6. Y. Zhang, Z. Chen, Z. Dong, M. Zhao, S. Ning, P. He, Preparation of raspberry-like adsorbed silica nanoparticles via miniemulsion polymeri- zation using a glycerol-functionalized silica sol. Int. J. Polym. Mater. Polym. Biomater. **62**, 397–401 (2013)
7. J.P. Rao, K.E. Geckeler, Polymer nanoparticles: Preparation techniques and size-control parameters. Prog. Polym. Sci. **36**, 887–913 (2011)
8. X. Wang, J.E. Hall, S. Warren, J. Krom, J.M. Magistrelli, M. Rackaitis, G.G.A. Bohm, Synthesis, characterization, and application of novel polymeric nanoparticles. Macromolecules **40**, 499–508 (2007)
9. N.N. Nassar, Iron oxide nanoadsorbents for removal of various pollutants from wastewater: An overview. Appl. Adsorb. Water Pollut. Control, 81–118 (2012)
10. M. Globe, *Preparation and Characterization of Monodisperse Magnetite sols in W/O Microemulsion*. (1983)
11. C. Bock, C. Paquet, M. Couillard, G.A. Botton, B.R. MacDougall, Size-selected synthesis of PtRu nano-catalysts: Reaction and size control mechanism. J. Am. Chem. Soc. **126**(25), 8028–8037 (2004)
12. X. Pang, L. Zhao, W. Han, X. Xin, Z. Lin, A general and robust strategy for the synthesis of nearly monodisperse colloidal nanocrystals. Nat. Nanotechnol. **8**(6), 426–431 (2013)
13. M.M. Husein, N.N. Nassar, Nanoparticle preparation using the single microemulsions scheme. Curr. Nanosci. **4**(4), 370–380 (2008)
14. F. Sagala, *Naturally Derived Silicate-Based Nanoparticles for Enhanced Oil Recovery in Sandstone Reservoirs*. (2020)
15. L.C. Varanda, C.G.S.D. Souza, C.J. Perecin, D.A.D. Moraes, D.F.D. Queiróz, H.R. Neves, et al., Chapter 3 - Inorganic and organic–inorganic composite nanoparticles with potential biomedical applications: synthesis challenges for enhanced performance, in *Materials for Biomedical Engineering*, ed. by V. Grumezescu, A. M. Grumezescu, (Elsevier, 2019), pp. 47–99
16. M.O. Besenhard, A.P. LaGrow, A. Hodzic, M. Kriechbaum, L. Panariello, G. Bais, et al., Co-precipitation synthesis of stable iron oxide nanoparticles with NaOH: New insights and continuous production via flow chemistry. Chem. Eng. J. **399**, 125740 (2020)
17. J.W. Mullin, 8 - Industrial techniques and equipment, in *Crystallization*, ed. by J. W. Mullin, 4th edn., (Butterworth-Heinemann, Oxford, 2001), pp. 315–402
18. M. Lok, Coprecipitation, in *Synthesis of Solid Catalysts*, (Wiley, 2009), pp. 135–151
19. B.L. Cushing, V.L. Kolesnichenko, C.J. O'Connor, Recent advances in the liquid-phase syntheses of inorganic nanoparticles. Chem. Rev. **104**(9), 3893–3946 (2004)
20. Z. Wu, S. Yang, W. Wu, Shape control of inorganic nanoparticles from solution. Nanoscale **8**(3), 1237–1259 (2016)
21. A.E. Nielsen, Precipitation. Croat. Chem. Acta **42**(2), 319–333 (1970)
22. J.-P. Jolivet, M. Henry, J. Livage, *Metal Oxide Chemistry and Synthesis: From Solution to Solid State* (Wiley-Blackwell, 2000)
23. D.R. Lide, *CRC Handbook of Chemistry and Physics*, 87th edn. (Taylor & Francis, 2006)

24. C. Jia, Y. Cheng, F. Bao, D. Chen, Y. Wang, pH value-dependant growth of α-Fe2O3 hierarchical nanostructures. J. Cryst. Growth **294**(2), 353–357 (2006)
25. G. Pandey, S. Singh, G. Hitkari, Synthesis and characterization of polyvinyl pyrrolidone (PVP)-coated Fe3O4 nanoparticles by chemical co-precipitation method and removal of Congo red dye by adsorption process. Int. Nano Lett. **8**(2), 111–121 (2018)
26. A. Chitsaz, M. Jalilpour, M. Fathalilou, Effects of PVP and CTAB surfactants on the morphology of cerium oxide nanoparticles synthesized via co-precipitation method. Int. J. Mater. Res. **104**(5), 511–514 (2013)
27. A. Radoń, A. Drygała, Ł. Hawełek, D. Łukowiec, Structure and optical properties of Fe3O4 nanoparticles synthesized by co-precipitation method with different organic modifiers. Mater. Charact. **131**, 148–156 (2017)
28. D.-H. Chen, Y.-Y. Chen, Synthesis of strontium ferrite nanoparticles by coprecipitation in the presence of polyacrylic acid. Mater. Res. Bull. **37**(4), 801–810 (2002)
29. J. Peng, F. Zou, L. Liu, L. Tang, L. Yu, W. Chen, et al., Preparation and characterization of PEG-PEI/Fe3O4 nano-magnetic fluid by co-precipitation method. Trans. Nonferrous Metals Soc. China **18**(2), 393–398 (2008)
30. I. Riva'i, I.O. Wulandari, H. Sulistyarti, A. Sabarudin, Ex-situ synthesis of polyvinyl alcohol(PVA)-coated Fe3O4 nanoparticles by coprecipitation-ultrasonication method. IOP Conf. Ser. Mater. Sci. Eng. **299**, 012065 (2018)
31. S. Akbari, S.M. Masoudpanah, S.M. Mirkazemi, N. Aliyan, PVA assisted coprecipitation synthesis and characterization of MgFe2O4 nanoparticles. Ceram. Int. **43**(8), 6263–6267 (2017)
32. M. Anbarasu, M. Anandan, E. Chinnasamy, V. Gopinath, K. Balamurugan, Synthesis and characterization of polyethylene glycol (PEG) coated Fe3O4 nanoparticles by chemical co-precipitation method for biomedical applications. Spectrochim. Acta A Mol. Biomol. Spectrosc. **135**, 536–539 (2015)
33. Y. Zhang, Z. Nan, Modified magnetic properties of MnFe2O4 by CTAB with coprecipitation method. Mater. Lett. **149**, 22–24 (2015)
34. D. Varghese, C. Tom, C.N. Krishna, Effect of CTAB on structural and optical properties of CuO nanoparticles prepared by coprecipitation route. IOP Conf. Ser. Mater. Sci. Eng. **263**, 022002 (2017)
35. L. Shen, Y. Qiao, Y. Guo, S. Meng, G. Yang, M. Wu, et al., Facile co-precipitation synthesis of shape-controlled magnetite nanoparticles. Ceram. Int. **40**(1, Part B), 1519–1524 (2014)
36. T. Fuchigami, S. Inagi, M. Atobe, *Organic Electrode Reactions. Fundamentals and Applications of Organic Electrochemistry*. (2014), pp. 1–10 and 45–82
37. A. Serrà, E. Vallés, Advanced electrochemical synthesis of multicomponent metallic nanorods and nanowires: Fundamentals and applications. Appl. Mater. Today **12**, 207–234 (2018)
38. F. Nasirpouri, Fundamentals and principles of electrode-position, in *Electrodeposition of Nanostructured Materials*, ed. by F. Nasirpouri, (Springer International Publishing, Cham, 2017), pp. 75–121
39. U.S. Mohanty, Electrodeposition: A versatile and inexpensive tool for the synthesis of nanoparticles, nanorods, nanowires, and nanoclusters of metals. J. Appl. Electrochem. **41**(3), 257–270 (2011)
40. D. Bera, S.C. Kuiry, S. Seal, Synthesis of nanostructured materials using template-assisted electrodeposition. JOM **56**(1), 49–53 (2004)
41. M.T. Reetz, W. Helbig, Size-selective synthesis of nanostructured transition metal clusters. J. Am. Chem. Soc. **116**(16), 7401–7402 (1994)
42. N. Sato, Chapter 7 - electrode reactions, in *Electrochemistry at Metal and Semiconductor Electrodes*, ed. by N. Sato, (Elsevier Science, Amsterdam, 1998), pp. 213–233
43. F. Nasirpouri, An overview to electrochemistry, in *Electrodeposition of Nanostructured Materials*, ed. by F. Nasirpouri, (Springer International Publishing, Cham, 2017), pp. 43–73
44. A. Takai, Y. Yamauchi, K. Kuroda, Facile formation of single crystalline Pt nanowires on a substrate utilising lyotropic liquid crystals consisting of cationic surfactants. J. Mater. Chem. **19**(24), 4205–4210 (2009)

45. Y. Song, R.M. Garcia, R.M. Dorin, H. Wang, Y. Qiu, E.N. Coker, et al., Synthesis of platinum nanowire networks using a soft template. Nano Lett. **7**(12), 3650–3655 (2007)
46. Y. Imura, H. Tanuma, H. Sugimoto, R. Ito, S. Hojo, H. Endo, et al., Water-dispersible ultrathin au nanowires prepared using a lamellar template of a long-chain amidoamine derivative. Chem. Commun. **47**(22), 6380–6382 (2011)
47. X. Gao, F. Lu, B. Dong, Y. Liu, Y. Gao, L. Zheng, Facile synthesis of gold and gold-based alloy nanowire networks using wormlike micelles as soft templates. Chem. Commun. **51**(5), 843–846 (2015)
48. Q. Zhou, X. Liu, Y. Zhao, N. Jia, L. Liu, M. Yan, et al., Single crystal tin nano-rod arrays electrodeposited by a soft template. Chem. Commun. **39**, 4941–4942 (2005)
49. A. Serrà, E. Gómez, J.F. López-Barbera, J. Nogués, E. Vallés, Green electrochemical template synthesis of CoPt nanoparticles with Tunable size, composition, and magnetism from microemulsions using an ionic liquid (bmimPF6). ACS Nano **8**(5), 4630–4639 (2014)
50. I. Kaminska, M. Jonsson-Niedziolka, A. Kaminska, M. Pisarek, R. Hołyst, M. Opallo, et al., Electrodeposition of well-adhered multifarious au particles at a solid|toluene|aqueous electrolyte three-phase junction. J. Phys. Chem. C **116**(42), 22476–22485 (2012)
51. M. Pérez-Page, E. Yu, J. Li, M. Rahman, D.M. Dryden, R. Vidu, et al., Template-based syntheses for shape controlled nanostructures. Adv. Colloid Interf. Sci. **234**, 51–79 (2016)
52. D. Bera, S.C. Kuiry, S. Patil, S. Seal, Palladium nanoparticle arrays using template-assisted electrodeposition. Appl. Phys. Lett. **82**(18), 3089–3091 (2003)
53. A.J. Fragoso-Medina, F. López-Saucedo, G.G. Flores-Rojas, E. Bucio, Chapter 11 - Sonochemical synthesis of inorganic nanomaterials, in *Green Sustainable Process for Chemical and Environmental Engineering and Science*, ed. by B. R. Inamuddin, M. I. Ahamed, A. M. Asiri, (Elsevier, 2021), pp. 263–279
54. A. Gedanken, Using sonochemistry for the fabrication of nanomaterials. Ultrason. Sonochem. **11**(2), 47–55 (2004)
55. M. Kamali, R. Dewil, L. Appels, T.M. Aminabhavi, Nanostructured materials via green sonochemical routes – Sustainability aspects. Chemosphere **276**, 130146 (2021)
56. B.M. Teo, *Ultrasonic Synthesis of Polymer Nanoparticles. Handbook of Ultrasonics and Sonochemistry* (Springer, Singapore, 2016), pp. 365–393
57. H. Xu, B.W. Zeiger, K.S. Suslick, Sonochemical synthesis of nanomaterials. Chem. Soc. Rev. **42**(7), 2555–2567 (2013)
58. A. Gedanken, Ultrasonic Processing to Produce Nanoparticles, in *Encyclopedia of Materials: Science and Technology*, ed. by B. KHJ, R. W. Cahn, M. C. Flemings, B. Ilschner, E. J. Kramer, S. Mahajan, et al., (Elsevier, Oxford, 2001), pp. 9450–9456
59. A. Gedanken, I. Perelshtein, 18 - Power ultrasound for the production of nanomaterials, in *Power Ultrasonics*, ed. by J. A. Gallego-Juárez, K. F. Graff, (Woodhead Publishing, Oxford, 2015), pp. 543–576
60. J.H. Bang, K.S. Suslick, Applications of ultrasound to the synthesis of nanostructured materials. Adv. Mater. **22**(10), 1039–1059 (2010)
61. J. Lee, *Importance of Sonication and Solution Conditions on the Acoustic Cavitation Activity. Handbook of Ultrasonics and Sonochemistry* (Springer, Singapore, 2016), pp. 137–175
62. F. Mohandes, M. Salavati-Niasari, Sonochemical synthesis of silver vanadium oxide micro/nanorods: Solvent and surfactant effects. Ultrason. Sonochem. **20**(1), 354–365 (2013)
63. C.U. Okoli, K.A. Kuttiyiel, J. Cole, J. McCutchen, H. Tawfik, R.R. Adzic, et al., Solvent effect in sonochemical synthesis of metal-alloy nanoparticles for use as electrocatalysts. Ultrason. Sonochem. **41**, 427–434 (2018)
64. M. D'Arienzo, R. Scotti, B. Di Credico, M. Redaelli, Chapter 13 - Synthesis and characterization of morphology-controlled TiO2 nanocrystals: Opportunities and challenges for their application in photocatalytic materials, in *Studies in Surface Science and Catalysis*, ed. by P. Fornasiero, M. Cargnello, (Elsevier, 2017), pp. 477–540
65. R.C. Mehrotra, Synthesis and reactions of metal alkoxides. J. Non-Cryst. Solids **100**(1), 1–15 (1988)

66. T. Athar, Chapter 17 - Smart precursors for smart nanoparticles, in *Emerging Nanotechnologies for Manufacturing*, ed. by W. Ahmed, M. J. Jackson, 2nd edn., (William Andrew Publishing, Boston, 2015), pp. 444–538
67. M. Parashar, V.K. Shukla, R. Singh, Metal oxides nanoparticles via sol–gel method: A review on synthesis, characterization and applications. J. Mater. Sci. Mater. Electron. **31**(5), 3729–3749 (2020)
68. L.L. Hench, J.K. West, The sol-gel process. Chem. Rev. **90**(1), 33–72 (1990)
69. U. Schubert, *Chemistry and Fundamentals of the Sol–Gel Process. The Sol-Gel Handbook*. (2015), pp. 1–28
70. M. Henry, J.P. Jolivet, J. Livage, Aqueous chemistry of metal cations: Hydrolysis, condensation and complexation, in *Chemistry, Spectroscopy and Applications of Sol-Gel Glasses*, ed. by R. Reisfeld, C. K. Jjørgensen, (Springer, Berlin/Heidelberg, 1992), pp. 153–206
71. *Hydrolysis of Metal Alkoxides and Synthesis of Simple Oxides by The Sol-Gel Method. The Chemistry of Metal Alkoxides*, (Springer, Boston, 2002), pp. 107–25
72. D.M. Smith, R. Deshpande, B.C. Jeffrey, Preparation of low-density aerogels at ambient pressure. MRS Proc. **271**, 567 (1992)
73. S.S. Ray, R. Gusain, N. Kumar, Chapter four - Adsorption in the context of water purification, in *Carbon Nanomaterial-Based Adsorbents for Water Purification*, ed. by S. S. Ray, R. Gusain, N. Kumar, (Elsevier, 2020), pp. 67–100
74. V. Purcar, V. Rădiţoiu, A. Dumitru, C.-A. Nicolae, A.N. Frone, M. Anastasescu, et al., Antireflective coating based on TiO2 nanoparticles modified with coupling agents via acid-catalyzed sol-gel method. Appl. Surf. Sci. **487**, 819–824 (2019)
75. S. Cai, Y. Zhang, H. Zhang, H. Yan, H. Lv, B. Jiang, Sol–gel preparation of hydrophobic silica antireflective coatings with low refractive index by base/acid two-step catalysis. ACS Appl. Mater. Interfaces **6**(14), 11470–11475 (2014)
76. S.V. Lazareva, N.V. Shikina, L.E. Tatarova, Z.R. Ismagilov, Synthesis of high-purity silica nanoparticles by sol-gel method. Eurasian Chem. Technol. J. **19**(4), 295–302 (2017)
77. S.A. Ibrahim, S. Sreekantan, Effect of pH on TiO2 nanoparticles via sol-gel method. Adv. Mater. Res. **173**, 184–189 (2011)
78. S. Hosseini Largani, P.M. Akbarzadeh, The effect of concentration ratio and type of functional group on synthesis of CNT–ZnO hybrid nanomaterial by an in situ sol–gel process. Int. Nano Lett. **7**(1), 25–33 (2017)
79. M.S. Tokumoto, S.H. Pulcinelli, C.V. Santilli, V. Briois, Catalysis and temperature dependence on the formation of ZnO nanoparticles and of zinc acetate derivatives prepared by the sol−gel route. J. Phys. Chem. B **107**(2), 568–574 (2003)
80. K.L. Choy, Chapter 12 - Vapor processing of nanostructured materials, in *Handbook of Nanostructured Materials and Nanotechnology*, ed. by H. S. Nalwa, (Academic Press, Burlington, 2000), pp. 533–577
81. L. Sun, G. Yuan, L. Gao, J. Yang, M. Chhowalla, M.H. Gharahcheshmeh, et al., Chemical vapour deposition. Nat. Rev. Methods Primers **1**(1), 5 (2021)
82. Chapter 1 Overview of Chemical Vapour Deposition, in *Chemical Vapour Deposition: Precursors, Processes and Applications. The Royal Society of Chemistry*, ed. by A. C. Jones, M. L. Hitchman, (2009), pp. 1–36
83. W. Chang, G. Skandan, S.C. Danforth, B.H. Kear, H. Hahn, Chemical vapor processing and applications for nanostructured ceramic powders and whiskers. Nanostruct. Mater. **4**(5), 507–520 (1994)
84. A. Tavakoli, M. Sohrabi, A. Kargari, A review of methods for synthesis of nanostructured metals with emphasis on iron compounds. Chem. Pap. **61**(3), 151–170 (2007)
85. Y.M. Manawi, S.A. Ihsanullah, T. Al-Ansari, M.A. Atieh, A review of carbon nanomaterials' synthesis via the Chemical Vapor Deposition (CVD) method. Materials **11**(5) (2018)
86. H. Lee, M.Y. Song, J. Jurng, Y.-K. Park, The synthesis and coating process of TiO2 nanoparticles using CVD process. Powder Technol. **214**(1), 64–68 (2011)

87. M. Kumar, Y. Ando, Chemical vapor deposition of carbon nanotubes: A review on growth mechanism and mass production. J. Nanosci. Nanotechnol. **10**(6), 3739–3758 (2010)
88. M. Meyyappan, A review of plasma enhanced chemical vapour deposition of carbon nanotubes. J. Phys. D. Appl. Phys. **42**(21), 213001 (2009)
89. J. Ramanujam, A. Verma, Photovoltaic properties of a-Si:H films grown by plasma enhanced chemical vapor deposition: A review. Mater. Express **2**(3), 177–196 (2012)
90. L. Martinu, O. Zabeida, J.E. Klemberg-Sapieha, Chapter 9 - Plasma-enhanced chemical vapor deposition of functional coatings, in *Handbook of Deposition Technologies for Films and Coatings*, ed. by P. M. Martin, 3rd edn., (William Andrew Publishing, Boston, 2010), pp. 392–465
91. C.A. Dorval Dion, J.R. Tavares, Photo-initiated chemical vapor deposition as a scalable particle functionalization technology (a practical review). Powder Technol. **239**, 484–491 (2013)
92. Y. van de Burgt, Laser-assisted growth of carbon nanotubes—A review. J. Laser Appl. **26**(3), 032001 (2014)
93. A.P. Caricato, A. Luches, Applications of the matrix-assisted pulsed laser evaporation method for the deposition of organic, biological and nanoparticle thin films: A review. Appl. Phys. A **105**(3), 565–582 (2011)
94. M.M. Husein, N.N. Nassar, Nanoparticle preparation using the single microemulsions scheme. Curr. Nanosci. **4**(4), 370–380 (2008)
95. A.K. Ganguli, A. Ganguly, S. Vaidya, Microemulsion-based synthesis of nanocrystalline materials. Chem. Soc. Rev. **39**(2), 474–485 (2010)
96. S. Wolf, C. Feldmann, Microemulsions: Options to expand the synthesis of inorganic nanoparticles. Angew. Chem. Int. Ed. **55**(51), 15728–15752 (2016)
97. M. Sanchez-Dominguez, K. Pemartin, M. Boutonnet, Preparation of inorganic nanoparticles in oil-in-water microemulsions: A soft and versatile approach. Curr. Opin. Colloid Interface Sci. **17**(5), 297–305 (2012)
98. J.-P. Ge, W. Chen, L.-P. Liu, Y.-D. Li, Formation of disperse nanoparticles at the oil/water interface in normal microemulsions. Chem. Eur. J. **12**(25), 6552–6558 (2006)
99. M. Husein, E. Rodil, J.H. Vera, Formation of silver bromide precipitate of nanoparticles in a single microemulsion utilizing the surfactant counterion. J. Colloid Interface Sci. **273**(2), 426–434 (2004)
100. M.M. Husein, E. Rodil, J.H. Vera, Preparation of AgBr nanoparticles in microemulsions via reaction of AgNO3 with CTAB counterion. J. Nanopart. Res. **9**(5), 787–796 (2007)
101. J. Eastoe, M.J. Hollamby, L. Hudson, Recent advances in nanoparticle synthesis with reversed micelles. Adv. Colloid Interface Sci. **128–130**, 5–15 (2006)
102. M.A. Malik, M.Y. Wani, M.A. Hashim, Microemulsion method: A novel route to synthesize organic and inorganic nanomaterials: 1st Nano Update. Arab. J. Chem. **5**(4), 397–417 (2012)
103. J.N. Solanki, Z.V.P. Murthy, Controlled size silver nanoparticles synthesis with water-in-oil microemulsion method: A topical review. Ind. Eng. Chem. Res. **50**(22), 12311–12323 (2011)
104. M.A. López-Quintela, J. Rivas, M.C. Blanco, C. Tojo, Synthesis of nanoparticles in microemulsions, in *Nanoscale Materials*, ed. by L. M. Liz-Marzán, P. V. Kamat, (Springer, Boston, 2003), pp. 135–155
105. C.M. Niemeyer, Nanoparticles, proteins, and nucleic acids: Biotechnology meets materials science. Angew. Chem. Int. Ed. **40**(22), 4128–4158 (2001)
106. J. Jiang, G. Oberdörster, P. Biswas, Characterization of size, surface charge, and agglomeration state of nanoparticle dispersions for toxicological studies. J. Nanopart. Res. **11**(1), 77–89 (2009)
107. A. Ghadimi, R. Saidur, H. Metselaar, A review of nanofluid stability properties and characterization in stationary conditions. Int. J. Heat Mass Transf. **54**(17–18), 4051–4068 (2011)
108. L. Wu, J. Zhang, W. Watanabe, Physical and chemical stability of drug nanoparticles. Adv. Drug Deliv. Rev. **63**(6), 456–469 (2011)
109. C. Lourenco, M. Teixeira, S. Simões, R. Gaspar, Steric stabilization of nanoparticles: Size and surface properties. Int. J. Pharm. **138**(1), 1–12 (1996)

110. M. Iijima, H. Kamiya, Surface modification for improving the stability of nanoparticles in liquid media. KONA Powder Particle J. **27**, 119–129 (2009)
111. H. ShamsiJazeyi, C.A. Miller, M.S. Wong, J.M. Tour, R. Verduzco, Polymer-coated nanoparticles for enhanced oil recovery. J. Appl. Polym. Sci. **131**(15) (2014)
112. M. Ranka, P. Brown, T.A. Hatton, Responsive stabilization of nanoparticles for extreme salinity and high-temperature reservoir applications. ACS Appl. Mater. Interfaces **7**(35), 19651–19658 (2015)
113. D.A. Ersenkal, A. Ziylan, N.H. Ince, H.Y. Acar, M. Demirer, N.K. Copty, Impact of dilution on the transport of poly (acrylic acid) supported magnetite nanoparticles in porous media. J. Contam. Hydrol. **126**(3), 248–257 (2011)
114. C. Barrera, A.P. Herrera, N. Bezares, E. Fachini, R. Olayo-Valles, J.P. Hinestroza, C. Rinaldi, Effect of poly (ethylene oxide)-silane graft molecular weight on the colloidal properties of iron oxide nanoparticles for biomedical applications. J. Colloid Interface Sci. **377**(1), 40–50 (2012)
115. N. Jain, Y. Wang, S.K. Jones, B.S. Hawkett, G.G. Warr, Optimized steric stabilization of aqueous ferrofluids and magnetic nanoparticles. Langmuir **26**(6), 4465–4472 (2009)
116. P.L. Golas, S. Louie, G.V. Lowry, K. Matyjaszewski, R.D. Tilton, Comparative study of polymeric stabilizers for magnetite nanoparticles using ATRP. Langmuir **26**(22), 16890–16900 (2010)
117. A. Tiraferri, K.L. Chen, R. Sethi, M. Elimelech, Reduced aggregation, and sedimentation of zero-valent iron nanoparticles in the presence of guar gum. J. Colloid Interface Sci. **324**(1–2), 71–79 (2008)
118. D.H. Napper, Steric stabilization. J. Colloid Interface Sci. **58**(2), 390–407 (1977)
119. A.-M. Sung, I. Piirma, Electrosteric stabilization of polymer colloids. Langmuir **10**(5), 1393–1398 (1994)
120. B.S.M. Claudio, L. De Castro, Nanoparticles from mechanical attrition. Synth. Funct. Surf. Treat. Nanoparticles, 1–14 (2002)
121. Y. Lu, S. Guan, L. Hao, H. Yoshida, *Review on the Photocatalyst Coatings of TiO2: Fabrication by Mechanical Coating Technique and Its Application*, (2015), pp. 425–464
122. M. Boutonnet Kizling, S.G. Järås, Appl. Catal. A **147**, 1–21 (1996)
123. Z.R. Ismagilov, O.Y. Podyacheva, O.P. Solonenko, V.V. Pushkarev, V.I. Kuz'min, V.A. Ushakov, N.A. Rudina, Catal. Today **51**, 411–417 (1999)
124. C.-J. Liu, G.P. Vissokov, B.W.L. Jang, Catal. Today **72**, 173–184 (2002)
125. H. Shim, J. Phillips, I.M. Fonseca, S. Carabinerio, Appl. Catal. A **237**, 41–51 (2002)
126. S. Hinokuma, K. Murakami, K. Uemura, M. Matsuda, K. Ikeue, N. Tsukahara, M. Machida, Top. Catal. **52**, 2108–2111 (2009)
127. S. Hinokuma, M. Okamoto, E. Ando, K. Ikeue, M. Machida, Catal. Today **175**, 593–597 (2011)
128. S. Hinokuma, M. Okamoto, E. Ando, K. Ikeue, M. Machida, Bull. Chem. Soc. Jpn. **85**, 144–149 (2012)
129. S. Hinokuma, Y. Katsuhara, E. Ando, K. Ikeue, M. Machida, Catal. Today **201**, 92–97 (2013)
130. S. Hinokuma, H. Fujii, Y. Katsuhara, K. Ikeue, M. Machida, Cat. Sci. Technol. **4**, 2990–2996 (2014)
131. S. Hinokuma, H. Kogami, N. Yamashita, Y. Katsuhara, K. Ikeue, M. Machida, Catal. Commun. **54**, 81–85 (2014)
132. S. Hinokuma, N. Yamashita, Y. Katsuhara, H. Kogami, M. Machida, Cat. Sci. Technol. **5** (2015). https://doi.org/10.1039/c1035cy00370a
133. Y. Agawa, S. Endo, M. Matsuura, Y. Ishii, ECS Trans. **50**, 1271–1276 (2012)
134. T. Fujitani, I. Nakamura, Angew. Chem. Int. Ed. **50**, 10144–10147 (2011)
135. K. Qadir, S.H. Kim, S.M. Kim, H. Ha, J.Y. Park, J. Phys, Chem. C **116**, 24054–24059 (2012)
136. S.H. Kim, C.H. Jung, N. Sahu, D. Park, J.Y. Yun, H. Ha, J.Y. Park, Appl. Catal. A **454**, 53–58 (2013)
137. T. Yoshitake, Y. Nakagawa, A. Nagano, R. Ohtani, H. Setoyama, E. Kobayashi, K. Sumitani, Y. Agawa, K. Nagayama, Jpn. J. Appl. Phys. **49**, 015503 (2010)

138. K. Hanada, T. Yoshida, Y. Nakagawa, T. Yoshitake, Jpn. J. Appl. Phys. **49**, 125503 (2010)
139. C. Qin, S. Coulombe, Mater. Lett. **60**, 1973–1976 (2006)
140. A.V. Stanishevsky, E.L. Tochitsky, J. Wide Bandgap Mater. **4**, 297–310 (1996)
141. A.S. Chaus, T.N. Fedosenko, A.V. Rogachev, Ľ. Čaplovič, Diamond Relat. Mater. **42**, 64–70 (2014)
142. B. Naik, S.M. Kim, C.H. Jung, S.Y. Moon, S.H. Kim, J.Y. Park, Adv. Mater. Interfaces **1**, 201300018 (2014)
143. S. Hinokuma, S. Misumi, H. Yoshida, M. Machida, Cat. Sci. Technol. **5**, 4249 (2015). https://doi.org/10.1039/c5cy00636h
144. A. Albanese, P.S. Tang, W.C.W. Chan, The effect of nanoparticle size, shape, and surface chemistry on biological systems. Annu. Rev. Biomed. Eng. **14**, 1–16 (2012)
145. N. Subcommittee of the National Science and T. Council, "National Nanotechnology Initiative Supplement to the President's 2019 Budget," no. August 2018, p. 24, (2019)
146. P. Buffat, J.P. Borel, Size effect on the melting temperature of gold particles. Phys. Rev. A **13**(6), 2287–2298 (1976)
147. J. Jortner, Cluster size effects. Zeitschrift für Phys. D Atoms, Mol. Clust. **24**(3), 247–275 (1992)
148. C.D. Didomenico, M. Lintz, L.J. Bonassar, Molecular transport in articular cartilage - What have we learned from the past 50 years? Nat. Rev. Rheumatol. **14**(7), 393–403 (2018)
149. S.D. Perrault, C. Walkey, T. Jennings, H.C. Fischer, W.C.W. Chan, Mediating tumor targeting efficiency of nanoparticles through design. Nano Lett. **9**(5), 1909–1915 (2009)
150. K. R. Backe, P. Skalle, O. B. Lile, *Shrinkage of Oil Well Cement Slurries*
151. P. J. Boul, P. M. Ajayan, *Nanotechnology Research and Development in Upstream Oil and Gas*, vol. 1901216, (2020)
152. Y. Bu, X. Hou, C. Wang, J. Du, Effect of colloidal nanosilica on early-age compressive strength of oil well cement stone at low temperature. Constr. Build. Mater. **171**, 690–696 (2018)
153. I. Panas, A. Martinelli, A. Matic, Accelerating effects of colloidal nano-silica for beneficial calcium – silicate – hydrate formation in cement. Chemical Physics Letters **392**, 242–248 (2004)
154. X. Pang, P. J. Boul, W. C. Jimenez, *IADC / SPE 168037 Nanosilicas as Accelerators in Oilwell Cementing at Low Temperatures*, no. March, pp. 4–6, (2014)
155. D. Enescu, M.A. Cerqueira, P. Fucinos, L.M. Pastrana, Recent advances and challenges on applications of nanotechnology in food packaging. A literature review. Food Chem. Toxicol **134**(May), 110814 (2019)
156. H. Mu, H. Gao, H. Chen, F. Tao, X. Fang, L. Ge, A nanosised oxygen scavenger : Preparation and antioxidant application to roasted sunflower seeds and walnuts. Food Chem. **136**(1), 245–250 (2013)
157. G.O. Noonan, A.J. Whelton, D. Carlander, T.V. Duncan, Measurement Methods to Evaluate Engineered Nanomaterial Release from Food Contact Materials. Comprehensive Reviews in Food Science and Food Safety **13**, 679–692 (2014)
158. Z. Zhang et al., NanoImpact Development of a standardized food model for studying the impact of food matrix effects on the gastrointestinal fate and toxicity of ingested nanomaterials. NanoImpact **13**, 13–25 (2019)
159. C.G. Otoni, P.J.P. Espitia, R.J. Avena-bustillos, T.H. Mchugh, Trends in antimicrobial food packaging systems: Emitting sachets and absorbent pads. FRIN **83**, 60–73 (2016)
160. H. Chung, M. Yu, Q.P. Nguyen, J. Pet. Sci. Eng. Nanotechnol. Oil Field Appl. Challenges. Impact **157**, 1160–1169 (2017)
161. A. Sánchez Jiménez et al., Safe(r) by design implementation in the nanotechnology industry. NanoImpact **20**(July) (2020)

Chapter 2
Nanoparticles as Potential Agents for Enhanced Oil Recovery

Farad Sagala, Afif Hethnawi, George William Kajjumba, and Nashaat N. Nassar

2.1 Introduction

Conventional oil recovery techniques, like primary and secondary methods, result in roughly one-third of the oil originally in place (OOIP), leaving a significant amount of trapped oil unrecovered [1, 2]. Accordingly, the world reserves are estimated to range up to 1.5 trillion barrels of oil [3]. Thus, it is estimated that this remaining trapped oil after these conventional recovery techniques would be nearly 1.0 trillion barrels [4]. Several EOR techniques commonly grouped as tertiary recovery schemes target this enormous, trapped oil [5–9]. However, getting an appropriate cost and effective approach to obtain this trapped oil after the conventional recovery techniques remains a misery, given that most of the current tertiary practices depend on oil prices [10, 11]. Hence, a search is desirable for viable, cost-effective, efficient and environmentally friendly methods.

Generally, EOR techniques are aimed at increasing the overall recovery factor (RF), which is the product of sweep (E_v) and displacement (E_D) efficiencies. To increase the RF, mechanisms such as oil-water interfacial tension reduction [12], wettability alteration [13] and fluid viscosity enhancement [14] are performed.

F. Sagala · A. Hethnawi · N. N. Nassar (✉)
Department of Chemical and Petroleum Engineering, University of Calgary, Calgary, Alberta, Canada
e-mail: nassar@ucalgary.ca

G. W. Kajjumba
Department of Civil and Environmental Engineering and Construction, University of Nevada, Las Vegas, NV, USA

N. N. Nassar et al. (eds.), *Nanoparticles: An Emerging Technology for Oil Production and Processing Applications*, Lecture Notes in Nanoscale Science and Technology, https://doi.org/10.1007/978-3-319-12051-5_2

Using common EOR methods, for example, chemicals, gas injection, etc., most of these mechanisms can be achieved. Selecting any EOR technique to apply, the objective is to attain any of these mechanisms. A successful EOR design and approach need to be not only efficient and reliable but also cost-effective. However, most of the current techniques are scientifically successful but exceedingly expensive thus paving a gap for searching new alternative approaches to recover the trapped oil in an efficient and cost-effective way.

Recently, effective techniques and approaches using nanoparticle technology are emerging as an alternative agent for improving the performance of EOR and have greatly shifted the perception of investigators towards the application of nanomaterials [15–19]. Nanotechnology refers to the manipulation, characterizing, producing and application of materials by orienting their architecture at the nanoscale [20]. Developments in nano applications have permitted researchers to formulate several exceptional nanomaterials with many probable applications in various fields such as wastewater treatment, medicine, drug delivery, energy, etc. [21–27]. The difference in their application is due to their exceptional orientation that alters their physical and chemical properties in comparison to their bulk counterparts [11]. The number of atoms in bulk materials, at the surface, is substantially less than those in the whole material; this makes their properties constant regardless of their shape and/or size [11]. Nevertheless, reducing the size results in several properties, for example, thermal resistance, catalytic activities, internal pressure, dispersion ability, intrinsic reactivity and quantum optical and electronic properties, all being altered [28]. This is because of the surface area to volume ratio that becomes large; thus the atoms at the surface become significantly more exposed to the surface of the material in comparison to the atoms in the bulk material; hence the surface energy increases [29]. Consequently, because nanoparticles present some propitious characteristics, their surface active sites can be used in various ways which have triggered research using these properties in oil and gas applications [17].

As thus, the instantaneous progress of nanotechnology application in the previous years in various applications has triggered their usage in the oil and gas industry, for various fields such as exploration, drilling, production, EOR, etc. [20, 30]. Because of the increased world energy demand due to the increasing population, researchers have continued to explore the mechanisms of nanomaterials as nanofluids, nano-emulsions or catalysts for hydrocarbons extraction [20], even from non-conventional resources [17].

The use of nanoparticles in EOR has gained attention by numerous researchers worldwide [17, 31, 32]. Nanoparticles can considerably enhance recovery for oil by modifying numerous fluid properties such as modifying the fluid viscosity, reducing the interfacial tension (IFT), improving the thermal conductivity and changing the rock wettability through the fluid-fluid and/or fluid-rock interaction [33–35]. Nanoparticles can be used in solving production challenges such as preventing deposition of asphaltene and wax and overcoming formation damage based on their size and adsorption capacity [36]. Studies on the applicability of nanomaterials in EOR have deduced that, due to their size, these materials can easily penetrate the reservoir pore space where conventional recovery techniques

such as polymers cannot reach. This grants an advantage since these nanomaterials can change the reservoir fluid properties and thus improve and/or enhance oil recovery [36]. Numerous nanoparticle applications in EOR have been performed extensively primarily in labs to understand the mechanism under which nanoparticles can recover trapped oil. The emphasis has been on mechanisms such as interfacial tension reduction [37], wettability alteration [19], oil viscosity reduction [38] and structural disjoining pressure [39] and how these mechanisms can vary with different nanoparticle types, morphologies and nanoparticle concentration. Luky et al. [40] investigated the impact of nanofluid flooding on IFT reduction, permeability reduction, retention of nanoparticles and how these factors can enhance oil recovery. The study was carried out in a glass micromodel under microscopic imagining which indicated that due to the pressure surgency that occurred during fluid injection, nanoparticles become adsorbed on the glass surface. Consequently, nanoparticle adsorption resulted in wettability alteration although there was permeability impairment that was observed. In their study subsequently, nanoparticle morphology, concentration and type were the key parameters that could trigger oil recovery. The author also noted that as nanoparticle concentration increases, IFT reduces but at a cost of impairing the absolute permeability. Ali et al. [41] examined the role of three types of nanoparticles, namely, aluminium oxide (Al_2O_3), titanium dioxide (TiO_2) and silica dioxide (SiO_2), on EOR using limestone rocks at various temperatures. They first investigated the transport mechanism of these nanomaterials in the porous medium and found out that the rate of nanoparticle adsorption on the rock surface was in the order $Al_2O_3 < TiO_2 < SiO_2$ with adsorption rates 8.2%, 27.8% and 43.4%, respectively. They moreover found out that these three nanoparticles could all alter the rock wettability of the limestone core from intermediate to water wet. Moreover, there was a noticeable decrease in oil viscosity in the presence of Al_2O_3 and TiO_2 nanoparticles at 50 °C and 60 °C. Other researchers [17, 42] used different nanoparticle types for EOR introducing different mechanisms. Figure 2.1 shows the enormous diversity of the nanomaterial application derived from their nature, morphologies and shapes. The figure also shows the fluids/media in which nanoparticles can be dispersed, the medium state of the nanoparticles and, notably, the several possible surface modifications the nanoparticles can be exposed to making them an important material in various fields of science. Nonetheless, there are fewer available studies in the literature addressing the amalgamation of the commonly used nanoparticles and their optimization parameters targeting recovery improvement. Therefore, this chapter presents the prospects and major analysis of the recently proposed nanoparticles and/or nanomaterials in EOR. The chapter further shades lights on the underlying oil recovery mechanisms of nanoparticles in EOR, major recovery parameters involved during oil recovery. Moreover, nanofluid stabilization methods applicable to nano-EOR have also been reviewed. Lastly, concerns and uncertainties that have been raised due to nanoparticle exposure have been covered. This chapter is helpful for readers, gaining insight into the enhancement of oil recovery using state-of-the-art concepts and fundamentals for nanofluids.

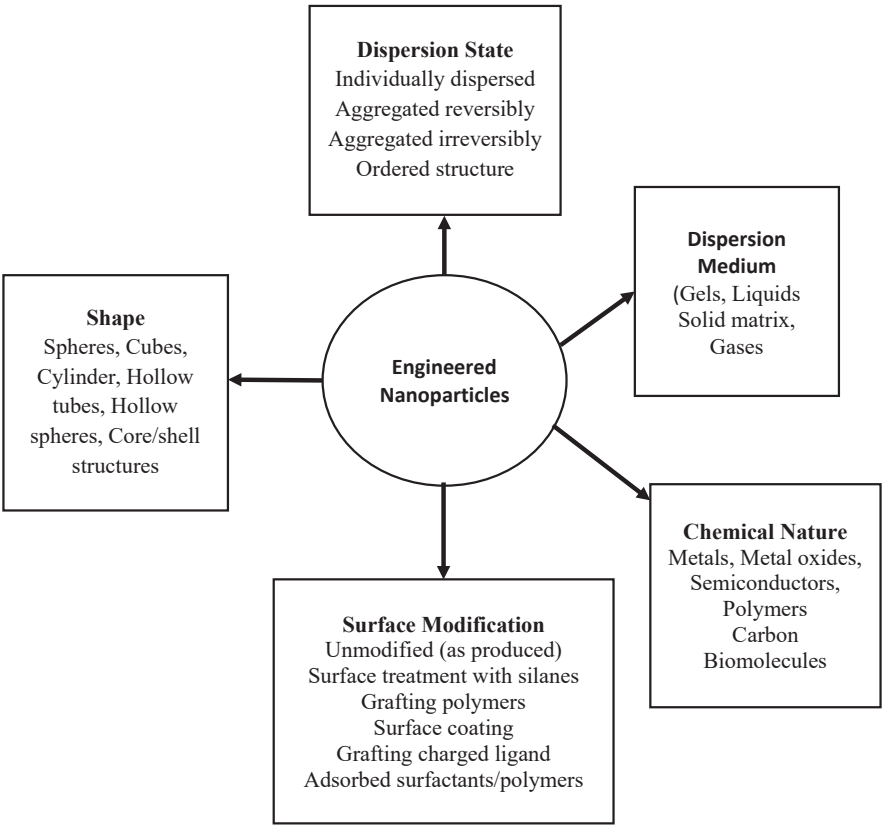

Fig. 2.1 Some of the highlights showing the contribution and diversity of engineered nanomaterials

2.2 Nanoparticle Types Used Commonly in EOR Applications

EOR is influenced by parameters like interfacial tension, viscosity, temperature and density [43, 44]. These parameters further affect the performance of nanoparticles during the EOR process. This section addresses some of the nanomaterials that have been applied in different EOR processes.

2.2.1 Silica Nanoparticles

Silica/silicon dioxide (SiO_2)/quartz is one of the most abundant minerals on Earth and is considered to be environmentally friendly [45] [46]. The thermal and surface area properties of SiO_2 make it an excellent material in EOR processes. SiO_2 hardly

changes at a temperature below 650 °C [47], thus its application in harsh environments during oil recovery [47]. During oil EOR, SiO_2 nanoparticles can be used solely or integrated with various materials [15, 48–50]. Zargartalebi et al. [51] enhanced the performance of an anionic surfactant by using surface-modified hydrophilic and hydrophobic silica nanoparticles. Through interfacial tension (IFT) and adsorption tests, it was revealed that as the concentration of SiO_2 nanoparticles increased, the IFT decreased until the optimal point was achieved—beyond which it remained relatively constant or slightly increased. At low nanoparticle concentration, the repulsive electrostatic forces between the particles and surfactants rev the diffusion of surfactant into the oil medium. In addition, the particles can aid the transportation of surfactants by acting as a carrier. However, as the concentration of nanoparticles increases, the nanoparticle-surfactant surface tension increase might hinder the release of surfactant, thus an IFT increase. Besides, at higher concentrations, the charged nanoparticles aggregate the surfactant causing uneven spreading at the water-oil interface.

Carrier materials also affect the performance of SiO_2 nanoparticles; the rate of adsorption within the matrix attenuates core permeability and alleviates pressure drop. The study of nanosilica adsorption onto limestone, sandstone and dolomite elicited that limestone has a higher adsorption potential (5.50 mg/g) followed by sandstone (1.27 mg/g), and barely any adsorption by dolomite [52]. However, the adsorption of SiO_2 nanoparticles by limestone and sandstone did not affect the permeability of the core. A significant pressure drop was observed in dolomite. To avoid pressure, drop and deformation damage, hydrophobic-lipophilic polysilicon and naturally wet polysilicon can offer a solution because they lower the IFT and wettability alteration. The introduction of hydrophobic-lipophilic polysilicon can reduce the IFT from 26.3 mN/m to 1.75 mN/m, alleviating oil recovery by 32.2%, while wet polysilicon can improve oil recovery by 28.6% [53]. However, care must be taken before such performance is implemented at a large scale. The ameliorated performance can be attributed to the presence of dispersing agents like ethanol that can lower the IFT [54]. Such dispersing agents have lower density compared to water which can attenuate the wetting angle, and they have high solubility of oil. In addition, SiO_2 can block the pores, reducing the oil recovery. That said, the application of SiO_2 nanoparticles in EOR is a promising approach because they are relatively cheap and can be modified from readily available materials like quartz. Table 2.1 summarizes the different SiO_2 nanoparticles and their performance.

2.2.2 Aluminium Oxide Nanoparticles

After silicon and oxygen, aluminium is the most abundant element in the Earth's crust; thus aluminium oxide has been widely investigated in EOR processes [17, 41, 55]. Al_2O_3 nanoparticles achieve EOR by attenuating viscous force [41, 56]. During oil exploration, after secondary flooding, more than 60% of the oil remains trapped in the reservoirs. Al_2O_3 nanoparticles can reduce oil-water IFT and reduce viscosity.

Table 2.1 Summary of studies showing investigated nanoparticle types in enhanced oil recovery

Type and size	Conditions	Reservoir type	Fluid properties	Mechanism of recovery	Remarks/conclusion	References
Silica (20 nm) coated with a zwitterionic polymer	Ambient conditions	Sandstone (Berea) Ø (17%)	Nanofluids 45 wt% DIW	IFT reduction Structural disjoining pressure Wettability alteration	Modified silica better than unmodified in IFT reduction 5 vol % additional oil could be recovered with modified silica	[209]
Silica (7 nm) No surface modification	Ambient conditions	Sandstone (Berea) Ø (15–22%) K (9–400 mD)	Oil 5.01 cP Brine (3.0 wt%) Nanofluids (0.01–0.1 wt%)	Wettability alteration Increasing NP concentration reduced IFT	Higher NP concentration reduces IFT but no additional oil because of pore blockage Increasing nanofluid concentration does not guarantee additional recovery	[16]
Silica (20 nm) No surface modification	Ambient pressure and temperature 55 °C	Sandstone (Berea) Ø (20%) K (400 mD)	Oil viscosity 98.88 cP Brine 20,000 ppm Nanofluids 10 vol% silica	Wettability alteration No noticeable IFT reduction	Structural disjoining pressure mechanism was verified using the formulated fluids 55% oil was recovered by silica nanofluid	[49]
Silica (7 nm) No surface modification	Pressure 1450 psi and temperature 25–80 °C	Sandstone (Berea) Ø (15–19%) K (100–600 mD)	Oil viscosity 5.1 cP Brine 3 wt % Nanofluids 0.05 wt %	Wettability alteration No significant IFT reduction	More oil was recovered from all wettability systems at high temperatures Again, at high temperatures, aggregation of nanoparticles can result in pressure jamming	[210]

Silica (<40 nm) No surface modification	Ambient pressure and temperature 50 °C	Sandstone (Berea) Ø (9.35–11.95%) K (0.68–0.95 mD)	Oil 20.9 Cp Brine (7500 ppm) Nanofluid (5–30 ppm)	Wettability alteration Viscosity reduction by increasing nanoparticle concentration	After nanoparticle adsorption, there was a noticeable increase in irreducible water saturation and Kr_o Additional 4.48–10.33% oil was recovered after nanofluid flooding 10 ppm was the optimum concentration Oil viscosity and asphaltene content were reduced with increasing concentration Low injection rates are suggested for improved nano-EOR	[197]
Silica (10 nm) Surface modified with hexanedioic acid	Ambient pressure and temperature 60 °C	Sandstone (Berea) Ø (14%) K (0.6 mD)	Oil 2.02 Cp Brine (3 wt %) Nanofluid (0.001–1 wt%)	Wettability alteration and IFT reduction	Silica surface was modified to obtain active silica that performed better than conventional silica	[111]
Silica (20 nm) No surface modification	Ambient conditions	Sandstone (Berea) Ø (19%) K (587 mD)	Nanofluid (0.01–0.5 wt%) Oil 4.6 Cp Brine (3 wt% NaCl)	Wettability alteration and IFT reduction	Great potential for using active silica for EOR free from surfactants Silica NPs found compatible with sandstone Extra 13% was recovered during nano flooding Less permeability impairment was noticed at low injection rates	[211]
Silica (5–15 nm) No surface modification	Ambient conditions	Carbonate (chalk) Properties not mentioned	n-Decane Brine (0–20 wt%) Nanofluids (0.5–4 wt%)	Wettability alteration	The exposure time of the nanofluids affects the rate of wettability alteration Adsorption of nanoparticles on the rock surface was found to be an irreversible process	[212]

(continued)

Table 2.1 (continued)

Type and size	Conditions	Reservoir type	Fluid properties	Mechanism of recovery	Remarks/conclusion	References
Silica (7 nm) Surface modified with benzimidazole	Ambient pressure and temperature 80 °C	Sandstone (Berea) Ø (20%) K (54 mD)	Oil 5.0 Cp Brine (5 wt %) Nanofluid (1 wt%)	Wettability alteration No significant IFT reduction	The structural disjoining force was the major mechanism for wettability alteration Additional 38% of the oil was recovered after 100 ppm nanofluid injection Surface modification reduces nanoparticle aggregation	[110]
Silica (8 nm)	Ambient conditions	NA (batch study)	Oil viscosity 120,000 and 2,200,000 cp Distilled water Nanofluids 10–10,000 ppm	Viscosity reduction No significant IFT reduction	Silica (8 nm) nanoparticles yielded the best viscosity reduction at 1000 ppm Oil viscosity reduction increases as the NP size increases	[213]
ZnO (31–36 nm)	Ambient conditions	Packed glass beads	Nanofluids 500–5000 ppm	IFT reduction	Highest oil recovery factor of 11.82% attributed to IFT reduction and wettability alteration	[73]
CNT (16–20.61 nm)	Ambient conditions	Packed glass beads	0.1–0.5 wt% CNT, distilled water Brine 3 wt%	IFT reduction and wettability alteration	Maximum oil recovery of 18.57% was obtained at 0.3 wt% of CNT	[214]

CNC unmodified (3–5 nm)	Ambient conditions	Sand pack and plugs (Ø (33–39%)) K (3–282 mD) Sandstone core Ø (16–17%) K (803–922 mD	0.1 wt% nanocellulose 0.3 wt% NaCl Single-phase flow study	No reported effect of CNP on IFT and wettability alteration	Neither of the two nanocellulose types seemed to adsorb significantly on the sand grains	[97]
CNC unmodified (6 nm)	Ambient pressure Temperature 60–120 °C	Sandstone core Ø (20.33–20.47%) K (803–922 mD)	0.5–2 wt% nanocellulose 0.1 wt% NaCl Oil viscosity 17.6 cp and 4 cp at 20 and 60 °C, respectively	Wettability alteration towards water wet Improving the oil sweep efficiency	CNC improved the sweep efficiency by increasing the brine viscosity Ultimate increase in oil recovery 3.4% OOIP due to CNC injection Difficult to ascertain the main mechanism leading to additional oil recovery	[215]
ZrO_2	Ambient pressure and temperature 70 °C	Carbonate Ø (20%) K (30 mD)	Oil viscosity 64 cts Distilled water Nanofluids 5 wt %	Wettability alteration	ZrO_2 nanofluids are wettability modifiers for carbonate formations Wettability change using ZrO_2 nanoparticles on carbonate rocks surface is a slow process	[82]
Al_2O_3 (40 nm)	Ambient pressure and temperature 70 °C	Carbonate (chalk) Ø (12.2–14.2%) K (0.3–0.13 mD)	Oil 64 Cp Brine 30,000 ppm Nanofluids (5 wt%)	Wettability alteration	$CaCO_3$ and SiO_2 gave better recovery compared to other types of nanoparticles used in this study	[56]

(continued)

Table 2.1 (continued)

Type and size	Conditions	Reservoir type	Fluid properties	Mechanism of recovery	Remarks/conclusion	References
Aluminium oxide (40 nm) Silica (20 nm) Titanium dioxide (10–30 nm) No surface modification	Ambient pressure Temperatures (25–60) ^{0}C	Carbonate (limestone) Ø (43%) K (3.12 D)	Degassed crude 21.7 Cp Brine 2.5 wt % Nanofluid 0.005 wt %	Wettability alteration Viscosity reduction IFT reduction Capillary force reduction	Based on the adsorption studies, Al_2O_3 had the lowest at 8.2%, TiO_2 27.8% and SiO_2 43.4% and this was related to surface charge	[41]
Al_2O_3 (21 nm)	Ambient conditions	Sandstone (Berea) Ø (20%) K (54 mD)	Oil viscosity 5.1 cp 0.05 wt % Brine 3 wt %	IFT reduction Wettability alteration Viscosity reduction	Stability of nanoparticles was improved by adding 1 wt % polyvinylpyrrolidone (PVP)	[58]
Al_2O_3 (21 nm)	Ambient conditions	Sand pack	Oil viscosity 5 cp Brine (30 g/l)	Wettability alteration IFT reduction Reduction of oil viscosity reduction of mobility ratio permeability alterations	Produced oil from alumina oxide NPs was lighter than the injected oil Ethanol was proposed as an alternative dispersing phase for nanoparticles	[17]
Aluminium oxide (35 nm) No surface modifications	2800 psi and temperature 50 °C	Sandstone (Berea) Ø (33%) K (2.19 D)	Heavy oil 64 cP Distilled water Nanofluids (100–10,000 ppm)	Wettability alteration IFT reduction	Nanoparticles were dispersed in SDS surfactant Performance of anionic surfactants can be improved by adding alumina NP with lower ratio	[19]
Al_2O_3 (21 nm)	Ambient conditions	Sandstone (Berea) Ø (17%) K (110 mD)	Brine 2.5 wt % Oil viscosity 40.38 cp Nanofluids (1–4) wt%	IFT reduction Wettability alteration	Al_2O_3 change the rock wettability from water-wet to a neutral wet state	[216]

γ-Al_2O_3 (>40 nm)	Ambient conditions	Sand pack	Nanofluids 0.1–1 wt % Brine (NaCl) DIW	Foam enhancement	Additional 14% recovered with the presence of Al_2O_3 nanoparticles	[147]
Alumina coated silica (20 nm)	Ambient conditions	Berea sandstone Ø (18–22%) K (125–606 mD)	Nanofluids (0.05–1 wt%) Oil viscosity 30 cp	Foam stability	Irreversible adsorption of NPs on the air-water interface resulted in foam stability 70–75% additional oil was recovered	[217]
Nanocellulose 0.8–1.2 μm No surface modification	Ambient pressure and temperature	Micro-glass model	Oil 80.4 Cp Brine 1 wt % Nanofluid 0.005 wt %	Nanocellulose improved the viscosity of the injected fluid IFT reduction in order of 10^{-1}mN/m	Nanofluids showed superior thickening ability and pronounced shear thinning property	[96]

With the right size, Al_2O_3 emulsify into an aqueous solution like sodium dodecyl sulphate; the emulsification of the particles can plummet the IFT to ultralow which enhances oil recovery. Emulsification is affected by particle size. When a nanofluid consisting of small Al_2O_3 nanoparticles was used to ameliorate oil recovery, a 63% improvement was registered compared to a nanofluid composed of large Al_2O_3 nanoparticles [56]. In another experiment, Al_2O_3 nanoparticles offer excellent wettability properties [19]. Al_2O_3 achieves wettability abilities by altering the contact angle which soars the water-wet conditions compared to oil-wet conditions. The enhancement of water-wet conditions results in the imbibition of water that restores the original core wettability conditions. When anionic surfactant was mixed with Al_2O_3, the residual water saturation of sandstone core improved from 7.0% to 23% by adding 0.1 g/L of nanoparticles [19]. Like SiO_2, Al_2O_3 barely achieves ultralow IFT and can affect the permeability of the core by aggregating in the pores [57]. Besides, Al_2O_3 nanoparticles have been reported to be unstable in strong ionic liquids like brine [58]. Although the process is slow at ambient conditions, brine facilitates the dissolving of Al_2O_3 to $AlCl_3$.

2.2.3 Nickel Oxide (NiO) Nanoparticles

During oil production and transportation from the reservoir, asphaltene, the solid compound of oil, is one of the major problems. Asphaltene aggregates in the core blocking the transportation of oil. NiO nanoparticles are promising materials to overcome the asphaltene challenge. NiO has a high binding for asphaltene and can disaggregate it from oil medium. When combined with CO_2, NiO nanoparticles enhance permeability and porosity of a core which ebb the precipitation of asphaltene in the core medium [59]. The dispersants can have a significant impact on the performance of NiO nanoparticles because they influence the angle and wettability properties. A comparison of water, brine, ethanol and diesel as NiO dispersants elicited that the presence of ethanol maximizes the EOR process [17]. NiO enhances oil recovery through viscosity attenuation. Modifying NiO with polymers can increase the sweep efficiency by increasing the stability of the nanofluid. When NiO nanoparticles were coated with xanthan polymer and flooded in the sand packed reactor, the recovery increased from 4.48% (NiO alone) to 5.98% [60]. The boosted performance is attributed to the reduction of viscous force.

2.2.4 Iron Oxide Nanoparticles

As mentioned earlier, asphaltene is one of the major causes of oil losses during exploration. Nanomaterials that can attenuate aggregation and/or adsorb asphaltene are of a great deal. Iron oxide nanoparticles offer an excellent solution owing to their high specific surface area, magnetic and catalytic properties [61, 62] [63].

Albeit metal oxides are promising asphaltene adsorbent in the reservoirs, the question is what happens to the metal oxide-asphaltene precipitates. The conversion of asphaltene to eco-friendly by-products like hydrogen can enhance the economic production of oil. The application of Fe_3O_4 nanoparticles revved the adsorption of asphaltene, and when gasification of adsorbed asphaltene, Fe_3O_4 presence attenuated the gasification temperatures from 500 °C to 380 °C [64]. The abatement of thermal temperatures validates the fact that Fe_3O_4 nanoparticles catalyse the conversion/cracking of asphaltene. Fe_3O_4 nanoparticles achieve this by lowering the activation of energies. When compared to NiO and Co_3O_4 nanoparticles, Fe_3O_4 offers the least reduction in activation energies [64]. However, the cost and ease of Fe_3O_4 production can offset this disadvantage.

2.2.5 Zinc Oxide (ZnO) Nanoparticles

The application of ZnO in enhancing oil recovery is still unsatisfactory as several researchers reported its unfavourable impacts on reservoir permeability [17]. These nanoparticles are known to display antibacterial, antifungal, UV filtering and anticorrosive properties. ZnO has many other applications such as rubber making [65, 66] and ceramic industry because of its higher density (5600 kg/m^3) [67]. Its other applications include acting as an additive for cement and in paints as a coating agent [68, 69]. Hassan et al. [70] reported some promising results of ZnO nanoparticles in EOR applications by recovering an additional 11.8% of oil initially in place. Their findings are questioned since the 0.05–0.5 wt% concentration of ZnO used in their study just resulted in only 2% IFT reduction. Although they concluded that this was the major mechanism for oil increment, this reduction is very insignificant to remobilize any trapped oil due to capillary forces. Moreover, the authors did not report any wettability measurements before and after the adsorption of the nanoparticles on the rock surface. Besides, the concentration of ZnO used by the authors was so high, and no experimental evidence was reported for the effect of this concentration on the rock properties since previous studies such as Ogolo et al. [17] had earlier reported the effect of such nanomaterials on the rock properties.

2.2.6 Zirconium Oxide (ZrO_2) Nanoparticles

ZrO_2 are another group of nanoparticles that elicit performance in EOR processes. ZrO_2 is a semiconduction material with catalytic, water-insoluble and low thermal conductivity properties. The ability to be moulded into different shapes (e.g. cubic, tetrahedral and amorphous) makes ZrO_2 an excellent candidate in EOR processes. ZrO_2 elicit significant EOR from carbonate cores by alternating the oil-water and water-wet properties. Addition of 0.05 wt% ZrO_2 enhanced oil recovery by changing oil-wet to water-wet properties [71]. The attenuation of contact angle from 152°

to 44° facilitates the movement of oil from the core. ZrO_2 also displays superior chemical and physical stability compared to silica and γ-alumina nanoparticles [72]. Albeit ZrO_2 show good performance in carbonate reservoirs, the behaviour of these nanoparticles in other cores need to be elucidated.

2.2.7 Carbon-Based Nanoparticles

Among the most common carbon materials expended in EOR include graphene oxide, carbon nanotubes (CNTs) and cellulose owing to their ability to reduce IFT, viscosity and wettability alternation, thus their ability to proliferate oil recovery. When used in the presence of polymers, carbon-based nanoparticles can enhance the thermal stability and improve the polymer aging resistance. With the addition of 300 mg/L of graphene oxide in 1700 mg/L of acrylamide-based polymer, the thermal stability increased from 90 °C to 135 °C, while the viscosity of the mixture was attenuated within 30 days [73]. The use of multi-walled CNT in water flooding experiments at 0.05 wt% improved the oil recovery to 31.8%, due to their hydrophobicity, with reported contact angle of 136° [74]. The presence of varying charge density on cellulose makes it a good material to reduce IFT, and the higher the charge density, the higher the EOR. Comparison of cellulose nanoparticles with charge density 0.72 and 1.51 meq/q elicited greater performance for cellulose with higher charge density because of their ability to form homogenous nanofluid. However, the performance of cellulose is attenuated in a saline environment, and their ability to adsorb on a rock further inhibits their implementation [75]. The adsorption causes pore closure and aggregation in the core. Table 2.1 summarizes the different metal and carbon-based nanoparticles that have the potential to be applied in EOR processes.

2.3 Nanoparticle Stabilization for EOR Application

Nanoparticles are classified as particles with various particle crystallinity with different shapes, sizes, surface areas and chemical compositions [76]. As their particle dimension reduces, the number of atoms at their surface increases exponentially resulting in a higher surface area compared to the bulk material. Nanomaterial can be modified to become hydrophilic, hydrophobic or double-faced (Janus) depending on their selected application, stabilizers or modifying agent used [77]. Nanoparticles for EOR applications in most cases are dispersed in fluids such as oil, deionized water and brine or gas to formulate nanofluids. However, in most cases because of their sizes and shapes, they are not stable and tend to aggregate forming sediments or clusters that diminish their dispersity [78]. Due to this aggregation and/or precipitation, large particles with non-uniform size distribution tend to form clusters, creating practical challenges and limitations for further applications [42, 58]. Accordingly, particle morphology, topology and size distribution require

monitoring to avoid aggregation that may limit their application. Destabilization of the agglomerated particles should be avoided to guarantee an outstanding performance of the nanoparticles in EOR. An increase of agglomerated particle size results in continuous destabilization of nanoparticles and several mechanisms can be involved. These mechanisms can quantitatively explain the stability of the colloids in terms of the energy barrier. This energy barrier represents the difference between the repulsion and the attraction energy as presented in Fig. 2.2. Significantly, overcoming this energy barrier would result in the particles approaching each other and hence coming into contact. The DLVO (Derjaguin, Landua, Verwery, and Overbeek) theory accurately describe the stability of the colloidal suspension by accounting for (1) aggregation of the colloidal particles, (2) the interaction among the ionic particles under aqueous conditions, and (3) the net force between the attractive van der Waals (vdW) force and the repulsive force generated by the double layers of other particles. Considering the previous points, DLVO Theory can observe the stability mechanism of the colloids in terms of energy barrier, which can be resulted from the difference between the repulsion and the attraction energy as shown in Fig. 2.2. As shown, the figure briefly visualizes two possible scenarios for the repulsion of the particles. In the first scenario (Fig. 2.2a), the repulsion force tends to be large, while in the second case (Fig. 2.2b), it is reduced, while the net total energy for both figures is presented by the solid line. For the first scenario, the

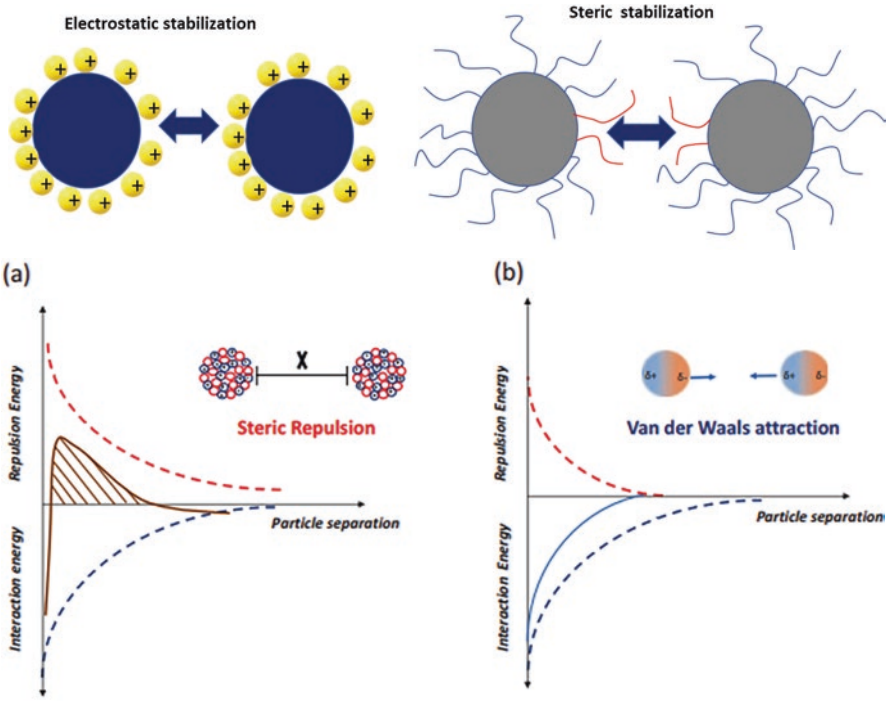

Fig. 2.2 Schematic representation of the stability mechanism according to DLVO theory, (**a**) with energy barrier and (**b**) without energy barrier. The schematic was drawn based on the concept presented in reference [83]

net energy curve holds a repulsion force that must be overcome when the particles are interacted by van der Waals attraction, such that exceeding the energy barrier (the area under the solid line) by destroying the net force that prevents the particles from interacting with each other, subsequently allows the particles to get attracted by van der Waals force. On the other hand, as shown in the second figure, overcoming the energy barrier is achieved at which the colloidal particles are rapidly flocculated by micro-flocculation. Hence, the determination of the stability mechanism highly depends on the ions present in the aqueous media as well as the actions of functionalizing agents that are vastly reported to functionalize the unstable particles. These agents can be considered as the driving force for using the nanoparticles in EOR. Therefore, the use of various additives have been reported, which include stabilizing agents like polymer or surfactant [79–81]. Changing the ionic strength around the colloidal particles has a significant effect on the stabilization mechanism. For instance, the stability of the nanoparticles can be reduced by double-layer compression, which causes a change in the ionic strength induced from the addition of different electrolytes, resulting in destabilizing of the colloids under unstable conditions [82]. Consequently, colloids get close to each other with the presence of thin electric double layers that contribute to overcoming the energy barrier and subsequent aggregation of the colloid's particles. More reduction of a double layer can be achieved if salts of counter-ion are added, exceeding double-layer repulsion that leads to coagulation of particles. Charge neutralization is one more mechanism that can cause lower stability for the nanoparticles. Charge neutralization is often carried out by absorption of metal hydrolysis species on the particle surface, such that a negative surface charge can be neutralized by using a positively charged ligands. To avoid exceeding the energy barrier through charge neutralization or double layer reduction, determination of zeta potential of the colloidal particles has to be an important concept [83]. It is essential to estimate the optimal dosage needed for a near point of zero charge of the particles. The stability of the nanoparticles can be enhanced via effective control of the zeta potential. This can be achieved by coating the nanoparticle surface with organic material such as surfactants and/or polymers that provide a steric repulsion between the nanoparticles.

2.4 Commonly Used Stabilization Techniques for EOR Application

Some stabilization techniques have been proposed to improve the stability and dispersibility of these nanoparticles, especially for EOR applications. These include ultrasonication, steric and electrostatic stabilization [84]. In the *ultrasonic* technique, nanoparticles are dispersed in liquids, such as water, oil or resins using a sonicator. The use of the ultrasonic method to stabilize nanomaterials has various advantages, among them is the homogenous dispersion of the materials in the liquid which can prevent the particles from precipitating [85].

On the other hand, electrostatic stabilization of nanoparticles is another technique for stabilizing nanoparticles when dispersed in a fluid. An illustration of this technique is shown in Fig. 2.2a based on the DLVO (Derjaguin, Landau, Verwey and Overbeek) theory [86]. When two particles are in contact, their interaction is linked to the repulsion potential of both the van der Waals and electric potential. It is important to note that one of the limitations of electrostatic stabilization is the fact that it is mostly applicable to only dilute systems. Also, other characteristics include, not being applicable to electrolyte sensitive systems, the agglomerated particles being hard to re-disperse and being difficult to apply in multiple phase systems.

Steric stabilization also referred to as polymeric stabilization is another technique commonly used for nanoparticle stabilization; it involves the addition of inhibitors such as surfactants and polymers or other modifiers that prevent nanoparticles from aggregating in suspensions by creating a favourable force of repulsion between the nanoparticles [87, 88]. As shown in Fig. 2.2a, adding polymers or surfactants covers the system in such a way that the long tails extend out into the solution improving the repulsive forces of attraction [89]. Colloidal particle stabilization via polymer encapsulation has been reported by researchers to greatly improve nanoparticle stability. This is because the nanoparticles stabilized by specific types of polymers such as polyampholyte and polyelectrolyte can remain stable even in harsh reservoir conditions [90]. Mikhil et al. [90] found out that nanoparticles stabilized with polyampholyte-based polymers can be used in reservoirs with higher salinity up to 120,000 mg/dm^3 and high temperature up to 90 °C with long-term colloidal stability. Also, polyelectrolyte polymers such as poly(acrylic acid), poly(vinyl pyrrolidone) or poly(styrene sulfonate) can be used to provide electrostatic repulsive force between nanoparticles and stabilize them in higher brine scenarios [91]. Nanoparticle encapsulation using polymers can be accomplished in two ways, i.e. "grafting from" and "grafting to" methods. With grafting from, the coating is achieved by first immobilizing an initiator on the nanoparticle surface, and then polymerization of the corresponding monomer follows. For grafting to, the encapsulation is achieved by grafting the polymer on the surface of the nanoparticle via electrostatic interaction which is the easier approach in most cases. For oil and gas application, polymers are coated on nanoparticles' surfaces using the grafting to technique [89]. In this method, polymers with functional groups that are reactive with groups on surfaces of nanoparticles are used to achieve the modification. These groups can include alcohols, carboxylic acid, silane, amine, phosphoric acid, etc. [92]. Various types of polymers have been used by different researchers for nanoparticle stabilization. For instance, Barrera et al. [93]. investigated the effect of poly(ethylene oxide)-silane on the suspension properties of iron oxide nanoparticles. The authors used an X-ray photoelectron spectroscopy initially to obtain information on the chemical nature of the nanoparticle surface before grafting; the surface consisted of a mixture of amine groups and grafted polymer. They found out that the exposure of the amine groups on the surface of the nanoparticle decreased as the polymer molecular weight increased. This indicated that the particles obtained consisted of single iron oxide cores coated with a polymer brush. The DLVO theory was used to analyze the particle stability considering electrostatic, magnetic, steric

and van der Waals interactions. Experimental results and suspension stability theory indicated that stability was achieved after the grafting process [93].

Nirmesh et al. [52] stabilized aqueous ferrofluids and magnetic nanoparticles of 6–8 nm diameter by grafting polyacrylamide copolymer (PAM) to form a thinnest steric stabilized layer attached to the iron oxide surface. The thermogravimetric analysis (TGA) showed an increase in weight of the dried particles with a consistent polymer coating of a 1 nm thickness which confirmed the existence of the polymer on the surface of the particles. The mass spectrometry and the dynamic light scattering were consistent with 4–5 nm increase in the hydrodynamic radius of the grafted nanoparticles, and the magnetization experiments indicated nonmagnetic surface layers which resulted from the attachment of poly(acrylic acid) block to the nanoparticle surface [52]. A similar study, conducted by Patricia et al., stabilized magnetite nanoparticles using polyelectrolyte polymer types; the colloidal stability of the particles was assessed by measuring the turbidity of the sediments after a given time of increasing the ionic strength. The sedimentation results were supported by conducting the dynamic light scattering measurement of the particle hydrodynamic diameter that remained suspended. At high PH, the polymers used because of their coordinative interaction with iron oxide surface improved the particle stability. The author's investigation provided a guideline for the design of polymeric stabilizers for magnetite nanoparticles according to the PH and ionic strength of the intended applications [33].

Sterically stabilized systems even under circumstances where the zeta potential of the system is close to zero remain well dispersed in the solution even with high brine salt concentrations [95]. Steric stabilization effectiveness is mainly attributed to the thermodynamics that results from adding polymeric chains to lesser volumes [96]. In comparison, steric stabilization since its thermodynamic method has some advantages over the electrostatic stabilization technique. Unlike electrostatic stabilization, in steric stabilization, particles can be re-dispersible and more enhanced stability can be achieved. Moreover, with this method, a higher nanoparticle concentration can be used, it is also not sensitive to electrolytes compared to the electrostatic method, and it is suitable for multiple phase systems. Notwithstanding the advantages of steric stabilization over the electrostatic method, using surfactants and polymers as stabilizing agents makes the underlying mechanism due to the presence of nanoparticles difficult to predict. Surfactants influence wettability alteration and oil-water IFT properties, while polymers affect nanofluid viscosity. Therefore, using them as stabilizing agents makes it hard to identify whether nanoparticles or surfactant/polymers contributed to the EOR process.

Electrostatic stabilization can also be amalgamated with steric stabilization to obtain a new technique normally referred to as electrosteric stabilization [100]. With this mechanism, aggregation of nanoparticles is prevented by the combined effects of electrostatic and steric stabilization usually associated with the adsorption of polyelectrolytes onto the particle surface. This can be achieved by attaching polymers/surfactants to a charged particle surface. In such situations, when two particles approach each other, both steric and electrostatic repulsion prevent the nanoparticles from agglomerating. Using both steric and electrostatic stabilization helps to make use of the unique qualities of each method. Electrostatically stabilized

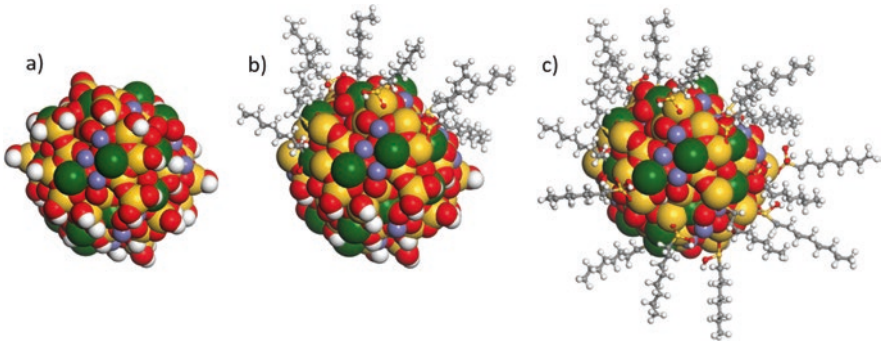

Fig. 2.3 (**a**) Representation of a 2 nm nanoparticle of pyroxene showing the hydroxylated surface. (**b**) Representation of half of the pyroxene nanoparticle reacted with the triethoxy(octyl)silane (ball and stick) anchored by the hydroxyls present on the surface. (**c**) Representation of the total pyroxene nanoparticle reacted with the triethoxy(octyl)silane (ball and stick) anchored by the hydroxyls present on the surface [114]. Permission related to the material excerpted were obtained from the American Chemical Society (ACS) and further permission should be directed to ACS

dispersions are kinetically stable but are very sensitive to the presence of electrolytes, while sterically stabilized dispersions are thermodynamically stable and are much less sensitive to the presence of electrolytes [100].

Ligand incorporation is another stability approach commonly used in the formulation of stable nanofluids. With this method, different organic functional groups are grafted on the surface of nanoparticles to improve their stability and dispersive ability in different solvents [101]. Organic ligand incorporation, in general, is among the most common method used to produce stable nanofluids especially for EOR application [102]. Commonly used ligands depending on their functional groups include carboxylic acid, amines, phosphonic acid, silanes and thiols [103–106]. A chemical reaction is one of the commonest strategies used to incorporate these organic ligands on the surface of the nanoparticles. With this approach, organic ligands are chemically bonded on the surface of the nanoparticles, and depending on the reaction condition, ligands form various types of interactions with the surface of the nanoparticle. For example, ligands with carboxylic acids-based ligands form three types of interactions, while phosphates functional groups can be modified with metal oxides via different five interaction modes [107, 108]. For the silane coupling agents with alkoxy groups and organic functional groups, they use the OH group on the nanoparticle surface as the reactive sites during the interaction as shown in Fig. 2.3. The silane coupling agents improve nanoparticle stability by introducing various organic functional groups on the particle surface that prevent them from aggregating. Organic ligands can also be anchored on the surface of the nanoparticles via the formation of non-chemically bonding interactions. In such scenarios, the ligand forms a weak bond complex via electrostatic interaction or van der Waals forces. For the case of carbon nanotubes (CNTs), surface modification via ligand incorporation can be achieved via various chemical reactions such as oxidative coupling, cycloaddition, halogenations and reductive [109]. Moreover, electrostatic stabilization combined with ligand incorporation has been reported as an effective way of obtaining more stable nanofluids especially for EOR applications

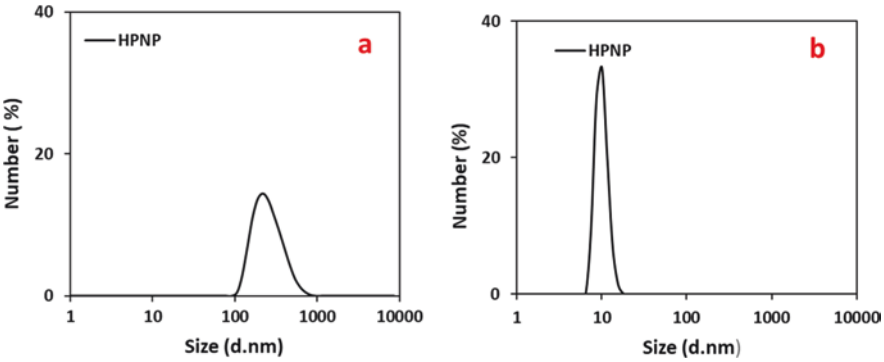

Fig. 2.4 Nanofluids of nanopyroxene functionalized with (**a**) triethoxy(octyl)silane pH 6.5 and (**b**) same solution pH adjusted to 9 [113, 115]. Permissions related to the material excerpted were obtained from ACS and further permission should be directed to ACS

[110–112]. As shown in Fig. 2.4, the nanofluids of nanopyroxene were functionalized with triethoxy(octyl)silane to generate hydrophobic pyroxene nanoparticles (HPNP). Changing the pH of the solution from 6.5 for solution (a) to 9 for solution (b) significantly improved the nanoparticle stability [113].

The difference between surfactant, polymer and ligand incorporation in nanoparticle stabilization is that in situations where the surfactant is used, as the name indicates, surfactants are surface-active materials. They chemically react with the surface of nanoparticles; thus the nanoparticle size does not increase since surfactants have shorter chain molecules with a polar head and hydrocarbon or non-polar chains. Surfactant heads attach to the surface of the nanoparticle, while the chain remains free to move in the surrounding medium. Polymers have large chains which entangle the particle and thus increase the size that results in modifications of nanoparticle properties. In situations where a capping agent or ligand is used, it just encloses the particle and does not react with the surface, therefore no effect on the nanoparticle morphology. However, for application purposes, the selection of either polymer, surfactant or ligand depends on various factors such as nanotype and intended application. For example, if nanoparticles are to be used for applications where we do not want much rise in viscosity, the surfactant is preferable. While for several promising biomedical applications capping by biomolecules is preferable, for oil recovery applications other factors such as compatibility with reservoir conditions may come into play.

2.5 Mechanisms of Enhancing Oil Recovery Using Nanoparticles

Various mechanisms of nano-EOR have been stated recently by various researchers using nanoparticles as nanofluids, nano-emulsions or catalysts. The most commonly reported and proposed mechanisms are detailed below.

2.5.1 Alterations of Wettability

Among the parameter that affects oil recovery includes wettability. Reservoir rock wettability plays a vital role during oil recovery [19, 116, 117]. It is one of the fundamental elements that influence the water flooding process, oil-water relative permeability, capillary pressure, residual oil saturation, tertiary oil recovery and control of the spatial fluid flow and dissemination in porous media [118]. Irrespective of the rock composition, most reservoirs are believed to have a mixed wettability system, meaning they are not completely oil wet or water wet [19]. It is normally preferable for the rock wettability to be changed to water wet during oil recovery since it can improve the water imbibition process. This can enhance oil recovery especially in the course of brine flooding [119]. However, during oil production, as the rock and fluid interact, the rock wettability changes to another state mostly oil-wet or intermediate wet state. Alteration of wettability to oil wet can also occur during drilling, for example, when using oil-based drilling fluids, wettability of the formation can switch to either oil wet, mixed or intermediate wet [120]. This happens because of the interactions and surface adsorption of the oil-based drilling fluids at the rock interface which results in a new wettability state at the rock surface [121]. Contact angle measurement is the commonest approach applied to study rock wettability. Contact angle measurements are typically taken with reference to the denser phase when either a liquid or gas is in contact with a solid surface. As a rule of thumb, based on Anderson, a surface is water wet when the measured contact angle via a denser phase is 0–75^0 and intermediate if 76–120^0 or oil wet if the contact angle is 120–180^0 [98]. Equation 2.1 illustrates the relationship between the solid and fluid in contact defined by the coefficient S. This spreading coefficient (S) can be defined in terms of the IFT between the present phase, in the case of oil, water and solid; S is written as Eq. 2.1.

$$S = \partial_{O/S} - \partial_{W/S} - \partial_{O/W} \tag{2.1}$$

where $\partial_{O/S,}$ $\partial_{W/S}$ and $\partial_{O/W}$ are the interfacial forces between oil, solid and water, respectively. The change in contact angle depends on the force imbalance at the interface; a water-wet system can be created when the spreading coefficient S is low due to lower IFT at the water-oil interface that can give a higher contact angle [98]. Also, the adhesion equation (Eq. 2.2) can be used to explain the effect of wettability alteration.

$$W = \partial\left(1 + cos\theta\right) \tag{2.2}$$

where W is the adhesive force retaining oil on the rock surface (mJ/m^2), ∂ is the IFT between oil and nanofluids (mN/m), θ is the contact angle of oil/rock surface/nanofluids (degree). From Eq. 2.2, the adhesive force responsible for holding oil on the rock surface W decreases as the wettability is altered towards water wet; this indicates that crude oil can easily flow, hence improving oil recovery. Recent, findings have proved that nanoparticles when dispersed in various fluids can change the rock fluid contact angle and change reservoir rock wettability towards stronger water-wet

conditions. Munshi et al. [122] used different nanoparticles of different types and sizes to determine their effect on contact angle. Indium oxide (IO) nanoparticle coated with Si substrates was used with demineralized water and diethylene glycol (DEG). The authors found out that nanoparticle size has a stronger effect on the contact angle.

For nanoparticles in size range from 14 to 620 nm, their contact angle varied between 24° and 67° when using deionized water droplet, and the angle varied between 15° and 60° for the nanofluid. They also noted that for the two fluids, the contact angle decreased as particle size reduces. Moreover, the attachment of nanoparticles on the rock surface can reduce the rock permeability which can affect the oil recovery. Therefore, optimal sizes and concentrations of nanoparticles are always desirable for effective performance. Wettability alteration and contact angle are mainly affected by the size, type, concentration and morphologies of the nanoparticles used. However, nanoparticle size can affect the transportation and adsorption capability of the nanoparticles in the porous medium. In a study conducted by Jianjia et al. [53], using 0.5 wt% silica nanofluids with three porous media to study the transportation, retention and adsorption characteristics of silica nanofluids in these reservoir formations, the results indicated that equilibrium adsorption was in the order sandstone > limestone > dolomite as 1.272, 5.501 and 0 mg, respectively. However, the authors noticed that these nanoparticles could easily flow in the sandstone medium without damaging the permeability in comparison to limestone and dolomite. Although there was noticeable adsorption of the nanoparticles in the limestone sample, no significant permeability damage was detected. Nevertheless, pressure drop was detected during the flooding experiments which showed that nanoparticle plugging could have taken place and permeability damage might have transpired.

Although surfactants alone are always used for wettability alteration, the integration of nanoparticles with surfactants has reported improved results compared to using either nanoparticles or surfactants alone. Karimi et al. [82] examined the role of zirconium oxide (ZrO_2) nanofluids when used as a wettability modifier in carbonate rock. Several nanofluids were prepared to contain ZrO_2 and a surfactant. Nanoparticle concentrations in the range of 1–5 wt% were applied for the study. After treatment with the nanofluids, the contact angle measurements showed that the nanofluids could change the rock wettability to a water wet, resulting in improved oil recovery. In another study performed by Juliana et al. [19], they integrated alumina-based nanofluids with an anionic surfactant in the range of 0.01–0.1 wt%. Wettability alteration was assessed by contact angle measurements and running imbibition tests. Results indicated that the nanofluids could alter the sandstone wettability to strong water wet. It was deduced that the efficiency of surfactants can be improved by combining them with nanoparticles at lower concentrations for wettability alterations.

Rasoul et al. [56] conducted a comparison study using different types of nanoparticles to change the carbonate rock wettability. The effect of different nanoparticles such as zirconium dioxide calcium carbonate, titanium dioxide, silicon dioxide, magnesium oxide, aluminium oxide, cerium oxide and carbon nanotubes on the

carbonate wettability was assessed by contact angle and imbibition tests. The results from the batch and continuous experiments confirmed silicon dioxide and calcium oxide as the best agents for EOR applications in carbonate reservoirs. Capillary pressure measurements moreover indicated an increase in irreducible water saturation after treatment with $CaCO_3$ nanofluids. Although the core flooding experiments were conducted at ambient conditions, reliable results may be obtainable when similar studies are performed at reservoir conditions.

2.5.2 Nanoparticle Application for Viscosity Reduction

Reduction of oil viscosity during oil production processes is important. In general, the maximum classical desired pipeline oil viscosity should not be more than 400 mPa·s at room temperature [123–125]. This is not the case however in many situations, and various approaches are suggested on how to reduce the oil viscosity. To reduce the heavy oil viscosity, thermal techniques are typically used for oil viscosity reduction [14]. Nanoparticles based on their catalytic and heat transfer abilities are being used during these thermal recovery processes to enhance their performance. Nanoparticles can work as catalysts during heavy hydrocarbon cracking and/or as an adsorbent for asphaltene disaggregation [42]. Studies have examined the application of nanomaterials during thermal recovery and promising results have been obtained. Wei et al. [126] applied nickel catalyst during heavy oil recovery by aquathermolysis process. The nanoparticles were prepared using a methylcyclohexane-water-n-octanol-AEO_9 emulsion system. It was noticed that nickel nanoparticles could work as catalysts during the aquathermolysis process. The results demonstrated that the molecular weight of the sample that was upgraded decreased significantly compared with the original crude oil sample. Moreover, the sulphur content dropped to 0.23% from 0.45%, and the resin and asphaltene content also reduced noticeably. After the upgrading reaction, the presence of the surfactant resulted in the formation of an emulsion type II water in oil (w/o) which further reduced the original crude viscosity to 2400 mPa·s at 50 °C. This was approximated to be 98.90%, demonstrating the capability of nickel catalysts as viscosity-reducing agents during heavy oil recovery. Esteban et al. [127] in another study used alumina and silica based nanoparticles for reducing the heavy crude oil viscosity. The impact was assessed by running asphaltene adsorption experiments with UV dynamic light scattering and vis spectrophotometry. In their study, the authors selected silica nanofluid because it had better adsorption capability for asphaltene during the batch experiments. 2.0 wt% of the surfactants were added to assess the surfactants' effect in the presence of the silica nanoparticles on oil viscosity reduction. Increasing the concentration of nanoparticles up to 1 wt% resulted in almost 90% viscosity reduction. The authors noted that the effectiveness of reducing the heavy oil viscosity can be enhanced by increasing the nanoparticle concentration which has also been reported elsewhere [78]. The core flooding tests also showed an improvement of 16% after primary recovery. They concluded that adsorption of the asphaltenes by

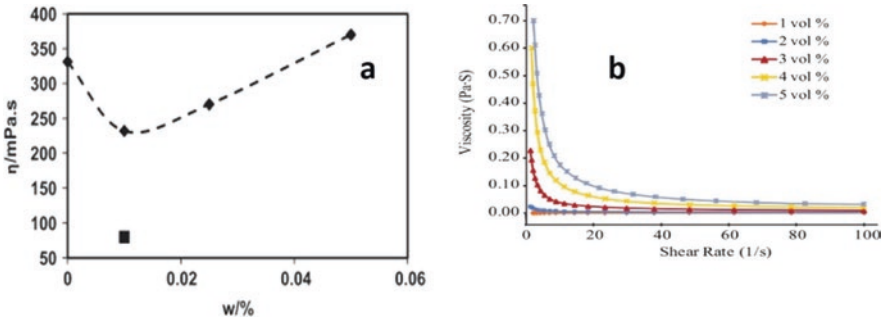

Fig. 2.5 Effects on nanoparticle concentration on viscosity **(a)** and **(b)** effect of shear rate on viscosity for different volumes of nanoparticle [128, 129], respectively. Permissions related to the material excerpted were obtained from Elsevier and further permission should be directed to Elsevier

nanoparticles is the main mechanism for reducing oil viscosity during heavy oil recovery. This study evidenced that a matrix of nanoparticle and surfactant fluid is more effective than surfactants or nanoparticles alone.

Esteban et al. [78] used different nanoparticles of various chemical nature that comprised of silica, iron oxide and aluminium oxide, and fascinating results were obtained. In their study, viscosity reduction in all cases assessed was noticed. A maximum viscosity reduction of 52% was obtained when 0.1 wt% silica nanoparticles were used. The authors pointed out that particle size, concentration and shear rate prejudiced changes in viscosity. As the particle size increases, viscosity reduction becomes insignificant, since the packing factor of the bigger nanosized flocks after aggregation results in less contact. Nevertheless, the changes in the fluid structure internally due to the increase in the shear rate slightly decreased the oil viscosity. They noted that having an optimal concentration nanoparticle concentration and size can result in lower oil viscosity as seen in Fig. 2.5.

2.5.3 Combination of Nanoparticles with Polymers for EOR

Polymers are normally used in EOR of both light and heavy oil. Researchers have endeavoured to study the macroscopic sweeping efficiency of polymer flooding in EOR [130]. They have deduced that polymers can increase the sweep efficiency mainly by the water shut off and hence permeability reduction or by increasing the viscosity of the water. They are suitable for moderate viscous oils since water flood sweeping efficiency is always lower due to viscous fingering and reservoir heterogeneity [131].

Nanoparticles integrated with polymers for EOR application has been reported recently. Experiments have been performed using polymers either by grafting them on the surfaces of the nanoparticles or by mixing them physically to improve the rheological properties of nano sol-based fluids. When nanoparticles are grafted on

the surface of the nanoparticle, the solution stability depending on the polymer type can significantly improve. Also, the particles that are obtained after grafting polymers on nanoparticles can be used to stabilize foams and emulsions [98]. Using nanoparticles integrated with polymers for EOR applications can result in improved oil recovery than when polymers alone are used. Synergizing polymers with nanoparticles assist in (1) improvement of the rheological behaviour of polymers by increasing the intrinsic viscosity and elasticity of the system which is mainly attributed to cross-linking properties of the nanoparticles [132, 133], (2) inhibition of polymer degradation by lowering the degree of degradation [134] and thermal stability improvement especially in harsh reservoir conditions [134] and (3) reduction of IFT and wettability change, especially to water wet, which has also been reported by adding silica nanoparticles to polymer [50]. Polyacrylamide clay-based nanofluid was used to improve a polymer flooding study during EOR. Cheraghian and Khalilinezhad centred on examining the impact of clay-based nanoparticles on the viscosity of a polymer and later on EOR for heavy oil. Core flooding results showed that the matrix of the polymer and nanoparticles could increase the oil recovery compared to polymer alone. With the injection of approximately 1 PV, the flooding test exhibited a 5% incremental oil recovery with the nanoclay sols [135].

Nanoparticles are economical and hold potential promises in recovering oil based on their properties; therefore more studies on polymer/nanoparticle integration are still required to understand their recovery mechanisms and potential. Nonetheless, for proper application and usage, their need for stability is paramount, especially in harsh reservoir conditions. Consequently, studies pertaining to their chemical limits in terms of stability and adsorption are still needed [98].

2.5.4 Nanoparticle-Augmented Surfactant for EOR

Similar to nanoparticle-polymer solutions, surfactant polymer solutions are also formed by either physical mixing or by grafting via electrostatic interactions. When nanoparticles are coated by surfactants, the surfactant forms a monolayer on the nanoparticle surface, and hence the nanoparticles become more hydrophobic and can be utilized to formulate emulsions and forms. However, this process depends on the sizes and shapes of the nanoparticles and their concentration. Also, the surfactant type and concentrations used during the formulation stage will influence their performance [136]. Studies of nanoparticle-based surfactants in EOR have been applied extensively [137–139]. Studies have suggested various types of surfactants for several purposes, mainly depending on the rock/mineral type and reservoir composition. The selection of inappropriate surfactants can result in poor flooding performance which can reduce oil recovery. Literature suggests that anionic based surfactants are preferable for sandstone formations, although occasionally, other types of surfactants have been used. For carbonate, cationic surfactants are preferable [140]. A synergy of nanoparticles with biosurfactants has also been recently reported. Wang et al. [141] dispersed SiO_2 nanoparticles in bio nanofluids. According

to the observations visually, absorbance optical measurement, zeta magnitude and particle size measurements indicated that nanofluids with the lowest concentration (25 ppm) were more stable compared to other concentrations. The wettability measurement results demonstrated that although bio nanofluids at any concentration could change the wettability of oil-wet sandstone substrate to water wet, the best performance was achievable when 1000 ppm was used. A flooding test using a micro-glass model with the bio nanofluid was conducted and showed that an additional 5% can be achieved by integrating nanoparticles with surfactant. The outcomes of this study showed that the matrix of SiO_2 with the bio surfactant not only remained stable but also potentially provided a method to enhance oil recovery.

2.5.5 Application of Nanoparticles for Foam Stability in EOR Applications

In the oil and gas industry, foams have been used extensively for mobility control during gas flooding to reduce gas channelling into fractured zones and zones with high permeability. Various types and concentrations of surfactants are usually used to generate foams [142], but unfortunately, those generated by surfactants alone are thermodynamically unstable, particularly at high reservoir temperatures [98]. Various researchers have shown interest in the role of nanoparticles in foam stabilization [39, 143–145]. The use of nanoparticles to stabilize foams results in a very stable lamella even at high salinity and temperatures moreover for extended periods [146]. Researchers have noted that even at a low concentration of 0.05 wt% of silica nanoparticles, a stabilized foam can be formed moreover at elevated temperatures of 95 ° C. At higher salinities still, it has been postulated that larger particle sizes are desirable for better foam stability [146]. Manan and coworkers investigated the role of various types of nanoparticles such as silicon dioxide, aluminium oxide, copper oxide and titanium dioxide with concentrations in the range of 0.1–1 wt% and a fixed concentration of AOS surfactant on foam stability. Displacement tests performed at room temperature and pressure were used to evaluate the oil recovery efficiency which revealed that most of the nanoparticles used could stabilize CO_2 foam at selected nanoparticle concentrations. From this study, the best foam stability of the nanoparticles tested was obtained with aluminium oxide nanoparticles [147]. However, David et al. [39] showed that silica was the most effective nanoparticle for foam stabilization from his study which is in contrast to what Manan et al. had reported. Recently, Songyan et al. [148] reported the effect of using SiO_2 nanoparticles together with a cationic surfactant CTAB during CO_2 foam flooding for EOR. CTAB/SiO_2 ratio 0.033 was selected, as the optimal concentration. The authors revealed that by increasing the concentration, the stabilization effect of CTAB/SiO_2 increases and then decreases. They concluded that silica nanoparticles stabilize CO_2 foam by mainly the following mechanisms: CO_2 coarsening bubble decrease, interfacial property improvement and liquid discharge reduction. The authors recommended the improvement of oil recovery efficiency via CTAB/SiO_2

foam rather than water flooding. Weipeng et al. [149] studied how AlOOH nanoparticles affect the performance of sodium dodecyl sulphate (SDS) stability under diverse conditions of temperature and salinity. The authors noticed that foam stability was at most when the SDS/AlOOH ratio 5:1 was used. They deduced that partially hydrophobic nanoparticles with a positive charge and smaller in size can be firmly attached to the foam interface forming a tight system, and hence a stabilized foam. Even in the presence of oil, the foam that was stabilized with the matrix of SDS and AlOOH could notably withstand adverse conditions. In another study conducted by Qian Sun et al. [136], the authors stabilized foam using hydrophobic SiO_2 nanoparticles with SDS. The EOR performance of the stabilized foam with the surfactant/nanoparticle matrix was assessed using a glass micromodel and a sand pack. They found out that the foam stability decreased as temperature increased. Moreover, the matrix of SiO_2 and SDS stabilized foam demonstrated better temperature tolerance than the foam stabilized by SDS alone due to the adsorption of nanoparticles on the bubble interface. Unlike the SDS foam, most of the bubbles stabilized with the matrix maintained a spherical shape for a longer span which improved the dilutional viscoelasticity, unlike the SDS foam. The flooding results showed that SiO_2/SDS stabilized foam could recover more oil than either brine or SDS flooding alone. Foam stability improvement resulted in better gas mobility control and channelling. For the sand pack flooding, the differential pressure increase was proportional to the concentration of SiO_2 in the nano-surfactant matrix. They reported that oil recovery increased only when the concentration of the nanoparticles was below 1.5 wt% and therefore recommended this integration for EOR applications. Yira et al. [150] examined the impact of SiO_2 nanoparticle charge on the stability of the foam using natural gas in a condensate reservoir. They stabilized the foam by adding modified silica nanoparticles with different surface acidities and polarities. Four of these modified silica-based nanoparticles were made and examined using a surfactant adsorption technique. The produced foam stability was assessed using displacement experiments, to ascertain the best possible nanoparticle concentration that can be used used. In the batch study, a half-life of 41% was achieved using the basic nanofluid and surfactant concentration of 0.05 wt% which was higher than the nanofluid without nanoparticles. The researchers attributed this difference to the formation of a steric layer that resulted because of nanoparticle adsorption on the surface of the bubble, hindering its contraction or expansion and allowing the nanostabilized foam to have more durability than the foam without the nanoparticles. In addition, the authors conducted displacement tests using methane gas to assess the perdurability of the foam stabilized with nanoparticles in the porous medium and the mobility reduction at reservoir temperature of 100 °C. While only 10% of the original oil was recovered when only foam flooding was used, an additional 18% was obtained when foam was synergized with nanoparticles. This was a result of the increased foam stability that in turn increased sweep efficiency. The results by these different researchers demonstrate the tremendous advantages that nanoparticles offer during foam EOR, as a result of their physical structure and morphologies. Still, more studies on nanoparticles of different types may be required to enable their adoption for other applications.

2.5.6 Using Nanoparticle Stabilized Pickering Emulsions for EOR Application

A Pickering emulsion results from solutions stabilized by solid particles that adhere at the interface of two phases [151]. This occurs when oil and water are mixed to form oil droplets that spread throughout the water. If solid particles are added to the solution, they attach to the interface preventing the drops from coalescing, hence forming a stabilized emulsion. Emulsion stability may depend on the properties such as the size of the particle, shape and particle surface chemistry. The contact angle of the particle will determine the adherence of the particle to the surface. With a smaller contact angle of the particle, the droplet is wetted by the particle and coalescence of the droplets will most probably not occur.

In adverse conditions of high temperature and pressure in the reservoir, colloidal solids and/or surfactants may be used for emulsion stability. However, surfactants are expensive and not stable in such conditions hence limiting their usage in such conditions. Rheological characteristics and stability of an emulsion may depend on its composition, operating temperature, size of the droplet, etc. [123]. Recently, the application of nanoparticles to stabilize emulsions has proved to offer better options because of their unique characteristics in comparison to a surfactant or colloidal emulsions. Nanoparticles can attach to the oil-water interface on the droplet surface irreversibly forming a monolayer and hence provide a stable emulsion applicable in severe reservoir conditions. Moreover, nanoparticles based on their size can easily move in the reservoirs which makes them applicable for EOR [11, 32].

Research has confirmed that nanoparticle-stabilized emulsions can improve oil recovery [152]. Sharma et al. [153] noted that injecting a polymer (0.5 PV) and Pickering emulsion (0.5 PV) in a Berea sandstone core sample was enough to provide up to 6% additional oil recovery after brine injection compared to the Pickering emulsion or polymer alone. Yoon et al. [154] used a silica colloidal solution dispersion of oil in water, which resulted in a stable emulsion that yielded a 4% additional oil recovery after brine injection. The adsorption of silica nanoparticles on the polymer and surfactant matrix by both van der Waals forces and electrostatic forces resulted in a stable emulsion. They noticed that the produced emulsion was able to flow in the porous medium easily due to improved mechanical stability of the emulsion in the presence of nanoparticles that resulted in improved oil recovery [154].

2.5.7 Inhibition of Wax and Asphaltene Deposition with Nanoparticles

During oil production, the changes in the reservoir conditions such as pressure and temperature may result in the deposition of organic solids on the rock surfaces such as wax and asphaltene [155]. Asphaltene due to its higher molecular weight and complex structure is among the most notable deposit that presents serious

challenges during oil production [156–158]. Asphaltenes vary for different oil; they normally consist of aromatic rings linked to hydrocarbon chains and also have other traces of heteroatoms and heavy metals which contribute to their complex structures [159].

When asphaltene deposits on the rock surface as a result of changes in the reservoir properties, the production cycle of the reservoir may be affected. Deposits of asphaltene on the rock surface also damage the formation and reduce the permeability due to pore blockage. Asphaltene deposits can cause pipeline clogging; their adsorption on the rock surface can result in wettability reversal, damage of production equipment due to corrosion and formation of petroleum coke [160–162]. Additionally, asphaltenes are amphiphilic in nature therefore can behave as surfactant and at times causes oil-water separation issues by creating reverse emulsions. As a result, asphaltenes should be avoided because of the challenges it presents, the increased costs and its environmental impact [163].

Deposited asphaltenes and wax are normally removed or prevented using methods such as injecting solvents, surfactants addition, cutting during wireline operations and a variety of other mechanical approaches [164–166]. However, these methods are expensive and not durable, because asphaltenes readily redeposit. Also, these conventional approaches used to prevent asphaltene deposition during production are not effective since the asphaltene inhibitors and the chemicals dispersed during treatment have similar chemical compositions [60]. Researchers are therefore eager to find smart materials and methods that are efficient, sustainable and cost-effective. These concerns have resulted in the emergence of research into the use of nanomaterials for asphaltene deposition prevention [79, 167–169] due to their distinctive characteristics which are vital for adsorption and changing asphaltene aggregation mechanism [169].

Several studies at the laboratory, pilot and field scale have examined the use of nanotechnology in asphaltene deposition inhibition. Nasser et al. [63] investigated the adsorption capability of various nanoparticles such as FeO_4, Co_3O_4, TiO_2, MgO, CaO and NiO. From their findings, the asphaltene adsorption capabilities were highest for CaO and lowest for TiO_2. They noted that, however, adsorption was mainly metal oxide type dependent [63]. Mohammadi et al. [168] investigated the role of TiO_2, ZrO_2 and SiO_2 nanoparticles in stabilizing asphaltene, concluding that because of the presence of hydrogen bonds in an acidic environment, TiO_2 nanoparticles could stabilize the asphaltene. These researchers concluded that depending on the surface chemistry of the adsorbent, asphaltene stability can be improved [168], similar to what Nassar et al. [170] found out when studying how the surface chemistry of the alumina-based nanoparticles affected the asphaltene adsorption capability. They concluded that asphaltene adsorption was highest for acidic nanoparticles and lowest for neutral nanoparticles. This indicates that using particular acids as modifying agents can accelerate the adsorbents and adsorbates' interactions.

Yousef et al. [79] carried out a study using three metal oxide types that included silica nanoparticles (SiO_2), nickel nanoparticles (NiO) and iron oxide (Fe_3O_4) nanoparticles to ascertain how they could absorb asphaltene. The authors noted that irrespective of the nanoparticle type, increasing n-heptane in the presence of the

adsorbent resulted in more adsorption. However, they pointed out that for selection purposes silicate nanoparticles had more affinity for asphaltene adsorption compared to NiO and Fe_3O_4.

Camilo et al. [169] examined the impact of 12 different types of nanoparticles on asphaltene adsorption. They observed the rapid adsorption of asphaltenes on the nanoparticle surface, which indicated that adsorbents show promise for the delay of the agglomeration and inhibition of the precipitation and deposition of asphaltenes. The authors determined that because adsorbents can adsorb and stabilize asphaltenes, the nanoparticles restored production, which resulted in improving oil recovery [169]. Stefanía et al. [167] studied the impact of nanoparticle size and surface acidity in inhibiting formation damage. They synthesized silica nanoparticles in the range of 11 to 240 nm and studied their ability to inhibit asphaltenes using batch-mode experiments. They performed the kinetics of asphaltene aggregation with and without nanoparticles using DLS experiments with different heptane-toluene ratios. They revealed that among the nanoparticles they studied, the smallest nanoparticle (11 nm) exhibited the highest adsorption rate for n-C7 asphaltenes. Modifying these same nanoparticles using acidic, basic and neutral treatments, as S11A, S11B and S11N, respectively, they discovered that the asphaltene adsorption followed the trend S11A $\gg$ S11B $\simeq$ S11N $\simeq$ S11. Finally, the researchers performed a displacement test to treat the asphaltene damaged core in porous media at reservoir conditions. Nanofluid treatment with silica nanoparticles increased the effective oil permeability and improved oil recovery, to 11%.

In a field trial that was reported by Zabala and coworkers [60], they used aluminium-based nanoparticles to inhibit formation damage that was caused by the deposited asphaltenes. They first conducted a core flood trial followed by a field test in the Cupiagua Sur oil field in Colombia. The field trail resulted in cumulative oil production of 150,000 barrels after injection of the nanofluids. The authors deduced that alumina-based nanofluids were stable for long periods in the formation and recommended them for reservoirs with very low permeability conditions [60].

It is clear from these investigations mentioned above that the use of nanoparticles for asphaltene inhibition may offer many benefits compared to the conventional chemical and mechanical methods commonly used, as a result of their chemical structures and surface functionality. Nevertheless, most of the reported studies are performed in labs rather than in the field. Notwithstanding their wide application in inhibiting asphaltene, during oil recovery, however more pilot and field test investigations are needed to provide a better understanding of their role in asphaltene deposition inhibition, thus allowing the technique to be more fully adopted in the industry.

It is also important to note that some oil contains significant amounts of paraffin, constituting the saturated fractions of the aliphatic compounds [171]. When the reservoir temperature falls below the wax appearance temperature (WAT), precipitation of wax occurs [172]. The precipitated wax crystals normally form a network structure at low deposited amounts approximately less than 1 wt % [173]. This

results in increased pour point, viscosity, yield stress and non-Newtonian flow behaviour of the waxy crude oils. In addition, pipeline transportation of waxy crude oil results in viscosity increase and pressure losses that affect the fluid flow [174]. Effective methods to prevent paraffin wax deposition remain a challenge during oil production. Current industrial practices for improving the flowability of waxy crude oil involve the addition of oil-soluble pour point depressant (PPD) such as poly(ethylene-vinyl acetate) and polymers, such as polyacrylate, that help to change the morphology of the crystals by crystal alteration and entropic repulsion [175]. Recently, researchers have also been motivated to look at nanoparticle application for wax inhibition especially when combined with the conventional polymers normally used. Wang et al. [176] compared the performance of nanohybrid PPDs with conventional poly(ethylene-vinyl acetate) (EVA). According to the authors, the microscopic images of precipitated wax crystals in the presence of nanohybrid PPDs showed that nanohybrid PPDs exhibit superior pour point depression than EVAs alone. Norrman et al. [177] studied the effects of the quantity of coating materials by functionalizing the nanoparticles with poly(octadecyl acrylate) (POA) on pour point depressants and comparing them with the bare nanoparticles. They used waxy oil to show the performance of the pour point. They primarily examined how nanoparticle coverage would impact their effectiveness. The adsorption of the POA on silica was assessed using a quartz crystal microbalance with dissipation (QCM-D). Nanoparticle's performance was tested by carrying out rheology experiments to assess differences in the strength of the wax gel that was formed, with differential scanning calorimetry (DSC) to determine the WAT and any crystallization difference and visually observe the formed wax with polarized microscopy. Rheological tests demonstrated that nanoparticles with a lower POA exposure had less effect on the size of the formed wax gel, while nanoparticles that had a full coverage of POA could lower the strength of the wax gel significantly. DSC results also demonstrated that the nanoparticles result in a drop in WAT and that there was less effect when nanoparticles with more than 100% coverage were used. DSC establishes that nanoparticle presence alters the behaviour of the wax crystallization, likely by introduction of double nucleation sites, hence causing a raise in crystallization. Polarized microscopy demonstrates that presence of nanoparticles resulted in formation of bigger particles compared to the added silica. Research demonstrates that optimizing the nanoparticles coated on wax gels is still possible, so that less particles can be used, hence improving their usability [177]. The possible mechanism proposed for this nanohybrid in wax inhibition includes crystal morphology modulation, gelation point reduction and rheological yield stress. Nanoparticles may also act as supplementary dispersed nucleation centres, forming more crystals of a smaller size, which may hinder growth as shown in Fig. 2.6. Because of various nucleation sites in the presence of the nanohybrid, wax crystals have a regular, spherical shape and a solid structure, which hampers the process of percolation that is required for the formation of a volume-spanning network of wax crystals, which results in free wax crystals with a modified morphology [178].

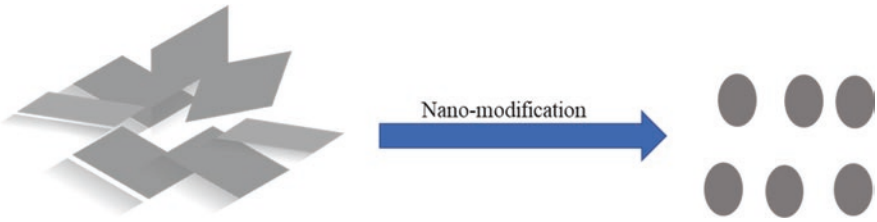

Fig. 2.6 Schematic representation of the morphological modulation

2.5.8 Structural Disjoining Pressure (SDP) Caused by Nanoparticles and the EOR Impact

Structural disjoining pressure can determine the spreading of fluid on the surface [94, 144]. Research has demonstrated that a wedge-film structure can be formed when nanoparticles exist in a contact region and three-phase contact region forming a driving force [39] as shown in Figs. 2.7 and 2.8.

SDP correlates with the fluid ability to adhere to the surface as a result of the imbalance between the solid, oil and aqueous phases [39]. When these interfacial forces lower the contact angle of the aqueous phase to almost 1°, this results in a wedge film, which acts to detach the formation fluids from the surface of formation [145]. The spreading coefficient of the fluid exponentially raises as the thickness of the film falls [110, 145]. The force for the spreading of the nanofluids is the film tension gradient ($\Delta\gamma$) or structural force which is directing in the direction of the wedge from the entire solution. At the vertex of the three-phase contact, the gradient is high due to the presence of nanoparticles occupying the wedge confinement as shown in Figs. 2.7 and 2.8**.** Also, as the gradient rises in the vertex direction of the wedge, nanoparticles are forced to adhere at the wedge tips [39]. Hua et al. [179] proposed that to improve the oil recovery with nanoparticles with the aid of SDP, the nanofluid should be formulated to contain smaller nanoparticles with a lower polydispersity. They observed that higher particle size disparities tend to lessen the SDP. It was further deduced that to maximize the SDP, the nanofluid formulated needs to have a high osmotic pressure of approximately 200 Pa for at least 10 vol% nanofluids. Trokhymchuk et al. [180] developed an analytical model by applying the Laplace transformation to estimate the SDP for any nanofluid solution. This simple model can be used to comprehend the liquid films' stability in presence of colloidal particles and is given by Eq. 2.3 as

$$\pi_{st}(h) = \begin{cases} -p & 0 < h < d \\ \pi_o \cos(\omega h + \varphi_2) e^{-kh} + \pi_1 e^{-\delta(h-d)}, & h > d \end{cases} \tag{2.3}$$

where d is the nanoparticle diameter, h is the thickness of the wedge film, the remaining parameters (π_o, π_1, ω, φ_2, k, δ) are fitted as cubic polynomials in terms of

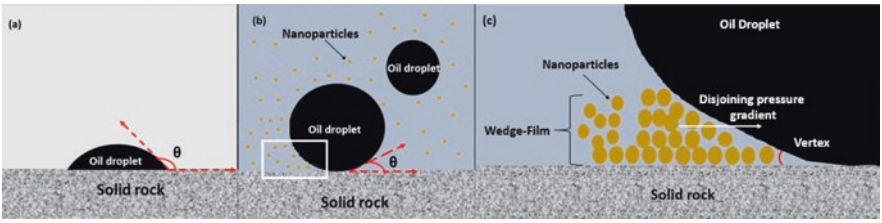

Fig. 2.7 Illustration of how nanoparticles detach oil from the surface due to the structural disjoining force

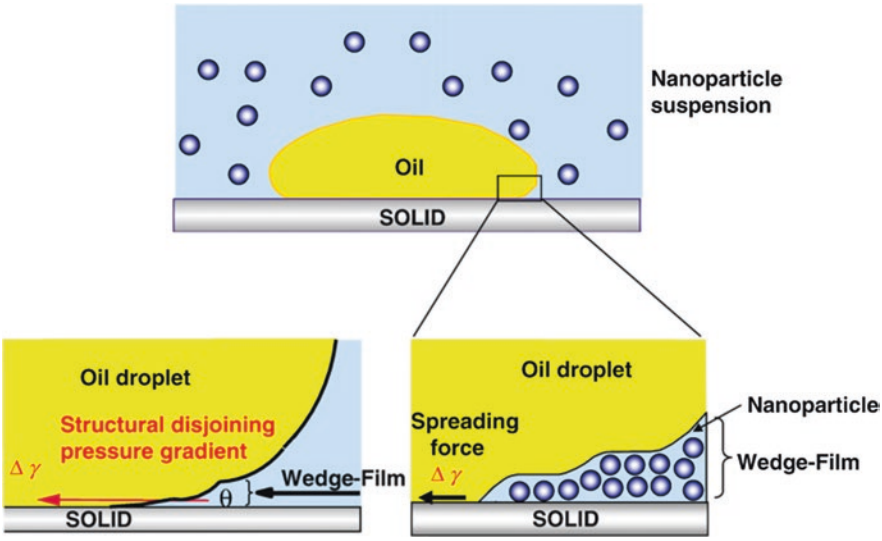

Fig. 2.8 Nanoparticle structuring in the wedge film results in an SDP [39]. Permissions related to the material were obtained from ACS and further permission should be directed to ACS

the nanofluid volume fraction (φ) and P represents the osmotic pressure which depends on the volume fraction of the nanofluids expressed as

$$\rho kT\left(\frac{1+\varphi+\varphi^2-\varphi^3}{\left((1-\varphi\right)^3}\right) \tag{2.4}$$

where ρ *is the* particle number density, k is the Boltzmann constant and T is the temperature. From the above expression, the SDP and osmotic pressure increase as the nanofluids' volume fraction increases. Also, for a higher SDP, a smaller three-phase contact angle between the nanofluids, oil and rock is needed.

2.5.9 *Nanoparticle Application in Heavy Oil Recovery*

Hashemi et al. [42] reported extensively the application of nanoparticles in heavy oil upgrading. The recovery of heavy oil can be achieved by using nanoparticles because it enhances heavy oil thermal conductivity or by in situ upgrading of heavy oil. Not only are nanoparticles able to improve the viscosity and density of the heavy oil, but some can also enhance the specific latent heat and the reservoir thermal conductivity. The thermal enhancement processes occur in reservoir rock with the help of electromagnetic (EM) heating, which uses the injected metal oxide nanoparticles. When exposed to high frequency, the nanoparticles associate themselves with the electromagnetic field, which leads to the emergence of particle movements with high frequency, heating the surrounding region by friction [181]. Also, the nanoparticles are used in in situ upgrading of heavy oil, as catalysts to crack heavy oil molecules chemically. Given the nanoparticle high surface area to volume ratio, it improves their catalytic performances of hydrocracking and hydrogenation inside the reservoir. In comparison to the micro-sized catalysts, nanoparticles can be well dispersed with nominal injectivity impacts.

2.6 Janus Nanoparticles Overview for EOR Application

The concept of Janus nanoparticle was introduced as early as 1989, by C. Casagrande et al. [16]. The authors prepared glass spherical particles, with one hemisphere hydrophilic and the other side hydrophobic, hence naming the objects “Janus beads”. This was in reference to the Roman gods that had two faces on one head, and since these designed objects had dual properties on one face, they considered them amphiphilic solids. They went ahead to study their properties at the oil-water interfaces and found out that they do act differently than ordinary solid particles and could mimic surfactants. Since then, research into Janus nanoparticles has continued to rise. These Janus nanoparticles can form a stable solution with a definite size and considerably reduce the IFT between two phases just like surfactants. Besides, because of their morphologies, Janus nanoparticles can combine various materials in an isolated structure at the nanoscale hence combining dissimilar properties in one unit [182, 183]. Furthermore, Janus nanoparticles with different functionalities, uniform size and morphological features are desirable in numerous fields of applications, e.g. catalysis and medicine. Due to their fascinating features and inherent properties, these Janus nanoparticles still have synthetic challenges that need to be addressed. One of the important issues that still require more investigation is suggesting more synthesis protocol of these anisotropic colloidal particles with less than 1 micrometre in bulk quantities, having the capability to regulate their morphology with defined control of their surface chemistry and the ability to produce these Janus nanoparticles in large quantities for various technological applications [184].

2.6.1 Synthesis of Janus Nanoparticles

Major progress pertaining to their synthesis has been recently reported, three main methods are normally used in synthesizing Janus nanoparticles, and these include self-assembly, phase separation and masking as seen in Fig. 2.9; these strategies use techniques such as microfluidic system, surface modification and Pickering emulsion [185]. The microfluidic method via phase separation can be scaled up to obtain Janus nanoparticles in large quantities; however, the resultant particles are normally relatively bigger due to the large size of fluidic channels making it an infeasible approach to obtain the required Janus particle sizes [186]. The most commonly used method for producing large amounts of Janus nanoparticles is masking via Pickering emulsions.

2.6.1.1 Synthesis of Nanoparticles Using the Masking Technique

In this method, part of the homogenous particle is isolated, and the remaining uncovered part is functionalized and/or modified with a chemical agent resulting in Janus particles with a double surface. This is achieved by kinetic immobilization or trapping the colloidal particles at the interface of liquid-liquid phases and liquid-solid phase or on a solid surface, and it is one of the most feasible methods for Janus nanoparticle preparation. This approach applies to any material and provides the option of modifying the trapped particles with different functional groups. The only setback with this method is only a few milligrams of particles are produced in one

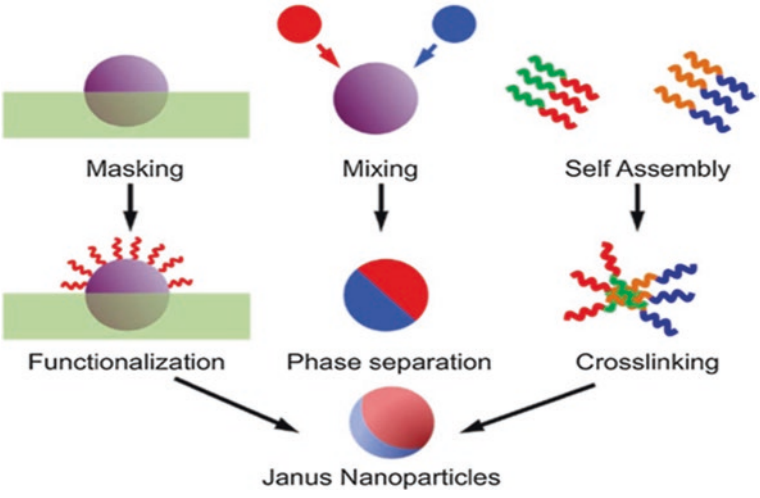

Fig. 2.9 Schematic illustration of the three main steps for the preparation of Janus nanoparticles [185]. Permissions related to the material were obtained from Elsevier and further permission should be directed to Elsevier

batch which makes it inapplicable for the production of large amounts of Janus nanoparticles for technological applications [185]. Janus nanoparticles in large quantities can be produced by trapping the homogenous nanoparticle between liquid-liquid and liquid-solid interface a process known as Pickering emulsion as explained in detail in the next subsection [184, 187, 188].

2.6.1.2 Pickering Emulsion

Pickering emulsions are a result of colloidal particle stability at the interface of two immiscible phases. These solid particles stabilize the droplets at the interface preventing coalescence by forming a mechanical monolayer between the two phases. These solid particles can be both organic and inorganic, e.g. nanoparticles, etc. Stability of the solid particles at the interface is achieved by particle diffusion onto the interfacial region, and these remain stable in mechanical equilibrium. Contact angle (θ) remains the key aspect in designing stable Pickering emulsion since it creates the particle position relative to the oil-water (o/w) interface. If the contact angle (θ) is less than 90, the o/w emulsion is more stable. On the contrary, w/o emulsion is favoured when the contact angle is greater than 90, as shown in Fig. 2.10.

Compared to conventional surfactants that reduce the interfacial tension between the o/w, Pickering emulsion can be formulated without IFT reduction. This is because of the higher Gibbs energy required to remove a particle from the oil-water interface which is higher compared to that of the conventional surfactant [190]. The desorption energy and emulsion stability are related, and both depend on the particle size, particle-particle and particle-oil interactions. If the particles are smaller, so that the effect of gravity is insignificant, the energy ($-\Delta_{int}G$) required to detach a particle of radius r from an oil-water interface of tension $\sigma_{o/w}$ is given by the equation

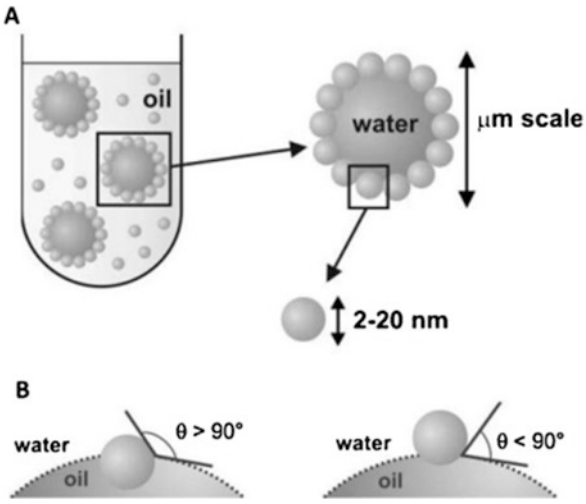

Fig. 2.10 Schematic representation of (A) solid particle stabilized w/o emulsion and (B) changing the position of solid particles at the o/w interface at different contact angles >90 and < 90 [189]. Permissions related to the material were obtained from Elsevier and further permission should be directed to Elsevier

$$-\Delta_{\text{int}}G = \pi r^2 \gamma_{\frac{o}{w}} \left(1 \pm \cos\theta_{\frac{o}{w}}\right)^2 \tag{2.5}$$

where the sign is negative when the particle is removed from the water phase and positive when the particle is removed from the oil phase. From the equation, the binding energy ($-\Delta_{int}G$) of the particles at the oil-water interface is dependent on the radius (r) of the particles as seen from Eq. 2.5; it decreases with a decrease in particle size. This size dependence allows nanoparticle assembly to achieve equilibrium at the interface which may not be the case for micrometre-size particles that may be trapped at an anon-equilibrium state. Therefore, to restrict the modification only on the liquid exposed surface requires delicate thermodynamic control of the interface.

2.6.1.3 Preparation of Janus Nanoparticles via Pickering Emulsion

Pickering emulsion-based system is highly favourable to produce Janus nanoparticles with anisotropic surface chemistry and controllable geometry in large quantities. Production of these large quantities of Janus nanoparticles has been achieved by the use of water-wax Pickering emulsion [188, 191]. Controlling the kinetic stabilization of these nanoparticles in wax droplets allows their fabrication in gram-sized quantities [191] as shown in Fig. 2.11.

Production of Janus nanoparticles using Pickering emulsion was first reported by Granick et al. [188], based on o/w Pickering emulsion of silica nanoparticles in the presence of paraffin wax. They dispersed the untreated hydrophilic silica nanoparticles in melted wax and then mixed it with water. After full adsorption of the

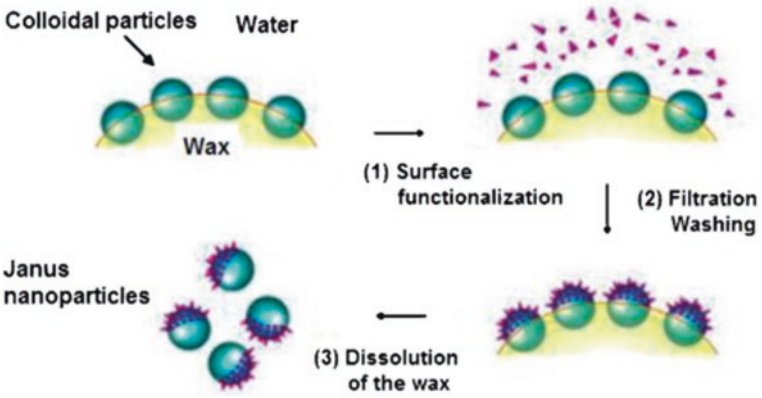

Fig. 2.11 Schematic step-by-step fabrication of Janus colloidal nanoparticles via Pickering emulsion process [191]. Permissions related to the material excerpted were obtained from Elsevier and further permission should be directed to Elsevier

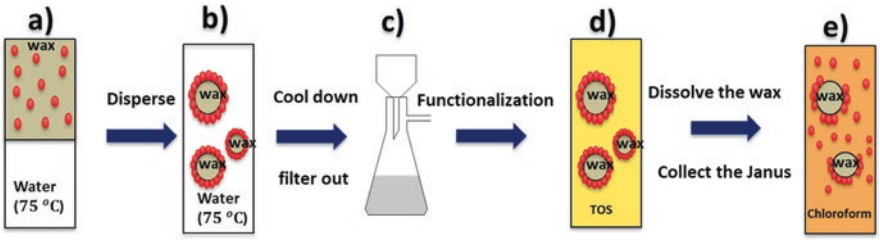

Fig. 2.12 Schematic representation for the preparation of Janus nanoparticles; (**a**) particles dispersed in an emulsion of water and melted wax, (**b**) adsorbed nanoparticles onto paraffin wax, (**c**) filtering of wax and washing of the weakly attached nanoparticles from the wax ball, (**d**) surface modification with silane (TOS), (**e**) finally particles obtained by dissolving the wax balls in chloroform and toluene

particles in wax, the system was cooled to lock the particles in the wax phase to kinetically stabilize them. Subsequently, the chemical modification was performed on the unprotected side as shown in Fig. 2.12. Wax was later dissolved in the organic solvents to release the Janus nanoparticles with the hydrophobic and hydrophilic parts. Using wax offers several advantages, such as stabilizing the particles during the chemical modification process, and avoids movements of the particle at the liquid-liquid interface [184]. Several research groups have followed the Granick method to prepare Janus nanoparticles; Zayed and coworkers have also synthesized Janus nanoparticles in large quantities using the same approach. In their work, they prepared Janus magnetic nanoparticles of 10–15 nm by immobilizing the magnetic nanoparticles on the surface of paraffin wax balls via water-molten wax emulsion. Later, salinization of the exposed side was accomplished using (3-aminopropyl) triethoxysilane (APTES), and waxes were dissolved subsequently in methanol and chloroform to obtain the wax-free Janus nanoparticles [192].

Using the Pickering emulsion technique to prepare Janus nanoparticles was described as a simple and cheaper way of producing large quantities of Janus nanoparticles by Liang et al. [188]; the authors gave three major advantages of using this technique; they concluded that this process is solution-based with approximately 50% yield which makes it easy to use. According to the authors, the benchtop experiments performed to date with this method have allowed the production of 0.1 g of particles in one batch. The authors concluded that since the emulsion process that forms the basis of this synthesis is achieved by mechanical mixing for a short time, the process is, therefore, simple, cheaper and scalable for larger Janus productions. Their third reason was that, unlike other alternative methods where the surface coverage of modified chemical makeup is controlled kinetically, the Pickering emulsion method offers the ability of surface coverage of modified chemical makeup to be controlled thermodynamically. The monodispersed surface coverage is better from batch to batch because the area coated depends thermodynamically on the contact angle between the particle surface and the liquid used in the emulsion.

2.6.2 *Janus Nanoparticle Application for Enhancing Oil Recovery*

Although numerous studies have been performed on nanoparticle application in oil and gas as previously discussed, most of the studies have focused on isotropic and homogeneous types of nanoparticles. The application of anisotropic nanoparticles in oil recovery is emerging, and there is evidence of oil improvement from recent studies that have been conducted mainly at laboratory scale. Dan Luo and coworkers have recently reported oil recovery improvement using Janus nanoparticle concentration in a saline environment. The authors performed a core flooding test by injecting a nano concentration of 0.01 wt% and noticed a 15.2% increment after water flooding. They attributed the recovery increment to the properties of the amphiphilic Janus nanoparticle that was trapped at the interface of oil-water and acted as a surfactant which resulted in an interfacial reduction. From their findings, the Janus nanosheet also formed a more stable climbing film that induced Marangoni stress forces which resulted in an easy flow of oil [193]. After that, several other researchers have continued to report their findings regarding the role of Janus nanoparticles for EOR application. Hairong et al. [194] conducted a study using silica Janus nanoparticles for EOR using sandstone cores. The authors synthesized silica-based amphiphilic Janus nanoparticles by grafting an organic hydrophobic chain (3-aminopropyl)triethoxysilane onto the SiO_2 nanoparticles' surface using a Pickering emulsion technique. Contact angle, interfacial tension and interfacial viscosity were employed to investigate the potential of the synthesized Janus silica nanoparticles to recover more residual oil. They found out that the interfacial properties between the oil-water interface could be enhanced. The IFT could be reduced from 30 mN/m to 2.28 mN/m, a 92.4% reduction, using a concentration of 0.05 wt% Janus nanoparticles. Based on the contact angle measurements, these nanoparticles could change the rock wettability to water wet. Moreover, their displacement study showed that up to 15.74% incremental oil recovery could be obtained by injecting 0.01 wt% Janus nanofluids. They attributed this increment to surfactant-like properties possessed by the Janus nanofluids which can enable them to form a stable interfacial film that can assist in reducing the IFT and recover more trapped oil. Notwithstanding their recent promising reported results, it is important to note this reported IFT reduction is still not in the ultralow range of 10^{-3}, a reduction that is required to mobilize more trapped oil during EOR. Nevertheless, it is evident to predict that the use of Janus nanoparticles in improving oil recovery is expected to offer many benefits, due to their physical assembly and structural morphologies. Similar to the previously mentioned nanoparticle types, also the application of Janus nanoparticles is still at the bench scale with no field application reported. Hence, more studies at all levels are still needed to have a clear phenomenology of their capability in EOR for proper adoption in the petroleum industry.

2.7 Effect of Various Factors on Nanoparticle Performance

Different parameters have been examined on oil recovery during nanofluid injection. A review of the majority of these factors that influence nanoparticle EOR is as follows.

2.7.1 Salinity Effect

It is important to find ways to support the stability of nanofluids in different saline environments during flooding, mainly for oil recovery applications. Nanofluids normally fail in presence of excessive salinity due to charge screening [99]. Nanoparticle retention in presence of brine solution may be due to charge interaction which results in the formation of clusters that affect the recovery [56]. However literature depicts that smaller particles with zero charge normally are noninteracting [56, 195]. Nanoparticles can be modified with polyelectrolytes especially in high salinity environments but still fail. However, specific polymers have been suggested that can effectively be applied in high saline environments. Mikhil et al. [99] noticed that colloidal stability in extreme salinity conditions can be achieved by stabilizing nanoparticles with polyampholyte-based polymers. The authors recommended such a matrix for reservoirs with higher salinities.

2.7.2 Effect of Nanoparticle Concentration

Nanoparticle EOR is greatly affected by the nanoparticle concentration used. A high concentration of particles does not guarantee improved oil recovery yields, and there is always desired optimum concentration required to maximize oil recovery. Teng et al. [196] examined the impact of the concentration of used silica nanoparticles on EOR. The used nanoparticle concentrations ranged between 0 and 1.0% at a fixed surfactant concentration as shown in Fig. 2.13. Subsequently, oil recovery increased with the nanoparticle concentration until it reached a plateau at 0.5 wt% where the nanoparticle concentration increase had no significant impact on oil recovery. Nanoparticle concentration above the optimum may result in core plugging, causing changes in the formation properties such as porosity and permeability. This may impact the flow of fluids as shown in Fig. 2.14, in which the impairment rose in correlation with the rise in the nanoparticle concentration [197].

2.7.3 Nanoparticle Type and Size

The nanoparticle type and size also impact oil recovery. Manan et al. [147] examined the impact of nanoparticles of Al_2O_3, SiO_2, TiO_2 and CuO, noting that adding nanoparticles improved oil recovery by recovering an extra 14% additional oil

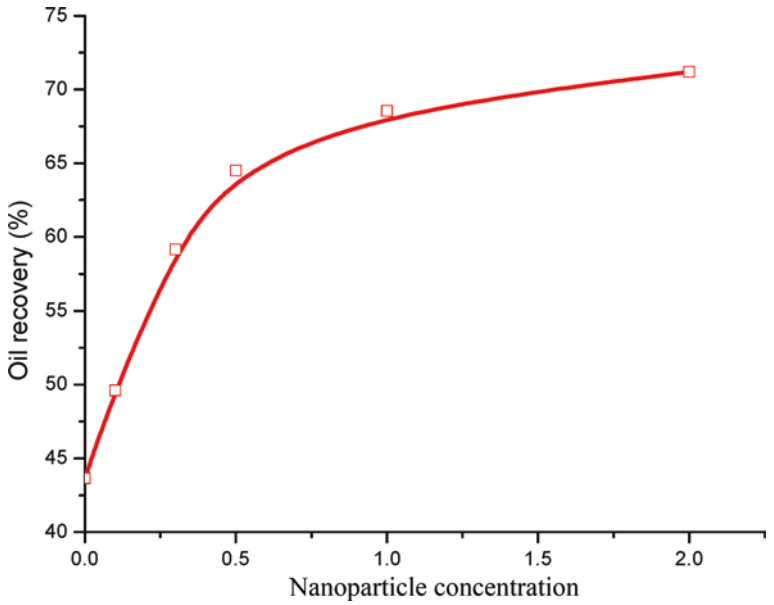

Fig. 2.13 Effect of nanoparticle concentration on oil recovery enhancement. Obtained from [196] after permission

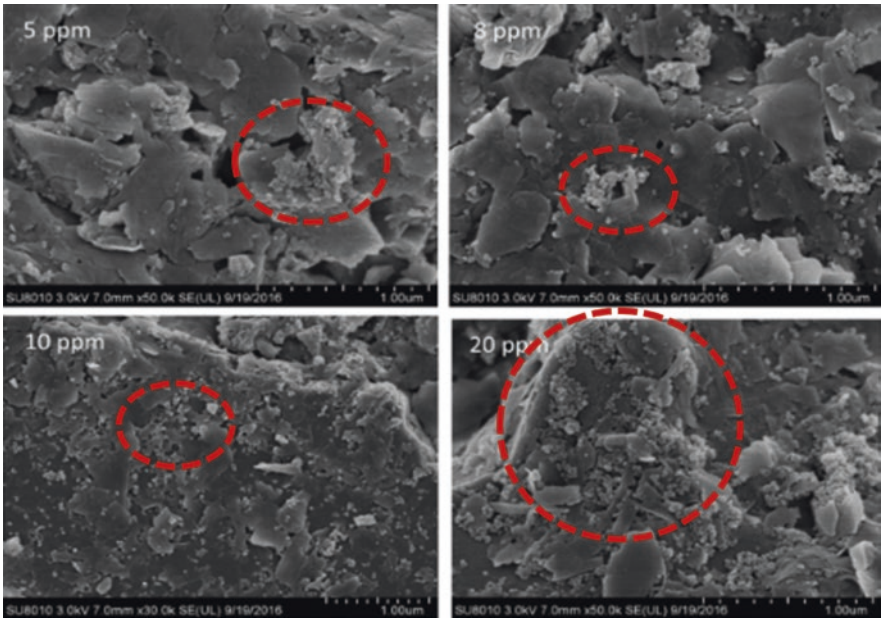

Fig. 2.14 SEM pictures of the core at different concentrations of nanoparticles indicating permeability impairment (red circles) caused by the injection of nanofluids [197]. Permissions related to the material excerpted were obtained from ACS and further permission should be directed to ACS

after water flooding. Despite these selections, the type of nanoparticle to use depends on its purpose, as some are best at changing wettability, others reducing oil viscosity, others adsorbing asphaltenes, others reducing IFT, etc. Understanding of the reservoir rock and fluid properties is necessary before the nanoparticle type selection based on the required objectives of nanofluid injection. For example, nanofluids that are comprised of zirconium dioxide, calcium carbonate, titanium dioxide, silicon dioxide, magnesium oxide, aluminium oxide, cerium oxide and carbon nanotube were chosen for EOR in a carbonate formation. The researchers performed a series of tests using spontaneous imbibition and contact angle measurements to determine the role of different nanofluids on wettability alteration for carbonate rocks. The authors found out that SiO_2 and $CaCO_3$ nanoparticles could notably change the wettability to stronger water wet compared to other types [56].

The size of the nanoparticle also impacts incremental oil recovery. Luky et al. [52] assessed the effect of some factors that influence nanoparticle EOR performance using hydrophilic silica nanoparticles with three sizes from 7 to 40 nm. The authors concluded that the size of the nanoparticles significantly impacted EOR. From their study, the smallest nanoparticle size gave the highest oil recovery. Similarly, decreasing nanoparticle size resulted in improved displacement efficiency that increased the oil recovery [52].

2.7.4 Effect of the Injection Rate

Injection rate impacts incremental oil recovery during nanofluid injection. Increasing the nanofluid injection rates lowers oil recovery. This is attributed to nanoparticle agglomeration, with an increased injection rate [52]. It is, therefore, impervious to optimize the injection rate to maximize oil recovery. Moreover, with increased injection rate, unfavourable mobility ratios may result due to viscous fingering in cases where the displacing fluid is less viscous than the displaced fluid which can lower the oil recovery [198, 199].

2.7.5 Effect of the Injection Sequence

Compared to continuous nanofluid injection, sequence injection of brine and nanofluids has proved a better option during nano-EOR flooding. This is because the nanofluids that normally agglomerate during nanofluid injection and often plug the pores can be washed away by the sequentially injected water unlike in continuous injection. Teng et al. [197] performed a study by injecting the same pore volumes in the rock but with a different sequence as shown in Fig. 2.15. The authors observed that as the number of injection cycles increased, more oil could be recovered. Further studies are required to examine the injection of nanofluids altered with water or brine, especially with different nanoparticle types, sizes and concentrations and at different wettability conditions of the porous medium.

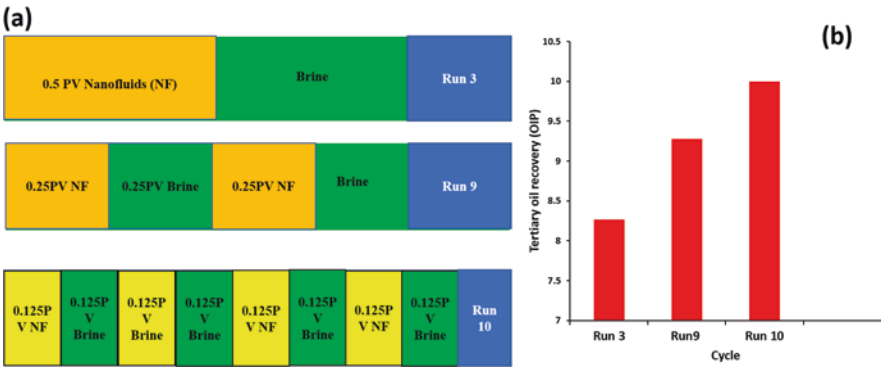

Fig. 2.15 On the left, (**a**) schematic of different tested injection schemes and on the right (**b**) tertiary oil recovery rates for the selected sequences [197]. Permissions related to the material were obtained from ACS and further permission should be directed to ACS

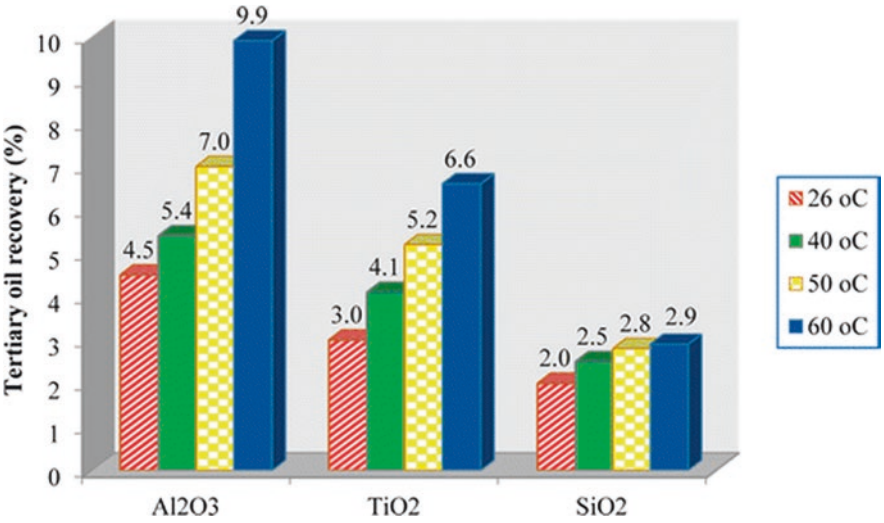

Fig. 2.16 Oil recovery via metal oxides-based nanofluids at various temperatures after brine flooding [41]. Permissions related to the material excerpted were obtained from ACS and further permission should be directed to ACS

2.7.6 Effect of Temperature

Temperature influences oil recovery in different aspects. It impacts the fluid flow and rheological behaviour especially oil since it can reduce its viscosity and IFT hence improving the oil recovery. Esfandyari et al. [41] used three metal oxides as nanofluids with fixed concentration of 0.005 wt% at temperatures ranging from 26 to 60 °C. Results showed that tertiary recovery improved as temperature increased as shown in Fig. 2.16.

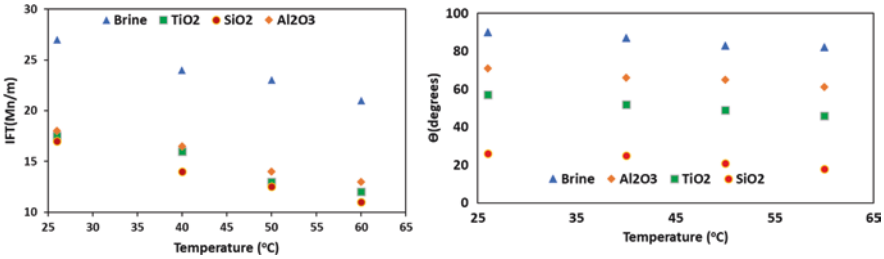

Fig. 2.17 Effect of temperature on IFT **(a)** and contact angle **(b)** [41]. Permissions related to the material excerpted were obtained from ACS and further permission should be directed to ACS

Recovery increment after water flooding was a result of the change in the contact angle and IFT in the presence of different nanofluids as the temperatures increased. This is shown in Fig. 2.17. At low temperatures, there was no significant change in the contact angle and IFT. As the temperature increased, both IFT and contact angle decreased which resulted in additional oil recovery.

2.8 Economic Analysis of Using Nanoparticles

Nanoparticle cost analysis estimations need to be assessed with the current market crude oil prices in the markets and the cost of the currently used EOR methods such as alkaline, polymers, surfactants, etc. in mind. This will help to determine the economic viability and adaptability of nanoparticles for pilot and field EOR applications. Most current studies have focused on and supported the use of mainly silica nanoparticles for EOR application especially in changing reservoir wettability from oil wet to water wet. However, the synthesis protocol for such materials may limit their scalability for field application. For example, looking at silica nanoparticle synthesis, which is one of the commonly used nanoparticles for EOR applications, the sol-gel procedure used in their synthesis and production involves the use of freeze-drying under nitrogen and calcination at higher temperatures which makes the entire synthesis process cumbersome and expensive [200, 201]. Therefore, there is a need to develop easy pathways that are effective and adaptable. The cost of the chemicals together with the equipment used in synthesizing nanoparticles should be economically justifiable and offer scalability options at low costs. Currently, no economic analysis has been developed to compare the oil prices with nanoparticle costs. This hinders the adoption of nanoparticles in the real field application of oil and gas.

2.9 Concerns and Uncertainties of Applying Nanoparticles in Oil and Gas Applications

Notwithstanding the role of nanotechnology in various applications such as medicine, environment, energy, etc., however, there still exist some major uncertainties and obstacles that need to be addressed [202]. Over the last decade, nanotechnology

has been viewed as environmentally friendly and many applications of nanomaterials have been reported. Despite its popularity, there remains less data on nanoparticles' effects on the environment because of few field applications [202]. Some initial findings reported that nanotechnology was safe for health [203]. For instance, The Royal Society and the Royal Academy of Engineering released a report which concluded that nanomaterials in several applications pose no new health risks [204]. Despite this, the related environmental benefits of nanoparticles are merged with risks that may be problematic and unpredictable, and also, there is scant information regarding disposal, reactivation usage, regeneration and other risks related to their exposure [205]. Karin et al. [206] demonstrated that plastic nanoparticles affect the survival of aquatic zooplankton and fish which can cause the behavioural disorder. Nevertheless, more finding while using other nanoparticles requires further investigations to understand their underlying effects. Given their shapes, some nanoparticles may easily match with some molecules like proteins and may therefore absorb when they contact body fluids and could potentially spread to sensitive body parts and damage them [207]. Studies have however proved that remedy management can help to reduce the environmental and health hazards associated with these nanoparticles [207]. Lowering contact with nanoparticles by using respirators has been proposed as a possible method of preventing the direct exposure of nanoparticles that may result in breathing difficulties [203]. For example, titanium, nickel, CNTs and cobalt have been hypothesized as nano types that are responsible for respiratory problems [207]. Ethical guidelines, test protocols and procedures need to be developed to provide proper and safer handling of nanomaterials for EOR usage. Agencies have started this procedure by offering improved healthy access and safety inspection pertaining nanoparticle usage. For instance, in America, the National Toxicology Program (NTP), National Center for Environmental Research of the Environmental Protection Agency (EPA), National Institute for Occupational Safety and Health (NIOSH) and the National Institute of Environmental Health Sciences have all been commissioned for application and risk assessment of nanomaterials [203, 208].

In summary, as a commendation to users of nanoparticles, less exposure and use of respirators/masks have been recommended as a way of lessening nanoparticle breathing that may damage the body organs [203].

2.10 Conclusions and Future Outlook

Many aspects of the petroleum industry may at one stage require the use of nanoparticles to improve their performance. At this time, researchers have shown how nanoparticles can be integrated with different recovery processes such as exploration, drilling, oil upgrading, etc. In this chapter, different types of nanoparticles used in EOR have been reviewed and their underlying mechanisms explored for different reservoir formation types. In this chapter also, the different stability techniques for nanofluids before their application as EOR agents have been reviewed. Notwithstanding the recovery potential of nanofluids, the introduction of effective

and simple synthesis protocols that are cheaper and effective is paramount for scaling options, especially for field applications. These nanoparticles need to be cheap and environmentally sustainable. Previous research has primarily focused on the application of isotropic (homogenous) nanoparticles, while only a few have examined double-sided nanoparticles in EOR. Therefore, more investigations are desirable that apply amphiphilic nanomaterials to understand their underlying mechanism.

Acknowledgements The authors are grateful to the Natural Sciences and Engineering Research Council of Canada (NSERC) for the financial support. The first author acknowledges the Islamic Development Bank in Jeddah, Saudi Arabia, for the financial support through his PhD study.

References

1. L.W. Lake et al., *Fundamentals of Enhanced Oil Recovery* (2014
2. R. Sen, Biotechnology in petroleum recovery: the microbial EOR. Prog. Energy Combust. Sci. **34**(6), 714–724 (2008)
3. N. Abas, A. Kalair, N. Khan. Review of fossil fuels and future energy technologies. Futures. 69, 31–49 (2015)
4. National Petroleum Council. *Enhanced Oil Recovery – An Analysis of the Potential for Enhanced Oil Recovery from Known Fields in the United States–1976–2000* (Washington, DC, 1976)
5. Bilak, R., *Enhanced oil recovery methods*. 2006, Google Patents
6. S.A. Siddiqui, Enhanced oil recovery methods. Masters Abstracts International (2010)
7. V. Alvarado, E. Manrique, Enhanced oil recovery: an updated review. Energies **3**(9), 1529–1575 (2010)
8. A.A. Yousef, S. Al-Saleh, M.S. Al-Jawfi. Improved/enhanced oil recovery from carbonate reservoirs by tuning injection water salinity and ionic content. in *SPE Improved Oil Recovery Symposium* (Society of Petroleum Engineers, 2012)
9. S. Thomas, Enhanced oil recovery-an overview. Oil Gas Sci. Technol.-Revue de l'IFP **63**(1), 9–19 (2008)
10. G. Maggio, G. Cacciola, A variant of the Hubbert curve for world oil production forecasts. Energy Policy **37**(11), 4761–4770 (2009)
11. X. Kong, M. Ohadi. Applications of micro and nanotechnologies in the oil and gas industry-overview of the recent progress. in *Abu Dhabi International Petroleum Exhibition and Conference* (Society of Petroleum Engineers, 2010)
12. D.O. Shah, *Improved Oil Recovery by Surfactant and Polymer Flooding* (Elsevier, 2012)
13. A.A. Abe, *Relative Permeability and Wettability Implications of Dilute Surfactants at Reservoir Conditions* (2005)
14. W.R. Shu, K.J. Hartman, *Thermal Recovery Method for Viscous Oil*. 1986. Google Patents
15. O. Torsater et al. Improved oil recovery by nanofluids flooding: an experimental study. in *SPE Kuwait International Petroleum Conference and Exhibition* (Society of Petroleum Engineers, 2012)
16. L. Hendraningrat, S. Li, O. Torsæter, A coreflood investigation of nanofluid enhanced oil recovery. J. Pet. Sci. Eng. **111**, 128–138 (2013)
17. N. Ogolo, O. Olafuyi, M. Onyekonwu. Enhanced oil recovery using nanoparticles. in *SPE Saudi Arabia Section Technical Symposium and Exhibition* (Society of Petroleum Engineers, 2012)
18. P.M. McElfresh, D.L. Holcomb, D. Ector. Application of nanofluid technology to improve recovery in oil and gas wells. in *SPE International Oilfield Nanotechnology Conference and Exhibition* (Society of Petroleum Engineers, 2012)

19. J. Giraldo et al., Wettability alteration of sandstone cores by alumina-based nanofluids. Energy Fuel **27**(7), 3659–3665 (2013)
20. M. Khalil et al., Advanced nanomaterials in oil and gas industry: design, application and challenges. Appl. Energy **191**, 287–310 (2017)
21. W. Shen et al., Preparation of solid silver nanoparticles for inkjet printed flexible electronics with high conductivity. Nanoscale **6**(3), 1622–1628 (2014)
22. R. Mout et al., Surface functionalization of nanoparticles for nanomedicine. Chem. Soc. Rev. **41**(7), 2539–2544 (2012)
23. R. Subbiah, M. Veerapandian, K.S. Yun, Nanoparticles: functionalization and multifunctional applications in biomedical sciences. Curr. Med. Chem. **17**(36), 4559–4577 (2010)
24. J. Cheng et al., Formulation of functionalized PLGA–PEG nanoparticles for in vivo targeted drug delivery. Biomaterials **28**(5), 869–876 (2007)
25. K. Yang et al., Multimodal imaging-guided photothermal therapy using functionalized graphene nanosheets anchored with magnetic nanoparticles. Adv. Mater. **24**(14), 1868–1872 (2012)
26. H. Chang, H. Wu, Graphene-based nanocomposites: preparation, functionalization, and energy and environmental applications. Energy Environ. Sci. **6**(12), 3483–3507 (2013)
27. E. Serrano, G. Rus, J. Garcia-Martinez, Nanotechnology for sustainable energy. Renew. Sust. Energ. Rev. **13**(9), 2373–2384 (2009)
28. J.M. Perez, Iron oxide nanoparticles: Hidden talent. Nat. Nanotechnol. **2**(9), 535–536 (2007)
29. Y. Lei et al., Increased silver activity for direct propylene epoxidation via subnanometer size effects. Science **328**(5975), 224–228 (2010)
30. C. Matteo et al., Current and future nanotech applications in the oil industry. Am. J. Appl. Sci. **9**(6), 784 (2012)
31. B. Suleimanov, F. Ismailov, E. Veliyev, Nanofluid for enhanced oil recovery. J. Pet. Sci. Eng. **78**(2), 431–437 (2011)
32. T. Zhang et al. Nanoparticle-stabilized emulsions for applications in enhanced oil recovery. in *SPE Improved Oil Recovery Symposium* (Society of Petroleum Engineers, 2010)
33. P.L. Golas et al., Comparative study of polymeric stabilizers for magnetite nanoparticles using ATRP. Langmuir **26**(22), 16890–16900 (2010)
34. P. Saravanan, R. Gopalan, V. Chandrasekaran, Synthesis and characterisation of nanomaterials. Def. Sci. J. **58**(4), 504 (2008)
35. A.K. Mittal, Y. Chisti, U.C. Banerjee, Synthesis of metallic nanoparticles using plant extracts. Biotechnol. Adv. **31**(2), 346–356 (2013)
36. C. Negin, S. Ali, Q. Xie, Application of nanotechnology for enhancing oil recovery–a review. Petroleum **2**(4), 324–333 (2016)
37. L. Hendraningrat, S. Li, O. Torsater. Effect of some parameters influencing enhanced oil recovery process using silica nanoparticles: An experimental investigation. in *SPE Reservoir Characterization and Simulation Conference and Exhibition* (Society of Petroleum Engineers, 2013)
38. H. Ehtesabi et al., Enhanced heavy oil recovery in sandstone cores using TiO2 nanofluids. Energy Fuel **28**(1), 423–430 (2013)
39. D. Wasan, A. Nikolov, K. Kondiparty, The wetting and spreading of nanofluids on solids: Role of the structural disjoining pressure. Curr. Opin. Colloid Interface Sci. **16**(4), 344–349 (2011)
40. L. Hendraningrat, L. Shidong. A glass micromodel experimental study of hydrophilic nanoparticles retention for the EOR project. in *SPE Russian Oil and Gas Exploration and Production Technical Conference and Exhibition* (Society of Petroleum Engineers, 2012)
41. A. Esfandyari Bayat et al., Impact of metal oxide nanoparticles on enhanced oil recovery from limestone media at several temperatures. Energy Fuel **28**(10), 6255–6266 (2014)
42. R. Hashemi, N.N. Nassar, P.P. Almao, Nanoparticle technology for heavy oil in-situ upgrading and recovery enhancement: Opportunities and challenges. Appl. Energy **133**, 374–387 (2014)
43. J.G. Speight, *The Chemistry and Technology of Petroleum* (CRC Press, 2014)
44. O.C. Mullins, The asphaltenes. Annu. Rev. Anal. Chem. **4**, 393–418 (2011)

45. F.J. Pettijohn, P.E. Potter, R. Siever, *Sand and Sandstone* (Springer Science & Business Media, 2012)
46. P. Darling, *SME Mining Engineering Handbook*, vol. 1 (SME, 2011)
47. L. Wang et al., The study of thermal stability of the SiO2 powders with high specific surface area. Mater. Chem. Phys. **57**(3), 260–263 (1999)
48. C.R. Miranda, L.S.D. Lara, B.C. Tonetto. Stability and mobility of functionalized silica nanoparticles for enhanced oil recovery applications. in *SPE International Oilfield Nanotechnology Conference and Exhibition* (Society of Petroleum Engineers, 2012)
49. H. Zhang, A. Nikolov, D. Wasan, Enhanced oil recovery (EOR) using nanoparticle dispersions: Underlying mechanism and imbibition experiments. Energy Fuel **28**(5), 3002–3009 (2014)
50. T. Sharma, S. Iglauer, J.S. Sangwai, Silica nanofluids in an oilfield polymer polyacrylamide: Interfacial properties, wettability alteration, and applications for chemical enhanced oil recovery. Ind. Eng. Chem. Res. **55**(48), 12387–12397 (2016)
51. M. Zargartalebi, R. Kharrat, N. Barati, Enhancement of surfactant flooding performance by the use of silica nanoparticles. Fuel **143**, 21–27 (2015)
52. N. Jain, Y. Wang, S.K. Jones, B.S. Hawkett, G.G. Warr, Optimized steric stabilization of aqueous ferrofluids and magnetic nanoparticles. Langmuir **26**(6), 4465–4472 (2009
53. J. Yu et al. Study of adsorption and transportation behaviour of nanoparticles in three different porous media. in *SPE Improved Oil Recovery Symposium* (Society of Petroleum Engineers, 2012)
54. A. Roustaei et al. An experimental investigation of polysilicon nanoparticles' recovery efficiencies through changes in interfacial tension and wettability alteration. in *SPE International Oilfield Nanotechnology Conference and Exhibition* (Society of Petroleum Engineers, 2012)
55. M.O. Onyekonwu, N.A. Ogolo. Investigating the use of nanoparticles in enhancing oil recovery. in *Nigeria Annual International Conference and Exhibition* (Society of Petroleum Engineers, 2010)
56. R. Nazari Moghaddam et al., Comparative study of using nanoparticles for enhanced oil recovery: wettability alteration of carbonate rocks. Energy Fuel **29**(4), 2111–2119 (2015)
57. H.M. Zaid et al. The effect of zinc oxide and aluminum oxide nanoparticles on interfacial tension and viscosity of nanofluids for enhanced oil recovery. in *Advanced Materials Research* (Trans Tech Publications, 2014)
58. L. Hendraningrat, O. Torsæter, Metal oxide-based nanoparticles: revealing their potential to enhance oil recovery in different wettability systems. Appl. Nanosci. **5**(2), 181–199 (2015)
59. A.E. Bayat, R. Junin. Transportation of metal oxide nanoparticles through various porous media for enhanced oil recovery. in *SPE/IATMI Asia Pacific Oil & Gas Conference and Exhibition* (Society of Petroleum Engineers, 2015)
60. R. Zabala et al. Nano-technology for asphaltenes inhibition in Cupiagua South Wells. in *IPTC 2014: International Petroleum Technology Conference* (2014)
61. P. Mukherjee et al., Fungus-mediated synthesis of silver nanoparticles and their immobilization in the mycelial matrix: a novel biological approach to nanoparticle synthesis. Nano Lett. **1**(10), 515–519 (2001)
62. M.A. Meyers, A. Mishra, D.J. Benson, Mechanical properties of nanocrystalline materials. Prog. Mater. Sci. **51**(4), 427–556 (2006)
63. N.N. Nassar, A. Hassan, P. Pereira-Almao, Metal oxide nanoparticles for asphaltene adsorption and oxidation. Energy Fuel **25**(3), 1017–1023 (2011)
64. N.N. Nassar, A. Hassan, P. Pereira-Almao, Application of nanotechnology for heavy oil upgrading: Catalytic steam gasification/cracking of asphaltenes. Energy Fuel **25**(4), 1566–1570 (2011)
65. C.A. Franco et al., Adsorption and subsequent oxidation of Colombian asphaltenes onto nickel and/or palladium oxide supported on fumed silica nanoparticles. Energy Fuel **27**(12), 7336–7347 (2013)

66. S.I. Hashemi et al., On the application of NiO nanoparticles to mitigate in situ asphaltene deposition in carbonate porous matrix. Appl. Nanosci. **6**(1), 71–81 (2016)
67. S. Rellegadla et al., An effective approach for enhanced oil Recovery using nickel nanoparticles assisted polymer flooding. Energy Fuel **32**(11), 11212–11221 (2018)
68. J.B. Gardiner, Studies in the morphology and vulcanization of gum rubber blends. Rubber Chem. Technol. **43**(2), 370–399 (1970)
69. Y. Lin et al., Graphene nanosheets decorated with ZnO nanoparticles: facile synthesis and promising application for enhancing the mechanical and gas barrier properties of rubber nanocomposites. RSC Adv. **5**(71), 57771–57780 (2015)
70. V. Sousa et al., Combustion synthesized ZnO powders for varistor ceramics. Int. J. Inorg. Mater. **1**(3–4), 235–241 (1999)
71. O. Oprea et al., ZnO applications and challenges. Curr. Org. Chem. **18**(2), 192–203 (2014)
72. A. Moezzi, A.M. McDonagh, M.B. Cortie, Zinc oxide particles: synthesis, properties and applications. Chem. Eng. J. **185**, 1–22 (2012)
73. H. Soleimani et al., Synthesis of ZnO nanoparticles for oil-water interfacial tension reduction in enhanced oil recovery. Appl. Phys. A **124**(2), 128 (2018)
74. N.N. Nassar et al., Iron oxide nanoparticles for rapid adsorption and enhanced catalytic oxidation of thermally cracked asphaltenes. Fuel **95**, 257–262 (2012)
75. R. Hashemi, N.N. Nassar, P. Pereira Almao, Enhanced heavy oil recovery by in situ prepared ultradispersed multimetallic nanoparticles: a study of hot fluid flooding for Athabasca bitumen recovery. Energy Fuel **27**(4), 2194–2201 (2013)
76. N.N. Nassar, M.M. Husein, Ultradispersed particles in heavy oil: Part I, preparation and stabilization of iron oxide/hydroxide. Fuel Process. Technol. **91**(2), 164–168 (2010)
77. X. Li et al., Effect of nanoparticles on asphaltene aggregation in a micro-sized pore. Ind. Eng. Chem. Res. (2018)
78. E.A. Taborda et al., Experimental and theoretical study of viscosity reduction in heavy crude oils by addition of nanoparticles. Energy Fuel **31**(2), 1329–1338 (2017)
79. Y. Kazemzadeh et al., Behavior of asphaltene adsorption onto the metal oxide nanoparticle surface and its effect on heavy oil Recovery. Ind. Eng. Chem. Res. **54**(1), 233–239 (2015)
80. N.N. Nassar, Iron oxide nanoadsorbents for removal of various pollutants from wastewater: an overview, in *Application of Adsorbents for Water Pollution Control*, (Bentham Science Publishers, Oak Park, 2012), pp. 81–118
81. L. Nwidee et al. *Nanofluids for enhanced oil recovery processes: wettability alteration using zirconium oxide*. in *Offshore Technology Conference Asia* (Offshore Technology Conference, 2016)
82. A. Karimi et al., Wettability alteration in carbonates using zirconium oxide nanofluids: EOR implications. Energy Fuel **26**(2), 1028–1036 (2012)
83. Teh, C. Y., Budiman, P. M., Shak, K. P. Y., & Wu, T. Y. (2016). Recent advancement of coagulation–flocculation and its application in wastewater treatment. *Industrial & Engineering Chemistry Research, 55*(16), 4363–4389
84. R. Gopalan, C.-H. Chang, Y. Lin, Thermal stability improvement on pore and phase structure of sol-gel derived zirconia. J. Mater. Sci. **30**(12), 3075–3081 (1995)
85. K. Tanabe, Surface and catalytic properties of ZrO2. Mater. Chem. Phys. **13**(3–4), 347–364 (1985)
86. X. Wang, L. Zhi, K. Müllen, Transparent, conductive graphene electrodes for dye-sensitized solar cells. Nano Lett. **8**(1), 323–327 (2008)
87. G. Jo et al., The application of graphene as electrodes in electrical and optical devices. Nanotechnology **23**(11), 112001 (2012)
88. M.D. Stoller et al., Graphene-based ultracapacitors. Nano Lett. **8**(10), 3498–3502 (2008)
89. L.L. Zhang, R. Zhou, X. Zhao, Graphene-based materials as supercapacitor electrodes. J. Mater. Chem. **20**(29), 5983–5992 (2010)
90. M. Pumera, Graphene-based nanomaterials for energy storage. Energy Environ. Sci. **4**(3), 668–674 (2011)

91. B.D. Nguyen et al., The impact of graphene oxide particles on viscosity stabilization for diluted polymer solutions using in enhanced oil recovery at HTHP offshore reservoirs. Adv. Nat. Sci. Nanosci. Nanotechnol. **6**(1), 015012 (2014)
92. D. Luo et al., Nanofluid of graphene-based amphiphilic Janus nanosheets for tertiary or enhanced oil recovery: high performance at low concentration. Proc. Natl. Acad. Sci., 201608135 (2016)
93. A. Barrabino, T. Holt, E. Lindeberg, *Graphene Oxide as Foam Stabilizing Agent for CO2 EOR* (2018)
94. D.T. Wasan, A.D. Nikolov, Spreading of nanofluids on solids. Nature **423**(6936), 156 (2003)
95. M.S. Alnarabiji et al., The influence of hydrophobic multiwall carbon nanotubes concentration on enhanced oil recovery. Procedia Eng. **148**, 1137–1140 (2016)
96. B. Wei et al., The potential of a novel nanofluid in enhancing oil recovery. Energy Fuel **30**(4), 2882–2891 (2016)
97. R.C. Aadland et al., *Identification of Nanocellulose Retention Characteristics in Porous Media* (2018)
98. H. ShamsiJazeyi et al., Polymer-coated nanoparticles for enhanced oil recovery. J. Appl. Polym. Sci. **131**(15) (2014)
99. M. Ranka, P. Brown, T.A. Hatton, Responsive stabilization of nanoparticles for extreme salinity and high-temperature reservoir applications. ACS Appl. Mater. Interfaces **7**(35), 19651–19658 (2015)
100. A.-M. Sung, I. Piirma, Electrosteric stabilization of polymer colloids. Langmuir **10**(5), 1393–1398 (1994)
101. X. Wang, R.D. Tilley, J.J. Watkins, Simple ligand exchange reactions enabling excellent dispersibility and stability of magnetic nanoparticles in polar organic, aromatic, and protic solvents. Langmuir **30**(6), 1514–1521 (2014)
102. M.-A. Neouze, U. Schubert, Surface modification and functionalization of metal and metal oxide nanoparticles by organic ligands. Monatshefte für Chemie/Chemical Monthly **139**(3), 183–195 (2008)
103. N. Erathodiyil, J.Y. Ying, Functionalization of inorganic nanoparticles for bioimaging applications. Acc. Chem. Res. **44**(10), 925–935 (2011)
104. L. Nobs et al., Current methods for attaching targeting ligands to liposomes and nanoparticles. J. Pharm. Sci. **93**(8), 1980–1992 (2004)
105. J.-C. Boyer et al., Surface modification of upconverting NaYF4 nanoparticles with PEG–phosphate ligands for NIR (800 nm) biolabeling within the biological window. Langmuir **26**(2), 1157–1164 (2009)
106. R. De Palma et al., Silane ligand exchange to make hydrophobic superparamagnetic nanoparticles water-dispersible. Chem. Mater. **19**(7), 1821–1831 (2007)
107. M. Khalil et al., Non-aqueous modification of synthesized hematite nanoparticles with oleic acid. Colloids Surf. A Physicochem. Eng. Asp. **453**, 7–12 (2014)
108. R. Boissezon et al., Organophosphonates as anchoring agents onto metal oxide-based materials: synthesis and applications. RSC Adv. **4**(67), 35690–35707 (2014)
109. H.-C. Wu et al., Chemistry of carbon nanotubes in biomedical applications. J. Mater. Chem. **20**(6), 1036–1052 (2010)
110. C. Dai et al., Spontaneous imbibition investigation of self-dispersing silica nanofluids for enhanced oil recovery in low-permeability cores. Energy Fuel **31**(3), 2663–2668 (2017)
111. Y. Li et al., Investigation of spontaneous imbibition by using a surfactant-free active silica water-based nanofluid for enhanced oil recovery. Energy Fuel **32**(1), 287–293 (2017)
112. J.R.. Baran Jr, O.J. Cabrera, *Use of Surface-Modified Nanoparticles for Oil Recovery*. 2006. Google Patents
113. F. Sagala et al., Nanopyroxene-based nanofluids for enhanced oil recovery in sandstone cores. Energy Fuel (2019)
114. F. Sagala et al., Nanopyroxene-based nanofluids for enhanced oil recovery in sandstone cores at reservoir temperature. Energy Fuel **33**(2), 877–890 (2019)

115. F. Sagala, A. Hethnawi, N.N. Nassar, Hydroxyl-functionalized silicate-based nanofluids for enhanced oil recovery. Fuel **269**, 117462 (2020)
116. S. Farad et al., Effect of wettability on oil recovery and breakthrough time for immiscible gas flooding. Pet. Sci. Technol. **34**(20), 1705–1711 (2016)
117. P. Pillai, A. Mandal, Wettability modification and adsorption characteristics of imidazole-based ionic liquid on carbonate rock: Implications for enhanced oil recovery. Energy Fuel (2019)
118. W. Anderson, Wettability literature survey–part 1 to part 6. J. Pet. Technol. **1986**, 1125–1144 (1987)
119. M. Salehi, S.J. Johnson, J.-T. Liang, Mechanistic study of wettability alteration using surfactants with applications in naturally fractured reservoirs. Langmuir **24**(24), 14099–14107 (2008)
120. J. Yan, J. Monezes, M.M. Sharma, Wettability alteration caused by oil-based muds and mud components. SPE Drilling Complet. **8**(01), 35–44 (1993)
121. R.S. Al-Maamari, J.S. Buckley, Asphaltene precipitation and alteration of wetting: the potential for wettability changes during oil production. SPE Reserv. Eval. Eng. **6**(04), 210–214 (2003)
122. A. Munshi et al., Effect of nanoparticle size on sessile droplet contact angle. J. Appl. Phys. **103**(8), 084315 (2008)
123. S.W. Hasan, M.T. Ghannam, N. Esmail, Heavy crude oil viscosity reduction and rheology for pipeline transportation. Fuel **89**(5), 1095–1100 (2010)
124. G.A. Núñez et al., Flow characteristics of concentrated emulsions of very viscous oil in water. J. Rheol. **40**(3), 405–423 (1996)
125. M. Schumacher, *Enhanced Recovery of Residual and Heavy Oils* (Noyes Publications, 1980)
126. W. Li, J.-h. Zhu, J.-h. Qi, Application of nano-nickel catalyst in the viscosity reduction of Liaohe extra-heavy oil by aqua-thermolysis. J. Fuel Chem. Technol. **35**(2), 176–180 (2007)
127. E.A. Taborda et al., Effect of nanoparticles/nanofluids on the rheology of heavy crude oil and its mobility on porous media at reservoir conditions. Fuel **184**, 222–232 (2016)
128. Y.H. Shokrlu, T. Babadagli, Viscosity reduction of heavy oil/bitumen using micro-and nano-metal particles during aqueous and non-aqueous thermal applications. J. Pet. Sci. Eng. **119**, 210–220 (2014)
129. F. Duan, D. Kwek, A. Crivoi, Viscosity affected by nanoparticle aggregation in Al_2O_3-water nanofluids. Nanoscale Res. Lett. **6**(1), 248 (2011)
130. D. Wever, F. Picchioni, A. Broekhuis, Polymers for enhanced oil recovery: a paradigm for structure-property relationship in aqueous solution. Prog. Polym. Sci. **36**(11), 1558–1628 (2011)
131. F. Wassmuth et al., Polymer flood application to improve heavy oil recovery at East Bodo. J. Can. Pet. Technol. **48**(02), 55–61 (2009)
132. L. Elias et al., Morphology and rheology of immiscible polymer blends filled with silica nanoparticles. Polymer **48**(20), 6029–6040 (2007)
133. A. Maghzi et al., An experimental investigation of silica nanoparticles effect on the rheological behaviour of polyacrylamide solution to enhance heavy oil recovery. Pet. Sci. Technol. **31**(5), 500–508 (2013)
134. L.J. Giraldo et al., The effects of SiO2 nanoparticles on the thermal stability and rheological behaviour of hydrolyzed polyacrylamide based polymeric solutions. J. Pet. Sci. Eng. **159**, 841–852 (2017)
135. G. Cheraghian, S.S. Khalilinezhad, Effect of nanoclay on heavy oil recovery during polymer flooding. Pet. Sci. Technol. **33**(9), 999–1007 (2015)
136. Q. Sun et al., Utilization of surfactant-stabilized foam for enhanced oil recovery by adding nanoparticles. Energy Fuel **28**(4), 2384–2394 (2014)
137. F. Liu et al., Effect of non-ionic surfactants on the formation of DNA/emulsion complexes and emulsion-mediated gene transfer. Pharm. Res. **13**(11), 1642–1646 (1996)
138. S. Friberg, P.O. Jansson, E. Cederberg, Surfactant association structure and emulsion stability. J. Colloid Interf. Sci. **55**(3), 614–623 (1976)

139. R.D. Shupe, J. Maddox Jr, *Surfactant oil recovery process usable in high temperature, high salinity formations*. 1978. Google Patents
140. C. Negin, S. Ali, Q. Xie, Most common surfactants employed in chemical enhanced oil recovery. Petroleum **3**(2), 197–211 (2017)
141. D. Wang et al., Synergistic effect of silica nanoparticles and Rhamnolipid on wettability alteration of low permeability sandstone rocks. Energy Fuel (2018)
142. J.P. Heller. *CO2 Foams in Enhanced Oil Recovery* (ACS Publications, 1994)
143. J. Yu, et al. Foam mobility control for nanoparticle-stabilized supercritical CO2 foam. in *SPE improved oil recovery symposium* (Society of Petroleum Engineers, 2012)
144. K. Kondiparty et al., Wetting and spreading of nanofluids on solid surfaces driven by the structural disjoining pressure: statics analysis and experiments. Langmuir **27**(7), 3324–3335 (2011)
145. A. Chengara et al., Spreading of nanofluids driven by the structural disjoining pressure gradient. J. Colloid Interface Sci. **280**(1), 192–201 (2004)
146. D.A. Espinoza et al. Nanoparticle-stabilized supercritical CO2 foams for potential mobility control applications. in *SPE Improved Oil Recovery Symposium* (Society of Petroleum Engineers, 2010)
147. M.A. Manan et al., Effects of nanoparticle types on carbon dioxide foam flooding in enhanced oil Recovery. Pet. Sci. Technol. **33**(12), 1286–1294 (2015)
148. S. Li et al., Properties of carbon dioxide foam stabilized by hydrophilic nanoparticles and hexadecyltrimethylammonium bromide. Energy Fuel **31**(2), 1478–1488 (2017)
149. W. Yang et al., Foams stabilized by in situ-modified nanoparticles and anionic surfactants for enhanced oil Recovery. Energy Fuel **31**(5), 4721–4730 (2017)
150. Y. Hurtado et al., Effects of surface acidity and polarity of SiO2 nanoparticles on the foam stabilization applied to natural gas flooding in tight gas-condensate reservoirs. Energy Fuel **32**(5), 5824–5833 (2018)
151. J. Pickering, Pickering emulsions. J. Chem. Soc (2001)
152. T. Sharma, G.S. Kumar, J.S. Sangwai, Comparative effectiveness of production performance of Pickering emulsion stabilized by nanoparticle–surfactant–polymer over surfactant–polymer (SP) flooding for enhanced oil recovery for Brownfield reservoir. J. Pet. Sci. Eng. **129**, 221–232 (2015)
153. T. Sharma et al., Use of oil-in-water Pickering emulsion stabilized by nanoparticles in combination with polymer flood for enhanced oil recovery. Pet. Sci. Technol. **33**(17–18), 1595–1604 (2015)
154. K.Y. Yoon et al., Core flooding of complex nanoscale colloidal dispersions for enhanced oil recovery by in situ formations of stable oil-in-water Pickering emulsions. Energy Fuel **30**(4), 2628–2635 (2016)
155. T. Montoya et al., A novel solid-liquid equilibrium model for describing the adsorption of associating asphaltene molecules onto solid surfaces based on the "chemical theory". Energy Fuel **28**(8), 4963–4975 (2014)
156. E. Rogel, C. Ovalles, M. Moir, Asphaltene stability in crude oils and petroleum materials by solubility profile analysis. Energy Fuel **24**(8), 4369–4374 (2010)
157. F. Adebiyi, V. Thoss, Spectroscopic characterization of asphaltene fraction of Nigerian Bitumen. Pet. Sci. Technol. **33**(2), 245–255 (2015)
158. J.C. Pereira et al., Resins: the molecules responsible for the stability/instability phenomena of asphaltenes. Energy Fuel **21**(3), 1317–1321 (2007)
159. H. Doryani, M.R. Malayeri, M. Riazi, Visualization of asphaltene precipitation and deposition in a uniformly patterned glass micromodel. Fuel **182**, 613–622 (2016)
160. S. Dubey, M. Waxman, Asphaltene adsorption and desorption from mineral surfaces. SPE Reserv. Eng. **6**(03), 389–395 (1991)
161. S. Kim, M. Boudh-Hir, G. Mansoori. *The role of asphaltene in wettability reversal*. in *SPE Annual Technical Conference and Exhibition* (Society of Petroleum Engineers, 1990)
162. J.J. Adams, Asphaltene adsorption, a literature review. Energy Fuel **28**(5), 2831–2856 (2014)

163. X. Yang, V.J. Verruto, P.K. Kilpatrick, Dynamic asphaltene– resin exchange at the oil/water interface: Time-dependent W/O emulsion stability for asphaltene/resin model oils. Energy Fuel **21**(3), 1343–1349 (2007)
164. L.C.R. Junior, M.S. Ferreira, A.C. da Silva Ramos, Inhibition of asphaltene precipitation in Brazilian crude oils using new oil-soluble amphiphiles. J. Pet. Sci. Eng. **51**(1–2), 26–36 (2006)
165. K.J. Leontaritis, G.A. Mansoori, Asphaltene deposition: a survey of field experiences and research approaches. J. Pet. Sci. Eng. **1**(3), 229–239 (1988)
166. Y.. Yin, A. Yen. Asphaltene deposition and chemical control in CO2 floods. in *SPE/DOE Improved Oil Recovery Symposium* (Society of Petroleum Engineers, 2000)
167. S. Betancur et al., Role of particle size and surface acidity of silica gel nanoparticles in inhibition of formation damage by asphaltene in oil reservoirs. Ind. Eng. Chem. Res. **55**(21), 6122–6132 (2016)
168. M. Mohammadi et al., Inhibition of asphaltene precipitation by TiO_2, SiO_2, and ZrO_2 nanofluids. Energy Fuel **25**(7), 3150–3156 (2011)
169. C.A. Franco et al., Nanoparticles for inhibition of asphaltenes damage: adsorption study and displacement test on porous media. Energy Fuel **27**(6), 2899–2907 (2013)
170. N.N. Nassar, A. Hassan, P. Pereira-Almao, Effect of surface acidity and basicity of aluminas on asphaltene adsorption and oxidation. J. Colloid Interf. Sci. **360**(1), 233–238 (2011)
171. H.P. Roenningsen et al., Wax precipitation from North Sea crude oils: 1. Crystallization and dissolution temperatures, and Newtonian and non-Newtonian flow properties. Energy Fuel **5**(6), 895–908 (1991)
172. R. Edwards, Crystal habit of paraffin wax. Ind. Eng. Chem. **49**(4), 750–757 (1957)
173. F. Yang et al., Scaling of structural characteristics of gelled model waxy oils. Energy Fuel **27**(7), 3718–3724 (2013)
174. L. Wardhaugh, D. Boger, Flow characteristics of waxy crude oils: application to pipeline design. AICHE J. **37**(6), 871–885 (1991)
175. F. Yang et al., Polymeric wax inhibitors and pour point depressants for waxy crude oils: a critical review. J. Dispers. Sci. Technol. **36**(2), 213–225 (2015)
176. F. Wang et al., The effect of nanohybrid materials on the pour-point and viscosity depressing of waxy crude oil. Chin. Sci. Bull. **56**(1), 14–17 (2011)
177. J. Norrman et al., Nanoparticles for waxy crudes: effect of polymer coverage and the effect on wax crystallization. Energy Fuel **30**(6), 5108–5114 (2016)
178. F. Yang et al., Hydrophilic nanoparticles facilitate wax inhibition. Energy Fuel **29**(3), 1368–1374 (2015)
179. E.O. Recovery, Using nanoparticle dispersions: Underlying mechanism and imbibition experiments Zhang, Hua; Nikolov, Alex; Wasan, Darsh. Energy Fuel **28**(5), 3002–3009 (2014)
180. A. Trokhymchuk et al., A simple calculation of structural and depletion forces for fluids/suspensions confined in a film. Langmuir **17**(16), 4940–4947 (2001)
181. H.C. Lau, M. Yu, Q.P. Nguyen, Nanotechnology for oilfield applications: Challenges and impact. J. Pet. Sci. Eng. **157**, 1160–1169 (2017)
182. 唐琛 张成亮, 杨振忠, *Large Scale Synthesis of Janus Submicrometer Sized Colloids by Seeded Emulsion Polymerization* (2010)
183. C. Tang et al., Large scale synthesis of Janus submicrometer sized colloids by seeded emulsion polymerization. Macromolecules **43**(11), 5114–5120 (2010)
184. C. Kaewsaneha et al., Preparation of Janus colloidal particles via Pickering emulsion: an overview. Colloids Surf. A Physicochem. Eng. Asp. **439**, 35–42 (2013)
185. M. Lattuada, T.A. Hatton, Synthesis, properties and applications of Janus nanoparticles. Nano Today **6**(3), 286–308 (2011)
186. S.-Y. Teh et al., Droplet microfluidics. Lab Chip **8**(2), 198–220 (2008)
187. N.P. Pardhy, B.M. Budhlall, Pickering emulsion as a template to synthesize Janus colloids with anisotropy in the surface potential. Langmuir **26**(16), 13130–13141 (2010)
188. S.J.. Liang Hong, S. Granick, Simple method to produce Janus colloidal particles in large. Am. Chem. Soc., 5 (2006)

189. A. Böker et al., Self-assembly of nanoparticles at interfaces. Soft Matter **3**(10), 1231–1248 (2007)
190. R. Aveyard, J.H. Clint, T.S. Horozov, Aspects of the stabilisation of emulsions by solid particles: Effects of line tension and monolayer curvature energy. Phys. Chem. Chem. Phys. **5**(11), 2398–2409 (2003)
191. A. Perro et al., Production of large quantities of "Janus" nanoparticles using wax-in-water emulsions. Colloids Surf. A Physicochem. Eng. Asp. **332**(1), 57–62 (2009)
192. Z.B.Z. Shawon, Synthesis and characterization of Janus magnetic nanoparticles and its application as an adsorbent. J. Chem. Eng. **27**(1), 64–68 (2013)
193. D. Luo et al., Nanofluid of graphene-based amphiphilic Janus nanosheets for tertiary or enhanced oil recovery: High performance at low concentration. Proc. Natl. Acad. Sci. U. S. A. **113**(28), 7711–7716 (2016)
194. H. Wu et al., Silica-based amphiphilic Janus nanofluid with improved interfacial properties for enhanced oil recovery. Colloids Surf. A Physicochem. Eng. Asp. **586**, 124162 (2020)
195. Y.V. Li, L.M. Cathles, L.A. Archer, Nanoparticle tracers in calcium carbonate porous media. J. Nanopart. Res. **16**(8), 2541 (2014)
196. T. Lu, Z. Li, Y. Zhou, Flow behavior and displacement mechanisms of nanoparticle stabilized foam flooding for enhanced heavy oil recovery. Energies **10**(4), 560 (2017)
197. T. Lu et al., Enhanced oil recovery of low-permeability cores by SiO_2 nanofluid. Energy Fuel **31**(5), 5612–5621 (2017)
198. T. Sharma, G. Suresh Kumar, J.S. Sangwai, Enhanced oil recovery using oil-in-water (o/w) emulsion stabilized by nanoparticle, surfactant and polymer in the presence of NaCl. Geosyst. Eng. **17**(3), 195–205 (2014)
199. Y. Ding et al. Low salinity hot water injection with addition of nanoparticles for enhancing heavy oil recovery under reservoir conditions. in *SPE Western Regional Meeting* (Society of Petroleum Engineers, 2018)
200. L.P. Singh et al., Sol-gel processing of silica nanoparticles and their applications. Adv. Colloid Interf. Sci. **214**, 17–37 (2014)
201. I.A. Rahman, V. Padavettan, Synthesis of silica nanoparticles by sol-gel: size-dependent properties, surface modification, and applications in silica-polymer nanocomposites — a review. J. Nanomater. **2012** (2012)
202. D.M. Kahan, D. Rejeski. Project on Emerging Nanotechnologies. 2009.
203. A. Nel et al., Toxic potential of materials at the nanolevel. Science **311**(5761), 622–627 (2006)
204. Royal Society. *Nanoscience and Nanotechnologies: Opportunities and Uncertainties* (Royal Society, 2004)
205. K.W. Powers et al., Research strategies for safety evaluation of nanomaterials. Part VI. Characterization of nanoscale particles for toxicological evaluation. Toxicol. Sci. **90**(2), 296–303 (2006)
206. K. Mattsson et al., Brain damage and behavioural disorders in fish induced by plastic nanoparticles delivered through the food chain. Sci. Rep. **7**(1), 11452 (2017)
207. R. Purohit et al., Social, environmental and ethical impacts of nanotechnology. Mater. Today Proc. **4**(4), 5461–5467 (2017)
208. N. Yekeen et al., A comprehensive review of experimental studies of nanoparticles-stabilized foam for enhanced oil recovery. J. Pet. Sci. Eng. **164**, 43–74 (2018)
209. S.K. Choi et al., Nanofluid enhanced oil recovery using hydrophobically associative zwitterionic polymer-coated silica nanoparticles. Energy Fuel **31**(8), 7777–7782 (2017)
210. L. Hendraningrat, O. Torsæter, Effects of the initial rock wettability on silica-based nanofluid-enhanced oil recovery processes at reservoir temperatures. Energy Fuel **28**(10), 6228–6241 (2014)
211. M.I. Youssif et al., Silica nanofluid flooding for enhanced oil recovery in sandstone rocks. Egypt. J. Petrol. (2017)
212. S. Al-Anssari et al., Wettability alteration of oil-wet carbonate by silica nanofluid. J. Colloid Interface Sci. **461**, 435–442 (2016)

213. E.A. Taborda et al., Experimental and theoretical study of viscosity reduction in heavy crude oils by addition of nanoparticles. Energy Fuel **31**(2), 1329–1338 (2017)
214. H. Soleimani et al., Impact of carbon nanotubes based nanofluid on oil recovery efficiency using core flooding. Results Phys. **9**, 39–48 (2018)
215. S.N. Molnes et al., Investigation of a new application for cellulose nanocrystals: a study of the enhanced oil recovery potential by use of a green additive. Cellulose **25**(4), 2289–2301 (2018)
216. E. Joonaki, S. Ghanaatian, The application of nanofluids for enhanced oil recovery: Effects on interfacial tension and coreflooding process. Pet. Sci. Technol. **32**(21), 2599–2607 (2014)
217. R. Singh, K.K. Mohanty, Foams stabilized by in-situ surface-activated nanoparticles in bulk and porous media. SPE J. **21**(01), 121–130 (2016)

Chapter 3
Nanoparticles as Adsorbents for Asphaltenes

Abdallah D. Manasrah, Tatiana Montoya, Azfar Hassan, and Nashaat N. Nassar

3.1 Introduction

Due to population growth, industrialization, and higher living standards, the total energy demand has increased worldwide, and it is expected to keep increasing by 33% in 2035 [1]. Hence, it is important to find an environmentally friendly, economic, and sustainable source to meet these demands. Considering renewable and non-renewable energy resources, still crude oil is a major player in meeting the global energy demand, and thus there is an interest in enhancing the oil and gas recovery to meet this demand. For instance, the oil sand reserves in Alberta are larger than the reserves of Iran, Iraq, or Russia and are second only in size to those of Saudi Arabia [2]. However, from these reserves, only 20% is easily extracted, and the remaining 80% should be recovered through Enhanced Oil Recovery (EOR) methods [2]. In addition, in some other reserves in the world can occur the formation damage [3]. This unwanted operational issue diminishes oil and gas recovery as well, limiting the reservoir productivity and causing deficient operation [4, 5]. This issue can be produced by interactions between the porous medium and reservoir fluids, resulting in other complications, like fines migration [6], asphaltene precipitation/deposition [7, 8], condensate banks [9], and alteration of the rock wettability [10], among others. In fact, the presence of asphaltenes in crude oil is one of the principal challenges in the oil industries nowadays. Common types of formation damage, like precipitation/deposition of asphaltenes in the reservoir and the production equipment [4, 11], are the hardest to pass. In addition, asphaltene deposition is a key factor in different domains of the oil industry, such as in wettability alteration of reservoir rock from water-wet to oil-wet, potential adsorption on reservoir rock

A. D. Manasrah · T. Montoya · A. Hassan · N. N. Nassar (✉)
Department of Chemical and Petroleum Engineering, University of Calgary, Calgary, Canada
e-mail: nassar@ucalgary.ca

N. N. Nassar et al. (eds.), *Nanoparticles: An Emerging Technology for Oil Production and Processing Applications*, Lecture Notes in Nanoscale Science and Technology, https://doi.org/10.1007/978-3-319-12051-5_3

[12, 13], plugging flow lines and deposition build-up [14], and refinery catalyst deactivation [15]. Consequently, these asphaltene-related problems cause significant production losses, in addition, to vastly increase in operational costs.

These kinds of problems, and the necessity to increase oil production, obligate researchers in removing the asphaltenes from oil and bitumen. Hence, several numbers of methods have been currently suggested to prevent asphaltene deposition, mainly in zones near wells [11]. Among these methods are included the recurring intervention through solvent soaking or continuous chemical injection [3, 16]. There are also chemical treatments including the incorporation of dispersants, anti-flocculants, coagulants, flocculants, and nonpolar solvents, among others; these methods are mainly employed to manage asphaltene precipitation/deposition [16, 17]. However, these conventional methods, such as chemical treatment, mechanical methods, thermal and biological, are expensive and in most of the cases they require complex equipment and additional staff on the location [3, 16]; also, they present reduced lastingness, can cause modifications in the fluid composition, and do not ensure the avoidance of asphaltene deposition after the treatment, in addition to their environmental concerns [3, 16]. Therefore, intensive research has been conducted for developing an alternative, cost-effective, and environmentally friendly technology to stabilize and remove the asphaltene. For those reasons, the interaction of asphaltenes with surfaces has drawn the attention of the researchers implementing a range of experimental analyses to investigate the adsorption of asphaltenes over several materials, such as silica [18, 19], alumina [19, 20], iron oxide [21], gold [18, 22–25], stainless steel [26], glass [27], and clay minerals [28–33]. This approach can be achieved by understanding the nature of these compounds and their interaction with the adsorbent to enhance heavy oil upgrading and recovery with low operational and capital cost.

Therefore, in recent years, nanotechnology revealed to have a significant impact on various industrial applications. Nanoparticles and/or nanofluids have been presented as alternatives for inhibiting the impairment caused by asphaltene precipitation and for in situ improvement of reservoir production [1, 34, 35]. Due to the unique properties of nanoparticles like high surface area/volume ratios, specific chemical reactivity, functional surfaces, and great dispersibility [1], they represent a prospect for an environmentally safe and economical option for heavy oil recovery and upgrading. Additionally, nanoparticles are very mobile in porous media since they are smaller than the relevant pore spaces, resulting in effective transport. These characteristics allow the capture and removal of the asphaltenes present in a reservoir, impacting directly on the enhancement of oil production, inhibiting formation damage and wettability alteration [36–38]. This chapter provides a summary of information related to the use of different families of nanoparticles for adsorption of asphaltenes from oil matrices. Topics covered include (1) role of nanoparticles as adsorbents, (2) models for asphaltene adsorption and disaggregation, and (3) factors affecting asphaltene adsorption.

The chapter also lists several factors and experimental conditions that impact the adsorption process and compares the adsorption parameters (i.e., capacities and affinities) of different families of nanomaterials.

3.1.1 Asphaltenes

Asphaltenes are considered the heaviest, most aromatic, and surface-active fraction of the crude oil, that is, insoluble in light paraffin, but soluble in light aromatics [7, 8, 39]. Usually, asphaltenes present a polyaromatic structure that has a few alkyl groups per aromatic ring; also they have some heteroatoms, like nitrogen, sulfur, oxygen, and metals, such as V, Fe, and Ni [40]. Thus, the presence of functional groups such as carboxyl, ketones, aldehydes, benzothiophenes, dibenzothiophenes, naftenobenzotiophenes, alkyl sulfides, aryl alkyl sulfides and aryl sulfides is likely to occur in asphaltene structure [8, 41]. The asphaltene structure is known for being complex; thus, a simplified description is that asphaltenes have a nucleus with one or more cross-linked polyaromatic hydrocarbons (PAHs) [8, 39, 42]. Several hypotheses on asphaltenes' chemical structures are found in literature; some of them are island, archipelago, continental, or rosary type [39, 42, 43]. The island architecture is composed of seven fused rings and one PAH; whereas the archipelago architecture is composed of more than one PAH per asphaltene molecule connected by alkyl chains [39, 44]. The continental type is formed by one or two PAHs but with a larger number of fused rings [43, 44]. The rosary-type asphaltenes are formed by two or more PAHs joined by flexible aliphatic chains. However, asphaltene structures are constantly updated due to complexity.

The Yen-Mullins model is widely used and accepted to describe asphaltenes' colloidal and molecular structure [8, 39, 45–48]. This model looks at the island-type architecture as the main molecular structure of asphaltenes. When asphaltene concentration increases, the self-associative behavior of asphaltenes results in the formation of nanoaggregates with sizes around 2 nm. Further increase in asphaltene concentration, i.e., higher concentration, the nanoaggregates form clusters with an average size of 5 nm and aggregation numbers <10 [39]. Due to its amphiphilic behavior, asphaltenes are prone to self-assemble and arrange in large aggregates that increase the HO viscosity [11, 49, 50]. Also, asphaltenes that have a high amount of sulfur integrate strong C-S and C=S bonds that results in an increase in the oil viscosity [51–53]. Additionally, the existence of large amounts of N and S in the asphaltene structure provides a route to the production of SOx, NOx, and H_2S during processing. These characteristics of asphaltenes make hard the production, transportation, and processing of heavy and extra-heavy oils.

3.1.2 Role of Nanoparticles as Adsorbents

Adsorption of asphaltenes over the surface of nanoparticles is an attractive topic for the oil industries. Because the asphaltenes' precipitation might occur in both heavy and light oils, the nanoparticles would remove asphaltenes faster, and this will make the remaining oil fraction movable and ready for commonly used processing [54, 55]. Additionally, the nanoparticles have been proven to act as catalysts by

integrating asphaltene adsorption and oxidation for upgrading asphaltenes into light usable distillates. Consequently, an increase in energy efficiency, reduction in capital cost, and enhanced performance and portability would result. Several types of adsorbents are introduced in the oil industry, and they exposed a significant impact on the upgrading of oil as an alternative approach for green and economical technology. The materials used in the adsorption can be classified into clays, rock minerals, minerals, glass, soils, silica, modified silica, alumina, silica-alumina, metals, metal oxides, several types of carbon, and polymers [7, 56]. It is worth mentioning is that the adsorption process is controlled by the structure of asphaltenes in addition to the physical and chemical characteristics of the adsorbent [57]. Also, the origin of asphaltenes is an important parameter to determine its structure, while the physical characteristics of adsorbents have an important effect in the adsorption process efficiencies, like surface area, surface morphology, pore diameter, internal pore volume, and pore distribution [58, 59]. It is worth noting that the possibility of diffusion problems and pore blocking is yet to occur when common porous adsorbents are employed for taking out asphaltenes [59]. Thus, reducing particle size, augmenting adsorbent porosity, and increasing surface area and pore diameter of the adsorbent may avoid those issues [7].

Accordingly, nanotechnology has emerged as an attractive area in heavy oil upgrading by asphaltene removal, air emission capture, wastewater treatment, etc. [60–65]. This is due to the exceptional physical and chemical properties of the nanoparticles like high surface area-to-volume ratio, excellent adsorption affinity, easy dispersion, and catalytic behaviors toward heavy hydrocarbons [66]. Therefore, the use of nanoparticles as adsorbent and catalyst for asphaltene adsorption and their following oxidation and/or pyrolysis was firstly introduced by Nassar group [67] and then followed by other research groups [68–70]. This cost-effective and environmental approach would have a positive impact on in situ and subsurface oil enhancing processes [66]. Various studies carried out by our research group used novel technologies for employing nanoparticles in oil upgrading and recovery processes, mainly for asphaltene remotion through adsorption and later after-adsorption decomposition [57, 66, 71]. Recently, it was confirmed by Dr. Nassar research group that the adsorption of asphaltenes will have an important impact in the oil industrials by employing the nanoparticles as suppressors to avoid or impede the precipitation of asphaltenes by in situ adsorption of asphaltenes inside the well [36, 72]. Moreover, nanoparticles proved their ability in dispersion and stabilization of asphaltene aggregates through adsorption coupled with their small size, and thus raising the idea to use them to prevent formation damage. Nanoparticles adsorb asphaltenes fast, preventing in this way asphaltene deposition by eliminating the coexistent flocculation and precipitation since the asphaltenes are stabilized inside the oil medium, resulting in an improved recovery. Furthermore, supported and unsupported nanoparticles have been used for asphaltene adsorption from oil continued by after-adsorption catalytic reactions. It was also confirmed that the adsorption of asphaltenes from oils on the nanoparticles will delay the asphaltene precipitation with variations in temperature, pressure, and composition [72, 73].

3.2 Modeling of Asphaltene Adsorption

3.2.1 Solid-Liquid Equilibrium (SLE) Model

As it is studied in this chapter, the interaction between asphaltenes and nanoparticles is defined by type and strength, and those characteristics depend on the functional groups and composition of the asphaltenes and the surface characteristics of the adsorbent [74]. Therefore, to understand the mechanism and kinetics of asphaltene adsorption, most of the studies have been done in batch mode [7, 29, 36, 67, 71, 75–80]. From those studies, two types of isotherms have been presented: Langmuir-type [81] and multilayer adsorption isotherms [74]. The first isotherm type indicates homogeneous monolayer coverage of asphaltenes over the nanoparticle surface [7, 76, 82], and the second isotherm type is usually depicted by Freundlich model and indicates aggregation and self-association behavior of the asphaltenes [7, 78, 83, 84]. Nevertheless, due to the complexity in the structure of asphaltenes and their propensity to self-associate in bigger molecules, Langmuir and Freundlich models give a short vision into the adsorption mechanism [74]. For this reason, Castro et al. [85] came up with a model for asphaltene adsorption based on molecular thermodynamics. This model successfully described asphaltene adsorption at equilibrium on rocks. Nonetheless, the model needs to find out ten molecular parameters making the usage of this model challenging and difficult.

Accordingly, Giraldo et al. [86] have proposed the Dubinin-Astakhov (DA) model built on the Polanyi theory [81] to ascribe asphaltene adsorption over surfaces of microparticles and nanoparticles. This model needs to find out three molecular parameters, related to the energy of the interactions: surface adsorbate, the maximum adsorbed amount, and the heterogeneity parameter. Nevertheless, DA model can not be used to describe the adsorption mechanism of self-associative molecules such as asphaltenes, especially at low loads and uniform dense region with moderate loads [74, 86]. Therefore, this chapter introduced a novel thermodynamic model built on the chemical theory [87, 88], named the solid-liquid equilibrium (SLE) model, to explain the adsorption performance of auto-assemble asphaltene molecules over several surfaces. The SLE model is linked to the thermodynamic equilibrium of asphaltene adsorption over surfaces taking into account the *i*-merization of the asphaltenes and their interaction with a solid surface but eliminating the pressure effect. The model is built up on the chemical equilibria, the equation of state, and the phase equilibrium. The SLE is expressed as:

$$C_E = \frac{\psi H}{1 + K\psi} \exp\left(\frac{\psi}{q_m A}\right) \tag{3.1}$$

where $\psi = \dfrac{-1 + \sqrt{1 + 4K\xi}}{2K}$, $\xi = \left(\dfrac{q_m q}{q_m - q}\right) A$, and q (mg/m^2) and q_m (mg/m^2) are the asphaltenes' uptake onto the nanoparticle surface and the maximum adsorption of the nanoparticles, respectively. A (m^2/mg) is the BET surface area per mass of

nanoparticles, and C_E (mg/g) is the equilibrium concentration of asphaltenes. The SLE parameters K (g/g) and H (mg/g) are the adsorption constants linked to the asphaltenes' self-assemble over the nanoparticles' surface and the Henry law constant, respectively [74].

3.2.2 Solid-Liquid Equilibrium Reservoir Conditions (SLE-RC) Model

In the previous section, it was presented the SLE model [74], which has been validated at low pressures, considering the theory by Talu and Meunier [88] and built on the chemical theory [87] to describe the solution behavior when the interaction forces are strong due to non-ideal conditions [74]. Because the pressure dependence has been usually ignored in most adsorption models for describing the adsorption behaviour of asphaltenes, in this part of the chapter a novel adsorption model to describe the asphaltene adsorption onto solid surfaces at high pressure and temperature is introduced [89]. For this purpose, the SLE model previously presented [74] is modified to include the pressure dependence providing thermodynamic evenness at usual reservoir conditions [89].

The adsorption isotherm equation based on the SLE model capable to describe the adsorption behavior under reservoir conditions (SLE-RC) is developed based on (i) the chemical equilibria, (ii) the equation of the state (EOS), and (iii) the phase equilibrium [89], and described in Figure 3.1 which shows the scheme for the derivations of the SLE-RC model.

After all the considerations and the mathematical treatment, the isotherm equation of the SLE-RC can be written as:

$$C = \frac{\Psi H}{1+\Psi K}\exp\left(\frac{\Psi}{N_m}\right)\exp\left[-\frac{v_{as}}{RT}\left(\delta_{as}-\delta_T\right)^2\right] \tag{3.2}$$

where K and Ψ are:

$$K = \frac{K_T RT}{SA} \tag{3.3}$$

$$\Psi = \frac{-1+\sqrt{1+4K\xi}}{2K} \tag{3.4}$$

where ξ is $\xi = NN_m/(N_m - N)$, N is the uptake (g/g), N_m is the maximum uptake (g/g), K_T is the reaction constant for dimer formation, SA is the specific surface area of the material [cm^2/g], v_{as} is the asphaltene molar volume [cm (g/g)3/mol], δ_{as} is the solubility parameter for asphaltenes [MPa$^{1/2}$], and δ_T [MPa$^{1/2}$] is the solubility parameter for the solvent reported in literature [90].

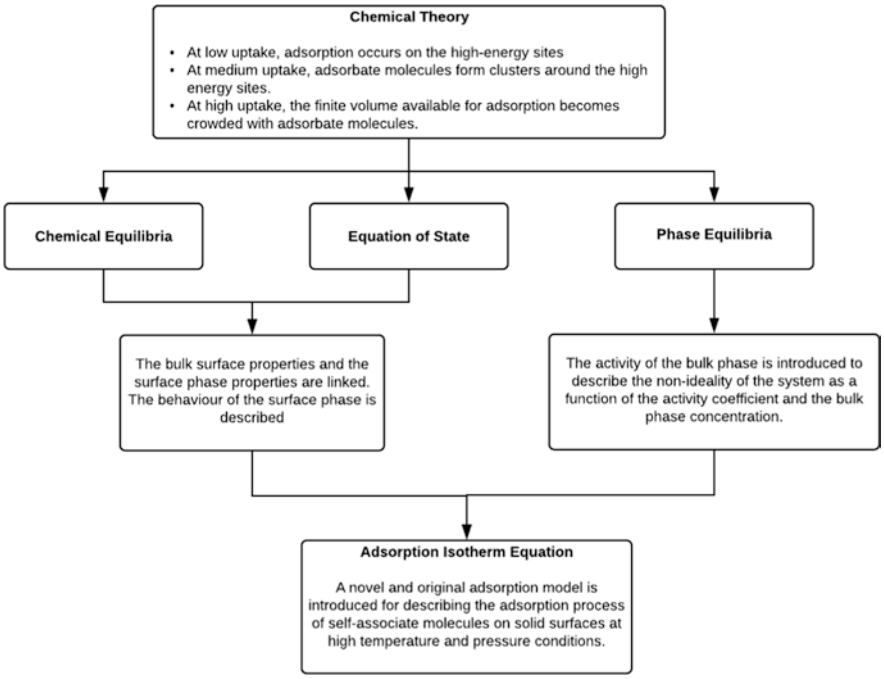

Fig. 3.1 Schematic representation of the deductions of the SLE-RC model [89]. Permissions related to the material presented were obtained from the American Chemical Society, copyright 2015, and further permission should be directed to the American Chemical Society; N.N. Nassar, T. Montoya, C.A. Franco, F.B. Cortés, P. Pereira-Almao. A New Model for Describing the Adsorption of Asphaltenes on Porous Media at a High Pressure and Temperature under Flow Conditions Energy & Fuels 29 (2015) 4210–4221

3.2.3 Disaggregation Model

It has been reported in the literature [91–97] several works about population balance models for describing the asphaltenes' increasing size but not considering asphaltene adsorption over nanoparticles. In this part of the chapter is presented a mathematical model that depicts the performance of asphaltene aggregation after accounting the adsorption of asphaltenes over nanoparticles [73]. In order to do this, a population balance model was proposed. This model assumed that asphaltenes under the presence of a shear rate are linked to the aggregation and fragmentation phenomena [93]. The population balance model that depicts the aggregation kinetics and fragmentation of asphaltenes was proposed in 2003 by Rahmani et al. [93]. The proposed model is established based on the theory that the aggregation is in its initial stages and rapidly growth of particles. When the aggregation increases and hydrodynamic stresses become of the order of the yield stress of the aggregates, the fragmentation becomes significant [98, 99]. Therefore, the model developed by Rahmani et al. [93], keeping the definition elaborated by Austin [98] and Friedlander

[100], was used to describe the kinetics of asphaltene aggregation, but a recently developed parameter that represents the inhibition produced by nanoparticles in the adsorption process was added to the model. An overview, the proposed model can be written as:

$$\frac{dn_i}{dt} = B - D - \frac{dq}{dt} \tag{3.5}$$

where $\frac{dn_i}{dt}$ is the concentration of the number of aggregates with size i, B is the term related to the appearance or aggregation of two particles of size i, D is the disappearance term in relation with the fragmentation owed to the collision of two particles with size i, and $\frac{dq}{dt}$ is the parameter tied in with the adsorption of asphaltene particles that do not interact on aggregation phenomena.

A more explained overview of the inhibition model of asphaltene aggregations [93, 100], when accounting adsorption on nanoparticles, is shown as follows:

$$\frac{dn_i}{dt} = \sum_{j+k=i} \alpha\beta_{jk}\left(V_j, V_k\right) n_j n_k - n_i \sum_{k=1}^{n_{\max}} \alpha\beta_{ik}\left(V_k, V_i\right) n_k - B_i n_i + \sum_{j=i+1}^{n_{\max}} \gamma_{i,j} B_j n_j - \frac{dq}{dt} \tag{3.6}$$

where, n_i is the number concentration of aggregates with size i (which means a simple aggregate contains i primary particles), β_{jk} is the collision frequency among particles of volumes V_j and V_k, α is the collision efficiency, B_i is the fragmentation rate of aggregates of size i, $\gamma_{i,j}$ is the fraction of volume of aggregates of size i originated by aggregates of size j, V_j/V_i, and n_{max} is the bigger size of particles that will create fragments of size i prior to fragmentation. In Eq. 3.6, the first term of the right side represents the formation of the particles of size i by collisions of particles j and k of minor size. The second term denotes the reduction of particles of size i by collisions with particles of any other size. The third term portrays the reduction of particles of size i by fragmentation, the fourth term explains the formation of particles of size i by fragmentation of biggest particles, and the fifth term refers to the adsorption of asphaltene particle that don't interact on aggregation phenomenon [73].

The collision frequency β_{jk} among particles of volumes V_j and V_k because of the Brownian motion and fluid shear is written in the following equation [93, 101]:

$$\beta_{jk} = \frac{2}{3}\frac{k_B T}{\mu}\left(\frac{d_i + d_j}{d_i d_j}\right)^2 + \frac{G}{6}\left(d_i + d_j\right)^3 \tag{3.7}$$

where k_B (1.38×10^{-23} m^2 kg s^{-2} K^{-1}) is the Boltzmann constant, T (K) is temperature, μ (Pa s) is the viscosity, and G (1/s) is the shear rate. The volume of a particle of size is written as:

$$V_i = \frac{fV_{i-1}}{1-\varepsilon} \tag{3.8}$$

where f is the sectional spacing, which is equal to 2 [93, 99, 102] and ε is the aggregate porosity which is assumed constant for aggregate formation from primary particles and can be used as a fitting parameter. The collision efficiency α is taken as 1.0 since bigger aggregates have fractal and porous structures [102–104]. In addition, the fragmentation rate B_i is defined as a function of particle volume [105, 106], as follows:

$$B_i = bV_i^a \tag{3.9}$$

where a = 1/3 and b is the rupture rate coefficient caused by shear fragmentation [93]. The coefficient b is used as a fitting parameter.

Then, the asphaltene aggregation inhibition parameter was included in the model utilizing adsorption kinetics of asphaltenes over the nanoparticles [73]. To determine the adsorption rate, it was used the double exponential model [107, 108]. This model is described by Eq. 3.10, as follows:

$$q_t = q_m - \frac{D_f}{M}\exp\left(-k_f t\right) - \frac{D_s}{M}\exp\left(-k_s t\right) \tag{3.10}$$

The double exponential model relates in two steps the kinetics of adsorption. As a result, k_f (min^{-1}), k_s (min^{-1}), D_f (mg/L), and D_s (mg/L) are the rate constants and adsorption coefficients of the fast and slow steps of the double exponential model, respectively, and q_m (mg/g) is the maximum amount of adsorbed asphaltenes [73].

3.3 Types of Nanoparticles for Asphaltene Adsorption

The adsorption process is commonly carried out by taking out asphaltenes from the heavy oil and dissolving them in a model solvent, like toluene or heptol (heptane + toluene). The batch adsorption usually takes place with a proportion of 1:10 (L/g) model oil solution/mass of the material at 298 K. Asphaltene adsorption over nanoparticles is established from the change in the concentration of asphaltenes in the oil solution before and after adding the nanoparticles. It is worth noting that the adsorption of asphaltenes over surfaces of materials is subjected to the type and strength of interactions among asphaltene and the material surface [40]. Several interparticle forces are accountable for this successful interaction among asphaltenes and the material surface as a result of functionalized groups on the asphaltenes, such as carboxylic, pyrrolic, pyridinic, thiophenic, and sulfite groups [85, 109]. The main forces that could promote these interactions are van der Waals, electrostatic, charge transfer, hydrogen bonding, and steric interactions [109]. Nassar et al. studied the adsorption of Athabasca asphaltenes utilizing different types of nanoparticles. The

authors obtained a monolayer of adsorbed asphaltenes over metal oxide nanoparticles [55, 110, 111], alumina [112], kaolin containing metal oxide nanoparticles [71], and modified kaolin [113]. Nassar et al. [55, 110, 111] reported the adsorption of n-C_7 asphaltenes from Athabasca vacuum residue over different types of metal oxide nanoparticles like NiO, Co_3O_4, Fe_3O_4, TiO_2, CaO, CeO_2, and ZrO_2. The authors disclosed that the adsorption of asphaltenes is highly influenced by the type of nanoparticles. In related studies with Iranian n-C_7 asphaltenes, Hosseinpour et al. [68] studied the adsorption of asphaltene over several acid/base metal oxide nanoparticles, such as NiO, Fe_2O_3, WO_3, MgO, $CaCO_3$, and ZrO_2. They got that the adsorption isotherms were Langmuir type with an adsorption capacity of 1.23–3.67 mg/m^2. In another study utilizing palladium and nickel oxide included on fumed silica nanoparticles, Franco et al. [114] obtained an important improvement in the adsorption of Colombian n-C_7 asphaltenes. The synergistic effect of these metal oxides might be achieved upon the incorporation. The authors realized that these supported nanoparticles promote the formation of type I adsorption isotherm, enabling subsequent processes of asphaltenes, as catalytic thermal cracking and the prevention of formation damage. Table 3.1 summarized the types of nanoparticles along with their maximum adsorption capacity on different types of extracted asphaltenes. As shown in the table, there is a variation in the maximum capacity (Q_m) of these nanoparticles which can be ascribed to a distinct degree of interaction among nanoparticle surface and asphaltenes as previously discussed. The polar interactions, for example, are mostly acid-base reactions taking place among adsorbate and adsorbent. From the presented outcomes so far, it can be reckoned that basic oxides and amphoteric oxides presented higher adsorption ability in comparison with acidic oxides, like TiO_2 and NiO. Nevertheless, the quality of adsorption determined by adsorption affinity values was higher for acidic oxides. This advises that intense interactions displayed among adsorbate and adsorbent may raise the catalytic impact of solids with high-affinity values for several reactions. It can be concluded that the electrostatic and van der Waals interactions are the most forceful interactions among the asphaltene aggregates and nanoparticles, and therefore the acid and base metal oxide nanoparticles can be used for the adsorption and efficient elimination of asphaltene aggregates from reservoir oils as a proposal for the in situ oil enhancement [69]. Alike insights were presented by other research groups for the adsorption of asphaltenes over various minerals and clays [56, 115–117]. Mohammadi et al. [35] utilized metal oxide nanoparticles, such as SiO_2, TiO_2, and ZrO_2, for improving the stability of asphaltene nanoaggregates through hydrogen bond formation at acidic environment. The authors found that TiO_2 nanofluids, in strong acidic condition, were behaving as a dispersant, therefore improving the stability of the asphaltenes and carrying out to an elevated precipitation onset point.

Furthermore, it was reported by Nassar et al. that the functionalized metal oxide nanoparticles over support like γ-Al_2O_3 (Al) or TiO_2 (Ti) have a higher adsorptive capacity than that of the support. Such finding is expected, as the metal oxides, NiO and/or PdO, have a high affinity toward the presented compounds in the asphaltene molecule such as pyridine, phenol, benzoic acid, and pyrrole [120]. Therefore, a significant increase in asphaltene adsorption was observed for the functionalized

Table 3.1 The maximum adsorption capacity of different extracted asphaltenes over different types of nanoparticles

Type of nanoparticles	Types of asphaltenes	Oil source	Amount adsorbed (mg/m^2)	Remarks	References
Co_3O_4	C_7-asphaltenes	Athabasca VR	1.76[a]	Amphoteric effect, <50 nm particle size	[110]
NiO	C_7-asphaltenes	Athabasca VR	0.58[a]	Acidic effect, <50 nm particle size	[110]
MgO	C_7-asphaltenes	Athabasca VR	1.35[a]	Basic effect, <50 nm particle size	[110]
CaO	C_7-asphaltenes	Athabasca VR	2.7[a]	Basic effect, <160 nm particle size	[110]
TiO_2	C_7-asphaltenes	Athabasca VR	0.54[a]	Acidic effect, <25 nm particle size	[110]
Fe_3O_4	C_7-asphaltenes	Athabasca VR	1.7[a]	Amphoteric effect, 20–30 nm particle size	[110]
Nano-alumina	C_7-asphaltenes	Athabasca bitumen	1.73[a]	Particle size <50 nm	[118]
Micro-alumina	C_7-asphaltenes	Athabasca bitumen	0.448[a]	Particle size 50–200 μm	[118]
γ-Al_2O_3	C_7-asphaltenes	Athabasca bitumen	88.50[a]	Particle size <50 nm	[67]
Fumed silica (S)	C_7-asphaltenes	Colombian	0.3569[a]	BET 389 m^2/g	[5]
SNi2	C_7-asphaltenes	Colombian	0.5698[a]	2wt%NiO supported-on-silica (S), BET 233.63 m^2/g	[5]
SPd2	C_7-asphaltenes	Colombian	0.7724[a]	2wt%PdO supported-on-silica (S), BET 205.15 m^2/g	[5]
SNi	C_7-asphaltenes	Colombian	0.6071[a]	1wt%NiO supported-on-silica (S), BET 290.31 m^2/g	[5]
SPd1	C_7-asphaltenes	Colombian	0.4742[a]	1wt%PdO supported-on-silica (S), BET 265.56 m^2/g	[5]
SNi1Pd1	C_7-asphaltenes	Colombian	0.5250[a]	1wt%NiO and PdO supported-on-silica (S), BET 201.50 m^2/g	[5]
SNi0.66Pd0.66	C_7-asphaltenes	Colombian	0.7083[a]	0.66 wt% of NiO and PdO supported-on-silica (S), BET 220.79 m^2/g	[5]

(continued)

Table 3.1 (continued)

Type of nanoparticles	Types of asphaltenes	Oil source	Amount adsorbed (mg/m^2)	Remarks	References
ZrO_2	C_7-asphaltenes	Athabasca vacuum residue	3.21[a]	Particle size 26 nm, BET 40 m^2/g	[119]
CeO_2	C_7-asphaltenes	Athabasca vacuum residue	2.65[a]	Particle size 16 nm, BET 50 m^2/g	[119]
TiO_2	C_7-asphaltenes	Athabasca vacuum residue	0.54[a]	Particle size 8 nm, BET183 m^2/g	[119]
NiO	C_7-asphaltenes	Iranian heavy oil	3.67[a]	Acidic surface, 45 nm particle size	[68]
Fe_2O_3	C_7-asphaltenes	Iranian heavy oil	3.52[a]	Amphoteric surface, 44 nm particle size	[68]
WO_3	C_7-asphaltenes	Iranian heavy oil	3.35[a]	Acidic surface, 44 nm particle size	[68]
MgO	C_7-asphaltenes	Iranian heavy oil	2.62[a]	Basic surface, 15 nm particle size	[68]
$CaCO_3$	C_7-asphaltenes	Iranian heavy oil	2.17[a]	Basic surface, 15 nm particle size	[68]
ZrO_2	C_7-asphaltenes	Iranian heavy oil	1.23[a]	Amphoteric surface, 20 nm particle size	[68]
Zeolite	C_7-asphaltenes	Colombia crude oil	0.892[a]	16 nm particle size	[36]
Silica gel	C_7-asphaltenes	Colombia crude oil	2.189[a]	Amorphous	[36]
Silica gel	C_7-asphaltenes	Colombia crude oil	13.158[a]	Crystalline	[36]
SNi5	C_7-asphaltenes	Colombia crude oil	8.961[a]	Crystalline silica with 5 wt % $Ni(NO_3)_2$	[36]
SNi15	C_7-asphaltenes	Colombia crude oil	16.367[a]	Crystalline silica with 15 wt % $Ni(NO_3)_2$	[36]

[a]Estimated from the Langmuir model

nanoparticles, as shown in Fig. 3.2, which describes the favorable interaction between the surface of the nanoparticle and the heteroatoms present in the asphaltene molecules like nitrogen and oxygen [120]. Similar adsorption behavior was observed for NiO and PdO supported invidiously on the TiO_2 particles (TiNi2 and TiPd2). Figure 3.3 shows the effect of functionalized metal oxides over Al support on the isotherms of Colombian n-C_7 asphaltenes at 298 K including the SLE model. As shown, the adsorption capacity is enhanced for the functionalized nanoparticles and the maximum uptake trends followed the order AlNi1Pd1 > AlPd2 > AlNi2 > Al. It is worth noting that the quantity of adsorbed asphaltenes on Ti nanoparticles

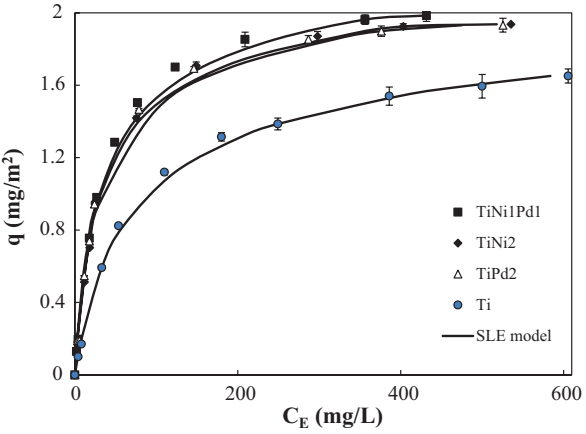

Fig. 3.2 Adsorption isotherms of n-C_7 asphaltene over Ti, TiNi2, TiPd2, and TiNi1Pd1 at 298 K. The symbols are experimental data, and the solid lines are the SLE model [121]. Permissions related to the material presented were acquired from Elsevier, and future permission should be directed to Elsevier; N.N. Nassar, C.A. Franco, T. Montoya, F.B. Cortés, A. Hassan. Effect of oxide support on Ni–Pd bimetallic nanocatalysts for steam gasification of n-C_7 asphaltenes, Fuel 156 (2015) 110–120

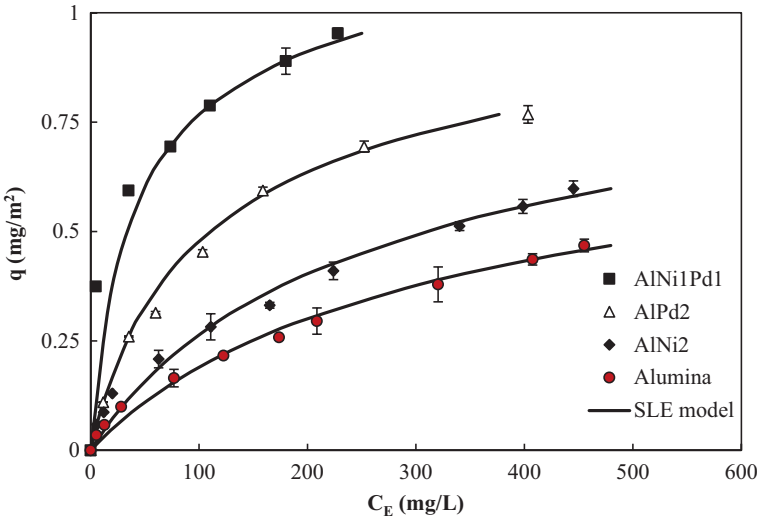

Fig. 3.3 Adsorption isotherms of n-C_7 asphaltene onto Al, AlNi2, AlPd2, and AlNi1Pd1 nanoparticles at 298 K along with the SLE model [121]. Permissions related to the material presented were acquired from Elsevier, and future permission should be directed to Elsevier; N.N. Nassar, C.A. Franco, T. Montoya, F.B. Cortés, A. Hassan. Effect of oxide support on Ni–Pd bimetallic nanocatalysts for steam gasification of n-C_7 asphaltenes, Fuel 156 (2015) 110–120

Table 3.2 Estimated parameters of the SLE model [121]

Nanoparticles	H (mg/g)	K (g/g) × 10^{-4}	q_m (mg/m^2)	χ^2
Ti	0.69	4.67	2.78	0.77
TiNi2	0.37	4.11	3.01	2.96
TiPd2	0.33	3.48	3.02	2.02
TiNi1Pd1	0.30	2.98	3.11	1.55
Al	1.89	3.82	1.30	1.84
AlNi2	1.62	3.56	1.51	2.13
AlPd2	0.73	2.58	1.55	0.70
AlNi1Pd1	0.25	2.38	1.67	1.13

Permissions related to the material presented were obtained from Elsevier, and future permission should be directed to Elsevier; N.N. Nassar, C.A. Franco, T. Montoya, F.B. Cortés, A. Hassan. Effect of oxide support on Ni–Pd bimetallic nanocatalysts for steam gasification of n-C_7 asphaltenes, Fuel 156 (2015) 110–120

is higher than for Al nanoparticles; in addition, Ni-Pd/ϒ-Al_2O_3 nanoparticles presented a lower uptake than Ni-Pd/TiO_2. The reason for that is due to the effect of the geometry on the adsorbent surface and the interactions between the metals which might affect the selectivity for several functional groups or heteroatoms in the asphaltenes [121]. Again, the values of SLE model parameters, which was proposed by our research group, were estimated and tabulated in Table 3.2 for the C_7-asphaltenes adsorption over functionalized metal oxide nanoparticles. As shown, the SLE model agrees perfectly with the experimental data for all the adsorption experiments which is confirmed by the low values of χ^2. It is worth noting that the adsorption affinity, represented as reciprocal H value, is increasing following the order of bimetallic > monometallic > support. Alike tendencies were obtained for the q_m parameter. Conversely, the K value, which is represented the degree of asphaltene self-association on active sites, was higher for the support compared with the functionalized nanoparticles. Because of the complicated structure of asphaltenes, their molecules can be self-associated and assemble as bigger molecules on the nanoparticles' surface. This finding was anticipated, as the low adsorbed amount of asphaltenes requires high energy to be adsorbed on the surface of the nanoparticles as monomers. Nevertheless, as the concentration at medium and high uptake is increased, asphaltenes will be aggregated over the maximum energy sites till the volume vacant for adsorption is occupied [122, 123]. In that place, and based on the chemical structure of adsorbent, the adsorption of asphaltene molecules is in a perpendicular and parallel or in flat configuration towards the aromatic part of the asphaltenes or heteroatoms present in their structure [114, 123].

3.3.1 Factors Affecting Asphaltene Adsorption

As discussed early, the adsorption of asphaltenes on the surface of nanoparticles was affected by several factors. These factors usually depend on the interactions among asphaltenes and the surface. This interaction is affected by the functional

Table 3.3 The effect of surface acidity of alumina on C_7-asphaltene adsorption extracted from Athabasca bitumen [112]

Adsorbent	pH value	Amount adsorbed (mg/m^2)	BET surface area m^2/g and avg. pore size (A)
Alumina acid	4.5	0.65	128, 60
Alumina basic	10	0.45	156, 54
Alumina neutral	7.5	0.50	154, 52

groups displayed on the surface and also to the side of asphaltenes in the environs of surface approximating for linking. Molecular interactions throughout adsorption are outcomes from intermolecular forces. These intermolecular forces are usually separated into three categories: dispersion forces, polar forces, and ionic forces. However, the acid-base interaction and electrostatic attraction were the most predominant forces promoting the asphaltene adsorption in nanoparticles. Fast adsorption of asphaltene aggregates onto γ-Al_2O_3 nanoparticles has been presented by Nassar et al. [112]. In that study, surface acidity on the asphaltene adsorption was investigated using alumina at different functionality groups to show the affinity toward asphaltene adsorption as summarized in Table 3.3. It was found that the asphaltene adsorption is highly impacted by the surface acidity and the adsorption capacities of asphaltenes onto the three aluminas followed the order acidic > basic and neutral. This was ascribed to the high surface areas of aluminas and the interaction of asphaltenes with the counter ions exhibited on alumina surface.

Furthermore, the effects of the adsorption method and temperature, types, and properties of nanoparticles and asphaltene characteristics on the asphaltene adsorption were also investigated.

3.3.2 Effect of Adsorption Method

Most of the reported studies on asphaltene adsorption were batch-mode experiments and presented that there are two varieties of adsorption isotherms, type I [5, 67, 80, 124] and type II [78, 84, 125]. The distinction between these two kinds could be due to many factors that are included in the asphaltene-asphaltene and asphaltene-solid surface interactions. Additionally, the method for the adsorption experiments has an important part in the obtained adsorption isotherm for understanding the interactions between adsorbate/adsorbate and adsorbate/adsorbent. The adsorption isotherms are commonly constructed using two different procedures; first, by varying the initial concentration of the adsorbate with a specified amount of adsorbent in a fixed volume of liquid [5, 117]. Second, by varying amounts of the adsorbent with a given amount of adsorbate in a fixed volume of liquid [127, 128]. It is worth mentioning is that the adsorption isotherms of a single molecule should not be impacted by the method by which they are achieved; thus, the suggested two methods should end up with the same results. However, this might not be true for

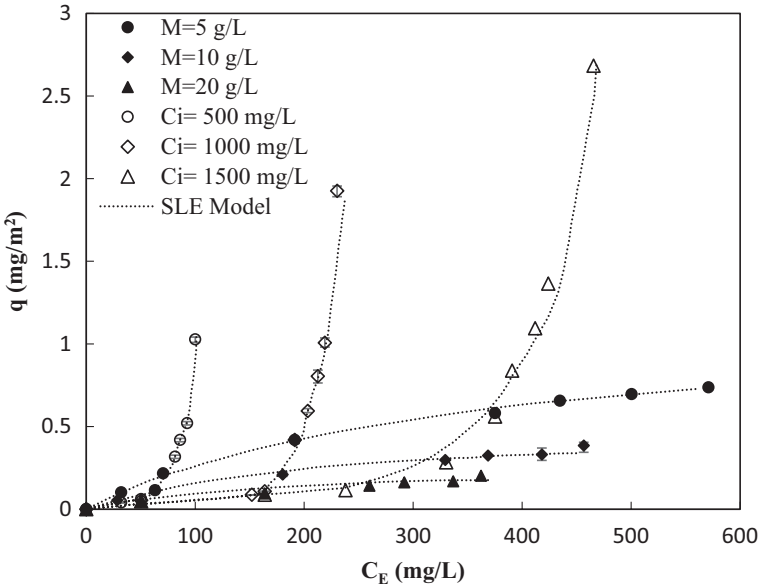

Fig. 3.4 Adsorption isotherms for asphaltene adsorption using method I and method II. Experimental conditions: temperature = 298 K, rpm = 200, and mixing time = 24 h [72]. Permissions related to the material excerpted were obtained from the American Chemical Society, copyright 2016, and further permission should be directed to the American Chemical Society; J.D. Guzmán, S. Betancur, F. Carrasco-Marín, C.A. Franco, N.N. Nassar, F.B. Cortés. Importance of the Adsorption Method Used for Obtaining the Nanoparticle Dosage for Asphaltene-Related Treatments, Energy & Fuels 30 (2016) 2052–2059

associating molecules such as asphaltenes, where the initial concentration can affect the aggregation behavior and, therefore, their adsorption. It was reported that the asphaltene adsorption over solid materials might be found as molecules, micelles, monomers, dimers, and nanoaggregates [7]. Therefore, it is necessary the select of suitable adsorption method, since this will help in obtaining the nanoparticle dosage for inhibiting/remediating asphaltene-related problems.

In that regard, to comprehend the impact of the adsorption method on asphaltene behavior, a study was conducted by Guzman et al. [72] on n-C_7 asphaltenes using silica nanoparticles. Figure 3.4 shows the constructed adoption isotherms for the adsorbed asphaltenes onto silica nanoparticles along with the SLE model fit at 298 K acquired by the method I at the different mass of the nanoparticles (M) and method II at a different initial concentration of asphaltene (C_i).

As shown in the figure, the adsorption isotherms obtained by method I are affected by the changing of the initial concentrations of n-C_7 asphaltenes. The size distribution of the aggregated asphaltene is varying with the initial concentration which is hindering the heteroatoms and functional groups, thus giving a decrease in the uptake [80, 129]. Consequently, a quick saturation of the vacant surface area was obtained by these aggregates, which resulted in a plateau for high

concentrations of asphaltenes as found for all three adsorption isotherms built by method I. Additionally, different adsorbed amounts were obtained based on the value of employed M for the three adsorption isotherms using method I. The upper isotherm belongs to $M = 5$ g/L, the middle isotherm belongs to $M = 10$ g/L, and the lower isotherm belongs to $M = 20$ g/L. For $C_E = 300$ mg/L, the uptake rises as the value of M is lower. On the other hand, the asphaltene adsorption isotherms obtained by method II at 298 K employing different values of C_i are also presented in Fig. 3.4. As shown, the three adsorption isotherms describe a type III behavior in accordance with the IUPAC [126]. These isotherms have been depicted in systems with low adsorbate-adsorbent affinities, which result in the generation of multiple layers of n-C_7 asphaltenes on the adsorbent surface [57, 130]. In this case, the form of each adsorption isotherm is ascribed to the decreasing of the nanoparticle vacant sites for adsorption by mass unit, due to the increment of the nanoparticle dosage which affects the interactions between the available nanoparticles and asphaltenes.

It can be concluded that the adsorption isotherms constructed by method II considerably deviate from those usually presented in the literature. Nonetheless, this method is a useful tool for obtaining the needed amount of nanoparticles according to the interactions of adsorbate-adsorbate and adsorbate-nanoadsorbent. In effect, this method is important in practice because the amount of asphaltenes at reservoir conditions is assumed invariable when treatments are applied.

3.3.3 *Effect of the Temperature*

The effect of temperature on the asphaltene adsorption was also investigated by Nassar et al. [67]. The adsorption experiments were carried out in the temperature range 298–328 K using γ-Al_2O_3 nanoparticles, and the results are shown in Fig. 3.5. As presented in the figure, the adsorption of asphaltenes over the surface of nanoparticles is decreased when temperature increments occur. Since the adsorption on the nanoparticle surface releases heat, such reduction in the asphaltene adsorption is expected. Nevertheless, the temperature effect affects the colloidal state of adsorbed asphaltenes on the surface which can be found as colloidal micelles, aggregates, or single molecules [131, 132]. Therefore, changing the colloidal condition of the asphaltenes results in a reduction in the adsorption capacity at high temperature due to the size decreasing in the asphaltene aggregate and asphaltene self-association [133].

3.3.4 *Effect of Pressure*

The pressure impact on asphaltene adsorption was investigated by Nassar et al. [89] through experimental adsorption test under-flow mode on porous media. The continuous adsorption experiments were carried out at three pressures 6.89, 10.34, and 17.24 MPa at 313 K onto a packed media of silica sand. They found out that

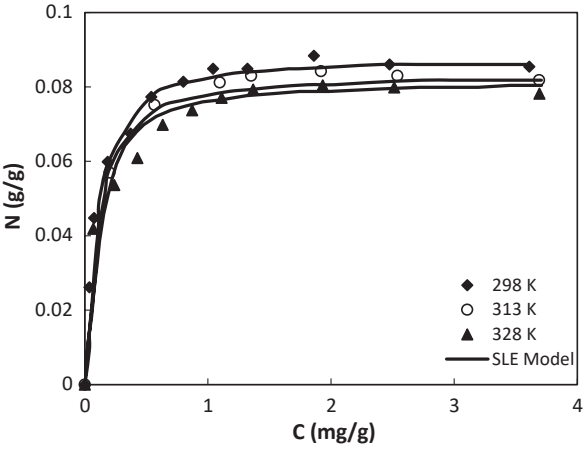

Fig. 3.5 Adsorption isotherm of asphaltenes onto γ-Al_2O_3 nanoparticles at a different temperature. The symbols are experimental data, and the solid lines are from the SLE model [67]. Permissions related to the material excerpted were obtained from the American Chemical Society, copyright 2010, and further permission should be directed to the American Chemical Society; N.N. Nassar. Asphaltene Adsorption onto Alumina Nanoparticles: Kinetics and Thermodynamic Studies, Energy & Fuels 24 (2010) 4116–4122

Table 3.4 Estimated parameters of the solid-liquid model at reservoir conditions in the SLE-RC model for different test pressures at 313 K [89]

	Value		
Parameter	6.89	10.34	17.24
H(mg/g)	8086.42	7030.61	3321.65
K(g/g)	1259.76	1440.82	1473.52
N_m(g/g)	0.00668	0.00708	0.00879
δ_{as}(MPa$^{1/2}$)	16.56	16.64	16.80
v_{as}(cm^3/Mol)	1040.4	1025.28	743.74
RMSE%	1.70	0.04	0.63

Permissions related to the material excerpted were obtained from the American Chemical Society, copyright 2015, and further permission should be directed to the American Chemical Society; N.N. Nassar, T. Montoya, C.A. Franco, F.B. Cortés, P. Pereira-Almao. A New Model for Describing the Adsorption of Asphaltenes on Porous Media at a High Pressure and Temperature under Flow Conditions Energy & Fuels 29 (2015) 4210–4221

asphaltene adsorption is pressure-dependent, obtaining type III (IUPAC classification) [134] isotherms shifting to the left as pressure increases, following the order on the adsorbed amount (N_m) as 17.24 > 10.34 > 6.89 MPa. On Table 3.4 are shown the results for the SLE-RC model that was validated with the obtained experimental results. It is worth noting on Table 3.4 that the solubility parameter δ_{as} rises as pressure rises, which agrees with what has been showed on literature [135–137], since

this is related to the fact that the system pressure is above the bubble point of the solvent (toluene) [89]. Also, the decrease of the molecular volume with pressure due to the solubility parameter is inversely proportional to the molar volume, which means that the solvent power required to solubilize asphaltenes increases and the molecular weight of the asphaltenes in the solvent decreases. On the other hand, the decreasing trend of the parameter *H* means that the affinity among the solid surface and the asphaltenes is high when the intermolecular forces among asphaltenes and the silica sand surface are favored with the increment in the pressure [74]. Inversely, the degree of asphaltene self-association related with the parameter *K* suggests that as the pressure increases, the asphaltenes adsorbed on the solid surface increase their self-association behavior, even though the self-association also depends on their molecular structure, the interaction between them, and its strength [84, 138].

3.3.5 Effect of Asphaltene Types and Properties

Usually, asphaltenes can be precipitated using one of two main solvents, namely, n-pentane and n-heptane [76, 110, 116, 139, 140]. Each solvent is responsible for precipitating different asphaltene characteristics in terms of molar mass, chemical composition, and physical characteristics, with different yields [76, 109]. Nonetheless, the adsorption performance might be changed as a consequence of the type of used precipitant. In this regard, an adsorption study on the two types of asphaltene samples was conducted onto NiO nanoparticles at 25 °C by independently extracting the asphaltene from vacuum residue using n-pentane (C_5) and n-heptane (C_7) [110]. C_7-asphaltenes and C_5-asphaltenes were individually dissolved in toluene with the goal of obtaining an insight into the impact of extracted asphaltene on the adsorption process. The adsorption results showed that the maximum uptake of C_5-asphaltenes is a little bit lower than that of C_7-asphaltenes. This is expected, as the adsorption behavior of the tested asphaltenes is different due to the presence of heteroatoms which makes them polar, as a consequence, stronger interactions occurred. Another reason is related to the high aromaticity in asphaltenes; bonding of π electrons to the empty d orbitals in transition metal oxides cannot be overlooked. It can be recalled that C_7-asphaltenes are more polar and aromatic than C_5-asphaltenes [141]. In addition, the colloidal conduct and molecular mass and structure of the asphaltenes affect adsorption too. In fact, it was reported that the C_5-asphaltenes have a higher resin amount than that of C_7-asphaltenes which could affect the colloidal behavior, thereby impacting the interactive forces among the asphaltene molecules and NiO nanoparticles [139]. Nonetheless, the initial uptake by NiO nanoparticles seems similar for both kinds of asphaltenes.

In another study, the effect of asphaltenes' molecular weights (MW) on the adsorption was also studied [55]. In this study, different molecular weights and sizes of visbroken asphaltenes were adsorbed onto Fe_3O_4 nanoparticles. The principal characteristics of the studied asphaltenes along with the Langmuir isothermal parameters are summarized in Table 3.5. The molecular weights of asphaltenes were obtained based on the established parameters from using exclusion (liquid)

Table 3.5 The properties of the considered asphaltenes along with the Langmuir isothermal parameters obtained at 298 K [55]

Type of asphaltenes	Log (MW)	H/C (atomic ratio)	N (wt%)	S (wt%)	Max. molecular size (nm)	Q_m (mmol/g)	K_L (L/mmol)
VBASP6	3.31	1.31	0.86	8.65	4.5	0.047	17.03
VBASP7	3.30	1.14	0.98	8.59	4.5	0.048	12.27
VBASP8	2.95	1.07	0.99	6.79	2.1	0.085	3.77
VBASP9	2.96	1.11	1.05	6.08	2.1	0.197	1.07

Permissions related to the material presented were granted by Elsevier, and future permission should be directed to Elsevier; N.N. Nassar, A. Hassan, L. Carbognani, F. Lopez-Linares, P. Pereira-Almao. Iron oxide nanoparticles for rapid adsorption and enhanced catalytic oxidation of thermally cracked asphaltenes, Fuel 95 (2012) 257–262

chromatography (SEC). It should be noted that the increasing aromaticity is one of the important features that have to be considered for thermally cracked asphaltenes, varying in this case from 0.43 for virgin asphaltenes to 0.60 for harshly cracked asphaltenes (VBASP9). From the SEC established parameters, the average molecular depictions including from 260 carbon atoms for virgin asphaltenes down to 64 carbon atoms for harshly cracked asphaltenes were determined. Their aromatic regions were from 113 down to 38 carbon atoms per average molecular depiction. Alkyl appendages were reduced in length from variations in thermal cracking.

Table 3.5 also compares the maximum uptake (Q_m) and adsorption affinities (K_L) obtained by the Langmuir model for the four types of asphaltenes. As shown, the uptake kept the order VBASP9 > VBASP8 > VBASP7 > VBASP6 which agrees with the kinetic efficiency results obtained for different asphaltene adsorption on the basis, portrayed by adsorption rate. However, the adsorption affinity had a reversed order. These discrepancies in the order might be ascribed to a different degree of interaction among the nanoparticle surface, in this case, iron oxide, and the type of asphaltenes. It has been published that iron oxide interacts strongly with asphaltenes and resin hydrocarbon group types and therefore impacts their H-bonding inclination and augments their retentive characteristics [21]. Moreover, the results also indicate that the molecular interaction among the p electrons of the aromatic ring with Fe will be augmented with the rise in the aromatic nature of asphaltenes. Also, the bond of N atoms with Fe cannot be excluded, especially when the asphaltene molecules line up parallel to the metal surface in a face-up position [142]. Based on that, high N content in harshly cracked asphaltenes would improve adsorption. Hence, the N content includes both, basic and non-basic nitrogen compounds, that can interact distinctively with the nanoparticles. In fact, iron compounds are predisposed to the selective adsorption of basic type nitrogen (pyridinic) instead of the non-basic (pyrrolic) [143]. Furthermore, the S content is playing a role in the adsorption performance. As shown in the table, the asphaltene adsorbed amount rises as the S content decreases. This reduction in the content of S with the reduction in the molecular weight of asphaltenes can be ascribed to the loss of alkyl moieties connected to the asphaltene structure by S-linkages that are eliminated simply by thermal cracking and thus decreases in S content. This leaves a nucleus that interacts effortlessly with the nanoparticles and ensures the adsorption [113].

3.3.6 *Effect of Nanoparticle Size*

We believe that the changes in nanosizes of particles can experience substantial alterations in their surface properties, including shape, topology, porosity, and surface area. As previously discussed, the nanoparticles have a strong ability to interact with polar heavy hydrocarbon molecules and have an effect on their consequent processing like adsorption. This is because of their incredible properties like high surface area-to-volume ratio and active surface functionality. Therefore, the size of nanoparticles might have an important influence on the adsorption performance of asphaltene by changing the size from 1 to 100 nm. To provide a better understanding of the impact of particle size and dispersion degree on the mechanistic behavior of asphaltene, many studies have been conducted by our research group for the first time [60, 61, 118, 144]. The nanosize impacts of NiO nanoparticles on adsorption of vacuum residue n-C_5 asphaltenes were studied which is also proved by our group on Quinolin-65 as a model molecule for asphaltene [61, 144, 145]. The authors gave important comprehension about the surface selectivity and activity and the role of particle size in the generation of more effective nanoadsorbent and catalysts for heavy hydrocarbon processes. Figure 3.6 shows the adsorption isotherms of n-C_5

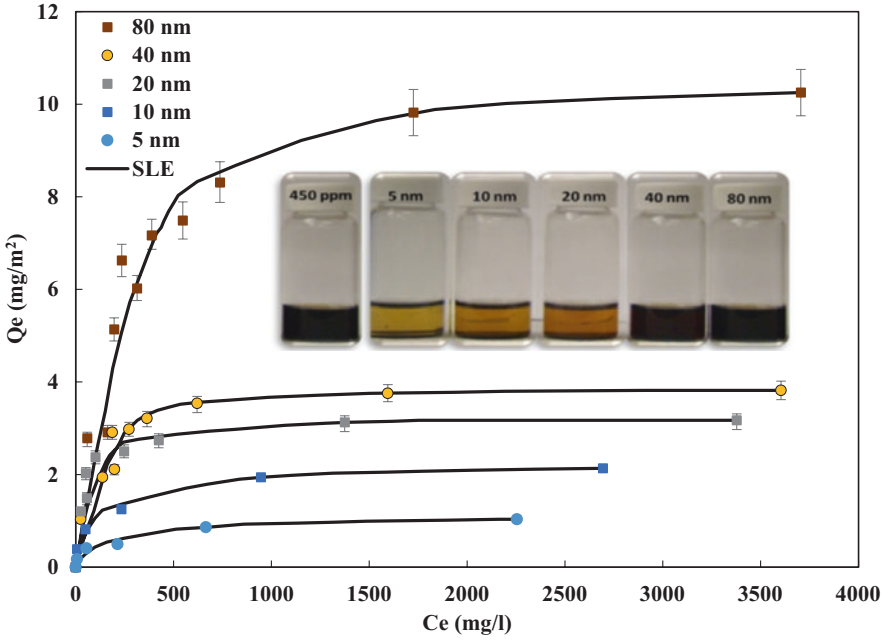

Fig. 3.6 The adsorption isotherms of vacuum residue n-C_5 asphaltenes over different-sized of NiO nanoparticles. The inset shows a picture of selected samples before and after adsorption [61]. Permissions related to the material excerpted were obtained from John Wiley and Sons, and further permission should be directed to John Wiley and Sons; N.N. Marei, N.N. Nassar, M. Hmoudah, A. El-Qanni, G. Vitale, A. Hassan. Nanosize effects of NiO nanosorbcats on adsorption and catalytic thermo-oxidative decomposition of vacuum residue asphaltenes, The Canadian Journal of Chemical Engineering 95 (2017) 1864–1874

asphaltenes onto different NiO nanoparticles of 5, 10, 20, 40, and 80 nm at 25 °C fitted with the SLE model. In addition, the figure provided with a photographer represents the variation in color of a control sample (450 mg/L) before and after adsorption. It is worth noting that the color change in the photograph presented the experimental adsorbed amount normalized per mass, not per surface area. As shown, all the sizes of NiO nanoparticles were succeeded in the adsorption of n-C_5 asphaltenes with different degrees in adsorption affinity and capacity. This finding confirms that the NiO-nanosized particles impact asphaltene adsorption behavior which can be due to the substantial variation in surface properties, topology, morphology, and textural properties of NiO nanoparticles after experiencing down in the nanoscale. Even though adsorption is given by a normalized surface area basis, a higher adsorption capacity can be observed for the largest particle size (80 nm) compared to the smaller sizes of NiO. This observation suggests that the adsorption behavior of n-C_5 asphaltenes goes far more than the increment or diminution in the surface areas and several conditions might be involved as intrinsic reactivity, dispersion ability, subsequent aggregation, asphaltene self-association, and the nanoparticle surface topology and morphology [110, 144]. Moreover, the fitting parameters of SLE model (K and H) were reduced with the reduction of the NiO nanosize from 80 nm to 5 nm, resulting in an increment of the adsorption affinity and a decrease of asphaltene aggregation degree.

In another study, it was found that the uptake of asphaltenes over different sizes of alumina (nano and micro) were affected by the surface area [118]. In this study, both types of aluminas with alike surface acidity but different particle size were used for asphaltene adsorption. It was noted that both aluminas were good in adsorbing asphaltenes with different degrees. Even though adsorption is given by a surface area basis, alumina nanoparticles presented higher adsorption affinity and adsorption capacity when compared to micro-alumina. This suggests that the increment in uptake and affinity of alumina with the reduction in the particle size goes far more than the increment in surface area and has other factors, as dispersion ability and intrinsic reactivity.

3.3.7 Effect of Coexisting Molecules on Asphaltene Adsorption

It is of paramount importance to inquire about the competitive adsorption process among several heavy molecules adsorbing onto a nanoparticle surface. Nonetheless, since asphaltenes' molecular structure is unestablished and is affected by the origin, there is a challenge in performing competitive adsorption on real crude for understanding the adsorption process. Therefore, model molecules such as violanthrone-79 (V-79) and Quinolin-65 (Q-65) have been utilized as model heavy compounds to imitate resin and asphaltene molecules, respectively, in several studies [60, 144, 146]. Recently, Montoya et al. [147] studied the adsorption onto different NiO nanoparticles of violanthrone-79 (V-79) and Quinolin-65 (Q-65) as model heavy compounds to imitate resin and asphaltene molecules, respectively, using three

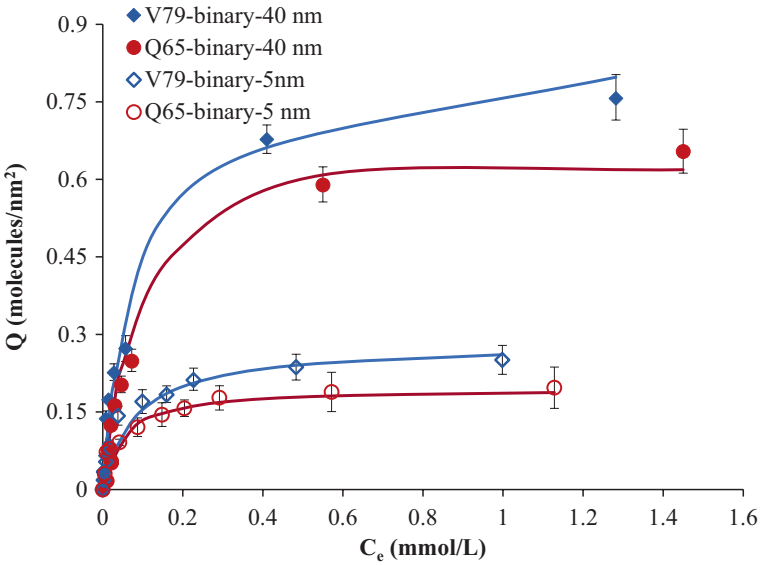

Fig. 3.7 Competitive adsorption isotherms of V-79 and Q-65 from the binary solutions onto the 5 nm NiO and 40 nm NiO nanoparticles. Nanoparticle dose, 10 g/L; temperature, 298 K; and experiment time = 24 h [147]. Permissions related to the material excerpted were obtained from the American Chemical Society, copyright 2020, and further permission should be directed to the American Chemical Society; T. Montoya, A. Amrollahi, G. Vitale, N. Hosseinpour, N.N. Nassar. Size Effects of NiO Nanoparticles on the Competitive Adsorption of Quinolin-65 and Violanthrone-79: Implications for Oil Upgrading and Recovery, ACS Applied Nano Materials (2020)

approaches: (1) individual adsorption, (2) simultaneous adsorption, and (3) displacement competitive adsorption; in addition, they used computational modeling to better understand the adsorption behavior. Figure 3.7 shows the simultaneous adsorption isotherms of V-79 and Q-65 from the binary solutions over the 5 nm NiO and 40 nm NiO nanoparticles. On Fig. 3.7, it can be observed that the adsorbed molar density of V-79 is higher than that of Q-65 onto both 5 nm NiO and 40 nm NiO nanoparticles. This was related to high interactions of V-79 with the surface sites of the nanoparticles, which was in agreement to the obtained computational modeling outcomes. Also, the adsorption uptake by surface area basis, of both V-79 and Q-65, onto the 5 nm NiO is lesser than that on 40 nm NiO. This was related to the lesser density of strong adsorption sites onto the surface of 5 nm NiO in comparison to the 40 nm NiO nanoparticles or the absence of a larger surface room. They also found that the strength of the adsorption interactions and the location of the adsorbing molecules are important parameters when working with competitive adsorption of V-79 and Q-65, concluding that V-79 molecules can substitute Q-65 and the Q-65 could be the predecessor of V-79.

Accordingly, it is worth noting that during asphaltene adsorption, competitive adsorption might take place between the maltene and asphaltene molecules to be adsorbed on sites and intervene in the adsorption effectiveness. Therefore, it is

important to study the effect of the presence of these coexisting molecules on the asphaltene adsorption. An experimental adsorption study was conducted on maltenes, asphaltenes, and bitumen using colloidal nanoparticles of γ-Al_2O_3 by independently dissolving them in toluene [67]. The adsorption isotherms fitted with the Langmuir model finding that the highest adsorption capacity was for the pure asphaltenes which is slightly higher than that for the bitumen. However, the pure maltenes show the lowest uptake. These discrepancies in the adsorption capacity can be ascribed to the chemical characteristics, molecular size, and structure of the oil, which impacts the interaction forces among the oil molecules and nanoparticles [139]. Moreover, the outcomes also showed that asphaltene molecules display the strongest interaction forces with the adsorbent surfaces. Nevertheless, having maltenes with a significant asphaltene concentration in the solution might have somehow an influence on this interaction which can alternate the organization of asphaltene molecules in the adsorbed layer and also asphaltene aggregates.

On the contrary, Franco et al. [148] investigated the impacts of resin I on the adsorption behavior of n-C_7 asphaltenes onto silica and hematite nanoparticles. The adsorption experiments were conducted varying n-C_7 asphaltene to resin I proportion such as 7:3, 1:1, and 3:7 and several concentrations of the asphaltene-resin mixture from 500 mg/L to 5000 mg/L. They obtained that resin I was behaving as a solvent at the concentrations they tested; this implied that resin I has no considerable impact on the asphaltene adsorption. In addition, they found that nanoparticles were more prone to adsorb asphaltenes than resin I. The amounts of n-C_7 asphaltenes and resin I adsorbed were determined by a novel method based on thermogravimetric (TGA) and softening point (SP) measurements.

3.3.8 Effect of N-Heptane/Toluene (H/T) Ratio

It is well-known that the asphaltenes could be having self-association to form various aggregates and colloids. Thus changing their colloidal state can cause formation damage and consequently impact the oil recovery efficiency [40, 149]. Therefore, an investigation on the adsorption behaviour of asphaltene aggregates on nanoparticle surface is of paramount importance. Based on the fact that asphaltenes are highly solubilized in toluene and totally precipitated in a solvent like n-heptane, it is important to understand the effect of asphaltene monomers, dimers, isomers, or nanoaggregates on adsorption process using the nanoparticles [29]. For that purpose, it was recommended to change the (n-heptane/toluene) H/T ratio from 0.0 to 0.45, because the high H/T ratio (>0.5) will increase the precipitation of asphaltenes if the other variables are kept constant [133]. It was observed that as the H/T ratio rises, the asphaltene adsorption rises on the surface of γ-Al_2O_3 nanoparticles [67]. This finding can be due to the reduction in the solubility of asphaltenes that increases asphaltene aggregation and self-association, translating into an increment in the adsorption [29, 133]. In another investigation, Franco et al. [129] tested the impacts of asphaltene aggregation on the adsorption process using NiO and/or PdO

Table 3.6 The SLE parameters of Colombian n-C_7 asphaltene adsorption from different heptol mixtures over fumed silica and SNi1Pd1 nanoparticles at 298 K [129]

Solvent	H (mg/g)	K (x10^{-4} g/g)	q_m (mg/m^2)	χ^2
Fumed silica				
Toluene	2.02	4.51	2.89	1.03
Heptol 20	1.59	4.96	2.97	1.65
Heptol 40	1.12	5.47	3.15	1.45
SNi1Pd1				
Toluene	1.77	2.16	6.36	0.36
Heptol 20	1.18	2.74	6.40	0.56
Heptol 40	1.07	3.29	6.58	0.77

nanoparticles added over fumed silica. In this study, various aggregate sizes of asphaltenes were obtained by changing different ratios of heptol (n-heptane and toluene) in quantities of 0, 20 (heptol 20), and 40 (heptol 40) % v/v n-heptane. The adsorption isotherms were depicted by the solid-liquid equilibrium (SLE) model, and the model parameters were presented in Table 3.6. As shown from the results that the SLE model fits perfectly with experimental data, as confirmed by the low values of χ^2. It is clearly observed that the adsorption capacity (qm), the adsorption affinity which is represented by the reciprocal of the H parameter, the K parameter of the SLE model, are increased with the increase in the ratio of heptol followed the trend of Heptol 40 > Heptol 20 > toluene for both nanoparticles. These findings suggested that the quantity of precipitant in the solution rises with a higher degree of asphaltene self-association on the active site of nanoparticles. However, for comparing different adsorbents at a set asphaltene concentration in the same solution, it can be concluded that the modified nanoparticles have less asphaltene self-association and a higher preference. This finding can be supported by the resulted qm and the inverse of H for SNi1Pd1 nanoparticles that present a higher adsorption affinity and capacity in comparison to the fumed silica nanoparticles. In contrast, the obtained K values of the SNi1Pd1 are lower in comparison to fumed silica, thus suggesting that the addition of NiO and PdO on the fumed silica surface facilitated the inhibition of the self-association of the asphaltenes.

On the other hand, Nassar et al. [67] investigated asphaltene aggregate size evolution with time for the n-C_7 asphaltenes AK18 in H/T 40 and H/T 20 along with the population balance model (PBM) fit as it is shown in Fig. 3.8. It can be observed in Fig. 3.8 an increment in the asphaltene aggregates' average size as the amount of n-heptane has increment too, with the maximum average size of 1086 nm and 842 nm for H/T 40 and H/T 20, respectively. It is worth noting that for both solutions the asphaltene average size increases until the maximum, and then it decreases. This is because under a shear condition the asphaltene growth kinetics requires both

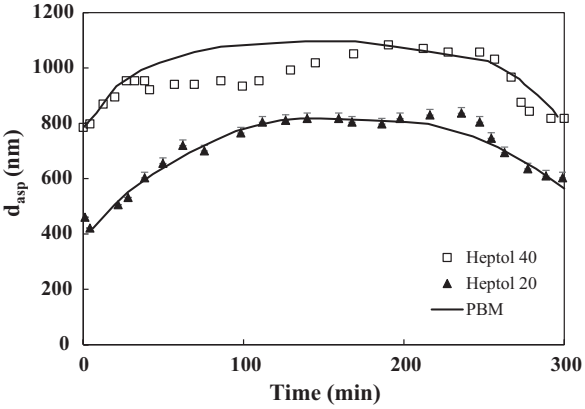

Fig. 3.8 Kinetics of virgin AK18 n-C_7 asphaltenes' aggregation-fragmentation at a temperature of 293 K in heptol 20 and heptol 40 solutions. The symbols are experimental data, and the solid lines are from the PBM model [73]. Permissions related to the material excerpted were obtained from the American Chemical Society, copyright 2015, and further permission should be directed to the American Chemical Society; N.N. Nassar, S. Betancur, S.c. Acevedo, C.A. Franco, F.B. Cortés. Development of a Population Balance Model to Describe the Influence of Shear and Nanoparticles on the Aggregation and Fragmentation of Asphaltene Aggregates, Industrial & Engineering Chemistry Research 54 (2015) 8201–8211

aggregation and fragmentation because of the collision of asphaltene aggregates [73].

Also, they found out that the parameters of the PBM model varied for each evaluated system. The aggregates porosity was 0.31 and 0.46 for H/T 20 and H/T 40, respectively, indicating that increasing the amount of n-heptane in the solutions decreases the solubility of the asphaltenes, causing the formation of larges aggregates, and then increases the aggregates porosity. This agrees with what has been reported in literature [93, 96]. However, for the breakup coefficient *b*, they did not find a strong dependence on the solvent composition, with values of 4.27×10^{-5} and 4.25×10^{-5} for H/T 20 and H/T 40 solutions, respectively. Finally, they studied the effect of nanoparticles in both systems (H/T 20 and H/T 40). From the PBM model, the ε parameter was reduced following the trend of virgin AK18 n-C_7 asphaltenes > magnetite > γ-alumina > silica, suggesting that smaller aggregates are resulting from the inclusion of nanoparticles to the system; the b parameter did not follow a clear trend, in terms of the kinetics of asphaltene aggregation-fragmentation, probably because the breakup coefficient could change as a function of the resultant asphaltene concentration and also may be affected by the presence of nanoparticles, and their characteristics such as size, shape, type, etc. [73].

3.3.9 *Effect of Water Content*

Water can be found in many steps during heavy oil recovery, upgrading, and processing. For practical application, it is important to investigate the impact of water on the asphaltenes' adsorption process. Therefore, an adsorption study was conducted on the asphaltenes using γ-Al_2O_3 nanoparticles by changing the quantity of water from 0.1 to 0.25 vol % under the invariable concentration of asphaltene 1500 mg/L at 298 K [67]. Take into account that the onset of phase distinction happens closely at 0.30 vol %. Worth noting is that it was not feasible to perform experiments at a water content higher than 0.25 vol % as the onset point of phase separation is around 0.30 vol%. It was observed that the adsorption capacity is linearly decreased with the water content. This observation can be explained by the fact that the hydrophilicity of the adsorbent surface will be increased with the water content, thus drives the asphaltenes away from the accessible sites [77]. Therefore, in the existence of water, asphaltenes can behave as surfactants. Therefore, they will work in stabilization of water drops inside a heavy oil matrix, producing emulsions and/or (w/o) microemulsions [150, 151]. This would draw asphaltenes to the water droplets instead of the nanoparticles, which generates a reduction in the adsorption. Also, the existence of water and emulsions can produce particle aggregation and cause reduction in the adsorption surface area, which impacts the uptake [151].

3.4 Conclusion and Future Remarks

This chapter looks into the current research trends for using the nanoparticle technology to remove and inhibit the asphaltenes from oil processing as an alternative technology that maximize recovery and upgrading of heavy oil while minimizing the environmental footprint. This chapter provides a good understanding of the effect of the adsorption process of the nanoparticles and gives an insight into the usage of nanotechnology for in situ improvement of heavy and extra-heavy oils. The following are the most relevant points that can be concluded from this chapter.

- Based on the unique properties of nanoparticles that differ from their bulk, nanoparticles have significant potential uses as an adsorbent for improving heavy oil upgrading and recovery.
- Complete asphaltene adsorption using different types of nanoparticles, such as silica, functionalized silica, and metal oxide, was rapidly obtained, which makes them a good option for preventing the precipitation and deposition of asphaltenes. That inhibition avoids flocculation and precipitation, which the polar compounds appear to be generating blocks of, and erase the trend to adsorb in multilayers, which can be caused by the polarity left by the initially adsorbed asphaltenes.
- The electrostatic and van der Waals forces are the strongest interactions among the asphaltene aggregates and surface of nanoparticles, and therefore the acid and base metal oxide nanoparticles can be utilized for the adsorption and effi-

cient remotion of asphaltene aggregates from oils as a focus for the in situ oil enhancement.

- The asphaltene adsorption was affected by several conditions that might be present in the oil industry, and it reduced as the water content and temperature increased. The water content will enhance the surface hydrophilicity of the nanoparticle, which moves the asphaltenes far from the adsorption places. In addition, water can aggregate the particle, thus reducing the uptake. Increments in the temperature will cause reduce in the asphaltene self-association.
- The effect of the presence of coexisting molecules, such as bitumen and maltenes, on the asphaltene adsorption was considered. Pure asphaltene seems to have a bigger adsorption capacity than bitumen or maltenes, indicating that adsorption was impacted by the chemical composition and size and structure of the oil.
- The effect of surface acidity of nanoparticles on the asphaltene adsorption was investigated using different aluminas with varying surface acidity. The asphaltenes were efficiently adsorbed on the three types of aluminas, where the acidic surface has the highest uptake, suggesting that the uptake is directly correlated to surface acidity of aluminas and playing a role in the adsorption process.
- The nanoparticle size has a considerable effect on the asphaltene adsorption. It was found for similar surface acidity of alumina that the adsorption capacity of nano-alumina is bigger than that of micro-alumina on a surface area basis. This was due to the high dispersion degree of nanoparticles. A similar finding was observed for NiO nanoparticles with sizes varying from 5 and 80 nm.
- It was found that the asphaltene adsorption process is affected by their types and properties. The adsorption was augmented with a reduction in the molecular weight of the asphaltenes. Reducing the asphaltene molecular weight improved the adsorption velocity, while the adsorption affinity increased as the molecular weight of asphaltenes increased.
- A model to describe the asphaltene aggregation-fragmentation without the existence of several nanoparticles that considers the adsorption process was formulated. The model reliability was based on population balance equations, and the adsorption parameter was added by using the double kinetic exponential model.
- The SLE model, which was proposed by our research group, is successfully implemented to fit the adsorption isotherms of asphaltene for different solvents with different volume ratios of n-heptane/toluene, different nanoparticles, different temperatures, etc. The model was used to explain the adsorption of asphaltenes over a surface based on thermodynamics, considering for the first time the i-mer generation of asphaltene, as a consequence of the interactions of asphaltene-asphaltene and asphaltene-solid surface.
- The functionalized fumed silica nanoparticles with nickel and palladium oxides were used for the adsorption of asphaltenes obtained from a Colombian extra-heavy crude oil. The SNi1Pd1 material had more preference for the asphaltenes than that of fumed silica. Additionally, the supported nanoparticles on fumed silica reduced the tendency of asphaltene self-association and improved the adsorption affinity as confirmed by the values of K and H terms of the SLE model. These findings showed that the supported material inhibited the self-association of asphaltenes.

- The effect of asphaltene self-association on the adsorption preference of functionalized and unfunctionalized nanoparticles toward the adsorption of asphaltenes was investigated. The adsorption of different asphaltenes' varying volume ratios of n-heptane/toluene was investigated. The outcomes indicated that the H term had the trend of toluene > heptol 20 > heptol 40, suggesting that the adsorption preference was augmented as the quantity of precipitant raised. In addition, the K term suggested that the asphaltene self-association onto the adsorbent surface raised in the order of heptol 40 > heptol 20 > toluene.
- Asphaltene adsorption isotherms' data at high-pressure conditions (reservoir conditions) were firstly used to validate a novel model based on the chemical theory to describe the influence of pressure on the interactions asphaltene-asphaltene and asphaltene-solid surface. Type III isotherms were obtained showing an increase in the asphaltene adsorbed amount when pressure increases.
- The effect of adsorption methods on the asphaltene adsorption was investigated. Method 1 consisted of an invariable dosage of nanoparticles in a set volume of liquid with the change on the initial concentrations of asphaltenes. Method 2 had varied dosages of nanoparticles to a set initial concentration of asphaltenes in solution. For various combinations of asphaltene initial concentrations and nanoparticle amount, adsorption isotherms of both types intersect each other, generating a "critical point" that coincides with the same starting concentration and nanoparticle dosage in the two methods.
- The effect of asphaltene source indicated that asphaltene nature and composition impact the adsorption process and that the form of the resulted adsorption isotherms depends mainly on the used method because of the self-associative nature of the adsorbate tested such as asphaltenes.

Keeping these abovementioned observations in mind, it is safe to assume that future use of nanoparticles in asphaltene adsorption is very much expected. Also, environmental challenges should be studied very deep to prevent any risks related to the indiscriminate utilization of nanoparticles. In this regard, recycling and re-using the spent nanoparticles could be very beneficial in terms of process economics as well as reduction of environmental footprint. This can be improved by giving magnetic properties to the nanomaterials, for example via core-shell preparations, between the nanoparticles for a specific use such as interfacial tension reduction, chemical enhanced oil recovery processes, inhibition of the formation damage, viscosity reduction, wettability alteration, among others. This can be applied to nanofluids for EOR processes as well. In addition, the synthesis of nanocomposites between commonly used nanomaterials and naturally occurring compounds such as dispersants or nanoparticles for uses in situ as nanofluids and subsurface could be achieved to give properties such as improving in the dispersibility nanoparticles in the medium; also, naturally occurring inorganic materials hold promise to decrease the asphaltene content of the oil and reduce the coke forming tendency (during petroleum refining operations) of the oil, resulting in partial upgrading of the oil. This may occur subsurface (in situ upgrading) or on the surface. However, lots of in-depth study toward the optimization of the adsorption process leading to the commercialization of the idea are still very much needed.

References

1. H. Rezvani, A. Khalilnezhad, P. Ganji, Y. Kazemzadeh, J. Mol. Liq. (2017)
2. Government of Alberta. Environmental Management of Alberta's Oil Sands. Resourceful. Responsible. (2009) environment.gov.ab.ca/info/library/8042.pdf (Accessed on March 5, 2020)
3. S. Betancur, J.C. Carmona, N.N. Nassar, C.A. Franco, F.B. Cortés, Ind. Eng. Chem. Res. **55**, 6122–6132 (2016)
4. T. Maqbool, A.T. Balgoa, H.S. Fogler, Energy Fuel **23**, 3681–3686 (2009)
5. C.A. Franco, T. Montoya, N.N. Nassar, P. Pereira-Almao, F.B. Cortés, Energy Fuel **27**, 7336–7347 (2013)
6. Z. You, A. Badalyan, P. Bedrikovetsky, M. Hand, D. Jenson, Productivity Decline Due to Fines Migration (Modelling and Field Case), *International Petroleum Technology Conference*, International Petroleum Technology Conference (2013)
7. J.J. Adams, Energy Fuel **28**, 2831–2856 (2014)
8. O.C. Mullins, Annu. Rev. Anal. Chem. **4**, 393–418 (2011)
9. G.A. Alzate, C.A. Franco, A. Restrepo, J.J. Del Pino Castrillon, D.L. Barreto Alvares, E. Murillo, A. Alberti, Evaluation of Alcohol-Based Treatments for Condensate Banking Removal, *SPE International Symposium and Exhibition on Formation Damage Control*, Society of Petroleum Engineers (2006)
10. F. Civan, *Reservoir Formation Damage* (Gulf Professional Publishing, 2015)
11. K. Leontaritis, J. Amaefule, R. Charles, SPE Production & Facilities **9**, 157–164 (1994)
12. R.S. Al-Maamari, J.S. Buckley, SPE Reserv. Eval. Eng. **6**, 210–214 (2003)
13. M. Mohammadi, M. Dadvar, B. Dabir, J. Mol. Liq. **238**, 326–340 (2017)
14. J.L. Creek, Energy Fuel **19**, 1212–1224 (2005)
15. D. Trimm, *Studies in Surface Science and Catalysis* (Elsevier, 1996), pp. 65–76
16. G.A. Mansoori, Socar Proc. **2010**, 12–23 (2010)
17. E.F. Ghloum, M. Al-Qahtani, A. Al-Rashid, J. Pet. Sci. Eng. **70**, 99–106 (2010)
18. A. Zahabi, M.R. Gray, T. Dabros, Energy Fuel **26**, 1009–1018 (2012)
19. D. Dudášová, A. Silset, J. Sjöblom, J. Dispers. Sci. Technol. **29**, 139–146 (2008)
20. M.F. González, C.S. Stull, F. López-Linares, P. Pereira-Almao, Energy Fuel **21**, 234–241 (2007)
21. L. Carbognani, Pet. Sci. Technol. **18**, 335–360 (2000)
22. M. Sedghi, L. Goual, W. Welch, J. Kubelka, J. Phys. Chem. B **117**, 5765–5776 (2013)
23. D. Harbottle, Q. Chen, K. Moorthy, L. Wang, S. Xu, Q. Liu, J. Sjoblom, Z. Xu, Langmuir **30**, 6730–6738 (2014)
24. A. Rudrake, K. Karan, J.H. Horton, J. Colloid Interface Sci. **332**, 22–31 (2009)
25. L. Goual, A. Abudu, Energy Fuel **24**, 469–474 (2009)
26. K. Xie, K. Karan, Energy Fuel **19**, 1252–1260 (2005)
27. S. Acevedo, J. Castillo, A. Fernández, S. Goncalves, M.A. Ranaudo, Energy Fuel **12**, 386–390 (1998)
28. Y. Tu, J. Woods, J. Kung, T. Mccracken, L. Kotlyar, B. Sparks, M. Dong, Clay Sci. **12**, 183–187 (2006)
29. T. Pernyeszi, A. Patzko, O. Berkesi, I. Dékány, Colloids Surf. A Physicochem. Eng. Asp. **137**, 373–384 (1998)
30. D. Dudášová, S. Simon, P.V. Hemmingsen, J. Sjöblom, Colloids Surf. A Physicochem. Eng. Asp. **317**, 1–9 (2008)
31. A. Jada, H. Debih, M. Khodja, J. Pet. Sci. Eng. **52**, 305–316 (2006)
32. A. Jada, H. Debih, Composite Interfaces **16**, 219–235 (2009)
33. G.C. Klein, S. Kim, R.P. Rodgers, A.G. Marshall, A. Yen, Energy Fuel **20**, 1973–1979 (2006)
34. R. Li, P. Jiang, C. Gao, F. Huang, R. Xu, X. Chen, Energy Fuel **31**, 188–197 (2016)
35. M. Mohammadi, M. Akbari, Z. Fakhroueian, A. Bahramian, R. Azin, S. Arya, Energy Fuel **25**, 3150–3156 (2011)

36. C.A. Franco, N.N. Nassar, M.A. Ruiz, P. Pereira-Almao, F.B. Cortés, Energy Fuel **27**, 2899–2907 (2013)
37. J. Giraldo, P. Benjumea, S. Lopera, F.B. Cortés, M.A. Ruiz, Energy Fuel **27**, 3659–3665 (2013)
38. B. Moradi, P. Pourafshary, F. Jalali, M. Mohammadi, M. Emadi, J. Nat. Gas Sci. Eng. **27**, 64–73 (2015)
39. O.C. Mullins, H. Sabbah, J.L. Eyssautier, A.E. Pomerantz, L. Barré, A.B. Andrews, Y. Ruiz-Morales, F. Mostowfi, R. McFarlane, L. Goual, Energy Fuel **26**, 3986–4003 (2012)
40. H. Groenzin, O.C. Mullins, Energy Fuel **14**, 677–684 (2000)
41. H. Groenzin, O.C. Mullins, Chem. A Eur. J. **103**, 11237–11245 (1999)
42. S. Acevedo, A. Castro, J.G. Negrin, A. Fernández, G. Escobar, V. Piscitelli, F. Delolme, G. Dessalces, Energy Fuel **21**, 2165–2175 (2007)
43. E. Durand, M. Clemancey, J.-M. Lancelin, J. Verstraete, D. Espinat, A.-A. Quoineaud, Energy Fuel **24**, 1051–1062 (2010)
44. J. Murgich, Mol. Simul. **29**, 451–461 (2003)
45. O.C. Mullins, Energy Fuel **24**, 2179–2207 (2010)
46. H. Sabbah, A.L. Morrow, A.E. Pomerantz, R.N. Zare, Energy Fuel **25**, 1597–1604 (2011)
47. Y. Ruiz-Morales, Can. J. Chem. **87**, 1280–1295 (2009)
48. T.F. Yen, J.G. Erdman, S.S. Pollack, Anal. Chem. **33**, 1587–1594 (1961)
49. R.R. Chianelli, M. Siadati, A. Mehta, J. Pople, L.C. Ortega, L.Y. Chiang, *Asphaltenes, Heavy Oils, and Petroleomics* (Springer, 2007), pp. 375–400
50. M. Ghanavati, M.-J. Shojaei, A.R. Sa, Energy Fuel **27**, 7217–7232 (2013)
51. S. Chavan, H. Kini, R. Ghosal, Int. J. Environ Sci Develop. **3**, 228 (2012)
52. W. Chuan, L. Guang-Lun, C.-J. Yao, K.-J. Sun, P.-Y. Gai, Y.-B. Cao, J. Fuel Chem. Technol. **38**, 684–690 (2010)
53. A.D. Manasrah, N.N. Nassar, L.C. Ortega, Fuel **215**, 865–878 (2018)
54. S.S. Alian, A.A. Omar, A.F. Alta'ee, I. Hani, Int. J. Chem. Mol. Nuclear Mat. Metall. Eng. **5**, 482–486 (2011)
55. N.N. Nassar, A. Hassan, L. Carbognani, F. Lopez-Linares, P. Pereira-Almao, Fuel **95**, 257–262 (2012)
56. M.S. Rana, V. Samano, J. Ancheyta, J. Diaz, Fuel **86**, 1216–1231 (2007)
57. C.A. Franco, N.N. Nassar, F.B. Cortés, J. Colloid Interface Sci. **433**, 58–67 (2014)
58. R. Syunyaev, R. Balabin, I. Akhatov, J. Safieva, Energy Fuel **23**, 1230–1236 (2009)
59. S. Acevedo, M.A. Ranaudo, C. García, J. Castillo, A. Fernández, Energy Fuel **17**, 257–261 (2003)
60. M. Hmoudah, N.N. Nassar, G. Vitale, A. El-Qanni, RSC Adv. **6**, 64482–64493 (2016)
61. N.N. Marei, N.N. Nassar, M. Hmoudah, A. El-Qanni, G. Vitale, A. Hassan, Can. J. Chem. Eng. **95**, 1864–1874 (2017)
62. A. El-Qanni, N.N. Nassar, G. Vitale, Chem. Eng. J. **327**, 666–677 (2017)
63. A. Hethnawi, A.D. Manasrah, G. Vitale, N.N. Nassar, J. Colloid Interface Sci. **513**, 28–42 (2018)
64. A.D. Manasrah, I.W. Almanassra, N.N. Marei, U.A. Al-Mubaiyedh, T. Laoui, M.A. Atieh, RSC Adv. **8**, 1791–1802 (2018)
65. A.D. Manasrah, T. Laoui, S.J. Zaidi, M.A. Atieh, Exp. Thermal Fluid Sci. **84**, 231–241 (2017)
66. R. Hashemi, N.N. Nassar, P.P. Almao, Appl. Energy **133**, 374–387 (2014)
67. N.N. Nassar, Energy Fuel **24**, 4116–4122 (2010)
68. N. Hosseinpour, A.A. Khodadadi, A. Bahramian, Y. Mortazavi, Langmuir **29**, 14135–14146 (2013)
69. A. Amrollahi Biyouki, N. Hosseinpour, N.N. Nassar, Energy Fuel **32**, 5033–5044 (2018)
70. N. Setoodeh, P. Darvishi, A. Lashanizadegan, J. Dispers. Sci. Technol. **39**, 711–720 (2018)
71. A. Hassan, F. Lopez-Linares, N.N. Nassar, L. Carbognani-Arambarri, P. Pereira-Almao, Catal. Today **207**, 112–118 (2013)
72. J.D. Guzmán, S. Betancur, F. Carrasco-Marín, C.A. Franco, N.N. Nassar, F.B. Cortés, Energy Fuel **30**, 2052–2059 (2016)

73. N.N. Nassar, S. Betancur, S.C. Acevedo, C.A. Franco, F.B. Cortés, Ind. Eng. Chem. Res. 54 (2015) 8201–8211
74. T. Montoya, D. Coral, C.A. Franco, N.N. Nassar, F.B. Cortés, Energy Fuel **28**, 4963–4975 (2014)
75. S. Rosales, I. Machín, M. Sánchez, G. Rivas, F. Ruette, J. Mol. Catal. A Chem. **246**, 146–153 (2006)
76. B. Marlow, G. Sresty, R. Hughes, O. Mahajan, Colloids Surf. **24**, 283–297 (1987)
77. A. Saada, B. Siffert, E. Papirer, J. Colloid Interface Sci. **174**, 185–190 (1995)
78. A.W. Marczewski, M. Szymula, Colloids Surf. A Physicochem. Eng. Asp. **208**, 259–266 (2002)
79. J.L.M. de la Cruz, I.V. Castellanos-Ramírez, A. Ortiz-Tapia, E. Buenrostro-González, C.D.L.A. Durán-Valencia, S. López-Ramírez, Colloids Surf. A Physicochem. Eng. Asp. **340**, 149–154 (2009)
80. F.B. Cortés, J.M. Mejía, M.A. Ruiz, P. Benjumea, D.B. Riffel, Energy Fuel **26**, 1725–1730 (2012)
81. S. Lowell, J.E. Shields, *Powder Surface Area and Porosity* (Springer, 2013)
82. H. Gaboriau, A. Saada, Chemosphere **44**, 1633–1639 (2001)
83. G. González, M.B. Moreira, Colloids Surf. **58**, 293–302 (1991)
84. S. Acevedo, M.A.A. Ranaudo, C. García, J. Castillo, A. Fernández, M. Caetano, S. Goncalvez, Colloids Surf. A Physicochem. Eng. Asp. 166 (2000) 145–152
85. M. Castro, J.L.M. de la Cruz, E. Buenrostro-Gonzalez, S. López-Ramírez, A. Gil-Villegas, Fluid Phase Equilib. **286**, 113–119 (2009)
86. J. Giraldo, N.N. Nassar, P. Benjumea, P. Pereira-Almao, F.B. Cortés, Energy Fuel **27**, 2908–2914 (2013)
87. J.M. Prausnitz, R.N. Lichtenthaler, E.G. de Azevedo, *Molecular Thermodynamics of Fluid-Phase Equilibria* (Pearson Education, 1998)
88. O. Talu, F. Meunier, AICHE J. **42**, 809–819 (1996)
89. N.N. Nassar, T. Montoya, C.A. Franco, F.B. Cortés, P. Pereira-Almao, Energy Fuel **29**, 4210–4221 (2015)
90. K. Mannistu, H. Yarranton, J. Masliyah, Energy Fuel **11**, 615–622 (1997)
91. D. Eskin, J. Ratulowski, K. Akbarzadeh, S. Pan, Can. J. Chem. Eng. **89**, 421–441 (2011)
92. N.H. Rahmani, T. Dabros, J.H. Masliyah, Chem. Eng. Sci. **59**, 685–697 (2004)
93. N.H. Rahmani, J.H. Masliyah, T. Dabros, AICHE J. **49**, 1645–1655 (2003)
94. A. Khoshandam, A. Alamdari, Energy Fuel **24**, 1917–1924 (2010)
95. H. Rahimi, A.R. Solaimany Nazar, Energy Fuel **24**, 1088–1093 (2009)
96. T. Maqbool, S. Raha, M.P. Hoepfner, H.S. Fogler, Energy Fuel **25**, 1585–1596 (2011)
97. A.R. Solaimany-Nazar, H. Rahimi, Energy Fuel **22**, 3435–3442 (2008)
98. L.G. Austin, Powder Technol. **5**, 1–17 (1971)
99. M. Hounslow, R. Ryall, V. Marshall, AICHE J. **34**, 1821–1832 (1988)
100. S.K. Friedlander, Smoke, dust and haze: Fundamentals of aerosol behavior, Wiley Interscience, 317, (1977)
101. M. Elimelech, J. Gregory, X. Jia, *Particle Deposition and Aggregation: Measurement, Modelling and Simulation* (Butterworth-Heinemann, 2013)
102. K.A. Kusters, S.E. Pratsinis, S.G. Thoma, D.M. Smith, Chem. Eng. Sci. **48**, 4119–4127 (1993)
103. P.T. Spicer, S.E. Pratsinis, AICHE J. **42**, 1612–1620 (1996)
104. T. Serra, X. Casamitjana, AICHE J. **44**, 1724–1730 (1998)
105. J. Pandya, L. Spielman, *Chem. Eng. Sci.*, vol 38 (1983)
106. J.D. Boadway, J. Environ. Eng. Div. **104**, 901–915 (1978)
107. A. Wilczak, T.M. Keinath, Water Environ. Res. **65**, 238–244 (1993)
108. N. Chiron, R. Guilet, E. Deydier, Water Res. **37**, 3079–3086 (2003)
109. O.P. Strausz, P.A. Peng, J. Murgich, Energy Fuel **16**, 809–822 (2002)
110. N.N. Nassar, A. Hassan, P. Pereira-Almao, Energy Fuel **25**, 1017–1023 (2011)
111. N.N. Nassar, A. Hassan, P. Pereira-Almao, Colloids Surf. A Physicochem. Eng. Asp. **384**, 145–149 (2011)
112. N.N. Nassar, A. Hassan, P. Pereira-Almao, J. Colloid Interface Sci. **360**, 233–238 (2011)

113. F. Lopez-Linares, L. Carbognani, A. Hassan, P. Pereira-Almao, E. Rogel, C. Ovalles, A. Pradhan, J. Zintsmaster, Energy Fuel **25**, 4049–4054 (2011)
114. C.A. Franco, F.B. Cortés, N.N. Nassar, J. Colloid Interface Sci. **425**, 168–177 (2014)
115. C.W. Angle, Y. Long, H. Hamza, L. Lue, Fuel **85**, 492–506 (2006)
116. S.F. Alkafeef, M.K. Algharaib, A.F. Alajmi, J. Colloid Interface Sci. **298**, 13–19 (2006)
117. K.R. Dean, J.L. McATEE Jr., Appl. Clay Sci. **1**, 313–319 (1986)
118. N.N. Nassar, A. Hassan, P. Pereira-Almao, Energy Fuel **25**, 3961–3965 (2011)
119. N.N. Nassar, A. Hassan, G. Vitale, Appl. Catal. A Gen. **484**, 161–171 (2014)
120. A.K. Zimmer, C. Becker, C.K. Chambliss, Energy Fuel **27**, 4574–4580 (2013)
121. N.N. Nassar, C.A. Franco, T. Montoya, F.B. Cortés, A. Hassan, Fuel **156**, 110–120 (2015)
122. T. Montoya, D. Coral, C.A. Franco, N.N. Nassar, F.B. Cortés, Energy Fuel **28**(8), 4963–4975 (2014)
123. C.A. Franco, N.N. Nassar, T. Montoya, M.A. Ruíz, F.B. Cortés, Energy Fuel **29**, 1610–1621 (2015)
124. T. Pernyeszi, I. Dékány, Colloids Surf. A Physicochem. Eng. Asp. **194**, 25–39 (2001)
125. M. Szymula, A.W. Marczewski, Appl. Surf. Sci. **196**, 301–311 (2002)
126. K. Sing, Pure Appl. Chem. **54**, 2201–2218 (1982)
127. L. Li, P.A. Quinlivan, D.R. Knappe, Carbon **40**, 2085–2100 (2002)
128. C. Ng, J.N. Losso, W.E. Marshall, R.M. Rao, Bioresour. Technol. **85**, 131–135 (2002)
129. C.A. Franco, N.N. Nassar, T. Montoya, M.A. Ruíz, F.B. Cortés, Energy Fuel **29**, 1610–1621 (2015)
130. C.A. Franco, M. Martínez, P. Benjumea, E. Patiño, F.B. Cortés, Adsorp. Sci. Technol. **32**, 197–207 (2014)
131. C. Drummond, J. Israelachvili, J. Pet. Sci. Eng. **45**, 61–81 (2004)
132. H.W. Yarranton, H. Alboudwarej, R. Jakher, Ind. Eng. Chem. Res. **39**, 2916–2924 (2000)
133. H. Alboudwarej, D. Pole, W.Y. Svrcek, H.W. Yarranton, Ind. Eng. Chem. Res. **44**, 5585–5592 (2005)
134. K.S. Sing, Pure Appl. Chem. **57**, 603–619 (1985)
135. S.I. Andersen, Fuel Sci. Technol. Int. **13**, 579–604 (1995)
136. A. Hirschberg, L. DeJong, B. Schipper, J. Meijer, Soc. Pet. Eng. J. **24**, 283–293 (1984)
137. R. De Boer, K. Leerlooyer, M. Eigner, A. Van Bergen, SPE Production & Facilities **10**, 55–61 (1995)
138. D. Browarzik, H. Laux, I. Rahimian, Fluid Phase Equilib. **154**, 285–300 (1999)
139. P. Ekholm, E. Blomberg, P. Claesson, I.H. Auflem, J. Sjöblom, A. Kornfeldt, J. Colloid Interface Sci. **247**, 342–350 (2002)
140. D.M. Sztukowski, M. Jafari, H. Alboudwarej, H.W. Yarranton, J. Colloid Interface Sci. **265**, 179–186 (2003)
141. R. Long, Am Chem Soc. Div. Pet. Chem. Prepr. (United States) **24** (1979)
142. A. Ortega-Rodriguez, F. Alvarez-Ramirez, S. Cruz, C. Lira-Galeana, J. Colloid Interface Sci. **301**, 352–359 (2006)
143. J.J. Habeeb, Method for Selectively Removing Basic Nitrogen Compounds from Lube Oils Using Transition Metal Halides or Transition Metal Tetrafluoroborates, Google Patents (1982)
144. N.N. Marei, N.N. Nassar, G. Vitale, Phys. Chem. Chem. Phys. **18**, 6839–6849 (2016)
145. A.D. Manasrah, A. El-Qanni, I. Badran, L.C. Ortega, M.J. Perez-Zurita, N.N. Nassar, React. Chem. Eng. **2**, 703–719 (2017)
146. F. López-Linares, L. Carbognani, M.F. González, C. Sosa-Stull, M. Figueras, P. Pereira-Almao. Energy Fuel **20**, 2748–2750 (2006)
147. T. Montoya, A. Amrollahi, G. Vitale, N. Hosseinpour, N.N. Nassar, ACS Appl. Nano Mater. (2020)
148. C.A. Franco, M.M. Lozano, S. Acevedo, N.N. Nassar, F.B. Cortés, Energy Fuel **30**, 264–272 (2015)
149. O.C. Mullins, H. Sabbah, J. Eyssautier, A.E. Pomerantz, L. Barré, A.B. Andrews, Y. Ruiz-Morales, F. Mostowfi, R. McFarlane, L. Goual, Energy Fuel **26**, 3986–4003 (2012)
150. J.D. McLean, P.K. Kilpatrick, J. Colloid Interface Sci. **196**, 23–34 (1997)
151. N.N. Nassar, M.M. Husein, Fuel Process. Technol. **91**, 164–168 (2010)

Chapter 4
Nanoparticles as Catalyst for Asphaltenes and Waste Heavy Hydrocarbons Upgrading

Abdallah D. Manasrah, Tatiana Montoya, Azfar Hassan, and Nashaat N. Nassar

4.1 Introduction

As a result of population growth and improvements in the quality of life, there has been a rapid increase in total energy demand worldwide and a depletion of conventional oil resources, resulting in a need for alternative, sustainable, and environment-friendly energy sources [1]. The global energy demand is expected to rise by 33% by 2035 [2]. To meet global energy demands while appropriately addressing environmental concerns, environment-friendly, cost-effective, efficient, innovative, and smart technologies for oil sands exploration and extraction need to be developed. Oil sands are currently one of the reliable supplies. Accordingly, great attention has been paid to unconventional resources such as heavy and extra-heavy crude oils to meet the global energy demand [1–4]; however, heavy crude oils have a large amount of high-molecular-weight polar hydrocarbons, such as asphaltenes, that cause high viscosities and low API gravity that strongly affect the production, transportation, and refinery processes [2–4]. These heavy polar hydrocarbons are also typically characterized by a low hydrogen-to-carbon atomic ratio (H/C) and a high initial boiling point and generally produce more than 50 wt% of residue with boiling points above 773 K [5, 6], which tends to inhibit light hydrocarbon conversion. In addition, heavy oils contain high levels of metals, such as Fe, Ni, and V, and heteroatoms, such as S, O, and N [7]. Heavy oils also contain appreciable amounts of sulfur-type compounds, including refractory compounds with strong bonds, such as C-S and C=S, that dramatically increase oil viscosity [8, 9]. Given high viscosity, high density, and the presence of metal and sulfur compounds, upgrading processes are essential to improve heavy oil quality to meet pipeline and market

A. D. Manasrah · T. Montoya · A. Hassan · N. N. Nassar (✉)
Department of Chemical and Petroleum Engineering, University of Calgary, Calgary, Canada
e-mail: nassar@ucalgary.ca

N. N. Nassar et al. (eds.), *Nanoparticles: An Emerging Technology for Oil Production and Processing Applications*, Lecture Notes in Nanoscale Science and Technology, https://doi.org/10.1007/978-3-319-12051-5_4

specifications. The H/C atomic ratio is typically used as an indicator of oil quality; a value near 1.5 is an indicator of high-quality crude, while a value near 0.8 is an indicator of poor-quality crude [10]. Accordingly, to improve the quality of heavy oil, its H/C atomic ratio should increase. The technologies currently used to improve heavy oil quality include carbon rejection, hydroprocessing, and gasification [11–13]. Carbon rejection processes include pyrolysis (e.g. visbreaking, coking, and rapid thermal pyrolyzer), separation or extraction (e.g. solvent deasphalting process, SDA), and cracking (e.g. VGO and VR FCC) [5, 6, 14–17]. Hydrocracking and steam cracking gasification are typical processes of hydrogen addition [18, 19]. Conventional hydroprocessing technologies still suffer from coke formation and catalyst poisoning as a result of metal deposition. Carbon rejection processes have simple configurations compared with hydrogen addition processes and do not require hydrogen injection and catalyst loading; however, this process produces lower yields and generates significant coke waste, giving it a large environmental footprint. Gasification has been a topic of research for many years [20, 21], and its development and commercialization have also been a subject of intense analysis [5, 22] as a promising technology for upgrading heavy hydrocarbons. To date, the best-known gasification process for heavy residue fraction upgrading is the "flexicoking" process developed by Exxon Mobil [23]. In flexicoking, residue is converted into synthetic gases, such as CO, H_2, CH_4, and CO_2. While flexicoking generates better quality liquid and forms less coke compared with the delay coking process, it suffers from a number of challenges including the need for good-quality feed to avoid coke formation, high catalyst loading, and the production of low-BTU waste gas [24]. Hence, there is an urgent need for new technologies that can merge with current technologies to enhance the quality of heavy oil and satisfy environmental regulations with lower operational costs. To this end, nanoparticle technology has recently emerged as a potential solution for a number of challenges facing the oil industry [22]. Nanoparticles technology has emerged as an attractive area of interest for heavy oil upgrading as asphaltene removal, air emission capture, and wastewater treatment become relevant. Because of their unique features and special physical and chemical properties, such as high surface area to volume ratio, high degree of dispersion, excellent adsorption affinity, and catalytic activity promotion, nanoparticles could be used as adsorbents and catalysts for enhancing heavy oil quality. Also, because of their small size, nanoparticles are highly mobile in porous media. Furthermore, nanoparticles offer potential for an environment-friendly and cost-effective approach for heavy oil recovery and upgrading because they can be prepared *in situ*, within the oil reservoir. Dr. Nassar's research group has explored nanoparticle technology to integrate carbon rejection with hydrogen addition processes. These studies have addressed the use of nanoparticles technologies for oil upgrading and recovery processes, particularly for asphaltene adsorptive removal and subsequent postadsorption decomposition. Nanoparticles were also employed as inhibitors to prevent or delay the precipitation of asphaltenes by *in situ* adsorption of asphaltenes within the well. Furthermore, supported and unsupported nanoparticles were employed for asphaltene adsorption from the oil matrix, followed by postadsorption catalytic decomposition [22, 25–37]. In this chapter, we

discuss the role of nanoparticles as adsorbents to remove heavy polar hydrocarbons from heavy oil and subsequently how they be used as catalysts for postadsorption decomposition of the adsorbed heavy hydrocarbons. The catalytic effect of different metal oxide nanoparticles on the thermo-oxidative decomposition of asphaltenes at isothermal and nonisothermal conditions will be evaluated using thermogravimetric analyses. In addition, the effects of nanoparticles in asphaltene steam gasification using a fixed bed reactor will be discussed. Thus, the following topics are covered in this chapter: (i) the role of nanoparticles as an adsorbent and their subsequent oxidation/decomposition of adsorbed species, (ii) factors affecting the thermo-oxidation and decomposition of asphaltenes such as the types and properties of nanoparticles, the source of asphaltenes and their properties, and the effect of adsorption affinity on the oxidation of adsorbed asphaltenes, and (iii) the use of isoconversional method for estimating the effective activation energies of the thermal decomposition reactions.

4.1.1 Role of Nanoparticles as Catalyst

Asphaltene adsorption and subsequent oxidation/combustion on nanoparticles has become an attractive topic for the heavy oil industry [28]. The nanoparticles are not only rapidly removing asphaltenes from the heavy oil and thus making the remaining fraction of oil transportable for conventional processing but also the nanoparticles can be employed as catalysts for upgrading asphaltenes into light usable distillates [5, 38, 39]. By integrating asphaltene adsorption and oxidation, important synergies could be realized, including a reduction in capital cost, an increase in energy efficiency, and enhanced performance and portability [40]. Many types of nanoparticles have been developed with greener technologies and cost-effective approaches that have proven to have a significant impact on the oil upgrading industry [28, 41]. These nanoparticles include glass, clay minerals, soils, minerals, rock minerals, silica, modified silica, alumina, silica-alumina, metals, metal oxides, various forms of carbon, and polymers [42]. Metal-based nanoparticles, for instance, exhibited extraordinary catalytic [43], electric [44], photosensitive [45], and magnetic [46] properties, as well as demonstrating their potential application in several fields of energy [47, 48], environment [49], engineering, and science [50]. Recently, extensive research has been performed that employs metal-based nanoparticles as adsorbent and catalyst "nanosorbcats" for oil upgrading and recovery processes [51–53] that can be positively applied for *in situ* and *ex situ* oil upgrading processes as a cost-effective and more environment-friendly approach. Asphaltenes can be selectively separated from oil by adsorbing them onto the surfaces of nanosorbcats and consequently, upgrading these heavy fractions into light utilizable distillates [5, 25]. It should be noted that asphaltenes upgrading is controlled by its chemical and physical structure in addition to the physical and chemical characteristics of the adsorbent [52]. The source of asphaltenes plays a significant role in determining its structure, while the physical properties of nanoparticles such as surface

morphology, surface area, internal pore volume, pore diameter, and pore distribution have contributed to the efficiency of the adsorption process [42, 54]. Another important factor to be considered is the potential for diffusion problems and pore plugging which are probable when using classical porous adsorbents for removing asphaltenes [55].

4.1.2 *Catalytic Effect of Nanosorbcat*

Nanoparticles can be employed as adsorbent/catalysts for separating asphaltenes followed by their catalytic decomposition [28, 37]. For instance, upgrading the heavy oil via *in situ* via catalytic cracking requires asphaltene adsorptive removal followed by catalytic thermal cracking or a hydrogenation reaction. Thus, before field application and well test performance, the catalytic effect of nanoparticles toward asphaltene cracking has to be determined. In search of an economically viable upgrading process for bitumen or heavy oil, an alternative processing scheme that may prove viable was proposed by Hassan et al. [53, 56] as shown in Fig. 4.1. This scheme requires the development of a catalyst capable of preferentially

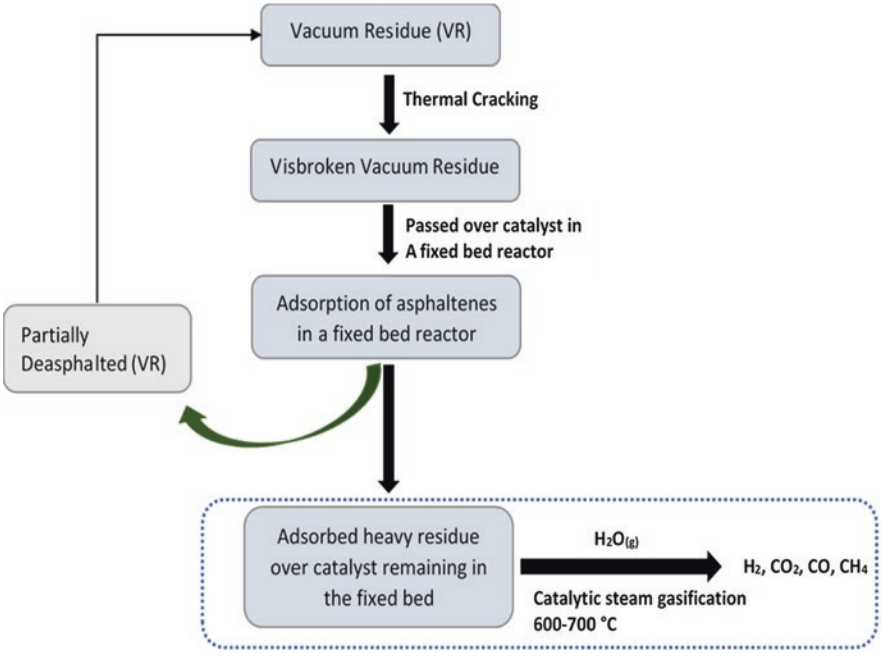

Fig. 4.1 Schematic representation of the total process for catalytic steam gasification of adsorbed asphaltenes and heavy asphaltene-like molecules [56]. (Permissions related to the material excerpted were obtained from American Chemical Society, copyright 2017, and further permission should be directed to American Chemical Society; Ref. [56])

adsorbing heavy polar hydrocarbons, like asphaltenes, and subsequently, its ability to perform low-temperature catalytic steam gasification of the adsorbed species. This approach can be achieved by constructing a setup capable of performing both adsorption and catalytic steam gasification in continuous operation using a fixed bed reactor. On the other hand, the adsorption process is conducted by extracting asphaltenes from the heavy oil and resolubilizing in a model solvent, such as toluene or heptol (heptane + toluene). Batch adsorption usually takes place with a ratio of 1:10 (L/g) model heavy oil solution/ mass of the nanoparticles. The adsorption of asphaltenes onto nanoparticles is determined from the change in the concentration of asphaltenes in the model oil solution (i.e. toluene) before and after mixing with the nanoparticles. It was confirmed that the adsorption of asphaltenes onto surfaces of nanoparticles depends on the type and strength of interactions between the asphaltene species and the solid surface. A number of interparticle forces are individually or collectively responsible for this successful interaction between asphaltenes and the surface that results from the presence of functionalized groups on the asphaltenes, including carboxylic, pyrrolic, pyridinic, thiophenic, and sulfite groups [57, 58]. The major forces that could contribute to these interactions are van der Waals, electrostatic, charge transfer, hydrogen bonding, and steric interactions [59]. After adsorption, the thermo-oxidative decomposition of the adsorbed asphaltenes over metal oxide nanoparticles can be performed using a simultaneous thermogravimetric analyzer (TGA/DSC) to measure the mass loss over oxidation temperature and/or time. For better understanding the catalytic effect and comparison purposes of nanosorbcat, a small amount (∼5–10 mg) of tested samples (including adsorbed asphaltenes and nanoparticles) should be placed in TGA and heated from room temperature at a specified heating rate to a specific temperature under atmosphere of air or nitrogen until no appreciable mass loss was observed. Although asphaltenes adsorption and thermal decomposition have been studied extensively [60–63], little work has been performed on the adsorption and subsequent catalytic thermal behavior of nanoparticles toward asphaltenes [37, 64, 65]. Different types of metal oxide nanoparticles were successfully employed for adsorptive removal [28] and subsequent oxidation [66], gasification [29], and decomposition [30] of asphaltenes for isothermal and nonisothermal conditions. Nassar et al. [28, 30, 37] reported about the adsorption of asphaltene and their subsequent oxidation onto different metal oxide nanoparticle surfaces, disclosing that the adsorption of asphaltenes is strongly dependent on the type of nanoparticles. Several types of nanoparticles were also reported for the adsorption of n-C_7 asphaltenes originated from Athabasca vacuum residue, such as NiO, Co_3O_4, Fe_3O_4, TiO_2, CaO, CeO_2, and ZrO_2 [33]. Furthermore, Nassar et al. [65] described the correlation between the adsorption affinity and the catalytic activity of metal oxide nanoparticles, suggesting that the higher the affinity for adsorption, the better the catalytic activity for asphaltene decomposition. These experimental findings also showed that the presence of nanoparticles decreases the activation energy of asphaltene decomposition, thus enhancing the reaction rate.

4.2 Oxidation of Asphaltenes

The adsorption and subsequent oxidation of asphaltenes on metal oxide nanoparticles were first introduced by Nassar et al. [37, 52, 64–66]. The measure of the catalytic effect of nanoparticles on the thermo-oxidative decomposition of asphaltenes typical employs the use of thermogravimetric analyses. This catalytic effect toward asphaltene oxidation is investigated by monitoring the mass and heat changes as temperature increases. The adsorbed asphaltenes samples should be heated under at least three different heating rates. It is worth mentioning that for better evaluation and comparison of the catalytic effect of nanoparticles on thermo-oxidative decomposition of asphaltenes, the amount of asphaltene adsorbed per surface area of nanoparticles should be kept fixed for all the selected nanoparticles. This would eliminate the effect of surface area and pinpoint the importance of the surface functionality of the nanoparticles toward asphaltene adsorption and subsequent oxidation. Additionally, the mass of tested sample should be the minimum to avoid mass transfer (diffusion) limitations.

When the asphaltenes are adsorbed onto nanoparticles, the oxidation appears to happen at much lower temperatures compares with the oxidation temperature of virgin asphaltenes (nonadsorbed), clearly supporting that the nanoparticles have a catalytic effect over asphaltenes oxidation as observed in several studies by Nassar et al. [37, 52, 64, 65]. Evidence of this can be seen in Fig. 4.2a and b, which shows the profiles for the differential of mass loss and heat flow, respectively, with the increase in the temperature at a heating rate of 10 °C/min, under air atmosphere, for virgin nC_7-asphaltenes as well as the adsorbed nC_7-asphaltenes onto nanoparticles [28]. As shown, the mass loss profile for nonadsorbed C_7-asphaltenes (virgin) can be divided into two regions over the oxides range of 400 and 550 °C: (1) low-temperature range (up to 400 °C) due to thermal cracking and (2) high-temperature range (beyond 400 °C) due to the complete oxidation to gaseous products. Since asphaltenes have heavy structure fractions in oil, no exothermicity associated with mass loss in the heat changes profile can be observed lower than 400 °C. This mass loss was therefore termed as low-temperature oxidation region where the major loss occurs due to bond scission as well as the incorporation of oxygen into the asphaltene matrix. Combustion in the presence of air occurs after 450 °C, as shown by the presence of an exotherm that follows the same profile as the mass loss. For the nanoparticles containing C_7-asphaltenes, the profile of mass loss and the heat evolved changed drastically. On the other hand, the oxidation/combustion of adsorbed nC_7-asphaltenes onto nanoparticles appears to happen at much lower temperatures (<350 °C). This reduction in oxidation temperature validates the idea that the nanoparticles considerably catalyze the oxidation of asphaltenes. Nassar et al. investigated the adsorption/oxidation of asphaltenes using different types of nanoparticles [28, 34, 35, 66]. During the adsorption process, the authors observed a monolayer of adsorbed asphaltenes using metal oxide nanoparticles [28, 35, 37], aluminas [64], modified kaolin, and kaolin containing metal oxide nanoparticles [67]. Table 4.1 summarizes the oxidation temperature and the activation energy of

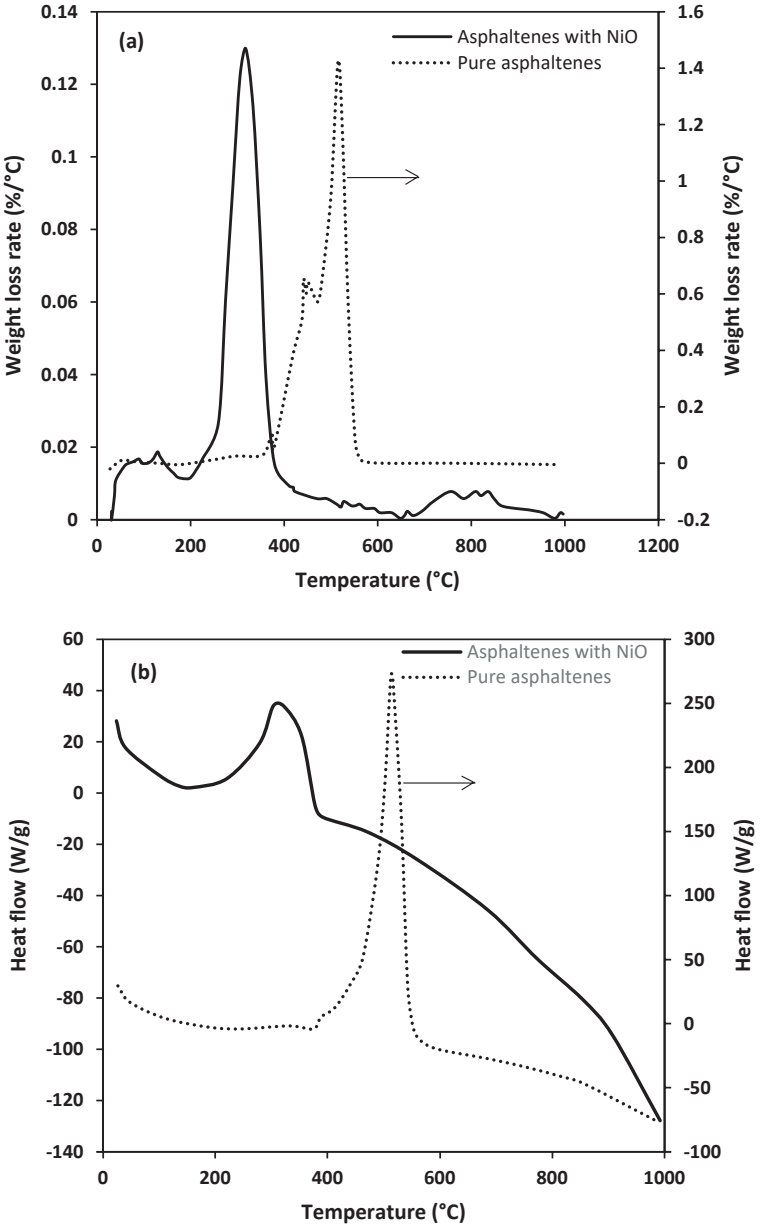

Fig. 4.2 DTG-DTA curves for asphaltenes oxidation with and without NiO nanoparticles, (**a**) the rate of mass loss with temperature, (**b**) the enthalpy changes with temperature [28]. (Permissions related to the material excerpted were obtained from American Chemical Society, copyright 2011, and further permission should be directed to American Chemical Society; Ref. [28])

Table 4.1 Effect of different types of nanoparticle on the oxidation properties of adsorbed asphaltenes

Type of nanoparticles	Size of NP	Oil source and type of asphaltenes	Activation energy (kJ/mol)	Oxidation temperature (°C)	Method used	Ref.
NiO	12 nm	C_7-asphaltenes, VR	57	280–325	Coats-Redfern	[37]
Co_3O_4	22 nm	C_7-asphaltenes	72	~300	Coats-Redfern	[37]
Fe_3O_4	22 nm	C_7-asphaltenes	43–61	~365	Coats-Redfern	[37]
Nanoalumina	48 nm	C_7-asphaltenes	16.72–39.83	250–440	Coats-Redfern	[65]
Microalumina	<200 μm	C_7-asphaltenes	12.56–38.22	300–440	Coats-Redfern	[65]
TiO_2	8 nm	C_7-asphaltenes	115–148	400	Ozawa–Flyn–Wall	[52]
ZrO_2	26 nm	C_7-asphaltenes	115–145	360	Ozawa–Flyn–Wall	[52]
CeO_2	16 nm	C_7-asphaltenes	50–120	330	Ozawa–Flyn–Wall	[52]
Acidic alumina	60 A, Avg. pore size	C_7-asphaltenes	27.2–52	320–350	Coats-Redfern	[64]
Neutral alumina	52 A, Avg. pore size	C_7-asphaltenes	17.9–47.0	320–350	Coats-Redfern	[64]
Basic alumina	54 A, Avg. pore size	C_7-asphaltenes	18.8–44.7	320–350	Coats-Redfern	[64]
NiO	12 nm, 107 m^2/g (BET)	C_7-asphaltenes	108.58	300 °C in 120 min	Ozawa–Flyn–Wall	[38]
Co_3O_4	22 nm, 41 m^2/g (BET)	C_7-asphaltenes	90.62	300 °C in 125 min	Ozawa–Flyn–Wall	[38]
Fe_2O_4	22 nm, 43 m^2/g (BET)	C_7-asphaltenes	153.34	300 °C in 280 min	Ozawa–Flyn–Wall	[38]

adsorbed asphaltenes over these different types of nanoparticles. All tested nanoparticles showed high catalytic activity for post adsorption oxidation. As shown, the oxidation temperature of asphaltene decreases by the range of 100–140 °C relative to the noncatalytic oxidation of virgin asphaltenes in the presence of metal oxide nanoparticles. However, for virgin nC_7-asphaltenes not adsorbed over nanoparticles, oxidation occurs between 400 and 550 °C, as discussed earlier. Moreover, the significant reduction in the activation energy values confirms the catalytic activity of nanoparticles toward asphaltene decomposition. A correlation between the

adsorption affinity and the catalytic activity of the metal oxide nanoparticles was reported, indicating that higher adsorption affinities increase the catalytic activity. Having an active surface is one of the important properties of an adsorbent/catalyst. For transition metal oxide nanoparticles, the adsorption affinity and catalytic activity are expected to be different depending on their differing surface characteristics and chemistry.

As demonstrated by Nassar et al. [64], a higher adsorption capacity per surface area was obtained for nanoalumina, demonstrating that surface acidity plays an important role in the adsorption affinity. In addition, the catalytic oxidation of adsorbed asphaltenes is highly affected by particle sizes [65, 68] and surface acidities [64]. This fact was supported by using two different alumina particles (micro and nanoparticles) that have different particle sizes and surface acidities. However, the catalytic activity for asphaltene oxidation was higher for microalumina compare with nanoalumina, revealing that the textural properties are more important than the particle size during the catalytic oxidation of asphaltenes.

To further understand the effect of surface acidity/basicity on the asphaltene oxidation performance, three different surface acidities of alumina containing adsorbed asphaltenes were investigated. It is evident that adsorption of asphaltene over alumina greatly enhanced the oxidation process and the oxidation process involving thermal cracking started as early as 400 °C. The acidic alumina has the highest adsorption of asphaltenes, and basic alumina has the highest catalytic activity toward asphaltene oxidation based on its surface area. Moreover, the transport of alumina nanoparticles suspended in an aqueous solution with potential adsorption value is feasible because the nanoparticles allowed the system to flow, demonstrating the inhibition of both precipitation and deposition as well as the enhanced durability against asphaltene damage in porous media [66].

It was also found that the mechanism function of asphaltene oxidation is strongly dependent on the type of nanoparticle, which is attributed to the different extent of chemisorption between asphaltenes and the nanoparticle surface [69]. For example, CeO_2 showed the lowest values of effective activation energy compared with other metal oxide nanoparticles like TiO_2 and ZrO_2 [52]. Such a low value of activation energy can be explained by the ability of CeO_2 to follow the Mars−Van Krevelen (MvK) mechanism [70]. Similar findings were reported by Hosseinpour et al. [71, 72] on Iranian n-C_7 asphaltenes using metal oxide nanoparticles for the adsorption and subsequent oxidation asphaltenes. It was observed that the profile of gases released in the decomposition process is particle-type dependent, confirming the catalytic role of the selected metal oxide nanoparticles. In another study, Franco et al. [73] showed that incorporating 1 wt% of nickel and palladium oxide onto fumed silica nanoparticles significantly enhanced the adsorption and subsequent oxidation of Colombian n-C_7 asphaltenes, because of the synergistic effect that could be achieved upon the incorporation of these metal oxides. Furthermore, the authors also found that these types of supported nanoparticles allow the formation of Type I adsorption isotherm, facilitating later processes of asphaltenes, such as catalytic thermal cracking and the inhibition of formation damage [25, 74].

4.2.1 Relationship Between Adsorption Affinity and Catalytic Activity of Nanoparticles

As discussed, the nanoparticles have demonstrated a strong affinity and catalytic activity toward asphaltene adsorption and oxidation. It is important to understand the relationship between adsorption affinity constant and the catalytic activity of nanoparticles. Such a correlation was investigated by Nassar et al. [37] by adsorbing and further oxidizing the C_7-asphaltenes over NiO and Fe_3O_4 nanoparticles. It was reported that NiO exhibits higher affinity constants than Fe_3O_4. The affinity constant is a measure of the interaction between adsorbate and adsorbent; the higher the value, the greater the strength of interaction. Accordingly, NiO presents the highest percent conversion at a provided temperature probably because of the strongest adsorbate–adsorbent interactions. On the other hand, Fe_3O_4, with the lowest adsorption affinity, shows the lowest catalytic activity. A comparison between adsorption affinity and catalytic activity of nanoparticles is presented in Fig. 4.3a and b which shows that the catalytic activity is directly related to affinity constant. Figure 4.3b shows the values of catalytic activity in terms of percent conversion at a given temperature and also in terms of onset temperature at a given percent conversion (30%). This led the authors to conclude that asphaltene adsorption and thermal decomposition are strongly affected by the type of metal oxide nanoparticles. Thus, a correlation between the adsorption affinity and the catalytic activity can be established; as the higher the affinity constant of the metal oxide, the better catalytic activity toward asphaltenes. It is worth noting that the affinity constant is a measure of the interaction between the asphaltenes and nanoparticles; the higher the value, the stronger the strength of interaction. Although the nanoparticles have comparable surface area and particle size, their catalytic activities are still different. This suggests that the surface area is not the only controlling parameter for the catalytic activity. It appears that the interactions between asphaltenes and nanoparticles are also of interest and play a role in catalytic activity. Similar observations have been reported in previous studies on the catalytic activity of the selected metal oxide nanoparticles toward asphaltene oxidation and gasification [25]. This correlation between the adsorption affinity constant and catalytic activity of nanoparticles was also supported in another study using aluminas at different surface acidities which proved that the adsorption affinity is affected by the basicity and acidity of nanoparticles [62]. For instance, Freundlich affinity factor (1/n), which is an indicator of adsorbate–adsorbent interaction correlates with the catalytic activity. The authors demonstrated that the catalytic activity increases as (1/n) value decreases. Therefore, alumina with basic surface has the lowest 1/n value, which depicts the strongest interactions, also has the lowest value of activation energy, consequently showing highest catalytic activity. The authors concluded that surface basicity of alumina affects the catalytic activity; the higher the surface basicity, the better the catalytic activity was.

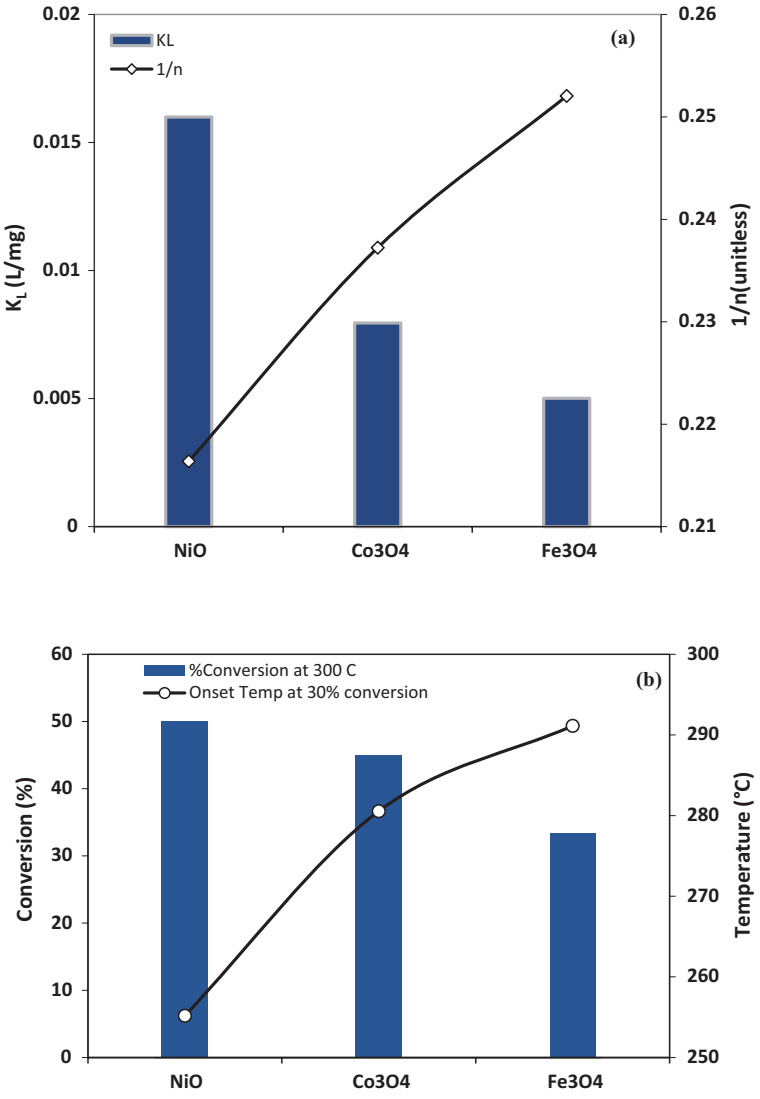

Fig. 4.3 The relationship between adsorption affinity and catalytic activity of nanoparticles, (**a**) Langmuir and Freundlich adsorption constants (K_L and 1/n) obtained in the previous study, (**b**) % conversion and oxidation of asphaltenes over nanoparticles [37]. (Permissions related to the material excerpted were obtained from Elsevier and further permission should be directed to Elsevier; Ref. [37])

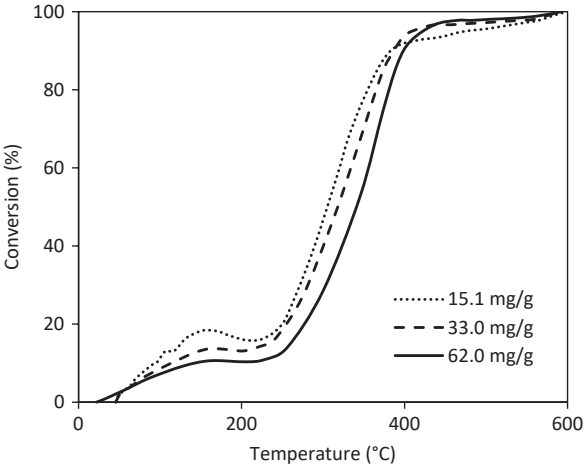

Fig. 4.4 Effect of the adsorbed amount of asphaltenes on the catalytic activity of Fe_3O_4 nanoparticles [37]. (Permissions related to the material excerpted were obtained from Elsevier and further permission should be directed to Elsevier; Ref. [37])

4.2.2 Effect of Asphaltene Loading on the Catalytic Activity of Nanoparticles

The dependence of asphaltenes loading on the catalytic activity of nanoparticles in terms of oxidation and conversion is experimentally verified by Nassar et al. [37]. These findings were demonstrated by oxidizing the adsorbed asphaltenes over metal oxide nanoparticles containing different adsorbed amount of asphaltenes. It is worth noting that increasing the initial concentration of asphaltenes will increase the adsorbed amount of asphaltenes onto nanoparticles. Figure 4.4 shows the catalytic activity of Fe_3O_4 for oxidation of different amount of adsorbed asphaltenes. It is clear that asphaltene oxidation is enhanced as the adsorbed amount of asphaltenes decreased. As the amount of nanoparticles is fixed, an increase in the adsorbed amount of asphaltenes results in the accumulation of asphaltene molecules onto the nanoparticle surfaces and reduces the active sites available for the reaction.

4.2.3 Effect of Asphaltenes Types on Oxidation

Typically, asphaltenes can be precipitated using one of two main solvents, namely, n-pentane and n-heptane [28, 61, 75–77]. Thus, the precipitated asphaltenes depend on the used solvent and present different characteristics of asphaltene in terms of molar mass, chemical composition, physical characteristics, and different yields [58, 75]. The adsorption and subsequent oxidation behavior might therefore be changed depending on the type of used precipitant. For instance, the maximum adsorption capacity of C_7-asphaltenes is slightly higher than that of C_5-asphaltenes over NiO nanoparticles [28]. Such findings can be explained by the polarity of structure due to the presence of heteroatoms which enhance the interactions. Thus,

it is useful to understand the catalytic effect of nanoparticles over different types of asphaltenes. Nassar et al. [35] evaluated the effect of four different molecular weights and sizes of visbroken asphaltenes on the adsorption and subsequent onto Fe_3O_4 nanoparticles. The adsorption results indicate that the molecular interaction between the p electrons of the aromatic ring with Fe is increased as the aromatic nature of asphaltenes increases. Also, the presence of heteroatoms like N atoms cannot be ruled out; higher N content in severely cracked asphaltenes would favor adsorption, especially if the N content offers both basic and non-basic nitrogen compounds which may interact differently with the nanoparticles. Additionally, the S content is playing a role in the adsorption performance; the lower the S the higher uptake of asphaltenes. Moreover, it was demonstrated that the oxidation of bulk asphaltenes depends on their properties; however, no systematic trends have been determined so far. It was also noticed that the oxidation temperature is different for the start and maximum percent conversion in the absence of nanoparticles. Nevertheless, in the presence of nanoparticles, the four types of asphaltenes showed identical conversion rates and oxidation temperatures. This confirms that the Fe_3O_4 nanoparticles have greatly enhanced the oxidation process, depicting the catalytic effect of the considered nanoparticles. For all asphaltenes, the oxidation process started at about 220 °C with nanoparticles, instead of about 380–400 °C in the absence of the nanoparticles. This decrease in temperature for oxidation reaction clearly shows the catalytic behavior of Fe_3O_4 nanoparticles toward asphaltenes oxidation. The estimated average activation energy of visbroken asphaltenes was approximately 82.5 kJ/mol, whereas in the presence of Fe_3O_4 nanoparticles, the average activation energy was 55.8 kJ/mol. From the above-mentioned results, it is evident that the presence of Fe_3O_4 nanoparticles caused a drop in the oxidation temperature and average activation energy, showing their catalytic effect. In addition, in the absence of nanoparticles, the four thermally cracked asphaltenes oxidized differently. However, when adsorbed onto Fe_3O_4 nanoparticles their oxidation behavior became similar, showing the enhanced catalytic effect of nanoparticles.

4.3 Estimation of the Activation Energy

The overall rate of solid-state reactions is generally described by Eq. 4.1 [87]:

$$\frac{d\alpha}{dt_\alpha} = k(T) f(\alpha) \tag{4.1}$$

where $d\alpha/dt\alpha$ is the reaction rate, α is the conversion degree, $k(T)$ is the rate constant, t is the time, T is the temperature, and $f(\alpha)$ is the reaction model. The dependence of the rate constant is usually described by the Arrhenius law:

$$k(T) = A\exp\left(-\frac{E}{RT}\right) \tag{4.2}$$

where E is the activation energy, A is the pre-exponential factor and R is the ideal gas constant. Using Eqs. 4.1 and 4.2, the following expression for the reaction rate is obtained.

$$\frac{d\alpha}{dt_\alpha} = A\exp\left(-\frac{E}{RT}\right) f(\alpha) \tag{4.3}$$

4.3.1 Estimation of Energy Activation at Isothermal Conditions

Separating the variables and the integrating Eq. 4.3 at isothermal conditions (constant temperature) yields Eq. 3.4 presented below [78].

$$g(\alpha) = \int_{\alpha}^{0} \frac{d\alpha}{f(\alpha)} = A\int_{t}^{0} \exp\left(-\frac{E}{RT}\right) dt = Aexp\left(-\frac{E}{RT}\right) t \tag{4.4}$$

where $g(\alpha)$ is the integral reaction model.

Taking the natural (Napierian) logarithm on both sides, Eq. 4.4 can also be written in linear form as follows:

$$\ln\left(g(\alpha)\right) = \ln(A) + \exp\left(-\frac{E}{RT}\right) + \ln(t) \tag{4.5}$$

Assuming E is constant, and after simple rearrangements Eq. 4.5 can be written as follows [78]:

$$\ln\left(t_{\alpha,i}\right) = \ln\left(\frac{g(\alpha)}{A}\right) + \frac{E}{RT_i} \tag{4.6}$$

where the subscript i is introduced to denote different isothermal temperature programs, $t\alpha_{,i}$ is the time for the reaction to reach a conversion α at different temperatures. Eq. 4.6 represents an integral method for isothermal reaction conditions. The values of E and the kinetic rate are determined from the slope and for the intercept of the plot $ln(t\alpha_{,i})$ against $1/T_i$, respectively. For more details see the work by Nassar et al. [38].

4.3.2 Estimation of Energy Activation at Non-Isothermal Conditions

For the non-isothermal heating rate, the following is defined:

$$\frac{d\alpha}{dT} = \frac{d\alpha}{dt} \times \frac{dt}{dT} \tag{4.7}$$

where $d\alpha/dT$ is the nonisothermal reaction rate, $d\alpha/dt$ is the isothermal reaction rate and dt/dT is the inverse of heating rate $1/\beta$. Substituting for Eq. 4.3:

$$\frac{d\alpha}{dT} = \frac{A}{\beta} \exp\left(-\frac{E}{RT}\right) f(\alpha) \tag{4.8}$$

Integrating Eq. 4.8:

$$g(\alpha) = \int_{\alpha}^{0} \frac{d\alpha}{f(\alpha)} = \frac{A}{\beta} \int_{T}^{0} \exp\left(-\frac{E}{RT}\right) dT \tag{4.9}$$

Equation 4.9 is known as the temperature integral and has no analytical solution [78]. Simplify an integration variable as follows:

$$x = -\frac{E}{RT} \tag{4.10}$$

Therefore, Eq. 4.9 becomes:

$$g(\alpha) = \int_{\alpha}^{0} \frac{d\alpha}{f(\alpha)} = \frac{AE}{\beta R} \int_{\infty}^{x} \frac{\exp(-x)}{x^2} dx \tag{4.11}$$

Calling $p(x) = \int_{\infty}^{x} \frac{\exp(-x)}{x^2} dx$, Eq. 4.11 can be written as follows:

$$g(\alpha) = \frac{AE}{\beta R} p(x) \tag{4.12}$$

A number of methods have been employed for E calculations based on different approximations used for $p(x)$, as will be shown below.

4.3.3 Estimation of Activation Energy Using OFW Method

In this method $p(x)$ could be approximated by series expansion. Effective activation energies were estimated using thermal analysis data and following the iso-conversional OFW method [79, 80] with the Doyle approximation [81, 82]. The OFW equation is expressed as follows:

$$\log(\beta) = \log\left(\frac{AE}{g(\alpha)R}\right) - 2.315 - 0.4567\frac{E}{RT} \tag{4.13}$$

where β is the heating rate, $\beta = dT/dt$, A (s^{-1}) is the pre-exponential factor, E (kJ/mol) is the effective activation energies, R (J/mol•K) is the ideal gas constant and T (K) is the reaction temperature, and α is the reaction conversion parameter that ranges between 0 and 1.0 and is expressed as:

$$\alpha = \frac{m_0 - m_t}{m_0 - m_f} \tag{4.14}$$

where m_0 is the initial sample mass, m_f is the final mass of the sample, and m_t is the sample mass at a given time. Hence, E is estimated from the slope of the best-fit line of the plot $\log(\beta)$ against $1/T$.

4.3.4 Estimation of Activation Energy Using KAS Method

In this method [83, 84], $p(x) \cong e^{-x}/x^2$, resulting in the following expression:

$$\ln\left(\frac{\beta_i}{T^2_{\alpha,i}}\right) = \ln\left(\frac{A_\alpha R}{E_\alpha}\right) + \ln\left(g(\alpha)\right) - \left(\frac{E_\alpha}{RT_{\alpha,i}}\right) \tag{4.15}$$

In this method, the activation energy ($E\alpha$) can be estimated from the plot of the left-hand side of Eq. 4.15 against $1/T\alpha_{,i}$ at a constant α for β_i.

4.3.5 Estimation of Activation Energy Using NLN Method

In the case of this advanced non-linear method developed by Vyazovkin and coworkers (NLN), it is based on a direct numerical integration of Eq. 4.9 [85]. According to this method, $p(x)$ in Eq. 4.12 is a function of $E\alpha$ and temperature. Therefore, Eq. 4.12 can be written as:

$$g(\alpha) = \frac{A_\alpha E_\alpha}{R} \sum_{N}^{j=1} J\left[E_\alpha, T_i(t_j)\right] \tag{4.16}$$

The main assumption of the NLN method is that the reaction model $g(\alpha)$ is independent of the heating rate β. For that reason, $J[E\alpha, T_i(t_j)]$ in Eq. 4.16 for any given conversion value α is the same for all experiments. Therefore, the evaluation of the activation energy in this case can be achieved at any value of α by finding $E\alpha$ that minimizes the following expression:

$$\Phi(E_\alpha) = \sum_{n}^{i=1} \sum_{n}^{j\neq i} \frac{J\left[E_\alpha, T_i(t_\alpha)\right]}{J\left[E_\alpha, T_j(t_\alpha)\right]} \tag{4.17}$$

where $J[E\alpha, T_i(t\alpha)]$ stands for the integral $\int_{t_\alpha}^{t_\alpha - \Delta\alpha} \exp\left(-\frac{E_\alpha}{RT_i(t)}\right)$. For more details see the work made by Nassar et al. [27].

Figure 4.5a and b shows isothermal kinetic curves for virgin asphaltenes and asphaltenes in the presence of nanoparticles of NiO. As seen in the figures, the kinetic curve shifts to the left as the temperature increases, indicating that the conversion rate increases with temperature. The estimated activation energies are presented in Table 4.2 [38]. Clearly, the presence of metal oxide nanoparticles with asphaltenes causes a dramatic shift in the reaction mechanism and a significant decrease in the activation energy of thermo-oxidative decomposition. Surprisingly, in the presence of nanoparticles, the values of activation energy followed the sequence NiO > Co_3O_4 > Fe_3O_4. This variation in activation energies can be attributed to differences in reaction mechanisms and limiting steps of the process [87]. Therefore, an estimate of the reaction kinetic rate is deemed necessary for comparison. In this case, the results showed that the activation energy of asphaltene thermos-oxidative decompositions decreased significantly in the presence of nanoparticles. Further, in the presence of nanoparticles the reaction kinetic rate was much faster. As seen, although NiO has the highest activation energy it still has the fastest reaction rate. This means that the thermo-oxidative decomposition reaction mechanism of asphaltene is also metal oxide-specific. Indeed the decomposition reaction rates followed the sequence NiO > Co_3O_4 > Fe_3O_4, which is in agreement with the order of adsorption affinity and catalytic activity at non-isothermal conditions reported in our previous studies [69, 78]. This again supports that the enhanced catalytic activity of metal oxide nanoparticles is not only a function of surface area or particle size but that the interaction between nanoparticle surface and asphaltene molecules are also of importance and can play major role in reaction mechanism [38].

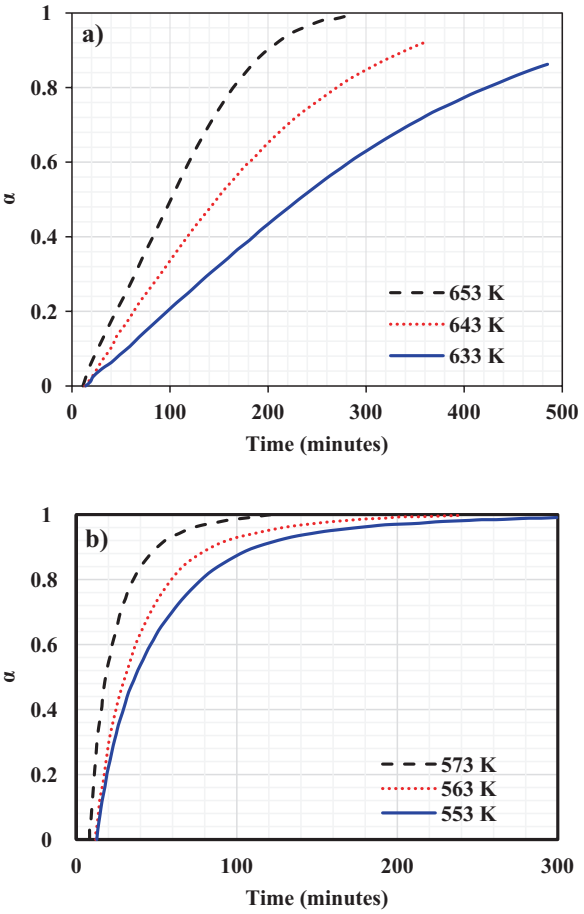

Fig. 4.5 Isothermal time plots for thermal oxidation of asphaltenes at different temperatures. (**a**) In the absence of nanoparticles. (**b**) In the presence of NiO nanoparticles [38]. (Permissions related to the material excerpted were obtained from Elsevier and further permission should be directed to Elsevier; Ref. [38])

Table 4.2 Estimated activation energy and kinetic rate for thermal oxidation of asphaltenes in the presence and absence of nanoparticles [38]

Material	Temperature (°K)	E_a (kJ)	dα/dt (min^{-1}) at 50% conversion
Virgin asphaltenes	633	153.34	0.005
	643		0.007
	653		0.011
Fe_3O_4-asphaltenes	553	76.11	0.015
	563		0.019
	573		0.026
Co_3O_4-asphaltenes	553	90.62	0.039
	563		0.056
	573		0.078
NiO-asphaltenes	553	108.58	0.040
	563		0.061
	573		0.091

Permissions related to the material excerpted were obtained from Elsevier and further permission should be directed to Elsevier; Ref. [38]

4.4 Pyrolysis of Asphaltenes

The *in situ* catalytic cracking of heavy oil is another attractive approach for heavy oil upgrading. As in the oxidation of heavy oil, it can also be upgraded by asphaltene adsorptive removal followed by catalytic thermal cracking or hydrogenation reaction. It is therefore important to understand the catalytic effect of nanoparticles on asphaltene cracking before the field and well test performance. Keep in mind that the thermal cracking of asphaltenes is challenging because of the temperature effect on asphaltenes produced from oil upgrading processes such as viscosity reduction and viscosity breaking [34]. Therefore, such application of an adsorbent and catalyst might be able to cope with a real feedstock of large molecules. In this case, nanoparticles may be employed as adsorbent/catalysts for separating asphaltenes followed by catalytic decomposition. As in visbreaking, similar to thermal cracking process, several variables control should be considered to the extent of cracking process. These conditions include temperature (455–510 °C), a residence time (2–6 min), and pressure (50–300 psi) at the heating coil outlet [14, 34]. Thus, such a process can be implemented by employing nanoparticles for the adsorption/catalytic stage after heating where asphaltenes are instable at this stage. This approach was thermally investigated under inert conditions for decomposition (pyrolysis) behavior of nanoparticles toward adsorbed asphaltene by Nassar et al., [30, 86]. After adsorbing asphaltene onto the surface of nanoparticles, the adsorbed asphaltenes was subjected to thermal decomposition using a thermogravimetric that monitored both mass and heat changes with increase in temperature. Using the nanoparticles will provide exceptional adsorptive and catalytic properties *in situ* adsorption and post-adsorption catalytic cracking of heavy hydrocarbons, such as asphaltenes, due to their small sizes, high surface area/volume ratios, and tunable chemical characteristics. This will provide additional insight into the challenges facing heavy oil recovery and upgrading as the nanoparticles can be used to sustain the heavy oil industry via the development of environmentally sound processes with cost-effective approaches. On this occasion, several studies were conducted to provide useful information about the catalytic effects of transition metal oxide and supported nanoparticles on asphaltene gasification. It was found that the presence of nanoparticles caused a significant decrease in the asphaltene decomposition temperature and activation energy. Table 4.3 shows the catalytic effect of adsorbed asphaltenes over different types of nanoparticles. The activation energies were calculated using the Ozawa–Flynn–Wall method. As shown, the high catalytic activity toward asphaltene decomposition followed the following order $NiO > Co_3O_4 > Fe_3O_4$, confirming that metal oxide nanoparticles can significantly enhance the thermal decomposition of asphaltenes reported by Nassar et al. [30]. In that study, the estimated activation energy followed the order $Fe_3O_4 > Co_3O_4 > NiO$, which again supports that NiO oxide has the highest catalytic activity toward asphaltene decomposition. It was stated that the thermal decomposition profile of virgin asphaltene could be fractionated into three steps: (1) low-temperature range (up to 350 °C) that is characterized by the breaking of intermolecular associations, which presents

Table 4.3 The catalytic effect of pyrolysis adsorbed asphaltenes over different types of nanoparticles

Type of nanoparticles	Types of Asphaltenes	Activation energy (kJ/mol)	The temperature at 40% conversion (°C)	Ref.
NiO	C_7-asphaltenes	134	336–357	[30]
Co_3O_4	C_7-asphaltenes	174	305–327	[30]
Fe_3O_4	C_7-asphaltenes	194	289–316	[30]
Silica (S)	n-C_7 asphaltenes	180	370–400	[86]
SNi2 (2 wt% NiO on S)	n-C_7 asphaltenes	135	350–370	[86]
SPd2 (2 wt% of PdO on S)	n-C_7 asphaltenes	117	230–250	[86]
SNi1Pd1*	n-C_7 asphaltenes	115	200–210	[86]

as the loss of alkyl chains, and weak chemical bonds such as sulfur bridges; (2) mid-temperature range (350–500 °C) which possibly depicting the rupture of longer alkyl groups and the opening of the polyaromatic ring; (3) high temperature range (beyond 500 °C), which shows further cracking resulting in coke formation. When it incorporated nanoparticles, on the other hand, the decomposition temperature significantly decreased; this lowering of pyrolysis temperature shows the catalytic activity of nanoparticles. The effect of the nanoparticles on post-adsorption catalytic thermal cracking of n-C_7 asphaltenes was investigated in another study using Ni-Pd nanocatalyst supported on fumed silica nanoparticles. It demonstrated that the catalytic thermal decomposition of n-C_7 asphaltenes in the presence of silica nanoparticles took place through two main steps. The first step takes place from 300 to 500 °C, which corresponds to the breaking of the alkyl side chains, while the second one occurs from 500 to 800 °C. The maximum peak of the rate of mass loss was shifted to the left by approximately 40 °C, in comparison with that of virgin n-C_7 asphaltenes, indicating that the reactions involved in this stage took place earlier than those for the virgin n-C_7 asphaltenes. For the functionalized nanoparticles, two peaks were observed for SNi2 and SPd2 below 660 °C [86]. It was found that SNi2 nanoparticles had a higher catalytic effect toward the *n*-C_7 asphaltene thermal cracking than the support, and at temperatures higher than 600 °C functionalized fumed silica nanoparticles with PdO lead to the suppression of coke formation. Nevertheless, the authors concluded that bimetallic nanoparticles (NiO and PdO) supported on silica nanoparticles showed the highest catalytic activity, this was attributed to the synergistic effects of NiO and PdO on the silica surface, which led to higher selectivity than the independent effects of the monometallic ones. Figure 4.6, panels a and b, shows a plot of the rate of mass loss for *n*-C_7 asphaltenes in the presence of Fumed silica and SNi1Pd1 nanoparticles. These findings were also supported by activation energy values, for the virgin n-C_7 asphaltenes, the activation energy ranged between 117 and 195 kJ/mol, while the activation energy ranged between 55 and 170 kJ/mol for SNi1Pd1. When the conversion percentage was less than 50%, the general trend for the effective activation energy was SNi1Pd1

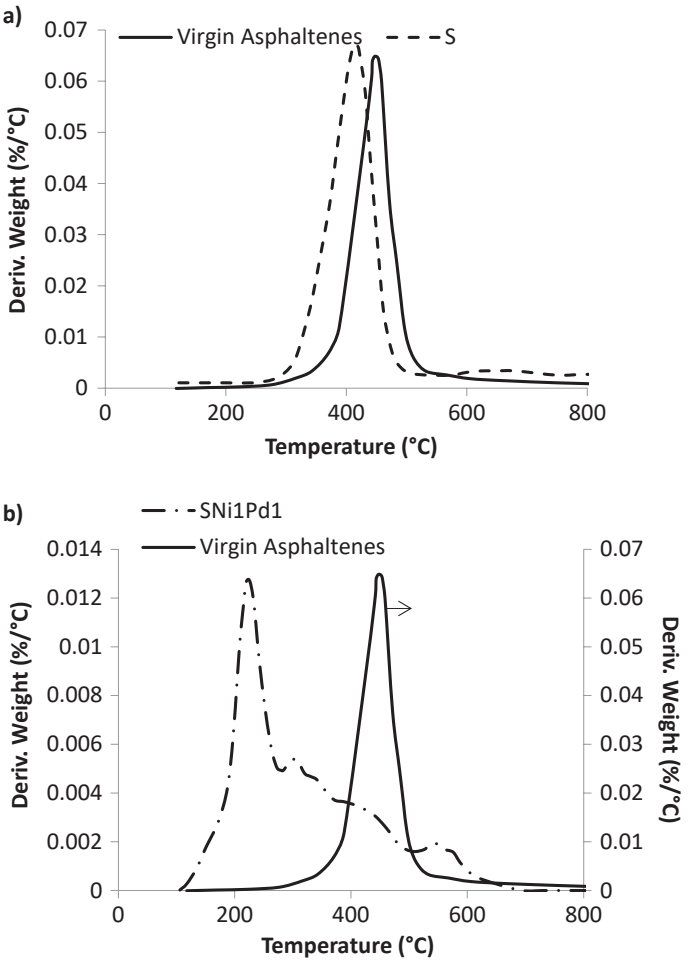

Fig. 4.6 Rate of mass loss of *n*-C_7 asphaltene via thermal cracking in the presence and absence of (**a**) of fumed silica nanoparticles and (**b**) bimetallic SHS. Amount adsorbed = 0.2 mg/m^2; argon flow = 100 cm^3/min, heating rate = 10 °C/min [86]. (Permissions related to the material excerpted were obtained from Springer Nature and further permission should be directed to Springer Nature; Ref. [86])

≈ SPd2 < SNi2 < S < virgin n-C_7 asphaltenes. However, for conversion percentages above 60%, the trend of activation energy was n-C_7 asphaltenes < SNi1Pd1 ≈ SPd2 < SNi2 ≈ S. Similar studies using Iranian C_7-asphaltenes were reported by Hosseinpour et al. [72] and Biyouki et al. [87], using metal oxide nanoparticles for adsorption and subsequent oxidation and pyrolysis. The authors found that the outcome gases in the process are particle-type dependent, confirming the catalytic role of the selected metal oxide nanoparticles.

4.5 Gasification of Asphaltenes

Over the last years, several technologies have emerged to improve the quality of heavy oil, including carbon rejection, hydroprocessing and gasification methods [3, 11, 88]. Carbon rejection processes include pyrolysis (e.g. visbreaking, coking and rapid thermal pyrolyzer), separation or extraction (e.g. solvent deasphalting process, SDA) and cracking (e.g. VGO and VR FCC) [6, 14–16]. Hydrocracking and steam cracking gasification, on the other hand, are typical processes of hydrogen addition [18, 19]. These conventional hydroprocessing technologies still suffer from coke formation, catalyst poisoning as a result of metal deposition, and produce lower yields [41]. Significant research has been carried out to develop techniques for hydrogen generation from heavy hydrocarbons. The most developed technologies for this purpose are reforming and gasification. Gasification seems to be a promising technology for upgrading heavy hydrocarbons. Gasification is a thermal process in which a carbonaceous feed is transformed into synthesis gas, which is primarily hydrogen, carbon monoxide, carbon dioxide, and steam which subsequently could be used to produce liquid hydrocarbons through the Fischer−Tropsch process [89]. The gasification reaction is a highly endothermic reaction performed under severe temperature, pressure, and C to O atomic ratio conditions [90]. Catalytic steam gasification, on the other hand, refers to a similar process occurring in the presence of a catalyst. As of today, the best-known gasification process for heavy residue fraction upgrading is the Flexicoking process developed by Exxon Mobil [24, 51]. Although it generates better quality liquid and forms less coke compared with the delay coking process, it suffers from several challenges including the need for good-quality feed to avoid coke formation, high catalyst loading, and the production of low-BTU waste gas.

In search of an economically viable upgrading process for bitumen or heavy oil, an alternative processing schematic representation of a benchtop plant that was built with the capacity of handling light as well as heavy hydrocarbon feeds is shown in Fig. 4.7. The plant consists of a 40 cm long and 1.9 (3.4″) cm diameter piton-type reactor and three reservoirs. The first reservoir had the feed (nC_5-asphaltenes +LCO), the second reservoir contained water, and the third contained toluene. All reservoirs were pressurized with N_2. The system utilized three pumps. For the toluene and water reservoirs, the pumps used were reciprocating pumps from ELDEX (model 1 L MP), while for the feed, the pump was an ISCO 500D screw-type pump. Two Swagelok back pressure regulators (0–500 psi) were employed to maintain the pressure during the two different modalities, adsorption and gasification experiments. A cold trap was installed (using a refrigerating and recirculating bath (LAUDA WK 300)) for the condensation of water and heavy hydrocarbon prior to the gas flow meter (model FMA-4000) and the on-line gas chromatography, was performed with an SRI 86106 analyzer. Omega K type thermocouples were used to keep track of process key temperatures, with a special configuration for the reactor, consisting of a custom 1/16″ (0.16 cm) profile probe with five reading points separated 5 cm. All readings were obtained with an OMEGA10 zone thermocouple

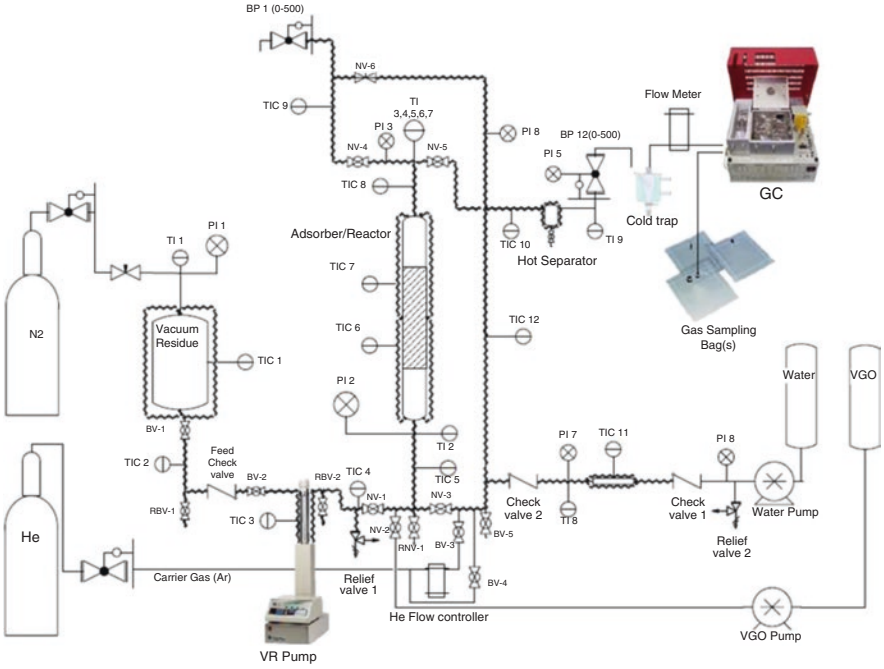

Fig. 4.7 Schematic representation of the adsorption/gasification plant [53]. (Permissions related to the material excerpted were obtained from Elsevier and further permission should be directed to Elsevier; Ref. [53])

scanner (model MDSSi8). The heating of the system was achieved using OMEGA heating tapes, along with K type wall thermocouples, all connected and controlled by two OMEGA PID (Proportional-Integral-Derivative) temperature controllers (model C6N16 TIC). The steam generation chamber consisted of a 1/4″ (0.64 cm) Swagelok tubing of approximately 30 cm length, filled with matching rings to improve the heat distribution, and heated with the elements previously mentioned. All connections were completed with Swagelok stainless steel tubing (1/4″& 1/8″). The ball valves and needle valves utilized were also Swagelok, as well as the different range of pressure gages all along with the system. The reactor was made of a stainless-steel tube, with an outer diameter (OD) of 3/4 in, the internal diameter (ID) of 0.62 in or ~ 1.57 cm and height of 27.67 cm for 30 g of catalyst. Additionally, 5 cm both on top and bottom were filled with an inert material (carborundum), to have a better distribution of flow, and heat only the middle section of the tube, in order to have a better temperature profile. For a better understanding of how the adsorption and gasification experiments were carried out, a brief description of the procedure is presented below. The procedure is divided into three main steps, (i) Adsorption; (ii) Cleaning; and (iii) Gasification as follows:

(i) Adsorption experiment: After filling the reactor with the catalyst (~30 g) in extrudate form, the feed was heated to 130 °C and pumped. The weight hourly

space velocity (WHSV) used for the adsorption process was 2 h^{-1}. The feed continued through the reactor column in the up-flow mode to adsorb asphaltenes from the feed onto the extrudate at a temperature of 250 °C. Oil samples were collected at fixed time intervals at the outlet of the liquid backpressure value. The zero time for asphaltenes breakthrough was considered the moment the first droplet of liquid from the reactor appeared.

(ii) Cleaning: When the adsorption process reached saturation (which was already known to be around two column volumes), the pumping of oil was stopped and the remaining heavy hydrocarbon in the porous medium was taken out of the system with the aid of vacuum gas oil (VGO) or toluene (depending upon the feed) and then steam to complete dissolving/cleaning whatever may be left inside the porous media.

(iii) Gasification: The catalytic steam gasification step started immediately after cleaning. Steam was generated and flushed through the reactor, exiting through the gas backpressure valve. The system temperature was increased gradually until it reached reaction temperatures of 530 °C and beyond. Steam gasification of the same adsorbed material was carried out at different temperatures. Liquid hydrocarbons and water were periodically drained from the cold trap separator. Gas analysis was performed every 30 min with an online GC when the system was at reaction temperature. The rate of liquid water injected during the gasification was 0.2 cm^3/min. Gas chromatography analyses were performed online using an SRI multiple gas analyzer model 8610#3, 120 V TCD & HID detectors, and an assemble of 3′ molecular sieve/6' Hayesep-D columns. The GC was previously calibrated with a hydrocarbon mixture gas and took 30 min for each analysis.

In that study, four types of metal kaolin based catalysts containing one alkali (K or Cs), one alkaline earth (Ca or Ba) metal oxides were tested using a stream consisting of n-C_5 asphaltenes dissolved in light cyclic oil (LCO) for catalytic steam gasification and compared [53]. The composition by wt% of the used catalysts are listed in Table 4.4. For 6K6Ca catalyst, it was reported that when the reaction temperature increased, the concentration of produced H_2 and CO decreased, and the CO_2 concentration increased. In addition, the abundance of H_2 would favor CH_4 producing reactions, and thus the ratio of H_2/CO_2 was decreased with an increase in the reaction temperature.

For a better understanding of the catalytic effect on the gasification of asphaltenes, Fig. 4.8 compares the gas composition at different temperatures for the four

Table 4.4 List of the catalyst composition in wt% employed in gasification of asphaltenes [53]

Catalyst	KOAc[a]	$Ca(OAc)_2$	$Ba(OAc)_2$	CsOAc	NiO	Sugar	Kaolin
6K6Ca	6	6	–	–	–	20	68
6K6Ba	6	–	6	–	–	20	68
3Ni6KBa	6	6	–	–	3	20	65
3Ni6Cs6Ba	–	–	6	6	3	20	65

[a]OAc = (CH_3COO)

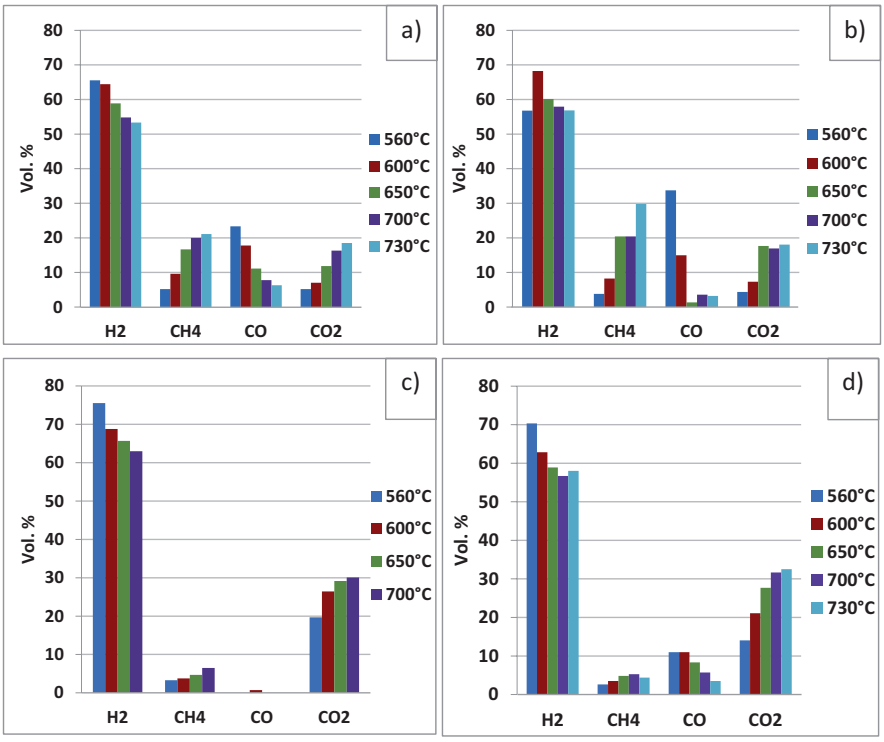

Fig. 4.8 Gas composition (vol%) at different temperatures comparison for the four catalysts (**a**) 6K6Ca (**b**) 6K6Ba (**c**) 3NiO6K6Ba (**d**) 3NiO6Cs6Ba [53]. (Permissions related to the material excerpted were obtained from Elsevier and further permission should be directed to Elsevier; Ref. [53])

catalysts. It can be observed that the H_2 and CO amounts are decreasing while CH_4 and CO_2 amounts are increasing corresponding with the increase in reaction temperature. As a comparison, in Fig. 4.8a and b, certain differences in CSG by 6K6Ca and 6K6Ba catalysts can be observed. The percentage of H_2 is slightly higher for the catalyst containing Ba, and the CO content decreases at a higher rate and reaches low values (<5%) at temperatures as low as 650 °C. For the 6K6Ba catalyst, the production of CH_4 and CO_2 appear to reach a plateau while it follows a trend for 6K6Ca catalysts; however, reaching similar values at higher temperatures. Comparing the catalytic steam gasification of 6K6Ba with 3NiO6K6Ba in Fig. 4.8b and c indicates that the addition of Ni seems to have significant effect. In addition to the reduction in CO percentage, the percentage of CH_4 also drops to roughly half of that obtained for 6K6Ba catalyst. Also, the content of H_2 is higher, with percentages higher than 60%. The authors demonstrated this to the spillover effect of H_2 by Ni. Moreover, the percentage of CO_2 is increased for the catalyst containing Ni. These behaviors seem to indicate more shift toward water–gas shift reaction, producing more H_2, CO_2, and less CO. Also, CH_4 producing reactions seem to have been

reduced, perhaps from the fact that less CO is available. By comparing 3NiO6K6Ba with 3NiO6Cs6Ba catalysts for CSG in Fig. 4.8c and d, it can be observed that there is less H_2 and higher CO percentages for the Cs containing catalyst. The authors noted that the CH_4 percentages decreased with the addition of Ni to the catalyst, an indication that methanation is reduced. A plausible explanation can be that less CO available for methanation is present in the gases. Also, catalyst 3NiO6Cs6Ba produces the highest amount of gases, followed by 6K6Ba, 3NiO6K6Ba and 6K6Ca.

In another study, the effect of oxide support types on the adsorption and subsequent steam gasification of adsorbed asphaltenes was explored over Ni–Pd bimetallic nanocatalysts supported on TiO_2 and ɣ-Al_2O_3 nanoparticles [51]. The functionalized nanoparticles were labeled by the initial letters of the support (Al or Ti) followed by the symbol of the cation of the resulting metal oxide after the calcination process and the weight percentage of the precursor hydroscopic salt used. Thus, nanoparticles of TiNiXPdY with 1 wt% of PdO and 1 wt% of NiO were denoted as TiNi1Pd. Figure 4.9 shows the estimated effective activation energies for the catalytic steam gasification of n-C_7 asphaltenes in the absence and presence of Ti, TiNi2, TiPd2 and TiNi1Pd1 nanoparticles as a function of the degree of conversion. E_α for virgin n-C_7 asphaltenes decreases with the degree of conversion [25], indicating that n-C_7 asphaltene gasification is not a single "homogeneous" step and actually involves more than one mechanism [25, 31]. Conversely, the trend of E_α for asphaltene gasification in the presence of nanoparticles is opposite of that of virgin n-C_7 asphaltenes, showing markedly lower effective activation energy compared

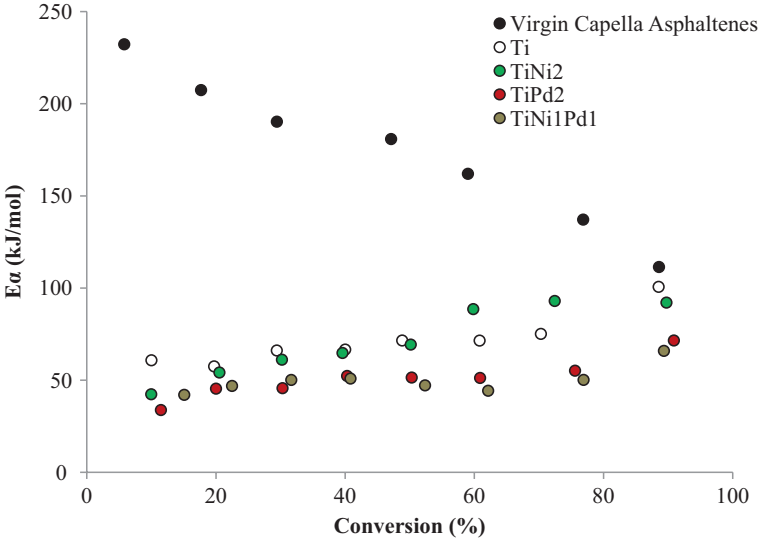

Fig. 4.9 Effective activation energies estimated by the OFW method for steam catalytic gasification of n-C_7 asphaltenes in the absence and presence of Ti, TiNi2, TiPd2 and TiNi1Pd1 nanoparticles [51]. (Permissions related to the material excerpted were obtained from Elsevier and further permission should be directed to Elsevier; Ref. [51])

with that of virgin n-C_7 asphaltene gasification. Thus, the trend of effective activation energy is affected by the nanoparticles present due to the occurrence of different reaction mechanisms. TiNi1Pd1 displayed the lowest activation energy throughout the process, suggesting that TiNi1Pd1 is more catalytically active toward n-C_7 asphaltene steam gasification, therefore confirming their synergistic effect. This synergistic effect could be explained by the combination of individual selectivities and the hybrid structures of Pd and Ni that lead to better surface electronegativity and hence more efficient catalytic activity [26, 91]. Similar observations were seen for the effective activation energy trends with Al support and the functionalized nanoparticles [51].

4.6 Conclusion and Future Remarks

This chapter provides important insights into the use of nanoparticle technology to adsorb and subsequent oxidation/decomposition of asphaltenes in oil processing as an alternative technology for recoverying and upgrading of heavy oil, thus minimizing the environmental footprint. It also gives insight into the influence of the adsorption process on the catalytic activity of the nanoparticles and provides a better understanding of the use of nanotechnology for *in situ* upgrading of heavy and extra-heavy oils. This chapter also supports the use of nanoparticles for heavy oil upgrading and processing as they are cost-effective approach since they can be prepared *in situ*. As a result, they have the potential to be developed into a future technology that may have a huge effect on the industrial and environmental impact. Below are the most important findings and points for using nanoparticles technology for oil recovery and upgrading:

- The unique properties of nanoparticles have considerable potential applications as an adsorbent and subsequent oxidation/ decomposition for enhancing heavy oil upgrading and recovery.
- The catalytic effect of nanoparticles was evaluated by employing the adsorptive removal of asphaltenes from heavy oil model solution followed by asphaltene oxidation. The nanoparticles showed high catalytic activity for asphaltenes oxidation.
- The metal oxide nanoparticles, such as TiO_2, ZrO_2, and CeO_2, were applied for the adsorption and subsequent catalytic oxidation of Athabascan C_7-asphaltenes. High catalytic activity for asphaltenes oxidation was observed. The kinetic study of the thermo-oxidative decomposition of asphaltenes in the presence and absence of nanoparticles was carried out using the Ozawa–Flyn–Wall (OFW).
- The kinetics study of the thermo-oxidative decomposition of asphaltenes in the presence and absence of different metal oxide nanoparticles was investigated at isothermal conditions. The kinetic results showed that an enhanced thermo-oxidative decomposition of asphaltenes associated with a change in reaction

mechanism and decrease of activation energy was obtained in the presence of nanoparticles.

- A set of metal oxide nanoparticles showed a high oxidation rate and low activation energy for asphaltenes oxidation in the following order $NiO > Co_3O_4 > Fe_3O_4$. Differences in activation energy for different nanoparticles suggest different reaction mechanisms.
- Functionalizing the silica nanoparticles has lowered the asphaltene oxidation temperature as well as the activation energy. The estimated activation energies of asphaltene oxidation in the presence and absence of nanoparticles by the OFW method confirmed that different nanoparticles utilized different reaction mechanisms.
- A correlation between the affinity constant and the catalytic activity has been revealed, the higher the affinity constant the greater the catalytic activity. Thus, the catalytic activity of nanoparticles might decrease as the adsorbed amount of asphaltenes onto nanoparticles increase.
- It was reported that adsorption capacity is also proportional to surface acidity. Acidic alumina, for example, has a higher adsorption affinity than the basic one. Conversely, the basic alumina has the highest catalytic activity toward asphaltene oxidation. A correlation between Freundlich affinity constant and the catalytic activity was established. Decrease 1/n values, favors the catalytic activity of the adsorbent.
- The effect of particle sizes on adsorption and oxidation of asphaltenes were investigated under similar surface acidity. The micro-alumina showed higher catalytic activity toward asphaltene oxidation than nano-alumina. This enhanced catalytic effect demonstrated by micro-alumina shows that textural properties play an important role in catalysis.
- It was found that nanoparticles portray different reaction mechanisms in the catalytic oxidation of asphaltenes and that the pathway followed is specific to the type of nanoparticle.
- It was observed that the temperature of asphaltene oxidation decreased in the order Heptol 40 > Heptol 20 > toluene, indicating that for larger aggregates, the catalytic activity of nanoparticles is reduced.
- The effect of nanoparticles on different types of visbroken asphaltenes obtained from thermally cracked vacuum residue was evaluated for adsorption and oxidation. Regardless of the types of asphaltenes, the presence of Fe_3O_4 nanoparticles caused a significant decrease in the oxidation temperature and average activation energy, depicting high catalytic activity.
- The effects of nanoparticle technology on the thermal cracking of n-C_7 asphaltenes were also investigated by performing a catalytic thermal cracking process using a TGA/FTIR system. The NiO and PdO supported on fumed silica nanoparticles were employed. The results showed that PdO supported on silica nanoparticles has better catalytic activity than NiO supported on silica nanoparticles. The mechanism function, kinetic parameters, and transition state thermodynamic functions for the thermal cracking of n-C_7 asphaltenes were nanoparticle dependent.

- The bimetallic nanoparticles (NiO and PdO) supported on silica nanoparticles showed the highest catalytic activity.
- The possibility of low-temperature catalytic steam gasification of adsorbed asphaltenes in a fixed bed reactor unit was also evaluated.
- The effect of incorporating alkali, alkaline earth and transition metal on catalytic activity for steam gasification was investigated. Incorporation of NiO nanoparticles promoted further H_2 production during the steam gasification of the adsorbed asphaltenes, leading to CO_2 and H_2 as major products with less side reactions.

To this end, as for any new technologies, there are a number of challenges facing the employment of nanoparticles for catalytic upgrading and recovery enhancement. The main goal of this chapter is to provide an overview of nanoparticle technology usage for enhancing the catalytic upgrading and recovery processes of crude oil. Furthermore, the chapter sheds light on the advantages of the employment of nanoparticles in heavy oil industry and addresses some of the limitations and challenges facing this new technology. The synthesis of nanoparticles could be performed via various techniques; however, the mass production of required nanoparticles and availability of surface facilities, the stability of produced volume, and control over the size of the particles are some of the important issues that should be addressed in any industrial applications. In addition, cost is very important parameter in any project since it is essential to acquire hi-tech control systems to avoid or mitigate any associated risks due to the nature of high pressure and temperature reaction conditions. The presence of nanoparticles inside the porous media and providing appropriate reaction conditions with required elements including hydrogen would result in recovery improvement as well as considerable quality enhancement in all three phases of liquid, gas, and solid. The enhancement of viscosity, API gravity, carbon residue content, sulfur, and nitrogen content in liquid phase was significant. Higher quality of produced gases in terms of hydrocarbon gases as well as less carbon dioxide emission in the gas phase and less amount of coke content in solid phase show a very promising future for the nanoparticles *in situ* implementation.

Also, environmental challenges should be considered in enough depth to mitigate any associated risks regarding the mass use of nanoparticles. In this regard, recovery and reusing the nanoparticles could be very beneficial in terms of process economics as well as the reduction of environmental footprints, which can be improved giving magnetic properties to the nanomaterials. Naturally occurring inorganic materials also hold promise to decrease the asphaltene content of the oil and reduce the coke-forming tendency (during petroleum refining operations) of the oil, resulting in the partial upgrading of the oil. This may occur subsurface (*in situ* upgrading) or on the surface. However, a lot of in-depth studies are still needed to optimize the adsorption process and lead to commercialization.

References

1. N. Berkowitz, J.G. Speight, The oil sands of Alberta. Fuel **54**(3), 138–149 (1975)
2. A. Shah et al., A review of novel techniques for heavy oil and bitumen extraction and upgrading. Energy Environ. Sci. **3**(6), 700–714 (2010)
3. L.C. Castaneda, J.A. Muñoz, J. Ancheyta, Current situation of emerging technologies for upgrading of heavy oils. Catal. Today **220**, 248–273 (2014)
4. C. Fan et al., The oxidation of heavy oil: Thermogravimetric analysis and non-isothermal kinetics using the distributed activation energy model. Fuel Process. Technol. **119**, 146–150 (2014)
5. A. Hassan et al., Development of a support for a NiO catalyst for selective adsorption and post-adsorption catalytic steam gasification of thermally converted asphaltenes. Catal. Today **207**, 112–118 (2013)
6. L. Carbognani et al., Selective adsorption of thermal cracked heavy molecules. Energy Fuel **22**(3), 1739–1746 (2008)
7. H. Groenzin, O.C. Mullins, J. Phys. Chem. A **103**, 11237 (1999)
8. S. Chavan, H. Kini, R. Ghosal*, Process for sulfur reduction from high viscosity petroleum oils*
9. C. Wu et al., Mechanism for reducing the viscosity of extra-heavy oil by aquathermolysis with an amphiphilic catalyst. J. Fuel Chem. Technol. **38**(6), 684–690 (2010)
10. J. Ancheyta, *Modeling and Simulation of Catalytic Reactors for Petroleum Refining* (Wiley, 2011)
11. Y. Zhang et al., Fundamentals of petroleum residue cracking gasification for coproduction of oil and syngas. Ind. Eng. Chem. Res. **51**(46), 15032–15040 (2012)
12. L. Castañeda, J. Muñoz, J. Ancheyta, Combined process schemes for upgrading of heavy petroleum. Fuel **100**, 110–127 (2012)
13. L. Atkins, T. Higgins, C. Barnes, *Heavy crude oil: global analysis and outlook to 2030.* Hart energy consulting report, 2010
14. O. Omole, M. Olieh, T. Osinowo, Thermal visbreaking of heavy oil from the Nigerian tar sand. Fuel **78**(12), 1489–1496 (1999)
15. M. Thomas et al., Visbreaking of Safaniya vacuum residue in the presence of additives. Fuel **68**(3), 318–322 (1989)
16. F. Rodriguez-Reinoso et al., Delayed coking: Industrial and laboratory aspects. Carbon **36**(1), 105–116 (1998)
17. E. Furimsky, Characterization of cokes from fluid/flexi-coking of heavy feeds. Fuel Process. Technol. **67**(3), 205–230 (2000)
18. M. Marafi, A. Stanislaus, M. Absi-Halabi, Heavy oil hydrotreating catalyst rejuvenation by leaching of foulant metals with ferric nitrate-organic acid mixed reagents. Appl. Catal. B Environ. **4**(1), 19–27 (1994)
19. M. Marafi, A. Stanislaus, Preparation of heavy oil hydrotreating catalyst from spent residue hydroprocessing catalysts. Catal. Today **130**(2), 421–428 (2008)
20. J. Van Dyk, M. Keyser, M. Coertzen, Syngas production from south African coal sources using Sasol–Lurgi gasifiers. Int. J. Coal Geol. **65**(3), 243–253 (2006)
21. H. Liu et al., Effect of pyrolysis time on the gasification reactivity of char with CO_2 at elevated temperatures. Fuel **83**(7), 1055–1061 (2004)
22. R. Hashemi, N.N. Nassar, P. Pereira Almao, Nanoparticle technology for heavy oil in-situ upgrading and recovery enhancement: Opportunities and challenges. Appl. Energy **133**, 374–387 (2014)
23. E. Mobil, *FLEXICOKING™ conversion technology*. [cited 2014]
24. C.E. Baukal Jr., *The John Zink Hamworthy Combustion Handbook: Volume 1-Fundamentals* (CRC Press, 2012)
25. C.A. Franco, N.N. Nassar, T. Montoya, F.B. Cortés, NiO and PdO supported on fumed silica nanoparticles for adsorption and catalytic steam gasification of Colombian c7-asphaltenes, in *Handbook on Oil Production Research*, ed. by J. Ambrosio, (Nova Science Publishers, Inc, Hauppauge, 2014)

26. C.A. Franco et al., Adsorption and subsequent oxidation of Colombian Asphaltenes onto nickel and/or palladium oxide supported on Fumed silica nanoparticles. Energy Fuel **27**(12), 7336–7347 (2013)
27. N.N. Nassar et al., Comparative study on thermal cracking of Athabasca bitumen. J. Therm. Anal. Calorim. **114**(2), 465–472 (2013)
28. N.N. Nassar, A. Hassan, P. Pereira-Almao, Metal oxide nanoparticles for asphaltene adsorption and oxidation. Energy Fuel **25**(3), 1017–1023 (2011)
29. N.N. Nassar, A. Hassan, P. Pereira-Almao, Application of nanotechnology for heavy oil upgrading: Catalytic steam gasification/cracking of asphaltenes. Energy Fuel **25**(4), 1566–1570 (2011)
30. N.N. Nassar, A. Hassan, P. Pereira-Almao, Thermogravimetric studies on catalytic effect of metal oxide nanoparticles on asphaltene pyrolysis under inert conditions. J. Therm. Anal. Calorim. **110**(3), 1327–1332 (2012)
31. N.N. Nassar, A. Hassan, G. Vitale, Comparing kinetics and mechanism of adsorption and thermo-oxidative decomposition of Athabasca asphaltenes onto TiO_2, ZrO_2, and CeO_2 nanoparticles. Appl. Catal. A Gen. **484**, 161–171 (2014)
32. F.B. Cortés et al., Sorption of Asphaltenes onto nanoparticles of nickel oxide supported on Nanoparticulated silica gel. Energy Fuel **26**(3), 1725–1730 (2012)
33. C. Franco et al., Kinetic and thermodynamic equilibrium of asphaltenes sorption onto nanoparticles of nickel oxide supported on nanoparticulated alumina. Fuel **105**(0), 408–414 (2013)
34. N.N. Nassar, A. Hassan, P. Pereira-Almao, Clarifying the catalytic role of NiO nanoparticles in the oxidation of asphaltenes. Appl. Catal. A Gen. **462**, 116–120 (2013)
35. N.N. Nassar et al., Iron oxide nanoparticles for rapid adsorption and enhanced catalytic oxidation of thermally cracked asphaltenes. Fuel **95**, 257–262 (2012)
36. N.N. Nassar, Asphaltene adsorption onto alumina nanoparticles: Kinetics and thermodynamic studies. Energy Fuel **24**(8), 4116–4122 (2010)
37. N.N. Nassar, A. Hassan, P. Pereira-Almao, Comparative oxidation of adsorbed asphaltenes onto transition metal oxide nanoparticles. Colloids Surf. A Physicochem. Eng. Asp. **384**(1), 145–149 (2011)
38. N.N. Nassar et al., Kinetics of the catalytic thermo-oxidation of asphaltenes at isothermal conditions on different metal oxide nanoparticle surfaces. Catal. Today **207**, 127–132 (2013)
39. H. Abbas et al., Adsorption of Algerian Asphaltenes onto synthesized Maghemite Iron oxide nanoparticles. Pet. Chem., 1–9 (2020)
40. P.S. Wallace, et al., *Heavy oil upgrading by the separation and gasification of asphaltenes*. In *1998 Gasification technologies conference*. 1998
41. A.D. Manasrah, G. Vitale, N.N. Nassar, Catalytic oxy-cracking of petroleum coke on copper silicate for production of humic acids. Appl. Catal. B Environ. **264**, 118472 (2020)
42. J.J. Adams, Asphaltene adsorption, a literature review. Energy Fuel **28**(5), 2831–2856 (2014)
43. E. Alizadeh-Gheshlaghi et al., Investigation of the catalytic activity of nano-sized CuO, Co3O4 and CuCo2O4 powders on thermal decomposition of ammonium perchlorate. Powder Technol. **217**, 330–339 (2012)
44. X. Luo et al., Application of nanoparticles in electrochemical sensors and biosensors. Electroanalysis: An International Journal Devoted to Fundamental and Practical Aspects of Electroanalysis **18**(4), 319–326 (2006)
45. M.K.K. Oo et al., Rapid, sensitive DNT vapor detection with UV-assisted photo-chemically synthesized gold nanoparticle SERS substrates. Analyst **136**(13), 2811–2817 (2011)
46. M. Khoobi et al., Polyethyleneimine-modified superparamagnetic Fe3O4 nanoparticles: An efficient, reusable and water tolerance nanocatalyst. J. Magn. Magn. Mater. **375**, 217–226 (2015)
47. R. Hashemi, N.N. Nassar, P. Pereira-Almao, Transport behavior of multimetallic ultradispersed nanoparticles in an oil-sands-packed bed column at a high temperature and pressure. Energy Fuel **26**(3), 1645–1655 (2012)

48. A.D. Manasrah et al., Surface modification of carbon nanotubes with copper oxide nanoparticles for heat transfer enhancement of nanofluids. RSC Adv. **8**(4), 1791–1802 (2018)
49. W.-X. Zhang, Nanoscale iron particles for environmental remediation: An overview. J. Nanopart. Res. **5**(3–4), 323–332 (2003)
50. M.E. Franke, T.J. Koplin, U. Simon, Metal and metal oxide nanoparticles in chemiresistors: Does the nanoscale matter? Small **2**(1), 36–50 (2006)
51. N.N. Nassar et al., Effect of oxide support on Ni–Pd bimetallic nanocatalysts for steam gasification of nC 7 asphaltenes. Fuel **156**, 110–120 (2015)
52. N.N. Nassar, A. Hassan, G. Vitale, Comparing kinetics and mechanism of adsorption and thermo-oxidative decomposition of Athabasca asphaltenes onto TiO2, ZrO2, and CeO2 nanoparticles. Appl. Catal. A Gen. **484**, 161–171 (2014)
53. A. Hassan et al., Catalytic steam gasification of n-C5 asphaltenes by kaolin-based catalysts in a fixed-bed reactor. Appl. Catal. A Gen. **507**, 149–161 (2015)
54. R. Syunyaev et al., Adsorption of petroleum asphaltenes onto reservoir rock sands studied by near-infrared (NIR) spectroscopy. Energy Fuel **23**(3), 1230–1236 (2009)
55. S. Acevedo et al., Adsorption of asphaltenes at the toluene− silica interface: A kinetic study. Energy Fuel **17**(2), 257–261 (2003)
56. A. Hassan et al., Catalytic steam gasification of athabasca visbroken residue by NiO–kaolin-based catalysts in a fixed-bed reactor. Energy Fuel **31**(7), 7396–7404 (2017)
57. M. Castro et al., Predicting adsorption isotherms of asphaltenes in porous materials. Fluid Phase Equilib. **286**(2), 113–119 (2009)
58. O.P. Strausz, P.A. Peng, J. Murgich, About the colloidal nature of asphaltenes and the MW of covalent monomeric units. Energy Fuel **16**(4), 809–822 (2002)
59. C. Drummond, J. Israelachvili, Fundamental studies of crude oil–surface water interactions and its relationship to reservoir wettability. J. Pet. Sci. Eng. **45**(1–2), 61–81 (2004)
60. H. Alboudwarej et al., Adsorption of asphaltenes on metals. Ind. Eng. Chem. Res. **44**(15), 5585–5592 (2005)
61. D.M. Sztukowski et al., Asphaltene self-association and water-in-hydrocarbon emulsions. J. Colloid Interface Sci. **265**(1), 179–186 (2003)
62. M.S. Akhlaq et al., Adsorption of crude oil colloids on glass plates: Measurements of contact angles and the factors influencing glass surface properties. Colloids Surf. A Physicochem. Eng. Asp. **126**(1), 25–32 (1997)
63. K.R. Dean, J.L. McATEE Jr., Asphaltene adsorption on clay. Appl. Clay Sci. **1**(4), 313–319 (1986)
64. N.N. Nassar, A. Hassan, P. Pereira-Almao, Effect of surface acidity and basicity of aluminas on asphaltene adsorption and oxidation. J. Colloid Interface Sci. **360**(1), 233–238 (2011)
65. N.N. Nassar, A. Hassan, P. Pereira-Almao, Effect of the particle size on asphaltene adsorption and catalytic oxidation onto alumina particles. Energy Fuel **25**(9), 3961–3965 (2011)
66. C.A. Franco et al., Adsorption and subsequent oxidation of colombian asphaltenes onto nickel and/or palladium oxide supported on fumed silica nanoparticles. Energy Fuel **27**(12), 7336–7347 (2013)
67. F. Lopez-Linares et al., Adsorption of Athabasca vacuum residues and their visbroken products over macroporous solids: Influence of their molecular characteristics. Energy Fuel **25**(9), 4049–4054 (2011)
68. T. Montoya, et al., *Size effects of NiO nanoparticles on the competitive adsorption of quinolin-65 and violanthrone-79: Implications for oil upgrading and recovery.* ACS Applied Nano Materials, 2020
69. C.A. Franco et al., Influence of Asphaltene aggregation on the adsorption and catalytic behavior of nanoparticles. Energy Fuel **29**(3), 1610–1621 (2015)
70. P. Mars, D.W. Van Krevelen, Oxidations carried out by means of vanadium oxide catalysts. Chem. Eng. Sci. **3**, 41–59 (1954)
71. N. Hosseinpour et al., Asphaltene adsorption onto acidic/basic metal oxide nanoparticles toward in situ upgrading of reservoir oils by nanotechnology. Langmuir **29**(46), 14135–14146 (2013)

72. N. Hosseinpour et al., Enhanced pyrolysis and oxidation of asphaltenes adsorbed onto transition metal oxides nanoparticles towards advanced in-situ combustion EOR processes by nanotechnology. Appl. Catal. A Gen. **477**, 159–171 (2014)
73. C.A. Franco, F.B. Cortés, N.N. Nassar, Adsorptive removal of oil spill from oil-in-fresh water emulsions by hydrophobic alumina nanoparticles functionalized with petroleum vacuum residue. J. Colloid Interface Sci. **425**, 168–177 (2014)
74. C.A. Franco et al., Nanoparticles for inhibition of asphaltenes damage: Adsorption study and displacement test on porous media. Energy Fuel **27**(6), 2899–2907 (2013)
75. B. Marlow et al., Colloidal stabilization of clays by asphaltenes in hydrocarbon media. Colloids Surf. **24**(4), 283–297 (1987)
76. S.F. Alkafeef, M.K. Algharaib, A.F. Alajmi, Hydrodynamic thickness of petroleum oil adsorbed layers in the pores of reservoir rocks. J. Colloid Interface Sci. **298**(1), 13–19 (2006)
77. P. Ekholm et al., A quartz crystal microbalance study of the adsorption of asphaltenes and resins onto a hydrophilic surface. J. Colloid Interface Sci. **247**(2), 342–350 (2002)
78. A.W. Coats, J. Redfern, Kinetic parameters from thermogravimetric data. Nature **201**(4914), 68–69 (1964)
79. T. Ozawa, A new method of analyzing thermogravimetric data. Bull. Chem. Soc. Jpn. **38**(11), 1881–1886 (1965)
80. J.H. Flynn, L.A. Wall, A quick, direct method for the determination of activation energy from thermogravimetric data. Journal of Polymer Science Part B: Polymer Letters **4**(5), 323–328 (1966)
81. C.D. Doyle, Kinetic analysis of thermogravimetric data. J. Appl. Polym. Sci. **5**(15), 285–292 (1961)
82. C.D. Doyle, Series approximations to the equation of thermogravimetric data. Nature **207**(4994), 290–291 (1965)
83. H.E. Kissinger, Reaction kinetics in differential thermal analysis. Anal. Chem. **29**(11), 1702–1706 (1957)
84. T. Akahira, T. Sunose, Method of determining activation deterioration constant of electrical insulating materials. Res Rep Chiba Inst Technol (Sci Technol) **16**(1971), 22–31 (1971)
85. S. Vyazovkin, Modification of the integral isoconversional method to account for variation in the activation energy. J. Comput. Chem. **22**(2), 178–183 (2001)
86. T. Montoya et al., Kinetics and mechanisms of the catalytic thermal cracking of asphaltenes adsorbed on supported nanoparticles. Pet. Sci. **13**(3), 561–571 (2016)
87. A. Amrollahi Biyouki, N. Hosseinpour, N.N. Nassar, Pyrolysis and oxidation of Asphaltene-born coke-like residue formed onto in situ prepared NiO nanoparticles toward advanced in situ combustion enhanced oil recovery processes. Energy Fuel **32**(4), 5033–5044 (2018)
88. Manasrah, A.D., Conversion of Petroleum Coke into Valuable Products Using Catalytic and Non-Catalytic Oxy-Cracking Reaction. 2018
89. C. Sosa, *Adsorption of heavy hydrocarbons for the purpose of hydrogen production*. 2007, MSc Thesis, University of Calgary, Calgary, AB, Canada
90. R.J. Lang, R.C. Neavel, Behaviour of calcium as a steam gasification catalyst. Fuel **61**(7), 620–626 (1982)
91. Y. Wu et al., Monodispersed Pd− Ni nanoparticles: Composition control synthesis and catalytic properties in the Miyaura− Suzuki reaction. Inorg. Chem. **50**(6), 2046–2048 (2011)

Chapter 5
Effect of Pressure on Thermo-oxidation and Thermocatalytic Oxidation of *n*-C_7 Asphaltenes

Oscar E. Medina, Jaime Gallego, Farid B. Cortés, and Camilo A. Franco

5.1 Introduction

A mechanistic and kinetic/thermodynamic understanding of asphaltene oxidation is crucial for determining the thermal reaction pathway of heavy (HO) and extra-heavy (EHO) crude oils in thermal enhanced oil recovery (TEOR) applications [1]. These methods use the heat exchange for reducing oil viscosity and therefore improve their mobility inside the reservoir. Technologies that involve the injection of oxidizing agents such as air and oxygen are widely used worldwide, known as combustion process [2, 3]. Furthermore, these fluids are less expensive and require less economic investment than the injection of other fluids such as steam and non-condensable gases [4, 5]. Despite these advantages, some limitations are associated with the combustion front and coke formation in the reservoir due to the high temperatures in these technologies [6]. Asphaltenes are the primary sources of coke [7]. Their composition of aliphatic chains surrounding aromatic rings makes them atypical structures, that once they lose the structures around them, they become more refractory, more condensable, and more massive [8]. Asphaltenes' thermal behavior is of great interest due to their coking tendency and catalyst deactivation during the injection of hot gases, mainly air or oxygen-rich fluids [9, 10]. Because of these

O. E. Medina · F. B. Cortés (✉) · C. A. Franco (✉)
Grupo de Investigación en Fenómenos de Superficie–Michael Polanyi, Departamento de Química y Petróleos, Facultad de Minas, Universidad Nacional de Colombia Sede Medellín, Medellín, Colombia
e-mail: oemedinae@unal.edu.co; fbcortes@unal.edu.co; caafrancoar@unal.edu.co

J. Gallego
Química de Recursos Energéticos y Medio Ambiente, Instituto de Química, Universidad de Antioquia UdeA, Medellín, Colombia
e-mail: andres.gallego@udea.edu.co

N. N. Nassar et al. (eds.), *Nanoparticles: An Emerging Technology for Oil Production and Processing Applications*, Lecture Notes in Nanoscale Science and Technology, https://doi.org/10.1007/978-3-319-12051-5_5

molecules' complexity, nanotechnology has been employed by several authors to improve the kinetic oxidation rate and reduce the energy required for the thermal asphaltene decomposition [11–13]. By evaluating different chemical natures of nanoparticles, it has been identified that its phase complexity is imperative for selective oxidation of asphaltenes [14–16]. Besides, the compensation effect can help understand the chemical reaction pathway during this process.

Nevertheless, there are no studies in the specialized literature that report the effect of pressure and compensation effect of asphaltene thermo-oxidation and thermocatalytic oxidation. In this sense, this research opens a new landscape on the oxidative behavior of the heaviest fractions of crude oil under the reservoir and in situ combustion conditions, providing the first insights in this area.

This chapter summarizes the main results obtained after robust research on the effect of pressure on nanotechnology-assisted oxidative phenomena. The topics include (*i*) advantages and disadvantages of the main thermal recovery methods; (*ii*) application of nanotechnology in low-pressure asphaltene reaction kinetics; (*iii*) theoretical insights about thermodynamic compensation effect; (*iv*) characterization of seven different *n*-C_7 asphaltenes; (*v*) synthesis and characterization of novel nanocatalysts; (*vi*) adsorption and modeling of asphaltenes on nanocatalysts; (*vii*) high-pressure thermogravimetric experiments on virgin asphaltenes, effect of pressure, and their chemical nature; (*viii*) thermocatalytic oxidation of asphaltenes at different pressures in the presence of various nanocatalysts; (*ix*) kinetic analysis based on effective activation energy and Arrhenius pre-exponential factor; and (*x*) discussion of the thermodynamic compensation effect. Eventually, this study leads to the elucidation of the asphaltene decomposition pathways in an oxidizing atmosphere and, therefore, a better understanding of EOR processes' improvement through nanotechnology.

5.2 Thermal Enhanced Oil Recovery Processes

Enhanced oil recovery (EOR) methods are used in the oil and gas industry for increasing the productive life of crude oil reservoirs [17]. Since 1950, for the production of heavy (HO) and extra-heavy crude oils (EHO), thermal (TEOR) processes are commonly used [18] to supply heat into the reservoir and vaporize part of the crude oil [19]. TEOR methods use the temperature as a tool to improve HO and EHO mobility by oil viscosity reduction. During the heating process, thermal expansion of rock and fluids, variation in capillary pressure, the volatilization of light hydrocarbons, and gravitational segregation occur. TEOR includes hot water injection, steam injection, in situ combustion, and electric heating [2, 3].

Steam is injected into the reservoir in different ways including cyclic steam injection (CSS), continuous steam injection, and steam-assisted gravity drainage (SAGD).

CSS also called Huff and Puff involves several steam injection periods for heating the reservoir in the near-wellbore area, using a single well that functions as an

injector for steam and producer for crude oil. Precisely, CSS consists of three main stages including (*i*) steam injection into the reservoir; (*ii*) soaking time, where the well is closed to production for heat exchange; and (*iii*) production time, where the well is opened for HO and EHO production. In the soaking period, the crude oil is heated, and its viscosity decreases [20]. Temperatures of around 200°C to 300°C are reached, and production rates remain high for a short time before decreasing. The steam-to-oil ratio increases as cycles progress, leading to decreased economic gain. A good design of the technique is necessary to achieve high productivity; this factor must consider permeability, oil viscosity, and injection depth [21, 22]. Approximately 30% of OOIP is recovered with CSS [23, 24].

Continuous steam injection is used as a recovery technique to extract denser crude oils and began around 1960 in California to complement recovery by cyclical steam injection [25]. A continuous heat supply by steam is required, and it is realized in the injection wells, so that the steam advances in the reservoir, transferring heat and decreasing the oil's viscosity. As the steam front progresses, steam condensation builds up, helping move crude oil to the producing wells. With this technique, 50% of the OOIP is recovered [26, 27]. Like cyclical steam injection, steam injection faces several economic and environmental challenges related to CO_2 emissions during steam generation. The steam generation water has problems such as handling large amounts of liquid and an additional dehydration facility for the separation of the generated emulsions [28].

Steam-assisted gravity drainage (SAGD) is a technique applied mainly to extra-heavy crudes and oil sands. It was invented by Dr. Roger Butler in Canada in 1970 due to the high viscosity of hydrocarbons in that country [29, 30]. SAGD is currently one of the most efficient recovery methods that achieve recoveries up to 70% of OOIP along with high production rates [31, 32]. The technique consists of drilling two horizontal wells, placing one at 4 m–6 m above the other. Steam is injected into the upper well to heat the crude oil, reduce its viscosity, and promote its movement to the lower well (production well). Injected steam creates a steam chamber that continuously expands to push condensed water and heated oil into the producing well. This technique's application is restricted by several factors, including geological environment, reservoir thickness, vertical and horizontal homogeneity, and high permeability.

Furthermore, the presence of gas and an aquifer can reduce the efficiency of the technique [33, 34]. On the other hand, the high volumes of water involved in steam generation and gas consumption as fuel can cause high costs. To solve these problems, variations on the technique have been proposed, such as chemical solvents and non-condensable gases [4, 5].

In situ combustion, the heat is generated in the reservoir by igniting a part of the crude oil. During the injection of fluids, surface heat is generated and transferred to the reservoir. Water is one of the generally used fluids, which can be injected as hot water or as steam [25, 35]. The methods of thermal recovery can be used in both horizontal and vertical wells. However, generally in horizontal wells, its application can be more complex and expensive. In horizontal wells, techniques such as expanded solvent with gravity drainage (ES-SAGD), vapor extraction (VAPEX),

and SAGD are used to improve the sweep efficiency, increase the contact area, and oil rate production [17].

In situ combustion is generated by injecting air or oxygen to ignite a small portion of the oil in the reservoir, reaching temperatures between 450°C and 600°C. Because heat originates in situ, heat losses are minimum, making it an efficient method [36, 37]. Exothermic oxidation reactions release a high amount of heat that helps improve the mobility of heavy oil, burning a small part. There are three methods of in situ combustion: (*i*) frontal combustion, where the ignition is generated near to the injector well and the hot zone advances in production direction; (*ii*) reverse combustion, where the front combustion advances in the opposite direction of airflow, and (*iii*) high-pressure air injection. This process does not involve recycling water and has a very low emission of gases. Therefore, it is the most crucial technique for exploiting heavy and extra-heavy crude oils [38].

The process begins with ignition, where a gas chamber consisting of air and flue gases forms at the combustion front. Through the combustion front propagation, continuous expansion of the gas chamber is generated, which helps to move the unburned oil towards the production wells [6]. The in situ combustion mechanism is described by well-defined zones, including the burned, combustion, cracking, evaporation, and steam area. These areas are characterized by having different temperatures and different saturations of oil and water [39, 40]. However, despite the many benefits that this technique offers, several limitations must be overcome, and that is not yet fully understood [41]. There is still no adequate control of the combustion front and the portion of burned oil or its heating rate. Furthermore, the primary sources of coke are asphaltenes, and to date, no studies of its oxidative behavior under reservoir conditions have been dated. Understanding these mechanisms and finding technologies that improve these fractions' reactivity could improve the efficiency of these technologies since many operations could be optimized to obtain a higher recovery factor.

5.3 Nanocatalysts for Asphaltene Decomposition and Heavy Oil Upgrading

In recent decades, nanotechnology has emerged as an innovative technology applicable to the oil and gas industry, especially in the remediation and inhibition of formation damage and potentializing EOR processes [42]. By convention, nanoparticles are in the range of 1 nm−100 nm. Their size and unique characteristics make them suitable for application in porous media [43]. Among nanoparticles' properties are their high surface area-to-volume ratio, their selectivity towards heavy components of crude oil, their unique optical and chemical characteristics, and the presence of active surfaces [44, 45].

The production of heavy and extra-heavy crudes is a challenge that the industry faces every day due to the high viscosity and low mobility. Thermal recovery

methods have proven to be very efficient in increasing the production of this type of hydrocarbon [18]. The increase in temperature and the injection of heat can occur in situ or through some fluid. This provides better sweep efficiency and an increase in recovery factor with decreased viscosity [22].

A synergy between nanotechnology and thermal recovery methods has emerged as an alternative to increase hydrocarbon production. In recent years, several studies have focused on the synthesis and development of catalytic nanoparticles that reduce the decomposition temperature of asphaltenes and resins, taking advantage of the temperatures generated by thermal recovery processes. Different materials have been employed, including non-functionalized and functionalized nanoparticles as mono- [46] and multi-elemental oxides [46, 47] for the asphaltene catalytic decomposition and HO and EHO upgrading [48]. Among the most recent studies, it has been employed nanocatalysts of SiO_2 [16, 49], TiO_2 [47], CeO_2 [50–52], and Al_2O_3 [47, 53, 54] resulting in significant reductions in the decomposition temperatures of asphaltenes in different atmospheres (air, steam, inert).

To evaluate the catalytic capacity of nanoparticles, low-pressure thermogravimetric analysis and differential scanning calorimetry (DSC) are commonly used. Among the first applications of nanoparticles for the oxidation of asphaltenes, Nassar et al. [55] investigated the adsorption and subsequent oxidation of Athabasca asphaltenes in different metal nanoparticles (NiO, Co_3O_4, and Fe_3O_4) [55]. The authors found reductions of more than 100°C in the asphaltene decomposition temperature in all cases, obtaining a better result for NiO nanoparticles. Furthermore, the surface acidity of the nanoparticles was evaluated in another study [56]. Basic, acid, and neutral alumina were assessed for the oxidation of Athabasca asphaltenes. The results show affinity increases as the acidic surface increases. On the contrary, catalytic activity is higher for basic alumina.

Besides, Fe_3O_4 nanoparticles were used for catalytic oxidation of different visbroken asphaltenes from a cracked vacuum residue. Results show a significant reduction in the oxidation temperature and average activation energy [57]. Also, TiO2, ZrO2, and CeO2 nanoparticles' catalytic activity has been investigated [58]. CeO_2 nanoparticles showed the highest performance for asphaltene catalytic oxidation, confirmed by the lowest effective activation energy trends and lowest values of Gibbs free energy and enthalpy changes.

On the other hand, fumed silica nanoparticles were functionalized with transition element oxides of Ni and Pd at different dosages for the oxidation of Colombian asphaltenes [16]. This study presents essential conclusions on the application of functionalized materials. First, a higher dosage of each metal in the mono-elemental nanoparticles increases the catalytic capacity of the material. Also, bi-elemental nanoparticles show better performance than mono-elemental nanoparticles. The application of transition elements can significantly improve the performance of TEOs, and the application of design of experiments can lead to the development of an optimal material to reduce the activation energy for the catalytic oxidation of asphaltenes, which has a dosage of 0.29% Ni and 1.32% Pd on the surface of the nanoparticle.

The influence of resins on the adsorption of asphaltenes on nanoparticles has also been studied. The results present different adsorption isotherm types according to the resin/asphaltene ratio. It was concluded that resins I do not significantly influence asphaltene adsorption on nanoparticles and help to solubilize in the medium [59]. Other works have focused on the effect of resins I on the catalytic decomposition of asphaltenes adsorbed on nanoparticles. A combined method of thermogravimetric analysis and softening point measurements was used to evaluate the adsorption of asphaltenes and resins I in heavy oil model solutions. The results of the catalytic behavior show that the presence of resins I do not significantly change the decomposition temperature of the asphaltenes adsorbed on the nanoparticles. However, the catalytic effect of the nanoparticles is affected by an increase in activation energy as the presence of resins increases in the system [60].

Despite all efforts to understand and optimize TEOR methods by nanotechnology application, the effect of pressure on the interaction of isolated asphaltene molecules and nanoparticles has not yet been reported in the literature. All these investigations have been evaluated at atmospheric pressure, without considering the high pressures to which the crude oils may be subjected in the reservoir and in situ combustion processes. The few works carried out under reservoir conditions directly evaluate the matrix of HO and EHO. Still, to optimize these processes, it is important to understand how the individual fractions behave, specifically the coke precursors in the reservoir, in nanoparticles' absence and presence.

5.4 Compensation Effect

Essentially, the rate of all thermally activated processes is described by the Arrhenius law, where the rate r is temperature-dependent, following the expression $r(T) = k_o e - E_a^{app} / k_B T$, where, k_B is the Boltzmann's constant. Kinetic parameters (E_a^{app} and k_o) determine the temperature dependence and overall rate, respectively, during thermal processes. Experimental studies have shown that in some systems, by varying E_a^{app} values, a thermodynamic compensation effect is reflected in k_o changes. A direct relationship between both parameters was found, described by Eq. (5.1)

$$\ln(k_o) = aE_a^{app} + b \tag{5.1}$$

The kinetic parameters characterizing the system, according to Eq. (X), are linearly related to E_a^{app} as a function of $\ln(k_o)$. The term "compensation effect" was introduced in 1908 by Wilson et al., by evaluating the electron emission phenomenon on a heated platinum surface in a hydrogen environment. Later, the compensation effect was used in catalysis processes, and it has been found that it is valid for a large number of homogeneous and heterogeneous chemical reactions. Since then, the compensation effect has been used to study thermal and nonthermal processes'

reaction mechanisms, including bulk diffusion, polymer dielectric relaxation, and electrical conduction, among others. In thermal reactions, the compensation effect is known as isokinetic relationship because the linear dependence of Eq. (5.1) leads to an isokinetic temperature ($T_{isokinetic}$) expressed by the slope of the line. This temperature implies that all the considered reactions have the same rate. However, $T_{isokinetic}$ is often outside the range of experimentally accessible reaction conditions. Commonly, the compensation effect of chemical reactions leads to real compensation in the rate, considering the values for a always positive. Nevertheless, despite the majority of the cases, there are a large of chemical processes that have negative values for a.

Despite many attempts to explain the compensation effect in different processes, the term is not universally accepted, arguing that the nature of Arrhenius's law is such that the experimental determination of kinetic parameters is associated with large statistical uncertainties which rise to a compensatory effect.

On the other hand, the compensation effect can be distinguishable and categorized according to the nature and range of the reactants and/or reaction conditions, together with the common constant and systematically modified features. The type I compensation effect for heterogeneous reactions is associated with modification of the chemical reaction or the catalysts. Type II represents the compensation effect for experimental condition variation (i.e., pressure, temperature, heating rate), and type III is associated with practical calculation changes. That is, the estimation of kinetic parameters is realized using different computational programs or different rate equations.

In this order, in this work, we will show that for a broad class of experimental conditions and catalysts with different active site distributions, the compensation effect can be explained. First, the type II compensation effect will be demonstrated by pressure changes during asphaltene oxidation in nanocatalysts' presence and absence. Then, the type I compensation effect will be explained using a different class of nanocatalysts.

5.5 Materials and Methods

5.5.1 Materials

5.5.1.1 Nanoparticles and N-C_7 Asphaltenes

Ceria-zirconia mixed oxide ($Ce_{0.62}Zr_{0.38}O_2$) as support and impregnated with Au and Pd noble oxides in 3:1 and 10:1 Au/Pd initial nominal molar ratios was used for asphaltene adsorption and subsequent catalytic oxidation. Nanocatalysts were synthesized by deposition-precipitation of Au followed by incipient wetness impregnation of Pd. Details of the synthesis procedure are found in our previous work [1]. The surface area (S_{BET}) of bi-elemental catalysts and support was $67\ m^2 \cdot g^{-1} \pm 2\ m^2 \cdot g^{-1}$. The final load of element oxides on surface support was determined by inductive

coupled plasma-atomic emission spectrometry (ICP-AES). Results demonstrate that the nominal molar ratio remains equal to 3:1 and 10:1 at the end of the synthesis process. According to the Au/Pd nominal molar ratio, functionalized nanocatalysts were named as 3:1AuPd and 10:1AuPd.

Also, STEM-XEDS analysis corroborates the formation of metallic particles in functionalized nanocatalysts. The crystal size of Au and Pd varies between 1 and 5 nm and the respective dispersions near to 36%, for both systems. Finally, by X-ray photoelectron spectroscopy, the main functional groups of each catalyst were obtained. These results are summarized in Table 5.1.

Initially, a single asphaltene source was used to evaluate the effect of pressure on its oxidation in the absence and presence of nanocatalysts. Then, six different asphaltenes were obtained from different HO and EHO around the world to address the chemical nature effect on reactivity at low- and high-pressure conditions. Asphaltene isolation was done by mixing *n*-heptane (99%, Sigma-Aldrich, St. Louis, MO) with the HO following the protocol described in the standard ASTM D2892 and ASTM D5236 [62–64]. The samples were characterized by elemental analysis (EA) estimated using a Thermo Flash elemental analyzer EA 1112 (Thermo Finnigan, Milan, Italy) to determine the C, H, S, O, and N content, following the protocol described in previous works [65]. The average molecular weight was estimated using a Knauer osmometer (Knauer, Berlin-Heidelberg, West Germany) calibrated with benzyl and using the steps enlisted in literature [66]. X-ray photoelectron spectrometry was performed on a Specs brand X-ray photoelectronic spectrometer (NAP-XPS) with a PHOIBOS 150 1D-DLD analyzer, using a monochromatic source of Al-Kα (1486.7 eV, 13 kV, 100 W) with step energy 90 eV and 20 eV for general and high-resolution spectra, respectively. Finally, ^{1}H NMR and ^{13}CNM were developed on a Bruker AMX 300 spectrometer (Karlsruhe, Germany) operating at 300 MHz, with a 5 mm inner diameter tube. The samples were dissolved in $CDCL_3$ (99.8%) containing traces of tetramethylsilane (TMS) used as standard internal solvents. Details of the procedure are found in a previous study [67]. Considering the results of EA, VPO, and ^{13}CNM, average molecule construction was done using Materials Studio (BOVIA, San Diego, CA, USA), following the Lee-Yang-Parr function and Clar's theory [68, 69].

Table 5.1 Superficial atomic content (%) of Ce, Au (4f signal), and Pd (3d signal) ions through XPS of bi-elemental catalysts supported on $Ce_{0.62}Zr_{0.38}O_{2\pm\delta}$

Catalyst	Ce3+ (atomic %)	Au^0 (atomic %)	$Au^{\delta+}$ (atomic %)	Pd^0 (atomic %)	Pd^{2+} (atomic %)
3:1AuPd[a]	20	100	0	37.7	62.3
10:1AuPd[a]	34	100	0	50.4	49.6

[a]Results acquired from previous work [61]

5.5.2 Methods

5.5.2.1 Adsorption Isotherms

The amount of asphaltenes adsorbed on the different nanocatalysts was determined by a colorimetric method using a UV-vis spectrophotometer Genesys 10S UV-VIS (Thermo Scientific, Waltham, MA, USA) at a wavelength fixed at 295 nm [70, 71]. Asphaltene initial concentrations were varied between 100 mg·L^{-1} and 1500 mg·L^{-1}. Besides, the toluene was used as a blank in the calibration curve and as an agent for dilution [72].

The procedure starts by adding the constant mass of nanoparticles to the prepared heavy oil model solutions in a ratio of 1:10 mass/volume. This solution to nanoparticles ratio is used to allow the adsorbent decantation for the UV-vis absorbance measurements. All samples were mixed at 200 rpm for 24 h at 25°C to ensure the equilibrium, unless otherwise specified. Then, by centrifugation, the nanoparticles containing asphaltenes were separated. Runs were done by triplicate, obtaining a deviation of 0.05 mg·L^{-1}. The amount of n-C_7 asphaltenes adsorbed "q" is calculated using the mass balance in Eq. (5.2)

$$q = \frac{\left(C_0 - C_E\right) \cdot M}{A} \tag{5.2}$$

where C_E (mg·L^{-1}) represents the n-C_7 asphaltene concentration in the equilibrium, M (L·g^{-1}) is the solution volume/nanoparticle mass ratio, and A (m^2·g^{-1}) denotes the surface area of the adsorbent.

5.5.2.2 Kinetic Study by High-Pressure Thermogravimetric Analysis

Kinetic analysis of n-C_7 asphaltenes oxidation assisted by nanocatalysts was carried out using a high-pressure thermogravimetric analyzer 750 (TA Instruments, Inc., Hüllhorst, Germany). The equipment operates with a uniform electromagnetic field generated by a magnetically levitated balance. Figure 5.1 shows a diagram of the gas supply system for the equipment. It comprises four gas mass flow controllers (MFCs) to guarantee a correct flow of the working gas at different pressures. Initially, the sample surface is cleaned under a vacuum at 0.00025 MPa for 10 min by N_2 injection at 5 mL·min^{-1}. Then, two runs are done at the same operation conditions due to flow effects, one for the sample to analyze and the other for the empty sample holder. Automatic correction is made by subtraction of the respective measurements.

Non-isothermal experiments were executed at different heating rates of 5°C·min^{-1}, 10°C·min^{-1}, and 15°C·min^{-1}. Air injection was done by a flow of 80 mL·min^{-1}, and the mass was fixed in 1 mg to avoid mass and heat diffusional effects [1, 73]. Thermal experiments were developed in three main subsections that

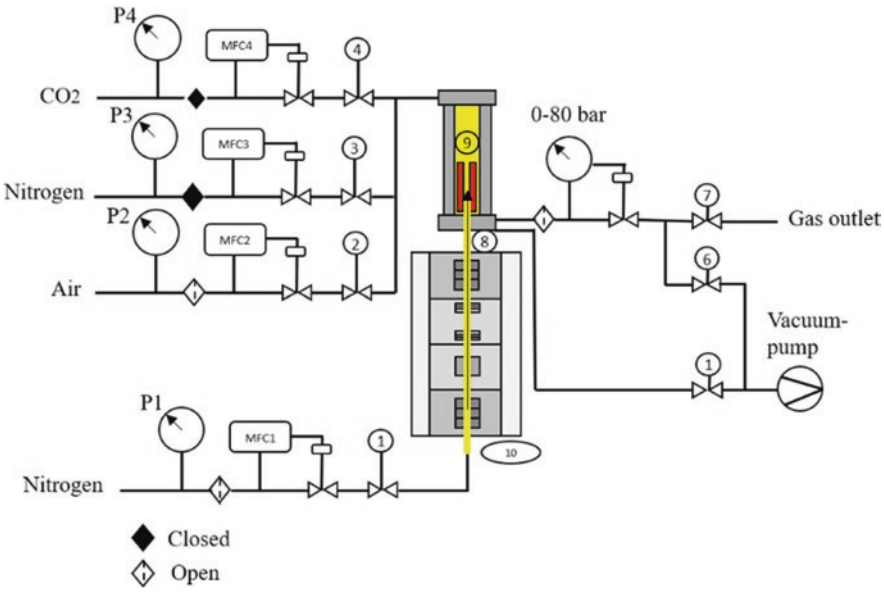

Fig. 5.1 Representative diagram for the gas supply system of the HP-TGA 750. (MCF# corresponds to gas mass flow controllers, P# the manometers, 1–6 are the automatic valves, 7 is the gas outlet pressure regulator, 8 is the tube balance, 9 is magnet levitated balance, and 10 is the high-pressure reaction furnace)

involve (*i*) virgin *n*-C_7 asphaltene oxidation for a single source in a wide range of pressures between 0.084 MPa and 7.0 MPa, (*ii*) oxidation of different sources of *n*-C_7 asphaltenes at low- and high-pressures, and (*iii*) oxidation of nanocatalysts containing *n*-C_7 asphaltenes.

5.6 Modeling

5.6.1 Solid-Liquid Equilibrium Model

This model, from the theory of adsorption and association of molecules over microporous surfaces [74], describes the adsorption and desorption isotherms using the following equations (Eqs. 5.3, 5.4 and 5.5).

$$C = \frac{\psi H}{1 + K\psi} e^{\left(\frac{\psi}{Q_m A}\right)} \tag{5.3}$$

$$K = \frac{K_T RT}{SA} \tag{5.4}$$

$$\psi = \frac{-1+\sqrt{1+4K\xi}}{2K} \tag{5.5}$$

where the concentration of asphaltenes in the equilibrium is represented by C ($mg \cdot g^{-1}$) and H ($mg \cdot g^{-1}$) refers to the affinity between the adsorbate-adsorbent couple. Similarly, K ($g \cdot g^{-1}$) indicates the self-association degree of n-C_7 asphaltenes on nanoparticles, and Q_m ($g \cdot g^{-1}$) is the maximum adsorption capacity of nanoparticles [75].

5.6.2 Activation Energy Estimation

Estimation of kinetic parameters (i.e., Arrhenius pre-exponential factor and activation energy) was done using a single power law equation bearing in mind the immediate reactivity of the materials. Ozawa-Wall-Flynn approximation was used to resolve non-isothermal experiments [76], leading the Eq. (5.6):

$$\ln\left[\frac{\beta F(\theta)}{P_{O_2}^n T^2}\right] = \ln\left(\frac{k_o R}{E_a}\right) - \frac{E_a}{RT} \tag{5.6}$$

where β ($°C \cdot min^{-1}$) is the heating rate, **P** (bar) is the oxygen partial pressure, n represents the order of oxidation reaction, E_a ($kJ \cdot mol^{-1}$) is the effective activation energy, k_o ($s^{-1} \cdot bar^n$) is the Arrhenius pre-exponential factor, and R ($J \cdot mol^{-1} \cdot K^{-1}$) is the ideal gas constant. Besides, $F(\theta)$ is represented by the expression ($\int d\theta / f(\theta) = -\ln(1-x)$) related to the volumetric consumption model [1, 73].

5.7 Results

5.7.1 Characterization of N-C_7 Asphaltenes

The elemental composition and average molecular weight results of the asphaltene samples are shown in Table 5.2. Carbon content varies between 81.0% and 85.0% while hydrogen content between 7.1% and 7.8%. Differences in heteroatom content between each sample were observed. The atomic percentage for nitrogen increases in the order SS < C < A ≈ D < E < F < B. Particularly, SS sample has a content below to 0.5%. Sulfur content is the predominant heteroatom in all samples, for values higher than 3.9%. Finally, oxygen content varies between 2.9% and 3.6%. On the other side, molecular weight increases in the order E < F < C < D < SS < A < B, according to the different elemental composition in each sample. A complete analysis is reported in a previous work [67].

Table 5.2 Elemental composition and average molecular weight of n-C_7 asphaltenes of different sources

Sample	Elemental mass fraction concentration ± 0.2%					M_W ± 5.0 g·mol^{-1}
	C	H	N	S	O	
SS	81.7	7.8	0.3	6.6	3.6	907.3
A[a]	82.6	7.3	1.5	5.4	3.2	950.3
B[a]	81.9	7.7	1.9	5.3	3.2	1051.6
C[a]	82.5	7.7	1.1	5.3	3.4	722.4
D[a]	83.0	7.2	1.5	5.4	2.9	717.3
E[a]	84.7	7.2	1.6	3.5	3.0	555.7
F[a]	84.3	7.1	1.8	3.9	2.9	650.9

[a]Results acquired from previous work [67]

Table 5.3 Carbon types present in whole n-C_7 asphaltenes and its fractions obtained by ^{13}C-NMR analysis

Carbon		Relative amount (%) in asphaltenes					
	SS	A[a]	B[a]	C[a]	D[a]	E[a]	F[a]
C_{ar}	64.48	62.12	68.2	65.9	60.3	55.6	57.8
C_{al}	35.51	37.9	31.8	34.1	39.7	44.4	42.2

[a]Results acquired from previous work [67]

Carbon type proton distribution was obtained by the combination of normalization and integration processes of the ^{13}C NMR patterns and are shown in Table 5.3. The carbon was divided into two important regions, one for the aliphatic carbon content and the other for the aromatic carbon. The former increases in the order B < C < SS < A < D < F < E, while aromatic content follows the opposite behavior.

According to the NMR spectral analysis results, combined with elemental analysis and average molecular weight (VPO), asphaltene molecules were computationally resolved and are shown in Fig. 5.2 a–g. For all samples, island structure type adjusts correctly the experimental results obtaining theoretical molecular weights of 903.1 g·mol^{-1}, 959 g·mol^{-1}, 1043 g·mol^{-1}, 724 g·mol^{-1}, 701 g·mol^{-1}, 570 g·mol^{-1}, and 660 g·mol^{-1} for SS, A, B, C, D, E, and F samples, respectively. These are deviations lower than 3.0% for all asphaltenes. Molecular formulas are also enlisted in each figure. Results demonstrate that structural and chemical differences exist in each sample evaluated.

5.7.2 Adsorption Isotherms

Adsorption isotherms for SS asphaltenes over nanocatalysts are shown in Fig. 5.3. According to the International Union of Pure and Applied Chemistry (IUPAC) [77], this isotherm type is characterized by a high affinity between the adsorbent-adsorbate couple. For a fixed asphaltene concentration, adsorption amount increases

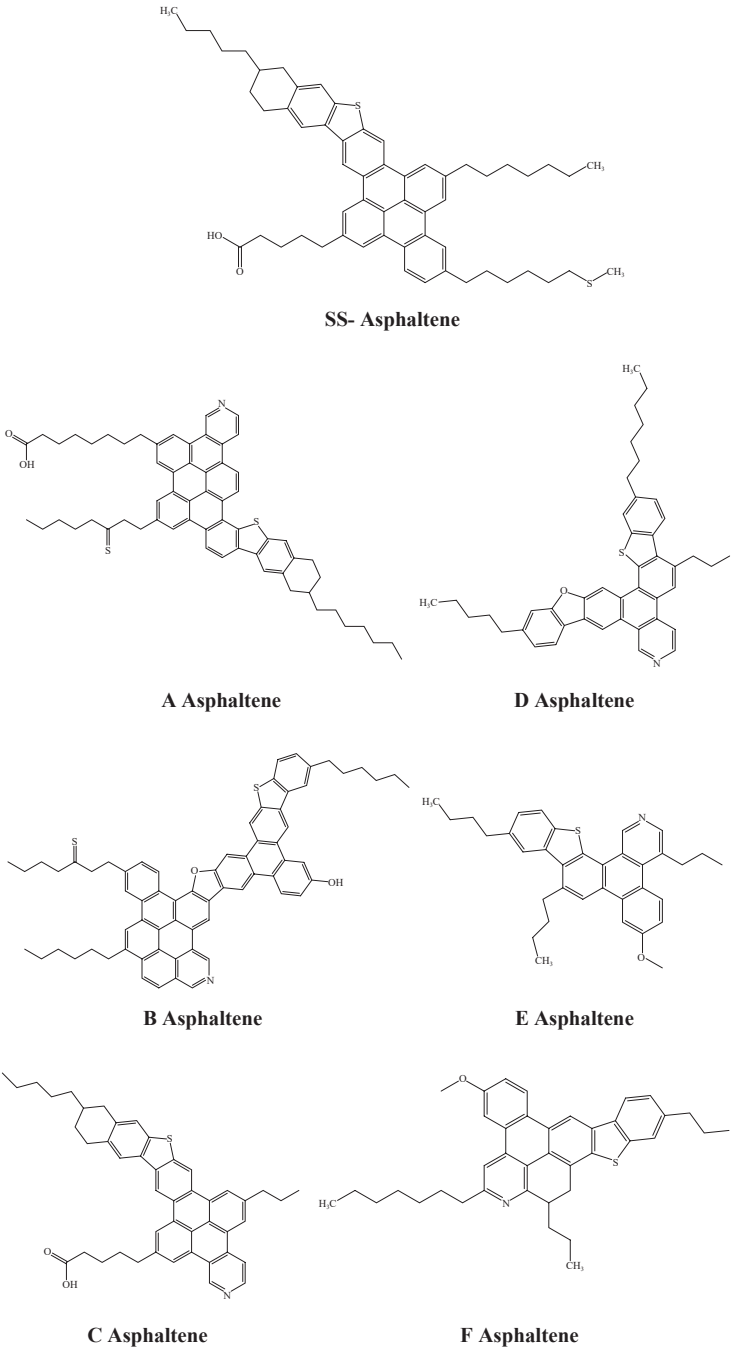

Fig. 5.2 Representative chemical structures for n-C_7 asphaltene samples constructed from results of NMR, elemental analysis, and average molecular weight. (Reproduced from Medina et al. [67] with permission)

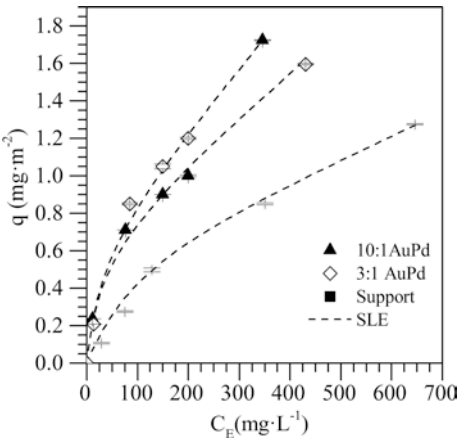

Fig. 5.3 *n*-C_7 asphaltene adsorption isotherms over support and functionalized nanocatalysts with different Au/Pd nominal molar ratios (3:1, and 10:1). (Taken with permission from Medina et al. [83])

in the order Support <3:1AuPd < 10:1AuPd. This trend is met throughout the range of concentrations evaluated. In the first instance, $Ce_xZr_{1-x}O_2$ mixed oxides show a high capacity for asphaltene uptake due to the affinity for the polyaromatic condensed structures for Ce^{3+} ions [50]. In addition, Zr^{4+} ions provide a higher capability to support by increasing the number of active sites for asphaltene adsorption and acid surface degree [78].

The incorporation of Au and Pd crystals improves the adsorption capacity and affinity according to the slope in Henry's region. Between both nanocatalysts, a nominal molar ratio of 10:1 shows a better performance than 3:1. According to XPS analysis, 10:1AuPd has a higher content of Pd0 ions, which can result in stronger chemical bonds with asphaltene molecules [79]. As was mentioned, Ce^{3+} plays a critical role in adsorption processes and is present in a higher load for 10:1 nanocatalyst [51]. These findings reveal that a heterogeneity surface is a key factor in increasing asphaltene adsorption, creating different selectivities for the nitrogen, oxygen, and sulfur functional groups of asphaltene structure. Compared with the literature, this study's selected nanocatalysts show a better performance [80–82].

5.7.3 High-Pressure Thermogravimetric Analysis

5.7.3.1 Effect of Pressure on N-C_7 Asphaltene Oxidation

Figure 5.4 shows the mass change and temperature profiles as a function of time for *n*-C_7 asphaltene oxidation at 6.0 MPa. This system was selected to illustrate the asphaltene oxidation behavior at high-pressure conditions. According to the mass change profile, the temperature was divided into four defined regions. The first region, named *oxygen chemisorption region* (OC), corresponds to the interval where an increase in asphaltene mass is observed, associated with incorporating oxygen atoms on its chemical structure from the oxygen-rich environment. The second

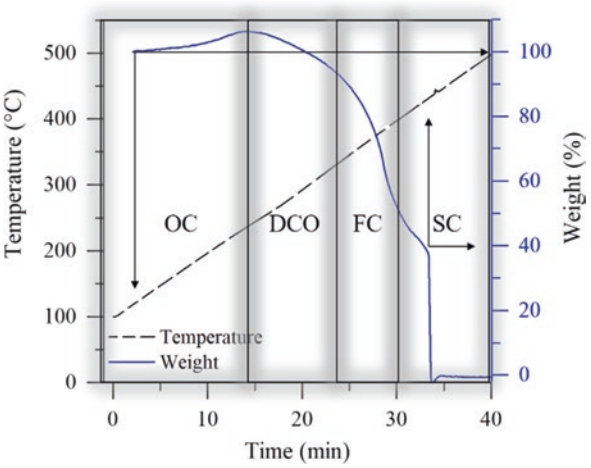

Fig. 5.4 Profiles for mass change and temperature for n-C_7 asphaltene oxidation at 6.0 MPa discretized in the four regions: (*i*) oxygen chemisorption (OC) region, (*ii*) decomposition of the chemisorbed oxygen (DCO) region, (*iii*) first combustion (FC) region, and (*iv*) second combustion (SC) region. Heating rate, 10°C·min^{-1}; airflow, 80 mL·min^{-1}; and sample mass, 6 mg. (Taken with permission from Medina et al. [73])

region, known as *decomposition of chemisorbed oxygen region* (DCO), is the temperature interval where the first decomposition and desorption of oxygenated compounds occurs, i.e., where mass sample begins its reduction. In this region, it also can occur the loss of lower molecular weight hydrocarbons and heteroatoms located in the branched structures. Then, for higher temperatures, the combustion phenomenon is divided into two main regions, *first* (FC) and *second combustion* (SC). These intervals were separated according to the thermal event close to 400°C, clearly observed in the temperature profile. The total consumption of asphaltenes is carried out at the end of SC. Each region is defined by a particular behavior associated with its mass change and mass change rate curves at the time of its decomposition in mathematical functions (conventionally Gaussian/Lorentzian), which perfectly describe the area under the DTG curve [16, 55, 56, 80, 84].

Then, the effect of pressure was evaluated on n-C_7 asphaltene oxidation. The results are shown in Fig. 5.5. Panels a–c show the rate for mass change and panels d–f the mass change profiles for pressures between 0.084 MPa to 6.0 MPa. According to the results, asphaltene oxidation is a pressure-dependent phenomenon, due to both profiles being modified with the increase in pressure [85–87]. For atmospheric pressure, the asphaltene profile is divided into low- and high-temperature regions. Contrasting, pressures higher than 0.3 MPa modify the oxidation behavior from 2 to 4 thermal events.

In the current context, panels a–c of the same figure shows that pressure generates a positive effect on asphaltene oxidation reflected in the number and intensity peaks of the rate for mass change. In panel a, a single peak is observed close to 450°C, which is in accordance with results reported for asphaltene oxidation at low pressures [88]. By contrast, in panels b and c, two peaks appear at 380°C and 450°C. Besides, a slight elevation is observed around 300°C. The lowers temperature peaks in the rate for mass change of asphaltene oxidation seem to arise from DCO and FC thermal events. On the other hand, panels d–f show that OC and DCO do not occur at low pressure since an increase in sample mass is not obtained for low

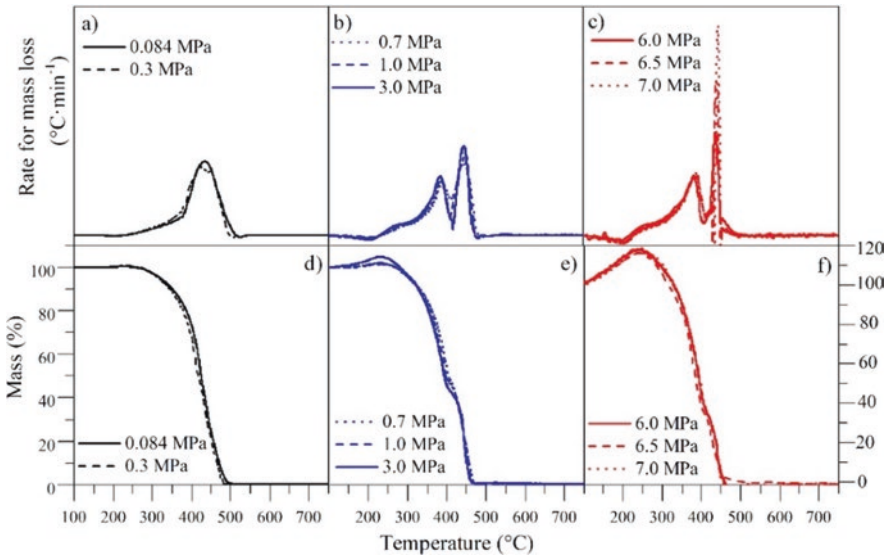

Fig. 5.5 (**a**–**c**) Rate for mass loss and (**d**–**f**) mass percentage for *n*-C_7 asphaltene oxidation at different pressures between 0.084 MPa and 7.0 MPa. Heating rate, 10°C·min^{-1}; airflow, 80 mL·min^{-1}; and sample mass, 1 mg. (Taken with permission from Medina et al. [73])

temperatures. These results suggest that oxygen chemisorption plays a vital role in asphaltene oxidation since the molecules become more reactive; hence there is an easy bond scission. Besides, the volatile content is driven off at lower temperatures [88]. The oxidation of heavy hydrocarbon structures occurs in the most reactive sites, i.e., peripherical molecules and heteroatoms.

Also, the basal plane of the aromatic structure could promote oxygen anchorage [8]. High-pressure's main effects promote the probability of oxygen atoms collision and, hence, higher kinetic energy [89, 90]. During SC the solid product obtained after FC is characterized for a low H/C ratio, high polarity, and aromaticity degree, since aliphatic structures react during DCO and FC regions, promoting aromatic condensation degree.

5.7.3.2 Thermo-Oxidation of Different N-C_7 Asphaltenes

The effect of the chemical nature of asphaltene over its oxidation was evaluated using six different asphaltene sources. Samples were named as A, B, C, D, E, and F asphaltenes. The thermograms were constructed at three different pressures (0.084 MPa, 3.0 MPa, and 6.0 MPa). Figure 5.6 shows the mass change and rate for mass change profiles for the systems evaluated.

Results show that the oxidation process depends directly on the asphaltene chemical structure and the increment of pressure remarks on the differences between the rate for mass change and mass change profiles. For all systems, asphaltene

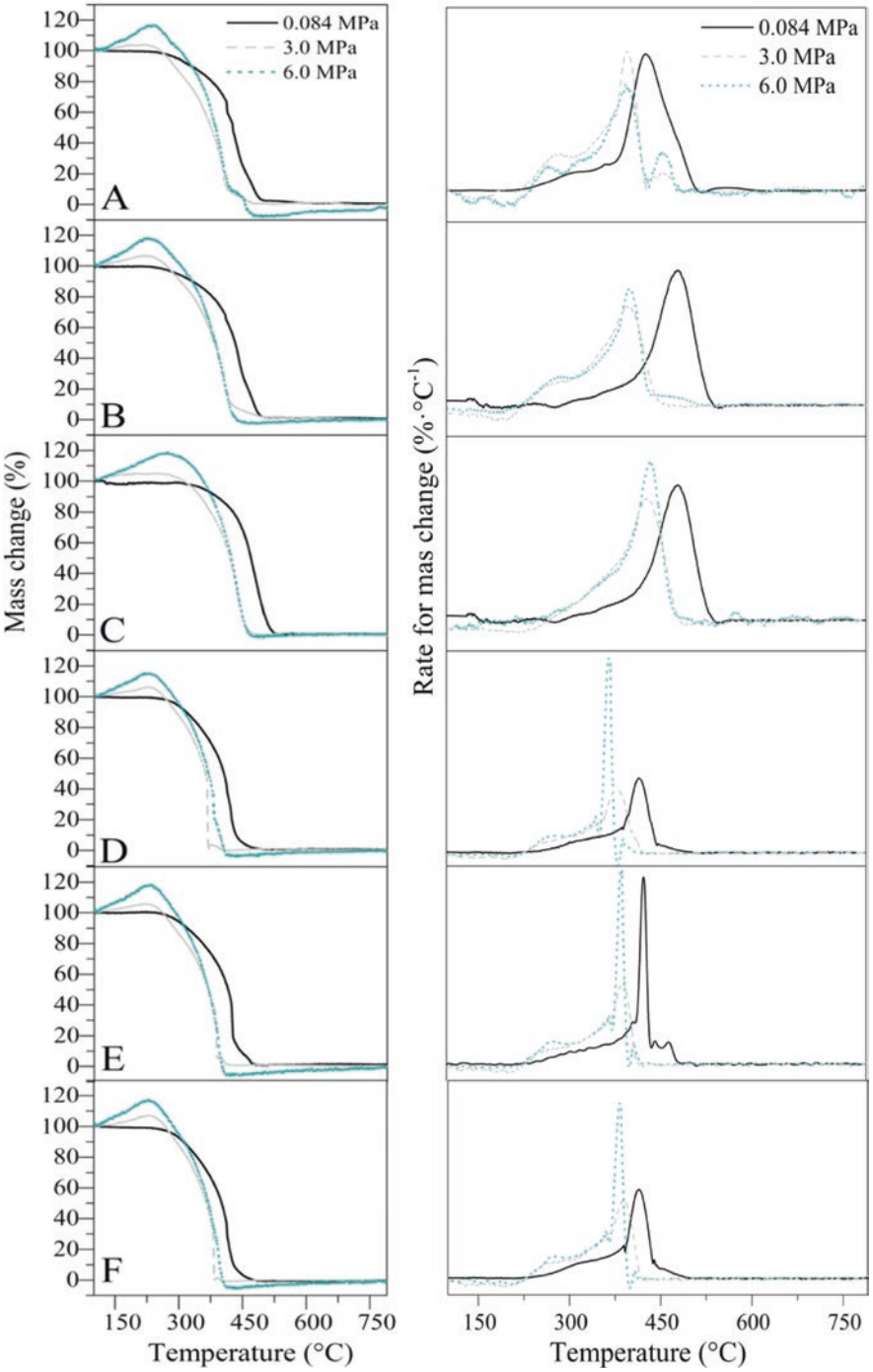

Fig. 5.6 Mass percentage and rate for mass change for different n-C_7 asphaltene oxidations at different pressures from 0.084 MPa to 6.0 MPa. Sample weight, 1 mg; heating rate, 10°C·min^{-1}; and airflow, 80 mL·min^{-1}. (Taken with permission from Medina et al. [67])

decomposition is defined by four thermal events as described in the previous section, for pressures higher than 3.0 MPa [91]. According to mass change profiles, oxygen chemisorption degree increases following the trend D < F < E < B < A < C. Substantial differences in the amount of oxygen chemisorbed in each sample can be associated with the amount of free radicals, heteroatoms, aromaticity degree, and diameter of clusters and aggregates. Free radicals vary according to the asphaltene source, between 10^{15} and 10^{20} spins·g^{-1}. The greater the amount of free radicals, the greater the chemisorption of oxygen [92]. Besides, the increase in pressure promotes an increase in oxygen chemisorbed percentage due to aggregates' thermal expansion [93]. A direct relationship between the content of carbonyl and carboxyl functional groups was found. Despite the increase in oxygen content following the order E ≈ F < D < A ≈ B < C, the amount of these functional groups increases as follows D < F < E < B < A < C, which agrees with OC%. Carboxyl groups are characterized by their easiness for being ionized by hydrogen proton releasing from OH^- group [94]; therefore oxygen is strongly activated in these active sites. On the other hand, according to ^{1}H-NMR results reported in previous work [67], the increase in aromatization degree and the decrease in alkylation degree favor the anchorage of oxygen molecules on asphaltene structure. As the number of fused rings in the polyaromatic core increases, the intermolecular interactions increase too [95]. Therefore, the formation of ketones, phenols, ethers, and alcohols takes place [91]. It has been reported that at low temperatures (100–150°C), ketones and aromatic ethers are the main oxygenated functional groups in asphaltene structures [92].

According to X-ray diffraction analysis, reported in previous work [67], the decrease in the cluster's diameter increases the mass gained in the OC region, because there is a bigger surface area/volume ratio for oxygen anchorage, added to the asphaltene molecular expansion by pressure effect.

DCO region also is favored by high-pressure systems, as the loss of mass increases in the order 3.0 MPa < 6.0 MPa. This is obtained for all samples. Between asphaltenes, the mass loss percentage increases in the order D < F < E < C < B < A. The samples with higher OC increment lost a higher mass in the DCO region. It implies that in effect during DCO occurs mainly the decomposition of the oxygenated structures, which at the same time are more reactive [91]. Besides, X-ray photoelectron spectroscopy analysis shows the influence of the different functional groups. Samples with the highest thioether content have shown the highest mass loss in DCO. This sulfur form is characterized to require low energy for oxidizing. Besides the position on saturated structure facilitates their decomposition at low temperatures [96]. As for 1H-NMR, according to the *H*α values, it was also found that a high content of methyl, ethyl, and methylene structures promotes a greater loss of mass in DCO region [97].

For combustion regions, the chemical nature of asphaltenes considerably influences the FC and SC behavior at high-pressure conditions. The asphaltenes with a high content of short aliphatic chains and heteroatoms located in branched structures decompose around 70% of their mass. According to the asphaltenes' initial composition, the remaining coke after this region will have a different composition due to the loss of peripheral substituents [98] and the ability to create steric

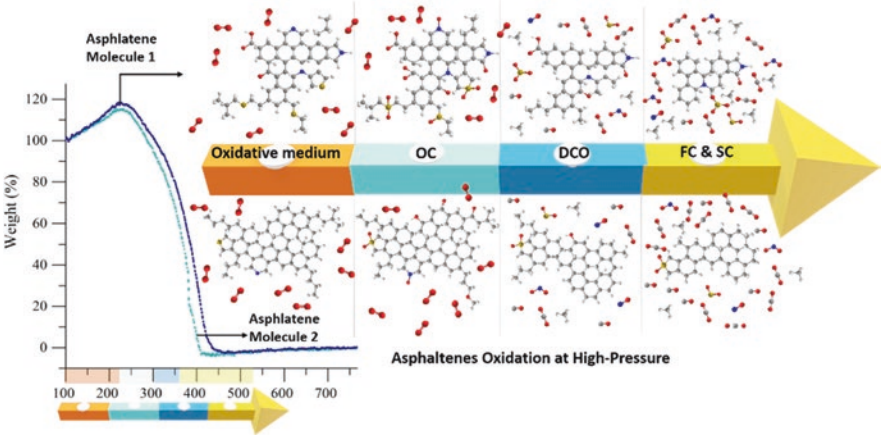

Fig. 5.7 Representative diagram for different n-C_7 asphaltene oxidations at high-pressure conditions. (Taken with permission from Medina et al.)

hindrance and prevent polyaromatic condensation [98]. This was corroborated by XRD results, where samples with high intensity for γ-band and low intensity for (002)-bands have favorable conditions for polyaromatic sheets stacked together to produce coke [99]. Hence, during SC, for samples with low content of aliphatic structures and high aromatic degree, a high amount of asphaltenes is required to decompose, independently of system pressure. In the current context, aromatic functional groups, including thiophenes, pyrroles, and pyridines, also promote a higher mass loss in SC, adding extra polar interactions between the aromatic structures [100]. Figure 5.7 shows the differences in the profiles obtained from two asphaltene molecules with different functional groups, different sizes of the aromatic nucleus, and different molecular weights, among others.

5.7.3.3 Thermocatalytic Oxidation of N-C_7 Asphaltenes

SS asphaltenes were selected to evaluate the effect of different nanocatalysts on asphaltene oxidation at high- and low- pressure conditions. Figure 5.8 shows the results in mass change and rate for mass change for asphaltene oxidation with (a) support, (b) 3:1AuPd, and (c) 10:1AuPd nanocatalysts at non-isothermal conditions. According to the profiles obtained, the presence of nanocatalysts maintains the decomposition of asphaltenes defined by 4 thermal events for pressures greater than 1.0 MPa, i.e., 0.7 MPa higher than in the absence thereof. This suggests that a more significant mass diffusion occurs for virgin molecules at lower pressures [101]. The mixed support shows an important reduction in asphaltene decomposition for all pressure evaluations. The inclusion of Zr^{4+} on the internal molecular structure of ceria improves their catalytic activity by the increment in oxygen storage capacity, directly related to redox reactions. As reported in the literature, the

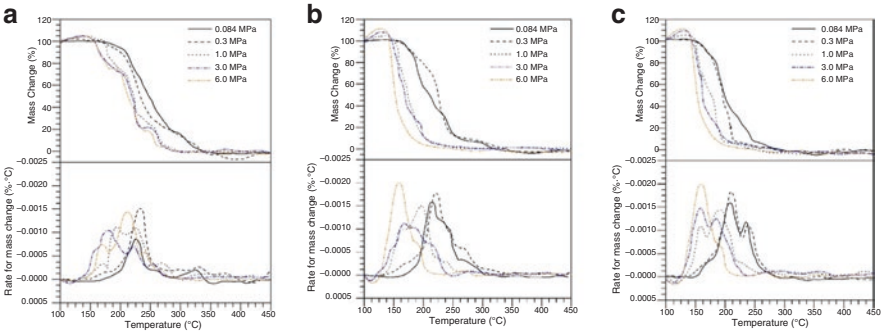

Fig. 5.8 Mass in percentage and rate for mass change for *n*-C_7 asphaltene oxidation in the presence and absence of bi-elemental catalysts 3:1AuPd and 10:1AuPd at different pressures from 0.084 MPa to 6.0 MPa. Sample weight, 1 mg; *n*-C_7 asphaltene load, 0.2 mg·m^{-2}; heating rate, 10°C·min^{-1}; and airflow, 80 mL·min^{-1}. (Taken with permission from Medina et al. [83])

couple Ce3+/C4+ plays an important role in asphaltene decomposition, being the main mechanism for hydrogen production in cracking processes. By using nanocatalysts, the oxygen chemisorbed decreases considerably at 6.0 MPa; however, the reactivity of samples is favored by this event, ending the total decomposition for the systems with higher OC%. Lower pressures present a higher OC% for adsorbed than virgin asphaltenes. For DCO region, nanocatalysts cause most of the asphaltene to decompose in this region at lower temperatures (< 230°C). Nevertheless, for lower pressures, the mass loss is equally distributed in the three decomposition regions. This is corroborated by the rate for mass change peaks. For low-pressure systems, the main decomposition peak is observed at 230°C, but pressures higher than 1.0 MPa show an increase in intensity peak at 160°C.

As literature reports, active sites on the support surface can improve the catalytic activity of the materials. In this study, two noble elements (Au and Pd) were used in different nominal ratios (10:1 and 3:1). From results, it is appreciated that similar to support, the four thermal events remain for high-pressure systems. Nevertheless, substantial differences in intensity and temperature peaks are obtained in each system [102]. Comparing with support, both functionalized nanocatalysts improve the oxidation behavior of asphaltenes by increasing oxygen chemisorption percentage, reduction of temperature peaks, and increase in intensity peaks at low temperatures and therefore its reduction at high temperatures. Besides, pressure increases improve the catalytic behavior of AuPd-based nanocatalysts. For lower pressures, the peak at 200°C and 190°C is predominant for 3:1AuPd and 10:1AuPd, respectively. These temperatures are reduced as pressure goes up, achieving 170°C and 160°C at 6.0 MPa for the same systems.

Oxygen chemisorption was higher for nanocatalysts with a higher amount of Au active phases (i.e., 10:1AuPd). Interactions between oxygen from the environment and noble elements favor the oxygen transfer to asphaltene molecules by spillover mechanism [103, 104]. In the current context, the DCO region is also favored in the same nanocatalyst trend described. As the carbonaceous molecules become oxygen-rich during OC, in DCO they lose a higher amount of mass. For example, 10: AuPd

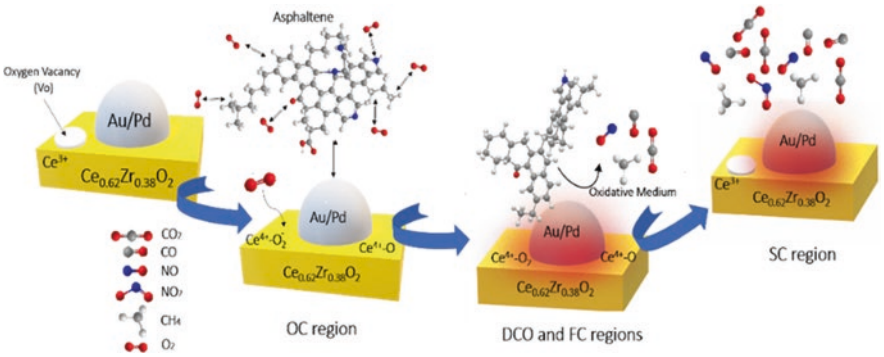

Fig. 5.9 Schematic illustration for thermocatalytic oxidation of n-C_7 asphaltenes using AuPd/$Ce_{0.62}Zr_{0.38}O_2$ nanocatalysts discretized in the four thermal regions. (Taken with permission from Medina et al. [83])

and 3:1AuPd lost 90% and 80% of the initial mass, respectively, during DCO zone at 6.0 MPa. In this sense, during FC and SC, the asphaltene mass loss is considerably reduced for high-pressure systems.

In addition, according to surface nanocatalysts characterization, the influence of different ions on asphaltene catalytic activity was found. High Pd^{2+} ions concentration promotes a detriment in catalytic activity, while Ce^{3+} and Au^0 increase the reactivity of the materials under the operational conditions. These results indicate that nanocatalysts require a good design based on structural and phase complexity for selective oxidation of asphaltenes [61, 105].

Figure 5.9 shows mechanistic insights about the catalytic oxidation process of n-C_7 asphaltene oxidation over bi-elemental nanocatalysts.

Figure 5.9 tries to present the main mechanisms that act in the decomposition of asphaltenes at high pressure. First, the adsorption of asphaltenes occurs mainly in the active phases of the noble elements. Simultaneously, with increasing temperature, the oxygen molecules adsorb onto the oxygen anion vacancies on the surface of the support (OC region). Here, oxidation of asphaltenes occurs during the OC region. When nanocatalysts acquire enough energy, the first oxygenated fractions decompose during DCO, a redox cycle takes place, and the first gaseous products are formed, including sulfur-, nitrogen-, and oxygen-based gases. Finally, at the end of the FC region, a solid with a high condensed and aromatic degree is obtained due to the loss of aliphatic chains. In SC, the total decomposition of the condensed molecules is generated.

5.7.4 Estimation of Kinetic Parameters

5.7.4.1 Asphaltene Oxidation at Different Pressures

The effective activation energy for SS asphaltenes oxidation was calculated for all systems at different pressure conditions, discretizing the total phenomenon in four thermal events. Plotting $\ln\left[\beta\left(-\ln\left(1-x\right)\right)\times\left(\mathrm{P}_{O_2}T^2\right)^{-1}\right]$ against $1{\cdot}T_i^{-1}$ and using the

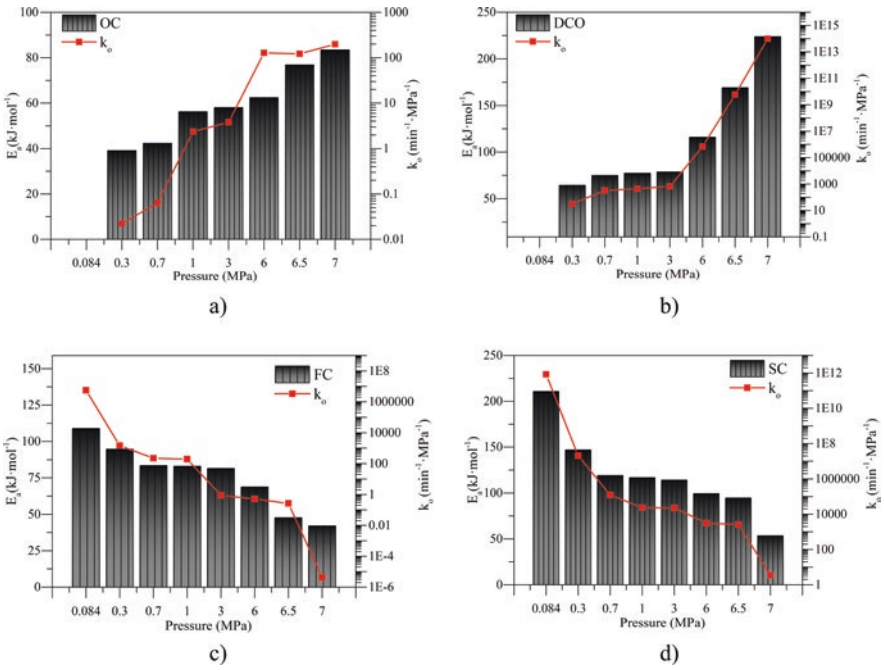

Fig. 5.10 Estimated kinetic parameters for *n*-C_7 asphaltene oxidation at different pressures discretized in different regions, including (**a**) oxygen chemisorption (OC), (**b**) decomposition of the chemisorbed oxygen (DCO) region, (**c**) first combustion (FC) region, and (**d**) second combustion (SC) region. (Results taken from Medina et al. [91])

slope and intercept of the straight line, E_a and k_o are obtained, respectively. Results are shown in Fig. 5.10 a–d. As temperature was divided into shorter intervals, a first-order reaction fits decomposition profiles correctly with $R^2 > 0.99$.

From panel (a) of Fig. 5.10, it is observed that E_a increases as pressure increases. Values vary between 39.12 kJ·mol^{-1} and 83.46 kJ·mol^{-1} in the pressure range evaluated. The amount of chemisorbed oxygen increases considerably for high-pressure systems; the energy to carry out this process also increases.

This same trend is followed for the DCO thermal event. Because with the increase in pressure, there are a greater number of oxygen structures formed, there is a greater energy expenditure in their decomposition.

Effective activation energies for DCO are higher than for the OC region, varying between 64.47 kJ·mol^{-1} and 223.84 kJ·mol^{-1}. Finally, for the combustion regions, the activation energy at lower pressures is higher than in DCO; however, for high pressures, FC and SC have lower values, due to the high degree of decomposed structures during DCO, and high conversion degree implies high activation energy values.

For the Arrhenius pre-exponential factor, it is observed dependency on the pressure system. Pressure modifies k_o values by several orders of magnitude [91]. As the number of accessible number states increases, Arrhenius values during OC are

varied due to the change in entropy change by the system's molecular disorganization and the formation of an activated complex.

5.7.4.2 Kinetic Analysis for Different N-C_7 Asphaltenes at High-Pressure Conditions

Kinetic analysis was done for the n-C_7 asphaltenes from different sources. Figure 5.11 shows the results obtained. From panels a–b, it is observed an increase in E_a during OC and DCO region as pressure increases for all samples. As it was

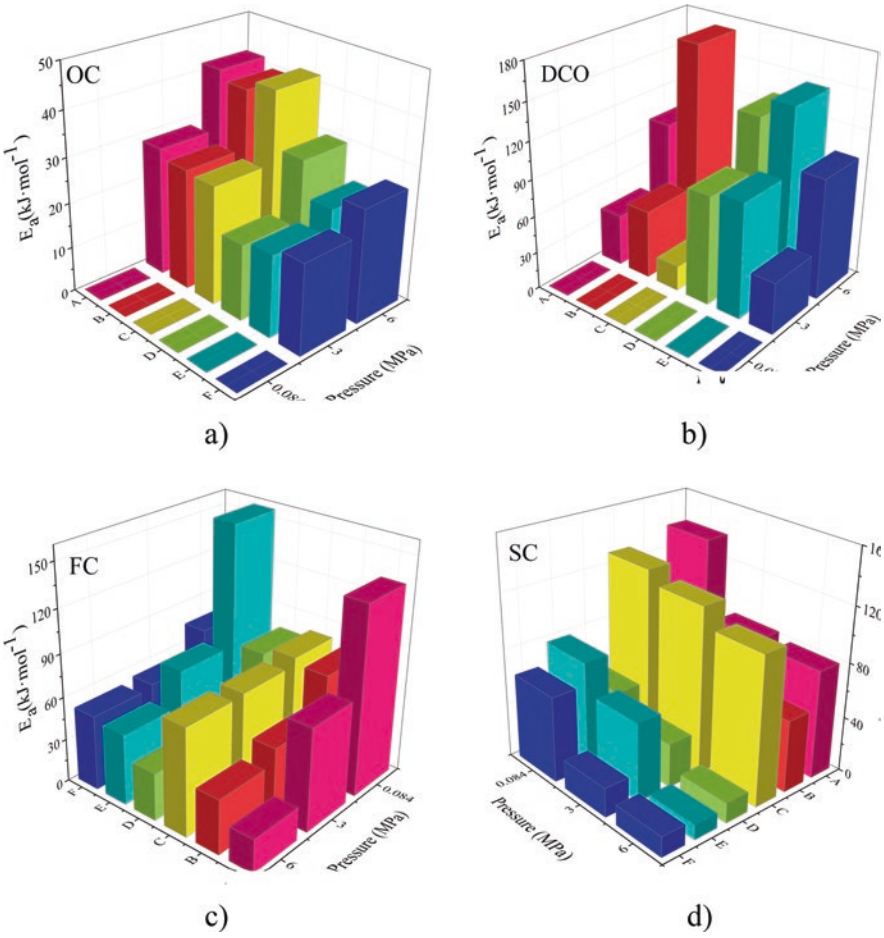

Fig. 5.11 Estimated effective activation energy for the oxidation of different n-C_7 at 0.084 MPa, 3.0 MPa, and 6.0 MPa discretized in different regions including (*a*) oxygen chemisorption (OC), (*b*) decomposition of the chemisorbed oxygen (DCO) region, (*c*) first combustion (FC) region, and (*d*) second combustion (SC) region. (Results are taken from Medina et al. [67])

explained, DCO depends on the functional groups formed during OC zone. Regardless of the chemical nature of asphaltene, by increasing pressure, the number of oxygenated structures increases, due to interactions with free radicals, heteroatoms, and aromatic rings, among others. Each asphaltene has different active sites for oxygen anchorage, and pressure favors this phenomenon in all cases [91, 106, 107]. On the other hand, the differences in E_a values between each sample are directly related to its chemical nature and origin. Samples with a higher aromatic degree show a higher activation energy value. Functional nitrogen and sulfur groups also affect these results. Aromatic nitrogen and sulfur reduce activation energy. The opposite is obtained for carboxyl and carbonyl groups. The high content of these groups increases the activation energy.

The values of E_a during DCO are higher than the obtained for OC, which is in accordance with the results previously exposed [91, 108]. Nevertheless, pressure generates a positive effect over asphaltene oxidation since the energy required to complete combustion zones is reduced.

On the other hand, asphaltenes with a smaller cluster size present lower E_a values during FC. This is due to the breakdown of alkyl side chains, making the asphaltenes more refractory at the end of this region. Finally, in SC region, several chemical reactions occur, including dealkylation/cyclization of aliphatic chains, combination/polymerization/condensation and peri-condensation of aromatic rings, and aromatization of naphthenic rings, mainly in asphaltenes like A, B, and C, reflected in their higher values for effective activation energy [9, 86, 109].

5.7.4.3 Kinetic Analysis for N-C_7 Asphaltene Catalytic Oxidation

Kinetic study was done for thermocatalytic oxidation of *n*-C_7 asphaltene based on effective activation energy. The values for both parameters are shown in Fig. 5.12. From results, it is appreciated that according to the chemical nature of nanocatalysts, E_a presents significant differences. The effect of pressure in the presence of nanocatalysts is the same as for virgin asphaltenes. Pressure increment implies higher energy values for OC and DCO thermal events and lower values for combustion zones. Besides, nanocatalysts with higher catalytic activity show higher energy values for OC and DCO regions. Contrasting with virgin asphaltenes, the adsorbed molecules reduces the activation energy around 17 kJ·mol^{-1} for the best system (10:1AuPd). This result could be associated with a faster consumption of heavy oil fraction in the active sites when increasing the system pressure [110–113]. As mentioned, DCO follows the same trend because higher energy is required to complete the decomposition of the oxygenated compounds. Nevertheless, due to the high mass loss during this region caused by the materials' catalytic activity, the E_a values for these systems are higher than for free asphaltenes. This increase is offset by the decrease in E_a for FC and SC events. Functionalized materials show the highest reduction in these thermal events related to the synergic effect between noble metals and ceria-zirconia support.

In all systems, both the chemical nature of the nanocatalyst and the system pressure changes the kinetic parameter values. For the case of pressure, it favors the global kinetic rate for *n*-C_7 asphaltene oxidation reactions, independently of the asphaltene source.

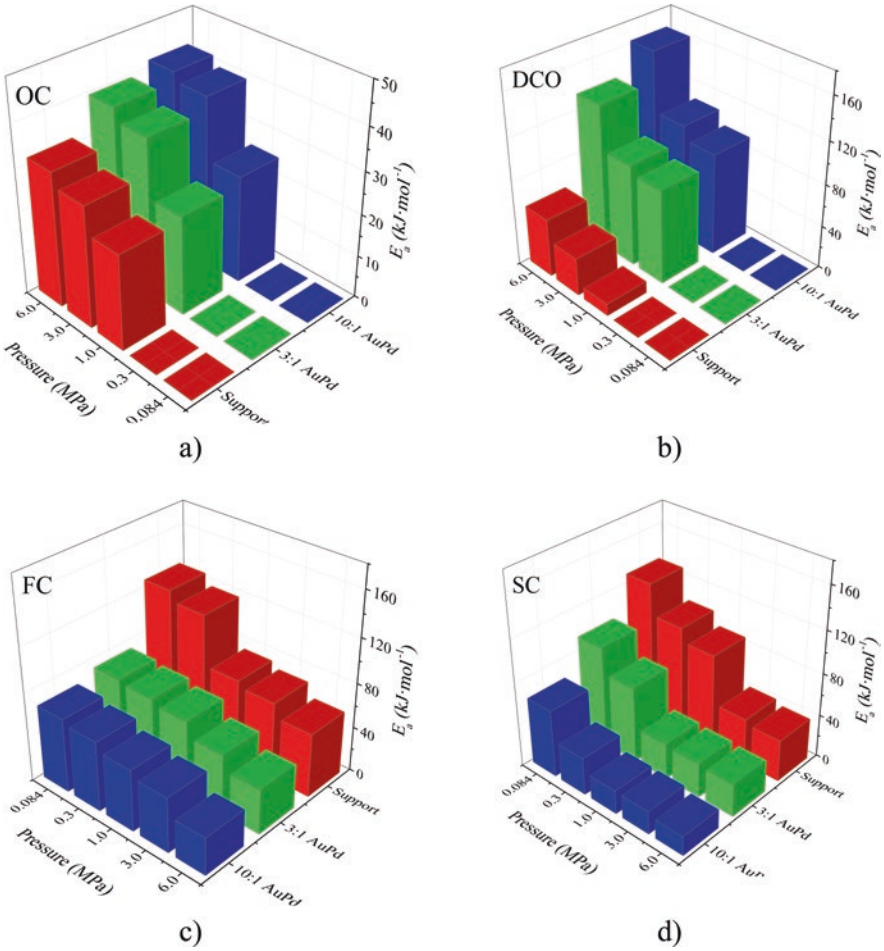

Fig. 5.12 Estimated effective activation energy for n-C_7 asphaltene oxidation with different nanocatalysts. Discretized in the different regions including (**a**) oxygen chemisorption (OC), (**b**) decomposition of the chemisorbed oxygen (DCO) region, (**c**) first combustion (FC) region, and (**d**) second combustion (SC) region. (Results are taken from Medina et al. [83])

5.7.5 Compensation Effect

5.7.5.1 Compensation Effect on N-C_7 Asphaltene Oxidation at Different Pressures

Figure 5.13 shows the experimentally measured effective activation energy (E_a) and ln(k_o) values for asphaltene oxidation discretized in different thermal regions known as oxygen chemisorption (OC), desorption of chemisorbed oxygen functional groups (DCO), first combustion (FC), and second combustion (SC), at pressures between 0.084 MPa and 7.0 MPa. A linear compensation effect (dotted line) was observed between E_a and ln(k_o). Standard deviations of 3.0%, 2.0%, 4.0%, and 5.0% were obtained for activation energy during OC, DCO, FC, and SC, respectively,

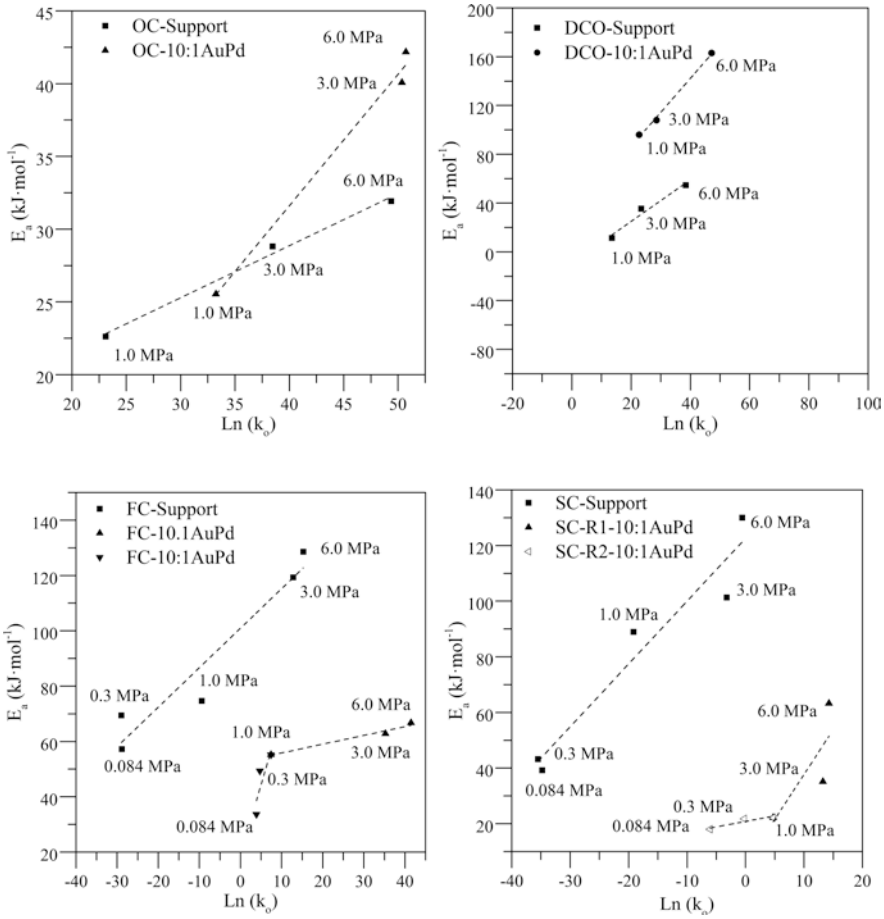

Fig. 5.13 Dependence of effective activation energy E_a on the logarithm of the Arrhenius pre-exponential factor k_o for asphaltene oxidation under different pressure conditions from 0.084 MPa to 7.0 MPa and different heating rates (HR) from 5°C·min^{-1} to 15°C·min^{-1}, divided into the four thermal events OC, DCO, FC, and SC. R# means the number of mechanisms of reaction to take control of each thermal event during asphaltene oxidation at different pressures

while ln(k_o) presents deviations lower than 3.0% in all regions. Many efforts have been made to explain several processes' thermodynamic compensation effect [114, 115]. It has been argued that large statistical uncertainties are associated with the nature of Arrhenius's law, due to the experimental determination of the kinetic parameters (i.e., E_a and k_o), and therefore, a compensatory effect is achieved [114, 116]. According to Fig. 5.1, the DCO, FC, and SC phenomena show a direct relationship between the E_a and ln(k_o) values. Unlike these, during OC, there is a variation in the linearity of this trend with the increase in pressure.

This result indicates that there are variations on the linear dependence of apparent activation energy and pre-exponential factor attributed to the number of ways in

which the heat can provide the energy needed to overcome the barrier to carry out the asphaltene oxidation at low temperatures with system pressure increases. This behavior indicates that entropy and enthalpy of activation are linearly related to each stage's activation energy, making evident the occurrence of a compensation effect in different stages [116]. In this zone, the oxidant's initiation likely proceeds by hydrogen abstraction, and the subsequent reaction of the asphaltene radicals can either lead to oxygen incorporation [117]. This corroborates the two mechanisms suggested by the compensation effect to carry out OC.

For the development of the DCO, FC, and SC regions, in the initial stage, the asphaltene decomposition was done along a reaction path with high activation energy and with relatively high negative values of ΔS^{T} due to the nature of the labile oxides in the new molecular (asphaltene*) oxygenated structure [118]. Therefore, there is a high value of k_o when E_a is high (i.e., for pressures >0.7 MPa). Although the same trend was observed in FC regarding DCO, lower activation energy values were obtained. During FC occurs the loss of aliphatic functional groups, dissociation of heteroatoms positioned in branched structures [119, 120], leading to a weaker interaction between the molecules and an almost unimolecular reaction with a relatively low ΔS^{T} negative value [118]. For low values of E_a, pre-exponential factor values are greatly reduced. At the end of this region, the asphaltene molecules change from a flaccid to a tight structure. Again, high E_a values are found, characteristic of the decomposition of the heaviest solid residue after the decomposition of the lightest groups in the asphaltene structure [120]. The increase of k_o makes a positive effect on the rate constant, compensated by the E_a increment, with a negative contribution to the rate constant.

5.7.5.2 Compensation Effect for Oxidation of N-C_7 Asphaltenes in the Presence of Nanocatalysts at Different Pressures

Figure 5.14 shows the effective activation energy as a function of $\ln(k_o)$ for asphaltene oxidation in the presence of support and AuPd-supported nanocatalysts between 0.084 MPa and 6.0 MPa. Results were presented according to the four thermal events that describe the asphaltene decomposition curves under high-pressure conditions. Throughout the results, it was identified as a linear correlation between the E_a values and $\ln(k_o)$ for a reaction developed at different pressures. This means that an increase of the reaction rate (i.e., the increment of the frequency factor) can be compensated with a rise in the E_a (and therefore reaction rate decrease), as system pressure changes. All experiments in which each nanocatalysts is involved fit to a single line with good correlation, suggesting that asphaltenes react under the same mechanism through the same intermediates as pressure is modified. However, between each nanocatalyst, two independent lines were obtained. In ceria-zirconia mixed oxide, oxygen chemisorption is controlled by oxygen activated by the functional groups of support and gas phase, known as lattice oxygen [121, 122]. Some research suggest that the main mechanism for asphaltene decomposition on ceria-based nanocatalysts is determined by the redox cycle (Ce^{4+}/Ce^{3+}) [51, 52, 123], and

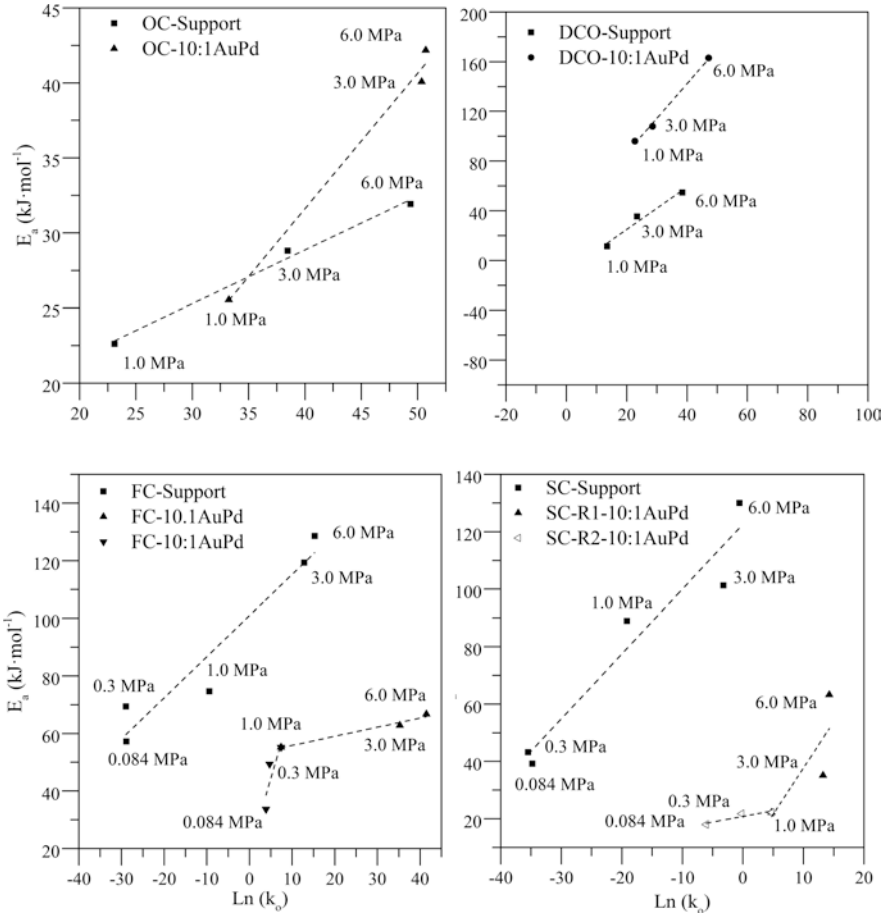

Fig. 5.14 Dependence of activation energy E_a on the logarithm of the pre-exponential factor k_o for the oxidation of nanoparticles containing asphaltenes under different pressure conditions from 0.084 MPa to 6.0 MPa, divided into the four thermal events OC, DCO, FC, and SC. R# means the number of mechanisms of reaction to take control in each thermal event during asphaltene oxidation at different pressures

the inclusion of isovalent and aliovalent Zr^{4+} on ceria fluorite structure improves the oxygen storage and hence the capability to reduce Ce^{4+} to Ce^{3+} [61, 105]. On the contrary, the incorporation of active phases of Pd and Au element oxides on the surface of ceria-zirconia mixed oxide modifies the asphaltene oxidation mechanism [124]. Oxygen chemisorption exists in the form of Au-O, Au = O, Au-O-Au, Pd = O, Pd-O-Pd, and Pd-O, being these phases more active and reactive for oxidation reactions [103, 104]. Compensation effect is attributed to the different activation energy associated with the heterogeneity of the surface, whose relative number is modified with pressure variations, also varying the adsorption capacity of reactants and products. These results show the importance of determining the structural complexity of

nanocatalysts for selective asphaltene oxidation. For example, the effective activation energy to create a surface oxygen vacancy in the upper oxygen layer of ceria-based materials is less on the surface of doped mixed oxide ($AuPd/Ce_{0.62}Zr_{0.38}O_2$) than it is on pure oxide.

DCO also shows that there are no changes in the global mechanism for asphaltene decomposition by varying the pressure as a linear dependency of activation energy against $\ln(k_o)$ was observed. Both variables vary in parallel ways. Nevertheless, according to the different chemical natures of each system, different reaction pathways are founded, following to the transition state theory (TST) for heterogeneous reactions [125, 126]. TST suggests that the concentration of the active sites plays a key role in the rate constant, showing a direct relationship. Hence, the changes in activation energy have been attributed to enthalpies' founded modifications on the different surfaces provided by Au, Pd, Ce, and Zr element oxides. For combustion FC and SC regions, two different pathways were found for 10:1AuPd nanocatalysts due to the heterogeneous surface and the different catalytic powers of each phase. At low pressures, there is another mechanism for asphaltene decomposition than at high pressures. This result corroborates the hypothesis that during OC the asphaltene structure is modified and its reactivity changes.

The addition of nanocatalysts does not change the trend of k_o and E_a during combustion zones. High values of the pre-exponential factor imply high values of effective activation energy. During FC, decomposition of groups occurs after the detachment of the oxygen groups in DCO, which are not as heavy as those that decompose in SC. This event is associated with low negatives values for ΔS^{T}. The opposite behavior is observed in SC, with the highest values for k_o and E_a. Hence, the change in compensation effect suggests a change in reaction mechanism, which strongly depends on the physicochemical properties of the nanocatalysts.

5.8 Conclusion

This work was focused on understanding the effect of pressure over the thermo-oxidation behavior of asphaltenes with and without nanocatalyst. Both thermo-oxidation and thermocatalytic oxidation of asphaltene showed a direct dependence on the system temperature and pressure. Unlike the results at low pressure, asphaltenes undergo marked oxidation at low temperatures when the system pressure is greater than 0.7 MPa and 1.0 MPa for virgin and adsorbed asphaltenes, respectively. The effective activation energy values using $AuPd/Ce_{0.62}Zr_{0.38}O_2$ nanocatalyst was reduced by more than 30% for all the pressures evaluated. Moreover, according to the distributed activation energy models, the decomposition of asphaltenes occurs in several simultaneous reactions of order n = 1 due to the multiple mechanisms involved in asphaltene oxidation/decomposition and molecular complexity.

Besides, it was found that the pressure follows the compensation effect for asphaltene mass loss in the presence and absence of nanocatalysts. Oxygen

chemisorption, a dominant event at high pressures and low temperatures, follows two different reaction mechanisms: hydrogen abstraction and free radical reactions. In the case of nanocatalysts, it has been suggested that the distribution of active sites with varying reactivity could explain the compensation effect. Here, it was found that each catalyst follows a global reaction mechanism as the pressure is changed. Despite that the asphaltene oxidation in the presence and absence of nanocatalysts follows the compensation effect with changes in the system pressure, a marked change in the OC region was observed, where the reaction pathway goes from two global mechanisms to one for the *n*-C_7 asphaltenes with and without nanocatalyst, respectively.

Compensation effect plots are useful to evaluate if the reaction pathway is changing by the change of any experimental variable, such as T, P, catalyst, and the molecular structure of the reagents (asphaltenes for this case), among others.

Acknowledgments The authors would like to acknowledge the Universidad Nacional de Colombia for their financial and logistical support.

References

1. O.E. Medina Erao, J. Gallego, C.M. Olmos, X. Chen, F.B. Cortés, C.A. Franco, Effect of multifunctional Nanocatalysts on n-C7 Asphaltene adsorption and subsequent oxidation under high pressure conditions. Energy Fuel (2020)
2. D.W. Green, G.P. Willhite, *Enhanced oil recovery* vol. 6: Henry L. Doherty Memorial Fund of AIME, Society of Petroleum Engineers Richardson, TX, (1998)
3. S. Thomas, Enhanced oil recovery-an overview. Oil & Gas Science and Technology-Revue de l'IFP **63**, 9–19 (2008)
4. T. Nasr, G. Beaulieu, H. Golbeck, G. Heck, Novel expanding solvent-SAGD process "ES-SAGD", in *Canadian International Petroleum Conference*, (2002)
5. P.A. Govind, S.K. Das, S. Srinivasan, T.J. Wheeler, Expanding solvent SAGD in heavy oil reservoirs, in *International Thermal Operations and Heavy Oil Symposium*, (2008)
6. A.-Y. Huc, *Heavy crude oils: from geology to upgrading: an overview*. Editions Technip, (2010)
7. X.-G. Dong, Q.-F. Lei, W.-J. Fang, Q.-S. Yu, Thermogravimetric analysis of petroleum asphaltenes along with estimation of average chemical structure by nuclear magnetic resonance spectroscopy. Thermochim. Acta **427**, 149–153 (2005)
8. P. Murugan, T. Mani, N. Mahinpey, K. Asghari, The low temperature oxidation of Fosterton asphaltenes and its combustion kinetics. Fuel Process. Technol. **92**, 1056–1061 (2011)
9. N.P. Freitag, Chemical-reaction mechanisms that govern oxidation rates during in-situ combustion and high-pressure air injection. SPE Reserv. Eval. Eng. **19**, 645–654 (2016)
10. X. Zhang, Q. Liu, Z. Fan, Enhanced in situ combustion of heavy crude oil by nickel oxide nanoparticles. Int. J. Energy Res. **43**, 3399–3412 (2019)
11. N.N. Nassar, A. Hassan, P. Pereira-Almao, Clarifying the catalytic role of NiO nanoparticles in the oxidation of asphaltenes. Appl. Catal. A Gen. **462**, 116–120 (2013)
12. M.M. Husein, S.J. Alkhaldi, In situ preparation of alumina nanoparticles in heavy oil and their thermal cracking performance. Energy Fuel **28**, 6563–6569 (2014)
13. F. Amin, A study on the adsorption and catalytic oxidation of Asphaltene onto nanoparticles. J. Pet. Sci. Technol. **7**, 21–29 (2017)

14. A. Amrollahi Biyouki, N. Hosseinpour, N.N. Nassar, Pyrolysis and oxidation of Asphaltene-born coke-like residue formed onto in situ prepared NiO nanoparticles toward advanced in situ combustion enhanced oil recovery processes. Energy Fuel **32**, 5033–5044 (2018)
15. A.A. Akhmadiyarov, I.T. Rakipov, A.A. Khachatrian, A.A. Petrov, S.A. Sitnov, A.V. Gerasimov, et al., Thermocatalytic upgrading of heavy oil by iron oxides nanoparticles synthesized by oil-soluble precursors. J. Pet. Sci. Eng. **169**, 200–204 (2018)
16. C.A. Franco, T. Montoya, N.N. Nassar, P. Pereira-Almao, F.B. Cortés, Adsorption and subsequent oxidation of colombian asphaltenes onto nickel and/or palladium oxide supported on fumed silica nanoparticles. Energy Fuel **27**, 7336–7347 (2013)
17. J. Barillas, T.D. Júnior, W. Mata, Improved oil recovery process for heavy oil: A review. Brazilian Journal of Petroleum and Gás **2** (2008)
18. J. Burger, P. Sourieau, M. Combarnous, H.J. Ramey, *Thermal methods of oil recovery*: Gulf Publishing Company, Book Division, (1985)
19. J. Alvarez, S. Han, Current overview of cyclic steam injection process. Journal of Petroleum Science Research **2** (2013)
20. P.S. Sarathi and D.K. Olsen, Practical aspects of steam injection processes: A handbook for independent operators, National Inst. for Petroleum and Energy Research, Bartlesville, OK, (1992)
21. M. Cokar, I.D. Gates, M.S. Kallos, Reservoir simulation of steam fracturing in early-cycle cyclic steam stimulation. SPE Reserv. Eval. Eng. **15**, 676–687 (2012)
22. Q. Jiang, B. Thornton, J. Russel-Houston, S. Spence, Review of thermal recovery technologies for the Clearwater and lower grand rapids formations in the cold lake area in Alberta. J. Can. Pet. Technol. **49**, 2–13 (2010)
23. R. Butler, C. Yee, Progress in the in situ recovery of heavy oils and bitumen. J. Can. Pet. Technol. **41** (2002)
24. J.C. de Souza Jr, D.F. Cursino, K.G. Padua, Twenty Years of Vapor Injection in Heavy-Oil Fields, in *SPE Latin American and Caribbean Petroleum Engineering Conference*, (2005)
25. E. Hanzlik, D. Mims, Forty years of steam injection in California-The evolution of heat management, in *SPE International Improved Oil Recovery Conference in Asia Pacific*, (2003)
26. D.W. Zhao, J. Wang, I.D. Gates, Thermal recovery strategies for thin heavy oil reservoirs. Fuel **117**, 431–441 (2014)
27. D.W. Zhao, J. Wang, I.D. Gates, An evaluation of enhanced oil recovery strategies for a heavy oil reservoir after cold production with sand. Int. J. Energy Res. **39**, 1355–1365 (2015)
28. A.J. Rosa, R. de Souza Carvalho, J.A.D. Xavier, *Engenharia de reservatórios de petróleo*: Interciência, (2006)
29. R. Butler, A new approach to the modelling of steam-assisted gravity drainage. J. Can. Pet. Technol. **24**, 42–51 (1985)
30. R. Butler, D. Stephens, The gravity drainage of steam-heated heavy oil to parallel horizontal wells. J. Can. Pet. Technol. **20** (1981)
31. L. Yang, D.-S. Zhou, Y.-h. Sun, SAGD as follow-up to cyclic steam stimulation in a medium deep and extra heavy oil reservoir, in *International Oil & Gas Conference and Exhibition in China*, (2006)
32. J. Jimenez, The field performance of SAGD projects in Canada, in *International petroleum technology conference*, (2008)
33. I. Gates, N. Chakrabarty, Optimization of steam-assisted gravity drainage in McMurray reservoir, in *Canadian International Petroleum Conference*, (2005)
34. S. Akin, S. Bagci, A laboratory study of single-well steam-assisted gravity drainage process. J. Pet. Sci. Eng. **32**, 23–33 (2001)
35. V. Alvarado, E. Manrique, Enhanced oil recovery: An update review. Energies **3**, 1529–1575 (2010)
36. C. Chu, A study of fireflood field projects (includes associated paper 6504). J. Pet. Technol. **29**, 111–120 (1977)

37. C. Cheih, State-of-the-art review of fireflood field projects (includes associated papers 10901 and 10918). J. Pet. Technol. **34**, 19–36 (1982)
38. A. Turta, S. Chattopadhyay, R. Bhattacharya, A. Condrachi, W. Hanson, Current status of commercial in situ combustion projects worldwide. J. Can. Pet. Technol. **46** (2007)
39. C. Wu, P. Fulton, Experimental simulation of the zones preceding the combustion front of an in-situ combustion process. Soc. Pet. Eng. J. **11**, 38–46 (1971)
40. L. Castanier, W. Brigham, Upgrading of crude oil via in situ combustion. J. Pet. Sci. Eng. **39**, 125–136 (2003)
41. N. Mahinpey, A. Ambalae, K. Asghari, In situ combustion in enhanced oil recovery (EOR): A review. Chem. Eng. Commun. **194**, 995–1021 (2007)
42. A.I. El-Diasty, A.M. Aly, Understanding the mechanism of nanoparticles applications in enhanced oil recovery, in *SPE North Africa Technical Conference and Exhibition*, (2015)
43. C.A. Franco, N.N. Nassar, M.A. Ruiz, P. Pereira-Almao, F.B. Cortés, Nanoparticles for inhibition of asphaltenes damage: Adsorption study and displacement test on porous media. Energy Fuel **27**, 2899–2907 (2013)
44. S. Mokhatab, M.A. Fresky, M.R. Islam, Applications of nanotechnology in oil and gas E&P. J. Pet. Technol. **58**, 48–51 (2006)
45. A.I. El-Diasty, A.M.S. Ragab, Applications of nanotechnology in the oil & gas industry: Latest trends worldwide & future challenges in Egypt, in *North Africa Technical Conference and Exhibition*, (2013)
46. F. Ariza, C. Andrés, Synthesis and application of supported metallic and multi-metallic oxides nanoparticles for in-situ upgrading and inhibition of formation damage, Ph.D. Thesis, Universidad Nacional de Colombia-Sede Medellín, Online, (2015)
47. N.N. Nassar, C.A. Franco, T. Montoya, F.B. Cortés, A. Hassan, Effect of oxide support on Ni–Pd bimetallic nanocatalysts for steam gasification of n-C7 asphaltenes. Fuel **156**, 110–120 (2015)
48. D. López, L.J. Giraldo, J.P. Salazar, D.M. Zapata, D.C. Ortega, C.A. Franco, et al., Metal oxide nanoparticles supported on macro-mesoporous Aluminosilicates for catalytic steam gasification of heavy oil fractions for on-site upgrading. Catalysts **7**, 319 (2017)
49. T. Montoya, B.L. Argel, N.N. Nassar, C.A. Franco, F.B. Cortés, Kinetics and mechanisms of the catalytic thermal cracking of asphaltenes adsorbed on supported nanoparticles. Pet. Sci. **13**, 561–571 (2016)
50. O.E. Medina, J. Gallego, D. Arias-Madrid, F.B. Cortés, C.A. Franco, Optimization of the load of transition metal oxides (Fe2O3, Co3O4, NiO and/or PdO) onto CeO2 nanoparticles in catalytic steam decomposition of n-C7 Asphaltenes at low temperatures. Nano **9**, 401 (2019)
51. O.E. Medina, J. Gallego, L.G. Restrepo, F.B. Cortés, C.A. Franco, Influence of the Ce4+/Ce3+ redox-couple on the cyclic regeneration for adsorptive and catalytic performance of NiO-PdO/CeO2±δ nanoparticles for n-C7 asphaltene steam gasification. Nano **9**, 734 (2019)
52. O.E. Medina, Y. Hurtado, C. Caro-Velez, F.B. Cortés, M. Riazi, S.H. Lopera, et al., Improvement of steam injection processes through nanotechnology: An approach through in situ upgrading and foam injection. Energies **12**, 4633 (2019)
53. C. Franco, E. Patiño, P. Benjumea, M.A. Ruiz, F.B. Cortés, Kinetic and thermodynamic equilibrium of asphaltenes sorption onto nanoparticles of nickel oxide supported on nanoparticulated alumina. Fuel **105**, 408–414 (2013)
54. L. Cardona Rojas, Efecto de nanopartículas en procesos con inyección de vapor a diferentes calidades, Msc Magister Thesis, Universidad Nacional de Colombia-Sede Medellín, Online, 2018
55. N.N. Nassar, A. Hassan, P. Pereira-Almao, Comparative oxidation of adsorbed asphaltenes onto transition metal oxide nanoparticles. Colloids Surf. A Physicochem. Eng. Asp. **384**, 145–149 (2011)
56. N.N. Nassar, A. Hassan, P. Pereira-Almao, Effect of surface acidity and basicity of aluminas on asphaltene adsorption and oxidation. J. Colloid Interface Sci. **360**, 233–238 (2011)

57. N.N. Nassar, A. Hassan, L. Carbognani, F. Lopez-Linares, P. Pereira-Almao, Iron oxide nanoparticles for rapid adsorption and enhanced catalytic oxidation of thermally cracked asphaltenes. Fuel **95**, 257–262 (2012)
58. N.N. Nassar, A. Hassan, G. Vitale, Comparing kinetics and mechanism of adsorption and thermo-oxidative decomposition of Athabasca asphaltenes onto TiO2, ZrO2, and CeO2 nanoparticles. Appl. Catal. A Gen. **484**, 161–171 (2014)
59. C.A. Franco, M.M. Lozano, S. Acevedo, N.N. Nassar, F.B. Cortés, Effects of resin I on Asphaltene adsorption onto nanoparticles: A novel method for obtaining asphaltenes/resin isotherms. Energy Fuel **30**, 264–272 (2015)
60. M.M. Lozano, C.A. Franco, S.A. Acevedo, N.N. Nassar, F.B. Cortés, Effects of resin I on the catalytic oxidation of n-C 7 asphaltenes in the presence of silica-based nanoparticles. RSC Adv. **6**, 74630–74642 (2016)
61. C.M. Olmos, L.E. Chinchilla, J.J. Delgado, A.B. Hungría, G. Blanco, J.J. Calvino, et al., CO oxidation over bimetallic au–Pd supported on ceria–zirconia catalysts: Effects of oxidation temperature and au: Pd molar ratio. Catal. Lett. **146**, 144–156 (2016)
62. L. Barre, D. Espinat, E. Rosenberg, M. Scarsella, Colloidal structure of heavy crudes and asphaltene solutions. Revue de l'Institut Français du Pétrole **52**, 161–175 (1997)
63. A. International, ASTM D5236–13, Standard Test Method for Distillation of Heavy Hydrocarbon Mixtures (Vacuum Potstill Method), *Annual Book of ASTM Standards,* (2013)
64. A. International, ASTM D2892, Standard Test Method for Distillation of Crude Petroleum (15-Theoretical Plate Column), *Annual Book of ASTM Standards,* (2016)
65. S.M. Lopes, P. Geng, Estimation of elemental composition of diesel fuel containing biodiesel. SAE International Journal of Fuels and Lubricants **6**, 668–676 (2013)
66. S. Acevedo, J. Castillo, V. Vargas, A. Castro, O.Z. Delgado, C.A.F. Ariza, et al., Suppression of phase separation as a hypothesis to account for nuclei or nanoaggregate formation by Asphaltenes in toluene. Energy Fuel (2018)
67. O.E. Medina, J. Gallego, N.N. Nassar, S.A. Acevedo, F.B. Cortés, C.A. Franco, Thermo-oxidative decomposition Behaviors of different sources of n-C7 Asphaltenes at high-pressure conditions. Energy Fuel (2020)
68. C. Lee, W. Yang, R.G. Parr, Results obtained with the correlation energy density functionals. Phys. Rev. B: Condens. Matter Mater. Phys **37**, 785 (1988)
69. H.L. Schmider, A.D. Becke, Optimized density functionals from the extended G2 test set. J. Chem. Phys. **108**, 9624–9631 (1998)
70. O.C. Mullins, Optical interrogation of aromatic moieties in crude oils and Asphaltenes, in *Structures and Dynamics of Asphaltenes*, ed. by O. C. Mullins, E. Y. Sheu, (Springer, Boston, MA, 1998). https://doi.org/10.1007/978-1-4899-1615-0_2
71. S. Goncalves, J. Castillo, A. Fernandez, J. Hung, Absorbance and fluorescence spectroscopy on the aggregation behavior of asphaltene–toluene solutions. Fuel **83**, 1823–1828 (2004)
72. N.N. Nassar, A. Hassan, P. Pereira-Almao, Application of nanotechnology for heavy oil upgrading: Catalytic steam gasification/cracking of asphaltenes. Energy Fuel **25**, 1566–1570 (2011)
73. O.E. Medina, J. Gallego, E. Rodríguez, C.A. Franco, F.B. Cortés, Effect of pressure on the oxidation kinetics of Asphaltenes. Energy Fuel **33**, 10734–10744 (2019)
74. O. Talu, F. Meunier, Adsorption of associating molecules in micropores and application to water on carbon. AICHE J. **42**, 809–819 (1996)
75. T. Montoya, D. Coral, C.A. Franco, N.N. Nassar, F.B. Cortés, A novel solid–liquid equilibrium model for describing the adsorption of associating asphaltene molecules onto solid surfaces based on the "chemical theory". Energy Fuel **28**, 4963–4975 (2014)
76. G.-S. Liu, S. Niksa, Coal conversion submodels for design applications at elevated pressures. Part II. Char gasification. Prog. Energy Combust. Sci. **30**, 679–717 (2004)
77. P. Schneider, Adsorption isotherms of microporous-mesoporous solids revisited. Appl. Catal. A Gen. **129**, 157–165 (1995)

78. M. Kurian, C. Kunjachan, Effect of lattice distortion on physical properties and surface morphology of nanoceria framework with incorporation of iron/zirconium. Nano-Structures & Nano-Objects **1**, 15–23 (2015)
79. A.E.E. Shilov, *Activation of Saturated Hydrocarbons by Transition Metal Complexes*, vol 5 (Springer Science & Business Media, 1984)
80. C.A. Franco-Ariza, J.D. Guzmán-Calle, F.B. Cortés-Correa, Adsorption and catalytic oxidation of asphaltenes in fumed silica nanoparticles: Effect of the surface acidity. Dyna **83**, 171–179 (2016)
81. F.B. Cortés, T. Montoya, S. Acevedo, N.N. Nassar, C.A. Franco, Adsorption-desorption of n-c7 asphaltenes over micro-and nanoparticles of silica and its impact on wettability alteration. CT&F-Ciencia, Tecnología y Futuro **6**, 89–106 (2016)
82. C.A. Franco, T. Montoya, N.N. Nassar, F.B. Cortés, NiO and PdO supported on Fumed silica nanoparticles for adsorption and catalytic steam gasification of Colombian n-C7 Asphaltenes. Handbook on Oil Production Research **26**, 101–145 (2014)
83. O.E. Medina, J. Gallego, C.M. Olmos, X. Chen, F.B. Cortés, C.A. Franco, Effect of multifunctional nanocatalysts on n-C7 Asphaltene adsorption and subsequent oxidation under high-pressure conditions. Energy & Fuels (2020) 2020/03/29
84. N.N. Nassar, A. Hassan, G. Luna, P. Pereira-Almao, Kinetics of the catalytic thermo-oxidation of asphaltenes at isothermal conditions on different metal oxide nanoparticle surfaces. Catal. Today **207**, 127–132 (2013)
85. O. Sonibare, R. Egashira, T. Adedosu, Thermo-oxidative reactions of Nigerian oil sand bitumen. Thermochim. Acta **405**, 195–205 (2003)
86. P. Murugan, N. Mahinpey, T. Mani, Thermal cracking and combustion kinetics of asphaltenes derived from Fosterton oil. Fuel Process. Technol. **90**, 1286–1291 (2009)
87. P.R. Herrington, Effect of concentration on the rate of reaction of asphaltenes with oxygen. Energy Fuel **18**, 1573–1577 (2004)
88. N. Hosseinpour, Y. Mortazavi, A. Bahramian, L. Khodatars, A.A. Khodadadi, Enhanced pyrolysis and oxidation of asphaltenes adsorbed onto transition metal oxides nanoparticles towards advanced in-situ combustion EOR processes by nanotechnology. Appl. Catal. A Gen. **477**, 159–171 (2014)
89. P. Hänggi, P. Talkner, M. Borkovec, Reaction-rate theory: Fifty years after Kramers. Rev. Mod. Phys. **62**, 251 (1990)
90. B.J. Berne, M. Borkovec, J.E. Straub, Classical and modern methods in reaction rate theory. J. Phys. Chem. **92**, 3711–3725 (1988)
91. O.E. Medina, J. Gallego, E. Rodriguez, C.A. Franco, F.B. Cortés, Effect of pressure on the oxidation kinetics of Asphaltenes. Energy Fuel (2019)
92. N.M. Sánchez, A. de Klerk, Low-temperature oxidative asphaltenes liquefaction for petrochemicals: Fact or fiction? Appl. Petrochem. Res. **6**, 97–106 (2016)
93. M. Gonçalves, M. Teixeira, R. Pereira, R. Mercury, J.D.R. Matos, Contribution of thermal analysis for characterization of asphaltenes from Brazilian crude oil. J. Therm. Anal. Calorim. **64**, 697–706 (2001)
94. D. Kuakpetoon, Y.-J. Wang, Structural characteristics and physicochemical properties of oxidized corn starches varying in amylose content. Carbohydr. Res. **341**, 1896–1915 (2006)
95. B.E. Ascanius, D.M. Garcia, S.I. Andersen, Analysis of asphaltenes subfractionated by N-methyl-2-pyrrolidone. Energy Fuel **18**, 1827–1831 (2004)
96. Y.B. Bava, M. Geronés, L.J. Giovanetti, L. Andrini, M.F. Erben, Speciation of Sulphur in asphaltenes and resins from Argentinian petroleum by using XANES spectroscopy. Fuel **256**, 115952 (2019)
97. F.S. AlHumaidan, A. Hauser, M.S. Rana, H.M. Lababidi, NMR characterization of Asphaltene derived from residual oils and their thermal decomposition. Energy Fuel **31**, 3812–3820 (2017)
98. O.C. Mullins, The modified yen model. Energy Fuel **24**, 2179–2207 (2010)

99. N.T. Nguyen, K.H. Kang, C.W. Lee, G.T. Kim, S. Park, Y.-K. Park, Structure comparison of asphaltene aggregates from hydrothermal and catalytic hydrothermal cracking of C5-isolated asphaltene. Fuel **235**, 677–686 (2019)
100. I. Fernandez, G. Frenking, Direct estimate of conjugation and aromaticity in cyclic compounds with the EDA method. Faraday Discuss. **135**, 403–421 (2007)
101. A. Martínez-Arias, M. Fernández-García, C. Belver, J. Conesa, J. Soria, EPR study on oxygen handling properties of ceria, zirconia and Zr–Ce (1: 1) mixed oxide samples. Catal. Lett. **65**, 197–204 (2000)
102. O.E. Medina, C. Olmos, S.H. Lopera, F.B. Cortés, C.A. Franco, Nanotechnology applied to thermal enhanced oil recovery processes: A review. Energies **12**, 4671 (2019)
103. C.M. Olmos, L.E. Chinchilla, E.G. Rodrigues, J.J. Delgado, A.B. Hungría, G. Blanco, et al., Synergistic effect of bimetallic au-Pd supported on ceria-zirconia mixed oxide catalysts for selective oxidation of glycerol. Appl. Catal. B Environ. **197**, 222–235 (2016)
104. U.S. Ozkan, R.B. Watson, The structure–function relationships in selective oxidation reactions over metal oxides. Catal. Today **100**, 101–114 (2005)
105. C.F. Zinola, Carbon monoxide oxidation assisted by interfacial oxygen-water layers. J. Solid State Electrochem. **23**, 883–901 (2019)
106. O. Senneca, N. Vorobiev, A. Wütscher, F. Cerciello, S. Heuer, C. Wedler, et al., Assessment of combustion rates of coal chars for oxy-combustion applications. Fuel **238**, 173–185 (2019)
107. S. Niksa, G.-S. Liu, R.H. Hurt, Coal conversion submodels for design applications at elevated pressures. Part I. devolatilization and char oxidation. Prog. Energy Combust. Sci. **29**, 425–477 (2003)
108. A. Zahabi, M.R. Gray, T. Dabros, Kinetics and properties of asphaltene adsorption on surfaces. Energy Fuel **26**, 1009–1018 (2012)
109. V. Calemma, P. Iwanski, M. Nali, R. Scotti, L. Montanari, Structural characterization of asphaltenes of different origins. Energy Fuel **9**, 225–230 (1995)
110. G. Duffy, L. Morpeth, A. Cousins, D. Roberts, J. Edwards, Investigation of the effect of total pressure on performance of the catalytic water–gas shift reaction using simulated coal-derived syngases. Catal. Commun. **11**, 272–275 (2009)
111. G. Chinchen, R. Logan, M. Spencer, Water-gas shift reaction over an iron oxide/chromium oxide catalyst.: II: Stability of activity. Appl. Catal. **12**, 89–96 (1984)
112. G. Chinchen, R. Logan, M. Spencer, Water-gas shift reaction over an iron oxide/chromium oxide catalyst.: I: Mass transport effects. Appl. Catal. **12**, 69–88 (1984)
113. K. Atwood, M. Arnold, E. Appel, Water-gas shift reaction. Effect of pressure on rate over an Iron-oxide-chromium oxide catalyst. Industrial & Engineering Chemistry **42**, 1600–1602 (1950)
114. C.A. Bennett, R.S. Kistler, K. Nangia, W. Al-Ghawas, N. Al-Hajji, A. Al-Jemaz, Observation of an isokinetic temperature and compensation effect for high-temperature crude oil fouling. Heat Transfer Engineering **30**, 794–804 (2009)
115. A.K. Galwey, M. Mortimer, Compensation effects and compensation defects in kinetic and mechanistic interpretations of heterogeneous chemical reactions. Int. J. Chem. Kinet. **38**, 464–473 (2006)
116. G. Gottstein, L. Shvindlerman, The compensation effect in thermally activated interface processes. Interface Science **6**, 267–278 (1998)
117. R. Javadli, A. de Klerk, Desulfurization of heavy oil–oxidative desulfurization (ODS) as potential upgrading pathway for oil sands derived bitumen. Energy Fuel **26**, 594–602 (2012)
118. K. Czajka, A. Kisiela, W. Moroń, W. Ferens, W. Rybak, Pyrolysis of solid fuels: Thermochemical behaviour, kinetics and compensation effect. Fuel Process. Technol. **142**, 42–53 (2016)
119. B. Wei, P. Zou, X. Zhang, X. Xu, C. Wood, Y. Li, Investigations of structure–property–thermal degradation kinetics alterations of Tahe Asphaltenes caused by low temperature oxidation. Energy Fuel **32**, 1506–1514 (2018)

120. W. Zijun, L. Wenjie, Q. Guohe, Q. Jialin, Structural characterization of gudao asphaltene by ruthenium ion catalyzed oxidation. Pet. Sci. Technol. **15**, 559–577 (1997)
121. C. Li, Q. Xin, Spillover and migration of surface species on catalysts, in *Proceedings of the 4th International Conference on Spillover*, (1997), p. 18
122. K. Fujimoto, Catalyst design based on spillover theory, in *Studies in Surface Science and Catalysis*, vol. 77, (Elsevier, 1993), pp. 9–16
123. O.E. Medina, C. Caro-Vélez, J. Gallego, F.B. Cortés, S.H. Lopera, C.A. Franco, Upgrading of extra-heavy crude oils by dispersed injection of NiO–PdO/CeO2±δ Nanocatalyst-based Nanofluids in the steam. Nano **9**, 1755 (2019)
124. F. Buciuman, F. Patcas, T. Hahn, A spillover approach to oxidation catalysis over copper and manganese mixed oxides. Chem. Eng. Process. Process Intensif. **38**, 563–569 (1999)
125. J.R. Alvarez-Idaboy, N. Mora-Diez, A. Vivier-Bunge, A quantum chemical and classical transition state theory explanation of negative activation energies in OH addition to substituted ethenes. J. Am. Chem. Soc. **122**, 3715–3720 (2000)
126. W.C. Conner Jr., A general explanation for the compensation effect: The relationship between ΔS‡ and activation energy. J. Catal. **78**, 238–246 (1982)

Chapter 6
Nanoparticles for Heavy Oil Upgrading

Sefatallah Ashoorian, Tatiana Montoya, and Nashaat N. Nassar

6.1 Introduction

The worldwide demand for energy has been steadily growing during the past decades. The latest published energy outlooks revealed that oil is still the paramount source of energy supply in the near future. Due to the depletion of conventional oil reservoirs and the soaring global demand for energy in recent years, unconventional oil reservoirs have become more attractive and gained interest from researchers and oil companies. However, due to their nature, these resources are hard to extract, process, and transport. Their exploitation process is both high-energy and water-intensive and also has considerable environmental footprints. Furthermore, these resources themselves usually contain components that have unfavorable environmental impacts. Also, these crudes do not meet the pipeline criteria and therefore need to be upgraded to be suitable for pipeline specifications. In situ upgrading is one promising method for recovering these reservoirs. In contrast to surface upgrading, it needs lower financial investment and substantially reduces the environmental hazard related to surface upgrading processes.

Due to the advances occurred in the field of nanotechnology in recent years, these methods have been utilized for heavy oil and bitumen in situ upgrading. One great example of these methods is the application of ultradispersed (UD) nanocatalysts for in situ upgrading of heavy oils and bitumen. Due to their exceptionally high surface area-to-volume ratio and active surface sites, UD nanocatalysts exhibit a

S. Ashoorian
Institute of Petroleum Engineering, School of Chemical Engineering, College of Engineering, University of Tehran, Tehran, Iran

T. Montoya · N. N. Nassar (✉)
Department of Chemical and Petroleum Engineering, University of Calgary, Calgary, Canada
e-mail: nassar@ucalgary.ca

N. N. Nassar et al. (eds.), *Nanoparticles: An Emerging Technology for Oil Production and Processing Applications*, Lecture Notes in Nanoscale Science and Technology, https://doi.org/10.1007/978-3-319-12051-5_6

unique catalytic and sorption properties. The use of UD nanocatalysts is a cost-effective and environmentally friendly method for recovering and upgrading unconventional reservoirs. Furthermore, these materials can also be used to inhibit or delay asphaltene precipitation, resulting in further oil recovery. However, similar to any other new technology, several challenges and problems are facing the nanoparticle application in the in situ upgrading process.

In this chapter, the recent advances in the field of UD nanocatalysts will be presented. Different aspects of the topic along with potential challenges and opportunities will be discussed. To this end first, a brief review of the current EOR method for heavy oil and bitumen recovery will be described. Next, the UD nanoparticle synthesis and application will be explained. H-donors will be reviewed next. Then the effect of nanocatalysts on the yielded liquid quality will be introduced. Different parameters like variations in crude viscosity, API, and sulfur content upon catalytic upgrading will be presented. After that nanocatalyst transport behavior in the porous media will be explained, followed by modeling the reaction kinetics of the in situ upgrading process. Finally, some issues related to nanoparticle recyclability and their environmental effect will be discussed.

6.2 The Current Enhanced Oil Recovery Processes

It is estimated that nearly 2.0*1012 of conventional crude oil and 5.0*1012 barrels of heavy oil will remain underground after natural depletion and utilizing the conventional production methods [1]. Enhanced oil recovery (EOR) methods aim to recover this portion of hydrocarbon reservoirs. Typically, EOR processes fall into three categories: thermal recovery, chemical flooding, and miscible displacement methods [2]. Although some researchers consider microbial EOR as a fourth branch, it has not been widely recognized since it has been rarely used in the field.

As a rule, thermal methods are suitable for high-viscosity crudes like heavy oil and bitumen, while chemical and miscible methods are preferred for lighter hydrocarbons like conventional oil. However, the choice of an EOR method depends on a variety of factors like geological characteristics, fluid property, and financial parameters which help the engineers decide on an optimum scenario.

6.3 Thermal EOR Methods

Since the recovery and upgrading of heavy oil and bitumen are the main topics of this book, a brief review of thermal EOR is presented in this section as it is the most prevalent EOR technique for such reservoirs. Thermal EOR has been used for more than 70 years ago and is known as the most sophisticated process to produce crude oil [1]. The best candidates for thermal EOR are mostly heavy oils (10–20° API) and tar sands ($\leq 10^{\circ} API$). Viscosity reduction can be regarded as the most important

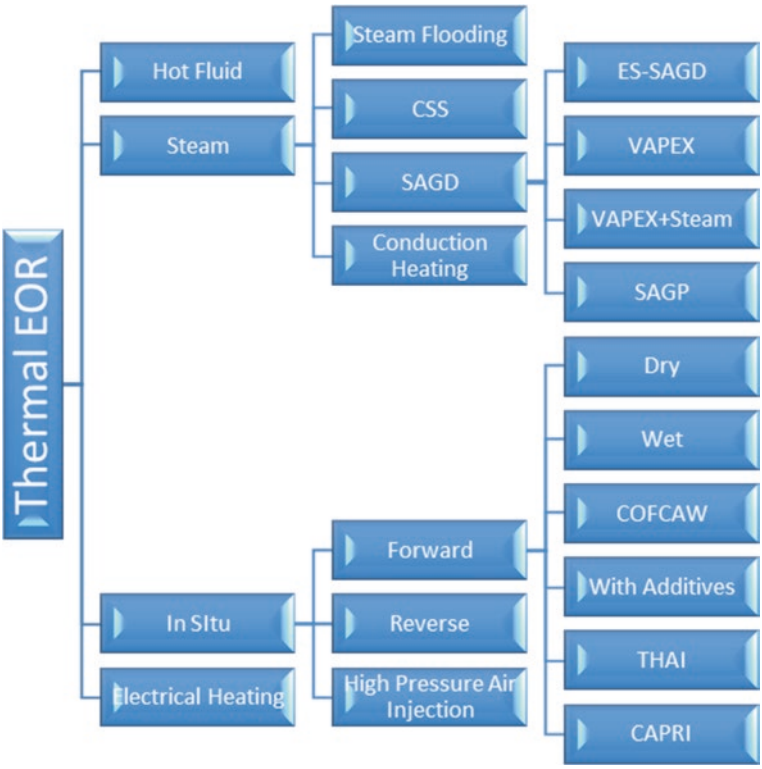

Fig. 6.1 Different thermal EOR methods

mechanism to produce heavy crudes in this technique; however, there are other active mechanisms like rock and fluid expansion, steam distillation, and visbreaking. Figure 6.1 shows currently used thermal methods. Thermal EOR generally falls into four categories: hot fluid injection, steam-based methods, in situ operations, and electrical heating. Each of these methods has its own advantages and disadvantages. Furthermore, it is noteworthy to mention that not all these techniques apply to a particular reservoir and their implementation relies on different factors like technical and financial parameters. In the following section, these methods are briefly presented.

6.3.1 Hot Fluid Injection

Hot fluid injection techniques refer to methods in which a preheated fluid – usually water – is injected into the reservoir in order to improve the mobility ratio by reducing the oil viscosity. Different fluids like water, air, and solvents might be used in

this technique. They might be preheated at the surface or heated using downhole heaters.

In its basic form, hot water is injected into the reservoir to sweep the oil [3]. Hot water is generally an immiscible displacement process in which oil is swept by hot and cold water. Except for some thermal effects, this mechanism is analogous to conventional water flooding, and before selecting this method, the same precautions must be taken that consider the possible consequences of swelling clay.

6.3.2 Steam-Based Methods

Steam-based methods which have been used commercially since the 1960s are believed to be the most advanced EOR techniques implemented in oil reservoirs and therefore have the least uncertainty in comparison with other techniques [4]. However, caution must always be taken while selecting these approaches just like any other EOR method [5].

Like any other thermal EOR method, the main concept behind steam-based processes is to reduce heavy oil viscosity so it can flow easily toward the production wells. Viscosity reduction, however, is not the only active mechanism in this technique, and other mechanisms such as emulsion drive, thermal expansion, solution gas drive, and steam distillation also contribute to the oil recovery process.

One important issue in steam-based processes is to reduce heat loss. If the wells are poorly insulated, then there is a high chance that significant heat loss occurs, resulting in poor performance and changing the technique from steam-based operations to hot water injection instead.

6.3.2.1 Steam Flooding (Steam Drive)

In steam flooding, the steam is continuously injected into the reservoir in order to create a steam zone which reduces the oil viscosity and also retains pressure for the oil displacement [6, 7].

The main difference between hot water injection and steam flooding is the effect of condensing vapor. In steam flooding, the presence of a gas phase results in the light components of the heavy oil to be distilled and carried away. Then by reducing the temperature, this phase would condense and reduce the oil viscosity during condensation, which improves the sweep efficiency [8].

Steam flooding recovery factor is usually higher than hot fluid injection and usually lies between 50 and 60% of the original oil in place, although recovery factors as high as 70% have also been reported [9]. The major drawbacks of this technique are the steam override, excessive heat loss, and higher costs as it is highly energy-intensive [2].

6.3.2.2 Cyclic Steam Stimulation

Cyclic steam stimulation (CSS), also known as huff-and-puff, is a three-stage technique which is operated on a single well. Figure 6.2 shows this process [10]. At first, the steam is injected into a well for a period of 1–3 months. Then the well is shut down, and the steam is allowed to distribute around the wellbore, a phase referred to as a soaking period. Finally, the well is opened to flow. The oil rate increases quickly to high values and stays constant for a while and is then followed by a decline [10]. The production continues until it reaches the economic limit and then the cycle is repeated. The steam-oil ratio for this process changes over time. It usually starts at 1:2 and increases to 1:3 or 1:4 as the number of cycles increases [11]. For this reason, this technique is usually used for one cycle, and then it is converted to the steam drive process.

There is a great interest in CSS since it has a quick payout; however the final recovery factors are much less than other thermal processes at around 10–40% of the OIIP. Moreover, as this process requires high-pressure injection, some considerations must be considered about the overburden pressure and also the reservoir geology. Like steam flooding, high costs related to steam generation and gravity override are the main concerns in this technique [8].

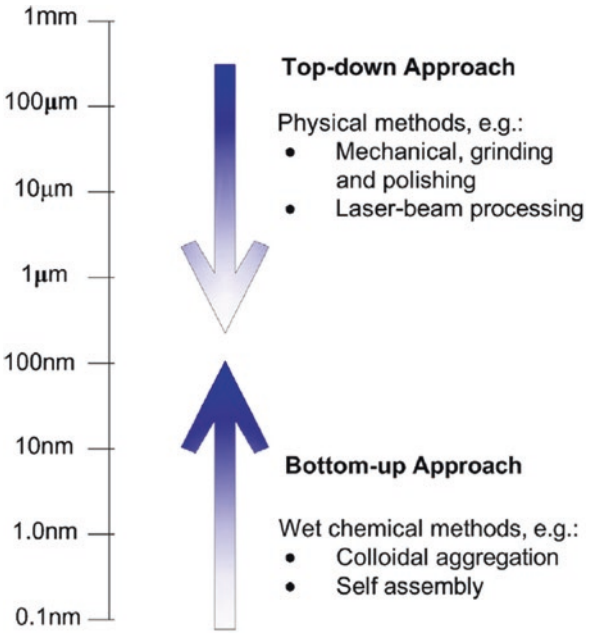

Fig. 6.2 Schematic representation illustrating the top-down and bottom-up approaches for nanocatalyst preparation [45]. Permissions related to the material excerpted were obtained from Bentham Science Publishers, copyright 2012, and further permission should be directed to Bentham Science Publishers; Nassar, N.N., Iron oxide nano adsorbents for removal of various pollutants from wastewater: an overview. Application of adsorbents for water pollution control, 2012: pp. 81–118

6.3.2.3 Steam-Assisted Gravity Drainage (SAGD)

SAGD was first proposed by Butler in the 1970s and was first tested for in situ recovery of Alberta bitumen in 1980 [12]. The main concept of SAGD is two parallel horizontal wells which lie on the same vertical plane. The upper well is responsible for high-pressure steam injection which forms a steam chamber that subsequently results in reducing the oil viscosity and drains the reservoir by gravity. The drained oil moves toward the lower well which is a production well, and the fluid is pumped to the surface. There are several important operational and geometric parameters in SAGD operation like rock permeability, reservoir heterogeneity, oil reservoir thickness, and well separation, which needs to be addressed; however high vertical permeability is considered the most important parameter as it is crucial to the performance of this method [13–16].

SAGD process is highly energy-intensive. This method results in a high amount of greenhouse gas emission, and a large volume of water is required to generate steam. Therefore, some variations of this technique have been proposed to decrease the high energy intensity of the process. VAPEX,[1] ES-SAGD,[2] and SAGP[3] are the most important variations which have been proposed so far.

VAPEX

Although VAPEX is a variation of a SAGD, it is not a thermal process [17]. The concept behind VAPEX is analogous to SAGD; however instead of steam, a solvent (or a mixture of solvents) is injected into the reservoir. The choice of a solvent depends on reservoir pressure and temperature. Typical solvents are ethane, propane, and butane which are injected along with a carrier gas like N_2 or CO_2. Viscosity reduction is the main active mechanism in this process for oil recovery. Since viscosity reduction in VAPEX relies on molecular diffusion and mechanical dispersion which are inherently slow processes, its efficiency is less than SAGD. The cost of solvent and probability of subterranean water contamination are among the most important concerns regarding this technique.

ES-SAGD

ES-SAGD lies between SAGD and VAPEX because it utilizes both steam and solvent in the injection well to reduce the crude viscosity. In fact, ES-SAGD benefits from both steam and solvent in order to increase efficiency with respect to VAPEX and decrease energy intensity compared to SAGD. Typical recovery factors between 40 and 60% have been reported for this process [18].

[1] Vapor extraction.

[2] Expanding solvent SAGD.

[3] Steam and gas push.

SAGP

This is another variation of the SAGD technique. In order to reduce the high energy demand to produce steam in the SAGD process, a non-condensable gas like natural gas or nitrogen is injected into the reservoir along with steam [19].

6.3.3 In Situ Combustion

In situ combustion (ISC) or fire flooding has been around since the 1920s [20–22]. This technique has been applied to hundreds of fields so far [23–25]; however only a few numbers of projects were economically favorable [25, 26]. ISC is achieved by igniting a portion of OIIP via injection of air or oxygen into the reservoir. This process creates a huge amount of heat which mobilizes the unburnt portion of the reservoir [25, 27]. Unlike steam-based methods in which the heat is transferred from outside of the reservoir, in situ heat creation in ISC results in very low heat loss which makes this technique energy-efficient. Moreover, since all reactions are taken place inside the reservoir, there is a minimal environmental footprint. Furthermore, a great advantage of this method is that ISC is able to partially upgrade the heavy crude and bitumen via thermal cracking. However, there are some drawbacks associated with ISC. The main problem that prevents its widespread usage is the difficulty associated with controlling the process, and gas overriding, channeling, and unfavorable gas-oil mobility ratios are the crucial problems. The main variations of ISC are forward combustion, dry or wet; reverse combustion; high-pressure air injection; THAI[4]; and THAI-CAPRI.[5]

In forward combustion, the combustion front movement is in the same direction as the air flows, but in reverse combustion, it is vice versa. When the air is being injected alone, the process is called dry combustion [28], while water injection can also be used during combustion to recover the heat from the burnt zone which is called wet combustion [29]. Reverse combustion performance in field tests was poor because the process is diminished due to the oxygen consumption before reaching the production well. In contrast to forward or reverse combustion, high-pressure air injection involves low-temperature oxidation of the crude. This process has been implemented on several light oil reservoirs. Due to the importance of THAI and THAI-CAPRI, processes in improving oil recovery, and in situ upgrading of heavy oil and bitumen, these methods are discussed separately in more detail in the following sections.

[4] Toe-heel-air-injection.

[5] Catalytic upgrading process in situ.

6.3.4 THAI

The toe-heel-air-injection is a novel process which was first performed by Petrobank in 2006, at Christiana Lake, Alberta, Canada [2]. The technique basically benefits from the ISC concepts; however unlike ISC, it uses a horizontal production well which helps to control the combustion front. In this technique, the air is injected from the vertical well, and then a combustion front is created by igniting a portion of reservoir oil. This front is propagated through the reservoir via a horizontal well from its toe to its heel which finally results in a stable combustion front and also eliminates the gas overriding problem [30, 31].

Another advantage of THAI over conventional ISC is a short-distance displacement of the mobilized oil. In ISC the mobilized oil must move hundreds of feet from the injection well to the vertical production well, whereas in THAI the mobilized oil moves only a couple of feet which yields more oil recovery and higher production rates [32]. Experimental studies show recovery factors as high as 80–85% for THAI which makes it an ideal technique for heavy oil and bitumen recovery [33]. Moreover, THAI is applicable to a higher number of candidate reservoirs compared to other techniques that cannot be used because of low reservoir pressure, high depth, or low thickness.

Partial in situ upgrading of the heavy oil and bitumen is a further benefit of the THAI process that is believed to occur via carbon rejection reactions (thermal cracking) in the coke and mobile oil zone (MOZ). This process is not only beneficial for the amount of oil recovery but also increases the oil quality which makes it easier for transportation and decreases the subsequent refinery operation costs. Experimental studies and pilot tests have shown a decrease of sulfur and heavy metal contents in the partially upgraded oil recovered by THAI [2]. In summary, THAI technique has the following advantages: higher recovery factor (around 80%) compared to the current steam-based or conventional ISC methods; partially upgrading the heavy crude and bitumen which makes them appropriate for pipeline transport and reduced refinery costs; the short flow path of the stimulated oil which reduces the instability associated with the longer flow path in conventional methods; and more environmentally friendly since less greenhouse gas is emitted and smaller surface footprints are associated with it.

Like any other EOR method, there are basic criteria which must be considered when selecting the THAI technique. The followings are some important parameters which need to be accounted for before THAI is chosen for a particular reservoir: there should not be any natural or hydraulic fractures in the reservoir; THAI is applicable in sandstone formations; the minimum thickness of the pay zone must be 6 m; in case of a bottom water drive existence, the thickness should be less than 30% of the oil zone; the viscosity and density of the crude should be higher than 200 mPa s and 900 kg/m^3, respectively; reservoir horizontal and vertical permeability should exceed 200 and 50 mD, respectively. Moreover, the value of $\frac{K_V}{K_H}$ should

be more than 0.25; the amount of water cut at the beginning of the THAI should be less than 70%.

It is noteworthy to consider that these are the necessary conditions which should be met before selecting THAI, however, the final decision depends on laboratory screening and reservoir simulation predictions of the process [34].

6.3.5 THAI-CAPRI

Heavy oil and bitumen transportation and refining have always been a major challenge for engineers. Surface upgrading has been used to modify the oil properties in order to meet the pipeline criteria; however surface upgrading can cost up to hundreds of millions of dollars [35]. In situ upgrading therefore seems to be a more favorable choice both financially and environmentally.

The idea of downhole catalytic upgrading using conventional ISC was first proposed by Moore et al. and Weissmann et al. [36–38]. In this process, a catalytic bed is placed in the reservoir near the production well. By passing the oil through the catalytic bed at a certain pressure and temperature, the catalytic reactions take place, and the upgraded oil drains into the production well. Although this process was tested successfully by Moore and Weissmann [36–38], there are two major problems with conventional ISC. First, the catalysts should be externally heated, and second, as the combustion front is not in contact with the production well, the oil passing the catalyst bed is relatively cold and can cause severe cocking, fouling the catalyst bed.

Despite conventional ISC, the THAI process seems to have great potential for inclusion in catalytic upgrading since its unique well geometries can prepare a suitable medium with desired pressure and temperature for catalyst activation.

As previously discussed in MOZ, thermal cracking reactions take place which can act as a precursor for the catalytic upgrading process in situ (CAPRI). The reactants in this process are combustion gases and water (steam). By passing these reactants through MOZ and their contact with the catalytic bed, the condition is prepared for catalytic upgrading of the previously partially upgraded oil (THAI). The equations governing the above reactions in THAI-CAPRI process are as follows [39]:

Thermal cracking (pyrolysis):

$$\text{Heavy residue} \rightarrow \text{Light oil} + \text{Coke} \tag{6.1}$$

Oxidation of coke (high-temperature oxidation):

$$\text{Coke} + \text{O}_2 \rightarrow \text{CO} + \text{CO}_2 + \text{H}_2\text{O} \tag{6.2}$$

Carbon rejection:

$$\text{CH}_x \rightarrow \text{CH}_{x_1} + \text{C}\left(x_1 > x\right) \tag{6.3}$$

Hydrogen addition:

$$\mathrm{CH}_x + \mathrm{H}_2 \rightarrow \mathrm{CH}_{x_1} \left(x_1 > x\right) \tag{6.4}$$

The required hydrogen responsible for upgrading the heavy oil and bitumen is thought to be formed by water-gas shift reactions [39]:

Gasification of hydrocarbon:

$$\mathrm{CH}_x \rightarrow \mathrm{C} + \frac{x}{2}\mathrm{H}_2 \tag{6.5}$$

$$\mathrm{C} + \mathrm{H}_2\mathrm{O}\left(\mathrm{steam}\right) \rightarrow \mathrm{CO} + \mathrm{H}_2 \tag{6.6}$$

$$\mathrm{C} + \mathrm{CO}_2 \rightarrow \mathrm{CO} \tag{6.7}$$

Water-gas shift:

$$\mathrm{CO} + \mathrm{H}_2\mathrm{O} \rightarrow \mathrm{CO}_2 + \mathrm{H}_2 \tag{6.8}$$

There are some challenges with the CAPRI process which need to be addressed before deciding on its application. Heavy oil and bitumen usually contain more than 5% sulfur and a high amount of heavy metals like Ni and Vanadium which can deactivate the catalyst quickly. Moreover, during thermal cracking of heavy oil and bitumen, coke is produced which can cover the catalyst bed and prevents its performance as a catalytic upgrader.

6.3.6 Electrical Heating

This method has not been used as much as the previously mentioned thermal methods. However, there have been some attempts to use electrical heating in order to increase oil recovery and in situ upgrading of the heavy oils. For example, ExxonMobil established a method called Electrofrac. In this technique, a conductive material is placed in hydraulic fractures of an oil shale which then forms a heating element [40]. Although these methods seem promising, they require a huge amount of electrical energy input, which may limit the possibility of their commercial use [2].

6.4 Ultradispersed Nanocatalysts

A catalyst is a substance that changes the rate of a chemical reaction and remains unaltered at the end of the process, making it possible to gain the desired products with a lower energy barrier.

A minimum amount of energy is required for a chemical reaction to occur. Catalysts help to reduce this required energy by providing active sites for adsorption and reaction where the products are created. For a catalytic reaction to occur, it is crucial for the reactant to attach to the catalyst active site. One drawback of conventional catalysts was the deactivation problems which occurred when the connection between catalyst and reactant was lost. For example, during in situ upgrading in the THAI-CAPRI process, coke deposition on catalytic beds usually resulted in their deactivation and affected the performance of the upgrading process.

UD nanocatalysts were developed mainly to overcome the pore plugging problem [41]. Due to their small size, which is usually around 100 nm, UD nanocatalysts offer a greater surface area, which means more active sites, resulting in a longer activation time. Another advantage of the UD nanocatalysts, compared to their conventional supported catalysts, is that the former can flow with the feedstock in the reaction media which makes the reaction time longer. In general, the advantages of nanocatalysts can be categorized as follows:

- Improved catalytic performance due to their large surface area-to-volume ratio.
- The increased probability of reactant-catalyst interaction due to the mobilization of nanocatalysts inside the reactor.
- The absence of any fixed bed and elimination of the necessity of catalyst replacement results in longer run times for conversion.
- In the absence of any pores in UD nanocatalysts, loss of activity will not occur compared to its supported catalyst counterpart [42].
- Successful field applications will reduce the operating costs as well as environmental issues associated with bitumen production such as greenhouse gas emission and solid waste by-products [43].
- Propagation of nanocatalysts inside the porous media and reacting in situ beside bitumen dissolution will result in viscosity reduction of the produced fluid.

Transition metals like Mo, Co, Ni, Fe, and Cr are usually used to form the UD nanocatalyst composition. Molybdenum is the most common transition metal used since it has superior performance in regard to increasing conversion and reducing the boiling point and micro carbon residue (MCR).

6.4.1 Synthesis of Nanoparticles

In order to manufacture nanoparticles, several methods have been proposed so far [41, 42, 44–48]. These methods can be classified into top-down and bottom-up methods as shown in Fig. 6.2 [45]. In top-down approaches, nanoparticles are prepared directly from bulk materials. They use physical methods such as milling or grinding, laser-beam processing, repeated quenching, and photolithography to generate isolated atoms [42]. Bottom-up approaches occur when molecular components as starting materials are linked with chemical reactions, nucleation, and growth processes, to promote the formation of nanoparticles [49–57].

Bottom-up methods consist of different approaches for nanocatalyst preparation, such as water-in-oil microemulsions or reversed micelles [41, 46, 52], chemical reduction [50], hot soap [49, 54], sol-gel [56], pyrolysis [57], and spray pyrolysis [55]. The water-in-oil microemulsion method is commonly used for the in situ formation of nanoparticles in a heavy oil matrix. An emulsion preparation is obtained by mixing oil, water, and a stabilizing agent such as surfactant [53]. Microemulsions have specific properties like very low interfacial tension, small microstructure, thermodynamic stability, and translucence, which make them suitable for a variety of applications [58]. The water-in-oil (w/o) microemulsion preparation technique is thoroughly described in the literature [41, 46, 52, 53]. In brief, a w/o emulsion is formed, and then an aqueous solution of corresponding metals is added to it. The sample is mixed for a certain time, and then a base aqueous solution is added to initiate nucleation and the growth of the nanoparticles, which remain stable in the suspension.

Nanocatalyst preparation can be achieved through mixing two reacting systems (one containing the precursor salt and the other a reducing agent) in the form of microemulsions [59]. Capek has reported a comprehensive study on the preparation of nanoparticles in w/o microemulsions with formulations for Fe, Pt, Ni, Au, Cd, Pd, Ag, and Cu. Therefore, microemulsions are deemed as a breakthrough for nanocatalyst preparation, particularly for in situ applications such as bitumen upgrading and recovery. For heavy oil conversion, an emulsion was developed in the presence of water claiming steam cracking of vacuum gas oil (VGO) catalyzed by a catalytic emulsion [60]. Furthermore, a hydroprocessing reaction was successfully catalyzed by implementing a catalytic nanoparticle solution prepared by the decomposition of w/o emulsion [61]. Thompson et al. investigated the Mo nanoparticle reaction performance for Athabasca bitumen upgrading [62]. They explored the formation of mixed oxy-carbides composed of MoO_2, MoO_3, and MoC as well as the agglomeration of nanocatalysts promoted by surfactant-media interactions in a lab-scale reactor packed with sand particles. In another attempt, a microemulsion method was utilized to prepare Ni, Mo, and Ni-Mo nanoparticle (approximately 10 nm) hydrodesulfurization with the potential of using for both surface and in situ upgrading [63]. Although nanocatalyst synthesis and preparation is believed to be fully established, their stability inside the prepared/reaction media and control over particle size as well as particle recovery and regeneration are still challenging issues that need to be addressed.

UD nanocatalyst mechanical separation and deposition have been investigated based on their movement inside the viscous fluid media in a cylindrical geometry [64]. These parameters were modeled based on 2D and 3D convective-dispersive models. Experimental data was used to validate these models [64]. According to the literature, the dispersion coefficient is a function of fluid medium properties (density, viscosity, and volumetric flux), and a high-dispersion coefficient value demonstrates the particle tendency for sedimentation in a medium [64]. Moreover, the "critical particle diameter" factor was defined to represent the particle deposition tendency [64]. Based on the particle and medium condition (i.e., initial particle concentration, velocity change, and medium viscosity change), sedimentation of

UD particles could take place followed by a change in the properties of the medium in a lower or higher critical particle diameter.

Alamolhoda et al. [65] proposed another technique to prepare catalyst for water-gas shift reactions (WGSR). This method avoided the impregnation, drying, and further calcination steps and produced active catalysts for low-temperature WGSR. The preparation method is appropriate and incorporates nickel and cerium efficiently into the silicate MFI structure; however before conducting the WGSR test, the produced catalyst must be activated in hydrogen at a high temperature to reduce the oxidation state of nickel. Therefore, the high surface area of the structured silicate-based catalyst provides a controlled reaction medium, while its pore structure increases the dispersion and lifespan of the catalytic active sites. The authors found that the catalysts produced catalyze and accelerate the WGSR with no methane production at 230°C. During the activity test, nickel catalyzed the WGSR, and cerium promoted the catalyst because of its ability to provide the required oxygen [66].

Particle size and sufficient quantity per volume of reactive oil are two main factors governing the UD nanocatalyst hydro conversion performance. Catalyst activity is dictated by its composition and the degree of dispersion. The catalysts in a well-dispersed condition favor the uptake of hydrogen, which results in the reduction of coke formation. In the following section, the performance of UD nanocatalysts versus conventional catalysts in in situ upgrading will be discussed.

6.5 Proof of Concept

As mentioned in the previous sections, the THAI-CAPRI process is one of the most efficient techniques for bitumen and heavy oil recovery. This technique benefits from both thermal cracking via combustion reactions and catalytic cracking. However catalytic deactivation upon asphaltenes, coke, metal, and heteroatom deposition is a major issue regarding this technique [67, 68]. Moreover, there exist many complications related to fixed-bed pattern design which could be eliminated by UD nanocatalyst application [69].

Hart et al. [70] investigated the performance of UD nanocatalysts in THAI-CAPRI operation and compared it to the conventional fixed-bed catalytic upgrading. Co-Mo/Al_2O_3 was used as a catalyst in a fixed-bed test at a temperature of 425°C, pressure 20 bar, and residence time of 10 min. A batch reactor was used for these UD nanocatalyst tests. The operational parameters, like residence time and catalyst-to-oil ratio (CTO), were kept the same to guarantee the dynamic similarity. The upgrading performance of each method was evaluated based on API gravity, viscosity reduction, impurity removal, and true boiling point distribution. According to their results, a fixed-bed technique could increase the API around 5.6°, while dispersed ultrafine catalysts enhance the API up to 8.7°. Viscosity is another important parameter which has a tremendous effect on heavy oil transportation.

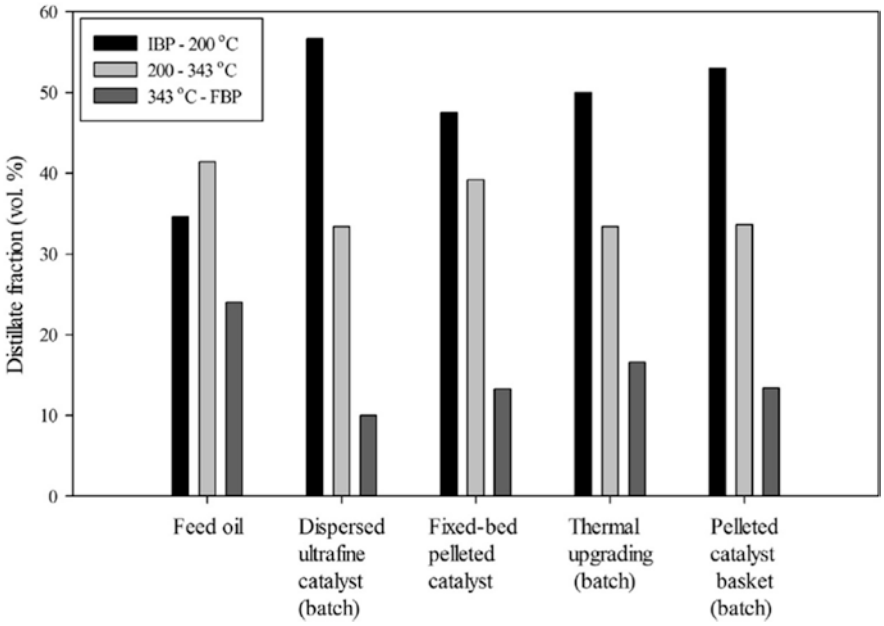

Fig. 6.3 UD nanocatalyst effect on fractions TBP for different systems [70]. Permissions related to the material excerpted were obtained from Elsevier, and further permission should be directed to Elsevier; Hart, A., M. Greaves, and J. Wood, A comparative study of fixed-bed and dispersed catalytic upgrading of heavy crude oil using-CAPRI. Chemical Engineering Journal, 2015. 282: pp. 213–223

A fixed bed was able to reduce the initial 1091 mPa s (feed oil) around 97.4%, to 28.4 mPa s. On the other hand, UD nanocatalysts could reduce the viscosity amount down to 7 mPa s which is again superior compared to its fixed-bed counterpart. Product oil true boiling point (TBP) was another criterion which was compared between the above methods. Figure 6.3 shows the TBP distribution results.

According to Fig. 6.3, UD nanocatalysts and fixed-bed catalysts could reduce the residue fraction from 24 vol% in the feedstock to 10 vol% and 13.3 vol%, respectively. Meanwhile, the gasoline fraction was increased from 34.6 vol% in the feedstock to 45.5 vol% for fixed-bed and 56.6 vol% for UD nanocatalysts. This could be attributed to the accessibility of active sites in the case of UD nanocatalysts so that heavy molecules have better access to them, while in fixed-bed catalysts, the long diffusion path length leads to pore plugging and deactivation [71, 72]. It is also noteworthy to mention that thermal cracking alone produced the most residue fraction among all cases, which shows the importance of catalytic cracking in reducing the residue fraction. UD nanoparticles also showed better performance in removing asphaltene, sulfur, and metals from the crude. Table 6.1 shows the amount of unwanted constituent removal for the 4 different scenarios.

Table 6.1 clearly shows that dispersed ultrafine nanoparticles surpass thermal cracking and fixed-bed catalyst techniques. The poorer performance of the

Table 6.1 Asphaltene, metal, and sulfur content before and after upgrading at 425°C, nitrogen reaction medium, 10 min residence, and 0.195 Reynolds number [70]

Impurities	THAI-produced oil	Fixed-bed catalyst	Thermal cracking	Dispersed ultrafine Co-Mo/Al_2O_3
Asphaltenes (wt% of feed oil)	10.40	4.88	3.79	2.32
Aluminum (ppm mass)	2	2	<1	<1
Boron (ppm mass)	6	3	4	2
Iron (ppm mass)	5	<1	<1	<1
Nickel (ppm mass)	41	24	8	7
Vanadium (ppm mass)	108	57	16	15
Ni + V (ppm mass)	149	81	24	22
Sulfur (wt% of feed oil)	3.52	2.50	2.08	2.16

Permissions related to the material excerpted were obtained from Elsevier, and further permission should be directed to Elsevier; Hart, A., M. Greaves, and J. Wood, A comparative study of fixed-bed and dispersed catalytic upgrading of heavy crude oil using-CAPRI. Chemical Engineering Journal, 2015. 282: pp. 213–223

fixed-bed catalysts is related to their large size, which results in lower surface area compared to ultrafine catalysts, therefore limiting access to their active sites.

In another study, Galarraga et al. [51] investigated the effectiveness of submicronic multimetallic catalysts in the bitumen hydrocracking process. In this study, NiWMo submicronic catalysts were derived from emulsified metallic aqueous solutions in order to evaluate their impact on bitumen upgrading. The experiments were conducted in a batch reactor at a total pressure of 3.45 MPa, temperature from 320 to 380°C, stirring speed of 500 rpm, and 3–70 h reaction times. They concluded that bitumen upgrading was enhanced by the proposed submicronic multimetallic catalysts by increasing the hydrogen-to-carbon ratio and decreasing both viscosity and coke formation.

6.6 Hydrogen Addition Processes

In the in situ upgrading technology, hydrogen addition processes allow the manipulation of the crude oil molecular composition by breaking bonds and adding hydrogen to those large molecular chains. This process leads to a higher H/C ratio and a slight density reduction of the fluid. In fact, this process makes the large molecules more reactive or more prone to crack. Other reactions eliminate contaminants and improve the quality of the fluid.

Hydrogen addition reactions are summarized in Table 6.2. The main characteristic is that the heavier the feedstock, the higher the severity of the conditions for treatment [61].

Table 6.2 Hydrogen addition reactions [61]

Process	Feed	Products	Operating conditions	Remarks
Hydrotreating	All cuts	Same as feed	72–2320 psi 260–400°C 0.15–10 h^{-1}	Hydrogenates the feed with 10% or less hydrocracking Removes sulfur, nitrogen, and metals
Hydrocracking	Medium and heavy cuts	Light gases Naphtha Kerosene Diesel fuel Lube oils	1450–2900 psi 350–430°C 0.2–2 h^{-1}	Changes the skeletal structure of the feed, by breaking C–C bonds
Mild hydrocracking	Medium and heavy cuts	Kerosene Diesel oil	725–1160 psi 350–440°C 0.2–2 h^{-1}	Same as hydrocracking, but at lower severity Hydrocracks 40% or less of the feed

As shown in Table 6.2, the main hydroprocesses are as follows: hydrotreating, hydrocracking, and mild hydrocracking. Hydrocracking is classified as a destructive hydrogenation process in which the carbon-carbon bond is broken, followed by hydrogenation. This process leads to saturated products with a lower boiling point. It consists of a combination of cracking, hydrogenation, isomerization, and treating operations [73]. On the other hand, hydrotreating is a nondestructive mild processing condition reaction. Its main objective is to eliminate contaminants like sulfur, nitrogen, oxygen, and metals. The most important hydrotreating processes are hydrodesulfurization (HDS), hydrodemetallization (HDM), hydro denitrogenation (HDN), and hydrogenation of complex structures [74].

6.6.1 Hydrogen Donors

As previously discussed, heavy oils encounter two major problems: transportation and processing. It is proven that both problems can be solved by utilizing upgrading techniques. Hydrogen addition and carbon rejection are two major mechanisms responsible for heavy crude oil upgrading. Carbon rejection is usually performed by delayed coking techniques, while hydrogen addition-based technologies mostly utilize catalytic hydroprocessing.

The benefits of the introduction of hydrogen during in situ upgrading offer much promise. In fact, hydrotreating processes play three important roles for heavy oils: desulfurization, pretreatment for fluid catalytic cracking processes, and hydrocracking [8]. Utilizing hydrogen donors is one approach used to add hydrogen to the upgrading process. The idea of using H-donors was first introduced in 1933 when it was employed for the hydrogenation of coke to treat oil residue. Since then, different H-donors were introduced and utilized for different applications but with the same concept of releasing hydrogen to enhance the specific operations [75].

H-donors are chemical compounds that have the ability to transfer hydrogen to heavy crude oil. Based on hydrogen donor capacity, cost, and degradation conditions, different H-donors have been introduced. It has been proven that the use of H-donors can significantly enhance the upgrading process.

A proper H-donor should be capable of diminishing the retrogressive reactions by capping free radicals. The rate of progressive and retrogressive reactions is controlled by the H-donor quality. Suitable H-donors like tetralin can promote the relative rates of the progressive reactions, whereas weak H-donors like naphthalene advance the retrogressive reactions [76, 77]. In the upcoming sections, different aspects of H-donors and their effect on upgrading will be discussed.

6.6.2 Different Types of H-Donors

Practically any organic compound which has a low oxidation potential can be utilized as an H-donor. The low oxidation potential allows H-donors to transfer the hydrogen(s) to the substrate under mild reaction conditions. The optimum donor selection is related to different parameters like the nature of the reaction, its availability, and its solubility in the reaction medium. Some H-donors are polyaromatics like pyrene, fluoranthene, and basic nitrogen compounds such as quinoline [78, 79]. Tetralin, decalin, and naphthalene are some other H-donors which have been used so far. Although these H-donors are so well known, problems associated with their recovery and reuse and their high prices made researchers use other H-donors like alcohols, hydroaromatic, cyclic ethers, and formic and ascorbic acids [80]. Some researchers have also used certain crude oil fractions as H-donors [81, 82]. These fractions are usually rich in compounds with condensed aromatic rings like alkyl naphthalene and phenanthrenes alkyls. In the following sections, some of the most popular model molecules which are used as H-donors are discussed in more detail.

6.6.3 The Applicability of H-Donors with UD Nanoparticles

In the previous sections, it was proven that the use of UD nanoparticles can overcome the problems associated with catalyst blockage during in situ upgrading of heavy oil. On the other hand, the in situ-generated hydrogen via water-gas-shift is not usually sufficient to diminish the amount of free radical formed during heavy oil pyrolysis, and to assist the upgrading process; an external source of hydrogen is required. H-donor addition is one of the methods which is used to provide the desired amount of hydrogen in the reservoir. Hart et al. [83] investigated the effect of cyclohexane as H-donors in UD catalytic upgrading of heavy oil. The results indicated that the presence of an H-donor could enhance the yield of the upgraded oil and also suppress coke yield [83]. Table 6.3 shows the effect of H-donor in enhancing the liquid yield product and reducing the coke formation. Their results

Table 6.3 Yields of liquid, gas, and coke after thermal and UD catalytic upgrading [83]

Experiment	Liquid (wt.%)	Gas (wt.%)	Coke (wt.%)
Thermal cracking + N_2	78.71 ± 0.11	13.35 ± 0.54	7.95 ± 0.43
Ultradispersed + N_2	83.79 ± 0.17	11.55 ± 0.19	4.67 ± 0.36
Ultradispersed + H_2	86.81 ± 0.47	10.45 ± 0.49	2.74 ± 0.03
Ultradispersed + N_2 + CH/oil (0.01)	86.97 ± 1.38	8.66 ± 1.62	4.38 ± 0.29
Ultradispersed + N_2 + CH/oil (0.02)	87.05 ± 1.23	8.93 ± 1.85	4.02 ± 0.13
Ultradispersed + N_2 + CH/o il (0.04)	87.94 ± 0.38	8.64 ± 0.22	3.43 ± 0.16
Ultradispersed + N_2 + CH/oil (0.06)	88.25 ± 1.28	8.56 ± 1.11	3.20 ± 0.18
Ultradispersed + N_2 + CH/oil (0.08)	88.76 ± 1.11	8.69 ± 1.20	2.55 ± 0.13

also demonstrated that by choosing the proper donor-oil ratio, upgrading with H-donors present better performance than using the hydrogen atmosphere.

6.6.4 Challenges and Opportunities

There are several methods to introduce hydrogen to the upgrading process. Using H-donors has some benefits over some conventional methods like injecting molecular hydrogen. Due to the low molecular weight of molecular hydrogen, it has a high diffusion capacity and is readily combustible, which results in a high-risk operation [75]. Moreover, using H-donors with thermal processes has some other advantages, including increased distillate yields, lower coke formation, the option of using several compounds depending on the technical and operational issues, and the process can be either pure thermal or catalytic.

On the other hand, like any other operational method, there are some drawbacks associated with H-donors: difficulties associated with H-donor separation from the product stream and the lack of any universal guideline for the H-donor application. The process effectiveness is highly dependent on the operating conditions and crude properties; the operation may not be fully predictable since the exact mechanism behind hydrogen transfer is not understood yet; the performance of external rehydrogenation cycles may be required to justify their cyclical hydrogen transfer.

6.7 Liquid Quality Enhancement

Evaluation of product quality is crucial in any upgrading process to determine the extent of the increased value of heavy feedstocks. Product quality determines the process cost-effectiveness, transportation pipe designs, as well as processing facility specifications [84]. It is therefore necessary to evaluate the quality of the liquid

streams produced based on hydrocarbon quality parameters like hydrogen-to-carbon ratio (H/C), API gravity, viscosity, MCR, sulfur, and nitrogen content.

6.7.1 H/C Atomic Ratio

One of the main characteristic properties of heavy oil and bitumen is the low value for the H/C ratio. The H/C ratio for different crude oil cuts is shown in Fig. 6.4 [85]. During the heavy oil upgrading, the H/C ratio increases. Cracking and hydrogenation are two main mechanisms in any thermal upgrading process in which heavy molecules decompose to lighter components with smaller molecules as well as higher H/C ratios [86]. Galarraga and Pereira-Almao [87] employed a batch mode to investigate the catalytic hydroprocessing reactions of Athabasca bitumen. They used nanocatalyst suspension in situ by using heavy oil emulsion and subsequently tested in a batch reactor working at marginal levels of hydrogen and sand for bitumen upgrading.

Their results revealed that nanocatalysts could promote the bitumen upgrading process by significantly increasing the H/C atomic ratio and reducing both viscosity

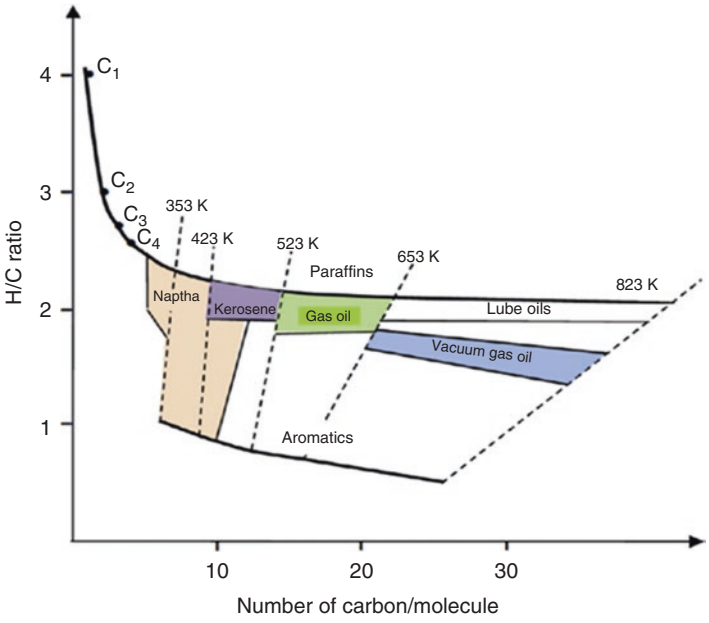

Fig. 6.4 Hydrogen-to-carbon ratio for the various petroleum cuts [86, 88] with permission. Permissions related to the material excerpted were obtained from Elsevier, and further permission should be directed to Elsevier; Hashemi, R., N.N. Nassar, and P.P. Almao, Nanoparticle technology for heavy oil in-situ upgrading and recovery enhancement: Opportunities and challenges. Applied Energy, 2014. **133**: pp. 374–387

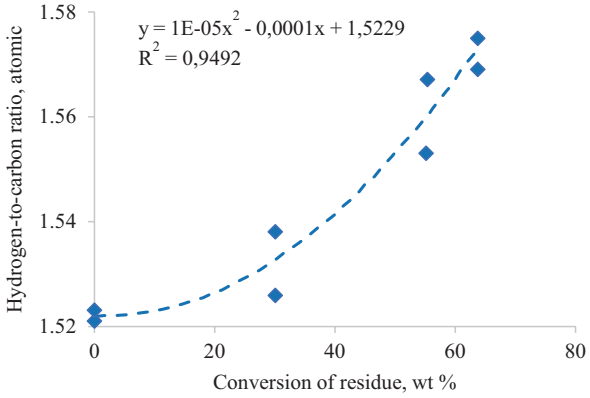

Fig. 6.5 Hydrogen-to-carbon ratio (H/C) of Athabasca bitumen at different conversions of residue for reaction performed at 653 K [87]. Permissions related to the material excerpted were obtained from the American Chemical Society, copyright 2010, and further permission should be directed to the American Chemical Society; Galarraga, C.E. and P. Pereira-Almao, Hydrocracking of Athabasca bitumen using submicronic multimetallic catalysts at near in-reservoir conditions. Energy & Fuels, 2010. 24(4): pp. 2383–2389

and coke formation [87]. Moreover, a remarkable reduction of sulfur and MCR was also observed. The H/C ratio enhancement as a function of residue conversion for products obtained at 653 K and 3.45 MPa is shown in Fig. 6.5. The graph shows a polynomial trend for H/C ratio enhancement, which clearly provides sufficient evidence for the effectiveness of nanocatalyst presence inside the porous media and effective incorporation of hydrogen within the liquid products. According to these results, nanocatalysts can increase the H/C ratio via hydrocracking followed by the hydrogenation process. Furthermore, higher H/C ratios take place at higher conversion values.

6.7.2 Viscosity Reduction and API Enhancement

Viscosity and API are the most important parameters regarding the pipeline specification requirements. One of the main ideas behind any upgrading process is to modify these parameters to make them suitable for fluid transport through the pipeline. For commercial transportation, bitumen API gravity should be in the range of 19–21° API, and bitumen viscosity should be decreased to approximately 250 cP at 283 K [89]. Reported results for both batch and pilot tests indicate the effectiveness of nanocatalysts in lowering the heavy oil and bitumen viscosity after upgrading [64, 87]. Surface upgrading and adding diluent has long been used to reduce the bitumen viscosity [90]. However, recent findings in the field of UD nanocatalyst application showed that these catalysts can be employed in situ to enhance the bitumen quality that can meet pipeline transportation criteria without any diluent

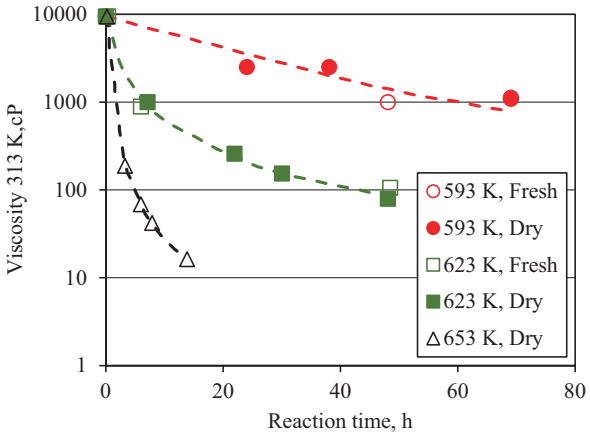

Fig. 6.6 Viscosity of liquid products from reaction at constant pressure of 3.45 MPa, temperatures of 593, 623, and 653 K, and at reaction times from 3 up to 70 h [87]. Permissions related to the material excerpted were obtained from Elsevier, and further permission should be directed to Elsevier; Hashemi, R., N.N. Nassar, and P.P. Almao, Nanoparticle technology for heavy oil in-situ upgrading and recovery enhancement: Opportunities and challenges. Applied Energy, 2014. **133**: pp. 374–387

addition. These results have been obtained by testing UD nanocatalysts in both batch and packed bed reactors in the presence of hydrogen. The performance of UD nanocatalysts from a batch reactor and packed bed reactor experiment is shown in Fig. 6.6 [87]. According to Fig. 6.6, nanocatalysts could substantially reduce the bitumen viscosity.

Reaction time and temperature are two main parameters affecting the bitumen viscosity. The results (batch and pilot tests) showed that the extent of viscosity reduction increases as the reaction time and temperature increase. The viscosity of the produced fluid is also dependent on the carrier type. The lighter the carrier, the more viscosity reduction will be achieved.

Figure 6.7 displays the results obtained for in situ oil upgrading technology (ISUT) in carbonate rocks already packed with Ni-Mo nanocatalyst [91]. In that method, the recovered vacuum residue from the produced oil is reinjected into the reservoir as a heat carrier along with nanocatalyst and hydrogen to provide the required energy for activating hydro-upgrading reactions. It is seen in Fig. 6.7, when there is less than 7% of VR conversion, there is a decrease of one order of magnitude in viscosity at 100°C. Also, at 35% conversion of VR, the viscosity was decreased by 99.8%. In addition, a reduction in the asphaltene content of 51% and an increment on the API gravity by 8° API were reported [91]. All these properties changed considerably due to the presence of the nanocatalyst; without it, unstable oil would result.

API is another significant parameter that can be evaluated in the bitumen upgrading process. When heavy oil or bitumen is upgraded, it results in lower density products which means higher API gravity of the produced liquid. The results of

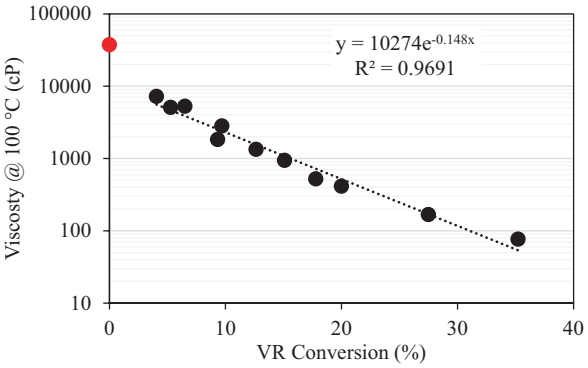

Fig. 6.7 Variation of viscosity based on VR (vacuum residue). Red dot corresponds to feed's properties [91]. Permissions related to the material excerpted were obtained from Elsevier, and further permission should be directed to Elsevier; Elahi, S.M., et al., In-situ upgrading and enhanced recovery of heavy oil from carbonate reservoirs using nanocatalysts: Upgrading reactions analysis. Fuel, 2019. **252**: pp. 262–271

batch and pilot plant tests revealed a significant increase in API gravity values during the upgrading of Athabasca bitumen in the presence of UD nanocatalysts [92]. According to these results, at different reaction times, the API for UD nanocatalysts is improved compared to their reference tests which lack the UD nanocatalysts. This implies the effectiveness of the UD nanocatalysts for improving the produced liquid quality by creating new reaction pathways and leading to higher levels of upgrading. The effect of the presence UD nanocatalysts in the reaction medium at different temperatures is shown in Fig. 6.8. It can be seen that UD nanocatalysts improved the upgrading process of the Athabasca bitumen.

6.7.3 Micro Carbon Reduction

Micro carbon residue is another quality enhancement criteria of a produced liquid after upgrading [92]. MCR content is measured based on the amount of carbon residue which is left behind after the thermal treatment of the heavy feedstocks. A low amount of MCR is desired in the produced liquids since it is a sign of a high-quality product. The obtained results in the literature proved the capability of UD nanoparticles to decrease the MCR amount of liquid products to a suitable extent [51, 94]. For example, the results of a batch reactor test for Athabasca bitumen catalytic hydrocracking showed that by implementing the UD nanocatalysts, the MCR content changed from 16 wt% in the blank experiment to about 11 wt% in the selected experimental conditions [51]. The same observations were also published regarding MCR reduction in produced samples for the continuous mode experiments [93].

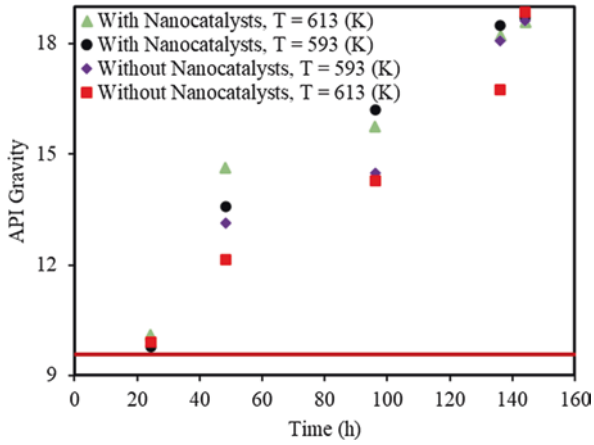

Fig. 6.8 API gravity of produced liquid samples from porous media at different times in the absence and presence of tri-metallic UD nanocatalysts at pressure of 3.5 MPa, hydrogen flow rate of 1 cm^3/min, and temperatures of 593 and 613 K [93]. Permissions related to the material excerpted were obtained from the American Chemical Society, copyright 2014, and further permission should be directed to the American Chemical Society; Hashemi, R., N.N. Nassar, and P. Pereira Almao, In situ upgrading of Athabasca bitumen using multimetallic ultradispersed nanocatalysts in an oil sands packed-bed column: Part 1. Produced liquid quality enhancement. Energy & fuels, 2014. **28**(2): pp. 1338–1350

6.7.4 Sulfur Removal

There are very strict regulations on the sulfur content of fossil combustibles based on environmental considerations [95], and the amount of sulfur in the final product of the refineries must be decreased to meet the minimum requirements of the environmental regulations. Hydrodesulfurization is considered as one of the most important reactions in hydrotreating processes which involves eliminating the sulfur from petroleum compounds to produce hydrogen sulfide as well as desulfurized compounds [86]. Dispersed catalysts, owing to their effective accessibility, generally show higher percentages of sulfur removal compared with supported catalysts [96–99].

The results of a sulfur content after upgrading with and without UD nanocatalysts in a continuous mode experiment are shown in Fig. 6.9. It can be seen that the amount of sulfur is decreased with time and temperature. The results also proved the efficiency of UD catalysts to enhance the product quality regarding sulfur content reduction. According to the results, UD nanocatalysts could decrease the amount of sulfur, especially at lower temperature samples. However, one important issue which needs to be considered is that sulfur removal is associated with hydrogen sulfide production, which can negatively impact nanocatalyst implementation inside the porous media.

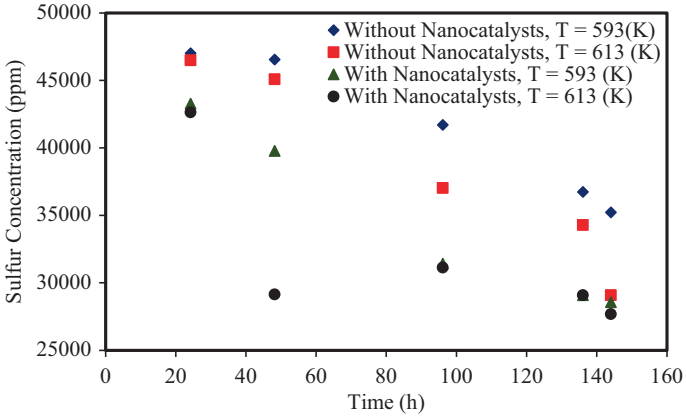

Fig. 6.9 Sulfur content of produced liquid samples from porous media at different times in the absence and presence of tri-metallic UD nanocatalysts at pressure of 3.5 MPa, hydrogen flow rate of 1 cm^3/min, and temperatures of 593 and 613 K [93]. Permissions related to the material excerpted were obtained from the American Chemical Society, copyright 2014, and further permission should be directed to the American Chemical Society; Hashemi, R., N.N. Nassar, and P. Pereira Almao, In situ upgrading of Athabasca bitumen using multimetallic ultradispersed nanocatalysts in an oil sands packed-bed column: Part 1. Produced liquid quality enhancement. Energy & fuels, 2014. **28**(2): pp. 1338–1350

6.7.5 Coke Formation Mitigation

In a typical thermal upgrading process, decomposition of heavy feedstocks occurs in the presence of hydrogen that saturate the free radicals and lead the production of lighter components as well as a great amount of coke and a considerable amount of light gas such as methane, ethane, and CO_2 [99, 100]. The use of catalysts in the reaction medium can result in fewer amounts of coke since catalysts can create new pathways in the reaction schemes [101].

Heavy oil and bitumen usually contain about 50 wt% of residue fraction with the normal boiling point higher than 818 K [102]. Catalyst deactivation due to metal deposition and coke formation is one major problem associated with the catalyst application in heavy feedstock catalytic upgrading [103]. Therefore, extensive research works have been conducted to improve the activity of the catalyst by introducing UD nanocatalysts which navigate along with the heavy feedstocks as well as catalyzing the upgrading processes [104]. Furthermore, UD nanocatalyst deactivation is less likely to happen than conventionally supported catalysts [105].

According to the literature, the use of nanocatalysts for Athabasca bitumen upgrading showed successful results, confirming the potential application of UD nanocatalysts for upgrading purposes. Tri-metallic nanocatalysts used in batch reactor tests for Athabasca bitumen upgrading could substantially reduce the coke formation with no detriment in residue conversion [87]. However, when the severity of conditions was increased, coke formation increased dramatically. The same results

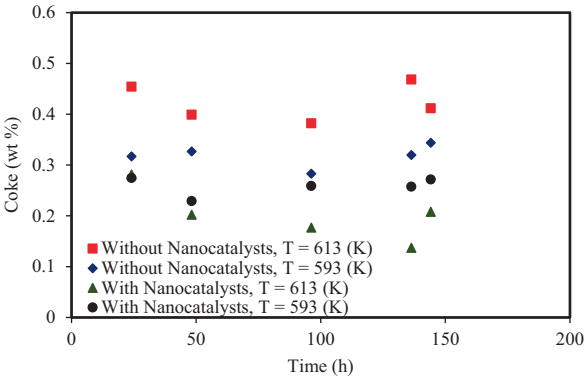

Fig. 6.10 Coke content of produced samples from porous media as a function of reaction time in the absence and presence of tri-metallic UD nanocatalysts at pressure of 3.5 MPa, hydrogen flow rate of 1 cm^3/min, and temperatures of 593 and 613 K [94]. Permissions related to the material excerpted were obtained from the American Chemical Society, copyright 2014, and further permission should be directed to the American Chemical Society; Hashemi, R., N.N. Nassar, and P. Pereira Almao, In situ upgrading of athabasca bitumen using multimetallic ultradispersed nanocatalysts in an oil sands packed-bed column: Part 2. Solid analysis and gaseous product distribution. Energy & fuels, 2014. **28**(2): pp. 1351–1361

are also obtained for continuous mode experiments which are shown in Fig. 6.10. As stated by Fig. 6.10, the presence of nanocatalysts inside the porous medium significantly improved the quality of produced samples regarding coke content [94].

The performance of UD nanocatalysts versus supported catalysts in reducing the amount of coke production is also an important topic. The results of supported catalysts versus dispersed ones demonstrated that during the upgrading of bitumen at typical upgrading conditions, the dispersed catalyst can reduce the coke formation more effectively than the supported catalyst. It was shown, however, that while UD nanocatalysts could reduce the coke formation up to a certain concentration, over which the catalytic particles acted as coke seeds and led to more coke formation [99].

6.8 Gas Emission Reduction

The significant amount of greenhouse gas (GHG) emissions is one of the main concerns related to the current upgrading technologies. Due to the severe side effects which these gases have on the environment, the governments start passing laws that limit the amount of GHG emissions. For example, the province of Alberta was the first in North America to legislate the GHG emission reduction for large industrial facilities [106]. Moreover, increasingly strict legislation limits on the level of fuel contaminants have forced the industry to explore novel cost-effective and environmentally friendly technologies for heavy feedstock processing [107].

In situ upgrading is one possible promising new technology that can enhance the quality of crude oil and decrease the level of contaminants such as sulfur and nitrogen as well as the GHG emissions to appropriate levels [108]. However, there is not sufficient information about the produced gases emitted during the in situ upgrading of heavy oils and bitumen by using nanocatalysts. A recent study by Hashemi et al. [93] explored the efficiency of nanocatalysts on gaseous emission reductions. They concluded that the presence of tri-metallic nanocatalysts promotes the hydrogenation reactions which led to a considerable reduction in CO_2 emission. According to their results, at high-pressure and high-temperature conditions, UD nanocatalysts could reduce the CO_2 emission by 50%, compared to the conventional medium that lacked nanocatalysts. Furthermore, UD nanocatalysts promote hydrocarbon gas production as a result of hydrocracking which can act as a diffusing solvent for enhancing heavy oil production. It is noteworthy to mention that gas emission during catalytic in situ upgrading is still a challenging topic that needs more laboratory investigations and pilot-scale testing in order to scrutinize its different aspects.

6.9 Nanocatalyst Transport Behavior Inside the Porous Media

In the previous sections, we have discussed the preparation and synthesis of nanocatalysts in a microemulsion system. The next important issue regarding the usage of nanocatalysts for bitumen upgrading would be the feasibility of nanocatalyst transport inside the porous media. This is a crucial topic since the efficiency of the UD nanocatalysts for heavy oil upgrading is highly related to the suitable placement of the nanocatalysts down in the reservoir. Although there have been many reports regarding the transport behavior of nanoparticles in the porous media [109], most of them focused on nanoparticle movement in deep bed filtration for wastewater treatments, so the obtained results are obviously not representative of the reaction conditions which exist in the oil sand base matrix.

In recent years, there have been some efforts to examine nanoparticle transport behavior in the porous media for oil reservoir conditions [93, 109–111]. In one attempt the transport behavior of metallic and multimetallic nanoparticles at typical pressure and temperature of the SAGD recovery process were investigated. The results showed the feasibility of the UD nanoparticle propagation in the oil-sand-packed bed column, as neither major permeability reduction nor pore plugging, was observed [93]. According to the results, nanoparticles tend to aggregate in both low and high permeability conditions. Moreover, the deposition tendency of the nanoparticles was highly dependent on the type of the metal, temperature, and sand pack permeability. Figure 6.11 demonstrates the breakthrough curves for different nanoparticle transportations through porous media at high pressure and temperature [111].

In another study, the transport behavior of nanocatalysts inside the porous media at a lower temperature was investigated. The results showed that nanocatalysts were able to propagate through the sand medium; however, larger agglomerated particles

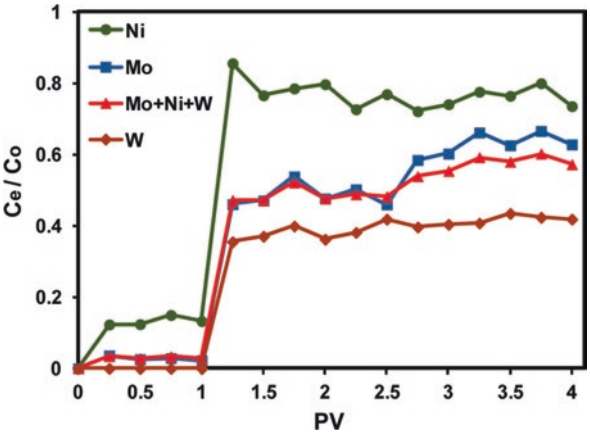

Fig. 6.11 Breakthrough curves for different multimetallic NPs suspended in VGO matrices in an oil-sand-packed bed column with clean silica sand of 100–140 mesh size saturated with Athabasca bitumen. Other test parameters are a residence time of 36 h, porosity of 33.7%, pressure of 3.5 MPa, and temperature of 320°C [111]. Permissions related to the material excerpted were obtained from the American Chemical Society, copyright 2012, and further permission should be directed to the American Chemical Society; Hashemi, R., N.N. Nassar, and P. Pereira-Almao, Transport behavior of multimetallic ultradispersed nanoparticles in an oil-sands-packed bed column at a high temperature and pressure. Energy & Fuels, 2012. **26**(3): pp. 1645–1655

were filtered out and remained inside the porous media [110]. According to these results, the sand media retained 14–18% of injected UD nanocatalysts, mainly at the bed entrance. However, this retention of nanocatalysts had a negligible effect on the pressure drop and caused no permeability damage inside the experimental medium.

Controlling the particle size during the injection and reaction times is one of the most important and challenging aspects of nanocatalyst transport inside the porous medium. This is crucial since the particle size would affect the pressure drop via permeability reduction, dispersion ability, adsorption affinity, and catalytic activity of nanoparticles inside the medium [93].

Another crucial topic in the sense of transport behavior of the nanocatalysts in the porous media is the mathematical modeling of this transportation. In fact, besides numerous experimental studies, valuable information on the concept of particle mass transfer can be provided by the robust mathematical modeling of nanocatalyst transport behavior inside the porous medium. Several researchers explored the modeling of mass transfer and deposition behavior of fine particles in cylindrical channels [64, 112–115]. In one of these novel studies [64], a mathematical model for nanocatalyst transport and deposition was developed that considers the geometry of the channel, fluid medium properties and characteristics, particle diameter and concentration, and the effects of the temperature on the particle agglomeration and deposition of nanocatalysts. This 2-D and 3-D convective-dispersive model, which provides the concentration profile of particles immersed in fluid media enclosed in a circular cross-section, was validated by experimental data obtained from an injection rig [64].

In short, nanocatalyst propagation inside the porous media is feasible, and UD multimetallic nanocatalysts could be controllably conveyed through oil sand porous media into a targeted heavy oil reservoir, where they could act as adsorbents/catalysts for the heavy oil upgrading process. However, the results showed that some parts of the injected particles could be retained inside the porous media. Nonetheless, the deposited particles inside the medium can potentially enhance the medium activity [116] and could be estimated by mathematical modeling [64].

6.10 Modeling of Reaction Kinetics

One of the important concepts related to in situ upgrading technology is the modeling of reaction kinetics. Generally, in chemical engineering, kinetic modeling is performed for effective process control and simulation of the reaction vessels. In in situ upgrading technology, process control is also of great importance to monitor the quality, exothermicity, and dilution and to reduce or eliminate the coke formation or oil instability. Therefore, modeling of reaction kinetics for in situ upgrading technology has great importance.

So far, several approaches have been proposed to model the reaction kinetics. Some of these methods are based on lumping techniques, while others used continuous mixture concepts. In general, the following methods have been presented to model the reaction kinetics [117]: lumping techniques, continuous mixture, structure-oriented lumping, and single event models.

Each of the abovementioned methods has its advantages and disadvantages. Due to complexities associated with the presence of large molecules like resins and asphaltenes, the lumping method has shown to be the best way to model the reaction kinetics in the case of bitumen and heavy oil upgrading [118–120]. In the following sections, some basic concepts related to kinetics are presented, and then catalytic hydroprocess reaction modeling techniques are discussed.

6.10.1 Kinetics

In order to comprehend the in situ upgrading process kinetics, it is crucial to learn about some basics of the chemical reactions. Reactions can be homogenous or heterogeneous. Reactions can also be classified based on their reversibility. The reaction is called irreversible when it is unidirectional and continues until the reactant is exhausted. On the other hand, reversible reactions can proceed in either direction based on the reactant and product concentration relative to the equilibrium condition. Catalytic heavy oil upgrading is a heterogeneous reaction. In this process, the reactant is adsorbed on the active site of the solid surface (catalyst) and reacts. The adsorption mechanism can be modeled by Langmuir-Hinshelwood isotherms.

It has been proven that the reaction rate constant is temperature dependent. This was first introduced by Svante Arrhenius and is described in the following equation known as Arrhenius equation:

$$k_A(T) = Ae^{-E/RT} \tag{6.9}$$

where A, E, R, and T are the pre-exponential factor or frequency factor, activation energy, universal gas constant, and absolute temperature, respectively. Any modeling of reaction kinetics should be able to predict the proper E and A for the desired system.

It is also noteworthy to mention the effect of the catalyst in enhancing the reaction rate based on the above equation. According to the collision theory, the frequency factor A is proportional to the number of collisions which can result in a reaction. Catalysts can provide a larger number of reaction sites and/or decrease the activation energy. Therefore, it can increase the chance of collision which leads to an increase in the frequency factor that finally results in increasing the rate constant and rate of reaction [121].

6.10.2 Reaction Kinetics Models

Different aspects of the heavy oil hydrocracking kinetics have been investigated based on proposed cracking reaction schemes [122–125]. Modeling the heavy crude oil reactions is a challenging task due to the complexities associated with the crude composition. Heavy crude oils and bitumen comprise thousands of different compounds and, most importantly, large molecules like asphaltenes and resins which make the modeling of reaction kinetic very complex. However, using the traditional lumping method along with defining the pseudo components is a common method for bitumen studies [118–120]. Group selection is one of the most important stages in this method. The number of groups will determine the amount of required experimental work for estimating the kinetic parameters. Generally, for modeling the reaction kinetics of bitumen, a first-order rate equation is used [126, 127].

In recent years, due to the advances in nanotechnology and proving the potential of UD catalyst application for enhancing the in situ upgrading process, several studies were performed to securitize the modeling of reaction kinetics for the UD catalytic hydrocracking. These models are mostly based on a famous lump model first proposed by Sanchez [124]. This model, which could precisely predict the product composition of heavy oil after hydrocracking, simply lumps the heavy oil to the following five different groups: residue (R), VGO, distillates (D), naphtha (N), and gases (G).

In a first attempt, Galarraga [58] applied the Sanchez model to study the kinetics of a catalytic hydrocracking process of crude oil. He used Ni-Mo-W UD catalysts for bitumen hydroprocessing in a batch reactor. After Galarraga obtained satisfactory evaluation results, Loria et al. [128] investigated the applicability of the lump

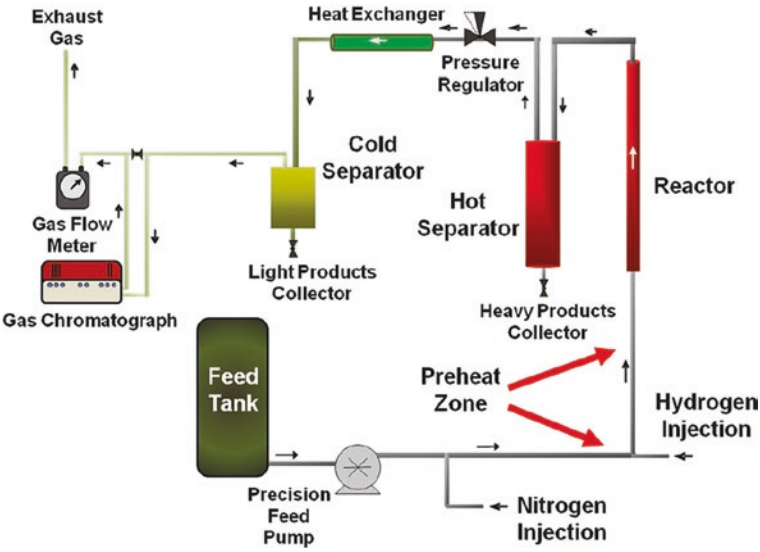

Fig. 6.12 Experimental setup used for evaluating the bitumen UD catalytic hydrocracking [128]. Permissions related to the material excerpted were obtained from the American Chemical Society, copyright 2011, and further permission should be directed to the American Chemical Society; Loria, H., et al., Kinetic modeling of bitumen hydroprocessing at in-reservoir conditions employing ultradispersed catalysts. Energy & Fuels, 2011. **25**(4): pp. 1364–1372

model to predict the kinetic parameters at a larger scale in a pilot plant test. The utilized pilot plant in this study is shown schematically in Fig. 6.12.

The results indicated that a great reduction in the viscosity of liquid products can occur based on the reaction temperature and residence time. They also proposed a modified model for UD catalytic hydrocracking which is shown in Fig. 6.13.

In another attempt, Da Silva De Andrade applied the same kinetic model to investigate the applicability of the Sanchez model to predict the kinetic parameters for ultradispersed catalytic hydrocracking of bitumen, vacuum residue, and pitch [129]. Their results demonstrate that the lump model is capable of predicting the kinetic parameter with high accuracy.

6.10.3 Model Description

This model consists of 5 lumps: residue (+550°C), VGO (343–545°C), distillates (216–343°C), naphtha (IBP – 216°C) and gases, and ten first-order reactions. Figure 6.14 shows the lumps and their reactions [124].

A kinetic expression is formulated for each component as a function of mass fraction and the kinetic constant which is shown below:

$$r_R = -\left(k_1 + k_2 + k_3 + k_4\right) \rightarrow y_R \tag{6.10}$$

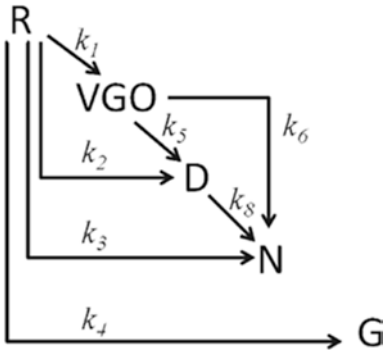

Fig. 6.13 Modified kinetic model for UD catalysts proposed by Loria et al. [128]. Permissions related to the material excerpted were obtained from the American Chemical Society, copyright 2011, and further permission should be directed to the American Chemical Society; Loria, H., et al., Kinetic modeling of bitumen hydroprocessing at in-reservoir conditions employing ultradispersed catalysts. Energy & Fuels, 2011. **25**(4): pp. 1364–1372

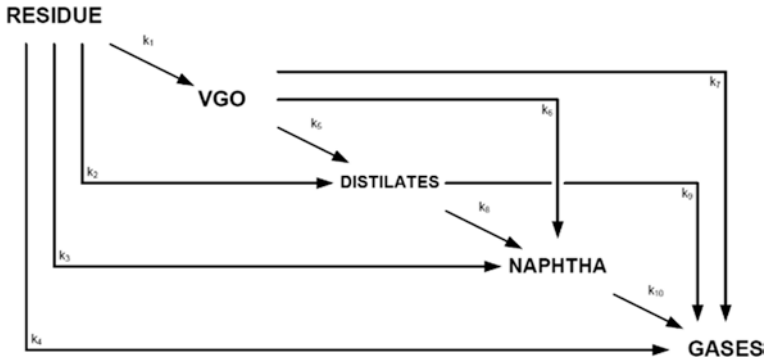

Fig. 6.14 Proposed kinetic model for the UD catalytic hydroprocessing of bitumen [124]. Permissions related to the material excerpted were obtained from the American Chemical Society, copyright 2005, and further permission should be directed to the American Chemical Society; Sánchez, S., M.A. Rodríguez, and J. Ancheyta, Kinetic model for moderate hydrocracking of heavy oils. Industrial & engineering chemistry research, 2005. **44**(25): pp. 9409–9413

$$r_{\mathrm{VGO}} = k_1 y_R - \left(k_5 + k_6 + k_7\right) \rightarrow y_{\mathrm{VGO}} \tag{6.11}$$

$$r_D = k_2 y_R + k_5 y_{\mathrm{VGO}} - \left(k_8 + k_9\right) \rightarrow y_D \tag{6.12}$$

$$r_N = k_3 y_R + k_6 y_{\mathrm{VGO}} + k_8 y_D - k_{10} \rightarrow y_R \tag{6.13}$$

$$r_G = k_4 y_R + k_7 y_{\mathrm{VGO}} + k_9 y_D + k_{10} \rightarrow y_N \tag{6.14}$$

where k, r, and y are reaction constant [h^{-1}], reaction rate [h^{-1}], and component mass fraction [wt%], respectively.

The results indicated that the proposed lump model could predict the kinetic parameters with an average percentage error of 3.11% and an overall correlation coefficient of 0.978, which indicates the suitability of the model for analyzing the UD catalytic hydrocracking of heavy oil and bitumen. There are also other studies which focused on the kinetics of the decomposition of bitumen and asphaltenes in the presence of the nanocatalysts. These studies also revealed some important aspects of the nanocatalyst hydrocracking and also the importance of the reaction kinetics modeling for such processes [130–134].

In another study, Elahi et al. [91] used the same lump model for heavy oil catalytic upgrading reactions in carbonate rocks. They found that the first reaction of the model (conversion of residue to VGO) played the most important role in the upgrading reactions and that reactions 7 and 9 do not have a significant impact on the overall reaction scheme, due to the negligible k values obtained. They therefore concluded that the gases were produced mainly from the residue and the naphtha cuts. Also, the authors found that the proposed model could successfully predict the products' distribution with an average error of 6% and with a good correlation to Arrhenius law.

6.11 Other Important Topics

6.11.1 Nanocatalyst Recycling

Nanocatalysts along with hydrogen incorporation aim to enhance the produced liquid quality via catalytic hydrocracking. As previously discussed, the fast deactivation of conventionally supported catalysts is one of the major disadvantages compared to UD nanocatalysts. UD nanocatalysts can also provide a desirable level of reaction activity and an option to implement at the well level [135]. Recyclability of the used nanocatalysts is a key bottleneck for their in situ application because recycling can lead to cost-saving as well as reducing the environmental footprint. Peluso, E. et al. [136] proposed a promising alternative for the downhole upgrading process. In this technique, nanocatalysts are injected inside the porous media through an injector well, and the upgraded oil is produced via recovery well. Produced liquid from the reservoir contains some active nanocatalysts inside the non-distillable residue which can be recycled and reinjected to the porous reservoir [136].

Understanding the nanocatalyst behavior with respect to stability and recyclability potential is of paramount importance since it can lead to favored economic outcomes. In one promising work, Peluso [136] demonstrated the feasibility of UD nanocatalyst recycling, although there is still the chance of particle agglomeration. However, the lack of extensive study in this area is quite tangible. In order to capture the main aspects of nanocatalyst recycling potential and challenges, it is crucial to perform more laboratory investigations and pilot-scale testing to make this technique economically beneficial for the existing heavy oil industry.

6.11.2 *Environmental Effect of Nanoparticles*

Nanotechnology is the science of controlling matters at the nanoscale [137], promising to enhance economics in different fields ranging from transportation to agriculture to health [138]. Over the last decade, numerous nanomaterials have been introduced to the marketplace [139] with direct and indirect application in society. Despite this fact, the effect of nanoparticles' exposure to human health and the environment is not clearly studied. Some research on this subject raised questions about the effects of these materials on humans and the environment [140]. From the environmental point of view, the benefits of nanoparticles are limited by potential challenges that may be difficult to predict. In addition, there is not sufficient information about the manufacturing, usage, and disposal of the nanomaterials and any associated risks from the exposure to nanomaterials [141]. Furthermore, detection methods, measurement, and analyzing and tracing the nanomaterials are still an ongoing area of research and development [142].

Nanoparticle applications as adsorbent/catalyst for heavy oil upgrading and recovery is a quite new and challenging chemical process, which like other areas of nanotechnology are faced with both opportunities and challenges. In this chapter, several challenges regarding the nanoparticle's application were addressed; however, there are still other issues which need to be fully scrutinized. For example, it is shown that some portions of injected nanofluids remain underground [93]. But the long-term effect of these deposited nanoparticles has not been studied. Furthermore, some operational issues like the possibility of groundwater contamination by the synthesized nanocatalysts should also be considered as an operational failure risk. Produced sustainable nanocatalysts show higher activity, higher selectivity, more efficient recovery, as well as durability and recyclability in a cost-effective process.

6.12 Conclusions

Due to their unique properties, nanoparticles have tremendous potential in oil and gas industry applications especially in the field of in situ catalytic upgrading of the heavy oils and bitumen. The in situ employment of nanoparticles would result in more oil recovery, as well as quality enhancement in all three produced phases of liquid, gas, and solid. Nanocatalysts demonstrate that they can enhance oil quality by viscosity reduction and API enhancement and are able to decrease the sulfur, nitrogen, metal, and MCR contents of the heavy oils via catalytic upgrading, which substantially increases the crude quality. Furthermore, they could considerably decrease GHG emissions.

Another important issue regarding the in situ application is the nanoparticle transport behavior in the porous media. The results exhibited that experimental studies along with mathematical modeling of the nanoparticle penetration inside the porous media and the reaction kinetics of the process can provide valuable information which helps to design a successful upgrading process.

Although the results obtained so far are a harbinger of the paramount effects of nanoparticles in the recovery and upgrading of the heavy oils and bitumen, there is still a long way ahead and a number of limitations and challenges which need to be addressed. For example, mass production of required nanoparticles, the stability of the produced volume, and the control over the size of the nanoparticles are some important topics that should be addressed in any industrial applications. Moreover, environmental considerations must be fully scrutinized before any mass usage of the nanoparticles in order to mitigate the associated risks. In this regard, nanoparticle recovery and reusing could be very promising in terms of process, economic, and environmental footprint reduction.

References

1. Thomas, S. (2008). Enhanced oil recovery-an overview. Oil & Gas Science and Technology-Revue de l'IFP, 63(1), 9-19.
2. Shah, A., Fishwick, R., Wood, J., Leeke, G., Rigby, S., & Greaves, M. (2010). A review of novel techniques for heavy oil and bitumen extraction and upgrading. Energy & Environmental Science, 3(6), 700-714.
3. Dietz, D. N. (1967, April). Hot-water drive. In 7th World Petroleum Congress. OnePetro.
4. Curtis, C., Kopper, R., Decoster, E., Guzman-Garcia, A., Huggins, C., Knauer, L., Minner, M., Kupsch, N., Linares, L.M., Rough, H. & Waite, M. (2002). Heavy-oil reservoirs. Oilfield Review, 14(3), 30-51.
5. Lake, L. W., Schmidt, R. L., & Venuto, P. B. (1992). A niche for enhanced oil recovery in the 1990s. Oilfield Review;(Netherlands), 4(1).
6. Ali, S. M. (1982, March). Steam Injection Theories-A Unified Approach. In SPE California Regional Meeting. OnePetro.
7. Meldau, R. F. (1979). Current steamflood technology. J Petrol Technol, 31(10), 1332-1342.
8. Speight, J. G. (2013). Enhanced recovery methods for heavy oil and tar sands. Elsevier.
9. W. G. Graves, J.E.L.D. Cardenas, M. E. Gurfinkel, A. W. Peats, *Heavy oil. 2007: Working Document of the NPC Global Oil & Gas Study*
10. Owens, W. D., & Suter, V. E. (1965). Steam stimulation–newest form of secondary petroleum recovery. Oil and Gas J, 82-87.
11. Alberta Chamber of Resources. 2002: Oil Sands Technology Roadmap
12. Butler, R. M. (1985). A new approach to the modelling of steam-assisted gravity drainage. Journal of Canadian Petroleum Technology, 24(03), 42-51.
13. Akin, S., & Bagci, S. (2001). A laboratory study of single-well steam-assisted gravity drainage process. Journal of petroleum science and engineering, 32(1), 23-33.
14. Kamath, V. A., Sinha, S., & Hatzignatiou, D. G. (1993, May). Simulation study of steam-assisted gravity drainage process in ugnu tar sand reservoir. In SPE Western Regional Meeting. OnePetro.
15. Queipo, N. V., Goicochea, J. V., & Pintos, S. (2002). Surrogate modeling-based optimization of SAGD processes. Journal of Petroleum Science and Engineering, 35(1-2), 83-93.
16. S. Purkayastha, *Control and Optimization of Steam Injection for Steam-Assisted Gravity Drainage (SAGD)*
17. Das, S. K., & Butler, R. M. (1995, October). Extraction of heavy oil and bitumen using solvents at reservoir pressure. In Technical meeting/petroleum conference of the South Saskatchewan section. OnePetro.
18. Gates, I. D. (2007). Oil phase viscosity behaviour in expanding-solvent steam-assisted gravity drainage. Journal of Petroleum Science and Engineering, 59(1-2), 123-134.

19. Jiang, Q., Butler, R., & Yee, C. T. (1998, June). The steam and gas push (SAGP)-2: mechanism analysis and physical model testing. In Annual Technical Meeting. OnePetro.
20. Grant, B. F., & Szasz, S. E. (1954). Development of an underground heat wave for oil recovery. Journal of Petroleum Technology, 6(05), 23-33.
21. Howard, F. A. (1923). U.S. Patent No. 1,473,348. Washington, DC: U.S. Patent and Trademark Office.
22. Wolcott, E. R. (1923). U.S. Patent No. 1,457,479. Washington, DC: U.S. Patent and Trademark Office.
23. Ali, S. M. (1972). A current appraisal of in-situ combustion field tests. Journal of Petroleum Technology, 24(04), 477-486.
24. Brigham, W. E., Satman, A., & Soliman, M. Y. (1980). Recovery correlations for in-situ combustion field projects and application to combustion pilots. Journal of Petroleum Technology, 32(12), 2132-2138.
25. Chu, C. (1977). A study of fireflood field projects (includes associated paper 6504). Journal of Petroleum Technology, 29(02), 111-120.
26. Cheih, C. (1982). State-of-the-art review of fireflood field projects (includes associated papers 10901 and 10918). Journal of Petroleum Technology, 34(01), 19-36.
27. Lake, L. W. (1989). Enhanced oil recovery.
28. Martin, W. L., Alexander, J. D., & Dew, J. N. (1958). Process variables of in situ combustion. Transactions of the AIME, 213(01), 28-35.
29. Dietz, D. N., & Weijdema, J. (1968). Wet and partially quenched combustion. Journal of Petroleum Technology, 20(04), 411-415.
30. Greaves, M., & Al-Shamali, O. (1996). In situ combustion isc process using horizontal wells. Journal of Canadian Petroleum Technology, 35(04).
31. Greaves, M., Tuwil, A. A., & Bagci, A. S. (1993). Horizontal producer wells in in situ combustion (ISC) processes. Journal of Canadian Petroleum Technology, 32(04).
32. Kendall, R., Chopra, S., Lines, L. R., Schmitt, D. R., & Batzle, M. L. (2010). Using time-lapse seismic to monitor the toe-to-heel-air-injection (THAI™) heavy-oil production process. In Heavy Oils: Reservoir characterization and production monitoring (pp. 275-284). Society of Exploration Geophysicists.
33. Greaves, M., Xia, T. X., Turta, A. T., & Ayasse, C. (2000, April). Recent laboratory results of THAI and its comparison with other IOR processes. In SPE/DOE Improved Oil Recovery Symposium. OnePetro.
34. Ameli, F., Alashkar, A., & Hemmati-Sarapardeh, A. (2018). Thermal Recovery Processes. Fundamentals of Enhanced Oil and Gas Recovery from Conventional and Unconventional Reservoirs.
35. Suncor, E., & Canadian Heavy Oil Association. (2005). Proceedings of the 2005 SPE/PS-CIM/CHOA International Thermal Operations and Heavy Oil Symposium: Heavy Oil: Integrating the Pieces.
36. Moore, R. G., Laureshen, C. J., Mehta, S. A., Ursenbach, M. G., Belgrave, J. D. M., Weissman, J. G., & Kessler, R. V. (1999). A downhole catalytic upgrading process for heavy oil using in situ combustion. Journal of Canadian Petroleum Technology, 38(13).
37. Weissman, J. G., Kessler, R. V., Sawicki, R. A., Belgrave, J. D. M., Laureshen, C. J., Mehta, S. A., ... & Ursenbach, M. G. (1996). Down-hole catalytic upgrading of heavy crude oil. Energy & fuels, 10(4), 883-889.
38. Weissman, J. G., & Kessler, R. V. (1996). Downhole heavy crude oil hydroprocessing. Applied Catalysis A: General, 140(1), 1-16.
39. Greaves, M., & Xia, T. (2001, June). CAPRI-Downhole catalytic process for upgrading heavy oil: Produced oil properties and composition. In Canadian international petroleum conference. OnePetro.
40. Secure Fuels from Domestic Resources*, The Continuing Evolution of America's Oil Shale and Tar Sands Industries* (U.S. Department of Energy, 2007), pp. 28–29
41. Husein, M. M., & Nassar, N. N. (2008). Nanoparticle preparation using the single microemulsions scheme. Current Nanoscience, 4(4), 370-380.

42. Niemeyer, C. M. (2001). Nanoparticles, proteins, and nucleic acids: biotechnology meets materials science. Angewandte Chemie International Edition, 40(22), 4128-4158.
43. Almao, P. P. (2012). In situ upgrading of bitumen and heavy oils via nanocatalysis. The Canadian Journal of Chemical Engineering, 90(2), 320-329.
44. Khoudiakov, M., Gupta, M. C., & Deevi, S. (2005). Au/Fe2O3 nanocatalysts for CO oxidation: a comparative study of deposition–precipitation and coprecipitation techniques. Applied Catalysis A: General, 291(1-2), 151-161.
45. Nassar, N. N. (2012). Iron oxide nanoadsorbents for removal of various pollutants from wastewater: an overview. Application of adsorbents for water pollution control, 81-118.
46. Nassar, N. N., & Husein, M. M. (2007). Study and modeling of iron hydroxide nanoparticle uptake by AOT (w/o) microemulsions. Langmuir, 23(26), 13093-13103.
47. Somorjai, G. A., Tao, F., & Park, J. Y. (2008). The nanoscience revolution: merging of colloid science, catalysis and nanoelectronics. Topics in Catalysis, 47(1), 1-14.
48. Wang, D., Xie, T., & Li, Y. (2009). Nanocrystals: Solution-based synthesis and applications as nanocatalysts. Nano Research, 2(1), 30-46.
49. Alivisatos, A. P., Johnsson, K. P., Peng, X., Wilson, T. E., Loweth, C. J., Bruchez, M. P., & Schultz, P. G. (1996). Organization of'nanocrystal molecules' using DNA. Nature, 382(6592), 609-611.
50. Bock, C., Paquet, C., Couillard, M., Botton, G. A., & MacDougall, B. R. (2004). Size-selected synthesis of PtRu nano-catalysts: reaction and size control mechanism. Journal of the American Chemical Society, 126(25), 8028-8037.
51. Galarraga, C. E. (2011). Upgrading Athabasca bitumen using submicronic NiWMo catalysts at conditions near to in-reservoir operation.
52. Gobe, M. (1983). Preparation and characterization of monodisperse magnetite sols in W/O microemulsion.
53. Hellweg, T. (2002). Phase structures of microemulsions. Current opinion in colloid & interface science, 7(1-2), 50-56.
54. Murray, C., Norris, D. J., & Bawendi, M. G. (1993). Synthesis and characterization of nearly monodisperse CdE (E= sulfur, selenium, tellurium) semiconductor nanocrystallites. Journal of the American Chemical Society, 115(19), 8706-8715.
55. Pluym, T. C., Powell, Q. H., Gurav, A. S., Ward, T. L., Kodas, T. T., Wang, L. M., & Glicksman, H. D. (1993). Solid silver particle production by spray pyrolysis. Journal of aerosol science, 24(3), 383-392.
56. Shen, S. C., Hidajat, K., Yu, L. E., & Kawi, S. (2004). Simple hydrothermal synthesis of nanostructured and nanorod Zn–Al complex oxides as novel nanocatalysts. Advanced Materials, 16(6), 541-545.
57. Yao, Y. L., Ding, Y., Ye, L. S., & Xia, X. H. (2006). Two-step pyrolysis process to synthesize highly dispersed Pt–Ru/carbon nanotube catalysts for methanol electrooxidation. Carbon, 44(1), 61-66.
58. Galarraga, C. E., Scott, C., Loria, H., & Pereira-Almao, P. (2012). Kinetic models for upgrading athabasca bitumen using unsupported NiWMo catalysts at low severity conditions. Industrial & engineering chemistry research, 51(1), 140-146.
59. Capek, I. (2004). Preparation of metal nanoparticles in water-in-oil (w/o) microemulsions. Advances in colloid and interface science, 110(1-2), 49-74.
60. Pereira, P., Marzin, R., Zacarias, L., Cordova, J., Carrazza, J., & Marino, M. (1999). U.S. Patent No. 5,885,441. Washington, DC: U.S. Patent and Trademark Office.
61. Vasquez, A. (2007, February). Synthesis, characterization and model reactivity of ultra dispersed catalysts for hydroprocessing. In Masters Abstracts International (Vol. 47, No. 03).
62. Thompson, J., Vasquez, A., Hill, J. M., & Pereira-Almao, P. (2008). The synthesis and evaluation of up-scalable molybdenum based ultra dispersed catalysts: effect of temperature on particle size. Catalysis letters, 123(1), 16-23.
63. Lapeira, C. C. (2009). Development of a new methodology for preparing nanometric Ni, Mo and NiMo catalytic particles using transient emulsions (Doctoral dissertation, University of Calgary, Department of Chemistry).

64. Molina, L., & Javier, H. (2009). Transport of catalytic particles immersed in fluid media through cylindrical geometries under heavy oil upgrading conditions (Vol. 70, No. 12).
65. Alamolhoda, S., Vitale, G., Hassan, A., Nassar, N. N., & Pereira Almao, P. (2019). Development and characterization of novel combinations of Ce-Ni-MFI solids for water gas shift reaction. The Canadian Journal of Chemical Engineering, 97(1), 140-151.
66. Li, Y., Fu, Q., & Flytzani-Stephanopoulos, M. (2000). Low-temperature water-gas shift reaction over Cu-and Ni-loaded cerium oxide catalysts. Applied Catalysis B: Environmental, 27(3), 179-191.
67. Hart, A., Shah, A., Leeke, G., Greaves, M., & Wood, J. (2013). Optimization of the CAPRI process for heavy oil upgrading: effect of hydrogen and guard bed. Industrial & Engineering Chemistry Research, 52(44), 15394-15406.
68. Shah, A. A., Fishwick, R. P., Leeke, G. A., Wood, J., Rigby, S. P., & Greaves, M. (2011). Experimental optimization of catalytic process in situ for heavy-oil and bitumen upgrading. Journal of Canadian Petroleum Technology, 50(11), 33-47.
69. Ortiz-Moreno, H., Ramírez, J., Sanchez-Minero, F., Cuevas, R., & Ancheyta, J. (2014). Hydrocracking of Maya crude oil in a slurry-phase batch reactor. II. Effect of catalyst load. Fuel, 130, 263-272.
70. Hart, A., Greaves, M., & Wood, J. (2015). A comparative study of fixed-bed and dispersed catalytic upgrading of heavy crude oil using-CAPRI. Chemical Engineering Journal, 282, 213-223.
71. Noguera, G., Araujo, S., Hernández, J., Rivas, A., Mendoza, D., & Castellano, O. (2012). A comparative activity study of a new ultra-dispersed catalyst system for a hydrocracking/hydrotreating technology using vacuum residue oil: Merey/Mesa. Chemical Engineering Research and Design, 90(11), 1979-1988.
72. Panariti, N., Del Bianco, A., Del Piero, G., & Marchionna, M. (2000). Petroleum residue upgrading with dispersed catalysts: Part 1. Catalysts activity and selectivity. Applied Catalysis A: General, 204(2), 203-213.
73. Speight, J. G. (1981). The Desulfurization of Heavy Oils and Residua, Mercel Dekker. Inc., NY, 119-127.
74. Leprince, P. (2001). Petroleum refining. Vol. 3 conversion processes (Vol. 3). Editions Technip.
75. Alema´n-Va´zquez, L. O., Torres-Mancera, P., Ancheyta, J., & Rami´rez-Salgado, J. (2016). Use of hydrogen donors for partial upgrading of heavy petroleum. Energy & Fuels, 30(11), 9050-9060.
76. Albertazzi, S., Rodríguez-Castellón, E., Livi, M., Jiménez-López, A., & Vaccari, A. (2004). Hydrogenation and hydrogenolysis/ring-opening of naphthalene on Pd/Pt supported on zirconium-doped mesoporous silica catalysts. Journal of Catalysis, 228(1), 218-224.
77. Liu, Y., & Fan, H. (2002). The effect of hydrogen donor additive on the viscosity of heavy oil during steam stimulation. Energy & fuels, 16(4), 842-846.
78. Satchell Jr, D. P. (2009). U.S. Patent No. 7,594,990. Washington, DC: U.S. Patent and Trademark Office.
79. E.L. Wilson Jr, W.N. Mitchell, *Hydrogen-donor coal liquefaction process,* USA Patent US 4210518, 1980
80. Derbyshire, F. J., Mitchell, T. O., & Whitehurst, D. D. (1981). U.S. Patent No. 4,292,168. Washington, DC: U.S. Patent and Trademark Office.
81. Chen, Q., Gao, Y., Wang, Z. X., & Guo, A. J. (2014). Application of coker gas oil used as industrial hydrogen donors in visbreaking. Petroleum science and technology, 32(20), 2506-2511.
82. Langer, A. W., Stewart, J., Thompson, C. E., White, H. T., & Hill, R. M. (1962). Hydrogen donor diluent visbreaking of residua. Industrial & Engineering Chemistry Process Design and Development, 1(4), 309-312.
83. Hart, A., Lewis, C., White, T., Greaves, M., & Wood, J. (2015). Effect of cyclohexane as hydrogen-donor in ultradispersed catalytic upgrading of heavy oil. Fuel Processing Technology, 138, 724-733.

84. Martínez-Palou, R., de Lourdes Mosqueira, M., Zapata-Rendón, B., Mar-Juárez, E., Bernal-Huicochea, C., de la Cruz Clavel-López, J., & Aburto, J. (2011). Transportation of heavy and extra-heavy crude oil by pipeline: A review. Journal of petroleum science and engineering, 75(3-4), 274-282.
85. Billon, A., & Bigeard, P. H. (2001). Chapter 10. Hydrocracking. Petroleum refining.
86. Gates, B. C., Katzer, J. R., & Schuit, G. C. (1979). Chemistry of catalytic processes. Mcgraw-Hill College.
87. Galarraga, C. E., & Pereira-Almao, P. (2010). Hydrocracking of Athabasca bitumen using submicronic multimetallic catalysts at near in-reservoir conditions. Energy & Fuels, 24(4), 2383-2389.
88. Hashemi, R., Nassar, N. N., & Almao, P. P. (2014). Nanoparticle technology for heavy oil in-situ upgrading and recovery enhancement: Opportunities and challenges. Applied Energy, 133, 374-387.
89. Pauls, R. W., Abboud, S. A., & Turchenek, L. W. (1996). Pollutant deposition impacts on lichens, mosses, wood and soil in the Athabasca Oil Sands area.
90. Anderson, B. S., Chambers, J. I., & McMurray, D. R. (1995, June). Market Outlook For Athabasca Bitumen--The Economics of Location. In SPE International Heavy Oil Symposium. OnePetro.
91. Elahi, S. M., Scott, C. E., Chen, Z., & Pereira-Almao, P. (2019). In-situ upgrading and enhanced recovery of heavy oil from carbonate reservoirs using nano-catalysts: Upgrading reactions analysis. Fuel, 252, 262-271.
92. Hassan, A., Carbognani, L., & Pereira-Almao, P. (2008). Development of an alternative setup for the estimation of microcarbon residue for heavy oil and fractions: Effects derived from air presence. Fuel, 87(17-18), 3631-3639.
93. Hashemi, R., Nassar, N. N., & Pereira Almao, P. (2014). In situ upgrading of Athabasca bitumen using multimetallic ultradispersed nanocatalysts in an oil sands packed-bed column: Part 1. Produced liquid quality enhancement. Energy & fuels, 28(2), 1338-1350.
94. Hashemi, R., Nassar, N. N., & Pereira Almao, P. (2014). In situ upgrading of athabasca bitumen using multimetallic ultradispersed nanocatalysts in an oil sands packed-bed column: Part 2. Solid analysis and gaseous product distribution. Energy & fuels, 28(2), 1351-1361.
95. Breysse, M., Djega-Mariadassou, G., Pessayre, S., Geantet, C., Vrinat, M., Pérot, G., & Lemaire, M. (2003). Deep desulfurization: reactions, catalysts and technological challenges. Catalysis Today, 84(3-4), 129-138.
96. Farshid, D., Reynolds, B. *Process for upgrading heavy oil using a highly active slurry catalyst composition*. USA Patent, US7431823B2, 2008
97. M.R. de Agudelo, C. Galarraga, *Catalyst for the simultaneous hydrodemetallization and hydroconversion of heavy hydrocarbon feedstocks*. USA patent US4729980A, 1988
98. de Agudelo, M. R., & Galarraga, C. (1991). A stable catalyst for heavy oil processing: III. Activity and selectivity. The Chemical Engineering Journal, 46(2), 61-68.
99. Kennepohl, D., & Sanford, E. (1996). Conversion of Athabasca bitumen with dispersed and supported Mo-based catalysts as a function of dispersed catalyst concentration. Energy & Fuels, 10(1), 229-234.
100. Sanford, E. C. (1995). Conradson carbon residue conversion during hydrocracking of Athabasca bitumen: Catalyst mechanism and deactivation. Energy & fuels, 9(3), 549-559.
101. Newson, E. (1975). Catalyst deactivation due to pore-plugging by reaction products. Industrial & Engineering Chemistry Process Design and Development, 14(1), 27-33.
102. Altgelt, K. H. (1993). Composition and analysis of heavy petroleum fractions. CRC press.
103. Ancheyta, J., Rana, M. S., & Furimsky, E. (2005). Hydroprocessing of heavy petroleum feeds: Tutorial. Catalysis today, 109(1-4), 3-15.
104. Pereira-Almao, P. (2007, May). Fine tuning conventional hydrocarbon characterization to highlight catalytic upgrading pathways. In Proceedings of Variability of the Oil Sands Resource Workshop, Lake Louise, AB.
105. Lee, D. K., Koon, P. S., Yoon, W. L., Lee, I. C., & Woo, S. I. (1995). Residual oil hydrodesulfurization using dispersed catalysts in a carbon-packed trickle bed flow reactor. Energy & fuels, 9(1), 2-9.

106. Jordaan, S. M. (2011). Governance of Impacts to Land and Water Resources from Oil Sands Development in Alberta. Laboratory on International Law and Regulation, UC San Diego, La Jolla.
107. Gosselin, P., Hrudey, S. E., Naeth, M. A., Plourde, A., Therrien, R., Van Der Kraak, G., & Xu, Z. (2010). Environmental and health impacts of Canada's oil sands industry. Royal Society of Canada, Ottawa, ON, 10.
108. McEachern, P. (2009). Environmental management of Alberta's oil sands.
109. Zamani, A., & Maini, B. (2009). Flow of dispersed particles through porous media—deep bed filtration. Journal of Petroleum Science and Engineering, 69(1-2), 71-88.
110. Zamani, A., Maini, B., & Pereira-Almao, P. (2010). Experimental study on transport of ultra-dispersed catalyst particles in porous media. Energy & Fuels, 24(9), 4980-4988.
111. Hashemi, R., Nassar, N. N., & Pereira-Almao, P. (2012). Transport behavior of multimetallic ultradispersed nanoparticles in an oil-sands-packed bed column at a high temperature and pressure. Energy & Fuels, 26(3), 1645-1655.
112. Adamczyk, Z., & Van De Ven, T. G. (1981). Deposition of particles under external forces in laminar flow through parallel-plate and cylindrical channels. Journal of Colloid and Interface Science, 80(2), 340-356.
113. Brady, J. F. (1994). The long-time self-diffusivity in concentrated colloidal dispersions. Journal of Fluid Mechanics, 272, 109-134.
114. Sarimeseli, A., & Kelbaliyev, G. (2004). Modeling of the break-up of deformable particles in developed turbulent flow. Chemical engineering science, 59(6), 1233-1240.
115. Yoshioka, N., Karaoka, C., & Emi, H. (1972). On the deposition of aerosol particles to the horizontal pipe wall from turbulent stream. Kagaku Kogaku, 36(9), 1010-1016.
116. Hashemi, R., Nassar, N. N., & Pereira Almao, P. (2013). Enhanced heavy oil recovery by in situ prepared ultradispersed multimetallic nanoparticles: A study of hot fluid flooding for Athabasca bitumen recovery. Energy & Fuels, 27(4), 2194-2201.
117. Ancheyta, J., Sánchez, S., & Rodríguez, M. A. (2005). Kinetic modeling of hydrocracking of heavy oil fractions: A review. Catalysis Today, 109(1-4), 76-92.
118. Gray, M. R. (1990). Lumped kinetics of structural groups: hydrotreating of heavy distillate. Industrial & engineering chemistry research, 29(4), 505-512.
119. Martens, G. G., & Marin, G. B. (2001). Kinetics for hydrocracking based on structural classes: Model development and application. AIChE journal, 47(7), 1607-1622.
120. Singh, J., Kumar, M. M., Saxena, A. K., & Kumar, S. (2005). Reaction pathways and product yields in mild thermal cracking of vacuum residues: A multi-lump kinetic model. Chemical Engineering Journal, 108(3), 239-248.
121. Gray, M. R. (2015). Upgrading oilsands bitumen and heavy oil. University of Alberta.
122. Alhumaizi, K. I., Akhmedov, V. M., Al-Zahrani, S. M., & Al-Khowaiter, S. H. (2001). Low temperature hydrocracking of n-heptane over Ni-supported catalysts: study of global kinetics. Applied Catalysis A: General, 219(1-2), 131-140.
123. Krishna, R., & Saxena, A. K. (1989). Use of an axial-dispersion model for kinetic description of hydrocracking. Chemical engineering science, 44(3), 703-712.
124. Sánchez, S., Rodríguez, M. A., & Ancheyta, J. (2005). Kinetic model for moderate hydrocracking of heavy oils. Industrial & engineering chemistry research, 44(25), 9409-9413.
125. Scherzer, J., & Gruia, A. J. (1996). Hydrocracking science and technology. Crc Press.
126. Köseoğlu, R. Ö., & Phillips, C. R. (1987). Kinetics of non-catalytic hydrocracking of Athabasca bitumen. Fuel, 66(6), 741-748.
127. Köseoğlu, R. Ö., & Phillips, C. R. (1988). Kinetic models for the non-catalytic hydrocracking of Athabasca bitumen. Fuel, 67(7), 906-915.
128. Loria, H., Trujillo-Ferrer, G., Sosa-Stull, C., & Pereira-Almao, P. (2011). Kinetic modeling of bitumen hydroprocessing at in-reservoir conditions employing ultradispersed catalysts. Energy & Fuels, 25(4), 1364-1372.
129. Da Silva De Andrade, F. J. (2014). Kinetic modeling of catalytic in situ upgrading for Athabasca bitumen, deasphalting pitch and vacuum residue (Master's thesis, Graduate Studies).

130. Nassar, N. N., Hassan, A., Luna, G., & Pereira-Almao, P. (2013). Kinetics of the catalytic thermo-oxidation of asphaltenes at isothermal conditions on different metal oxide nanoparticle surfaces. Catalysis today, 207, 127-132.
131. Nassar, N. N., Hassan, A., Luna, G., & Pereira-Almao, P. (2013). Comparative study on thermal cracking of Athabasca bitumen. Journal of thermal analysis and calorimetry, 114(2), 465-472.
132. Nassar, N. N., Hassan, A., & Pereira-Almao, P. (2011). Application of nanotechnology for heavy oil upgrading: Catalytic steam gasification/cracking of asphaltenes. Energy & Fuels, 25(4), 1566-1570.
133. Nassar, N. N., Hassan, A., & Pereira-Almao, P. (2012). Thermogravimetric studies on catalytic effect of metal oxide nanoparticles on asphaltene pyrolysis under inert conditions. Journal of thermal analysis and calorimetry, 110(3), 1327-1332.
134. Nassar, N. N., Hassan, A., & Vitale, G. (2014). Comparing kinetics and mechanism of adsorption and thermo-oxidative decomposition of Athabasca asphaltenes onto TiO2, ZrO2, and CeO2 nanoparticles. Applied Catalysis A: General, 484, 161-171.
135. Nares, H. R., Schachat, P., Ramirez-Garnica, M. A., Cabrera, M., & Noe-Valencia, L. (2007, April). Heavy-crude-oil upgrading with transition metals. In Latin American & caribbean petroleum engineering conference. OnePetro.
136. Peluso, E. (2011). Hydroprocessing full-range of heavy oils and bitumen using ultradispersed catalysts at low severity (Vol. 73, No. 05).
137. Bergeson, L. L., & Auerbach, B. E. T. H. A. M. I. (2004). Reading the small print. In Environmental Forum (Vol. 21, No. 2, pp. 30-32). THE ENVIRONMENTAL LAW INSTITUTE.
138. Morris, J., & Willis, J. (2007). US Environmental Protection Agency nanotechnology white paper. US Environmental Protection Agency, Washington, DC.
139. Kahan, D. M., & Rejeski, D. (2009). PRoject on emeRging nanotechnologies.
140. Nel, A., Xia, T., Mädler, L., & Li, N. (2006). Toxic potential of materials at the nanolevel. science, 311(5761), 622-627.
141. Thomas, T., Thomas, K., Sadrieh, N., Savage, N., Adair, P., & Bronaugh, R. (2006). Research strategies for safety evaluation of nanomaterials, part VII: evaluating consumer exposure to nanoscale materials. Toxicological Sciences, 91(1), 14-19.
142. Breggin, L. K., & Carothers, L. (2006). Governing uncertainty: the nanotechnology environmental, health, and safety challenge. Colum. J. Envtl. L., 31, 285.

Chapter 7
Nanotechnology Applications for Viscosity Reduction of Heavy and Extra-Heavy Oils: A Review

Laura C. Bohorquez, Juan J. Insignares, Daniel Montes, Richard D. Zabala, Raul Osorio, Carlos A. Franco, Adriana Henao, Farid B. Cortés, and Camilo A. Franco

7.1 Introduction

With rising worldwide oil demand, heavy oil (HO) and extra-heavy oil (EHO) deposits have become a resource of great interest, accounting for at least half of all recoverable oil (IEA). The majority of HO is found in the following regions: the Orinoco Belt (Venezuela), Alberta (Canada), some regions of the Gulf of Mexico, and Northeast China [1]. Nonetheless, this type of crude oil has unfavorable physicochemical properties such as a low °API (American Petroleum Institute) gravity (not exceeding 20 °API) [2] and high viscosity that negatively impact the quality of these crude oils, which decreases their value and competitiveness within the market while increasing the operating costs related to their production/recovery and transport [3, 4]. These limitations are commonly associated with a high content of heavy compounds, mainly formed by resins and asphaltenes. The latter are some of the most complex crude oil molecules, and due to this complexity, no studies have deciphered them entirely. However, they are known for a high content of heteroatoms [5, 6], such as oxygen (O), nitrogen (N), and sulfur (S), that generate dipole moments inducing self-association between asphaltenes molecules [6, 7]. The self-aggregation ability of asphaltenes and the interaction of resins with the supramolecular

L. C. Bohorquez · J. J. Insignares · A. Henao
Fundación Universidad de América, Bogotá, Colombia

D. Montes · F. B. Cortés (✉) · C. A. Franco (✉)
Grupo de Investigación en Fenómenos de Superficie – Michael Polanyi, Facultad de Minas, Universidad Nacional de Colombia-Sede Medellín, Medellín, Colombia
e-mail: fbcortes@unal.edu.co; caafrancoar@unal.edu.co

R. D. Zabala · R. Osorio · C. A. Franco
Ecopetrol S.A., Puerres, Colombia

N. N. Nassar et al. (eds.), *Nanoparticles: An Emerging Technology for Oil Production and Processing Applications*, Lecture Notes in Nanoscale Science and Technology, https://doi.org/10.1007/978-3-319-12051-5_7

asphaltene assemblies give rise to the formation of a viscoelastic network, which is the main cause of the high viscosity typically observed in this type of fluid [8].

Due to these molecular interactions, the recovery factor of these crudes is 19% [9], which is less than the average of conventional deposits. This poor recovery makes their cost-benefit ratio unprofitable. Furthermore, they require increased energy expenditure for artificial lifting mechanisms, mainly progressive cavity pump (PCP) and electric submersible pumps (ESP) [10]. Crude oil acquires a gel consistency when at rest, which, among other issues, makes transport problematic, causing damage in pipelines due to corrosion, plugging, and other mechanisms. These problems increase the costs for maintenance of the pipelines as more power is needed in the suction and discharge pumps, which leads to a significant volume of these crudes being transported by tank car with potentially limited road access [3].

A wide variety of in situ techniques aimed at viscosity reduction have emerged to improve mobility at reservoir conditions and for surface transport. Thus, thermal recovery processes such as thermal injection, gas injection, catalysis for in situ upgrading [11, 12], and deasphalting [13], among others [11, 14, 15], are some of the main viscosity reduction methods. Thermal injection is problematic with regard to the diffusion of heat towards the formation, reducing thermal efficiencies, so that much energy is lost. Furthermore, high temperatures can cause unwanted transformations, and dissolutions of minerals that can cause damage via a reduction of permeability, alteration of wettability, and thermal degradation [16]. Moreover, gas injection results in low mobility rates, mainly due to the low viscosity of gases compared with the high viscosity of HOs.

Different techniques are similarly applied to improve the transportation of HOs, including dilution with lighter hydrocarbons [17], oil in water (o/w) emulsions [18], pipeline heating [19], pumping stations [20], and friction reduction (annular flow) [21]. These techniques are more energy-efficient because they do not require substantial equipment or facility development, which leads to a reduction in operating expenditures. However, these techniques generate high operating costs by requiring large amounts of solvents and diluents, which usually are not always readily available [22]. Furthermore, diluents are volatile compounds that modify upon evaporation before and while acting on the crude oil [23]. The effects of these mechanisms are not permanent and have a low perdurability in the viscosity reduction [24].

In this context, nanotechnology becomes one of the most attractive alternatives for improving the existing viscosity reduction mechanisms both at reservoir conditions and for surface transport. Based on previous studies [25], the use of nanotechnology in recovery processes decreases the energy required [26] by the aforementioned existing methods and increases recovery factor [27]. Other studies have evaluated nanoparticles and nanofluids of different chemical natures that lead to viscosity reductions up to 30% [28] and 90% [29], respectively.

In the oil industry, nanotechnology has attracted great research interest in the development and application of nanomaterials in different processes. Nanotechnology can be used in HO recovery processes to optimize existing mechanisms to reduce viscosity, energy consumption, and environmental impact [30–32].

Other studies have evaluated the effect of nanoparticles/nanofluids as viscosity reducers of HO and EHO by core flooding tests at reservoir conditions, demonstrating that the addition of nanoparticles increases the crude mobility and allows for oil recovery factor to increase by 16% [29]. These results have been validated in field trials in which crude oil production has been increased by more than 300 bopd [33].

The main objective of this section is to provide a review of the literature focused on the different mechanisms by which nanoparticles reduce the viscosity of HO and EHOs. Thus, the review accounts for the rheological properties of HO and EHOs, focusing mainly on viscosity. We then explain the mechanisms of interaction between nanoparticles and heavy fractions of crude oils, such as asphaltenes and resins. Subsequently, we describe different nanotechnology applications for viscosity reduction, including ultrasound cavitation, deasphalting, improved oil recovery (IOR) stimulation, and reduction of diluent consumption in transport. Finally, we present three field trials in Colombian oil fields where nanoparticles/nanofluids have been applied.

This chapter has been divided into five sections, including the introduction section. The second section describes HO and EHO rheological properties, such as viscosity, thixotropy, and yield point, accounting for their molecular weights and microstructures. This section also presents the composition and rheological behavior of heavy crudes as non-Newtonian and pseudoplastic fluids. The third section presents the main mechanisms of interaction between crude oil heavy fractions and nanoparticles generated by the adsorption phenomenon. We evaluate the effects of textural properties such as roughness, hydrodynamic diameter and surface area, chemical nature, and nanoparticle concentration. Section four details the different applications for reducing the viscosity of HO and EHO, assisted by nanoparticles categorized into surface processes and at reservoir conditions, designed to improve the mobility of crude oils in recovery and reduce the consumption of solvents such as naphtha. The final section presents three field trial cases wherein viscosity reduction is assisted by nanotechnology.

7.2 Properties of Heavy and Extra-Heavy Crude Oil

Crude oil physicochemical properties are related to their processing and commercialization quality and account for their classification into light, intermediate, heavy, and extra-heavy crude oils [34]. Among the predominant characteristics of HOs and EHOs are their unfavorable rheological properties such as high viscosities and their specific low gravity that does not exceed 20 °API [2]. Therefore, these crudes are categorized as low-quality resources [35]. Moreover, their limited mobility generates issues during extraction, transport [4, 23], and refining [36]. However, these properties are not alone in their negative impact. Rheological behavior also causes problems as these oils have a high content of heavy compounds, mainly asphaltenes and resins [37].

HOs are composed of saturated, aromatic, resins and asphaltenes (SARA) [38], in which the content of asphaltenes and resins significantly influence behavior due to their complexity. Asphaltenes are very polar aromatic compounds due to the presence of heteroatoms (oxygen, nitrogen, and sulfur) in their molecular structure. Heteroatoms produce a high dipole moment that allows asphaltenes to self-assembly. This ability, in conjunction with the presence of resins, leads to the formation of a 3D microstructure (viscoelastic network) that reduces the mobility of crudes by increasing their viscosity [39].

Moreover, according to previous studies, the asphaltenes can be described by their solubility and by their suppression of phase separation (SPS) [40], which refers to the formation and maintenance in solution of a new nuclei phase based on the asphaltene subfractions. In this way, asphaltenes are established to be a blend which is divided into two subfractions, A1 and A2 [40, 41]. This asphaltenes blend may present multiple interaction mechanisms for both fractions; however, fraction A1 predominantly interacts via hydrogen bonds, van der Waals forces, and acid–base interactions, while in fraction A2, stacking interactions predominate. Type A1 molecules are soluble in toluene at very low concentrations (approximately 90 mg•L^{-1}). At this concentration, the solid phase separation occurs, forming nuclei wherein type A1 molecules predominate. This separation is the main cause of the self-aggregation tendency of asphaltenes. Nevertheless, for asphaltenes to remain in solution, fraction A2 must be present, because when they intersperse with type A1 molecules, they penetrate into their micropores, thereby inhibiting the growth of the nuclei and the separation of the phases [41]. For this reason, these nuclei are considered a solid solution of A1-A2 [40, 41]. A molecular mechanics model simulating the previously mentioned nucleus phase is shown in Fig. 7.1.

However, in light crude oils, the asphaltene–asphaltene interactions tend to produce a lack of stability in the fluid matrix and are precipitated and subsequently deposited [42]. Thus, resins play a very important role in the structure of HOs, as they are polar and interact with asphaltene aggregates positioning on their surface in order to penetrate the micropores of asphaltenes and break the aggregation system providing such stability [43–45]. Resins have a high affinity with the A1 fraction found in solution due to the A2 fraction. Hence, resins enter in a "competition" with fraction A2 by the active sites of fraction A1 [43], which results in a 3D microstructure that triggers pseudoplastic behavior characteristic of a non-Newtonian fluid [46].

HOs and EHOs are considered colloidal blends because the heavy fractions are properly dispersed and stabilized in the blend, nevertheless there is no solution process [47, 48]. Consequently, heavy fractions are stabilized in the continuous phase, mainly because the resins prevent asphaltene precipitation. Stability effects are related to their non-Newtonian rheological behavior such as thixotropy, viscoelasticity [49] and yield stress [50]. Thixotropic behavior is characterized by a decrease of viscosity over time as the fluid undergoes shear stress, in the same way that it increases its viscosity over time when the flow is terminated [51, 52]. This behavior occurs because the interaction forces generated by the viscoelastic network are not

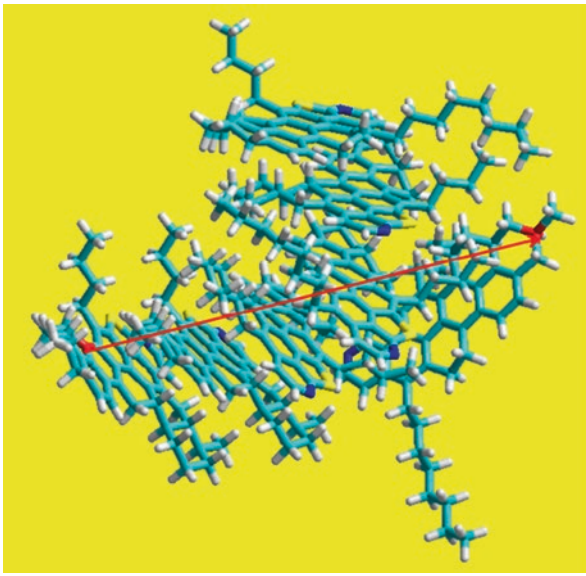

Fig. 7.1 Graphical representation of a molecular model of an asphaltene. (Reprinted with permission from Acevedo et al. [40]; Copyright 2018, ACS publications)

strong enough to withstand shear stress when the fluid is in motion, and the crude oil microstructure is broken down [40]. However, as soon as the fluid is left to rest, this network can be rebuilt. The impact of thixotropic mixtures is more severe at low temperatures, introducing problems associated with surface processes such as flow obstruction in pipes [53], gel formation, and difficulties in restart operations after the fluid has been static [54].

Viscoelasticity refers to the behavior of a fluid with properties between those of a pure solid and a pure liquid [48]. It is commonly related to thixotropy, and although every thixotropic fluid is viscoelastic, not all viscoelastic fluids are thixotropic. Hence, HOs and EHOs exhibit viscoelastic behavior [49]. In addition to these two properties, fluids may demonstrate yield stress, the minimum shear stress required for the fluid to start flowing [50]. All fluids can exhibit different rheological behaviors, especially when conditions vary. To understand the cause of these fluids' behaviors under variable conditions, it is necessary to understand their composition and structure [39, 55].

Viscoelastic networks are the main cause of the high viscosities of HOs. Viscosity is one of the most complex properties when working with HOs and EHOs because they exhibit great resistance to flow through the porous environment and pipes due to cohesion effects and adhesion of their internal particles [30]. These effects are problematic at reservoir conditions and on the surface.

7.3 Interaction Between Nanoparticles and Heavy Crude Oil Fraction

The interaction between nanoparticles and oil heavy fractions is mainly based on an adsorption process [56–58]. The adsorption phenomenon occurs when a solid can retain particles of a fluid on its surface after contact with the fluid. It describes the ability of the nanoparticle to retain asphaltenes on its surface. There are two types of adsorption: (*i*) physical adsorption or physisorption [59] and (*ii*) chemical adsorption or chemisorption [60–62]. The first type is reversible and is caused by electrostatic or dipolar attraction forces between asphaltenes and the nanoparticle's surface. The second is irreversible, occurs via chemical joints [63], and is due to the fact that the products are different from the reactants after desorption [64].

Because ions are not common in asphaltenes, it is difficult to achieve a chemical interaction. This interaction is commonly a physisorption process, characterized by its weak (van der Waals and dipolar) forces [57].

To better understand the process of interaction between nanoparticles and asphaltenes, the liquid–solid balance model (SLE) [65] was developed. In this model, the behavior of adsorption isotherms is studied, as the shape of their curve is significant in understanding the adsorptive phenomenon in terms of affinity and selectivity [57]. Asphaltene adsorption isotherms on the surface of different solids are related to the initial concentration of adsorbate (Co) and the amount adsorbed in the balance (q), taking into account three main parameters: the Henry's Law constant (H), constant on i-mer reactions (K), and the maximum amount of adsorption (q_m). Under these parameters, the process of adsorption of asphaltenes on the nanoparticle's surface may be explained in two main stages. The first stage implies the formation of a monolayer represented by the type I isotherms [66–68] consisting mainly of the most polar fractions. This layer presents the strongest interactions between nanoparticle and asphaltenes [40]. Once the monolayer has been saturated (all the active sites of the nanoparticle's surface have been occupied), the second stage begins, during which other layers are formed above the monolayer [69]. The interactions at this stage are between asphaltenes, so they tend to be weaker. Thus, the formation of a multilayer continues. Most studies have focused on understanding the adsorptive phenomena of asphaltenes and nanoparticles that follow predominantly type I and type III isotherms [43]. These reactions depend on the complexity of asphaltene self-association due to their influence on the interaction between adsorbate and adsorbent [58]. In addition, the methodology by which it is evaluated can affect the construction of the isothermal curve. Guzman et al. [58] proposed two different methods for asphaltenes of different origins (AspA and AspB). In method 1, a given amount of adsorbent in a fixed volume of liquid was exposed to a varying initial concentration of the adsorbate. In method 2, a known amount of asphaltenes in a fixed volume of liquid was exposed to a variable dosage of nanoparticle. The results are shown in Fig. 7.2. The isotherms intersect at a critical point, when they are operating under equal conditions. Method 1 is representative of type I isotherms and method 2 of type III isotherms. Another factor to consider in the construction of

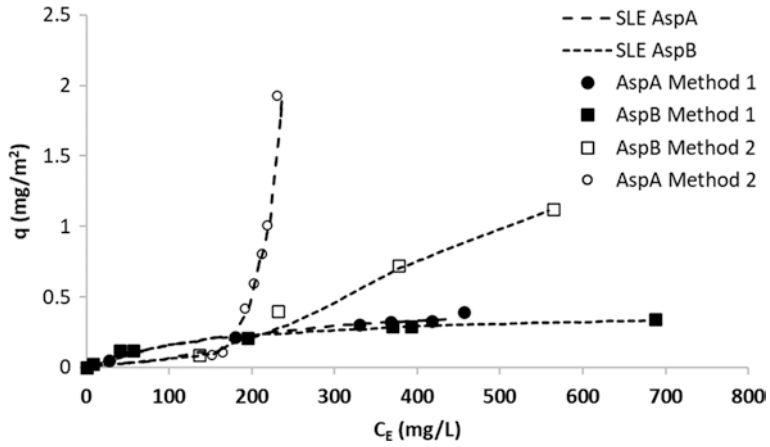

Fig. 7.2 Adsorption isotherms for models 1 and 2 against AspA and AspB. (Reprinted with permission from Guzmán et al. [58]; Copyright 2016, ACS publications)

isotherms is the origin of asphaltenes as it affects the asphaltene-asphaltene and asphaltene–nanoparticle interactions in which AspBs demonstrate greater adsorption capacity than AspAs.

When nanoparticles are added to crude oil, they interact directly with fraction A1 because the interaction between the nanoparticle and the A1 fraction is greater than the attraction forces between A1 molecules [70]. Moreover, fraction A1 has the highest polarity and, therefore, the lowest solubility. Under these conditions, the A1 fraction is most strongly attracted to the surface of the nanoparticle. During this process, the nanoparticle extracts fraction A1 from the viscoelastic network to retain it on its surface. This activity reduces aggregate size and subsequently alters the microstructure of crude oil, which disrupts the viscoelastic asphaltenes network [71]. Although type I resins present in the viscoelastic network may affect the nanoparticle–asphaltene interactions, recent studies have shown that adsorption of resins depends solely on their chemical nature and affinity for the nanoparticle [70]. Furthermore, the adsorption of asphaltenes is higher than the adsorption of resins. Therefore, the presence of resins loses importance in the adsorption process of asphaltenes.

Nanoparticles can adsorb certain heavy components of crude oil, such as asphaltenes and resins. However, previous studies have shown that nanoparticles have a higher affinity for asphaltenes than for resins [65, 71]. As shown in Fig. 7.3, three nanoparticles of different chemical natures were evaluated using adsorption isotherms [72]. The results showed an adsorption capacity in the order $SiO_2A > SiO_2 > Al_2O_3$. Figure 7.3 shows each nanoparticle's ability to reduce the size of asphaltene aggregates over a specific time, indicating that the asphaltene–nanoparticle interaction achieves network disruption and thereby reduces the size of asphaltene aggregates, leading to viscosity reduction [29]. As seen in Fig. 7.4, the SiO_2A nanoparticle achieves a greater reduction in the aggregate size of asphaltenes

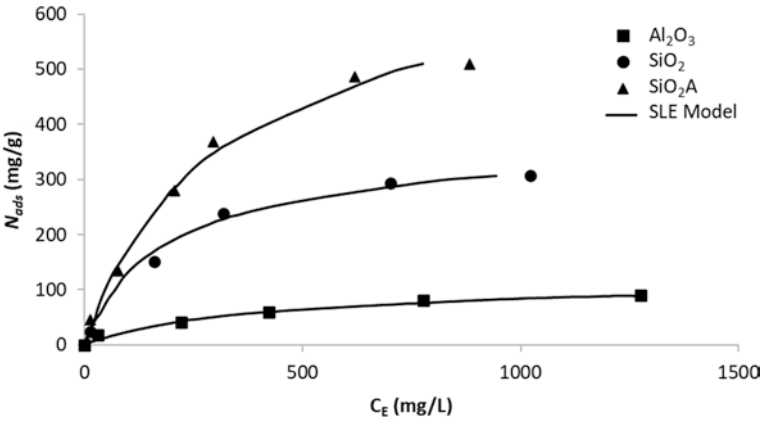

Fig. 7.3 SLE model of SiO_2A, SiO_2, and Al_2O_3 nanoparticles at 298 K. (Reprinted with permission from Taborda et al. [29]; Copyright 2016, Elsevier)

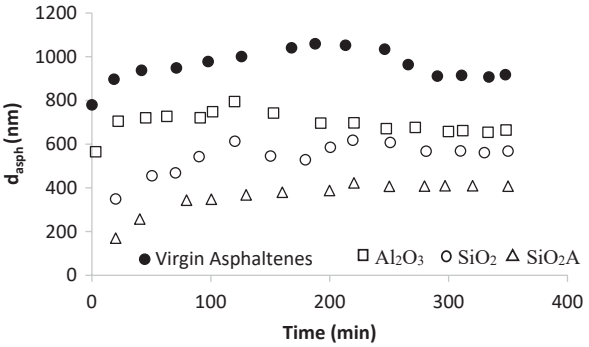

Fig. 7.4 Reduction of asphaltene aggregate size in the presence of SiO_2A, SiO_2, and Al_2O_3 nanoparticles vs. time. (Reprinted with permission from Taborda et al. [29]; Copyright 2016, Elsevier)

in a shorter time than Al_2O_3 and SiO_2 nanoparticles. As a result, it is possible to state that the greater the adsorption capacity, the greater the nanoparticle's ability to reduce the aggregate size of asphaltenes [29].

To analyze the viscoelastic behavior of crude oil, viscoelasticity is analyzed in terms of *i*) the storage modulus (G′), which is the ability of a material to store energy and deform after being submitted to stress, and *ii*) the loss modulus (G″), which indicates the material's ability to dissipate energy through the flow. If G′ > G″, the material is considered a viscoelastic solid. Conversely, if G″ > G′, it is a viscoelastic fluid [39, 73, 74]. Figure 7.5 shows the viscoelastic behavior of a heavy crude oil a) in the absence of nanoparticles and b) in the presence of nanoparticles relative to its phase angle (δ), which is generated in the response of the crude oil to the oscillatory stimulus [28].

In Fig. 7.5a and b, the behavior of a viscoelastic fluid is demonstrated as G″ > G′. However, the presence of nanoparticles results in a change in the fluid's internal structure, which is reflected in the decrease of G′ and G″ as well as an increase in the phase angle, as shown in Fig. 7.5b. The decrease of G′ and G″ values observed

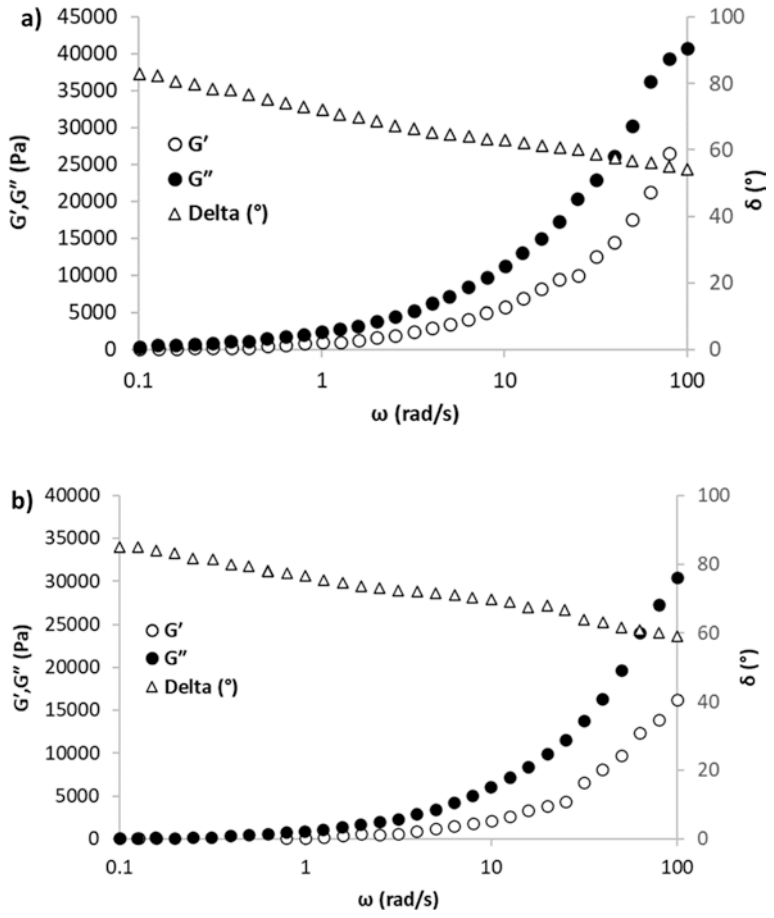

Fig. 7.5 The viscoelastic moduli for crude oil (**a**) in the absence and (**b**) presence of SiO_2 nanoparticles at 298 K. (Reprinted with permission from Taborda et al. [28]; Copyright 2016, Elsevier)

in Fig. 7.5b compared to Fig. 7.5a indicates a reduction in elastic and viscous contributions suggesting a more liquid-like than solid-like response and demonstrating a crude oil viscosity reduction [28].

Often, when HOs are subjected to an increasing shear rate, their viscosity decreases; however, with the addition of nanoparticles, crude oils reduce their viscosity without being subjected to stress [29, 75]. The modification of the fluid's microstructure and the disruption of the viscoelastic network of asphaltenes generates a change in the rheological properties of crude oil [28]. A more Newtonian behavior [63] appears in crude oil after adding the nanoparticles, suggesting a reduction in the pseudoplastic and thixotropic behaviors of the fluid [28, 32].

The viscosity reduction assisted by nanoparticles is due to the change of HO microstructure. As shown in Fig. 7.6, the oil matrix changes with the addition of

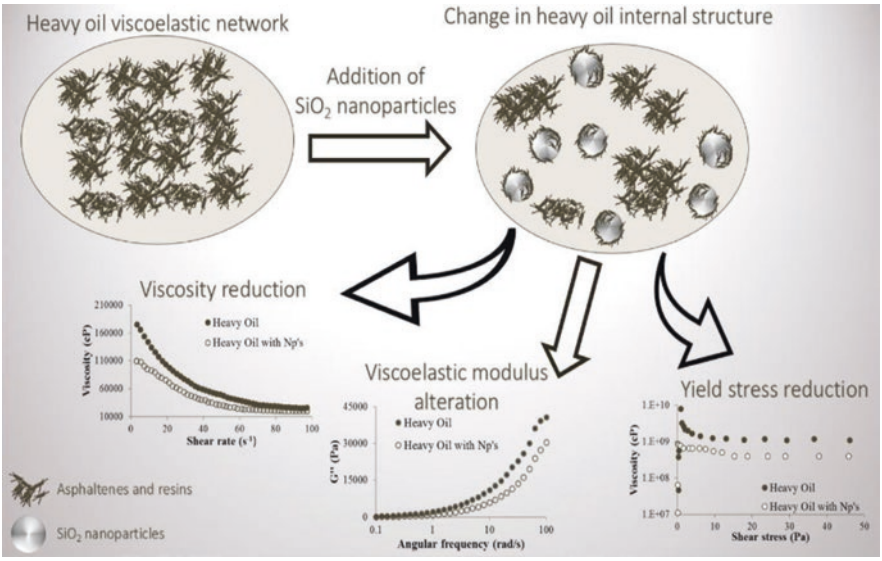

Fig. 7.6 Change of the heavy oil internal structure in the presence of SiO_2 nanoparticles. (Reprinted with permission from Taborda et al. [28]; Copyright 2016, Elsevier)

SiO_2 nanoparticles that disrupt the viscoelastic network formed by asphaltene aggregates in the presence of resins [28]. In this way, the viscoelastic network disruption is responsible for generating a decrease in fluid viscoelasticity and yield stress behavior [50], leading to viscosity reduction [39].

7.3.1 Effects of the Textural Properties of Nanoparticles

Textural properties play an important role in asphaltene–nanoparticle interaction, mainly influencing nanoparticles' adsorption capacity for asphaltenes. These properties include roughness [54], surface area, size [76], and hydrodynamic diameter [77]. Multiple authors [40, 41] have considered roughness a primary parameter in the formation of the monolayer in the adsorption process as it consists of the A1 fraction occupying the active nanoparticle sites and possibly generates a surface area blockage by steric effects. Montes et al. [54] evaluated the effect of textural properties of four SiO_2 nanoparticles obtained from different synthesis routes and silicon precursors and concluded that the availability of active surface sites substantially affects the adsorption process. However, roughness and surface area also play an important role in this phenomenon. Figure 7.7 shows the effect of (a) silica nanoparticle roughness and (b) silica nanoparticle surface area. Figure 7.7a suggests that increasing roughness may increase viscosity reduction. Figure 7.7b shows a possible increase in the viscosity reduction with an increase in surface area, except

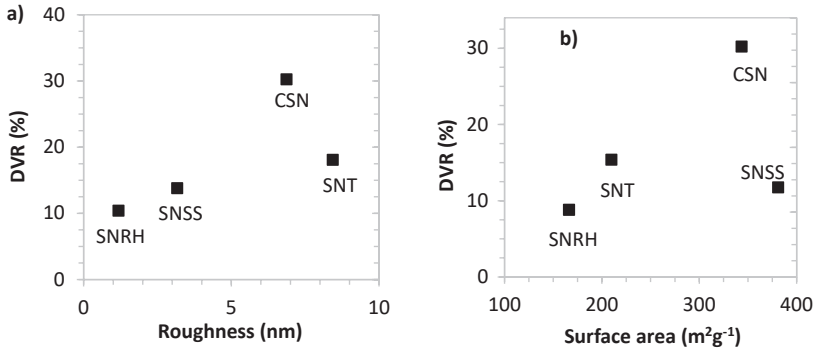

Fig. 7.7 Effect of four different silica nanoparticles' (**a**) roughness and (**b**) surface area on the degree of viscosity reduction (DVR) of heavy oil. (Reprinted with permission from Montes et al. [54]; Copyright 2020, ACS Omega)

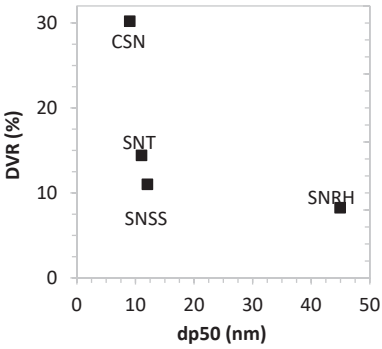

Fig. 7.8 Effect of the hydrodynamic diameter (dp50) on the degree of viscosity reduction (DVR) for four different silica nanoparticles. (Reprinted with permission from Montes et al. [54]; Copyright 2020, ACS Omega)

for one case. However, the study concluded that the number rather than the extent of active sites exposed on its surface was critical, since it is in the active sites where asphaltenes will be adsorbed. This property is linked to the size of the nanoparticles: an increase in viscosity reduction is seen as the size of the nanoparticle decreases [32]. This result can be associated with the nanoparticles' easy dispersion and diffusion in solution [76], generating greater interaction with asphaltenes and thereby increasing their contact area. As shown in Fig. 7.8, the hydrodynamic diameter is inversely proportional to viscosity reduction, as the lower the hydrodynamic diameter, the greater the reduction of viscosity. This is because it is linked to the exposure of functional groups on the surface of the nanoparticle. Thus, asphaltene adsorption strongly depends on the hydrodynamic diameter, nanoparticle size in suspension, and the type of active site.

7.3.2 Chemical Nature of the Effects of Nanoparticles

Several studies have evaluated the reduction of viscosity in the presence of multiple nanoparticle chemical types, including alumina [32, 78], silica [29, 32, 54], iron [32, 79], and nickel [31], among others. Modification of the nanoparticle's surface acidity has also been evaluated by several authors, who determined that such modification can affect their interaction forces. The above observation mainly depends on the number of basic and acidic centers of the specific asphaltene [32] and the chemical composition of the nanoparticle. As a result, several comparative studies have evaluated the nanoparticle's ability to reduce viscosity based on its surface acidity [76].

Viscosity reduction is related to the adsorptive capacity of the nanoparticle, and usually, higher adsorptive capacity results in greater viscosity reduction [58, 80]. The silica nanoparticle has been one of the most widely used in viscosity reduction processes as it has been shown to have a high adsorption capacity for *n*-C7 asphaltenes, which is mainly attributed to the presence of its silanol group [81]. For this reason, its surface composition has been evaluated for its effect on the nanoparticle's textural properties. However, as discussed in the previous section, the presence of the silanol group and the availability of active nanoparticle sites depend largely on its adsorption capacity. Using adsorption isotherms, Betancur et al. [76] assessed the effect of modifying the surface acidity of the silica nanoparticle (Fig. 7.9). The isotherms constructed were of type III, as four silica nanoparticles with different surface acidities were evaluated. The nanoparticle S11A, which corresponds to a silica nanoparticle with an acidic surface, has a greater adsorption capacity for *n*-C7 asphaltenes. This is likely due to the nanoparticle's surface

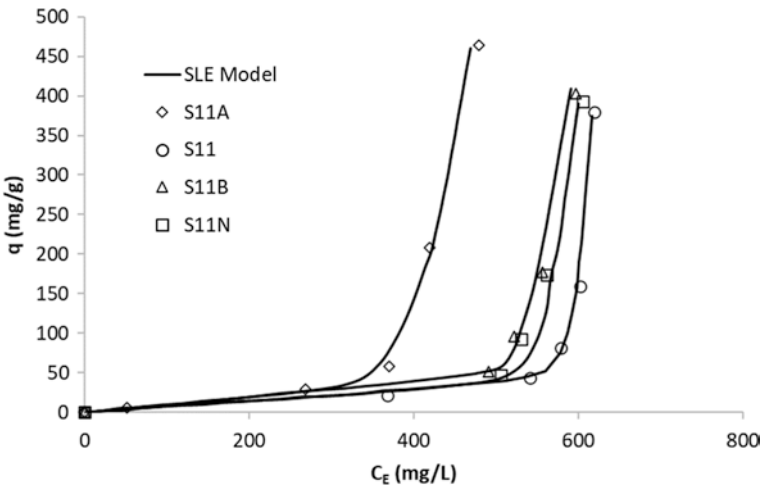

Fig. 7.9 Adsorption isotherms in the presence of S11A nanoparticles with an acidic surface, S11B with a basic surface, S11N with a neutral surface, and S11 for no surface modification. (Reprinted with permission from Betancur et al. [76]; Copyright 2016, Ind. Eng. Chem. Beef)

usually exhibiting increased acidity, enhancing the presence of silanol hydroxyl (Si-OH), which are the primary molecules responsible for increasing the interaction between the nanoparticle surface and asphaltenes. Therefore, increasing its acidity enhances the presence of silanol groups (Si-OH) in nanoparticles and their capacity to interact with the hydroxyl groups of asphaltenes [28, 32].

Alumina nanoparticles demonstrate a rapid adsorption and reach equilibrium in 2 h, which can be attributed to spontaneous and exothermic adsorption since the surface of the alumina nanoparticle is basic [41, 49, 71]. There is also evidence of a high affinity between adsorbent and adsorbate in the formation of isotherms Type I corresponding to the Langmuir model [71]. As with the silica nanoparticle, alumina has the Al-OH group, increasing its ability to interact with asphaltenes.

Other nanoparticles of interest are magnetite and hematite. Shayan et al. [79] determined that hematite reacts exothermically, generating a faster adsorption and balance capacity than magnetite, which demonstrated endothermic adsorption [82]. The thermodynamic behavior of each nanoparticle is linked to the acidity or basicity of its surface [82], and the acid surface of the magnetite increases its adsorption capacity as it attracts the hydroxyl groups of asphaltenes. In contrast, hematite's basic surface adsorbs protons and the adsorption produced heat; this process was primarily responsible for its exothermic behavior [79, 82].

This evidence allows us to speculate that viscosity reduction mechanisms depend heavily on the adsorption process through polar interactions between the surface of the nanoparticle and asphaltenes. These forces are commonly generated by acid–base interactions, which can be measured via an adsorption affinity value represented by the affinity constant (H) [83]. In addition, nanoparticles have demonstrated better performance when functionalized with other metallic elements [80]. This improvement is mainly due to the increased selectivity of the nanoparticle's active sites accompanied by a greater capacity for the stabilization of asphaltenes on the surface of the nanoparticle [84]. However, functionalized nanoparticles do not always favor the reduction of the viscosity of heavy crudes since the presence of metal oxide in their support tends to reduce their surface area and the availability of active sites with respect to the concentration of nanoparticles. Montes et al. [31] evaluated a functionalized NiO nanoparticle on nanoparticulate silica to reduce the viscosity of heavy crude oils and achieved a viscosity reduction at time 0 of approximately 13% (Fig. 7.10). The authors compared the viscosity reduction of specific percentages of four nanoparticles with different chemical nature (SiO_2, Fe_3O_4, Al_2O_3, and SiNi). SiO_2, Fe_3O_4, and Al_2O_3 nanoparticles were evaluated at a shear rate of 5 s^{-1}, a temperature of 30 °C, and a concentration of 1000 mg•L^{-1}. The functionalized nanoparticle SiNi was evaluated under the following conditions: 1000 mg•L^{-1} of SiNi nanoparticles, at time 0, 25 °C, and 10 s^{-1} [31]. The order of viscosity reduction capacity of the nanoparticles was $SiO_2 > Al_2O_3 > Fe_3O_4 >$ SiNi. This result is mainly due to the presence of the silanol group (Si-OH), which increases the nanoparticle–asphaltene interaction [76] because, as mentioned above, nanoparticles increase their tendency to attract hydroxyl groups from asphaltene molecules.

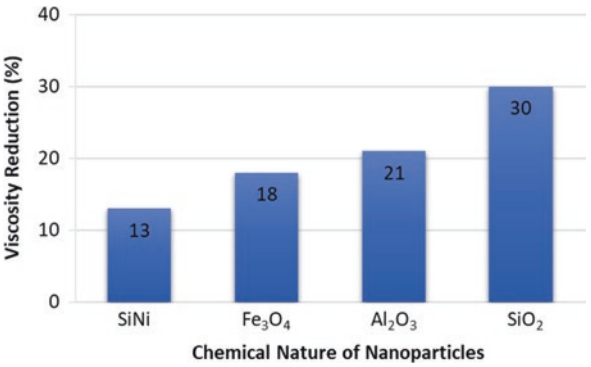

Fig. 7.10 Viscosity reduction percentages vs. the chemical nature of nanoparticles (SiO_2, Fe_3O_4, Al_2O_3, and SiNi) were evaluated at a shear rate of 5 s^{-1}, a temperature of 30 °C and a concentration of 1000 mg•L^{-1}. (Data obtained from Montes et al. [31] and Taborda et al. [28])

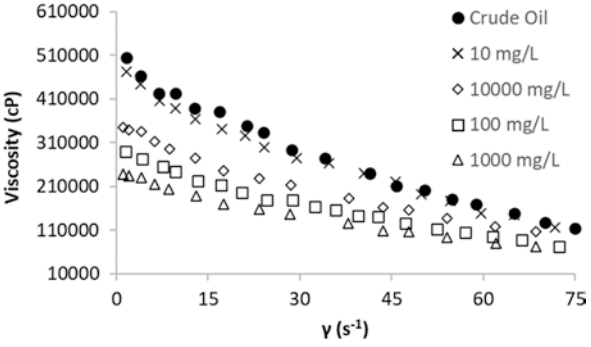

Fig. 7.11 The viscosity of heavy oil in the presence of SiO_2 nanoparticles at different (10, 100, 1000, 10,000 mg•L^{-1}) concentrations in relation to shear rate. (Reprinted with permission from Taborda et al. [32]; Copyright 2017, Elsevier)

7.3.3 Effect of Nanoparticle Concentration

Several authors have focused on evaluating the effects of nanoparticle concentration on reducing the viscosity of HOs [28, 32, 70]. Figure 7.11 shows the change in crude oil viscosity in the presence of nanoparticles at different concentrations ranging from 10 mg•L^{-1} to 10,000 mg•L^{-1} vs. shear rate, which does not exceed 75 s^{-1}. As noted, the shape of the curve indicates a shear-thinning behavior typical of a non-Newtonian fluid [28]; when the nanoparticles are added, the viscosity is reduced. This behavior is potentiated by increasing the nanoparticle concentration up to 1000 mg•L^{-1}, considered an optimal concentration. At a concentration of 10,000 mg•L^{-1}, a reduction in viscosity is still observed but to a lesser degree. This observation results from the particle's packaging effects, which might block the nanoparticle active sites and thereby reduce the interaction energy/forces [32]. Another reason that 1000 mg•L^{-1} is considered an optimal concentration is related to the nanoparticle's size. The concentration directly affects its size, and it is intended to have a small size to provide greater availability of active sites on its surface [76].

In conclusion, increasing the concentration of nanoparticles to an optimal value, usually 1000 mg•L^{-1}, maximizes viscosity reduction. From this value, an increase in the nanomaterial dosage generates negligible increases in viscosity reduction.

7.3.4 Nanofluid Implementation

Nanofluids provide another approach, specifically how they provide a medium for nanoparticle injection and greater nanoparticle dispersion [29]. Nanofluids consist of a carrier fluid (diluent/dispersant) and nanoparticles, wherein the diluent is responsible for providing a soluble phase in the crude oil [24, 30, 85]. The dispersant acting as a surfactant performs two main functions: keeping the nanoparticle suspended and avoiding its self-aggregation to increase its active site availability [86, 87]. One of the factors influencing the availability of active nanoparticle sites is related to the hydrodynamic diameter, representing a suspended nanoparticle diameter calculation through the DLS method [77]. A smaller hydrodynamic diameter increases the availability of active sites because nanoparticles with smaller diameters act individually, allowing all active sites to be available.

Montes et al. [24] evaluated the use of nanofluids for viscosity reduction and its perdurability over time (30 days), increasing viscosity in the presence and absence of nanoparticles (Fig. 7.12).

When only the carrier fluid was used, an 80% increase in viscosity was evident because diluents are highly volatile and tend to evaporate. On the other hand, nanofluid in the presence of silica nanoparticles did not increase viscosity as significantly (20%). This observation is attributed to the fact that the adsorption process is considered irreversible [88], affecting the cohesive forces of asphaltenes, avoiding the formation of viscoelastic networks, and following the increase in viscosity. Therefore, the nanoparticle not only fulfills the role of reducing viscosity, but also has an effect on its perdurability, which is an important factor in reducing the viscosity of heavy crude oils, as it can reduce dilution costs for the transport of these crude oils [86].

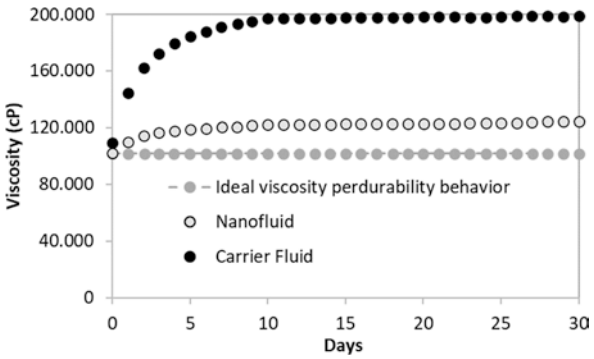

Fig. 7.12 Evaluation of the durability of viscosity reduction in the presence and absence of nanoparticles from 0 to 30 days. (Reprinted with permission from Montes et al. [24]; Copyright 2019, Energies)

7.4 Different Nanotechnology Applications for Viscosity Reduction

7.4.1 Reduction of Solvent Consumption for Transport

The development of these mechanisms occurs mainly in transport and facilities [89]. The characteristics of HOs also make these processes more complex. Their high viscosity leads to the use of solvents that manage to produce a blend between light crudes and heavy crudes that balances the viscosities and improves crude mobility. These solvents can be liquids such as naphtha [90] and diesel [91] or gasses such as CO_2 [92]. The addition of nanoparticles for cold processes in transport reduces naphtha consumption and increases the viscosity reduction perdurability [93]. This outcome is based on two main assumptions: (i) solvent dissolution of heavy crude fractions and (ii) redistribution of the viscoelastic network generated by the absorption processes and catalytic capacity of the nanoparticles [94].

To form the nanofluid, the nanoparticles must be dispersed in the carrier fluid. This action results in a synergic effect that leads to better performance in viscosity reduction.

Taborda et al. [94] studied the effect of SiO_2 nanoparticles on reducing naphtha consumption. A rheological evaluation concluded that nanofluid composed of biodiesel and 1000 mg•L^{-1} SiO_2 nanoparticles (BNF) was the best performing viscosity-reducing agent for HO. As shown in Fig. 7.13, the addition of 10% BNF + 13% naphtha reduced naphtha consumption by 52%, at which the HO reached its lowest viscosity. The study also provided an economic analysis that demonstrated a potential reduction of dilution costs with approximately 50% energy savings, representing a savings of more than USD 2.5 million/day. Furthermore, decreased energy consumption in pumping by 11% to HO and 37% to EHO was equivalent to more than USD 5500/day, generating a savings of over USD 2 million/year. The study proposed that a higher volume of oil might be transported as more net oils mass can be pumped, reducing capital expenditures.

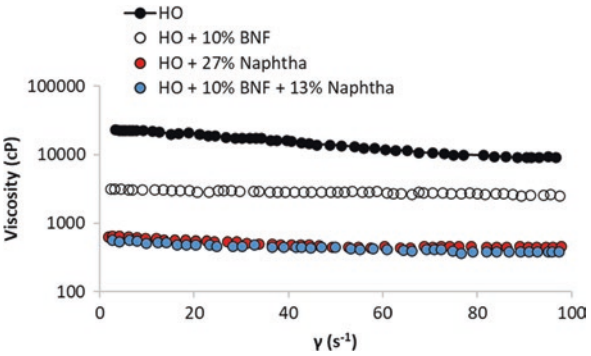

Fig. 7.13 Viscosity reduction as a function of shear rate of mixes of heavy oil with BNF and naphtha. (Reprinted with permission from Taborda et al. [94]; Copyright 2017, Elsevier)

7.4.2 *Ultrasonic Cavitation*

Ultrasonic cavitation involves irradiating ultrasound to disaggregate asphaltenes. This phenomenon is caused by an increase in energy resulting from the vibration to which they were exposed, thus decreasing the ability of asphaltene to interact with other asphaltene molecules [33, 75]. Another phenomenon that can occur in cavitation is the improvement by bubble formation. These bubbles are unstable and, upon collapse, generate an increase in temperature and pressure in the crude oil, managing to break the oil's heavy fractions, which are then hydrogenated by a hydrogen donor [31, 75, 80]. Montes et al. [31] evaluated viscosity reduction by ultrasonic cavitation assisted by SiO_2 nanoparticles functionalized with Ni nanocrystals. Added nanoparticles generated a synergic effect and reduced viscosity by three mechanisms: adsorption, disaggregation, and upgrading [31, 75, 80]. As shown in Fig. 7.14a, the exposure time increasing from 0–90 min improved viscosity reduction by 44% and an asphaltenes content reduction of 16% in the presence of silica nanoparticles. This observation is related to the increase in bubbles during the cavitation process. In addition, there was an increase in DVR (Fig. 7.14b), where only by adding the nanoparticles, the DVR at time 0 increased by 12% [31].

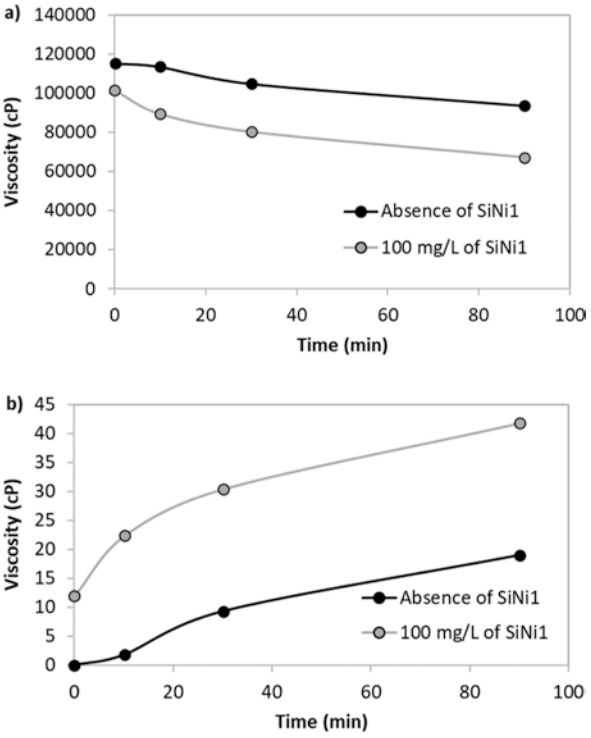

Fig. 7.14 (**a**) Viscosity and (**b**) DVR of heavy oil in the ultrasonic cavitation process in the presence and absence of 100 mg•L^{-1} SiNi1 nanoparticles. (Reprinted with permission from Montes et al. [31]; Copyright 2018, DYNA)

7.4.3 *Deasphalting*

Solvent deasphalting (SDA) consists of removing the heavy fraction of crude oil, resulting in the separation of two fractions: crude deasphalting (DAO) and pitch (asphaltenes and resins) [13]. This separation is achieved by adding high amounts of solvents to the crude where asphaltenes are not stable, causing them to self-aggregate and further precipitate so that, due to gravity effects, they are subsequently deposited [13, 95] and form residues known as pitch. Deasphalting is performed to improve crude oil quality and reduce viscosity by removing asphaltene aggregates from the DAO. Guzman et al. evaluated the effect of SiO_2 nanoparticles on a solvent deasphalting process for DAO quality improvement, comparing conventional SDA and deasphalting with improved solvent (e-SDA) with SiO_2 nanoparticles [96]. The results included an increase in API gravity of 14% under the e-SDA spray, as well as a reduction in viscosity in DAO greater than 50% compared to conventional deasphalting, caused by Si_2O nanoparticle synergic effects on DAO and pitch performances [96]. As shown in Fig. 7.15, DAO and pitch yields are inversely proportional when a) the pitch increases and b) the DAO decreases. This occurs because as the solvent to oil ratio (SOR) increases, the resins are solubilized, preventing them from playing their role as an interfacial agent with asphalts [96–98]. Therefore, asphaltenes are aggregated and precipitated, increasing pitch

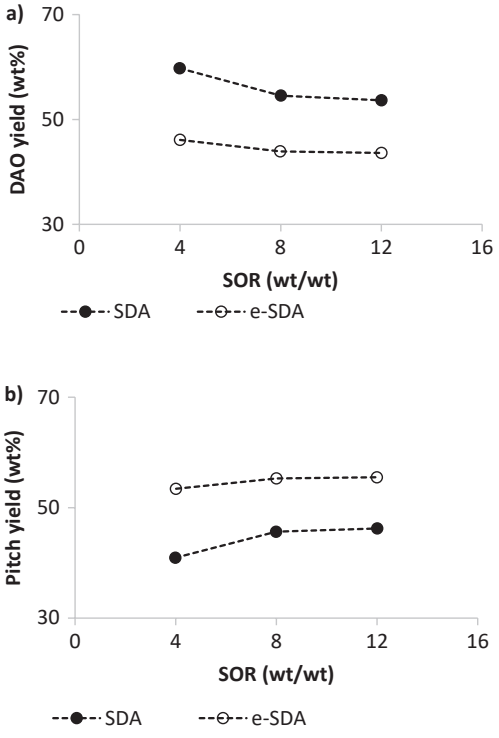

Fig. 7.15 Effect of the solvent to oil ratio in a) DAO and b) pitch yields for the SDA with (e-SDA) and without (SDA) SiO_2 nanoparticles. (Reprinted with permission from Guzmàn et al. [96]; Copyright 2017, Hindawi)

performance and decreasing the presence of asphalts in DAO, thus improving their quality [98]. Deasphalting in the presence of nanoparticles (e-SDA) provides a higher pitch yield due to the phenomenon of adsorption between silica nanoparticles and asphaltenes [99–101], as adsorbing them onto their surface facilitate their precipitation and separation of the oil matrix. In addition, deasphalting with improved solvent (e-SDA) reduces the required amount of solvent in the process.

7.5 Field Trials for IOR Stimulation

The Colombian oil industry has expressed great interest in developing nanotechnology for viscosity reduction due to its high amount of HO and EHO reserves. As a result, with the assistance of the state, academia, and industry, Colombia has been positioned as one of the pioneering countries in the field application of nanofluids/nanoparticles.

Zabala et al. [27] assessed the improvement of HO mobility in two Colombian fields by reducing viscosity using oil-based nanofluids (OBNs) containing nanoparticles. Field A produced an EHO of 8°API, and the reservoir showed a permeability between 800–400 mD and a porosity between 16–20%. Field B produced an HO of 13°API, and the reservoir showed a permeability between 500–1000 mD and a porosity between 16–22%.

The study developed a displacement test from a porous media with core plugs from each field under reservoir conditions and obtained an increase in oil recovery. Two field trials were conducted in each field. In field A, into the CHA and CHB wells were injected 86 bbl and 107 bbl of nanofluid, respectively. After nanofluid injection, the wells were closed for a soaking process for 12 h. The results showed an instant increase in the oil rate of approximately 310 bopd for the CHA well and 87 bopd for CHB, mainly due to the crude oil's viscosity reduction. In the first 9 days after the job, there was a reduction in viscosity of approximately 98%. The authors concluded that the treatment was economically viable as the increase in production lasted until day 269, and the capital invested was recovered in the first 90 days. Figure 7.16a shows the viscosity behavior within the first 300 days after treatment, which is reflected in well production performance. Figure 7.16b provides a record of the residual nanoparticles in the well.

In field B, the pilot wells were CNA and CNB in which 200 bbl and 150 bbl of nanofluids, respectively, were injected at a slow rate. After nanofluid injection, the wells were closed for the soaking process for approximately 12–18 h. The production increases were 270 bopd and 280 bopd for the CNA and CNB wells, respectively. The treatment effectiveness in field B remained for 174 d. Although the performance in field A was superior, the capital invested was recovered in just 4 months. Furthermore, the treatment achieved a viscosity reduction of 47% in the first 30 days (Fig. 7.17a).

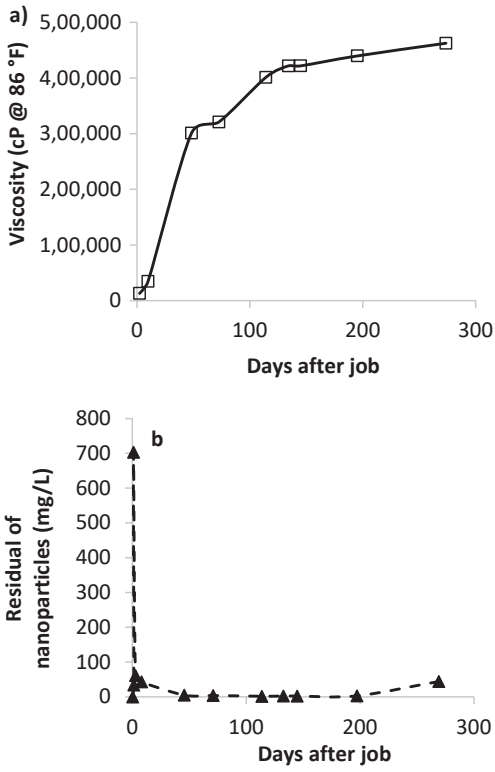

Fig. 7.16 (**a**) Viscosity and (**b**) residual nanoparticles vs. days after job. (Reprinted with permission from Zabala et al. [27]; Copyright 2016, SPE)

Another field trial in well C, in which a stimulation process was assisted by nanofluids using coiled tubing, was applied to improve oil mobility and viscosity reduction to reduce operating expenditures and consumption of naphtha and other solvents. The job was applied in a HO field in Colombia in which viscosity was approximately 608.600 cP at 86 °F.

The trial began by injecting 45 bbl of pre-flow into well C to increase the nanoparticle efficiency. Subsequently, 150 bbl of nanofluids and 101 bbl of organic pill were injected and displaced by 32 bbl of brine to decrease interfacial tension. After the nanofluid injection, the well was closed for a soaking process of 12 h. Figure 7.18 shows the production curve for well C before and after the stimulation assisted by nanofluids. Before stimulation, 861 bopd was produced. On 27 December, the stimulation of well C began to increase the production rate, and an increase of approximately 600 bopd was achieved. Three months later, the production reached an average value of 1600 bopd and remained at that production level.

The production increase was related to the viscosity reduction, and the viscosity reduction was due to the adsorption capacity of the nanoparticle. Before the stimulation process assisted by nanofluids, a viscosity reduction of approximately 82% was achieved (Fig. 7.19). Therefore, for 3 months, there was an approximately

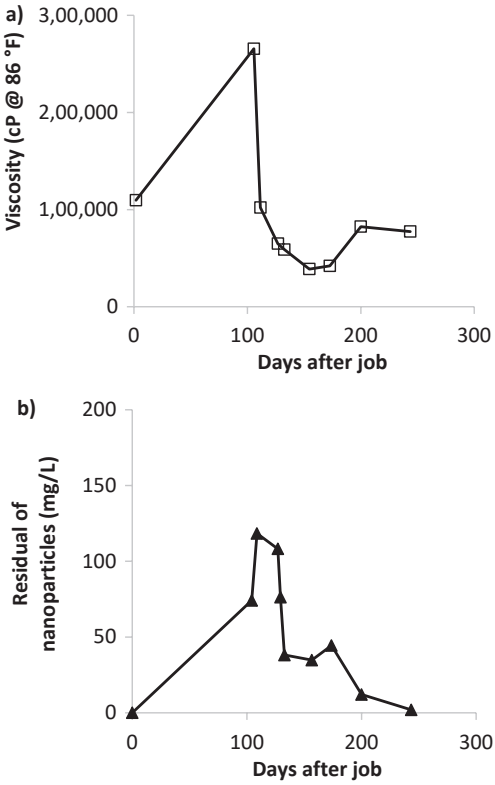

Fig. 7.17 (**a**) Viscosity and (**b**) residual of nanoparticles vs. days after job. (Reprinted with permission from Zabala et al. [27]; Copyright 2016, SPE)

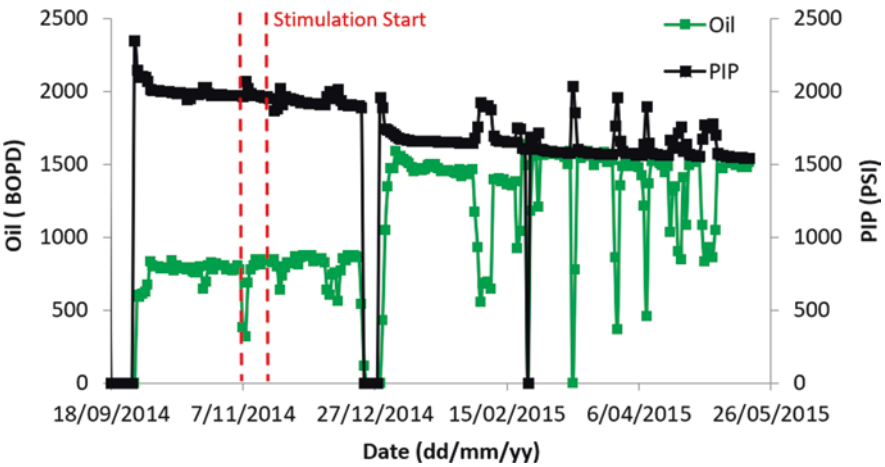

Fig. 7.18 Well production before and after stimulation assisted by nanofluids and PIP wells vs. time

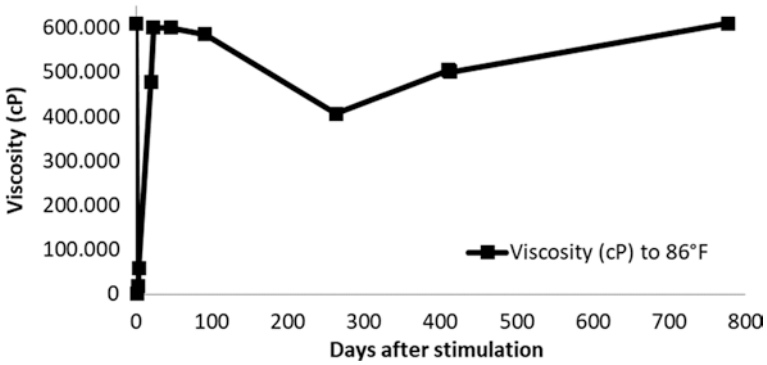

Fig. 7.19 Viscosity reduction at 86 ° F vs. time

100% reduction in naphtha consumption. Viscosity reached its initial value 800 days after the trial. At approximately 10 months after the stimulation, a profit greater than USD 2.1 million was reported with an investment of approximately USD 738 thousand, showing a high cost-benefit ratio of the project.

7.6 Conclusions

Nanotechnology is presented in the oil industry as a novel alternative for improving existing recovery mechanisms. This chapter shows that the adsorption capacity of nanoparticles for oil heavy fraction substantially enhances oil recovery as nanofluids and nanocatalysts in processes such as DOA, ultrasound cavitation, and reduction in naphtha consumption.

Nanoparticles can adsorb the heavy fractions of crude oils on their surface, mainly due to active sites' availability. Viscosity can be reduced by different mechanisms but always involves disrupting the viscoelastic network formed mainly by asphaltenes and resins. Moreover, viscosity reduction mechanisms depend heavily on the adsorption process occurring through polar interactions between the surface of the nanoparticle and asphaltene, the chemical nature of which is closely related to that of the nanoparticle surface. Finally, the results of field trials showed the importance of the perdurability of nanofluid viscosity reduction in the technical-economic results of the treatments.

Acknowledgments The authors would like to acknowledge Universidad Nacional de Colombia Sede Medellín, Fundación Universidad de América and Ecopetrol S.A. for financial and logistical support.

References

1. A. Hinkle, E.-J. Shin, M.W. Liberatore, A.M. Herring, M. Batzle, Correlating the chemical and physical properties of a set of heavy oils from around the world. Fuel **87**(13–14), 3065–3070 (2008)
2. A. Demirbas, H. Alidrisi, M. Balubaid, API gravity, sulfur content, and desulfurization of crude oil. Pet. Sci. Technol. **33**(1), 93–101 (2015)
3. R. Urquhart, Heavy oil transportation-present and future. J. Can. Petrol. Technol. **25**(02) (1986)
4. D. Escojido, O. Urribarri, J. Gonzalez, Part 1: Transportation of heavy crude oil and natural bitumen, in *13th World Petroleum Congress*, (World Petroleum Congress, 1991)
5. O.C. Mullins, The asphaltenes. Annu. Rev. Anal. Chem. **4**, 393–418 (2011)
6. S. Asomaning, A. Watkinson, Petroleum stability and heteroatom species effects in fouling of heat exchangers by asphaltenes. Heat Transfer Eng. **21**(3), 10–16 (2000)
7. M. Ghanavati, M.-J. Shojaei, S.A. Ahmad Ramazani, Effects of asphaltene content and temperature on viscosity of Iranian heavy crude oil: Experimental and modeling study. Energy Fuel **27**(12), 7217–7232 (2013)
8. O.C. Mullins et al., Advances in asphaltene science and the Yen–Mullins model. Energy Fuel **26**(7), 3986–4003 (2012)
9. G. Maya et al., *Estatus de la recuperación mejorada de petróleo en Colombia* (Ecopetrol SA, 2008)
10. K.E. Brown, Overview of artificial lift systems. J. Pet. Technol. **34**(10), 2,384–2,396 (1982)
11. K. Guo, H. Li, Z. Yu, In-situ heavy and extra-heavy oil recovery: A review. Fuel **185**, 886–902 (2016)
12. R. Hashemi, N.N. Nassar, P. Pereira Almao, Enhanced heavy oil recovery by in situ prepared ultra dispersed multimetallic nanoparticles: A study of hot fluid flooding for Athabasca bitumen recovery. Energy Fuel **27**(4), 2194–2201 (2013)
13. J.M. Lee et al., Separation of solvent and deasphalted oil for solvent deasphalting process. Fuel Process. Technol. **119**, 204–210 (2014)
14. S. Melcon, *Oil Recovery by In Situ Combustion* (Google Patents, 1965)
15. P. Vanmeurs, M.H. Waxman, H.J. Vinegar, *In-Situ Steam Drive Oil Recovery Process* (Google Patents, 1987)
16. D.B. Bennion, An overview of formation damage mechanisms causing a reduction in the productivity and injectivity of oil and gas producing formations. J. Can. Petrol. Technol. **41**(11) (2002)
17. E. Guevara, J. Gonzalez, G. Nuñez, Highly viscous oil transportation methods in the Venezuela oil industry, in *Exploration, Production Downstream (Refining and Petrochemicals)-Fifteenth World Petroleum Congress*, (1997), pp. 495–502
18. D. Rimmer, A. Gregoli, J. Hamshar, E. Yildirim, *Pipeline Emulsion Transportation for Heavy Oils* (ACS Publications, 1992)
19. J. Charlot, J. Couderc, J. Le Page, Heavy oil processing. A synthesis of the Asvahl results, in *European Communities symposium. 3*, 1988, pp. 898–917
20. B.M. Yaghi, A. Al-Bemani, Heavy crude oil viscosity reduction for pipeline transportation. Energy Sources **24**(2), 93–102 (2002)
21. D. Joseph, R. Bai, K. Chen, and Y. Renardy, "Core-Annular Flows, Annual Review of Fluid Mechanics," 1997
22. A. Miadonye, N. Latour, V. Puttagunta, A correlation for viscosity and solvent mass fraction of bitumen-diluent mixtures. Pet. Sci. Technol. **18**(1–2), 1–14 (2000)
23. A. Saniere, I. Hénaut, J. Argillier, Pipeline transportation of heavy oils, a strategic, economic and technological challenge. Oil Gas Sci. Technol. **59**(5), 455–466 (2004)
24. D. Montes, W. Orozco, E.A. Taborda, C.A. Franco, F.B. Cortés, Development of nanofluids for perdurability in viscosity reduction of extra-heavy oils. Energies **12**(6), 1068 (2019)

25. N.A. Ospina Gómez, *Evaluación de la aplicación de nanofluidos para mejoramiento in-situ del crudo pesado* (Escuela de Química y Petróleos, 2015)
26. L. Cardona Rojas, *Efecto de nanopartículas en procesos con inyección de vapor a diferentes calidades* (Ingeniería de Petróleos, 2018)
27. R. Zabala, C. Franco, F. Cortés, Application of nanofluids for improving oil mobility in heavy oil and extra-heavy oil: A field test, in *SPE Improved Oil Recovery Conference*, (Society of Petroleum Engineers, 2016)
28. E.A. Taborda, V. Alvarado, C.A. Franco, F.B. Cortés, Rheological demonstration of alteration in the heavy crude oil fluid structure upon addition of nanoparticles. Fuel **189**, 322–333 (2017)
29. E.A. Taborda, C.A. Franco, S.H. Lopera, V. Alvarado, F.B. Cortés, Effect of nanoparticles/nanofluids on the rheology of heavy crude oil and its mobility on porous media at reservoir conditions. Fuel **184**, 222–232 (2016)
30. J.E. Aristizábal-Fontal, F.B. Cortés, C.A. Franco, Viscosity reduction of extra heavy crude oil by magnetite nanoparticle-based ferrofluids. Adsorp. Sci. Technol. **36**(1–2), 23–45 (2018)
31. D. Montes, F.B. Cortés, C.A. Franco, Reduction of heavy oil viscosity through ultrasound cavitation assisted by NiO nanocrystals-functionalized SiO2 nanoparticles. Dyna **85**(207), 153–160 (2018)
32. E.A. Taborda, C.A. Franco, M.A. Ruiz, V. Alvarado, F.B. Cortes, Experimental and theoretical study of viscosity reduction in heavy crude oils by addition of nanoparticles. Energy Fuel **31**(2), 1329–1338 (2017)
33. C.A. Franco, R. Zabala, F.B. Cortés, Nanotechnology applied to the enhancement of oil and gas productivity and recovery of Colombian fields. J. Pet. Sci. Eng. **157**, 39–55 (2017)
34. R.G. Santos, W. Loh, A.C. Bannwart, O.V. Trevisan, An overview of heavy oil properties and its recovery and transportation methods. Braz. J. Chem. Eng. **31**(3), 571–590 (2014)
35. I. Hénaut, L. Barré, J. Argillier, F. Brucy, R. Bouchard, Rheological and structural properties of heavy crude oils in relation with their asphaltenes content, in *SPE International Symposium on Oilfield Chemistry*, (Society of Petroleum Engineers, 2001)
36. T.F. Yen, G.V. Chilingarian, *Asphaltenes and Asphalts, 2: Part B* (Elsevier, 2000)
37. S.W. Hasan, M.T. Ghannam, N. Esmail, Heavy crude oil viscosity reduction and rheology for pipeline transportation. Fuel **89**(5), 1095–1100 (2010)
38. S. Rudyk, Relationships between SARA fractions of conventional oil, heavy oil, natural bitumen and residues. Fuel **216**, 330–340 (2018)
39. R.F. Visintin, R. Lapasin, E. Vignati, P. D'Antona, T.P. Lockhart, Rheological behavior and structural interpretation of waxy crude oil gels. Langmuir **21**(14), 6240–6249 (2005)
40. S.C. Acevedo et al., Suppression of phase separation as a hypothesis to account for nuclei or nanoaggregate formation by asphaltenes in Toluene. Energy Fuel **32**(6), 6669–6677 (2018)
41. O.E. Medina, C. Olmos, S.H. Lopera, F.B. Cortés, C.A. Franco, Nanotechnology applied to thermal enhanced oil recovery processes: A review. Energies **12**(24), 4671 (2019)
42. O. León et al., Adsorption of native resins on asphaltene particles: A correlation between adsorption and activity. Langmuir **18**(13), 5106–5112 (2002)
43. J. Pereira, I. López, Interacciones resinas-asfaltenos: correlación con la precipitación de asfaltenos. Ciencia **14**(1) (2011)
44. M.M. Lozano, C.A. Franco, S.A. Acevedo, N.N. Nassar, F.B. Cortés, Effects of resin I on the catalytic oxidation of n-C 7 asphaltenes in the presence of silica-based nanoparticles. RSC Adv. **6**(78), 74630–74642 (2016)
45. C.A. Franco, M.M. Lozano, S. Acevedo, N.N. Nassar, F.B. Cortés, Effects of resin I on asphaltene adsorption onto nanoparticles: A novel method for obtaining asphaltenes/resin isotherms. Energy Fuel **30**(1), 264–272 (2016)
46. R.P. Chhabra, Non-Newtonian fluids: An introduction, in *Rheology of Complex Fluids*, (Springer, 2010), pp. 3–34
47. R. Weltmann, H. Green, Rheological properties of colloidal solutions, pigment suspensions, and oil mixtures. J. Appl. Phys. **14**(11), 569–576 (1943)
48. J. Mewis, N.J. Wagner, Thixotropy. Adv. Colloid Interf. Sci. **147**, 214–227 (2009)

49. S. Maity, J. Ancheyta, L. Soberanis, F. Alonso, M. Llanos, Alumina–titania binary mixed oxide used as support of catalysts for hydrotreating of Maya heavy crude. Appl. Catal. A Gen. **244**(1), 141–153 (2003)
50. G. Ovarlez, L. Tocquer, F. Bertrand, P. Coussot, Rheopexy and tunable yield stress of carbon black suspensions. Soft Matter **9**(23), 5540–5549 (2013)
51. A. Metzner, R. Otto, Agitation of non-Newtonian fluids. AICHE J. **3**(1), 3–10 (1957)
52. S. Mortazavi-Manesh, J.M. Shaw, Thixotropic rheological behavior of Maya crude oil. Energy Fuel **28**(2), 972–979 (2014)
53. F.S. Ribeiro, P.R.S. Mendes, S.L. Braga, Obstruction of pipelines due to paraffin deposition during the flow of crude oils. Int. J. Heat Mass Transf. **40**(18), 4319–4328 (1997)
54. D. Montes, J. Henao, E.A. Taborda, J. Gallego, F.B. Cortés, C.A. Franco, Effect of textural properties and surface chemical nature of silica nanoparticles from different silicon sources on the viscosity reduction of heavy crude oil. ACS omega **5**(10), 5085–5097 (2020)
55. J. Murgich, Intermolecular forces in aggregates of asphaltenes and resins. Pet. Sci. Technol. **20**(9–10), 983–997 (2002)
56. C.A. Franco, T. Montoya, N.N. Nassar, F.B. Cortés, Nioand pdo supported on fumed silica nanoparticles for adsorption and catalytic steam gasification of colombian c7asphaltenes, in *Handbook on Oil Production Research*, (Nova Science Publishers, Hauppauge, 2014), pp. 101–145
57. S. Betancur Márquez, Desarrollo de nanopartículas basadas en sílice para la inhibición de la precipitación/depositación de asfáltenos, Escuela de Procesos y Energía
58. J.D. Guzmán, S. Betancur, F. Carrasco-Marín, C.A. Franco, N.N. Nassar, F.B. Cortés, Importance of the adsorption method used for obtaining the nanoparticle dosage for asphaltene-related treatments. Energy Fuel **30**(3), 2052–2059 (2016)
59. H.J. Kreuzer, Z.W. Gortel, *Physisorption Kinetics* (Springer, 2012)
60. J. Muscat, D. Newns, Chemisorption on metals. Prog. Surf. Sci. **9**(1), 1–43 (1978)
61. M. León, E. Díaz, S. Bennici, A. Vega, S. Ordónez, A. Auroux, Adsorption of CO2 on hydrotalcite-derived mixed oxides: Sorption mechanisms and consequences for adsorption irreversibility. Ind. Eng. Chem. Res. **49**(8), 3663–3671 (2010)
62. G. Pan, Y. Qin, X. Li, T. Hu, Z. Wu, Y. Xie, EXAFS studies on adsorption–desorption reversibility at manganese oxides–water interfaces: I. irreversible adsorption of zinc onto manganite (γ-MnOOH). J. Colloid Interface Sci. **271**(1), 28–34 (2004)
63. P.A. Webb, *Introduction to Chemical Adsorption Analytical Techniques and their Applications to Catalysis* (Micromeritics Instrument Corp. Technical Publications, 2003)
64. B. O'Shaughnessy, D. Vavylonis, Irreversibility and polymer adsorption. Phys. Rev. Lett. **90**(5), 056103 (2003)
65. T. Montoya, D. Coral, C.A. Franco, N.N. Nassar, F.B. Cortés, A novel solid–liquid equilibrium model for describing the adsorption of associating asphaltene molecules onto solid surfaces based on the "chemical theory". Energy Fuel **28**(8), 4963–4975 (2014)
66. I. Langmuir, The constitution and fundamental properties of solids and liquids. Part I. solids. J. Am. Chem. Soc. **38**(11), 2221–2295 (1916)
67. S. Lowell, J.E. Shields, *Powder Surface Area and Porosity* (Springer, 2013)
68. J. Rouquerol, F. Rouquerol, P. Llewellyn, G. Maurin, K.S. Sing, *Adsorption by Powders and Porous Solids: Principles, Methodology and Applications* (Academic, 2013)
69. J. Delgado et al., Efecto de la adición de moléculas anfífilas sobre las propiedades de la película de asfaltenos en la interfase aire-agua. Rev. Ingeniería UC **19**(2), 16–24 (2012)
70. E.A. Taborda, C.A. Franco, V. Alvarado, F.B. Cortés, A new model for describing the rheological behavior of heavy and extra heavy crude oils in the presence of nanoparticles. Energies **10**(12), 2064 (2017)
71. N.N. Nassar, Asphaltene adsorption onto alumina nanoparticles: Kinetics and thermodynamic studies. Energy Fuel **24**(8), 4116–4122 (2010)

72. S.B. Márquez, F.B. Cortés, F.C. Marín, *Desarrollo de Nanopartículas basadas en Sílice para la Inhibición de la Precipitación/Depositación de Asfaltenos* (MSc Investigación, Ingenieria de Petróleos, Universidad Nacional de Medellin, 2015)
73. M.T. Ghannam, S.W. Hasan, B. Abu-Jdayil, N. Esmail, Rheological properties of heavy & light crude oil mixtures for improving flowability. J. Pet. Sci. Eng. **81**, 122–128 (2012)
74. D. Lesueur, The colloidal structure of bitumen: Consequences on the rheology and on the mechanisms of bitumen modification. Adv. Colloid Interf. Sci. **145**(1–2), 42–82 (2009)
75. D.M. Pinzón, Rheological demonstration of heavy oil viscosity reduction by nio/sio 2 nanoparticles-assisted ultrasound cavitation, in *SPE Annual technical conference and exhibition*, (Society of Petroleum Engineers, 2018)
76. S. Betancur, J.C. Carmona, N.N. Nassar, C.A. Franco, F.B. Cortés, Role of particle size and surface acidity of silica gel nanoparticles in inhibition of formation damage by asphaltene in oil reservoirs. Ind. Eng. Chem. Res. **55**(21), 6122–6132 (2016)
77. S. Bhattacharjee, DLS and zeta potential–what they are and what they are not? J. Control. Release **235**, 337–351 (2016)
78. N.N. Nassar, A. Hassan, P. Pereira-Almao, Effect of the particle size on asphaltene adsorption and catalytic oxidation onto alumina particles. Energy Fuel **25**(9), 3961–3965 (2011)
79. N.N. Shayan, B. Mirzayi, Adsorption and removal of asphaltene using synthesized maghemite and hematite nanoparticles. Energy Fuel **29**(3), 1397–1406 (2015)
80. D. Montes, E.A. Taborda, M. Minale, F.B. Cortés, C.A. Franco, Effect of the NiO/SiO2 nanoparticles-assisted ultrasound cavitation process on the rheological properties of heavy crude oil: Steady state rheometry and oscillatory tests. Energy Fuel **33**(10), 9671–9680 (2019)
81. N.N. Nassar, S. Betancur, S.C. Acevedo, C.A. Franco, F.B. Cortés, Development of a population balance model to describe the influence of shear and nanoparticles on the aggregation and fragmentation of asphaltene aggregates. Ind. Eng. Chem. Res. **54**(33), 8201–8211 (2015)
82. R.M. Cornell, U. Schwertmann, *The Iron Oxides: Structure, Properties, Reactions, Occurrences and Uses* (Wiley, 2003)
83. N.N. Nassar, A. Hassan, P. Pereira-Almao, Comparative oxidation of adsorbed asphaltenes onto transition metal oxide nanoparticles. Colloids Surf. A Physicochem. Eng. Asp. **384**(1–3), 145–149 (2011)
84. C. Huh, H. Daigle, V. Prigiobbe, M. Prodanovic, *Practical Nanotechnology for Petroleum Engineers* (CRC Press, 2019)
85. S. Betancur et al., Importance of the Nanofluid preparation for ultra-low interfacial tension in enhanced oil recovery based on surfactant–nanoparticle–brine system interaction. ACS omega **4**(14), 16171–16180 (2019)
86. O.E. Medina, C. Caro-Vélez, J. Gallego, F.B. Cortés, S.H. Lopera, C.A. Franco, Upgrading of extra-heavy crude oils by dispersed injection of nio–pdo/ceo2±δ nanocatalyst-based nanofluids in the steam. Nanomaterials **9**(12), 1755 (2019)
87. D. Galeano-Caro, J. Villegas, J.H. Sanchez, F.B. Cortés, S.H. Lopera, C.A. Franco, Injection of Nanofluids with Fluorosurfactant-modified nanoparticles dispersed in a flue gas stream at very low concentration for enhanced oil recovery (EOR) in tight gas–condensate reservoirs. Energy Fuel **34** (2020)
88. F.B. Cortés, T. Montoya, S. Acevedo, N.N. Nassar, C.A. Franco, Adsorption-desorption of nc 7 asphaltenes over micro-and nanoparticles of silica and its impact on wettability alteration. CT&F-Ciencia, Tecnología y Futuro **6**(4), 89–106 (2016)
89. J. Bear, M.Y. Corapcioglu, *Fundamentals of Transport Phenomena in Porous Media* (Springer, 2012)
90. S. Gharfeh, A. Yen, S. Asomaning, D. Blumer, Asphaltene flocculation onset determinations for heavy crude oil and its implications. Pet. Sci. Technol. **22**(7–8), 1055–1072 (2004)
91. X. Li, Y. Du, G. Wu, Z. Li, H. Li, H. Sui, Solvent extraction for heavy crude oil removal from contaminated soils. Chemosphere **88**(2), 245–249 (2012)
92. D.A. Redford, M.R. Hanna, *Gaseous and Solvent Additives for Steam Injection for Thermal Recovery of Bitumen from Tar Sands* (Google Patents, 1981)

93. R. Hashemi, N.N. Nassar, P.P. Almao, Nanoparticle technology for heavy oil in-situ upgrading and recovery enhancement: Opportunities and challenges. Appl. Energy **133**, 374–387 (2014)
94. E.A. Taborda, V. Alvarado, F.B. Cortés, Effect of SiO2-based nanofluids in the reduction of naphtha consumption for heavy and extra-heavy oils transport: Economic impacts on the Colombian market. Energy Convers. Manag. **148**, 30–42 (2017)
95. G. Brons, J.M. Yu, Solvent deasphalting effects on whole cold lake bitumen. Energy Fuel **9**(4), 641–647 (1995)
96. J.D. Guzmán, C.A. Franco, F.B. Cortés, An enhanced-solvent deasphalting process: effect of inclusion of SiO2 nanoparticles in the quality of deasphalted oil. J. Nanomater. **2017** (2017)
97. S.L. Kokal, J. Najman, S.G. Sayegh, A.E. George, Measurement and correlation of asphaltene precipitation from heavy oils by gas injection. J. Can. Petrol. Technol. **31**(04) (1992)
98. S.I. Andersen, J.G. Speight, Petroleum resins: Separation, character, and role in petroleum. Pet. Sci. Technol. **19**(1–2), 1–34 (2001)
99. C.A. Franco, N.N. Nassar, M.A. Ruiz, P. Pereira-Almao, F.B. Cortés, Nanoparticles for inhibition of asphaltenes damage: Adsorption study and displacement test on porous media. Energy Fuel **27**(6), 2899–2907 (2013)
100. C.A. Franco, N.N. Nassar, T. Montoya, M.A. Ruíz, F.B. Cortés, Influence of asphaltene aggregation on the adsorption and catalytic behavior of nanoparticles. Energy Fuel **29**(3), 1610–1621 (2015)
101. J.J. Adams, Asphaltene adsorption, a literature review. Energy Fuel **28**(5), 2831–2856 (2014)

Chapter 8
Using Nanoparticles as Gas Foam Stabilizing Agents for Enhanced Oil Recovery Applications

Yazan Mheibesh, Farad Sagala, and Nashaat N. Nassar

8.1 Introduction

8.1.1 Background

Oil recovery from a conventional reservoir involves three distinct but intimately connected recovery mechanisms: the primary recovery, which is the oil production using the inherent reservoir pressure; the secondary recovery, which is the recovery of oil by pressure maintenance operations including water flooding; and the enhanced oil recovery (EOR), which is the extraction of oil by either thermal, chemicals, or gas flooding techniques. The primary and secondary oil recovery mechanisms can recover up to one-third of the present oil in a reservoir while two-thirds of the oil will remain unrecovered [3, 76, 116, 144]. Tertiary or enhanced oil recovery (EOR) methods are targeted to economically produce 65% of the remaining hydrocarbon initially in place at the end of both the primary and secondary recovery mechanisms [65]. The performance of EOR is evaluated based on the macroscopic and microscopic efficiencies. The macroscopic displacement efficiency refers to the ability of the displacing fluid in contact with the reservoir in a volumetric sense both areally and vertically [65]. On the other hand, the microscopic displacement efficiency addresses the ability of the displacing fluid to mobilize the residual oil in the pore scale [35]. The microscopic displacement efficiency is closely related to the dimensionless capillary number which is the ratio between the viscous and interfacial forces. In a typical brine flooding (secondary recovery), the capillary number is within the range of (10^{-7}–10^{-6}) [84]. Increasing the capillary number to the range of

Y. Mheibesh · F. Sagala · N. N. Nassar (✉)
Department of Chemical and Petroleum Engineering, University of Calgary, Calgary, AB, Canada
e-mail: nassar@ucalgary.ca

N. N. Nassar et al. (eds.), *Nanoparticles: An Emerging Technology for Oil Production and Processing Applications*, Lecture Notes in Nanoscale Science and Technology, https://doi.org/10.1007/978-3-319-12051-5_8

(10^{-4}–10^{-3}) can reduce the residual oil saturation to 10% [79]. Moreover, the residual oil saturation reaches zero as the capillary number is increased to 10^{-2} [78]. To achieve this capillary number, the interfacial tension has to be within the range of (10^{-2}–10^{-3}) mN/m [153]. Although chemical EOR can effectively decrease the interfacial tension to ultralow values, it has not been applied widely in the past due to the high costs of chemicals and low oil prices [84].

The most common EOR method implemented in field applications is the gas EOR which contributes to about 39% of the entire world EOR project production [7, 10, 58]. Gas EOR methods include the injection of inert or hydrocarbon gases including methane, nitrogen, carbon dioxide, or air for reservoir pressure maintenance and residual oil recovery [142]. About 38% of US EOR project production is referred to as CO_2 injection [100]. The high focus on CO_2 implementation in EOR projects is attributed to minimizing the environmental aspects of the greenhouse emissions (GHE) as well as the desirable miscible properties of CO_2. However, the oil recovery from field applications of gas EOR is considered lower than anticipated as a result of early gas breakthrough and gravity override. Several applications of the oil industry involve utilizing foams including fire retardants and synthesis of porous materials [24, 25, 121], hydraulic fracturing [71, 130], and finally EOR [54]. Foam is considered one of the most promising technologies to overcome the gravity override and viscous fingering of gas EOR. Foams are capable of enhancing the macroscopic sweep efficiency of the gas flood by blocking the high permeable zones, increasing the apparent viscosity of gas, and diverting it towards unswept reservoir zones. Despite the high potential of foams in enhancing oil recovery, the stability of foams is still a major concern due to film thinning and bubble coalescence. One of the ultimate approaches to enhance the stability of surfactant-stabilized foams can be nanoparticles as suggested in the literature [108]. This is mainly attributed to nanoparticles and their ability to irreversibly adsorb and stabilize the foam liquid films [19, 74, 167]. The focus of this chapter is to summarize the main concepts of foam stability and the current status of foam stabilization by nanoparticles including the mechanisms and crucial parameters influencing foam stability. Moreover, remarkable studies also illustrate the role of nanoparticles in enhancing both the static and dynamic foam stabilities. Lastly, some field application overview and future commendations/research gaps for nanoparticle-stabilized foam are addressed in this chapter.

8.1.2 Need for Foam EOR

Theoretically, a miscible gas flood can recover most of the crude oil in a swept zone [152]. However, field applications showed that oil recovery by miscible CO_2 is much lower than anticipated which can go up to 20% of the OOIP [15]. The main obstacle of gas EOR is the low volumetric sweep efficiency due to the gravity override, the gas fingering, and reservoir heterogeneity, as depicted in Fig. 8.1 [26, 29,

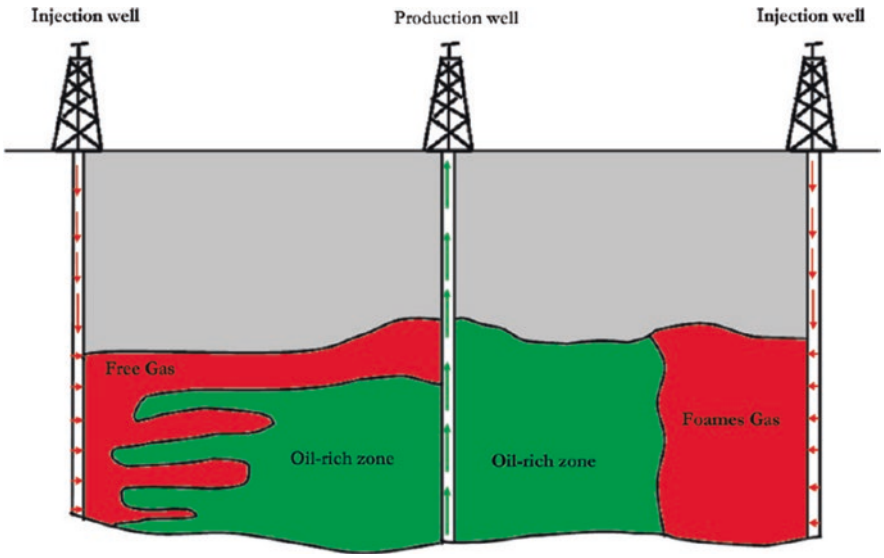

Fig. 8.1 Comparison between the volumetric sweep efficiency of gas and foam floods [60]. Permissions related to the material excerpted were obtained from ACS, and further permission should be directed to ACS; Farajzadeh, R., Andrianov, A., & Zitha, P. L. J. (2010). Investigation of Immiscible and Miscible Foam for Enhancing Oil Recovery. Industrial & Engineering Chemistry Research, 49(4), 1910–1919. doi: https://doi.org/10.1021/ie901109d

110]. The density difference between the gas and displaced fluid causes the gravity override of gas which results in an early gas breakthrough [5]. Moreover, the existence of fractured zones and heterogeneity in reservoir permeability can form high-mobility channels of the low-viscosity gas, thus lowering the macroscopic displacement efficiency of a gas flood [137, 141]. These drawbacks of gas flooding hinder the oil recovery by CO_2 gas flooding even though it has a high microscopic displacement efficiency [137]. Despite the high potential of surfactant flooding in recovering residual oil, it can only be implemented when oil prices are relatively high because of surfactant high costs and surfactants retention [94]. These addressed challenges of both gas and surfactant EOR methods led to conceptualizing of foam as a promising EOR approach [5, 179]. Literature suggests that generation of foam by a combination of both surfactant and gas flooding is cost-effective and enhances the sweep efficiency [5, 134]. Foam increases the sweep efficiency by reducing gas mobility via blockage of some flow channels, trapping gas so that its relative permeability will be reduced, and it can also increase the gas effective viscosity [5, 57, 97, 107, 134, 137].

In contrast with gas flooding, foam mainly recovers oil by the following mechanisms: it increases the viscosity of injected gas (the displacing fluid) for a more stable displacement process. Secondly, it diverts gas to more unswept oil-bearing zones by diverting gas from high permeable zones [5, 9, 60].

8.2 Foam Principles

One of the colloidal dispersion kinds is foam in which gas phase (internal/disperse phase) is dispersed in a continuous liquid phase (external phase). Gas bubbles are separated by a thin liquid film called lamellas which meet at a vertex called the plateau border. Figure 8.2a depicts a 2-D section of a foam surface. In two-dimensional slices of foam, the three lamellas meeting at the plateau border will have an angle of 120 (polyhedral angle). In three dimensions four lamellas will be meeting at the plateau border with an angle of 109.6 (tetrahedral angle). Finally, foams are thermodynamically unstable, and the arrangements of films in the foam are a result of both the surface tensions and contracting forces along with the liquid films [140].

The structure of gas bubbles in a foam can be either spherical or polyhedral cells. When the foam is wet or in a liquid phase, the shape of the gas bubbles will be spherical. However, due to the effect of gravity, foam can start drying resulting in a more polyhedral shape as shown in Fig. 8.2b [4, 18, 45, 46].

Surfactants are considered the most common foaming agent. The most common foam generation and evaluation methods of a solution containing foaming agents are the Bartsch method (shaking), the Bikerman method (sparging), and the Ross-Miles method. Based on the Bartsch method, foam is generated by mechanical shaking of a specific amount of solution placed in a closed container at a specific frequency [124]. In the Bikerman method, a specific volume of solution is placed in a cylinder while gas is being sparged at a specific flow rate through an orifice or porous disk placed at the bottom [124]. In the Ross-Miles method, a portion of the

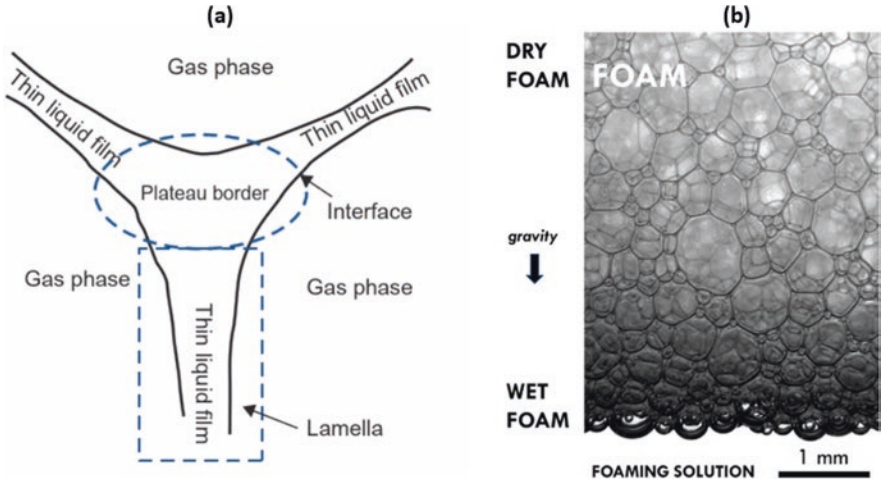

Fig. 8.2 (**a**) 2-D section of a foam [143]. Permissions related to the material excerpted were obtained from Elsevier and further permission should be directed to Elsevier; J. Sheng (2013). Enhanced Oil Recovery Field Case Studies. Oxford, UNITED STATES: Elsevier Science & Technology. (**b**) Wet and dry foam structures. Permissions related to the material excerpted were obtained from Elsevier and further permission should be directed to Elsevier [45]

solution is being placed in a cylinder while a portion of the liquid phase is being poured from the top to generate foam from a specific height [124].

The main concepts to be considered when dealing with the foaming behavior of a solution include foamability and foam stability. According to Carey and Stubenrauch [27], foamability characterizes the ability of a solution to produce foam which can be evaluated as the time needed to achieve a specific volume of foam. The rate at which surfactant molecules adsorb and the total amount of surfactant molecules adsorbed at the water/gas interface are the main factors controlling the foamability of a surfactant solution [27]. Thus, high foamability refers to a foam possessing a rapid surfactant adsorption rate, a high surface elasticity, and surface viscosity properties [27, 122]. The main principles of foam stability will be discussed in the following section.

8.3 Fundamentals of Foam Stability

A foaming agent that can be surfactant, macromolecule, or fine solids is required to generate foam by reducing interfacial energy thus increasing the interfacial area and reducing the mechanical energy input between the gas and liquid phases. To form a more stable foam, effects of foam destabilizing processes have to be minimized, including the film thinning (i.e., lamellas become thinner without changing the total surface area of the bubbles), coalescence (i.e., lamellas rupture, and gas bubbles merge to form bigger bubbles), and coarsening or Oswald ripening (i.e., gas flux from smaller to bigger bubbles). The main factors affecting foam stability include gravity drainage, capillary suction, surface elasticity, foam bulk, surface viscosity, repulsion, electric double layer, dispersion force attraction, and steric repulsion forces [140, 165].

According to the Young-Laplace equation, interfacial tension (σ) causes pressure difference (ΔP) to exist across a curved surface between the interface of gas (G) and liquid (L) phases. Equations (8.1 and 8.2) show the pressure difference (ΔP) across an interface of a wet foam bubble with a radius (R) where P_G, P_L are the pressure of the gas and liquid phases, respectively. Equation (8.3) shows the pressure difference of more complex foam bubbles with principal radii of curvature (R_1, R_2) [140].

$$\Delta P = P_G - P_L \tag{8.1}$$

$$\Delta P = \frac{2\sigma}{R} \tag{8.2}$$

$$\Delta P = \frac{\sigma}{\frac{1}{R_1} + \frac{1}{R_2}} \tag{8.3}$$

The Young-Laplace equation illustrates that the pressure inside a foam bubble (P_G) exceeds the outside pressure (P_L). Moreover, the pressure difference at the interface is also dependent on the foam bubble radius (R).

Due to variations in a foam bubble principal radii as shown in Fig. 8.3 between measured radius from a plateau border (R_B) and measured radius from a lamella (R_A), an additional pressure difference occurs between the liquid inside a film (P_A) and liquid in a plateau border (P_B). The pressure of a liquid in the foam film increases with an increase of measured radius. Thus, the liquid will flow from the film (relatively bigger radius R_A) to the plateau border (relatively smaller radius R_B) which causes film thinning resulting in lower foam stability [140].

Free energy of a gas bubble in foam increases with an increase in bubble size. As surfactant molecules adsorb a monolayer on the interface between a gas bubble and a liquid film, surface tension and free surface energy will be decreased. Thus, the thin liquid film will be stabilized due to surface tension reduction and increase in interfacial viscosity which provides mechanical resistance to film thinning and rupture. Equation (8.4) shows the general Gibbs adsorption for a binary isothermal system containing excess electrolyte. This equation thermodynamically describes the reduction of free surface energy due to surfactant adsorption when surfactant adsorption is considered as a monolayer while surface curvature is not great [140]

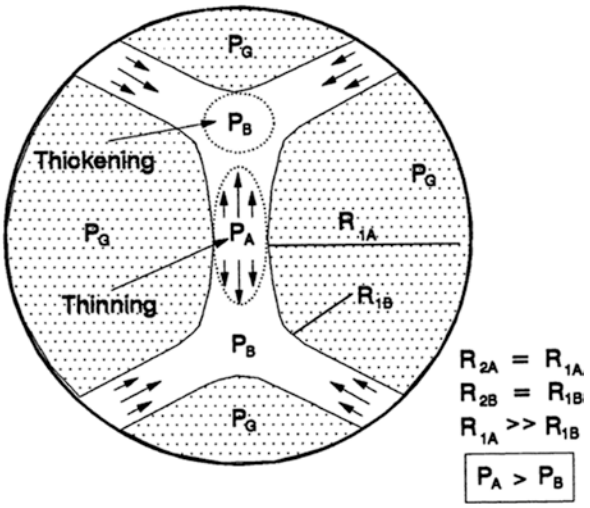

Fig. 8.3 Pressure difference across curved surfaces in a foam lamella due to variation in bubble principal radii. R_{1A} and R_{1B} are the radii from the right side of the liquid film, while R_{2A} and R_{2B} are from the left side of the liquid film [140]. Permissions related to the material excerpted were obtained from ACS, and further permission should be directed to ACS; Schramm, L. L., & Wassmuth, F. (1994). Foams: Basic Principles. In Foams: Fundamentals and Applications in the Petroleum Industry (Vol. 242, pp. 3–45): American Chemical Society

$$\Gamma_s = -\left(\frac{1}{RT}\right)\left(\frac{d\sigma}{d\ln C_s}\right) \tag{8.4}$$

where (Γ_s) is the surface excess of surfactant (mol/cm^2), (R) is the gas constant, (T) is the absolute temperature, (σ) is the surface or interfacial tension, and (C_s) is the solution concentration of surfactant in (M). Due to gravity forces, the liquid starts draining from liquid films until it is being balanced by capillary forces as described previously by the Young-Laplace equation. As a result, the thinning process leads to further foam collapse [140]. Surface elasticity of foam films increases foam ability to withstand deformations without rupturing. When a foam film is stabilized by surfactant adsorption undergoes a sudden expansion, the expanded portion of the film will have a lower degree of surfactant adsorption compared to the unexpanded film portion due to the increase in surface area. Thus, surface tension increases locally providing resistance for more film expansion by producing an immediate surface contraction by viscous forces. Hence, liquid flows from the low-surface tension region to the high-surface tension region as shown in Fig. 8.4. The diffusion of surfactant from bulk liquid to the expanded foam portion can be more quick in thick films compared to thin foam films. In thin foam films, not enough surfactant molecules will be transferred and adsorbed on the interface and achieve equilibrium quickly after film expansion. This phenomenon is called the Gibbs-Marangoni effect which is significant in stabilizing foam against thin film rupture and rapid deformation. This effect explains why a foam having low film surface tension cannot stabilize foam, because it does not having sufficient surface elasticity to reach equilibrium after surface expansion or contraction [140].

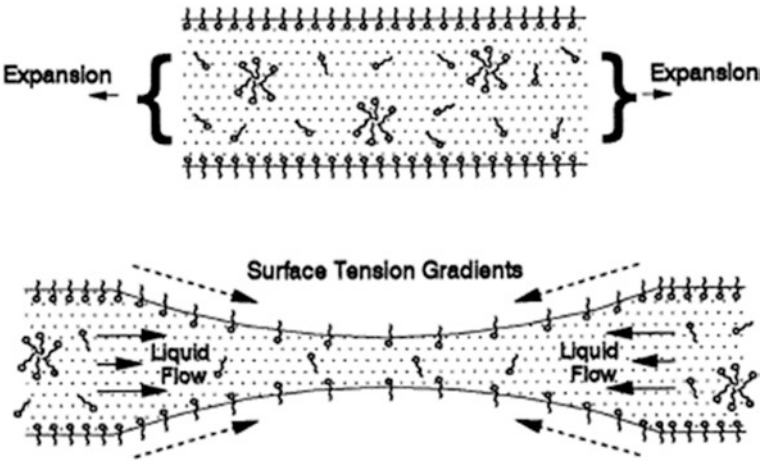

Fig. 8.4 Surface tension gradients in a film due to expansion [140]. Permissions related to the material excerpted were obtained from ACS, and further permission should be directed to ACS; Schramm, L. L., & Wassmuth, F. (1994). Foams: Basic Principles. In Foams: Fundamentals and Applications in the Petroleum Industry (Vol. 242, pp. 3–45): American Chemical Society

To form a stable foam, both lower surface tension and surface elasticity properties are required. Surface elasticity in foams is a dynamic property measuring the resistance against the creation of surface tension gradients and the rate of disappearance of these gradients in the system. In foam stability studies, there are two types of surface elasticity, the Gibbs and the Marangoni surface elasticities. The Gibbs surface elasticity (E_G) is an equilibrium surface measurement occurring when the number of surfactant molecules in the thin foam is very low so that the surfactant cannot restore surface concentration equilibrium after deformation. The Marangoni surface elasticity (E_M) is a nonequilibrium or time-dependent surface measurement occurring when there is enough amount of surfactant molecules in the foam for restoring the surface concentration equilibrium. Figure 8.5 compares between Gibbs and Marangoni surface elasticities after surface expansion. Equation (8.5) shows the Gibbs surface elasticity for a foam film (E_G) where (σ) is the surface tension and (A) is the geometric area of the surface. The surface elasticity for foam accounts for the effect of two gas/liquid interfaces so factor 2 is introduced in Eq. (8.5) [140].

$$E_G = \left(\frac{2\, d\sigma}{d \ln A} \right) \tag{8.5}$$

Viscous forces in foam, including both the surface and bulk viscosities, can affect the rate of bubble coalescence and film drainage. These forces can indirectly

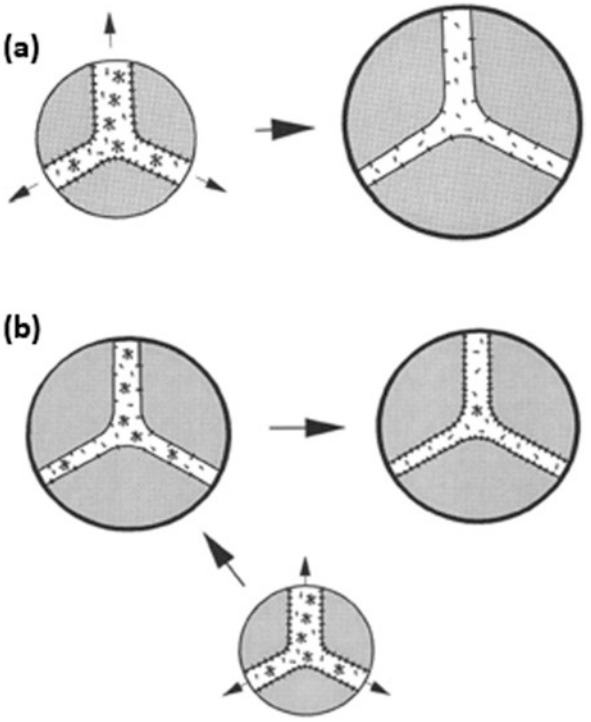

Fig. 8.5 Illustration of (**a**) Gibbs surface elasticity measurement occurring when the number of surfactant molecules is very low, (**b**) Marangoni surface elasticity measurement occurring when enough number of surfactant molecules exists in the foam for restoring the surface concentration equilibrium after film expansion [140]. Permissions related to the material excerpted were obtained from ACS, and further permission should be directed to ACS; Schramm, L. L., & Wassmuth, F. (1994). Foams: Basic Principles. In Foams: Fundamentals and Applications in the Petroleum Industry (Vol. 242, pp. 3–45): American Chemical Society

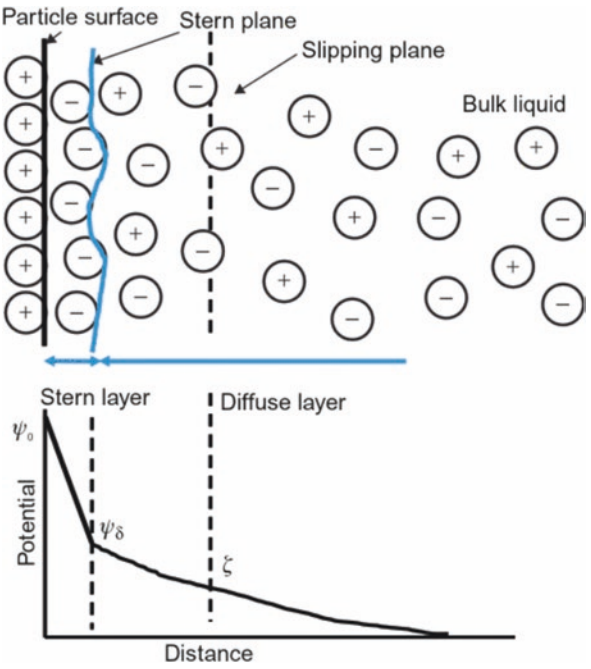

Fig. 8.6 Illustration of ELD of a charged foam lamella [143]. Permissions related to the material excerpted were obtained from Elsevier, and further permission should be directed to Elsevier; J. Sheng (2013). Enhanced Oil Recovery Field Case Studies. Oxford, United States: Elsevier Science & Technology

stabilize foam by resisting foam film thinning and rupturing processes. Thinning of thick foam lamellas is mainly resisted by bulk viscosity, while surface viscosity hinders the thinning of thin films [140].

A foam film stabilized by ionic surfactants adsorbed on the interface influences the distribution of nearby ions. Thus, ions with the same charge are repelled, while counter-charged ions are attracted to the film interface. This results in an electric double layer (ELD) consisting of both inner adsorbed ions and a diffuse layer. The diffuse layer consists of attracted ions by electric forces, and thermal motion will be formed. Depending on foam film thickness and charge density, the ELD opposes foam film thinning process when the charged interfaces of both film interfaces approach each other due to repulsive forces. Figure 8.6 depicts an electric double layer on one side of a foam film and the electric potential for a charged foam lamella [140].

Moreover, disjointing pressure, hydrostatic pressure difference between gas bubbles and bulk liquid, plays a significant role in keeping lamellas interfaces apart from each other. It accounts for electrical, dispersion, and steric (Van der Waals) forces operating across the foam lamellas [140].

8.4 Effect of Nanoparticles on Foam Stabilization

Despite the advantages of foam in increasing the oil recovery over conventional gas enhanced oil recovery processes, solely stabilized foams by surfactants have undesirable properties hindering foam flooding applications in enhanced oil recovery

projects. Low foam stability in harsh reservoir conditions such as high temperature and salinity makes conventional foams fail to meet the production requirements [98]. Moreover, adsorption of surfactants to the rock surface and surfactant decomposition in harsh reservoir environments results in weak foam formation resulting in poor sweep efficiency [7, 97].

Generally, dispersed solids help in the formation of more stable foams. They can increase the foam bulk viscosity and provide more foam film mechanical stability by solid adsorption on the gas/liquid interface [140]. Several studies showed that nanoparticles can play a significant rule in foam stability at high temperatures and salinity conditions by synergistic effect or physicochemical interactions between nanoparticles and surfactants [7]. Adsorption of nanoparticles on the liquid-gas interface enhances the foam dilatational elasticity and hinders the water flow at the bubble surface, thus preventing bubble coarsening, and slows down film thinning [47, 83, 113].

8.4.1 Mechanisms of Foam Stabilized by Surfactant and Nanoparticles

Interactions between nanoparticles-interface, surfactants-interface, and nanoparticles-surfactants count for foam film stabilization. There are several mechanisms of foam stabilization by nanoparticles proposed in the literature including particle detachment energy, particle arrangement during film drainage, maximum capillary pressure of coalescence, and the growing of aggregates [7, 146].

8.4.1.1 Particle Detachment Energy

Adsorption of nanoparticles at the film interface between gas and liquid is irreversible. The affinity of nanoparticles at the liquid interface is affected by the hydrophilic or lipophilic characters of the nanoparticles [129]. The required energy to remove a particle from the gas/liquid interface (ΔE) is expressed in Eq. (8.6) when the gravity and buoyancy forces are neglected due to the small size of the nanoparticles [20].

$$\Delta E = \pi R^2 \sigma_{aw} \left(1 \pm \cos\theta\right)^2 \tag{8.6}$$

where (ΔE) is the energy required to remove a particle from the interface, (R) is the nanoparticle radius, (σ_{aw}) is the gas/water interfacial tension, and (θ) is the contact angle between nanoparticles and the liquid. The sign in the bracket is negative for transfer from water and positive for transfer from oil or gas phase. This equation explains that the reduction in interfacial tension at the interface by surfactants can

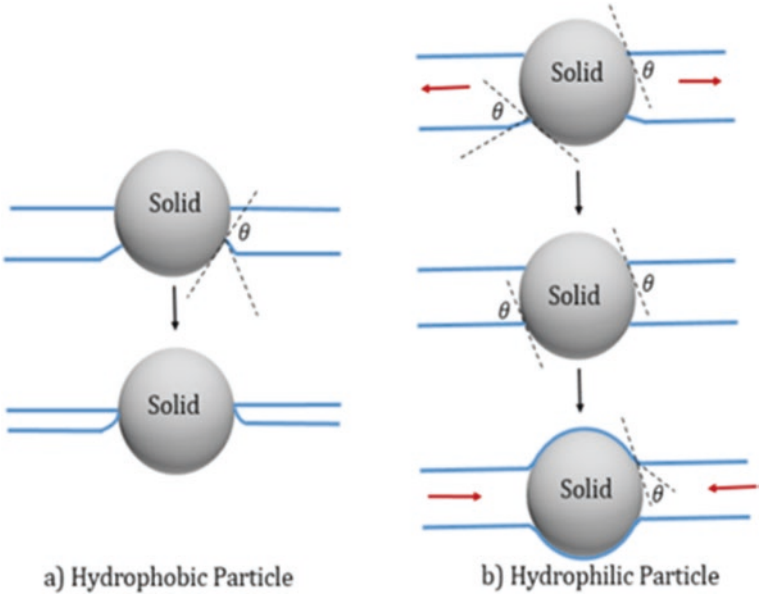

Fig. 8.7 Contact angle between solid particle and surfactant solution: (**a**) Hydrophobic particle ($\theta > 90°$), (**b**) hydrophilic particle ($\theta < 90°$) [7]. Permissions related to the material excerpted were obtained from ACS, and further permission should be directed to ACS; AlYousef, Z., Almobarky, M., & Schechter, D. (2017). Enhancing the Stability of Foam by the Use of Nanoparticles. Energy & fuels, 31(10), 10620–10627

lower the detachment energy resulting in lower foam stability. In the case of the high hydrophilic ($\theta < 30°$) or hydrophobic ($\theta > 150°$) particle wettability, the detachment energy will be reduced resulting in lower foam stability [146]. Figure 8.7 depicts the lipophile and hydrophile characterization of nanoparticles depending on contact angles between solids and liquid.

8.4.1.2 Particle Arrangement During Film Drainage

Depending on the wettability of the solid, adsorbed nanoparticles inside a thin film can form either a monolayer of bridging particles, a bilayer of closed-packed particles, or a network of particles aggregates as shown in Fig. 8.8 [77]. The network of particle aggregates occurs when there is an excess of solids inside the foam films. It is considered the most effective mechanism in foam stabilization because it keeps the gas bubbles separated by resisting dragging, hence slowing foam coalescence and liquid drainage [7].

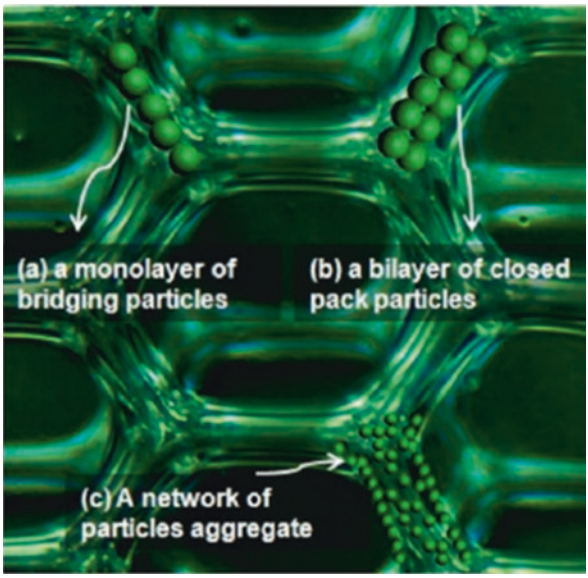

Fig. 8.8 Particle arrangement during film drainage [146]. Permissions related to the material excerpted were obtained from ACS, and further permission should be directed to ACS; Singh, R., & Mohanty, K. K. (2015). Synergy between Nanoparticles and Surfactants in Stabilizing Foams for Oil Recovery. Energy & Fuels, 29(2), 467–479. doi: https://doi.org/10.1021/ef5015007

8.4.1.3 Maximum Capillary Pressure of Coalescence

With the presence of nanoparticles adsorbed to the foam films, the maximum capillary pressure a liquid film can withstand before rupture increases [42]. This threshold pressure is referred to as the maximum capillary pressure of coalescence ($P_c^{\max}$) which results in more foam stability as $P_c^{\max}$ increases [146]. In the absence of nanoparticles, foam films are flat, while they do not have to be flat in the presence of nanoparticles, which provides a barrier against film thinning [7]. Equation (8.7) expresses that the maximum capillary pressure of coalescence ($P_c^{\max}$) is dependent on the packing parameter (p), air/liquid interfacial tension, particles radius (R), and contact angle (θ).

$$P_c^{\max} = p\frac{2\sigma_{aw}}{R}\cos\theta \tag{8.7}$$

In the case of hydrophobic solids ($\theta > 90°$), the film ruptures due to liquid drainage. On the other hand, if the solid particles are hydrophilic ($\theta < 90°$), liquid film starts thinning until it becomes flat as capillary pressure moves the liquid towards the solid particles [7, 146]. As a result, the film thinning process will be stopped which helps in maintaining foam stability, as shown previously in Fig. 8.7.

8.4.1.4 Growing Aggregates

The stability of foam films can be increased by nanoparticles as a result of particle aggregation and cork formation. Using silica nanoparticles at high concentrations (concentration > 2 wt.%,) helps in improving foam stability by increasing film viscosity [7, 28].

8.4.2 Experimental Techniques of Foam Stability Evaluation

The main experimental methods of foam stability by surfactant-nanoparticles for enhanced oil recovery include bulk stability tests, interfacial and dilatational elasticity experiments, and foam displacement tests [175]. In static foam tests, the decay of foam height, bubble size, and gas quality are evaluated over time both in the presence and absence of crude oil. These experiments indicate the effect of nanoparticles on slowing foam decay and coalescence rate. Interfacial tension and dilatational elasticity experiments evaluate the stability of foam films under expansion and contraction effects. Finally, foam displacement tests evaluate the ability of foam in increasing apparent viscosity of the displacing fluid, enhancing the flood mobility ratio, and its effect on oil recovery.

8.4.2.1 Bulk Foam Stability Tests

In bulk foam stability tests, foam generated by gas and the surfactant-nanoparticle dispersion is received in a transparent cylindrical testing tube to assess the foam physical properties over time. Foamability can be indicated by the change in foam height, bubble size distribution, and liquid holdup as a function of time. Effects of temperature, pressure, salinity, surfactant concentration, nanoparticle concentration, and crude oil could be evaluated in this type of foamability test. In this method, foam stability can be evaluated based on foam height and half-life time, bubble size distribution, vertical foam film, and confocal laser scanning microscopy tests.

Foam Height and Half-Life Time

As the generated foam is received in a cylindrical column, it starts decaying with time. The measured height of the foam column at a given time indicates foam stability. The time of foam height decay is slower in more stable foams. Half-life time is the time required for a foam column to decay to its half original height. Normalized foam height can be expressed as shown in Eq. (8.8). This test can be used to evaluate the effect of surfactants and/or nanoparticle concentrations on foam stability when the foam is in contact with crude oil. Figure 8.9 shows a typical diagram of a foam stability device used for bulk foam stability evaluation.

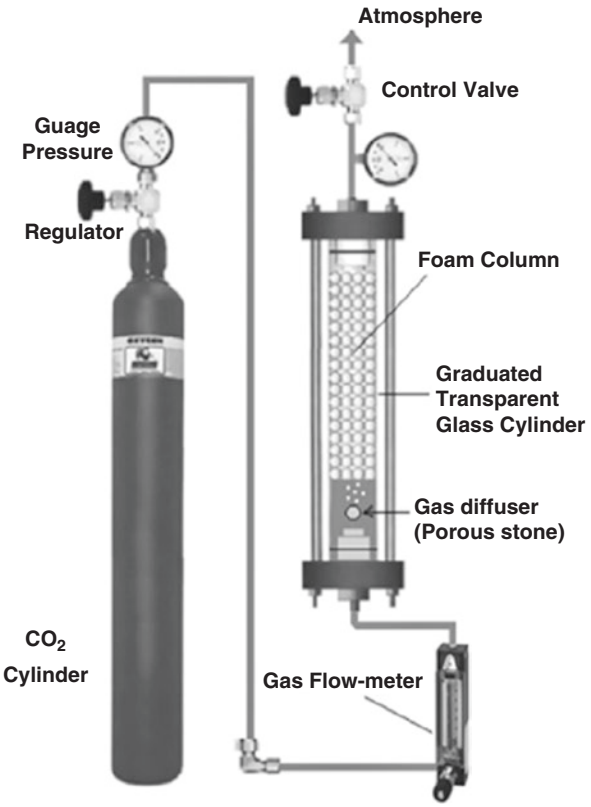

Fig. 8.9 Typical foam evaluation device for bulk foam stability evaluation [16]. Permissions related to the material excerpted were obtained from Elsevier, and further permission should be directed to Elsevier; Bayat, A. E., Rajaei, K., & Junin, R. (2016). Assessing the effects of nanoparticle type and concentration on the stability of CO_2 foams and the performance in enhanced oil recovery. Colloids and Surfaces A: Physicochemical and Engineering Aspects, 511, 222–231. doi: https://doi.org/10.1016/j.colsurfa.2016.09.083

$$\text{Normalized foam height} = \frac{\text{foam height @ time}(t)}{\text{foam height @ foam formation}} \tag{8.8}$$

Bubble Size Evaluation

Investigation of bubble size distribution helps in understanding the foam coalescence and film rupture mechanisms, especially by the use of microscopic pictures. Generally, the radius of foam bubbles is small when the foam is formed, but the size of the gas bubbles starts growing as a result of lamella rupturing. The effect of absorbed nanoparticles at the liquid films on delaying foam rupture can be studied by this method [97]. Figure 8.10 compares the gas bubble sizes of several surfactant solutions and surfactant-nanoparticle solutions. Foam coarsening was delayed in the case of the surfactant-nanoparticles solution, while foam bubble sizes of surfactant solution increased relatively faster indicating lower foam stability. Analyzing the foam bubble size and size distribution helps in understanding the effect of nanoparticles in enhancing foam stability as introduced by Xue et al. [171]. The

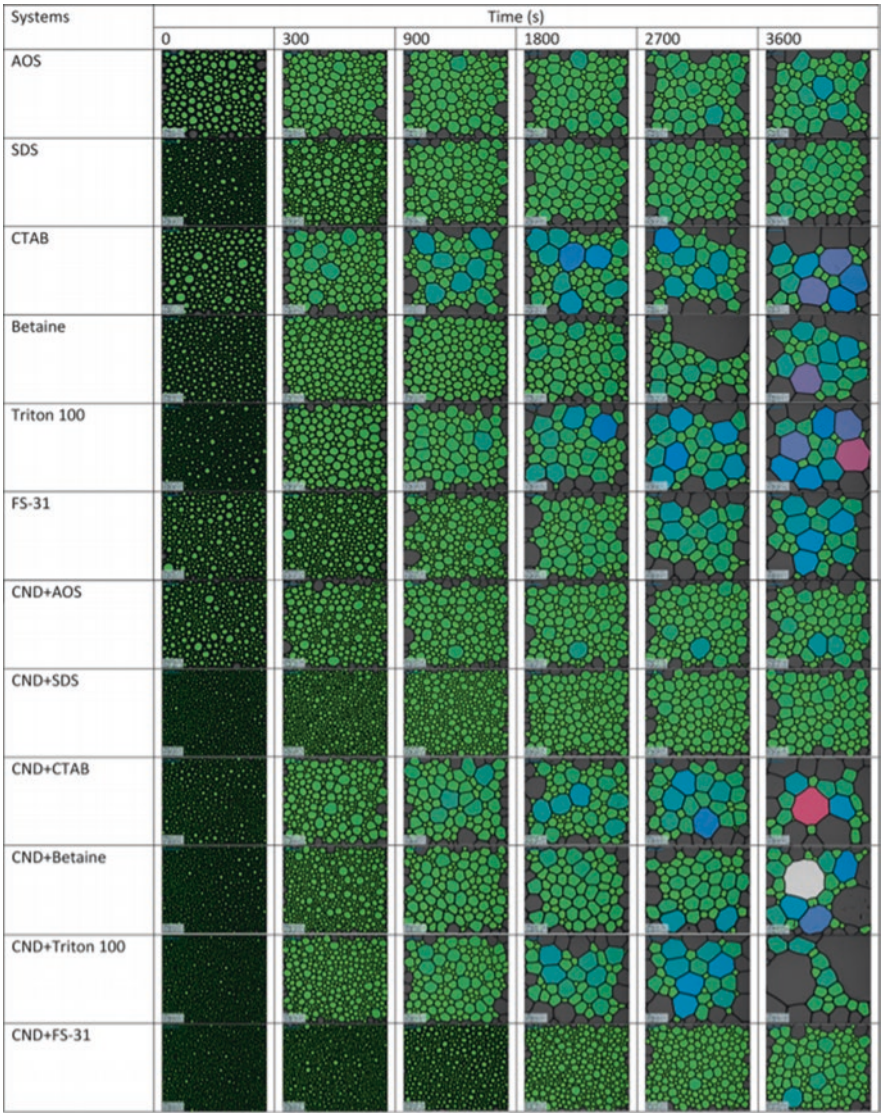

Fig. 8.10 Comparison between bubble sizes with time of foam stabilized by surfactants only and foam stabilized by surfactant-carbon nanodot (CND) [136]. Permissions related to the material excerpted were obtained from ACS, and further permission should be directed to ACS; Sakthivel, S., Adebayo, A., & Kanj, M. Y. (2019). Experimental Evaluation of Carbon Dots Stabilized Foam for Enhanced Oil Recovery. Energy & Fuels, 33(10), 9629–9643. doi: https://doi.org/10.1021/acs.energyfuels.9b02235

captured picture of foam morphology generated in a glass bead pack over time was used to calculate the Sauter mean diameter (D_{sm}) and the dimensionless polydispersity (U_{poly}) as expressed in Eqs. (8.9) and (8.10). A smaller change in foam Sauter

mean diameter over time indicates higher foam stability and delayed foam coarsening and coalescence. The insignificant change in the polydispersity indicates more uniformity in bubble shape over time [171, 175].

$$D_{sm} = \frac{\Sigma D_i^3}{\Sigma D_i^2} \tag{8.9}$$

$$U_{\text{poly}} = \frac{1}{D_{med}} \frac{\Sigma D_i^3 \left| D_{med} - D_i \right|}{\Sigma D_i^3} \tag{8.10}$$

where D_{sm} and U_{poly} are the Sauter mean diameter and the Polydispersity averaged over at least 100 bubbles. D_i and D_{med} are the diameter of a foam bubble and the median of the volume-averaged bubble diameter in the foam, respectively.

Vertical Foam Film Tests

In these tests, microscopes are used to observe the foam morphology to understand the effects of surfactants and/or nanoparticles on film thinning, film thickness, foam stability, and the location of adsorbed surfactants and/or nanoparticles. These tests show that nanoparticles can form three-dimensional networks enhancing the foam bubbles [146]. Figure 8.11 compares between a vertical foam film stabilized by surfactant only and a foam film stabilized by the surfactant-nanoparticle mixture. It shows that the surfactant-nanoparticle mixture delayed both the foam film thinning and rupturing. In Fig. 8.12b, when nanoparticles with fluorescence properties were used, nanoparticles were shown to be adsorbed at the interface and the Gibbs-Plateau border.

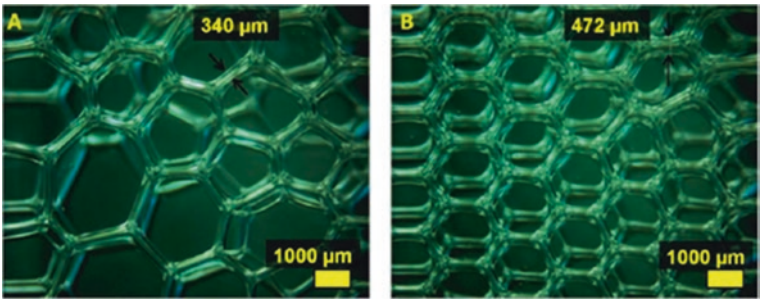

Fig. 8.11 Comparison between foam film morphologies and thicknesses of (**a**) foam stabilized by surfactant, (**b**) foam stabilized by surfactant and nanoparticles [146]. Permissions related to the material excerpted were obtained from ACS, and further permission should be directed to ACS; Singh, R., & Mohanty, K. K. (2015). Synergy between Nanoparticles and Surfactants in Stabilizing Foams for Oil Recovery. Energy & Fuels, 29(2), 467–479. doi: https://doi.org/10.1021/ef5015007

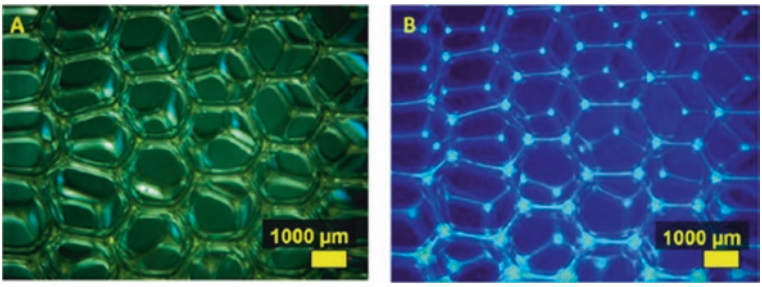

Fig. 8.12 Vertical foam film stabilized by surfactant-nanoparticle mixture captured at (**a**) visible light, (**b**) UV light [146]. Permissions related to the material excerpted were obtained from ACS, and further permission should be directed to ACS; Singh, R., & Mohanty, K. K. (2015). Synergy between Nanoparticles and Surfactants in Stabilizing Foams for Oil Recovery. Energy & Fuels, 29(2), 467–479. doi: https://doi.org/10.1021/ef5015007

8.4.2.2 Interfacial Tension and Dilatational Viscoelasticity Measurements

Interfacial tension and viscoelastic modulus are important parameters for the evaluation of foam generation and stability. In the absence of crude oil, surface tension controls the foam generation [7]. An increase in the viscoelastic modulus of foam films enhances foam stability against contraction and expansion [97]. Experiments of emulsions stabilized by surfactants and numerical simulations indicated that higher surface dilatational elasticity may decrease the Oswald ripening rates thus increasing foam stability [63, 113, 159]. In the presence of crude oil, interfacial tension properties between gas, water, and oil (σ_{wg}, σ_{wo}, σ_{og}) can be used to evaluate the effect of oil on foam stability, as will be discussed in the coming sections. The viscoelastic modulus (ε) in (mN/m) is expressed in Eq. (8.11) [97], where (γ) is the interfacial tension in (mN/m) and (A) is the surface area in (m^2).

$$\varepsilon = \frac{d\gamma}{d \ln A} \tag{8.11}$$

8.4.2.3 Application of Foam in the Porous Media Experiments

The effect of stabilized foam by surfactant-nanoparticle solution on enhancing oil recovery can be tested using porous media experiments. Micromodels, sand packs, and core flooding can be used for testing the foam apparent viscosity and its effect on oil recovery and mobility ratio enhancements. Micromodels can be used to study the pore scale effect of foam in EOR processes and its physical structure within the porous media at lower pressure experiments [118]. Core flooding experiments can mimic EOR processes under real reservoirs conditions. From differential pressure drop data in porous media experiments, apparent viscosity and mobility reduction factor can be calculated. An increase in pressure drop in foam flooding experiments

is related to the increase in gas apparent viscosity [111]. Apparent foam viscosity (μ_{app}) in a core flooding experiment is mathematically expressed in Eq. (8.12) [111].

$$\mu_{app} = \frac{k\Delta P}{u_t L} \tag{8.12}$$

where k is the core permeability, ΔP is the pressure difference, u_t is the total superficial velocity, and L is the core length.

Steady-state foam flow behavior can be classified into low-quality and high-quality foam regimes concerning the gas volumetric fraction in the total injected fluids or the foam quality (f_g) [30, 135]. Low-quality foam regime is characterized by a high superficial velocity of water (U_w) and low superficial velocity of gas (U_g) [22]. When the superficial velocity of gas (U_g) is high whereas the superficial velocity of water is low (U_w), foam flow regime is considered a high-quality foam regime [22]. These flow regimes can be clearly distinguished in the pressure gradient (ΔP) contours concerning superficial velocities of gas and water as illustrated in Fig. 8.13. The nearly vertical (ΔP) contours express the high-quality regime, while the nearly horizontal (ΔP) contours express the low-quality foam regime [22].

Higher apparent foam viscosity significantly attributes in higher foam strength [5]. Pressure gradient and apparent foam viscosity increase with the increase in the foam quality in the low-quality foam regime [37, 107]. Then, both the pressure gradient and the apparent foam viscosity decrease with the increase in the foam quality in the high-quality foam regime [37, 107]. Effect of increase in foam quality on the pressure and the apparent foam viscosity in foam displacement experiments in porous media is illustrated in Fig. 8.14.

The behavior of foam bubbles varies in the porous media in the different foam regimes. In the low-quality foam regime, foam bubbles are spaced and separated by thick liquid films [75, 107]. Hence, as the foam quality increases, apparent foam viscosity will also increase [37, 56, 135]. On the other hand, foam bubbles are packed and separated by individual liquid films in the high-quality foam regime [75, 107]. Moreover, as the foam quality increase in the high-quality foam regime, apparent foam viscosity will decrease as a result of an increase in the gas saturation and capillary pressure [61]. Hence, the foam will be unstable due to foam bubble coarsening [61]. Overall, in the high-quality foam regime, foam is stable when capillary pressure is lower than a limiting capillary pressure (P_c^*) [37]. Figure 8.15 expresses the concept of the limiting capillary pressure at which foam becomes unstable when foam quality is increased.

Injected foam in porous media can be either continuous or discontinuous gas foam as illustrated in Fig. 8.16. Gas bubbles in the discontinuous gas foam are separated by liquid lamellas, while gas channels are connected in the case of continuous gas foam [56, 107]. Accounting for this behavior is essential for understanding the foam mobility in porous media [5]. Discontinuous gas foam is capable of increasing apparent viscosity, while continuous gas foam can only reduce the gas relative

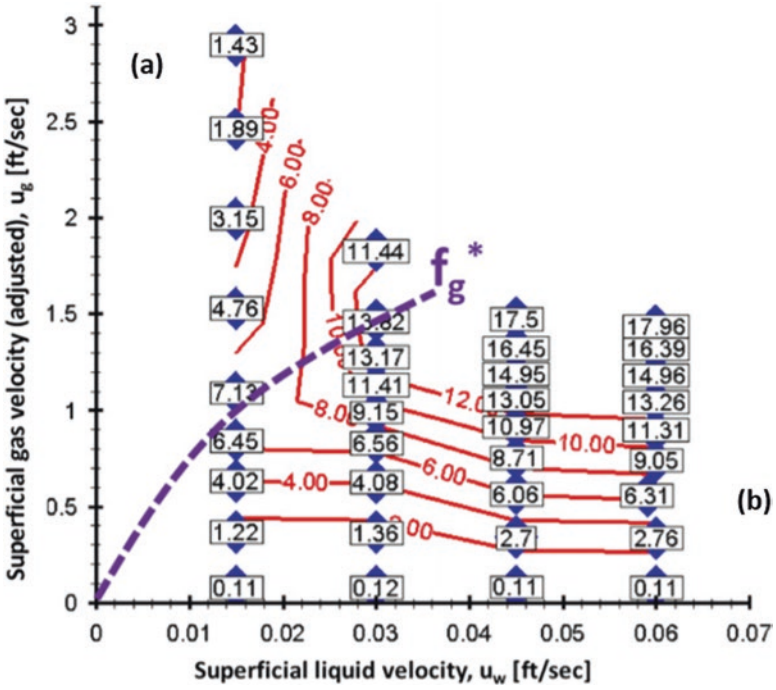

Fig. 8.13 Pressure gradient (psi/ft) contours as a function of gas and water superficial velocities of nitrogen gas foam in a horizontal pipe (0.5 wt% FA-406, 0.38/0.5 in ID/OD nylon pipe): (**a**) high-quality foam regime, (**b**) low-quality foam regime [62]. Permissions related to the material excerpted were obtained from Elsevier, and further permission should be directed to Elsevier; Gajbhiye, R. N., & Kam, S. I. (2011). Characterization of foam flow in horizontal pipes by using two-flow-regime concept. Chemical Engineering Science, 66(8), 1536–1549. doi: https://doi.org/10.1016/j.ces.2010.12.012

permeability [75, 107]. Hence, for the best mobility control foam, gas has to be discontinuous [5].

The ratio of total mobility of gas/brine to foam mobility is called the mobility reduction ratio (*MRF*). A higher reduction factor indicates higher foam stability [81]. It can be calculated from the ratio of pressure drop across the core during foam flooding (ΔP_f) to the pressure drop of the gas-only (ΔP_g). Equation (8.13) expresses the mobility reduction factor [81].

$$MRF = \frac{\left[\frac{kA\Delta P}{QL}\right]_f}{\left[\frac{kAvP}{QL}\right]_g} = \frac{\Delta P_f}{\Delta P_g} \tag{8.13}$$

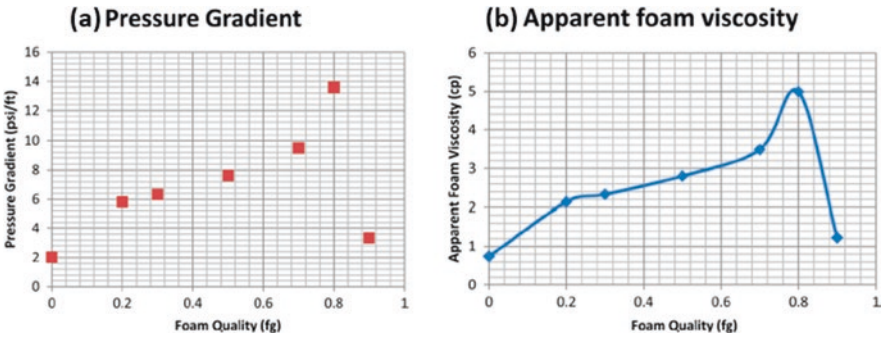

Fig. 8.14 Effect of increasing foam quality on (**a**) pressure gradient, (**b**) apparent foam viscosity. Carbonate core was used to construct these figures, while total injection rate was (0.05 ft^3/d) [5]. Permissions related to the material excerpted were obtained from ACS, and further permission should be directed to ACS; Al Sumaiti, A., Shaik, A. R., Mathew, E. S., & Al Ameri, W. (2017). Tuning Foam Parameters for Mobility Control using CO2 Foam: Field Application to Maximize Oil Recovery from a High Temperature High Salinity Layered Carbonate Reservoir. Energy & Fuels, 31(5), 4637–4654. doi: https://doi.org/10.1021/acs.energyfuels.6b02595

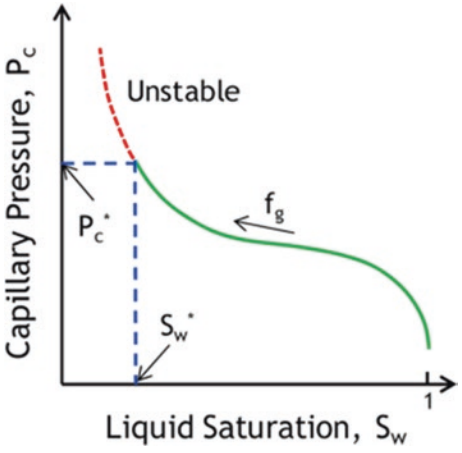

Fig. 8.15 Limiting capillary pressure concept for foam stability [61]. Permissions related to the material excerpted were obtained from ACS, and further permission should be directed to ACS; Farajzadeh, R., Lotfollahi, M., Eftekhari, A. A., Rossen, W. R., & Hirasaki, G. J. H. (2015). Effect of Permeability on Implicit-Texture Foam Model Parameters and the Limiting Capillary Pressure. Energy & Fuels, 29(5), 3011–3018

where k is the core permeability, A is the cross-sectional area of the core, ΔP is the pressure drop Q is the injection rate, and L is the core length. The subscripts f and g are for the foam and gas, respectively.

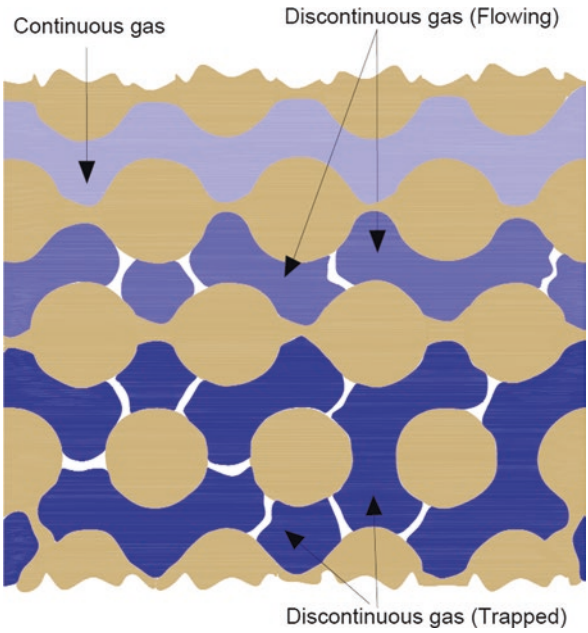

Fig. 8.16 Illustration of continuous and discontinuous gas (flowing and trapped) foams flow in porous media

8.5 Critical Parameters Influencing Foam Stability

In this section, the main crucial parameters influencing foam stability are discussed extensively.

8.5.1 Temperature

Generally, literature results suggest that increasing the temperature of a foam dispersion has a detrimental effect on foam stability. Static foam stability measurements indicate a decline in foam half-life time of liquid drainage as the temperature is increased [97, 163]. Moreover, the interfacial tension between gas and water increases, while dilatational viscoelasticity modulus decreases as a result of temperature elevation as depicted in Fig. 8.17 [97]. Consequently, both the foam stability and foam generation rate are declined with the increase in foam dispersion temperature [13, 97, 115, 156, 175, 177]. As a result, apparent foam viscosity can also decrease with the increase in temperature [8, 170].

The reduction of foam stability with the increase in temperature is attributed to several reasons. Increasing temperature cause ineffective adsorption of surfactant molecules and nanoparticles at foam lamellae as a result of thermal agitation and energetic movement of nanoparticles and surfactant molecules [97, 175, 177]. Increasing the temperature also contributes to decreasing the foam viscosity due to

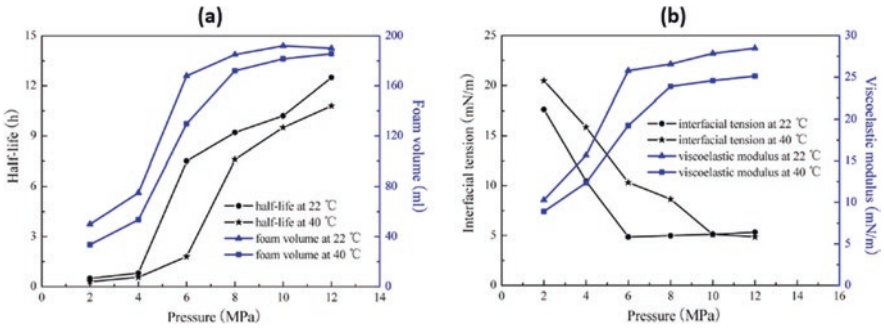

Fig. 8.17 Effect of increasing temperature from 22 to 40 °C and pressure from 2 to 12 MPa on CO_2 foam properties of SDS/SiO_2 dispersion: (**a**) foam volume and half-life time, (**b**) interfacial tension and viscoelastic modulus [97]. Permissions related to the material excerpted were obtained from ACS, and further permission should be directed to ACS; Li, S., Li, Z., & Wang, P. (2016). Experimental Study of the Stabilization of CO_2 Foam by Sodium Dodecyl Sulfate and Hydrophobic Nanoparticles. Industrial & Engineering Chemistry Research, 55(5), 1243–1253. doi: https://doi.org/10.1021/acs.iecr.5b04443

the escalation of both the gas diffusion and liquid drainage from the foam films [148, 172, 175]. Hence, the foam stability is crucially impacted as a result of foam film thinning and Ostwald ripening. Furthermore, an increase in water evaporation rate also contributes to foam film thinning [97, 175, 177].

8.5.2 Pressure

Increasing pressure can increase foam stability as suggested by Li et al. [97] In their study, CO_2 foam stability of SDS/SiO_2 dispersion was enhanced as indicated from half-life time, foam volume, surface tension, and viscoelastic measurements when pressure was increased from 2 to 12 MPa. Figure 8.17 indicates the increase in foam half-life time, volume, viscoelastic modulus, and the decrease in surface tension due to the increase in pressure. Moreover, generated CO_2 foam volume and density was increased gradually as pressure was raised as shown in Fig. 8.18. Li et al. [97] attributed the increase in foam volume and the enhancement of foam stability as pressure was increased due to the phase change of CO_2. The density of CO_2 increases dramatically from the gas phase to the supercritical phase. Hence, the fluid discharged from the CO_2 foam will be decreased as explained by Li et al. [97] which enhanced the foam stability in addition to resulting in desirable interfacial property behavior.

However, Emrani and Nasr-El-Din [53] reported the opposite effect of increasing pressure on CO_2 foam stability of AOS/SiO_2 at 75°F. It was claimed that the increase in CO_2 solubility with the increase in pressure decreased the foam half-life time leading to a faster liquid drainage rate as shown in Fig. 8.19. Finally, further research needs to be conducted to explain the causes of such completely different behavior of foam half-life time and volume when pressure is increased.

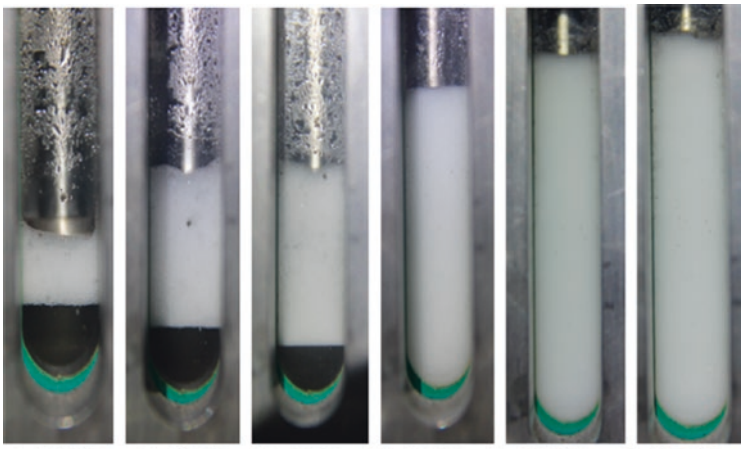

Fig. 8.18 Morphology of CO_2 foam of SDS/SiO_2 foam at pressure 2–12 MPa [97]. Permissions related to the material excerpted were obtained from ACS, and further permission should be directed to ACS; Li, S., Li, Z., & Wang, P. (2016). Experimental Study of the Stabilization of CO_2 Foam by Sodium Dodecyl Sulfate and Hydrophobic Nanoparticles. Industrial & Engineering Chemistry Research, 55(5), 1243–1253. doi: https://doi.org/10.1021/acs.iecr.5b04443

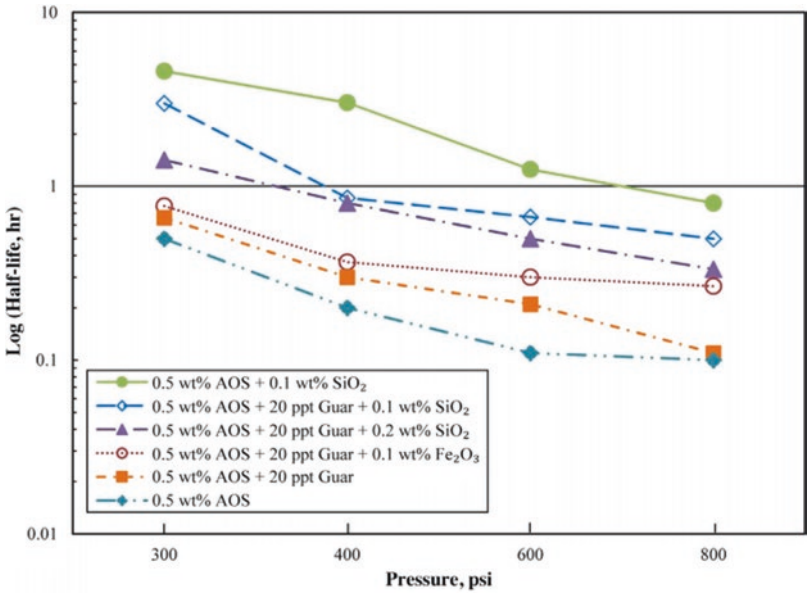

Fig. 8.19 Effect of pressure on CO_2 foam half-life time of AOS/SiO_2 at 25 °C while SiO_2 concentration was fixed at 0.1 wt.% [52]. Permissions related to the material excerpted were obtained from Elsevier, and further permission should be directed to Elsevier; Emrani, A. S., & Nasr-El-Din, H. A. (2017a). An experimental study of nanoparticle-polymer-stabilized CO_2 foam. Colloids and Surfaces A: Physicochemical and Engineering Aspects, 524, 17–27. doi: https://doi.org/10.1016/j.colsurfa.2017.04.023

8.5.3 *Salinity*

The presence of electrolytes is a crucial parameter influencing both the stability of surfactant molecules and nanoparticles in a foam dispersion. The stability of a surfactant-stabilized foam depends on both the concentration and the type of cation salts whether it is a monovalent, divalent, or multivalent. Kumar and Mandal [93] studied the effect of NaCl concentration on foam height for several surfactants including SDS, CTAB, and Tween 80. Their results indicated a relative increase in foam height after 50 min as salt concentration was less than 1 wt.% NaCl. However, as salinity was increased above 1 wt.% NaCl, foam height after 50 min declined. Figure 8.20 summarizes the effect of NaCl salinity on foam height after 50 min, while concentrations of SDS, CTAB, and Tween 80 were at the critical micelle concentration. Impact of salinity on a surfactant-stabilized foam increases due to the presence of divalent or multivalent ions. This is mainly due to the high tendency of surfactants to influentially react with existing cations such as Ca^{2+} and Mg^{2+} in formation brines which results in surfactant precipitation [162, 175].

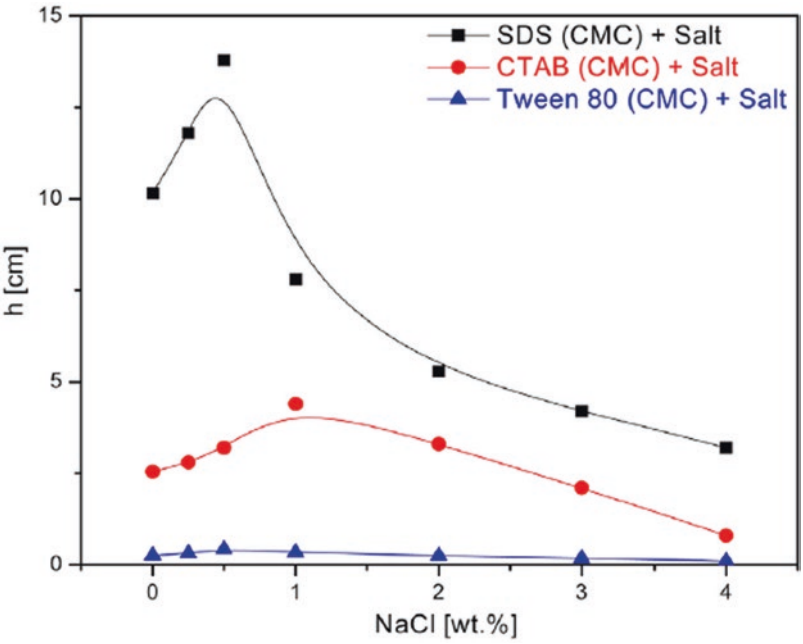

Fig. 8.20 Effect of salt concentration on foam height after 50 min in the presence of different surfactants [93]. Permissions related to the material excerpted were obtained from Elsevier, and further permission should be directed to Elsevier; Kumar, S., & Mandal, A. (2017). Investigation on stabilization of CO_2 foam by ionic and nonionic surfactants in presence of different additives for application in enhanced oil recovery. Applied Surface Science, 420, 9–20. doi: https://doi.org/10.1016/j.apsusc.2017.05.126

Derjaguin-Landau-Verwey-Overbeek (DLVO) theory suggests that the stability of a nanoparticle-stabilized foam is controlled by the sum of the repulsive electrostatic forces and the Van der Waals forces [173, 175]. The Van der Waals attraction forces become greater than the electrostatic repulsion forces as a result of the increase in solution salinity [21, 172]. This can be indicated from the low zeta potential measurements [44, 91]. Hence, the presence of a high concentration of monovalent and divalent ions can cause nanoparticle aggregation resulting in either stabilizing or destabilizing foam depending on the location of agglomeration (liquid phase, continuous liquid phase, or at the gas/liquid interface) [175].

According to Yekeen et al. [175], moderate aggregation of nanoparticles due to the presence of electrolytes at the gas/liquid interface can enhance foam stability. On the other hand, excessive particle accumulation at the interface or in the liquid phase can prevent the migration of nanoparticles to the gas/liquid interface which will eventually destabilize the foam.

8.5.4 Zeta Potential and pH

Zeta potential measures the magnitude of electrostatic repulsion/attraction between suspended particles and is considered a major property in evaluating the stability of colloidal dispersions and emulsions [117]. More stable emulsions possess higher magnitudes of electrostatic forces and consequently higher zeta potential measurements [117]. The major property affecting the zeta potential of a colloidal dispersion is the pH. Adding an acid to an emulsion reduces the magnitude of zeta potential, while adding an alkali increases the magnitude of the zeta potential [17].

In acidic environments, protonation of surfactants occurs, resulting in a reduction in the molecules' surface-active properties. As a result, surfactant aggregation can occur. Hence, it is more favored to keep an emulsion in the alkali environment for more stability [34].

Singh, Panthi, Weerasooriya, and Mohanty [150] evaluated the effect of pH alternation on the foam stability of tristyrylphenol propoxy carboxylate (TSP-PO45-COOH). This is an anionic surfactant which contains a carboxyl group which is a pH-sensitive unit as shown in Fig. 8.21. This surfactant dispersion was able to produce a fine bubble texture (bubble size <200 μm) in the alkali pH range. However, decreasing the pH by either adding acid or CO_2 injection resulted in foam destabilization behavior. Singh et al. [150] explained that the protonation of the carboxyl unit is responsible for foam destabilization. Moreover, the acidic pH causes a cloudy/unclear surfactant solution due to aggregation as reported from DLS and TEM test as shown in Fig. 8.22. Figure 8.23 shows the foam behavior due to pH alternation.

Recently, several surfactants were reported to generate stable foams in acidic environments including switchable amine surfactants. Switchable amine surfactants such as Ethomeen C/12, Duomeen TTM, and Duomeen CTM perform as nonionic surfactants in neutral pH and convert to cationic surfactants at low pH due to

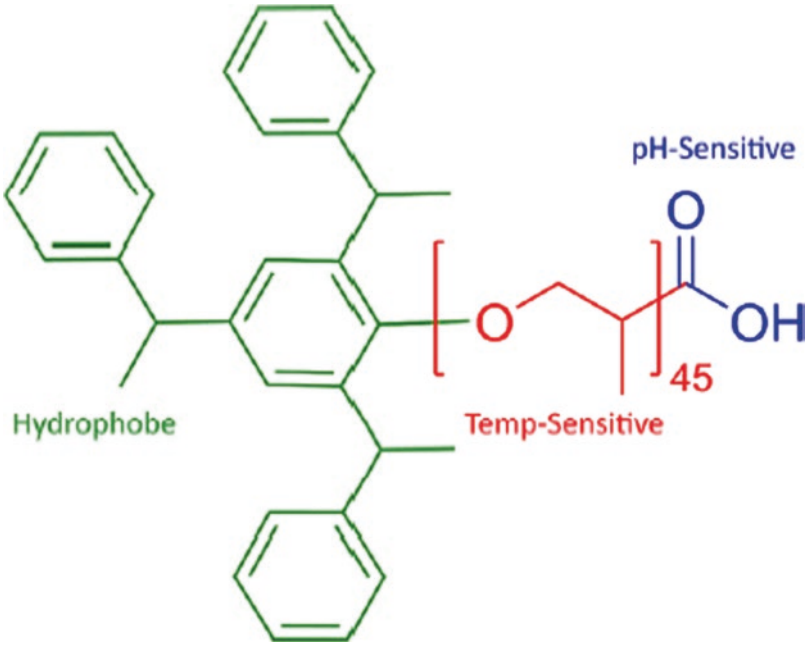

Fig. 8.21 Structure of TSP-PO45-COOH [150]. Permissions related to the material excerpted were obtained from ACS, and further permission should be directed to ACS; Singh, R., Panthi, K., Weerasooriya, U., & Mohanty, K. K. (2018). Multistimuli-Responsive Foams Using an Anionic Surfactant. Langmuir, 34(37), 11010–11020. doi: https://doi.org/10.1021/acs.langmuir.8b01796

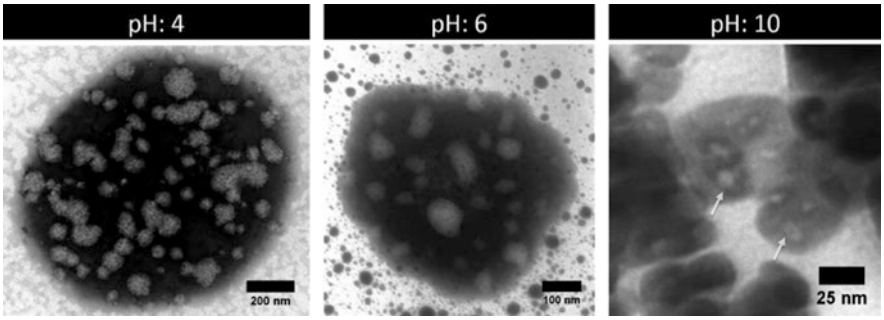

Fig. 8.22 TEM pictures showing the effect of pH alternation on growing aggregates of TSP-PO45-COOH surfactant [150]. Permissions related to the material excerpted were obtained from ACS, and further permission should be directed to ACS; Singh, R., Panthi, K., Weerasooriya, U., & Mohanty, K. K. (2018). Multistimuli-Responsive Foams Using an Anionic Surfactant. Langmuir, 34(37), 11010–11020. doi: https://doi.org/10.1021/acs.langmuir.8b01796

Fig. 8.23 Effect of pH alternation on foam stability of TSP-PO45-COOH surfactant [150]. Permissions related to the material excerpted were obtained from ACS, and further permission should be directed to ACS; Singh, R., Panthi, K., Weerasooriya, U., & Mohanty, K. K. (2018). Multistimuli-Responsive Foams Using an Anionic Surfactant. Langmuir, 34(37), 11010–11020. doi: https://doi.org/10.1021/acs.langmuir.8b01796

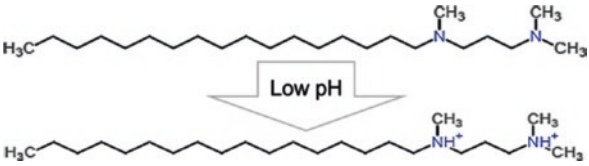

Fig. 8.24 Schematic of protonation of a switchable surfactant from the nonionic to the cationic form due to protonation at low pH conditions [38]. Permissions related to the material excerpted were obtained from ACS, and further permission should be directed to ACS; Rattanaudom, P., Shiau, B.-J., Suriyapraphadilok, U., & Charoensaeng, A. (2021). Effect of pH on silica nanoparticle-stabilized foam for enhanced oil recovery using carboxylate-based extended surfactants. Journal of Petroleum Science and Engineering, 196, 107729. doi: https://doi.org/10.1016/j.petrol.2020.107729

protonation as shown in Fig. 8.24 [32, 33, 50]. These surfactants are capable of producing stable CO_2 at pH between 4 and 6 [31].

Generally, stable nanoparticle dispersion at a specific pH range can enhance surfactant foam stability. Rattanaudom, Shiau, Suriyapraphadilok, and Charoensaeng [128] compared the effect of pH alternation on the N_2 foam stability of an anionic carboxylate extended surfactant with the effect of the addition of partially hydrophobic silica nanoparticles to the surfactant solution. Their results indicated that the presence of nanoparticles increased the foam half-life time when pH was increased from 3 to11 as displayed in Fig. 8.25. Figure 8.26 shows the zeta potential of the surfactant dispersion at 0.5 wt.% concentration and the 0.5 wt% surfactant dispersion with 100 ppm hydrophobic silica nanoparticles.

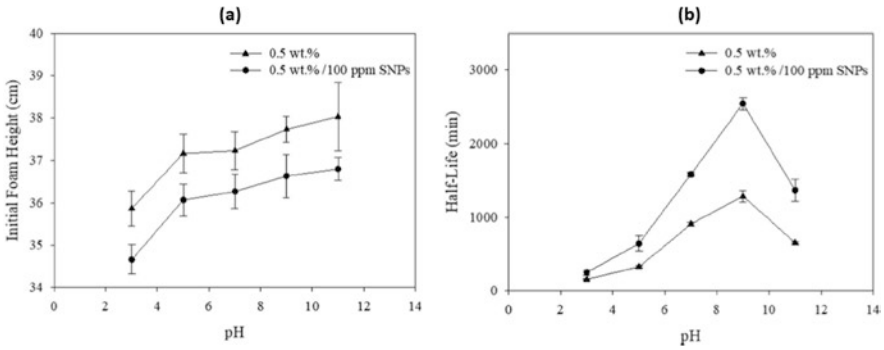

Fig. 8.25 Comparison between the effect of pH alternation on foam stability of carboxylate surfactant at 0.5 wt.% with the addition of hydrophobic silica nanoparticles at 100 ppm concentration: (**a**) foam initial height, (**b**) foam half-life time [128]. Permissions related to the material excerpted were obtained from Elsevier, and further permission should be directed to Elsevier; Rattanaudom, P., Shiau, B.-J., Suriyapraphadilok, U., & Charoensaeng, A. (2021). Effect of pH on silica nanoparticle-stabilized foam for enhanced oil recovery using carboxylate-based extended surfactants. Journal of Petroleum Science and Engineering, 196, 107729. doi: https://doi.org/10.1016/j.petrol.2020.107729

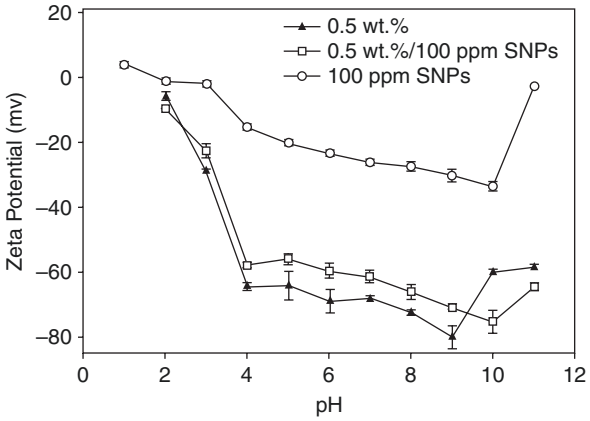

Fig. 8.26 Zeta potential of 0.5 wt.% surfactant solution, 0.5 wt.% surfactant, and 100 ppm silica solution and nanoparticle dispersion at 100 ppm concentration [128]. Permissions related to the material excerpted were obtained from Elsevier, and further permission should be directed to Elsevier; Rattanaudom, P., Shiau, B.-J., Suriyapraphadilok, U., & Charoensaeng, A. (2021). Effect of pH on silica nanoparticle-stabilized foam for enhanced oil recovery using carboxylate-based extended surfactants. Journal of Petroleum Science and Engineering, 196, 107729. doi: https://doi.org/10.1016/j.petrol.2020.107729

8.5.5 Gas Type

Foam performance and properties crucially depend on the gas types used for foam generation. The main gases utilized in gas EOR include methane, carbon dioxide, nitrogen, and air. In foam stability studies, carbon dioxide, nitrogen, and air received the most attention since they are nontoxic, nonflammable, and cost-effective [175].

Compared to CO_2, N_2 and air can form a stable foam in both ambient and reservoir conditions. Aarra, Skauge, Solbakken, and Ormehaug [2] evaluated the properties of N_2 and CO_2/AOS surfactant foams due to pressure variation (30–280 bar) while temperature and gas quality were fixed at 50 °C and 80%, respectively. Core flooding experiments in a Berea sandstone core indicated that N_2 was able to form a stable foam at both low and high pressures. However, the pressure drop in the CO_2 foam core flooding was significantly decreased as pressure was increased from 30 to 280 bar. Figure 8.27 compares the differential pressure of N_2 and CO_2 foams core flooding experiments at both low and high pressures.

The change in CO_2 foam properties between ambient and reservoir conditions is attributed to the phase change of CO_2 from the subcritical to the supercritical state. Moreover, the high solubility of CO_2 in water increases gas diffusion between foam bubbles resulting in both lamella rapturing and film thinning [68, 175]. Due to the high solubility of CO_2, less gas volume generates foam compared to less soluble gases such as N_2 [1, 174]. Furthermore, dissolved CO_2 gas in water produces carboxylic acid which also influences foam stability and film thickness via screening of the Van der Waals and electrostatic forces [11, 59].

Despite the physical change of CO_2 at high pressure and temperature conditions, several surfactants and nanoparticles were reported to be capable of generating stable supercritical CO_2 foams. Mainly, switchable amine surfactants [5, 38], the

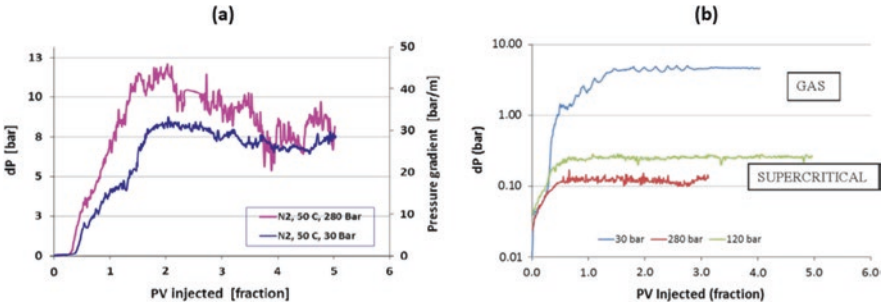

Fig. 8.27 Pressure gradient of foam core flooding experiments at both low and high pressure conditions of (**a**) N_2, (**b**) CO_2 while temperature and gas quality were 50 °C and 80%, respectively [2]. Permissions related to the material excerpted were obtained from Elsevier, and further permission should be directed to Elsevier; Aarra, M. G., Skauge, A., Solbakken, J., & Ormehaug, P. A. (2014). Properties of N2- and CO_2-foams as a function of pressure. Journal of Petroleum Science and Engineering, 116, 72–80. doi: https://doi.org/10.1016/j.petrol.2014.02.017

zwitterionic surfactant LDMAA [170], and the anionic surfactant AMPHOAM [170] can produce supercritical CO_2 foams at elevated pressure and temperature conditions. Organic ligand-graphed silica nanoparticles also showed the ability to stabilize supercritical CO_2 foams [8]. These surfactants and nanoparticles will be explained in further detail in the following sections.

8.5.6 Crude Oil

Crude oil is composed of complex mixtures of hydrocarbon and nonhydrocarbon components. Main hydrocarbon components include paraffin, aromatics, and naphthenes, while nonhydrocarbons contain sulfur, nitrogen, and oxygen compounds [112]. The variety of oil composition can significantly influence both the physical and chemical properties of any petroleum fluid [119, 160]. Hence, crude oil properties are significant in evaluating foam stability whether it will not destabilize the foam or only spread on liquid films or even enter the foam lamellas [111]. The main concepts discussed in the literature for evaluating the effect of crude oil on foam stability include the spreading and entering coefficients, lamella number, bridging coefficient, and the pseudo-emulsion film theory [160].

8.5.6.1 The Spreading and Entering Coefficients

To explain foam stability qualitatively in the presence of crude oil, the following coefficients can be used: spreading (S) and entering (E) coefficients as expressed in Eqs. (8.14) and (8.15). Negative values of the entering (E) and spreading coefficients (S) indicate that the oil does not affect foam stability. On the other hand, a positive value of S indicates that oil will spread on the foam films causing film rupture as depicted in Fig. 8.28 [160].

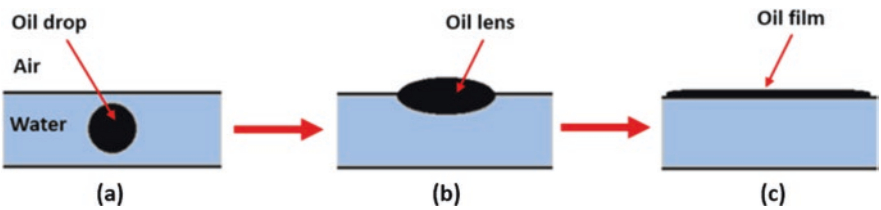

Fig. 8.28 Illustration of: (**a**) oil drop within the solution, (**b**) non-spreading oil system ($S < 0$), and (**c**) spreading system ($S > 0$) [103]. Permissions related to the material excerpted were obtained from ACS, and further permission should be directed to ACS; Lobo, L., & Wasan, D. T. (1993). Mechanisms of aqueous foam stability in the presence of emulsified nonaqueous-phase liquids: structure and stability of the pseudoemulsion film. Langmuir, 9(7), 1668–1677. doi: https://doi.org/10.1021/la00031a012

$$S = \sigma_{wg} - \sigma_{wo} - \sigma_{og} \tag{8.14}$$

$$E = \sigma_{wg} + \sigma_{wo} - \sigma_{og} \tag{8.15}$$

where σ_{wg}, σ_{wo}, and σ_{og} are the gas and water interfacial tensions with oil.

8.5.6.2 The Bridging Coefficient

When the value of the bridging coefficient (B) as expressed in Eq. (8.16) is positive, the presence of crude oil will destabilize the foam films regardless of the sign of the spreading coefficient (S). Figure 8.29 illustrates the bridging effect of oil in a foam liquid film ($B > 0$) [7, 41, 70, 111, 131, 160].

$$B = \sigma_{wg}^2 + \sigma_{wo}^2 - \sigma_{og}^2 \tag{8.16}$$

where σ_{wg}, σ_{wo}, and σ_{og} are the gas and water interfacial tensions with oil.

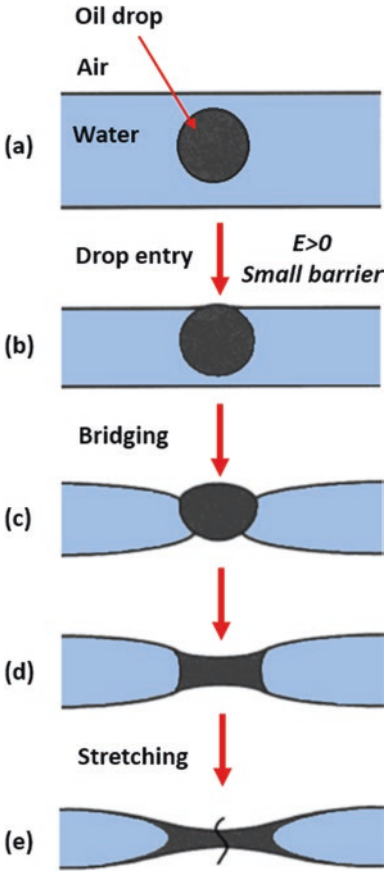

Fig. 8.29 Illustration of oil bridging-stretching mechanism of foam film destruction: (**a**–**c**) formation of an oil bridge, (**c**–**e**) stretching of an oil bridge due to uncompensated capillary pressures at the oil-water and oil-air interfaces, and (**e**) oil bridge rupture at the its thinnest central region [43]. Permissions related to the material excerpted were obtained from ACS, and further permission should be directed to ACS; Denkov, N. D., Cooper, P., & Martin, J.-Y. (1999). Mechanisms of Action of Mixed Solid–Liquid Antifoams. 1. Dynamics of Foam Film Rupture. Langmuir, 15(24), 8514–8529. doi: https://doi.org/10.1021/la9902136

8.5.6.3 Lamella Number

Lamella number (L) as expressed in Eq. (8.17) represents the tendency of oil to become emulsified and imbibed into foam films. When lamella number is less than 1, spreading and entering coefficients are negative which results in a more stable foam. When lamella number is between 1 and 7, the oil will moderately destabilize the foam which results in a negative spreading and positive entering coefficients. Finally, when the lamella number is greater than 7, the oil will destabilize the foam, and both S and E will be positive. Figure 8.30 illustrates the effect of oil on the stability of three types of foam (A, B, C) and the variations of the foam lamella number [138, 139, 160]

$$L = \frac{0.15\sigma_{wg}}{\sigma_{wo}} \tag{8.17}$$

where σ_{wg} and σ_{wo} are the water/gas and the water/oil interfacial tensions, respectively.

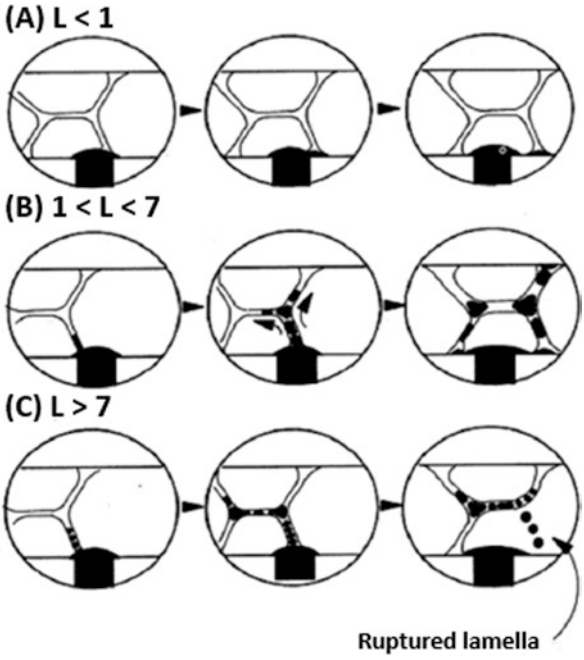

Fig. 8.30 Comparison between foam stability in contact with oil of: (**a**) foam type A ($L < 1$), (**b**) foam type B ($1 < L < 7$), and (**c**) foam type C ($L > 7$) [138]. [2]. Permissions related to the material excerpted were obtained from Elsevier, and further permission should be directed to Elsevier; Schramm, L. L., & Novosad, J. J. (1990). Micro-visualization of foam interactions with a crude oil. Colloids and Surfaces, 46(1), 21–43. doi: https://doi.org/10.1016/0166-6622(90)80046-7

8.5.6.4 Pseudo-Emulsion Film

Foam stability in presence of oil is significantly related to the stability of pseudo-emulsion films [90, 109, 127, 164]. A pseudo-emulsion film is defined as the thin liquid film existing between an oil droplet and the gas phase [160]. The oil will remain in the liquid lamella if the pseudo-emulsion film is stable, whereas oil may form a lens at the gas/water interface if the pseudo-emulsion film is ruptured. Hence, foam can break down [160]. Figure 8.31 expresses the possible configurations of the oil depending on the pseudo-emulsion film stability.

8.5.7 Surfactants

Foaming agents or surfactants are required for foam generation. Surfactant molecules stabilize liquid films via adsorption at the water/gas interface. Hence, the water molecules at the interface are replaced by a layer of surfactant molecules with a lower energy level [120, 166]. The selection of the appropriate surfactants for any EOR project is a challenging task. Surfactant concentration, hydrophilic-lipophilic balance (HLB), gas type, temperature, pH, and salinity are crucial factors impacting the effectiveness of foam stabilization by surfactants. The main surfactants reported in the literature for possessing foamability and foam stabilization properties for EOR applications are summarized in Table 8.1.

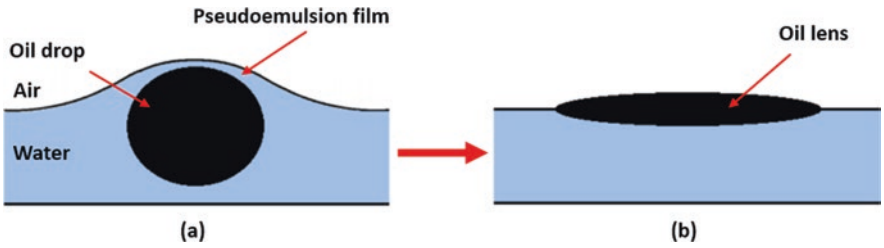

Fig. 8.31 (**a**) Stable pseudo-emulsion film, and (**b**) unstable pseudo-emulsion film [103]. Permissions related to the material excerpted were obtained from ACS, and further permission should be directed to ACS; Lobo, L., & Wasan, D. T. (1993). Mechanisms of aqueous foam stability in the presence of emulsified nonaqueous-phase liquids: structure and stability of the pseudo-emulsion film. Langmuir, 9(7), 1668–1677. doi: https://doi.org/10.1021/la00031a012

Table 8.1 Main surfactants tested for foam stabilization

Surfactant type	Short name	Chemical name	Reference
Anionic	APS	Alcohol propoxy sulfate	[117]
	AOS	Alpha olefin sulfonate	[117]
	SDS	Sodium dodecyl sulfate	[9]
	AMPHOAM	–	[170]
	AES	Sodium fatty alcohol polyoxyethylene ether sulfate	[123]
	FRC-1	–	[104]
	ENORDET A031	–	[6]
Cationic	CTAB	Dodecyl trimethyl ammonium bromide	[27]
	Ethomeen C/12	Bis(2-hydroxyethyl cocoalkylamine)	[38]
	Duomeen TTM	*N*,*N*,*N*′ -trimethyl-*N*′ -tallow-1,3-diaminopropane	[38]
	Duomeen CTM	*N*,*N*,*N*′ -trimethyl-*N*′ -coco-1,3-diaminopropane	[38]
Zwitterionic	FS	Perfluoroalkyl betaine surfactant	[9]
	LDMAA	Lauryldimethylammonio acetate	[170]
	LAPB	Lauramidopropyl betaine	[66]
	OA-12	$C_{14}H_{31}NO$	[163]
Nonionic	C_{12}DMPO	Dodecyl dimethyl phosphine oxide	[27]
	FC	Fluorochemical	[9]
	β-$C_{12}G_2$	*n*-dodecyl-β-D-maltoside	[23]
	Triton CG-110	Alkyl polyglucoside	[147]
	Tween 80	Polysorbate 80	[93]
	TX-100	$C_{34}H_{62}O_{11}$	[163]
	$C_{12}E_{23}$	Lauryl alcohol polyoxyethylene ether	[99]

8.5.8 Nanoparticles

Extensive foam stability studies suggest that nanoparticles may be a promising technique for enhancing both the static and dynamic foam stability. Insofar, it was proved that nanoparticles are capable of increasing foam half-life time, delay the foam bubble coalescence and coarsening rates, and maintain small bubble sizes with time. Moreover, they significantly increase the viscoelastic modulus of liquid while decreasing the gas/water surface tension. Foam displacement experiments indicated that nanoparticles could play a significant role in maintaining higher foam apparent viscosities. Hence, they contribute to better foam stability. Nanoparticle type, surface wettability, size, and concentration are the main crucial factors influencing the effectiveness of nanoparticles in enhancing foam stability.

8.5.8.1 Nanoparticle Type

Several nanoparticle types have been investigated for foam stabilization including silica nanoparticles, metal oxides, graphene oxides, and ash materials. Silica nanoparticles are the most common type of nanoparticles applied in foam stability studies [175]. Bayat et al. [16] studied the effect of nanoparticle type on the stability of CO_2 foam. Evaluated nanoparticles were silica (SiO_2), hydrophilic metal oxide including aluminum oxide (Al_2O_3), titanium dioxide (TiO_2), and copper oxide (CuO) at an optimum concentration of 0.008 wt.%. Static and dynamic foam stability experiments indicated that SiO_2 and Al_2O_3 were the best nanoparticles types for stabilizing CO_2 foam. The foam half-life times of SiO_2, Al_2O_3, TiO_2, and CuO were 28.1, 24.6, 20.1, and 17.9 min, respectively. Finally, total oil recoveries by foam displacement in sand packs achieved by SiO_2, Al_2O_3, TiO_2, and CuO were 71.7%, 65.7%, 58.2%, and 57.3%, respectively.

Several researchers evaluated the potential of fly ash, particulate matter (PM), and graphene oxides as a CO_2 foam stabilizer [48, 67, 95, 106, 149]. Fly ash or PM is a waste material produced from coal power generation plants [106, 149]. Although fly ash materials are cheap and can be used as CO_2 foam stabilizers, the grain sizes are too large for injection in the reservoirs [149]. To minimize the sizes of fly ash materials, high-frequency ultrasonic grinding (ball milling process) was used [48, 149, 175]. However, producing nanoparticles from fly ash material requires several steps of dilution which makes the quantification of the concentration of the produced nanoparticles very challenging [48, 67]. Similarly, particle growth of graphene oxides causes it to be unsuitable for implementation in reservoirs [14]. Literature results suggest that nanoparticles can improve the stability of foam without the respect of the nanoparticle types [175], especially if it poses the optimum surface wettability, size, and concentration, as explained in the next section.

8.5.8.2 Nanoparticle Surface Wettability

Surface wettability of nanoparticles plays a significant role in foam generation by nanoparticles and provides an essential indication of the particle surface activity [175]. Literature results demonstrated that the hydrophilic-lipophilic balance (HLB) and the hydrophilic-CO_2-philic balance (HCB) contributes to the surface wettability of nanoparticles [175]. Hence, the correct choice of HCB is crucial for the generation of nanoparticle-stabilized CO_2 foams [168].

The wettability of nanoparticles can usually be indicated via the measurement of the contact angle at the gas/liquid interface [36]. The ideal contact angle reported in the literature for foam stabilization by nanoparticles is within the range of 40–70° [77, 85, 97, 125, 146, 156], According to other researchers, the contact angle is preferred to be in the range of 60–90° [98]. As the nanoparticles possess the optimum contact angle, it will be adsorbed efficiently and irreversible at the gas/water interface due to the highly associated particles' detachment energy [19, 74, 167].

Table 8.2 Selected nanoparticles surface modification from the literature

Nanoparticle type	Surface modification/surfactant/polymer	Hydrophilicity/contact angle	Reference
Silica (SiO_2)	Polyethene glycol (PEG)	Hydrophilic	[55]
	Methylsilylmodifed (Siu)	Partially hydrophobic	[168]
	Methyl coated with dichloro dimethyl silane	30°	[118]
	PEG, physical mixing with AOS	Hydrophilic	[146]
	Surface modified, physical mixing with SDS	Partially hydrophobic/122.22°	[97]
	Alumina-coated, surface modifier, physical mixing with AOS	Hydrophilic	[147]
	Surface modified, physical mixing with CTAB	Hydrophilic/38.63°	[98]
	Physical mixing with viscoelastic surfactant (VES) and AOS		[81]
	Physical mixing with TX-100, SDBS, CTAB, or OA-12 surfactants	Hydrophilic	[163]
	Saline modified, physical mixing with linear alcohol ethoxylate (C12-C16) surfactant	Less hydrophilic	[133]
	Physical mixing with polymer (PAM)	Hydrophilic	[126]
	Coated with dimethylsiloxane, physical mixing with FRC1 anionic surfactant	Hydrophobic	[104]
	Physical mixing with lauryl alcohol polyoxyethylene ether ($C_{12}E_{23}$) nonionic surfactant	Hydrophilic	[99]
	Surface modified by silane KH560, physical mixing with ethoxylated amine surfactant	Hydrophilic	[181]
Fly ash	Physical mixing with AOS	Hydrophilic	[48]
Iron oxide (Fe_3O_4)	Physical mixing with AOS	Hydrophilic	[51]
	Surface modification by 4-methyl-2-pentanone, physical mixing with SDS and HPAM	Contact angles (12.7°, 20.6°, 57.5°, and 97.3°)	[102]

On the other hand, at contact angles, less than 30° or higher than 150°, particles' detachment energy will be reduced [175].

According to Yekeen et al. [175], several techniques can be used to modify the surface wettability of nanoparticles for foam stabilization. Firstly, the extent of salinization can be altered by dichloro dimethyl silane. Secondly, surface-active agents (surfactants or polymers) can be coated on the surface of the nanoparticles. Thirdly, surface modification of the nanoparticles can be achieved by in situ hydrophilization of the nanoparticles or mixing it with surfactants. Table 8.2 summarizes the main approaches of nanoparticle surface modification illustrated in the literature.

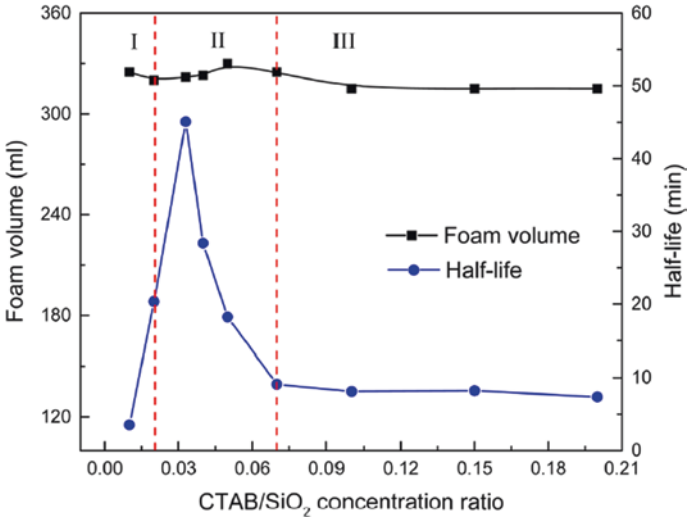

Fig. 8.32 Effect of CTAB/hydrophilic silica nanoparticle concentration ratio on CO_2 foam stability [98]. Permissions related to the material excerpted were obtained from ACS, and further permission should be directed to ACS; Li, S., Qiao, C., Li, Z., & Wanambwa, S. (2017). Properties of Carbon Dioxide Foam Stabilized by Hydrophilic Nanoparticles and Hexadecyltrimethylammonium Bromide. Energy & Fuels, 31(2), 1478–1488. doi: https://doi.org/10.1021/acs.energyfuels.6b03130

8.5.8.3 Effect of Nanoparticles Size

The performance of nanoparticles in foam stabilization is crucially impacted by the size of nanoparticles [85]. Generally, foam stability decreases as the size of the nanoparticles increases, and smaller nanoparticles generate more stable foams [175]. Tang, Xiao, Tang, and Jiang [158] studied the effect of silica nanoparticle size variation (sizes in the range of 20–700 nm) on the stability of SDS air foams. Their results indicated that smaller size nanoparticles are better for foam stabilization. Moreover, foam apparent viscosity also increases with decreasing the size of nanoparticles [89]. Figure 8.32 compares the apparent viscosity of CO_2 foam stabilized by varied sizes of silica nanoparticles (12–80 nm).

Smaller sizes of nanoparticles attribute to better foam stability for several factors. Mainly, smaller nanoparticles can migrate faster than bigger nanoparticles to the gas/water interface [40]. Hence, the adsorption and concentration of nanoparticles at the gas/water interface will increase providing more liquid film stability [89, 175]. Moreover, the attachment energy of nanoparticles at the gas/water interface is increasing with the increase in particle size [154, 172].

8.5.8.4 Effect of Nanoparticle Concentration

Literature results indicated that nanoparticle concentration is crucial for the evaluation of foam stability. At low nanoparticle concentration, the number of nanoparticles adsorbed at the water/gas interface could be not sufficient for enhancing the stability of the liquid film [175]. Kim, Taghavy, DiCarlo, and Huh [88] demonstrated that beyond a threshold of nanoparticle concentration, adsorbed nanoparticles at the gas/water interface become sufficient for enhancing the stability of the liquid. As the nanoparticle concentration in the solution increases, more nanoparticles will be adsorbed at the gas/water interface contributing to enhancing the liquid film elastic properties and slowing down both the liquid drainage and film thinning processes [175]. However, beyond the optimum nanoparticle concentration, aggregation of nanoparticles can impact the foam stability negatively [86]. According to Z. Li et al. [96], nanoparticle aggregation results in particles exerting gravity force exceeding the foam bubble anti-deformation capacity. Consequently, film thinning rate increases as a result of liquid discharge under the gravity effect of the aggregated nanoparticles [175]. The synergistic effect between nanoparticles and surfactants enhances the foam stabilization process. However, optimum nanoparticle concentration will be significantly impacted by the type of surfactant utilized, its chain length, and concentration [175]. Investigated synergy effect between silica nanoparticles and surfactants for CO_2 foam stabilization demonstrated that foam half-life time increases as the surfactant-nanoparticle concentration is increased until it reaches an optimum concentration ratio [97, 98]. However, beyond this optimum concentration ratio, the foam will be destabilized, as shown in Fig. 8.32.

S. Li et al. [98] explained that increasing the concentration ratio between CTAB and the hydrophilic silica nanoparticles (original contact angle with water is 38.63°) between 0.02 and 0.07 achieved the most stable foam (7 times the stability of CTAB alone) as shown in region (II) in Fig. 8.32. However, there was no obvious synergistic effect due to further increase in the CTAB/SiO_2 concentration ratio (region III), which results in lower foam stability compared to the region (II).

8.6 Various Studies Conducted on Foam Stability Using Nanoparticles

Foam studies can be conducted by using nitrogen, methane, and carbon dioxide. Literature results are expressed based on different gas types used for foam generation.

8.6.1 Nitrogen

Singh and Mohanty [145] evaluated the effect of alumina-coated silica nanoparticles on the stability of immiscible N_2 foam. These hydrophilic nanoparticles were unable to stabilize foam without the addition of a PG surface modifier. PG surface

modifier was able to change the wettability of nanoparticles to partially hydrophobic thus helping in the formation of more stable and fine foam bubbles at nanoparticle concentration of 1 wt.% and surface modifier of (0.05 wt.%). [7] showed that anionic alpha olefin sulfonate (0.5 wt.%) and surface-modified silica nanoparticle (0.5 wt.%) solution was able to stabilize foam in the prescience of crude oil. Foam half-life time was increased as the concentration of nanoparticles was increased. Moreover, the increase in surfactant-solid dispersion salinity to 1 wt.% of NaCl showed a desirable effect on enhancing foam stability and delaying foam height decay. On the other hand, in the absence of crude oil, the addition of solids had a minor effect on foam stability.

Nitrogen foam stabilized by surfactants-nanoparticles can have the ability to increase oil recovery after water flooding. According to Singh and Mohanty, oil recovery by N_2 foam stabilized by 0.5 wt.% Titon nonionic surfactant increased the oil recovery by 13.4% OOIP after water flooding. On the other hand, oil recovery by N_2 foam stabilized by 0.05 wt.% PG surface modifier and 1 wt.% alumina-coated silica nanoparticles increased the oil recovery by 22.6% OOIP after water flooding. This indicates that stabilizing N_2 foam by nanoparticles does not only increase the oil recovery, but it also helps in lowering the amount of surfactant concentration required [7, 145].

Evaluation of foam stability by calculation of spreading, entering, and bridging coefficients helps in understanding the effects of change of experimental conditions such as salinity on foam stability. [7] showed that blends of nanoparticles were not able to stabilize foam since crude oil had an antifoaming effect which can be expressed by positive values of the bridging coefficient (B) for both 0 and 1 wt.% of nanoparticles as shown in Table 8.3. On the other hand, when solution salinity was increased to 1 wt.% of NaCl, the bridging coefficient (B) became negative, or crude oil was no longer acting as an antifoaming agent. It is worth mentioning that the value of entering coefficient (E) stayed positive when salinity was increased. This indicates that the crude oil had affected the foam stability to some extent, whereas the foam was still relatively stable since oil drops were not spreading on the surface of foam films. This can be indicated by the negative values of the spreading coefficient (S). Table 8.4 shows a selected nitrogen foam studies from the literature and the oil displacement recovery for each experiment.

Table 8.3 Spreading (S), entering (E), and bridging (B) coefficients calculated from IFT measurements at 25 °C [7]

	0 wt.% NaCl		1 wt.% NaCl	
Coefficient	0 wt.% NPs	1 wt.% NPs	0 wt.% NPs	1 wt.% NPs
S	−5.5	−5.1	−4.5	−3.9
E	5.7	4.7	1.8	1.3
B	39	8.7	−74.9	−72.4

Permissions related to the material excerpted were obtained from ACS, and further permission should be directed to ACS; AlYousef, Z., Almobarky, M., & Schechter, D. (2017). Enhancing the Stability of Foam by the Use of Nanoparticles. Energy & fuels, 31(10), 10620–10627

Table 8.4 Evaluation of the effect of surfactant-nanoparticle dispersion on oil recovery

Nanoparticle type	Surfactant/ surface modifier	Nanoparticle surface modification	Experimental conditions									Gas	Oil recovery	Reference
			Temperature (C °)	Pressure (psi)	Salinity	Nanoparticle concentration	Surfactant concentration	Core lithology	ϕ	k (md)	Gas quality (%)			
Alumina-coated silica	Non anionic (triton)	From hydrophilic to partially hydrophobic	Room temperature	750	–	0	0.5 wt.%	Sandstone	20%	442	80	Immiscible N_2	13.4% additional after water flooding	[145]
Alumina-coated silica	PG	From hydrophilic to partially hydrophobic	Room temperature	750	–	1 wt.%	0.05 wt.% surface modifier	Sandstone	22%	585	90	Immiscible N_2	22.6% additional after water flooding	[145]
Surface-modified silica	Anionic AOS	Surface-modified	25	1200	1 NaCl wt.%	0	0.5 wt.%	Sandstone	21.84%	1.55	90	N_2	41.45% total recovery after water and foam flooding	[7]
Surface-modified silica	Anionic AOS	Surface-modified	50	1200	1 NaCl wt.%	0.5 wt.%	0.5 wt.%	Sandstone	20.55%	1.69	90	N_2	49.05% total recovery after water and foam flooding	[7]

8.6.2 Carbon Dioxide

CO_2 has many advantages over other gases such as N_2 and CH_4 which makes it the most favorable gas in enhanced oil recovery. Mainly, it can achieve a supercritical state at most reservoir conditions, and it can be miscible in crude oil which helps in improving the microscopic displacement efficiency of residual oil [64]. Injected CO_2 foam can be either in the supercritical state or normal CO_2. Several researchers confirmed the ability of nanoparticles in stabilizing CO_2 foams. Surface-modified nanoparticles have the following advantages in foam stabilization. They can stabilize CO_2 foam under high temperature and high salinity concentrations [77, 80, 92, 161, 180]. Nanoparticles can migrate in the porous media and are less prone to adsorb on the surface of rock formations compared to surfactants [69, 178]. Since the molecules of CO_2 lacks a permanent dipole, the hydrocarbon chain of a surfactant will be more inclined towards the water phase instead of being at the gas/liquid interface due to the weak Van der Waals forces [169]. In contrast, the surface-modified nanoparticles can have an affinity for both CO_2 and water which increases the binding forces between CO_2 and water resulting in more foam stability [155]. Due to the high solubility of CO_2 in water, gas diffusion between bubble films results in bubble coarsening thus decreasing the foam lifetime as a result of the Ostwald ripping effect [171]. Adsorption of nanoparticles on the gas/liquid interface can reduce the gas diffusion by contact area reduction between gas bubbles and liquid films [97]. Literature suggests that CO_2 foam can be stabilized either by brine-nanoparticle solution or by the surfactant-nanoparticle solution. In the following sections, the main results of CO_2 foam studies are discussed.

8.6.2.1 CO_2 Foam Stabilization by Brine-Nanoparticle Solution

These studies mainly focus on the in situ generation of stabilized CO_2 foam in porous media without the need for surfactants. To mitigate problems of surfactant retention during enhanced oil recovery, surface-modified nanoparticles can be used for CO_2 foam formation and stabilization. Nanoparticles such as silica, fly ash, or nano-clay can be commercially fumed by using polyethene glycol or PEG process and cost USD 4/lb [82]. Espinoza et al. [55] investigated the effect of surface-modified silica nanoparticles on increasing supercritical CO_2 foam viscosity by using two types of surface-modified silica nanoparticles: hydrophilic coated nanoparticles with polyethene glycol and salt-tolerant nanoparticles. These nanoparticles were able to form stable foam and increase the flow resistance by 2–18 times compared to the CO_2 brine solution without nanoparticles by using only (0.5 wt.%) of nanoparticle concentration. The study was performed at 95 °C and 1350–1400 psi in a column of 180-micrometer glass beads. This study indicated that the threshold shear rate is independent of the ratio between the injected CO_2/brine ratio. Yu, An, Mo, Liu, and Lee [176] used other surface-modified silica nanoparticles that were able to increase the apparent foam viscosity and mobility by 1.5–2.5 times and 9 times higher than CO_2/brine solution when nanoparticle concentration was between 2500 and 10,000 ppm. Moreover, a sandstone core flooding experiment that was

conducted by the same research team showed that the pressure drop increased from 50 to 870 psi when brine and CO_2 foam stabilized by nanofluid was used at 5000 ppm concentration. However, despite their promising results of controlling CO_2 mobility, this nanofluid cannot form foam when salinity is higher than 2 wt.% NaCl due to nanoparticle agglomeration.

Yu et al. [178] evaluated the effect of supercritical CO_2 foam stabilized by (5000 ppm) silica nanoparticles on oil recovery via core flooding experiments. Two sandstone cores were used (permeability was 31 and 270 mD), salinity was (2 wt.% NaCl), and temperature and pressure were 20 °C and 1200 psig, respectively. Additional oil recovery in the two sandstone cores by CO_2-nanofluid after brine flooding was 48.7% and 35.8% OOIP. At the end of the core flooding experiment, one of the cores (31 mD) was tested against nanoparticle retention in the porous media. Nanoparticles losses were found to be 3.3% of the total injected in the core flooding experiment. It is expected that minor nanoparticles losses in reservoir flooded by nanoparticle-stabilized foams were due to strong attractions between the nanoparticles and the gas/liquid interface [12]. According to A. Worthen et al. [168] methyl-coated silica nanoparticles can form more stable foams than polyethene glycol (PEG)-coated silica nanoparticles. Nguyen et al. [118] demonstrated that 50% of methyl-coated silica nanoparticles were able to stabilize CO_2 foam for 10 days at a concentration of 1 wt.%. On the other hand, bare silica nanoparticles and 75% methyl-coated silica nanoparticles were not able to generate foam when mixed with CO_2, while sodium dodecyl sulfate (SDS) formed less stable foam. Moreover, due to the coalescence of SDS surfactant foam, foam density decreased from 31 to 9 bubbles/mm^2, while bubble diameter increased from 83 to 198 μm during the experiment period (20 h). During the same experiment period, methyl-coated silica nanoparticles were able to maintain a foam density of 29 bubbles/mm^2 with a diameter of 72 micrometers, and changes were negligible for the next 10 days as shown in Fig. 8.33.

To evaluate the stability of CO_2 foam stabilized by methyl-coated silica nanoparticles in presence of crude oil, Nguyen et al. [118] performed gas flooding experiments by using CO_2 and CO_2 foam stabilized by nanoparticles in a micromodel saturated with medium to heavy oil (API gravity of 24) at 22 °C and 600 psi. Water flooding resulted in a recovery of 41% OOIP. When water flooding was followed by CO_2 injection, additional recovery was 5% OOIP. On the other hand, CO_2 foam stabilized by nanoparticles resulted in 15% OOIP additional oil recovery. Figure 8.34 compares the oil recovery and the macroscopic displacement efficiency for brine, CO_2, and CO_2 foam floods in a micro model.

Nguyen et al. [118] reported a reduction in the oil-in-water emulsion sizes in the case of nanoparticle-stabilized CO_2 foam. This effect is attributed to the active nanoparticles at the oil-water interface. This mechanism contributes to enhancing the oil recovery by CO_2 foam. Similarly, in EOR methods, smaller oil-in-water emulsion sizes improve the recovery rates [39]. By using fluorescence imaging at the microscale, Nguyen et al. [118] were able to quantify the sizes of oil-in-water and water-in-oil emulsion sizes as shown in Fig. 8.35. Oil-in-water emulsion sizes in the CO_2 flooding were reported to have an average size of 7.8 μm, while it was

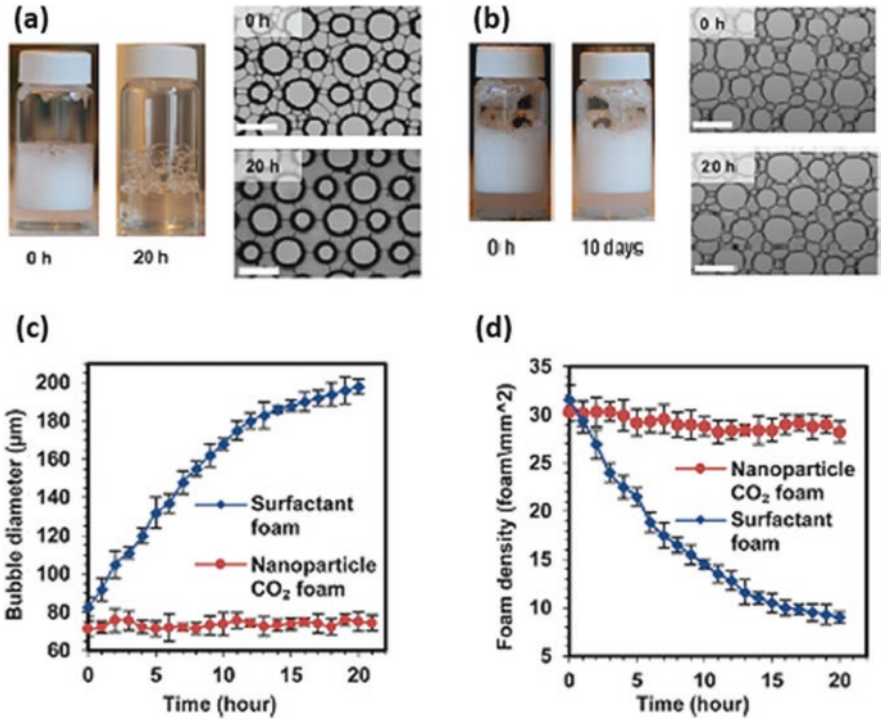

Fig. 8.33 (**a**) Foam sample stabilized only by SDS surfactant, (**b**) foam stabilized by nanoparticles, (**c**) change in bubble diameter of nanoparticle-stabilized foams with time, (**d**) change in foam density of surfactant- and nanoparticle-stabilized foams with time [118]. Permissions related to the material excerpted were obtained from ACS, and further permission should be directed to ACS; Nguyen, P., Fadaei, H., & Sinton, D. (2014). Pore-Scale Assessment of Nanoparticle-Stabilized CO2 Foam for Enhanced Oil Recovery. Energy & Fuels, 28(10), 6221–6227. doi: https://doi.org/10.1021/ef5011995

1.7 μm in the case of CO_2 nanoparticle foam. Thus, surface-active nanoparticles were able to reduce the oil-in-water emulsion sizes by 80%.

Alzobaidi et al. [8] demonstrated the effect of surface-modified silica nanoparticles on the increasing CO_2 foam apparent viscosity at harsh reservoir conditions. Silica nanoparticles utilized in their study were low coverage (LC), medium coverage (MC), and high coverage (HC) organic ligand nanoparticles. Nanoparticle dispersions of concentration of 1 wt.% were stabilized when salinity was 15 wt.% TDS at 3000 psi. Glass bead pack and sandstone core flooding experiments demonstrated the significant role of coated silica nanoparticles in maintaining high CO_2 foam viscosity up to 35 cP and bubble sizes in the order of 40 μm. Figure 8.36 compares the apparent foam viscosity against foam quality for the three types of nanoparticles at pressure, temperature, and salinity of 3000 psig, 25 °C, and 15 wt.% TDS, respectively. The apparent foam viscosity increased as the coverage of the silica nanoparticles increases from low coverage to high coverage. Moreover, apparent viscosity

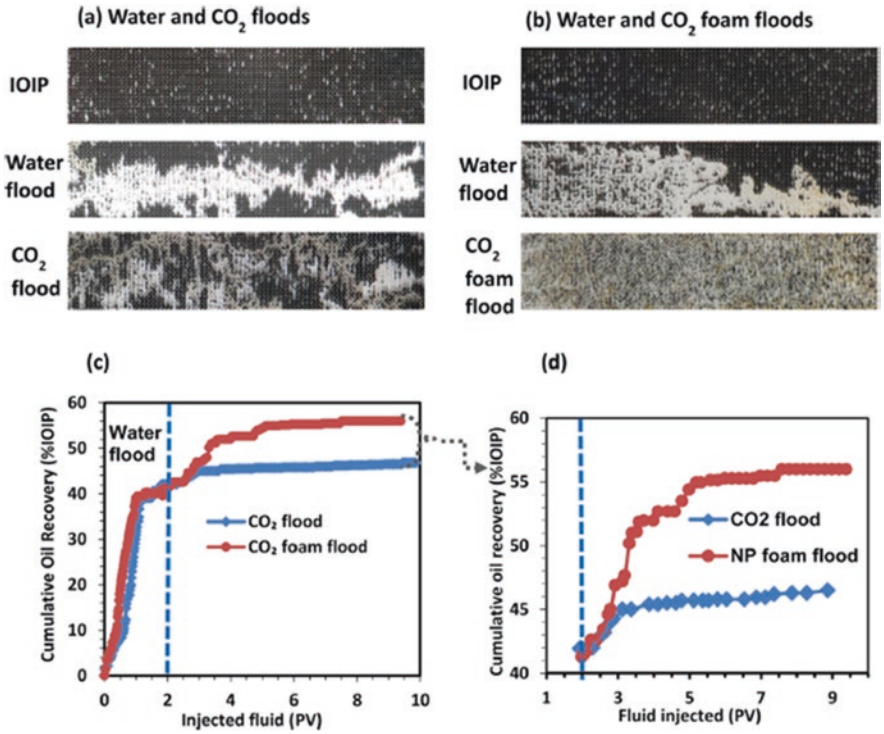

Fig. 8.34 Comparison between (**a**) water and CO_2 floods, (**b**) water and CO_2 foam stabilized by 50% methyl-coated silica nanoparticles [118]. Permissions related to the material excerpted were obtained from ACS, and further permission should be directed to ACS; Nguyen, P., Fadaei, H., & Sinton, D. (2014). Pore-Scale Assessment of Nanoparticle-Stabilized CO_2 Foam for Enhanced Oil Recovery. Energy & Fuels, 28(10), 6221–6227. doi: https://doi.org/10.1021/ef5011995

increased with an increase in foam quality; then it started decreasing after the transition foam quality (85%). Figure 8.37 compares the bubble sizes and apparent foam viscosity against foam quality for the MC and HC nanoparticles at pressure, temperature, and salinity of 3000 psig, 80 °C and 15 wt.% TDS, respectively. Finally, in core flooding experiments by using Boise and Berea sandstone cores, apparent foam viscosity was 26 cP at pressure, temperature, salinity, and foam quality of 3000 psig, 70 °C, 15 wt.% TDS, and 75%, respectively.

Rognmo et al. [132] performed another study on the effect of surface-modified silica nanoparticles on supercritical CO_2 at high salinity and pressure. Silica nanoparticles were surface modified to enhance hydrophobicity and salt tolerance. Nanoparticle dispersion at a concentration of 1500–5000 ppm was stable at a temperature of 40 °C for 75 days at salinity up to 20 wt.% NaCl and 5 wt.% $CaCO_3$. Moreover, nanoparticle dispersion dynamic stability was also tested at a concentration of 3000 ppm at temperatures 20, 60, and 120 °C and salinity between 15 and 25 wt.%. Constant pressure drop when the injection rate was fixed revealed that nanoparticle dispersion was stable. Rognmo et al. [133] evaluated the effect of

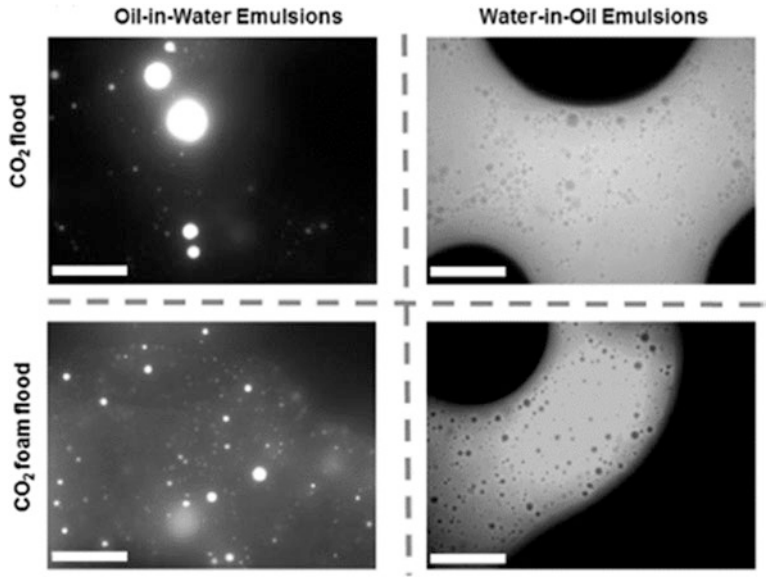

Fig. 8.35 Comparison between the oil-water and water-in-oil emulsion sizes in the cases of CO_2 and CO_2 foam floods [118]. Permissions related to the material excerpted were obtained from ACS, and further permission should be directed to ACS; Nguyen, P., Fadaei, H., & Sinton, D. (2014). Pore-Scale Assessment of Nanoparticle-Stabilized CO2 Foam for Enhanced Oil Recovery. Energy & Fuels, 28(10), 6221–6227. doi: https://doi.org/10.1021/ef5011995

co-injection of brine-silica nanoparticle dispersion and supercritical CO_2 at a foam quality of 70% and salinity of 1 wt.% NaCl on oil recovery and pressure drop. Surfactant used was a linear alcohol ethoxylate (C12–C16) at a concentration of 10,000 ppm. Core flooding experiments of 12 Bentheimer sandstone core plugs at 90 bar and 60 °C indicated that supercritical CO_2-nanoparticle dispersions enhanced the oil recovery compared to the injection of supercritical CO_2 and brine. The average increase in the oil recovery and the pressure drop gradient (calculated from the end of water flooding) of co-injection of supercritical CO_2 and brine (70% foam quality) was 8.2% OOIP and 39%, respectively. On the other hand, co-injection of 1500 ppm nanoparticles, 10,000 ppm surfactant dispersion, and supercritical CO_2 (70% foam quality) increased the oil recovery by 10.1–14.4% OOIP, while the increase in the pressure drop gradient was between 68 and 118%. Finally, injection of 5000 ppm nanoparticle dispersion and supercritical CO_2 at 70% foam quality increased the oil recovery by 15.4% OOIP, and the increase in the pressure drop gradient was 191%. On the other hand, co-injection of 1 wt.% of linear alcohol ethoxylate and supercritical CO_2 at foam quality of 70% increased oil recovery by 15.9% OOIP, while the pressure drop decreased by 13%. This indicates that the generated foam was not stable without the addition of silica nanoparticles. Figure 8.38 demonstrates the additional oil recovery and increase in pressure drop when nanoparticles were used compared to CO_2 flood and brine flood without

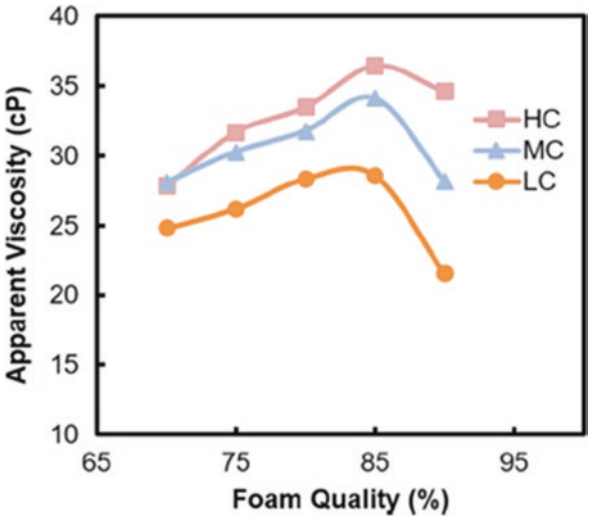

Fig. 8.36 Comparison between apparent viscosity behavior of the three types of nanoparticles with the increase in foam quality at pressure = 3000 psig, temperature = 25 °C, and salinity = 15 wt.% TDS [8]. Permissions related to the material excerpted were obtained from ACS, and further permission should be directed to ACS; Alzobaidi, S., Lotfollahi, M., Kim, I., Johnston, K. P., & DiCarlo, D. A. (2017). Carbon Dioxide-in-Brine Foams at High Temperatures and Extreme Salinities Stabilized with Silica Nanoparticles. Energy & Fuels, 31(10), 10680–10690

co-injection of surfactant (baseline). Figure 8.39 summarizes the average increase in oil recovery and pressure drop of each case as explained above.

Bayat et al. [16] assessed the effect of hydrophilic metal oxides (Al_2O_3, TiO_2, CuO) on enhancing the stability of CO_2 foam and increasing oil recovery. Best foam stability was obtained at nanoparticle concentration of 0.008 wt.% for all nanoparticle types. Evaluation of foam morphology and bubble size indicated that the bubble sizes of CO_2 foam stabilized by Al_2O_3, TiO_2, and CuO nanoparticles were 400, 500, and 600 μm, respectively. Hence, Al_2O_3 nanoparticles are better in CO_2 foam stabilization than TiO_2 and CuO nanoparticles since bubble coalescence rate was slower. Figure 8.40 compares the morphology and bubble sizes of CO_2 foam stabilized by SiO_2, Al_2O_3, TiO_2, and CuO nanoparticles. Increment in oil recovery by using CO_2 foam stabilized by Al_2O_3, TiO_2, and CuO nanoparticles was 12.3, 6.5, and 5.1% OOIP, respectively, while oil recovery increased by 17.4% OOIP in the case of CO_2 foam stabilized by SiO_2.

Graphene oxides (GO) are surface-active particles capable of the creation of very stable emulsions with organic solvents [87]. Amphiphilicity of GO is dependent on the particle sizes [105]. Smaller GO particles tend to have higher hydrophilicity due to the high density of –COOH on its edges and epoxy groups on the particle surface [105]. Thus, amphiphilicity of GO oxides can be altered by changing particle size or by partially reducing the particle oxygen content [101].

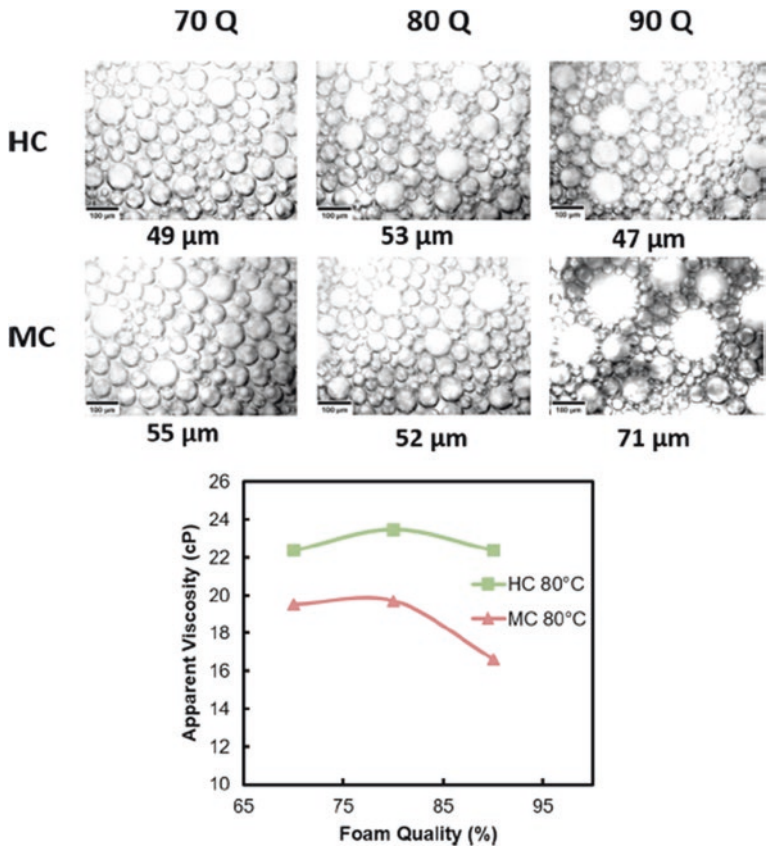

Fig. 8.37 Comparison between CO_2 foam bubble sizes and apparent viscosity of HC and MC nanoparticles at pressure = 3000 psig, temperature = 80 °C, and salinity = 15 TDS% [8]. Permissions related to the material excerpted were obtained from ACS, and further permission should be directed to ACS; Alzobaidi, S., Lotfollahi, M., Kim, I., Johnston, K. P., & DiCarlo, D. A. (2017). Carbon Dioxide-in-Brine Foams at High Temperatures and Extreme Salinities Stabilized with Silica Nanoparticles. Energy & Fuels, 31(10), 10680–10690

Partially reduced GO were efficient in stabilizing CO_2 in water which can improve foam stability due to large surface area of these particles [101]. Barrabino et al. [14] reduced the size of graphene oxides from 4–30 µm to 260–295 nm and tested their ability to produce stable CO_2 foams with synthetic seawater. Their study revealed that GO was able to generate foam, but the partially reduced graphene oxides and graphene in the nano range had a determinant effect on CO_2 foamability. Barrabino et al. [14] reported that nanographene can be partially reduced to achieve less hydrophilicity while considering the reduction angle. Table 8.5 summarizes selected studies of CO_2 foam stabilization by nanoparticles for enhancing oil recovery and maintaining high apparent foam viscosity.

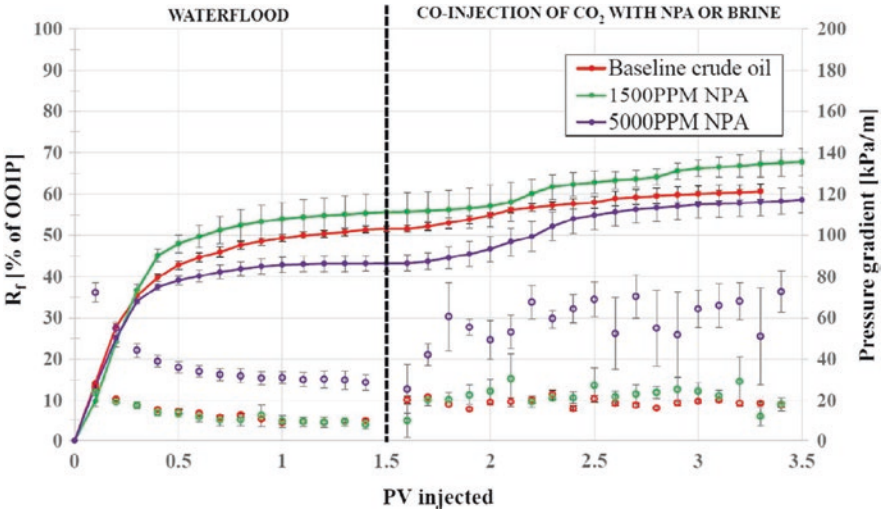

Fig. 8.38 Oil recovery (solid points and lines) and pressure drop comparison between CO_2 injection, 1500–5000 ppm by mass nanoparticle dispersion, and supercritical CO_2 at temperature, pressure, and salinity of 60 °C, 90 bar, and 1 wt.% NaCl [133]. Permissions related to the material excerpted were obtained from Elsevier, and further permission should be directed to Elsevier; Rognmo, A. U., Heldal, S., & Fernø, M. A. (2018). Silica nanoparticles to stabilize CO_2-foam for improved CO_2 utilization: Enhanced CO_2 storage and oil recovery from mature oil reservoirs. Fuel, 216, 621–626. doi: https://doi.org/10.1016/j.fuel.2017.11.144

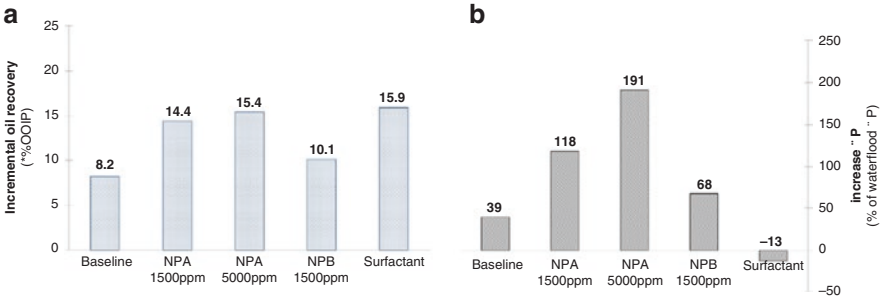

Fig. 8.39 (**a**) Additional oil recovery and (**b**) increase in pressure drop of supercritical CO_2 foam stabilized by nanoparticles (types NPA and NPB of different hydrophobicity) at temperature, pressure, salinity, surfactant concentration, and foam quality of 60 °C, 90 bar, 1 wt.% NaCl, 10,000 ppm, and 70%, respectively [133]. Permissions related to the material excerpted were obtained from Elsevier, and further permission should be directed to Elsevier; Rognmo, A. U., Heldal, S., & Fernø, M. A. (2018). Silica nanoparticles to stabilize CO_2-foam for improved CO_2 utilization: Enhanced CO_2 storage and oil recovery from mature oil reservoirs. Fuel, 216, 621–626. doi: https://doi.org/10.1016/j.fuel.2017.11.144

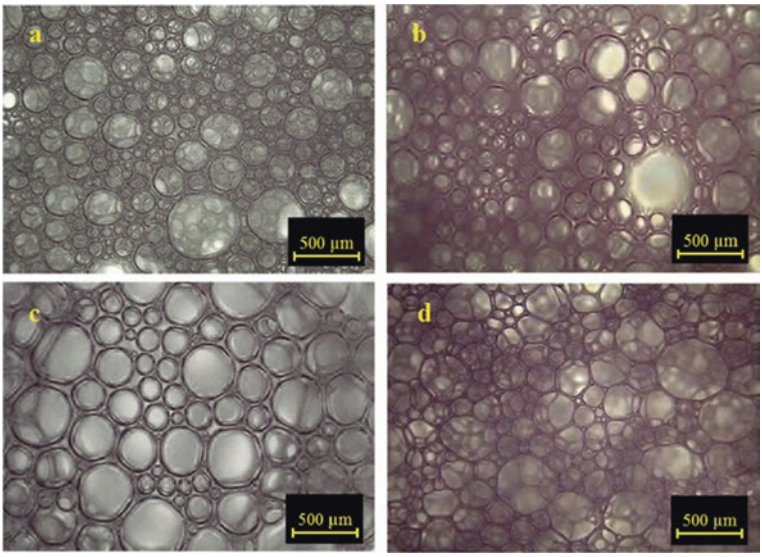

Fig. 8.40 Comparison between bubble sizes of CO_2 foam stabilized by (**a**) SiO_2, (**b**) Al_2O_3, (**c**) TiO_2, and (**d**) CuO nanoparticles [16]. Permissions related to the material excerpted were obtained from Elsevier, and further permission should be directed to Elsevier; Bayat, A. E., Rajaei, K., & Junin, R. (2016). Assessing the effects of nanoparticle type and concentration on the stability of CO_2 foams and the performance in enhanced oil recovery. Colloids and Surfaces A: Physicochemical and Engineering Aspects, 511, 222–231. doi: https://doi.org/10.1016/j.colsurfa.2016.09.083

8.6.2.2 Effect of Nanoparticle Surface Modification on CO_2 Foam Stability

The synergistic effect between nanoparticles and surfactants has received high attention as a significant mechanism for foam stability in EOR applications. Nevertheless, nanoparticles with certain hydrophobicity can be irreversibly adsorbed to the gas/liquid interface at lower energy compared to surfactant. Moreover, nanoparticles increase the density of surfactant molecules capable of stabilizing the foam interface. This effect can improve the interfacial tension between gas and liquid and increase the mechanical elasticity of foam lamellas, hence hindering the foam coalescence, rupturing, and liquid drainage compared to using surfactants only as a foam stabilizing agent. Main studies of CO_2 foam stabilization by modified nanoparticles and surfactants have been reported.

S. Li et al. [98] investigated the synergistic effect between hydrophilic silica nanoparticles (contact angle 38.63° with water) and CTAB on the stabilization of CO_2 foam. In their study, the concentration of silica nanoparticles was fixed at 1.5 wt.%, while CTAB concentration was changed from 0 to 0.3 wt.%. Initially, when surfactant concentration was low, the zeta potential of the silica nanoparticles and CTAB showed negative measurements indicating low adsorption between CTAB positive ions on the surface of the nanoparticles. Hence, the nanoparticles

Table 8.5 Selected studies of CO_2 foam stabilization by nanoparticles for enhancing oil recovery and maintaining high apparent foam viscosity

Nanoparticle type	Nanoparticle size (nm)	Nanoparticle surface modification	Experimental conditions											Effect on apparent viscosity/pressure drop/oil recovery	Reference
			Temperature (°C)	Pressure (psi)	Salinity	NPs concentration	Shear rate (s^{-1})	Porous media	Phi (%)	k (mD)	Oil	Gas	Gas quality (%)		
Silica	5	Hydrophilic coated with PEG	95	1352–1400	0	0.05 wt.%	1300	Glass bead pack column				Super critical CO_2	5.0–29.0	Flow resistance was 2–18 times gas viscosity	[55]
		Salt-tolerant coated with PEG			4 wt.% NaCl	0.5 wt.%									
Silica	20–100	Coated with PEG	25	1500 psig	Brine	2500–10,000 ppm	1419	Glass beadpack column				Super critical CO_2	2.0–11.0	(1) Apparent viscosity was between 1.5 and 2.5 times higher; (2) mobility was 9 times higher; (3) viscosity of foam was decreased when CO2/brine ratio was varied from 2 to 11	[176]
Silica	10.–40.	Coated silica	25	1500 psig	2 wt.% NaCl	5000 ppm		Berea sandstone	17.36	33.01		Super critical CO_2	20	(1) Pressure drop was 50 psi after brine flooding; (2) pressure drop increased up to 870 psi after CO2/brine-nano-dispersion flooding	[114]
Silica	17–20	Coated silica	20	1200 psig	2 wt.% NaCl	5000 ppm		Berea sandstone	17.4	31		Super critical CO_2	50%	(1) Pressure drop decreased from 834 to 786 psig during brine flooding; (2) as 5 PV of CO2/nanoparticles injected, pressure drop increased to 1750 psig; (3) additional oil recovery CO2/nanoparticles was 48.7%	[178]
									20.5	270				Additional oil recovery CO2/nanoparticles was 35.8%	

Silica	12	50% methyl-coated silica nanoparticles	22	600	1 wt.%	1 wt.%		Glass micromodel			Light oil (API 37)	CO_2		Additional oil recovery was 11%	[118]
											Medium to heavy oil (API 24)			Additional oil recovery was 15%	
											Heavy oil (API 14)			Additional oil recovery was 8%	
Silica	40	Hydrophilic	27		2.5 wt.% brine saturate, water flooding 0.3 wt% NaCl	0.008 wt.%		Sand packs	~43.4	~2300	Malaysian crude oil (density of 0.863 g/cm^3 and viscosity of 21.7 ± 0.02 cp at 26 °C)	CO_2		Additional oil recovery was 17.4%	[16]
AlO_3														Additional oil recovery was 12.3%	
TiO_2														Additional oil recovery was 6.5%	
CuO														Additional oil recovery was 5.1%	
Silica	Less than 50	Low coverage (LC), medium coverage (MC), high coverage (HC) ligands grafted to the nanoparticles	25–80	3000 psig	15 wt.% TDS	1 wt.%	2270	Glass bead pack	34	22,000		CO_2	70–90	(1) Apparent viscosity increased with increase in ligand grafting; (2) maximum apparent viscosity was 36 CP; (3) average bubble size was 40 micrometer	[8]
		MC, HC	25–70	2800 psig										Maximum apparent viscosity was 26 cP	
Silica		Hydrophilic	60–80	90 bar	2–20 wt%	1500–5000 ppm		Bentheimer sandstone	20–25	1100–2600	Crude oil (density of 0.849 g/cm^3 at 20 °C)	Super critical CO_2		Oil recovery increased to 14.1%, and the effects of high temperature and salinity were minimal	[132, 133]

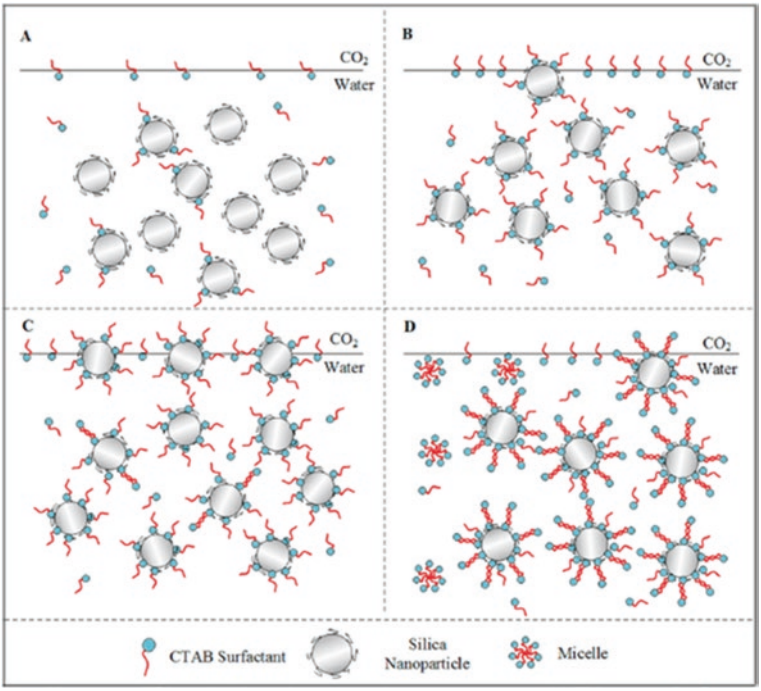

Fig. 8.41 Adsorption of the silica nanoparticles to the interface with an increase in surfactant concentration [98]. Permissions related to the material excerpted were obtained from ACS, and further permission should be directed to ACS; Li, S., Qiao, C., Li, Z., & Wanambwa, S. (2017). Properties of Carbon Dioxide Foam Stabilized by Hydrophilic Nanoparticles and Hexadecyltrimethylammonium Bromide. Energy & Fuels, 31(2), 1478–1488. doi: https://doi.org/10.1021/acs.energyfuels.6b03130

were still hydrophilic. As surfactant concentration was increased, more surfactant molecules were able to adsorb on the surface of the nanoparticles resulting in the formation of a monolayer of adsorption stage ($CTAB/SiO_2$ ratio between 0.02 and 0.033). This behavior was indicated by the positive zeta potential measurements. Due to the adsorption of surfactant molecules on the silica nanoparticles, the silica nanoparticles became hydrophobic hence escaping from the bulk phase and starts adsorbing on the gas/liquid interface. On the other hand, the double adsorption stage of surfactant molecules on the surface of the nanoparticles occurred due to further increase in surfactant concentration ($CTAB/SiO_2$ ratio between 0.033 and0.07) resulting in movement of nanoparticles from the gas/liquid interface back to the bulk phase as demonstrated in Fig. 8.41.

CO_2 foam half-life time and viscoelasticity were significantly increased due to the alternation of nanoparticle hydrophobicity by CTAB compared to using CTAB only. The rate of foam coalescence was delayed, and liquid hold up was significantly enhanced at $CTAB/SiO_2$ ratio of 0.033 (0.05 wt.% CTAB, 1.5 wt.% SiO_2) due to adsorption of nanoparticles at the gas/liquid interface. On the other hand, CO_2

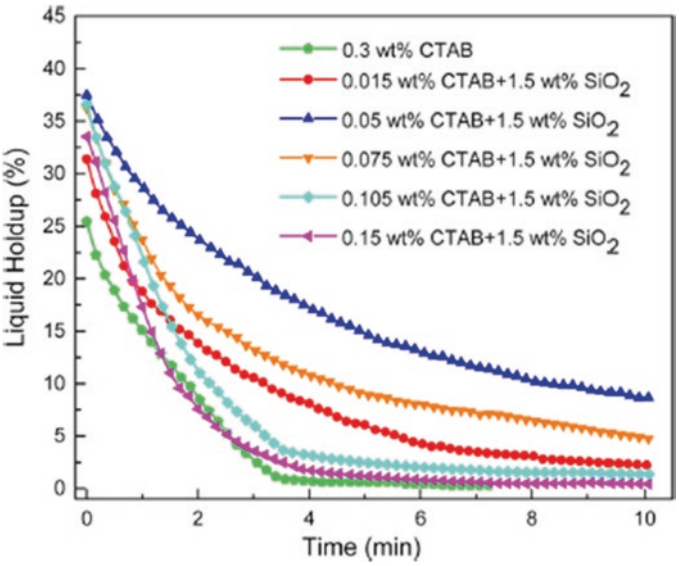

Fig. 8.42 CO_2 foam liquid holdup at different CTAB concentrations [98]. Permissions related to the material excerpted were obtained from ACS, and further permission should be directed to ACS; Li, S., Qiao, C., Li, Z., & Wanambwa, S. (2017). Properties of Carbon Dioxide Foam Stabilized by Hydrophilic Nanoparticles and Hexadecyltrimethylammonium Bromide. Energy & Fuels, 31(2), 1478–1488. doi: https://doi.org/10.1021/acs.energyfuels.6b03130

foam stabilized by CTAB at 0.3 wt.% without nanoparticles showed lower foam liquid holdup and half-life time and thus lower foam stability. Figure 8.42 shows the liquid holdup of CO_2 foam at different CTAB/SiO_2 concentrations. Finally, micromodel displacement experiments showed that CO_2 foam was able to increase the total oil recovery from 45% OOIP (at the end of water flooding) to 74.3% OOIP.

P. Wang et al. [163] compared the effect of several types of surfactants and hydrophilic silica nanoparticles on CO_2 foam stability. Surfactants used in this study include CTAB (cationic), SDBS (anionic), TX-100 (nonionic), and OA-12 (zwitterionic). The stability of CO_2 foam was decreased for all surfactant/nano-dispersion as salinity and temperature were increased from 0 to 30,000 mg/L and 30 to 70 °C, respectively. The best foam stability effect was achieved by a zwitterionic surfactant (OA-12) at nanoparticle and surfactant concentrations of 0.5 wt.% and 0.02 wt.%, respectively. The synergy between hydrophilic silica nanoparticles and OA-12 enhanced the CO_2 foam stability by lowering the surface tension and increasing the viscoelasticity modulus. Moreover, the intensity of CO_2 foam lamellas was reinforced by the formation of the three-dimensional network structure. Figure 8.43 illustrates the effect of hydrophilic silica nanoparticles in CO_2 foam stabilization. S. Li et al. [99] investigated the effect of silica nanoparticles hydrophilicity on CO_2 foam stability in the presence of nonionic surfactant ($C_{12}E_{23}$).

The best synergistic effect between four types of hydrophilic silica nanoparticles and $C_{12}E_{23}$ was reported when contact angle with water was minimum (20.12°). Due

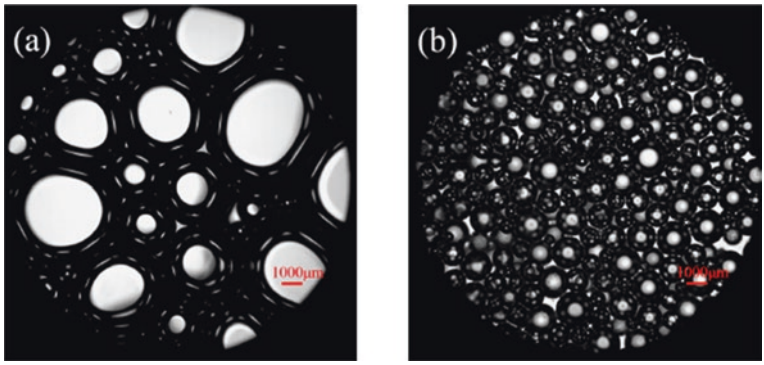

Fig. 8.43 Comparison between CO_2 foam morphology: (**a**) foam stabilized by surfactant (0.02 wt.% OA-12), (**b**) foam stabilized by surfactant-NPs (0.02 wt.% OA-12, 0.5 wt.% SiO_2) [163]. Permissions related to the material excerpted were obtained from ACS, and further permission should be directed to ACS; Wang, P., You, Q., Han, L., Deng, W., Liu, Y., Fang, J., … Dai, C. (2018). Experimental Study on the Stabilization Mechanisms of CO_2 Foams by Hydrophilic Silica Nanoparticles. Energy & Fuels, 32(3), 3709–3715. doi: https://doi.org/10.1021/acs.energyfuels.7b04125

to surfactant adsorption on the surface of the nanoparticles, the contact angle became 78° achieving the best foam stability at a surfactant concentration of 2.49 mM and nanoparticle concentration of 1.5 wt.%. As a result of the synergistic effect between hydrophilic silica and $C_{12}E_{23}$, CO_2 foam half-life was 30 times greater than surfactant foam, and interfacial viscoelastic modulus increased from 5.1 to 25.2 mN/m. Figure 8.44 shows the delay in CO_2 bubble coalescence of $C_{12}E_{23}$/SiO_2 dispersion compared to $C_{12}E_{23}$ foam in the microscopic model.

The role of hydrophobic nanoparticles in foam stability have also been reported. S. Li et al. [97] studied the synergistic effect between anionic surfactant (SDS) and hydrophobic silica nanoparticles (122.22° contact angle with water) at SDS/SiO_2 concentration ratio of 0.1–0.4 for CO_2 foam stabilization. Zeta potential measurements of SDS/SiO_2 dispersion revealed that the silica particle had a positive charge. Hence, most of the nanoparticles would be in the gas phase when SDS concentration is low. As the SDS/SiO_2 ratio increased, zeta potential started decreasing and reached zero when the SDS/SiO_2 ratio was 0.17. This indicates a reduction in nanoparticle hydrophobicity resulting in modulating the position of silica nanoparticles from the gas phase to the gas/liquid interface. Further increase in the SDS/SiO_2 ratio results in negative zeta potential measurements. When SDS/SiO_2 ratio reaches 0.4, nanoparticles become mostly hydrophilic. Hence, the stabilization effect of SDS/SiO_2 will be minimal since most of the nanoparticles will be already dispersed in the liquid phase. Figure 8.45 illustrates the position of the silica nanoparticles concerning the gas/liquid interface when SDS/SiO_2 concentration ratio was increased from 0.05 to 0.67.

S. Li et al. [97] reported that the synergistic effect between SDS/SiO_2 enhanced the CO_2 foam stability by the alternation of the interfacial properties. Viscoelastic

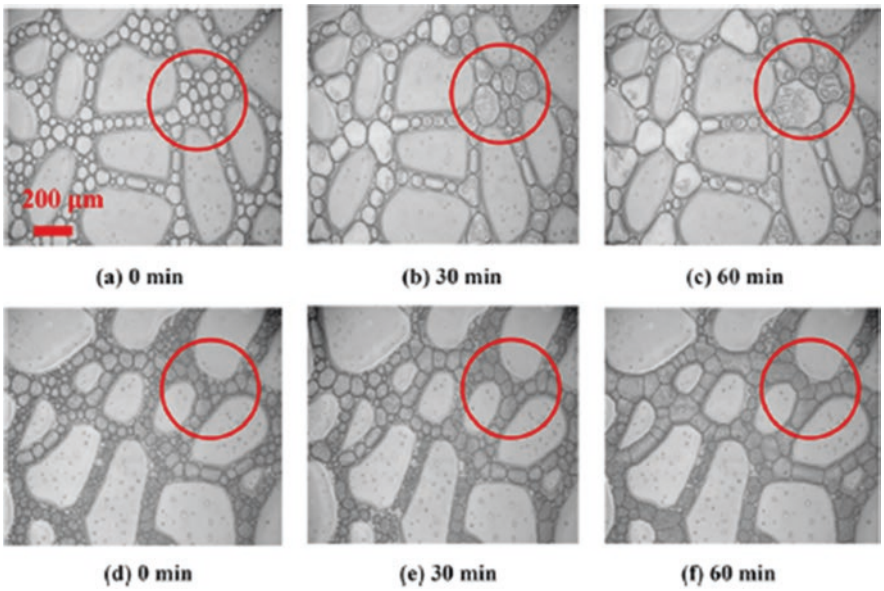

Fig. 8.44 (**a**–**c**) Stability of 2.49 mM $C_{12}E_{23}$ foam with time, (**d**–**f**) stability of 2.49 mM $C_{12}E_{23}$ and 1.5 wt.% silica foam with time [99]. Permissions related to the material excerpted were obtained from ACS, and further permission should be directed to ACS; Li, S., Yang, K., Li, Z., Zhang, K., & Jia, N. (2019). Properties of CO2 Foam Stabilized by Hydrophilic Nanoparticles and Nonionic Surfactants. Energy & Fuels, 33(6), 5043–5054. doi: https://doi.org/10.1021/acs.energyfuels.9b00773

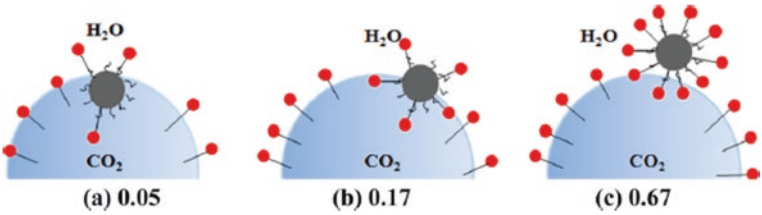

Fig. 8.45 Modulating the silica nanoparticle position from: (**a**) gas phase, (**b**) gas/liquid interface, (**c**) liquid phase. This figure indicates a middle section of a foam column [97]. Permissions related to the material excerpted were obtained from ACS, and further permission should be directed to ACS; Li, S., Yang, K., Li, Z., Zhang, K., & Jia, N. (2019). Properties of CO2 Foam Stabilized by Hydrophilic Nanoparticles and Nonionic Surfactants. Energy & Fuels, 33(6), 5043–5054. doi: https://doi.org/10.1021/acs.energyfuels.9b00773

modulus increased gradually as SDS/SiO_2 was increased to 0.17; then it decreased due to a further increase in SDS/SiO_2 ratio. At elevated temperatures, CO_2 foam stability was enhanced by addition of SiO_2 compared to using SDS alone. Increasing temperature lowers the viscoelastic modulus and increases the interfacial tension of SDS/SiO_2 dispersion. On the other hand, increasing pressure is beneficial for foam

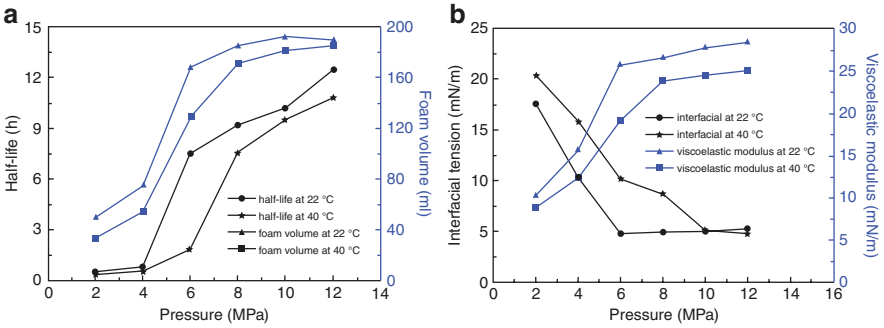

Fig. 8.46 (**a**) Foam half-life and volume of SDS/SiO_2 CO_2 foam at different temperatures and pressures, (**b**) interfacial properties of SDS/SiO_2 CO_2 foam at different temperatures and pressures [97]. Permissions related to the material excerpted were obtained from ACS, and further permission should be directed to ACS; Li, S., Li, Z., & Wang, P. (2016). Experimental Study of the Stabilization of CO2 Foam by Sodium Dodecyl Sulfate and Hydrophobic Nanoparticles. Industrial & Engineering Chemistry Research, 55(5), 1243–1253. doi: https://doi.org/10.1021/acs.iecr.5b04443

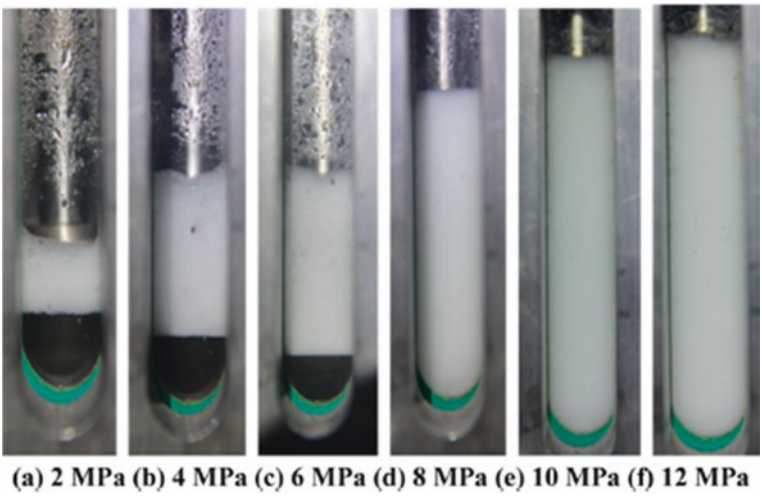

Fig. 8.47 Increase in SDS/SiO_2 CO_2 foam volume with an increase in pressure at 40 °C [97]. Permissions related to the material excerpted were obtained from ACS, and further permission should be directed to ACS; Li, S., Li, Z., & Wang, P. (2016). Experimental Study of the Stabilization of CO2 Foam by Sodium Dodecyl Sulfate and Hydrophobic Nanoparticles. Industrial & Engineering Chemistry Research, 55(5), 1243–1253. doi: https://doi.org/10.1021/acs.iecr.5b04443

stability by increasing foam half-life (foam half-life is 10 times higher) and interfacial properties as shown in Fig. 8.46. This effect was reported due to achieving the supercritical state of CO_2. Hence, CO_2 becomes liquid above 31.2 °C and 7.28 MPa. Figure 8.47 shows the increase in CO_2 foam volume due to pressure increase.

S. Li et al. [97] tested the efficiency of CO_2 foam in oil recovery stabilized by several SDS/SiO_2 concentration ratios at 50 °C and 8 MPa backpressure. Pressure difference and oil recovery results were optimum when SDS/SiO_2 concentration was 0.17. These results indicate that the best surfactant-nanoparticle concentration ratio to achieve CO_2 foam stability in the static foamability test is also the same as in the oil displacement tests. The maximum pressure difference and additional oil recovery results by water flooding followed by CO_2 foam stabilized by SDS/SiO_2 were 1.4 MPa and 75%, respectively.

Q. Liu et al. [102] studied the effect of surface modification of Fe_3O_4 nanoparticles on enhancing CO_2 foam stability. In the nanoparticle surface modification, 1,2-epoxy dodecane was grafted to the surface of the nanoparticles to alter its hydrophobicity. The alternation process of the hydrophobicity of the nanoparticles included the dispersion of Fe_3O_4 nanoparticles into a 4-methyl-2-pentanone solution while using NaOH aqueous solution as a catalyst. Then, the 1,2-epoxy dodecane was added to the aqueous dispersions. The surface modification reaction of the nanoparticles was conducted at 110 °C, while mechanical stirring speed was 300 rpm for 4 h under N_2 protection. More details of the Fe_3O_4 nanoparticles surface modification procedure are explained by Q. Liu et al. [102].

The identification of the surface functional groups by FTIR and TGA of the modified Fe_3O_4 nanoparticles indicated an effective grafting of the 1,2-epoxy dodecane (the hydrophobic functional group) to the surface of the nanoparticles. The contact angle between deionized water and the unmodified Fe_3O_4 nanoparticles was 12.7°, while the prepared Fe_3O_4 nanoparticles had the following contact angles: 20.6°, 57.5°, and 94.3°.

Evaluation of CO_2 foam stability of 0.1 wt.% Fe_3O_4, 0.2 wt.% SDS, and 0.1 wt.% HPAM dispersions by static foam stability tests, surface shear viscosity measurements, and core flooding experiments demonstrated the capability of surface-modified Fe_3O_4 to enhance foam stability. The best foam stability performance was achieved by the 94.3° wetting angle nanoparticles. They were able to increase the shear viscosity from 2650 to 5200 mPa.s, while enhancement in oil recovery was only 0.86% in a low permeability core oil displacement experiment by nano-dispersion foam.

8.7 Challenges of Field Implementation of Nanoparticle-Stabilized Foams

Although nanoparticle-stabilized foam is one of the most promising technologies for enhanced oil recovery and mitigation of the drawbacks of gas EOR, no pilot/field implementation of nanoparticle-stabilized foams have been reported in the literature [175]. However, the current status of nanoparticle-stabilized foams is still an important research focus. Yekeen et al. [175] summarized the main obstacles of field implementation of nanoparticle-stabilized foams including the uncertainty of the

economic aspects of nanoparticle-stabilized foams within the current low oil prices, nanoparticle agglomeration, and the environmental consequences of nanoparticles. Nanoparticles investigated in the literature for foam stabilization are developed from low-cost and commercially available raw materials including silica, fly ashes, and metal oxides; then surface modification is applied to the surface of the nanoparticles such as polyethene glycol (PEG) [82]. However, there is still no cost analysis demonstrating the economic advantages of nanoparticle utilization as a foam stabilizing agent in contrast with other foaming stabilization agents including surfactants or polymers [175]. Stability of a nanoparticle dispersion is crucially impacted by media conditions including salinity, temperature, pH, and nanoparticle concentration. In lab-scale foam studies, homogenous nanoparticle-surfactant dispersion can be prepared by ultrasonic vibration and surface modification of nanoparticles to avoid nanoparticle agglomeration [157]. However, the stability of nanoparticle dispersion in field-scale foam EOR is still unknown due to the lack of foam implementation in field or pilot applications [175]. In high salinity and high temperature environments, the screening effect of an electrostatic double layer (EDL) by reservoir electrolytes and the increased effect of particle collisions at high-temperature increments increase the risk of particle agglomeration [72, 73, 175] Hence, the aggregation of nanoparticles increases the hydrodynamic diameter of particles which could be in microns resulting in serious reservoir damage due to pore throats blockage. Finally, log-jamming and mechanical entrapment are the main identified mechanisms of nanoparticle pore channel blockage [49, 151, 157].

8.8 Conclusion, Recommendations, and Future Remarks

In this chapter, an extensive review of nanoparticle application for foam stability has been performed. Based on the existing literature, and from the phenomenological point of view, it can be argued that nanoparticle-stabilized foam offers a better alternative compared to surfactant-stabilized foam during gas EOR. Furthermore, nanoparticles of a given type and moderately hydrophobic surface at given optimum concentrations offer better stabilization options at the interfaces between immiscible fluids. Nevertheless, understanding the fundamental foam mechanisms, involved at the pore scale in the porous media coupled with nanoparticle agglomeration, is some of the current challenges of foam stabilized nanoparticles. Experimental studies and reported findings on the essential parameters of nanoparticle-stabilized foam performance are limited, and those that are reported are contradicting. It is important to note that the presence of nanoparticles at the air-water interface of the foam results in the draining of the oil from the foam films and their migration and accumulation at the edges enhance the foam stability and delay coalescence of the bubbles. Furthermore, the synergistic effect between nanoparticles and surfactants enhances the foam stabilization process. However, optimum nanoparticle concentration will depend largely on the surfactant type used and the concentration and operating conditions. It is also important to note that the aggregation of

nanoparticles at high salinity and high temperature and pressure could significantly increase or decrease foam stability depending on the aggregation magnitude. The potential benefit of producing nanoparticle-stabilized foam from fly ash and other low-cost nanoparticles, coupled with nanoparticle-stabilized foam visualization at the pore scale, and the fluid diversion mechanisms of nanoparticle-stabilized foam are exhilarating areas for further studies. Despite the extensive studies available in the literature, there are still some gaps in the nanoparticle-stabilized foam studies. Most of nanoparticle foam stabilization studies focus on sandstone formation, glass bead, or sand pack porous media, while less research has been conducted on carbonate formations. Also, the uncertainty of economic viability, nanoparticle agglomeration coupled with the uncertainty of health, and environmental hazards of nanoparticles are some of the existing challenges of nanoparticle-stabilized foam applications. In field applications, the purity of injected gases will differ over time due to gas recycling during the production process [170]. The effect of variation in gas composition or gas dilution on nanoparticle-stabilized foams is still unclear. Additionally, grafting surfactants on the surface of nanoparticles instead of physical mixing is another direction of research that has not been addressed recently that requires further investigations. Finally, there is still a need for pilot applications of nanoparticle-stabilized foams for field-scale performance evaluation of nanoparticle-stabilized foams.

Acknowledgments The authors gratefully acknowledge the Natural Sciences and Engineering Research Council of Canada (NSERC). The second author thanks the Islamic Development Bank (IDB) for its support during his internship at Dr. Nassar Research Group at the University of Calgary.

Nomenclature

A	Surface area, also used as the cross-sectional area of a core
B	Bridging coefficient
C_s	Surfactant concentration in solution
D_i	Diameter of a foam bubble
D_{med}	Median of the volume-averaged bubble diameter in the foam
D_{sm}	Sauter mean diameter
E	Entering coefficient
ΔE	Energy required to remove particle from the gas/liquid interface
E_G	Gibbs surface elasticity
E_M	Marangoni surface elasticity
f_g	Foam quality
k	Core permeability
L	Lamella number, core length
MRF	Mobility reduction ratio
$P_c^{\max}$	Maximum capillary pressure

P_c^*	Limiting capillary pressure
P_G, P_L	Pressure on each side of an interface (gas, liquid)
ΔP	Pressure difference across an interface or pressure change
p	Nanoparticle packing parameter
Q	Injection rate
R	Radius of a curved surface or interface, also used as the gas constant, radius of nanoparticles
S	Spreading coefficient
R_1, R_2	Principal radii of curvature of a surface or interface
T	Absolute temperature
U_g	The superficial velocity of the gas
U_{poly}	Polydispersity
U_w	The superficial velocity of water
u_t	The total foam superficial velocity
σ	Surface or interfacial tension
σ_{og}	The interfacial tension between oil and gas
σ_{wo}	The interfacial tension between water and oil
σ_{wg}	The interfacial tension between water and gas
ε	Viscoelastic modulus
θ	Contact angle
Γ_s	Surface excess concentration of surfactant

References

1. M.G. Aarra, P.A. Ormehaug, A. Skauge, S.K. Masalmeh, Experimental study of CO2- and methane- foam using carbonate core material at reservoir conditions. Paper presented at the SPE Middle East oil and gas show and conference, Manama, Bahrain, 2011. https://doi.org/10.2118/141614-MS
2. M.G. Aarra, A. Skauge, J. Solbakken, P.A. Ormehaug, Properties of N2- and CO2-foams as a function of pressure. J. Pet. Sci. Eng. **116**, 72–80 (2014). https://doi.org/10.1016/j.petrol.2014.02.017
3. V.O. Abramov, A.V. Abramova, V.M. Bayazitov, L.K. Altunina, A.S. Gerasin, D.M. Pashin, T.J. Mason, Sonochemical approaches to enhanced oil recovery. Ultrason. Sonochem. **25**, 76–81 (2015). https://doi.org/10.1016/j.ultsonch.2014.08.014
4. S. Akbari, A. Nour, R. Yunus, A. Farhan, Biosurfactants as promising multifunctional agent: A mini review. Int. J. Innov. Res. Sci. Stud. **1**, 1–6 (2018)
5. A. Al Sumaiti, A.R. Shaik, E.S. Mathew, W. Al Ameri, Tuning foam parameters for mobility control using CO2 foam: Field application to maximize oil recovery from a high temperature high salinity layered carbonate reservoir. Energy Fuel **31**(5), 4637–4654 (2017). https://doi.org/10.1021/acs.energyfuels.6b02595
6. Z. AlYousef, D. Schechter, The synergy of surfactant and nanoparticles: Towards enhancing foam stability. Paper presented at the SPE Kuwait oil & gas show and conference, Mishref, Kuwait, 2019. https://doi.org/10.2118/198190-MS

7. Z. AlYousef, M. Almobarky, D. Schechter, Enhancing the stability of foam by the use of nanoparticles. Energy Fuel **31**(10), 10620–10627 (2017). https://doi.org/10.1021/acs.energyfuels.7b01697
8. S. Alzobaidi, M. Lotfollahi, I. Kim, K.P. Johnston, D.A. DiCarlo, Carbon dioxide-in-brine foams at high temperatures and extreme salinities stabilized with silica nanoparticles. Energy Fuel **31**(10), 10680–10690 (2017). https://doi.org/10.1021/acs.energyfuels.7b01814
9. A. Andrianov, R. Farajzadeh, M. Mahmoodi Nick, M. Talanana, P.L.J. Zitha, Immiscible foam for enhancing oil recovery: Bulk and porous media experiments. Ind. Eng. Chem. Res. **51**(5), 2214–2226 (2012). https://doi.org/10.1021/ie201872v
10. N. Anuar, M.H. Yunan, F. Sagala, A. Katende, The effect of WAG ratio and oil density on oil recovery by immiscible water alternating gas flooding. Am. J. Sci. Technol. **4**(5), 80–90 (2017)
11. A. Aronson, V. Bergeron, M.E. Fagan, C.J.C. Radke, S.A. Physicochemical, E. Aspects, The influence of disjoining pressure on foam stability and flow in porous media. Colloids Surf. A Physicochem. Eng. Asp. **83**(2), 109–120 (1994)
12. A. Aroonsri, A.J. Worthen, T. Hariz, K.P. Johnston, C. Huh, S.L. Bryant, Conditions for generating nanoparticle-stabilized CO2 foams in fracture and matrix flow. Paper presented at the SPE annual technical conference and exhibition, New Orleans, LA, USA, 2013. https://doi.org/10.2118/166319-MS
13. S. Banerjee, E. Hassenklöver, J.M. Kleijn, M.A. Cohen Stuart, F.A.M. Leermakers, Interfacial tension and wettability in water–carbon dioxide systems: Experiments and self-consistent field modeling. J. Phys. Chem. B **117**(28), 8524–8535 (2013). https://doi.org/10.1021/jp400940s
14. A. Barrabino, T. Holt, E. Lindeberg, An evaluation of graphene oxides as possible foam stabilizing agents for CO_2 based enhanced oil recovery. Nanomaterials (Basel, Switzerland) **8**(8), 603 (2018). https://doi.org/10.3390/nano8080603
15. G. Batôt, M. Fleury, E. Rosenberg, L. Nabzar, M. Chabert, Foam propagation in rock samples: Impact of oil and flow characterization. Paper presented at the SPE EOR conference at oil and gas West Asia, Muscat, Oman, 2016. https://doi.org/10.2118/179855-MS
16. A.E. Bayat, K. Rajaei, R. Junin, Assessing the effects of nanoparticle type and concentration on the stability of CO2 foams and the performance in enhanced oil recovery. Colloids Surf. A Physicochem. Eng. Asp. **511**, 222–231 (2016). https://doi.org/10.1016/j.colsurfa.2016.09.083
17. E.J. Behrens, *Investigation of Loss of Surfactants During Enhanced Oil Recovery Applications-Adsorption of Surfactants onto Clay Materials* (Institutt for kjemisk prosessteknologi, 2013)
18. D. Beneventi, B. Carre, A. Gandini, Role of surfactant structure on surface and foaming properties. Colloids Surf. A Physicochem. Eng. Asp. **189**(1), 65–73 (2001). https://doi.org/10.1016/S0927-7757(01)00602-1
19. B.P. Binks, Particles as surfactants – Similarities and differences. Curr. Opin. Colloid Interface Sci. **7**(1), 21–41 (2002). https://doi.org/10.1016/S1359-0294(02)00008-0
20. B.P. Binks, S.O. Lumsdon, Influence of particle wettability on the type and stability of surfactant-free emulsions. Langmuir **16**(23), 8622–8631 (2000). https://doi.org/10.1021/la000189s
21. B.P. Binks, M. Kirkland, J.A. Rodrigues, Origin of stabilisation of aqueous foams in nanoparticle–surfactant mixtures. Soft Matter **4**(12), 2373–2382 (2008). https://doi.org/10.1039/B811291F
22. C.S. Boeije, W. Rossen, Fitting foam-simulation-model parameters to data: I. Coinjection of gas and liquid. SPE Reserv. Eval. Eng. **18**(02), 264–272 (2015). https://doi.org/10.2118/174544-PA
23. J. Boos, W. Drenckhan, C. Stubenrauch, Protocol for studying aqueous foams stabilized by surfactant mixtures. J. Surfactant Deterg. **16**(1), 1–12 (2013). https://doi.org/10.1007/s11743-012-1416-2

24. C. Boyère, C. Jérôme, A. Debuigne, Input of supercritical carbon dioxide to polymer synthesis: An overview. Eur. Polym. J. **61**, 45–63 (2014). https://doi.org/10.1016/j.eurpolymj.2014.07.019
25. R. Butler, I. Hopkinson, A.I. Cooper, Synthesis of porous emulsion-templated polymers using high internal phase CO2-in-water emulsions. J. Am. Chem. Soc. **125**(47), 14473–14481 (2003). https://doi.org/10.1021/ja037570u
26. B.T. Campbell, F.M. Orr, Jr., *Flow Visualization for CO2/Crude Oil Displacements* (1985)
27. E. Carey, C. Stubenrauch, Foaming properties of mixtures of a non-ionic (C12DMPO) and an ionic surfactant (C12TAB). J. Colloid Interface Sci. **346**(2), 414–423 (2010). https://doi.org/10.1016/j.jcis.2010.03.013
28. F. Carn, A. Colin, O. Pitois, M. Vignes-Adler, R. Backov, Foam drainage in the presence of nanoparticle−surfactant mixtures. Langmuir **25**(14), 7847–7856 (2009). https://doi.org/10.1021/la900414q
29. D. Chakravarthy, V. Muralidharan, E. Putra, D.S. Schechter, Application of x-ray CT for investigation of CO2 and WAG injection in fractured reservoirs. Paper presented at the Canadian International Petroleum Conference, Calgary, AB, USA, 2004. https://doi.org/10.2118/2004-232
30. Q. Chen, M. Gerritsen, A.R. Kovscek, Modeling foam displacement with the local equilibrium approximation: Theory and experiment verification. Paper presented at the SPE Annual Technical Conference and Exhibition, Denver, CO, USA, 2008. https://doi.org/10.2118/116735-MS
31. Y. Chen, A.S. Elhag, B.M. Poon, L. Cui, K. Ma, S.Y. Liao, … K.P. Johnston, Ethoxylated cationic surfactants for CO2 EOR in high temperature, high salinity reservoirs. Paper presented at the SPE improved oil recovery symposium, Tulsa, OK, USA, 2012. https://doi.org/10.2118/154222-MS
32. Y. Chen, A.S. Elhag, B.M. Poon, L. Cui, K. Ma, S.Y. Liao, et al., Switchable nonionic to cationic ethoxylated amine surfactants for CO2 enhanced oil recovery in high-temperature, high-salinity carbonate reservoirs. SPE J. **19**(02), 249–259 (2014). https://doi.org/10.2118/154222-PA
33. Y. Chen, A.S. Elhag, P.P. Reddy, H. Chen, L. Cui, A.J. Worthen, et al., Phase behavior and interfacial properties of a switchable ethoxylated amine surfactant at high temperature and effects on CO2-in-water foams. J. Colloid Interface Sci. **470**, 80–91 (2016). https://doi.org/10.1016/j.jcis.2016.02.028
34. K.-O. Choi, N.P. Aditya, S. Ko, Effect of aqueous pH and electrolyte concentration on structure, stability and flow behavior of non-ionic surfactant based solid lipid nanoparticles. Food Chem. **147**, 239–244 (2014). https://doi.org/10.1016/j.foodchem.2013.09.095
35. B.C. Craft, M. Hawkins, *Applied Petroleum Reservoir Engineering* (Pearson, Upper Saddle River, 2015)
36. Z.G. Cui, Y.Z. Cui, C.F. Cui, Z. Chen, B.P. Binks, Aqueous foams stabilized by in situ surface activation of CaCO3 nanoparticles via adsorption of anionic surfactant. Langmuir **26**(15), 12567–12574 (2010). https://doi.org/10.1021/la1016559
37. L. Cui, K. Ma, M. Puerto, A.A. Abdala, I. Tanakov, L.J. Lu, et al., Mobility of Ethomeen C12 and carbon dioxide (CO2) foam at high temperature/high salinity and in carbonate cores. SPE J. **21**(04), 1151–1163 (2016). https://doi.org/10.2118/179726-PA
38. C. Da, G. Jian, S. Alzobaidi, J. Yang, S.L. Biswal, G.J. Hirasaki, K.P. Johnston, Design of CO2-in-water foam stabilized with switchable amine surfactants at high temperature in high-salinity brine and effect of oil. Energy Fuel **32**(12), 12259–12267 (2018). https://doi.org/10.1021/acs.energyfuels.8b02959
39. T.W. de Haas, H. Fadaei, U. Guerrero, D. Sinton, Steam-on-a-chip for oil recovery: The role of alkaline additives in steam assisted gravity drainage. Lab Chip **13**(19), 3832–3839 (2013). https://doi.org/10.1039/C3LC50612F
40. R. Deleurence, C. Parneix, C. Monteux, Mixtures of latex particles and the surfactant of opposite charge used as interface stabilizers – Influence of particle contact angle, zeta

potential, flocculation and shear energy. Soft Matter **10**(36), 7088–7095 (2014). https://doi.org/10.1039/C4SM00237G
41. N.D. Denkov, Mechanisms of foam destruction by oil-based antifoams. Langmuir **20**(22), 9463–9505 (2004). https://doi.org/10.1021/la049676o
42. N.D. Denkov, I.B. Ivanov, P.A. Kralchevsky, D.T. Wasan, A possible mechanism of stabilization of emulsions by solid particles. *J. Colloid Interface Sci.* **150**(2), 589–593 (1992). https://doi.org/10.1016/0021-9797(92)90228-E
43. N.D. Denkov, P. Cooper, J.-Y. Martin, Mechanisms of action of mixed solid−liquid antifoams. 1. Dynamics of foam film rupture. Langmuir **15**(24), 8514–8529 (1999). https://doi.org/10.1021/la9902136
44. J.L. Dickson, B.P. Binks, K.P. Johnston, Stabilization of carbon dioxide-in-water emulsions with silica nanoparticles. Langmuir **20**(19), 7976–7983 (2004). https://doi.org/10.1021/la0488102
45. W. Drenckhan, S. Hutzler, Structure and energy of liquid foams. Adv. Colloid Interf. Sci. **224**, 1–16 (2015). https://doi.org/10.1016/j.cis.2015.05.004
46. W. Drenckhan, D. Langevin, Monodisperse foams in one to three dimensions. Curr. Opin. Colloid Interface Sci. **15**(5), 341–358 (2010). https://doi.org/10.1016/j.cocis.2010.06.002
47. Z. Du, M.P. Bilbao-Montoya, B.P. Binks, E. Dickinson, R. Ettelaie, B.S. Murray, Outstanding stability of particle-stabilized bubbles. Langmuir **19**(8), 3106–3108 (2003). https://doi.org/10.1021/la034042n
48. A.A. Eftekhari, R. Krastev, R. Farajzadeh, Foam stabilized by fly ash nanoparticles for enhancing oil recovery. Ind. Eng. Chem. Res. **54**(50), 12482–12491 (2015). https://doi.org/10.1021/acs.iecr.5b03955
49. H. Ehtesabi, M.M. Ahadian, V.J.E. Taghikhani, Enhanced heavy oil recovery using TiO2 nanoparticles: Investigation of deposition during transport in core plug. Energy Fuel **29**(1), 1–8 (2015)
50. A.S. Elhag, C. Da, Y. Chen, N. Mukherjee, J.A. Noguera, S. Alzobaidi, et al., Viscoelastic diamine surfactant for stable carbon dioxide/water foams over a wide range in salinity and temperature. J. Colloid Interface Sci. **522**, 151–162 (2018). https://doi.org/10.1016/j.jcis.2018.03.037
51. A.S. Emrani, H.A. Nasr-El-Din, Stabilizing CO2-foam using nanoparticles. Paper presented at the SPE European formation damage conference and exhibition, Budapest, Hungary, 2015. https://doi.org/10.2118/174254-MS
52. A.S. Emrani, H.A. Nasr-El-Din, An experimental study of nanoparticle-polymer-stabilized CO2 foam. Colloids Surf. A Physicochem. Eng. Asp. **524**, 17–27 (2017a). https://doi.org/10.1016/j.colsurfa.2017.04.023
53. A.S. Emrani, H.A. Nasr-El-Din, Stabilizing CO2 foam by use of nanoparticles. SPE J. **22**(02), 494–504 (2017b). https://doi.org/10.2118/174254-PA
54. R.M. Enick, D.K. Olsen, J.R. Ammer, W. Schuller, Mobility and conformance control for CO2 eor via thickeners, foams, and gels – A literature review of 40 years of research and pilot tests. Paper presented at the SPE improved oil recovery symposium, Tulsa, OK, USA, 2012. https://doi.org/10.2118/154122-MS
55. D.A. Espinoza, F.M. Caldelas, K.P. Johnston, S.L. Bryant, C. Huh, Nanoparticle-stabilized supercritical CO2 foams for potential mobility control applications. Paper presented at the SPE improved oil recovery symposium, Tulsa, OK, USA, 2010. https://doi.org/10.2118/129925-MS
56. A.H. Falls, G.J. Hirasaki, T.W. Patzek, D.A. Gauglitz, D.D. Miller, T. Ratulowski, Development of a mechanistic foam simulator: The population balance and generation by snap-off. SPE Reserv. Eng. **3**(03), 884–892 (1988). https://doi.org/10.2118/14961-PA
57. A.H. Falls, J.J. Musters, J. Ratulowski, The apparent viscosity of foams in homogeneous bead packs. SPE Reserv. Eng. **4**(02), 155–164 (1989). https://doi.org/10.2118/16048-PA

58. S. Farad, H.K. Nsamba, A. Al Hassan, W. Joseph, I. Kabenge, Effect of pH and slug ratio of alkaline surfactant polymer alternating gas flooding on oil recovery. Am. Assoc. Sci. Technol. **3**(2), 47–52 (2016)
59. R. Farajzadeh, A. Andrianov, H. Bruining, P.L.J. Zitha, Comparative study of CO2 and N2 foams in porous media at low and high pressure−temperatures. Ind. Eng. Chem. Res. **48**(9), 4542–4552 (2009). https://doi.org/10.1021/ie801760u
60. R. Farajzadeh, A. Andrianov, P.L.J. Zitha, Investigation of immiscible and miscible foam for enhancing oil recovery. Ind. Eng. Chem. Res. **49**(4), 1910–1919 (2010). https://doi.org/10.1021/ie901109d
61. R. Farajzadeh, M. Lotfollahi, A.A. Eftekhari, W.R. Rossen, G.J.H. Hirasaki, Effect of permeability on implicit-texture foam model parameters and the limiting capillary pressure. Energy Fuel **29**(5), 3011–3018 (2015). https://doi.org/10.1021/acs.energyfuels.5b00248
62. R.N. Gajbhiye, S.I. Kam, Characterization of foam flow in horizontal pipes by using two-flow-regime concept. Chem. Eng. Sci. **66**(8), 1536–1549 (2011). https://doi.org/10.1016/j.ces.2010.12.012
63. D. Georgieva, V. Schmitt, F. Leal-Calderon, D. Langevin, On the possible role of surface elasticity in emulsion stability. Langmuir **25**(10), 5565–5573 (2009). https://doi.org/10.1021/la804240e
64. R.B. Ghahfarokhi, United States Patent No. (2019)
65. D.W. Green, G.P. Willhite, *Enhanced Oil Recovery*, vol 8 (Texas, United States of America: Society of Petroleum Engineers, 1998)
66. F. Guo, S. Aryana, An experimental investigation of nanoparticle-stabilized CO2 foam used in enhanced oil recovery. Fuel **186**, 430–442 (2016). https://doi.org/10.1016/j.fuel.2016.08.058
67. F. Guo, J. He, P.A. Johnson, S.A. Aryana, Stabilization of CO2 foam using by-product fly ash and recyclable iron oxide nanoparticles to improve carbon utilization in EOR processes. Sustain. Energy Fuels **1**(4), 814–822 (2017). https://doi.org/10.1039/c7se00098g
68. J.E. Hanssen, M. Dalland, Increased oil tolerance of polymer-enhanced foams: Deep chemistry or just "Simple" displacement effects? Paper presented at the SPE/DOE Improved Oil Recovery Symposium, Tulsa, OK, USA, 2000. https://doi.org/10.2118/59282-MS
69. T.R. Hariz, *Nanoparticle-Stabilized CO2 Foams for Potential Mobility Control Applications* (The University of Texas at Austin, Austin, 2012)
70. W.D. Harkins, A general thermodynamic theory of the spreading of liquids to form duplex films and of liquids or solids to form monolayers. J. Chem. Phys. **9**, 552 (1941)
71. P.C. Harris, Dynamic fluid-loss characteristics of CO2-foam fracturing fluids. SPE Prod. Eng. **2**(02), 89–94 (1987). https://doi.org/10.2118/13180-PA
72. R. Hashemi, N.N. Nassar, P. Pereira-Almao, Transport behavior of multimetallic ultradispersed nanoparticles in an oil-sands-packed bed column at a high temperature and pressure. Energy Fuel **26**(3), 1645–1655 (2012). https://doi.org/10.1021/ef201939f
73. R. Hashemi, N.N. Nassar, P. Pereira Almao, Nanoparticle technology for heavy oil in-situ upgrading and recovery enhancement: Opportunities and challenges. Appl. Energy **133**, 374–387 (2014). https://doi.org/10.1016/j.apenergy.2014.07.069
74. A. Heydarian, R. Kharrat, S. Heydarian, A. Hashemi, Impact of nano-particles on static performance of surfactant foams. J. Am. Sci. **9**(6) (2013)
75. G.J. Hirasaki, J.B. Lawson, Mechanisms of foam flow in porous media: Apparent viscosity in smooth capillaries. Soc. Pet. Eng. J. **25**(02), 176–190 (1985). https://doi.org/10.2118/12129-PA
76. G. Hirasaki, C.A. Miller, M. Puerto, Recent advances in surfactant EOR. SPE J. **16**(04), 889–907 (2011). https://doi.org/10.2118/115386-PA
77. T.S. Horozov, Foams and foam films stabilised by solid particles. Curr. Opin. Colloid Interface Sci. **13**(3), 134–140 (2008). https://doi.org/10.1016/j.cocis.2007.11.009
78. J. Hou, Z. Liu, S. Zhang, X.a. Yue, J. Yang, The role of viscoelasticity of alkali/surfactant/polymer solutions in enhanced oil recovery. J. Pet. Sci. Eng. **47**, 219–235 (2005). https://doi.org/10.1016/j.petrol.2005.04.001

79. A.M. Howe, A. Clarke, J. Mitchell, J. Staniland, L. Hawkes, C. Whalan, Visualising surfactant enhanced oil recovery. Colloids Surf. A Physicochem. Eng. Asp. **480**, 449–461 (2015). https://doi.org/10.1016/j.colsurfa.2014.08.032
80. T.N. Hunter, R.J. Pugh, G.V. Franks, G.J. Jameson, The role of particles in stabilising foams and emulsions. Adv. Colloid Interf. Sci. **137**(2), 57–81 (2008). https://doi.org/10.1016/j.cis.2007.07.007
81. A.F. Ibrahim, A. Emrani, H. Nasraldin, Stabilized CO2 foam for EOR applications. Paper presented at the Carbon Management Technology conference, Houston, TX, USA, 2017. https://doi.org/10.7122/486215-MS
82. S. Jikich, CO2 EOR: Nanotechnology for mobility control studied. J. Pet. Technol. **64**(07), 28–31 (2012). https://doi.org/10.2118/0712-0028-JPT
83. S.I. Kam, W.R. Rossen, Anomalous capillary pressure, stress, and stability of solids-coated bubbles. J. Colloid Interface Sci. **213**, 329 (1999)
84. M.S. Kamal, I.A. Hussein, A.S. Sultan, Review on surfactant flooding: Phase behavior, retention, IFT, and field applications. Energy Fuel **31**(8), 7701–7720 (2017). https://doi.org/10.1021/acs.energyfuels.7b00353
85. S.I. Karakashev, O. Ozdemir, M.A. Hampton, A.V. Nguyen, Formation and stability of foams stabilized by fine particles with similar size, contact angle and different shapes. Colloids Surf. A Physicochem. Eng. Asp. **382**(1), 132–138 (2011). https://doi.org/10.1016/j.colsurfa.2010.09.023
86. M. Khajehpour, S.R. Etminan, J. Goldman, F. Wassmuth, S. Bryant, Nanoparticles as foam stabilizer for steam-foam process. SPE J. **23**(06), 2232–2242 (2018). https://doi.org/10.2118/179826-PA
87. J. Kim, L. Cote, F. Kim, W. Yuan, K. Shull, J. Huang, Graphene oxide sheets at interfaces. J. Am. Chem. Soc. **132**(23), 8180–8186 (2010). https://doi.org/10.1021/ja102777p
88. I. Kim, A. Taghavy, D. DiCarlo, C. Huh, Aggregation of silica nanoparticles and its impact on particle mobility under high-salinity conditions. J. Pet. Sci. Eng. **133**, 376–383 (2015). https://doi.org/10.1016/j.petrol.2015.06.019
89. I. Kim, A.J. Worthen, K.P. Johnston, D.A. DiCarlo, C. Huh, Size-dependent properties of silica nanoparticles for Pickering stabilization of emulsions and foams. J. Nanopart. Res. **18**(4), 82 (2016). https://doi.org/10.1007/s11051-016-3395-0
90. K. Koczo, L.A. Lobo, D.T. Wasan, Effect of oil on foam stability: Aqueous foams stabilized by emulsions. J. Colloid Interface Sci. **150**(2), 492–506 (1992). https://doi.org/10.1016/0021-9797(92)90218-B
91. T. Kostakis, R. Ettelaie, B.S. Murray, Effect of high salt concentrations on the stabilization of bubbles by silica particles. Langmuir **22**(3), 1273–1280 (2006). https://doi.org/10.1021/la052193f
92. P.M. Kruglyakov, S.I. Elaneva, N.G. Vilkova, About mechanism of foam stabilization by solid particles. Adv. Colloid Interf. Sci. **165**(2), 108–116 (2011). https://doi.org/10.1016/j.cis.2011.02.003
93. S. Kumar, A. Mandal, Investigation on stabilization of CO2 foam by ionic and nonionic surfactants in presence of different additives for application in enhanced oil recovery. Appl. Surf. Sci. **420**, 9–20 (2017). https://doi.org/10.1016/j.apsusc.2017.05.126
94. L.W. Lake, *Enhanced Oil Recovery* (Prentice Hall, Englewood Cliffs, 1989)
95. D. Lee, H. Cho, J. Lee, C. Huh, K. Mohanty, Fly ash nanoparticles as a CO2 foam stabilizer. Powder Technol. **283**, 77–84 (2015). https://doi.org/10.1016/j.powtec.2015.05.010
96. Z. Li, Z. Liu, B. Li, S. Li, Q. Sun, S. Wang, Aqueous foams stabilized with particles and surfactants. Paper presented at the SPE Saudi Arabia section technical symposium and exhibition, Al-Khobar, Saudi Arabia, 2012. https://doi.org/10.2118/160840-MS
97. S. Li, Z. Li, P. Wang, Experimental study of the stabilization of CO2 foam by sodium dodecyl sulfate and hydrophobic nanoparticles. Ind. Eng. Chem. Res. **55**(5), 1243–1253 (2016). https://doi.org/10.1021/acs.iecr.5b04443

98. S. Li, C. Qiao, Z. Li, S. Wanambwa, Properties of carbon dioxide foam stabilized by hydrophilic nanoparticles and hexadecyltrimethylammonium bromide. Energy Fuel **31**(2), 1478–1488 (2017). https://doi.org/10.1021/acs.energyfuels.6b03130
99. S. Li, K. Yang, Z. Li, K. Zhang, N. Jia, Properties of CO2 foam stabilized by hydrophilic nanoparticles and nonionic surfactants. Energy Fuel **33**(6), 5043–5054 (2019). https://doi.org/10.1021/acs.energyfuels.9b00773
100. M. Liu, A. Andrianov, W.R. Rossen, Sweep efficiency in CO2 foam simulations with oil. Paper presented at the IOR 2011-16th European symposium on improved oil recovery, 2011
101. C. Liu, J. Zhang, I. Orcid, X. Sang, X. Kang, B. Zhang, et al., CO(2)/water emulsions stabilized by partially reduced graphene oxide. ACS Appl. Mater. Interfaces **9**(20), 17613–17619 (2017)
102. Q. Liu, H. Qu, S. Liu, Y. Zhang, S. Zhang, J. Liu, et al., Modified Fe3O4 nanoparticle used for stabilizing foam flooding for enhanced oil recovery. Colloids Surf. A Physicochem. Eng. Asp., 125383 (2020). https://doi.org/10.1016/j.colsurfa.2020.125383
103. L. Lobo, D.T. Wasan, Mechanisms of aqueous foam stability in the presence of emulsified non-aqueous-phase liquids: Structure and stability of the pseudoemulsion film. Langmuir **9**(7), 1668–1677 (1993). https://doi.org/10.1021/la00031a012
104. T. Lu, Z. Li, D. Hou, Z. Xu, X. Ban, B. Zhou, Experimental and numerical evaluation of surfactant-nanoparticles foam for enhanced oil recovery under high temperature. Energy Fuel **34**(1), 1005–1013 (2020). https://doi.org/10.1021/acs.energyfuels.9b03000
105. J. Luo, L. Cote, V. Tung, A. Tan, P. Goins, J. Wu, J. Huang, Graphene oxide nanocolloids. J. Am. Chem. Soc. **132**(50), 17667–17669 (2010). https://doi.org/10.1021/ja1078943
106. Q. Lv, T. Zhou, X. Zhang, B. Zuo, Z. Dong, J. Zhang, Enhanced oil recovery using aqueous CO2 foam stabilized by particulate matter from coal combustion. Energy Fuel **34**(3), 2880–2892 (2020). https://doi.org/10.1021/acs.energyfuels.9b04066
107. K. Ma, *Transport of Surfactant and Foam in Porous Media for Enhanced Oil Recovery Process* (Rice University, 2013)
108. M. Manan, S. Farad, A. Piroozian, M. Esmail, Effects of nanoparticle types on carbon dioxide foam flooding in enhanced oil recovery. Pet. Sci. Technol. **33**(12), 1286–1294 (2015)
109. D.J. Manlowe, C.J. Radke, A pore-level investigation of foam/oil interactions in porous media. SPE Reserv. Eng. **5**(04), 495–502 (1990). https://doi.org/10.2118/18069-PA
110. S.K. Masalmeh, H. Hillgartner, R.A.-M. Al-Mjeni, X. Jing, Simultaneous injection of miscible gas and polymer (SIMGAP) to improve oil recovery and sweep efficiency from layered carbonate reservoirs. Paper presented at the SPE EOR Conference at Oil & Gas West Asia, Muscat, Oman, 2010. https://doi.org/10.2118/129645-MS
111. E.S. Mathew, A.R. Shaik, A. Al Sumaiti, W. AlAmeri, Effect of oil presence on CO2 foam based mobility control in high temperature high salinity carbonate reservoirs. Energy Fuel **32**(3), 2983–2992 (2018). https://doi.org/10.1021/acs.energyfuels.7b03490
112. W.D. McCain, *The Properties of Petroleum Fluids* (Pennwell Books, Tulsa, 1990), p. 19900301
113. M.B.J. Meinders, T. van Vliet, The role of interfacial rheological properties on Ostwald ripening in emulsions. Adv. Colloid Interf. Sci. **108–109**, 119–126 (2004). https://doi.org/10.1016/j.cis.2003.10.005
114. D. Mo, J. Yu, N. Liu, R.L. Lee, Study of the effect of different factors on nanoparticle-stablized CO2 foam for mobility control. Paper presented at the SPE Annual Technical Conference and Exhibition, San Antonio, TX, USA, 2012. https://doi.org/10.2118/159282-MS
115. D. Mo, B. Jia, J. Yu, N. Liu, R. Lee, Study nanoparticle-stabilized CO2 foam for oil recovery at different pressure, temperature, and rock samples. Paper presented at the SPE Improved Oil Recovery Symposium, Tulsa, OK, USA, 2014. https://doi.org/10.2118/169110-MS
116. M. Morvan, P. Moreau, G. Degre, J. Leng, C. Masselon, J. Bouillot, A. Zaitoun, New viscoelastic fluid for chemical EOR. Paper presented at the SPE international symposium on oilfield chemistry, The Woodlands, TX, USA, 2009. https://doi.org/10.2118/121675-MS
117. C. Negin, A. Saeedi, Q. Xie, Most common surfactants employed in chemical enhanced oil recovery. Petroleum **3** (2016). https://doi.org/10.1016/j.petlm.2016.11.007

118. P. Nguyen, H. Fadaei, D. Sinton, Pore-scale assessment of nanoparticle-stabilized CO2 foam for enhanced oil recovery. Energy Fuel **28**(10), 6221–6227 (2014). https://doi.org/10.1021/ef5011995
119. A.D. Nikolov, D.T. Wasan, D.W. Huang, D.A. Edwards, The effect of oil on foam stability: Mechanisms and implications for oil displacement by foam in porous media. Paper presented at the SPE annual technical conference and exhibition, New Orleans, LA, USA, 1986. https://doi.org/10.2118/15443-MS
120. G. Palazzo, D. Berti, *Colloidal Foundations of Nanoscience* (Elsevier, 2014)
121. C. Palocci, A. Barbetta, A. La Grotta, M. Dentini, Porous biomaterials obtained using supercritical CO2−water emulsions. Langmuir **23**(15), 8243–8251 (2007). https://doi.org/10.1021/la700947g
122. R.J. Pugh, Foaming, foam films, antifoaming and defoaming. Adv. Colloid Interf. Sci. **64**, 67–142 (1996). https://doi.org/10.1016/0001-8686(95)00280-4
123. C. Qian, A. Telmadarreie, M. Dong, S. Bryant, Synergistic effect between surfactant and nanoparticles on the stability of foam in EOR processes. SPE J. **25**(02), 883–894 (2020). https://doi.org/10.2118/195310-PA
124. M.D. Rad, *Natural Gas Foam Stabilization by a Mixture of Oppositely Charged Nanoparticle and Surfactant and the Underlying Mechanisms.* Master of Science, University of Calgary. (2018)
125. R. Rafati, A.S. Haddad, H. Hamidi, Experimental study on stability and rheological properties of aqueous foam in the presence of reservoir natural solid particles. Colloids Surf. A Physicochem. Eng. Asp. **509**, 19–31 (2016). https://doi.org/10.1016/j.colsurfa.2016.08.087
126. K. Raghav Chaturvedi, R. Kumar, J. Trivedi, J.J. Sheng, T. Sharma, Stable silica nanofluids of an oilfield polymer for enhanced CO2 absorption for oilfield applications. Energy Fuel **32**(12), 12730–12741 (2018). https://doi.org/10.1021/acs.energyfuels.8b02969
127. K.T. Raterman, An investigation of oil destabilization of nitrogen foams in porous media. Paper presented at the SPE annual technical conference and exhibition, San Antonio, TX, USA, 1989. https://doi.org/10.2118/19692-MS
128. P. Rattanaudom, B.-J. Shiau, U. Suriyapraphadilok, A. Charoensaeng, Effect of pH on silica nanoparticle-stabilized foam for enhanced oil recovery using carboxylate-based extended surfactants. J. Pet. Sci. Eng. **196**, 107729 (2021). https://doi.org/10.1016/j.petrol.2020.107729
129. F. Ravera, E. Santini, G. Loglio, M. Ferrari, L. Liggieri, Effect of nanoparticles on the interfacial properties of liquid/liquid and liquid/air surface layers. J. Phys. Chem. B **110**(39), 19543–19551 (2006). https://doi.org/10.1021/jp0636468
130. V.G. Reidenbach, P.C. Harris, Y.N. Lee, D.L. Lord, Rheological study of foam fracturing fluids using nitrogen and carbon dioxide. SPE Prod. Eng. **1**(01), 31–41 (1986). https://doi.org/10.2118/12026-PA
131. J.V. Robinson, W.W. Woods, A method of selecting foam inhibitors. J. Soc. Chem. Ind. **67**(9), 361–365 (1948). https://doi.org/10.1002/jctb.5000670908
132. A.U. Rognmo, N. Al-Khayyat, S. Heldal, I. Vikingstad, O. Eide, S.B. Fredriksen, … M.A. Ferno, Performance of silica nanoparticles in CO2-foam for EOR and CCUS at tough reservoir conditions. Paper presented at the SPE Norway one day seminar, Bergen, Norway, 2018a. https://doi.org/10.2118/191318-MS
133. A.U. Rognmo, S. Heldal, M.A. Fernø, Silica nanoparticles to stabilize CO2-foam for improved CO2 utilization: Enhanced CO2 storage and oil recovery from mature oil reservoirs. Fuel **216**, 621–626 (2018b). https://doi.org/10.1016/j.fuel.2017.11.144
134. W.R. Rossen, W.J. Renkema, Success of foam SAG processes in heterogeneous reservoirs. Paper presented at the SPE annual technical conference and exhibition, Anaheim, CA, USA, 2007. https://doi.org/10.2118/110408-MS
135. W.R. Rossen, M.W. Wang, Modeling foams for acid diversion. SPE J. **4**(02), 92–100 (1999). https://doi.org/10.2118/56396-PA

136. S. Sakthivel, A. Adebayo, M.Y. Kanj, Experimental evaluation of carbon dots stabilized foam for enhanced oil recovery. Energy Fuel **33**(10), 9629–9643 (2019). https://doi.org/10.1021/acs.energyfuels.9b02235
137. O.O. Samuel, *Effect of Reservoir Heterogeneity on Immiscible Foam Enhanced Oil Recovery* (Delft University of Technology, 2009)
138. L.L. Schramm, J.J. Novosad, Micro-visualization of foam interactions with a crude oil. Colloids Surf. **46**(1), 21–43 (1990). https://doi.org/10.1016/0166-6622(90)80046-7
139. L.L. Schramm, J.J. Novosad, The destabilization of foams for improved oil recovery by crude oils: Effect of the nature of the oil. J. Pet. Sci. Eng. **7**(1), 77–90 (1992). https://doi.org/10.1016/0920-4105(92)90010-X
140. L.L. Schramm, F. Wassmuth, Foams: Basic principles, in *Foams: Fundamentals and Applications in the Petroleum Industry*, vol. 242, (American Chemical Society, 1994), pp. 3–45
141. D. Shan, W.R. Rossen, Optimal injection strategies for foam IOR. Paper presented at the SPE/DOE improved oil recovery symposium, Tulsa, OK, USA, 2002. https://doi.org/10.2118/75180-MS
142. S. Shayegi, P.A. Schenewerk, J.M. Wolcott, *Enhancement of Residual Oil Recovery Using a Mixture of Nitrogen or Methane Diluted with Carbon Dioxide in a Single-Well Injection Process* (Google Patents, 1998)
143. J. Sheng, *Enhanced Oil Recovery Field Case Studies* (Elsevier Science & Technology, Oxford, 2013)
144. L. Siggel, M. Santa, M. Hansch, M. Nowak, M. Ranft, H. Weiss, … J. Tinsley, A new class of viscoelastic surfactants for enhanced oil recovery. Paper presented at the SPE improved oil recovery symposium, Tulsa, OK, USA, 2012. https://doi.org/10.2118/153969-MS
145. R. Singh, K.K. Mohanty, Foams stabilized by in-situ surface activated nanoparticles in bulk and porous media. Paper presented at the SPE annual technical conference and exhibition, Amsterdam, The Netherlands, 2014. https://doi.org/10.2118/170942-MS
146. R. Singh, K.K. Mohanty, Synergy between nanoparticles and surfactants in stabilizing foams for oil recovery. Energy Fuel **29**(2), 467–479 (2015). https://doi.org/10.1021/ef5015007
147. R. Singh, K.K. Mohanty, Foams stabilized by in-situ surface-activated nanoparticles in bulk and porous media. SPE J. **21**(01), 121–130 (2016). https://doi.org/10.2118/170942-PA
148. R. Singh, K.K. Mohanty, Nanoparticle-stabilized foams for high-temperature, high-salinity oil reservoirs. Paper presented at the SPE annual technical conference and exhibition, San Antonio, TX, USA, 2017. https://doi.org/10.2118/187165-MS
149. R. Singh, A. Gupta, K.K. Mohanty, C. Huh, D. Lee, H. Cho, Fly ash nanoparticle-stabilized CO2-in-water foams for gas mobility control applications. Paper presented at the SPE annual technical conference and exhibition, Houston, TX, USA, 2015. https://doi.org/10.2118/175057-MS
150. R. Singh, K. Panthi, U. Weerasooriya, K.K. Mohanty, Multistimuli-responsive foams using an anionic surfactant. Langmuir **34**(37), 11010–11020 (2018). https://doi.org/10.1021/acs.langmuir.8b01796
151. T. Skauge, K. Spildo, A. Skauge, Nano-sized particles for EOR. Paper presented at the SPE improved oil recovery symposium, 2010
152. R.L. Slobod, H.A. Jr. Koch, High-pressure gas injection- mechanism of recovery increase. Paper presented at the drilling and production practice, New York, NY, USA, 1953
153. K. Spildo, A.M. Johannessen, A. Skauge, Low salinity waterflood at reduced capillarity. Paper presented at the SPE improved oil recovery symposium, Tulsa, OK, USA, 2012. https://doi.org/10.2118/154236-MS
154. A. Stocco, E. Rio, B.P. Binks, D. Langevin, Aqueous foams stabilized solely by particles. Soft Matter **7**(4), 1260–1267 (2011). https://doi.org/10.1039/C0SM01290D
155. Y.Q. Sun, T. Gao, The optimum wetting angle for the stabilization of liquid-metal foams by ceramic particles: Experimental simulations. Metall. Mater. Trans. A Phys. Metall. Mater. Sci. **33**, 3285–3292 (2002). https://doi.org/10.1007/s11661-002-0315-y

156. Q. Sun, Z. Li, S. Li, L. Jiang, J. Wang, P. Wang, Utilization of surfactant-stabilized foam for enhanced oil recovery by adding nanoparticles. Energy Fuel **28**(4), 2384–2394 (2014). https://doi.org/10.1021/ef402453b
157. X. Sun, Y. Zhang, G. Chen, Z.J.E. Gai, Application of nanoparticles in enhanced oil recovery: A critical review of recent progress. Energies **10**(3), 345 (2017)
158. F.-Q. Tang, Z. Xiao, J.-A. Tang, L. Jiang, The effect of SiO2 particles upon stabilization of foam. J. Colloid Interface Sci. **131**(2), 498–502 (1989). https://doi.org/10.1016/0021-9797(89)90192-6
159. S. Tcholakova, Z. Mitrinova, K. Golemanov, N.D. Denkov, M. Vethamuthu, K.P. Ananthapadmanabhan, Control of Ostwald ripening by using surfactants with high surface modulus. Langmuir **27**(24), 14807–14819 (2011). https://doi.org/10.1021/la203952p
160. A.K. Vikingstad, *Static and Dynamic Studies of Foam and Foam-Oil Interactions.* PhD, University of Bergen, (2006)
161. T.-F. Wang, J.-X. Wang, L. Han, J.-H. Wang, Y. Zhu, Study on the stabilizing effect of aluminum hydroxide nanoparticles on foams. J. Xian Shiyou Univ., 78–81 (2012)
162. S. Wang, Y. Shi, B.-M. Li, Neural representation of cost–benefit selections in rat anterior cingulate cortex in self-paced decision making. Neurobiol. Learn. Mem. **139**, 1–10 (2017). https://doi.org/10.1016/j.nlm.2016.12.003
163. P. Wang, Q. You, L. Han, W. Deng, Y. Liu, J. Fang, et al., Experimental study on the stabilization mechanisms of CO2 foams by hydrophilic silica nanoparticles. Energy Fuel **32**(3), 3709–3715 (2018). https://doi.org/10.1021/acs.energyfuels.7b04125
164. D.T. Wasan, K. Koczo, A.D. Nikolov, Mechanisms of aqueous foam stability and antifoaming action with and without oil, in *Foams: Fundamentals and Applications in the Petroleum Industry*, vol. 242, (American Chemical Society, 1994), pp. 47–114
165. D. Weaire, S. Hutzler, P.-G. Gennes, The physics of foams. Phys. Today **54** (2001). https://doi.org/10.1063/1.1366070
166. T. Witten, P. Pincus, *Structured Fluids: Polymers, Colloids* (Surfactants, 2010)
167. A. Worthen, H. Bagaria, Y. Chen, S.L. Bryant, C. Huh, K.P. Johnston, Nanoparticle stabilized carbon dioxide in water foams for enhanced oil recovery. Paper presented at the SPE improved oil recovery symposium, Tulsa, OK, USA, 2012. https://doi.org/10.2118/154285-MS
168. A. Worthen, H. Bagaria, Y. Chen, S. Bryant, C. Huh, K. Johnston, Nanoparticle-stabilized carbon dioxide-in-water foams with fine texture. J. Colloid Interface Sci. **391**, 142–151 (2013). https://doi.org/10.1016/j.jcis.2012.09.043
169. D. Xing, B. Wei, W. McLendon, R. Enick, S. McNulty, K. Trickett, et al., CO2-soluble/nonionic, water-soluble surfactants that stabilize CO2-in-brine foams. SPE J. **17**(4), 1172–1185 (2012). https://doi.org/10.2118/129907-PA
170. Z. Xue, K. Panthi, Y. Fei, K.P. Johnston, K.K. Mohanty, CO2-soluble ionic surfactants and CO2 foams for high-temperature and high-salinity sandstone reservoirs. Energy Fuel **29**(9), 5750–5760 (2015). https://doi.org/10.1021/acs.energyfuels.5b01568
171. Z. Xue, A. Worthen, A. Qajar, I. Robert, S.L. Bryant, C. Huh, et al., Viscosity and stability of ultra-high internal phase CO2-in-water foams stabilized with surfactants and nanoparticles with or without polyelectrolytes. J. Colloid Interface Sci. **461**, 383–395 (2016). https://doi.org/10.1016/j.jcis.2015.08.031
172. W. Yang, T. Wang, Z. Fan, Highly stable foam stabilized by alumina nanoparticles for EOR: Effects of sodium cumenesulfonate and electrolyte concentrations. Energy Fuel **31**(9), 9016–9025 (2017a). https://doi.org/10.1021/acs.energyfuels.7b01248
173. W. Yang, T. Wang, Z. Fan, Q. Miao, Z. Deng, Y. Zhu, Foams stabilized by in situ-modified nanoparticles and anionic surfactants for enhanced oil recovery. Energy Fuel **31**(5), 4721–4730 (2017b). https://doi.org/10.1021/acs.energyfuels.6b03217
174. N. Yekeen, A.K. Idris, M.A. Manan, A.M. Samin, A.R. Risal, T.X. Kun, Bulk and bubble-scale experimental studies of influence of nanoparticles on foam stability. Chin. J. Chem. Eng. **25**(3), 347–357 (2017). https://doi.org/10.1016/j.cjche.2016.08.012

175. N. Yekeen, M.A. Manan, A.K. Idris, E. Padmanabhan, R. Junin, A.M. Samin, et al., A comprehensive review of experimental studies of nanoparticles-stabilized foam for enhanced oil recovery. J. Pet. Sci. Eng. **164**, 43–74 (2018). https://doi.org/10.1016/j.petrol.2018.01.035
176. J. Yu, C. An, D. Mo, N. Liu, R.L. Lee, Foam mobility control for nanoparticle-stabilized supercritical CO2 foam. Paper presented at the SPE improved oil recovery symposium, Tulsa, OK, USA, 2012a. https://doi.org/10.2118/153336-MS
177. J. Yu, N. Liu, L. Li, R.L. Lee, Generation of nanoparticle-stabilized supercritical CO2 foams. Paper presented at the Carbon Management Technology conference, Orlando, FL, USA, 2012b. https://doi.org/10.7122/150849-MS
178. J. Yu, D. Mo, N. Liu, R. Lee, The application of nanoparticle-stabilized CO2 foam for oil recovery. Paper presented at the SPE international symposium on oilfield chemistry, The Woodlands, TX, USA, 2013. https://doi.org/10.2118/164074-MS
179. Y. Zeng, R. Farajzadeh, A.A. Eftekhari, S. Vincent-Bonnieu, A. Muthuswamy, W.R. Rossen, et al., Role of gas type on foam transport in porous media. Langmuir **32**(25), 6239–6245 (2016). https://doi.org/10.1021/acs.langmuir.6b00949
180. S.Y. Zhang, *Foams Stabilized by Laponite/Surfactants and HMHEC/Surfactants* (Shandong University, Shandong, 2008)
181. X. Zhang, G. Zhang, J. Ge, Y. Wang, CO foam stabilized with switchable surfactants and modified nanoparticles effected by PH and salinity. Paper presented at the SPE Europec featured at 82nd EAGE Conference and Exhibition, Amsterdam, The Netherlands, 2020. https://doi.org/10.2118/200584-MS

Chapter 9
Influence of Surfactant Adsorption on Surface-Functionalized Silica Nanoparticles for Gas Foam Stability

Yira Hurtado, Daniel López, Sergio H. Lopera, Farid B. Cortés, and Camilo A. Franco

9.1 Introduction

Gas injection into oil fields represents about 39% of enhanced oil recovery (EOR) methods used worldwide [1]. However, this technique is limited by the mobility difference between displacing (gas) and displaced (crude oil) fluids, causing gravitational segregation, fingering, and gas channeling to previously depleted areas [2]. Through foam injection, gas mobility and its relative permeability are reduced because the apparent gas viscosity increases when it is trapped in bubbles [3]. Consequently, a uniform displacing front is maintained throughout the reservoir that mobilizes the crude oil, mitigating the limitations of the gas injection technique and improving oil recovery [4, 5]. However, foam use is limited because bubbles are unstable; consequently, foam effectiveness in long-term treatments is insufficient [6]. To improve the stability and long-term performance of foams, two mechanisms have been used: to supply a high volumetric gas fraction to the foaming solution to increase the number of bubbles in the foam and make them smaller and to increase the viscosity by incorporating surfactants, polymers, and/or foam boosters to reduce foam mobility and in turn improve stability [7, 8].

Y. Hurtado · D. López · F. B. Cortés (✉) · C. A. Franco (✉)
Grupo de Investigación en Fenómenos de Superficie–Michael Polanyi, Departamento de Química y Petróleos, Facultad de Minas, Universidad Nacional de Colombia Sede Medellín, Medellín, Colombia
e-mail: yvhurtadoc@unal.edu.co; dalopezsu@unal.edu.co; fbcortes@unal.edu.co; caafrancoar@unal.edu.co

S. H. Lopera
Grupo de Investigación en Yacimientos de Hidrocarburos, Departamento de Química y Petróleos, Facultad de Minas, Universidad Nacional de Colombia Sede Medellín, Medellín, Colombia
e-mail: shlopera@unal.edu.co

N. N. Nassar et al. (eds.), *Nanoparticles: An Emerging Technology for Oil Production and Processing Applications*, Lecture Notes in Nanoscale Science and Technology, https://doi.org/10.1007/978-3-319-12051-5_9

One of the strategies used to increase foam stability is reinforcing its structure with nanoparticles [2, 9–27] to prevent or mitigate two of the factors causing foam instability: gas diffusion between bubbles and the drainage of the liquid phase [9, 10]. Silica nanoparticles have shown great versatility in EOR processes because they remain well-dispersed in brines and decrease the surface tension between reservoir fluids [28–30]. In the foam system, nanoparticles locate at the gas-liquid interface of each bubble, so they must have a specific wettability that can be acquired by surfactant adsorption on the nanoparticle surface or surface modifications during the synthesis process [9, 11, 15, 16, 31]. Therefore, the interactions between surfactant molecules and nanoparticles play an essential role in foam stability [11, 16, 31, 32]. According to the literature, the mechanisms of surfactant-nanoparticle interactions depend on surfactant type and nanoparticle characteristics [24, 25, 31, 33]. In the case of oxide nanoparticles, such as silica, and anionic surfactants, such as alpha olefin sulfonates (AOSs), it is suggested that the adsorption is promoted by opposite charges between the interacting species [33], although the adsorption of surfactant and nanoparticles of similar charges is possible due to the presence of dissolved ions at appropriate pH [34–36]. The adsorption process leads to a partition of the adsorbed surfactant from the fluid to the nanoparticle surface, so only the free surfactant can promote bubble formation. Hence, the amount of nanoparticles in the foam solution determines not only the stability but also the formation of foam bubbles [14, 16]. The decrease in the interfacial tension between the liquid and gaseous phases is attributed to the surfactant in aqueous solution, which generates foam. Simultaneously, the surfactant adsorbed on nanoparticles allows them to remain in colloidal suspension and improves their wettability so that they can suspend at the air-liquid interface [25, 37, 38]. Therefore, both surfactant and nanoparticle concentrations affect foam stability [16]. Thus, studying surfactant-nanoparticle interfacial interactions could help in determining the concentrations of nanoparticles and surfactant in the foam solution to promote highly stable foams [16]. Although some studies showed the benefits of using nanoparticles to stabilize foams [15, 37, 39, 40], complex interaction mechanisms between nanoparticles and surfactants and optimal nanoparticle and surfactant concentrations to improve foam stability have not been investigated. In this work, we extended our previous work on natural gas foams stabilized with silica nanoparticles and investigated how surfactant adsorption to nanoparticles affects foam stability. The effect of nanoparticle concentration on the wettability and availability of surfactant at the gas-liquid interface was also evaluated.

9.2 Foam Injection in EOR Processes

Based on the co-injection of a large amount of gas into a surfactant solution to generate a gas bubble system surrounded by a thin liquid film called lamellae, the foam injection has been extensively developed to overcome gas injection drawbacks [41–43]. Since 1958, when Boud and Holbrook patented their foam injection technique

[44], several academic and industrial works have been reported [43, 45] for EOR applications. In general, the foam injection mechanism relies on macroscopic and microscopic factors that provide advantages over other EOR methods [43]. In particular, a system composed of gas bubbles in a liquid film provides higher apparent viscosity in comparison with a single gas system, improving the macroscopic sweep efficiency [45]. Due to the presence of surfactant compounds in the gas bubble-fluid system, the contact between the displacement fluid with the reservoir fluids promotes the reduction of the interfacial tension between the oil and water phases, reducing capillary forces at the pore level and promoting the mobilization of the trapped residual oil [46, 47]. Thus, the applicability of foams becomes attractive in the oil and gas industry, where traditional flooding becomes challenging, especially in low-permeability and/or high-temperature reservoirs [48].

Several variables, such as reservoir conditions, surfactant type, adsorption capability of the surfactant onto the rock surface, rock surface mineralogy, wettability, and petrophysical properties of oil and water phases, influence foam generation [6]. Due to their metastable nature at reservoir conditions, foams begin to coalesce when the liquid solution drains from the lamellae, reducing its thickness and increasing the capillary pressure of the system [42]. In general, pressure increases foam stability due to higher miscibility of surfactant compounds in the gaseous phase; however, the temperature increase reduces surfactant solubility in the brine and improves its degradation [6]. Besides, many studies show the detrimental effect of reservoir fluids in foam stability, whereas the reservoir brine could affect electrostatic double-layer forces, promoting the break of the foam [49]. The dispersion of oil droplets into the gas bubble system acts as an antifoaming agent via the promotion of a new interface and, thus, the realignment of surfactant compounds within interfaces [50]. Besides, foams could remain stable if a pseudo-emulsion within the oil phase and the liquid film is created [47]. However, the most important parameters for foam stability are the nature of the surfactant, its concentration in the foam solution, and its interactions with the reservoir fluids and rock surface. Surfactant molecules act as a surface-active agent that modifies interfacial forces within the liquid and gaseous phases, enhancing bubble formation and stability. However, surfactant adsorption onto the rock surface leads to a loss of the surfactant and its subsequent reduction in the foam solution. Hence, a reduction in the available surface-active agents adsorbed onto the air-water interface decreases the stabilization of foam lamellae, suggesting that the effectiveness of foam injection depends on the selection of the most suitable surfactant that can lead to high foam stability but possesses low adsorption affinity to the rock surface in reservoir conditions.

Surfactant adsorption onto the rock surface constitutes an important concern for EOR because the reduction in the available surface-active agents adsorbed onto gas-liquid interface decreases the stabilization of foam lamellae [34]. In comparison with cationic surfactants, nonionic and anionic surfactants are currently used as foaming agents, such as AOS and sodium dodecyl sulfate (SDS), due to its low adsorption rate. According to several investigations, foam stability is enhanced with the increase in surfactant concentration; however, foam stability is maximized at a threshold concentration [51]. In the presence of different salts, this threshold

concentration and foam stability are affected due to the modification of electrostatic forces in the aqueous solution [51, 52]. Selecting surfactant dosage without considering reservoir fluid interactions and the adsorption of the surfactant onto the rock surface leads to the underestimation of the initial surfactant concentration for foam stabilization [34]. Commonly, nanoparticles have been applied to foam solutions due to the capacity of nanomaterials to migrate to the gas-liquid interface, blocking gas diffusion and liquid drainage [10, 53–55]. However, although the nanomaterials reinforce the bubble structure, they can act as a carrying agent of adsorbed surfactant molecules from the bulk surface to the gas-liquid interface, inhibiting the surfactant adsorption onto the rock surface, increasing the number of surface-active molecules in the interface, and thus enhancing the foam stability. Consequently, the effects of surfactant-nanoparticle interactions on foam stability have been overlooked. We performed a comprehensive study on the interfacial interactions at the nanoparticle surface between nanoparticles and adsorbed surfactants to determine the effects of nanoparticle surface properties on foam stability and surfactant adsorption.

9.3 Nanoparticles for Natural Gas Foam Stability

Nanoparticle-surfactant mixtures have been applied to stabilize emulsions and foams for various applications in the gas and oil industry [24]. For example, the incorporation of nanoparticles in foam systems improved oil recovery up to 64% and reduced the mobilization of the injected gas, showing promising solutions for foam injection in EOR operations. Foam stability depends on several surface and morphological properties of nanoparticles, such as size, shape, surface wettability, interactions with the foaming agent, and concentration in the foam solution [55]. The main mechanism of gas diffusion blockage and liquid drainage is related to the adsorption and accumulation of nanoparticles at the gas-liquid interface, leading to the following three main modes proposed by Horozov [56]: (1) bridging particles, (2) a close-packed particles, and (3) a network of particle aggregates. However, because of the nature of most metal oxide nanoparticles, a reversible adsorption of the nanoparticles on the gas-liquid interface is expected, affecting foam stability [53] Besides, an amphiphilic surface nature is required to promote nanoparticle migration from the bulk surface and the attachment to the gas-liquid interface [15, 53, 57].

In general, hydrophobic and modified hydrophilic nanoparticles with adsorbed amphiphilic molecules are currently used to enhance foam stability, including foam agents used for bubble formation [24, 35, 53, 57, 58]. Yu et al. [59] evaluated CO_2 foams in water stabilized by silica nanoparticles with varying hydrophobicity and showed that nanoparticles with moderate wettability (i.e., contact angle near 60°) showed the most stable foam. However, nanoparticles chemically modified with hydrophobic compounds lead to poor dispersion and can increase the operating cost with a relatively low increase in foam stability [24]. According to several studies,

the adsorption of amphiphilic molecules such as foam agents on the nanoparticle surface provides better insights into increased foam stability [36, 58, 60]. The orientation away from the nanoparticle surface of the chain side of the amphiphilic molecule modifies surface wettability, increasing the amphiphilic behavior of the nanoparticle due to the presence of polar and nonpolar functional groups around the nanoparticle surface. Based on the interactions between the surfactant and nanoparticle, the surface wettability of the nanoparticle after the adsorption process and thus the capacity of the nanoparticle to migrate and locate onto the gas-liquid interface are modified. Although several types of nanoparticles, such as SiO_2, Al_2O_3, and $CaCO_3$, and surfactant, such as AOS, SDS, hexadecyl trimethyl ammonium bromide, and sodium dodecylbenzene sulfonate, have been evaluated, there remain some concerns related to the influences of the adsorbed surfactant in the foam stability via the mobilization of nanoparticles from the bulk to the gas-liquid interface and possible synergistic effect between the adsorbed and non-adsorbed surfactant molecules at the interface [16, 24, 34, 42, 43, 49, 53, 55, 57, 58, 60]. Based on our previous work where silica nanoparticles were used to study the effects of surface acidity and polarity [16], in this work, we aimed to determine the role of the adsorbed and non-adsorbed surfactant molecules in the enhancement of foam stability in the presence of silica nanoparticles with various net surface charges using AOS as the foaming agent.

9.4 Materials and Methods

9.4.1 Materials

SiO_2 nanoparticles purchased from Sigma Aldrich (St. Louis, Missouri, United States) were subjected to several surface modifications to determine the effects of acidity and polarity on the interactions with the surfactant. A certain amount of the nanomaterial was subjected to the acidification (SiO_2/A) and basification (SiO_2/B) processes, and one was grafted with petroleum vacuum residue (SiO_2/VR), while another was left unmodified. The synthesis procedure was detailed in our previous work [16]. The samples were characterized using an Autosorb-1 (Quantachrome Instruments, Boynton Beach, United States) device to estimate the surface area (SBET) by nitrogen adsorption isotherms at −196 °C. The NanoPlus-3 (Micromeritics, GA, 183 United States) device was used for hydrodynamic diameter (dp_{50}) and ζ potential measurements at pH 7. Finally, the total surface acidity was obtained using the temperature-programmed desorption method (TPD-NH_3) in a ChemBET/TPD (Quantachrome Instruments, Boynton Beach, United States).

The foam solution (surfactant P) composed mainly by AOS compounds as the active agent was purchased from Nalco S.A. (Bogota, Colombia) and used as received. Based on the absorbance measurements of surfactant solutions in a GENESYS™ 10S UV-Vis spectrophotometer (Thermo Scientific, Waltham, MA,

USA), the critical micelle concentration (CMC) in deionized water was close to 2000 mg•L^{-1}. At this concentration, it was found that the size of the surfactant P micelles was 18 nm. The natural gas injected for foam generation involved methane (93.5 wt.%) and a low-molecular-weight hydrocarbon (6.5 wt.%). Finally, a representative synthetic brine of a tight gas condensate reservoir, composed of NaCl, $CaCl_2$, $MgCl_2 \cdot 6H_2O$, KCl, and $BaCl_2 \cdot 2H_2O$, was employed in nanofluid preparation.

9.4.2 Methods

9.4.2.1 Nanofluid Preparation

In preparing foam nanofluid, a known mass of nanoparticles was added into the brine solution with a certain concentration of surfactant P. After the incorporation of nanoparticles, the dispersion was stirred for 2 h at 600 rpm using a magnetic stirrer (Cimarec Digital Stirring Hot Plate, Thermo Scientific) and then sonicated for 30 min at room temperature in an ultrasound probe (Elmasonic E 60 H, Elma Schmidbauer GmbH) using 37-kHz ultrasonic frequency. To ensure proper nanoparticle dispersion, nanoparticle aggregation kinetics before and after the ultrasound process was determined.

9.4.2.2 Surfactant Adsorption Experiments

Surfactant batch adsorption was conducted using a fixed surfactant concentration of 1000 mg•L^{-1} and nanoparticle dosages from 0.5 to 5 g•L^{-1}. The surfactant solution was prepared in brine; then, the nanoparticles were added. The mixture was stirred for 2 h at 600 rpm and left to stand for 12 h to ensure that the adsorption equilibrium was reached. The ultrasound was omitted for the nanoparticles to precipitate faster. Then, the mixtures were centrifuged, and the obtained precipitate was dried at room temperature. About 5 mg precipitate was used to perform the thermogravimetric analyses using a thermogravimetric analyzer (TGA Q50, TA Instruments). The sample was heated in an air atmosphere (flow rate, 100 mL•min^{-1}) from 30 to 800 °C at a rate of 5 °C•min^{-1}. The thermogravimetric test was also performed on virgin nanoparticles as a control. The difference in weight loss accounted for the adsorbed surfactants on the nanoparticle surface, Q (milligrams of surfactant per gram of nanoparticle, mg•g^{-1}), and the equilibrium concentration, C_E (mg•L^{-1}), was the amount of surfactant that was not adsorbed and remained free in solution. Both Q and C_E were estimated based on the TGA results and the following mass balance [61–63]:

$$Q = \left(C_i - C_E\right)\frac{V}{M} \tag{9.1}$$

where C_i (mg•L^{-1}) is the initial concentration of surfactant P, V (L) is the surfactant solution volume, and M (g) is the nanoparticle dosage. All tests were performed at least three times to confirm repeatability and calculate standard deviations. The standard deviations for all measurements did not exceed 54.3 mg·L^{-1}.

9.4.2.3 Foam Stability Tests

Foam stability in the absence and presence of nanoparticles was evaluated by placing a 10 mL of surfactant solution or nanofluid in a graduated glass concentric cylinder. In the internal cylinder, the foam was generated by the injection of 4.0 L•min^{-1} natural gas through a porous disk located at the bottom of the cylinder. The employed experimental setup is shown in Fig. 9.1. When the foam reached the top of the column, the gas injection was stopped. Hot water (70 °C) was circulated through the outer cylinder for temperature control [37]. The foam height was recorded as a function of time. The half-life, the time passed until 50% of the foam remained in the column, was taken as an indication of stability.

9.4.2.4 Foam Flooding Test

Based on a typical low-permeability gas condensate reservoir, natural gas flooding was conducted in the presence of surfactant P solutions at 1000 mg·L^{-1} in the absence and presence of nanoparticles to obtain oil recovery curves after foam

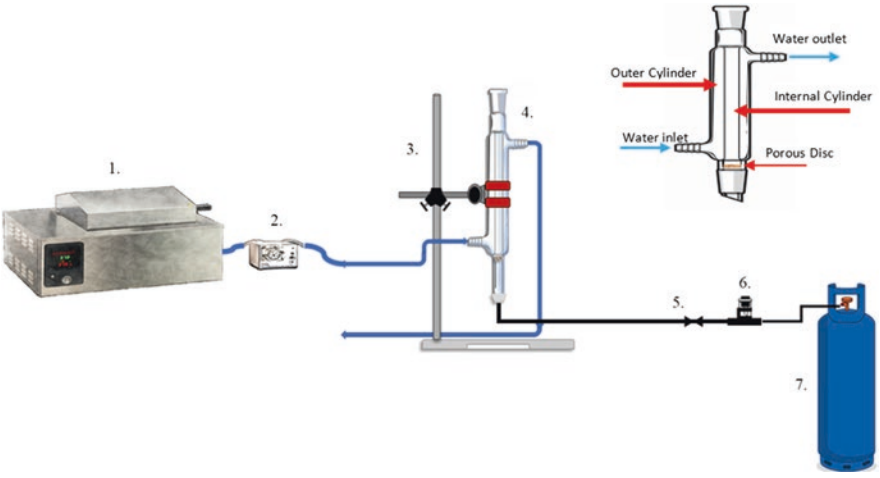

Fig. 9.1 Schematic representation of the experimental setup to perform foam stability tests in the absence and presence of nanoparticles. Flow rate, 4.0 L•min^{-1}; temperature, 70 °C. 1, Hot water bath; 2, peristaltic pump; 3, universal support; 4, graduated concentric cylinder with a porous disk at the bottom; 5, check valve; 6, flow regulator; 7, nitrogen tank

Table 9.1 Mean hydrodynamic diameter (dp50), surface area (SBET), ζ potential at pH 7 (ζ), and total surface acidity values of SiO_2 nanoparticles

Material	dp50 (nm)	SBET ($m^2 \cdot g^{-1}$)	ζ (mV)	Total acidity ($mmol \bullet g^{-1}$)
SiO_2	11	389.0	−23.6	2.16
SiO_2A	42	255.7	−19.7	2.85
SiO_2B	82	91.1	−17.7	1.51
SiO_2VR[a]	109	250.8	−18.9	0.31

[a]The nanoparticles were estimated in a mass fraction of 3.7% through thermogravimetric analyses [16]

injection. The test was conducted at a reservoir temperature of 212°F and pore and confining pressures of 35.85 and 8.27 MPa, respectively. A sandstone core with 7% porosity and 65.1 mD absolute permeability was used. Further information and additional tests can be found in our previous work [16].

9.5 Results

9.5.1 Nanoparticle Characterization

The nanoparticle characterization is summarized in Table 9.1. The findings showed that the nanoparticles without any surface modification exhibited an SBET of 389 $m^2 \cdot g^{-1}$, a hydrodynamic diameter of 11 nm, and a total acidity of 216 $mmol \bullet g^{-1}$. Also, in aqueous solutions at pH 7, the nanoparticles remained stable due to the high magnitude of the ζ potential of the nanoparticles. The surface modification of the SiO_2 nanoparticles led to the redistribution of surface atoms, promoting the aggregation of nanomaterials. This generates an increase in the hydrodynamic diameter, a decrease in the surface area, and the modification of acidic sites [30]. Modified nanoparticles had SBET values between 90 and 250 $m^2 \cdot g^{-1}$, hydrodynamic diameters from 40 to 110 nm, and surface total acidities between 0.3 and 2.85. The ζ potential values after the modification process decreased based on surface modification type. The reduction in the ζ potential value for the modified nanoparticles suggests a low increase in hydrophobicity degree [24], whereas SiO_2/VR showed the highest hydrophobicity. However, at pH 7, all nanoparticles remained dispersed in the aqueous bulk phase.

9.5.2 Surfactant Adsorption

Figure 9.2 shows the free surfactant concentration after the adsorption process onto SiO_2, SiO_2/A, SiO_2/B, and SiO_2/VR as a function of dosage. From Fig. 9.2, it can be observed that the surfactant concentration in nanofluids after adsorption equilibrium

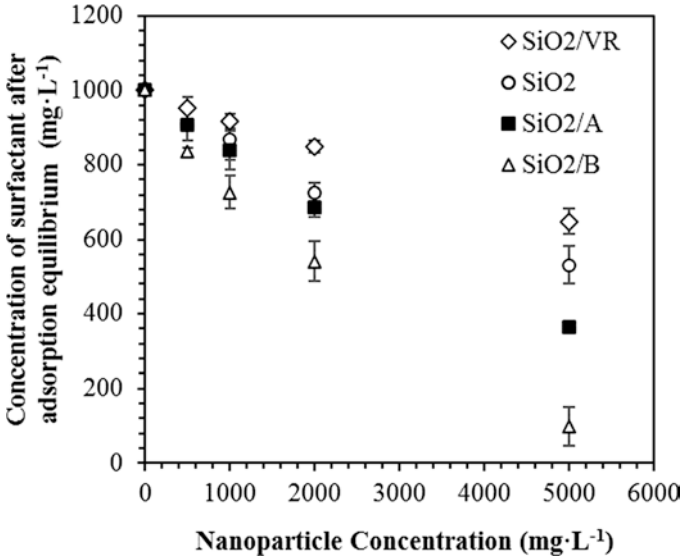

Fig. 9.2 Surfactant P concentration in solution after adsorption onto SiO_2, SiO_2/A, SiO_2/B, and SiO_2/VR nanoparticles for dosages of 500 mg•L^{-1}, 1000 mg•L^{-1}, 2000 mg•L^{-1}, and 5000 mg•L^{-1}, respectively. Surfactant initial concentration = 1000 mg•L^{-1}; stirring rate = 600 rpm; temperature = 25 °C

was reached decreases as the nanoparticle dosage increases. SiO_2/B and SiO_2/VR are the ones that have the widest gap when it comes to surfactant after adsorption equilibrium (C_E). In this sense, the amount of surfactant adsorbed is higher for SiO_2/B than that for SiO_2/VR, where the free surfactant in brine solutions at the highest nanoparticle dosage was reduced by 35.1%, 46.8%, 63.4%, and 90.2% for SiO_2/VR, SiO_2, SiO_2/A, and SiO_2/B systems, respectively, suggesting that the surface characteristics of the nanoparticles determine surfactant adsorption in the system. Currently, AOS compounds act as an anionic surfactant with a polar side mainly composed of the sulfonate functional group (SO_3^-) and a hydrocarbon chain with a length in the range of C_{12}–C_{18} as the nonpolar side in the surfactant structure [64, 65]. Considering that the adsorption experiments were conducted below the CMC value of surfactant P, surfactant monomers would interact with the nanoparticle surface based on their affinity to polar/nonpolar functional groups on the surface of the nanoparticles. In general, the acidification and basification processes alter the electrostatic forces of the nanoparticle due to changes in the amount of silanol (Si–OH) and siloxane (O–Si–O) functional groups exposed to the surface of the nanomaterial [16, 30, 66, 67]. Based on the obtained ζ potential values, these processes reduce surface negative charges (i.e., the net charge of the nanoparticles), supporting the interaction between the sulfonate group of surfactant P and SiO_2/B and SiO_2/A. Thus, inferring that the net surface charge of the nanoparticles determines the presence of feasible electrostatic interactions between the adsorbate and adsorbent is possible [24]. However, this adsorption mechanism was not observed

in the presence of SiO_2/VR. Vacuum residue used to modify the surface of the nanoparticles is mainly composed of the heavy components of the crude oil, which promotes the attachment of several hydrocarbon fractions onto the SiO_2 surface, increasing its hydrophobicity [57]. In that case, surfactant P could migrate to the nanoparticle surface due to the alignment of the chain side via weak interaction forces, such as hydrogen bonds and London forces. These weak forces reduce the adsorption strength of surfactant P on SiO_2/VR, leading to high surfactant concentration in the brine solutions, as shown in Fig. 9.2.

The adsorption of surfactant P onto silica nanoparticles changes surface wettability due to the orientation and subsequent alignment of surfactant molecules on the nanoparticle surface [11]. Figure 9.3 shows a schematic representation of the surface of the nanoparticles in the presence and absence of surfactant P for SiO_2 and SiO_2/VR. Once the adsorption process was complete, the nanoparticles had the appropriate wettability to position themselves at the interface and slowed down the gas diffusion between bubbles and the thinning of the lamella by the liquid drainage [15, 57].

Further, the stability of the foam is governed by two mechanisms: reduction in interfacial tension between gas and aqueous phases and reduction in interbubble gas diffusion. When the foam is being generated, the main mechanism stabilizing the foam is the reduction in interfacial tension; consequently, a high C_E can lead to enhanced foam stability. Over time, the disproportionation of gas bubbles, or the change in the diameter of bubbles caused by the gas diffusion between them, leads to the disappearance of bubbles with small diameters and becomes the main stabilization mechanism. The nanoparticles that migrate to the interface due to the change in wettability granted by the surfactant must combat the second mechanism of foam destabilization. The nanoparticles at the interface can act as a solid membrane in the lamella and decrease the gas diffusion and liquid drainage between bubbles, reducing their coalescence and increasing foam stability [25, 37, 39, 68–71].

9.5.3 Foam Stability

Figure 9.4 shows foam height as a function of time. The foam was generated by injecting natural gas to the column containing brine solutions with 1000 mg•L^{-1} surfactant P and nanoparticles at 500, 1000, 2000, and 5000 mg•L^{-1}. During the test, the temperature was maintained at 70 °C. The partition coefficient of the surfactant in the nanofluid depends on the nanoparticle nature, where part of the surfactant is free in the solution to promote the formation of bubbles and the rest is adsorbed on the surface of the nanoparticles, encouraging stabilization of the foam by the migration of the nanomaterials to the interface of the bubbles. If the nanoparticles do not become partially hydrophobic by surfactant adsorption, they remain in the liquid face and eventually locate in the plateau borders of the bubbles, slowing down the liquid drainage of the lamella. The fluids containing SiO_2/B and SiO_2/VR have a better performance at a concentration of 500 mg•L^{-1}, indicating enhanced

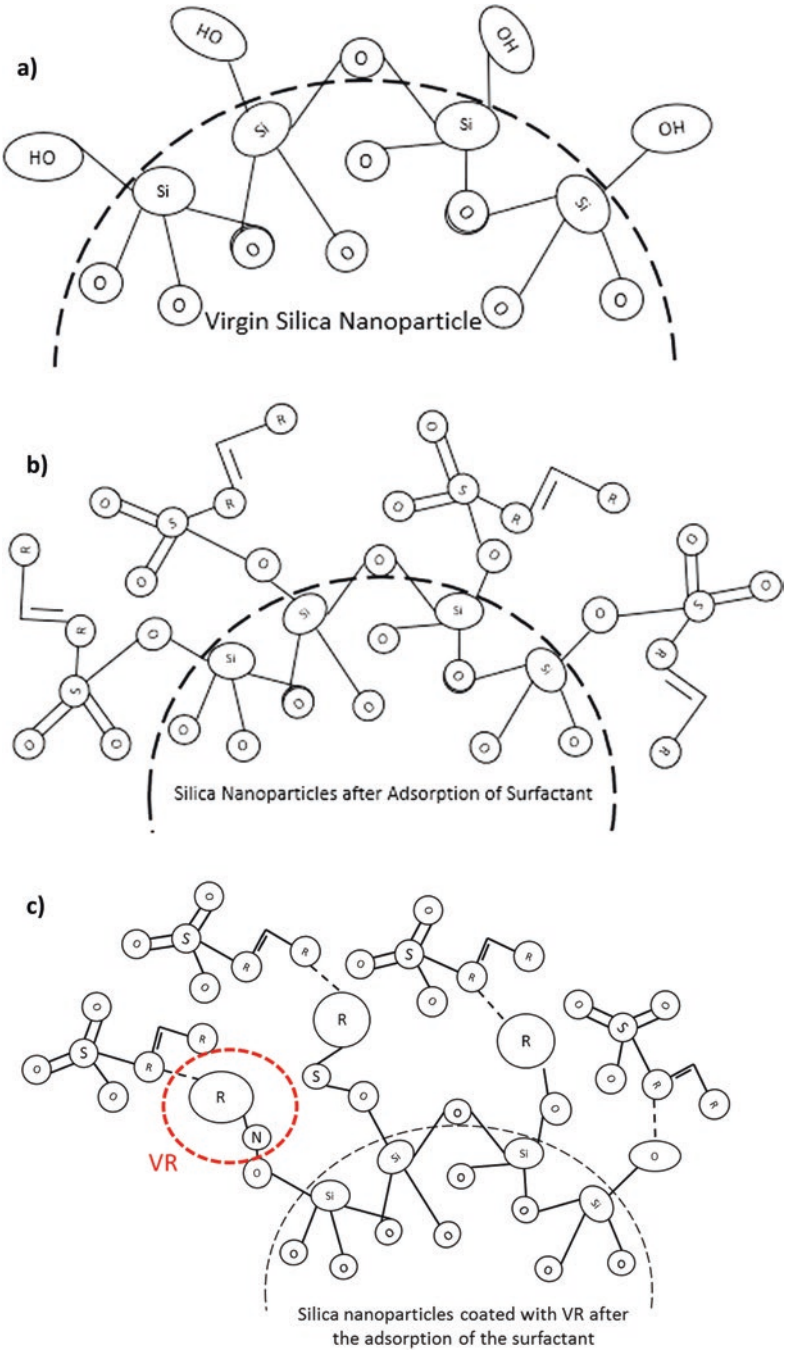

Fig. 9.3 Schematic representation of surfactant P alignment on SiO_2 nanoparticles after the adsorption process. (**a**) SiO_2 in the absence of the adsorbed surfactant, (**b**) SiO_2 in the presence of the adsorbed surfactant, and (**c**) SiO_2 coated with vacuum residue (VR) in the presence of the adsorbed surfactant

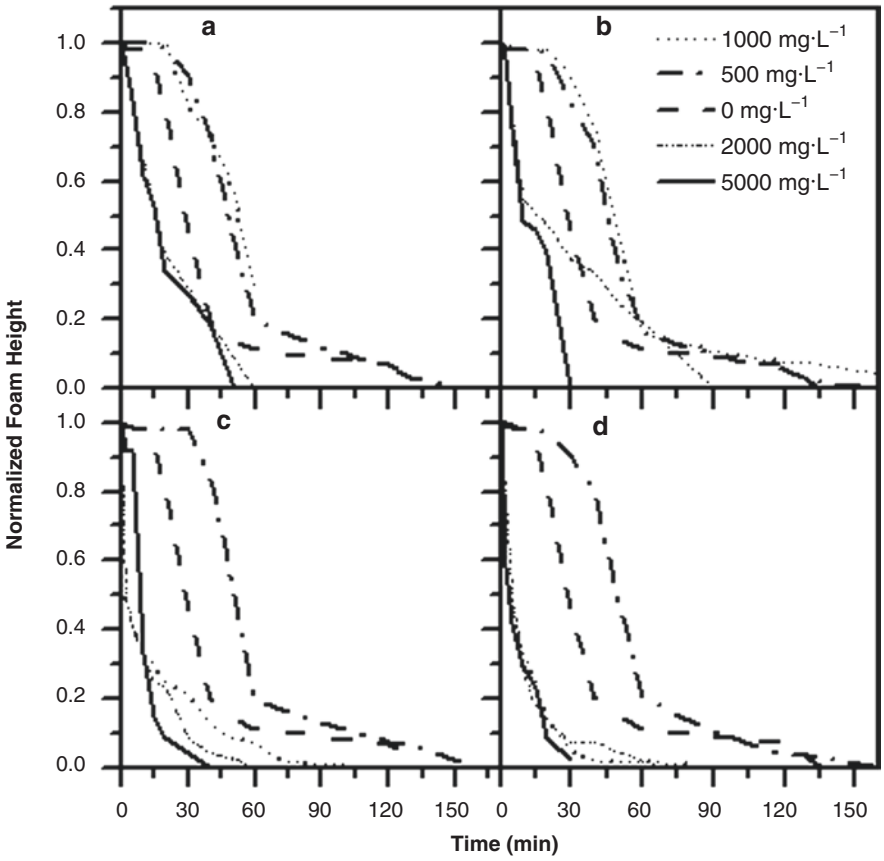

Fig. 9.4 Stability tests of foams generated by natural gas injection using AOS (surfactant P) with and without (**a**) SiO_2, (**b**) SiO_2A, (**c**) SiO_2B, and (**d**) SiO_2VR nanoparticles. Natural gas flow, 4 L•min^{-1}; temperature, 70 °C

foam stability (half-life) of 63% and 70%, respectively. The foam stabilization in the presence of nanoparticles depends on the interactions within the surfactant compound, nanoparticle size, shape, concentration, and surface wettability [41]. In this sense, the induction of a more oil-wet surface due to the high adsorption amount displayed by SiO_2/B improves the alignment of these nanoparticles in the bubble, thereby increasing the stability of the foam by decreasing gas diffusion. For the case of SiO_2/VR, the inherent hydrophobicity of these nanoparticles due to the presence of heavy oil fractions on its surface increases the foam stability due to a feasible alignment of the nanoparticles in the gas-liquid interface. Therefore, the foam stabilization due to the nanoparticles occurring at low concentrations for SiO_2/B and SiO_2/VR is because they have a higher degree of hydrophobicity than other materials [16]. However, for concentrations above 500 mg•L^{-1}, there is a drastic reduction

in foam height for samples containing SiO_2/B and SiO_2/VR. As the concentration of the nanoparticles increases, interactions with the surfactant molecules at the nanoparticle surface increase, leading to a competition for surfactant between the fluid bulk and the surface of the nanoparticles. When an adequate proportion of surfactant is reached, achieving improved foam stability is possible. If nanoparticle concentration exceeds that equilibrium point, the durability of the foam is negatively affected as there is not enough surfactant to decrease the interfacial tension between the gas and liquid at the bubble interface [11, 31]. As the concentration of nanoparticles increases, the partition coefficient in the nanofluid varies. The free surfactant migrates from the fluid bulk to the nanoparticle surface; consequently, there is less surfactant available to form the bubbles; thus, the first mechanism of foam stabilization is negatively affected. Besides, nanofluids containing SiO_2 and SiO_2/A generate a more stable foam at a higher concentration of nanoparticles (1000 mg•L^{-1}) because the partition coefficient of the surfactant in the nanofluid is affected by the affinity between nanoparticles and surfactants.

Figure 9.5 shows foam half-life as a function of nanoparticle concentration for each nanofluid. The half-life of the foam first increases with increasing nanoparticle concentration until it reaches a maximum value. From that point forward, the foam half-life drastically diminishes. This behavior is congruent with the two abovementioned mechanisms of foam stabilization. In the absence of nanoparticles, foam stability depends only on the reduction in interfacial tension due to the presence of the surfactant. In the presence of nanoparticles, foam stability depends on the reduction in gas diffusion and liquid drainage in the lamellae that decrease the coalescence of the bubbles. The reduction in coalescence is, therefore, the result of the

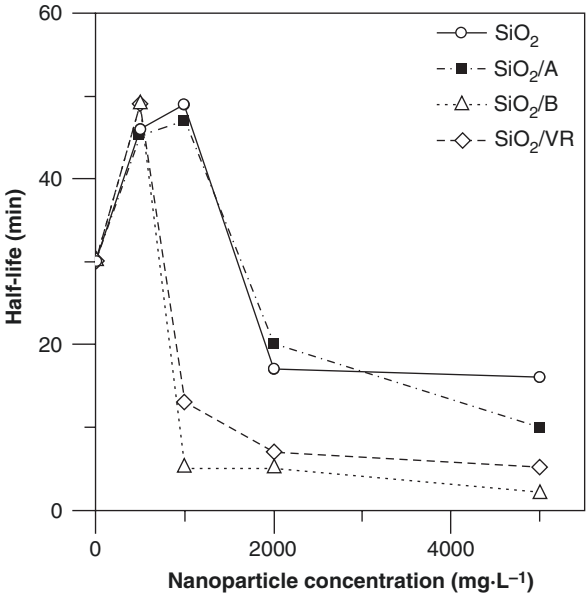

Fig. 9.5 Foam half-life as a function of nanoparticle concentration. Foams are generated by natural gas injection into aqueous solutions of AOS (surfactant P) with and without SiO_2, SiO_2/A, SiO_2/B, and SiO_2/VR nanoparticles. Natural gas flow, 4 L•min^{-1}; temperature, 70 °C

nanoparticles with adequate wettability being positioned at the interface. However, if the concentration of nanoparticles is too high, the first mechanism of foam stabilization is affected, and the foam half-life decreases due to the low concentration of free surfactant in the brine solution [24, 31]. Finally, the maximum point changes with the nature of the nanoparticle. The nanofluids with SiO_2/B and SiO_2/VR reach their maximum points at lower concentrations than those with SiO_2 and SiO_2/A, showing that the surface wettability and surfactant-nanoparticle interactions play a vital role in the half-life of the foam.

9.5.4 Foam Flooding Test

The foam stability results showed that SiO_2/B and SiO_2/VR demonstrate higher foam stability at the lowest nanoparticle dosage, suggesting that the wetting character of the nanomaterial before and after surfactant adsorption plays an important role in foam stability. Considering that high surfactant adsorption could prevent the loss of surface-active compounds in the porous media and thus enhance the foam flooding process, surfactant P solutions in the absence and presence of SiO_2/B were evaluated in reservoir conditions for crude oil recovery. Natural gas displacement was first conducted to ensure the preferential flow channels in the porous media. Figure 9.6 shows the oil recovery curves during the foam flooding test. The increase in the foam stability improves the blockage of the preferential channels in the porous media, thereby allowing a better sweep of the noncontacted zones and improved oil recovery [16, 34, 53, 56, 69, 72, 73].

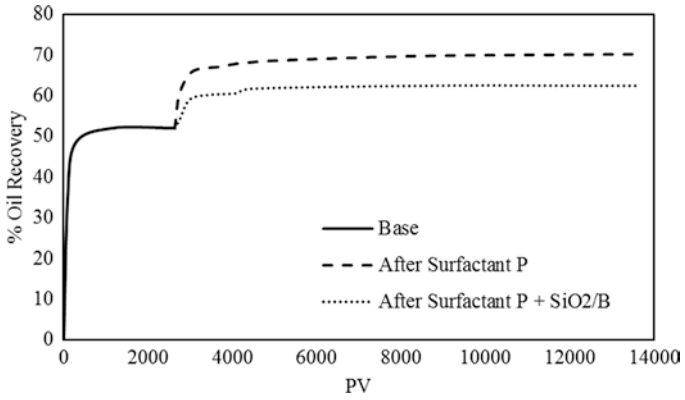

Fig. 9.6 Oil recovery curves for natural gas flooding (base) and foam flooding after surfactant P in the absence and presence of SiO_2/B. (Reproduced from Hurtado et al. [16] with permission)

9.6 Conclusions

Incorporating nanoparticles in foam solutions increases foam stability due to the alignment of nanomaterials at the bubble-fluid interface, avoiding the liquid drainage of the lamella and reducing the interbubble gas diffusion. However, the effectiveness of foam stability improvement is determined by the adsorption affinity of surfactant P to the nanoparticle surface. The orientation and subsequent alignment of surfactant molecules on the nanoparticle surface change surface wettability, where the exposed chain side of AOS increases the hydrophobicity of the nanoparticles and enhances nanoparticle migration to the gas-liquid interface. The adsorption of surfactant P on the nanoparticles reduces the surfactant concentration in the brine solutions to 35.1% for SiO_2/VR and 90.2% for SiO_2/B, which means that less surfactant is available to reduce interfacial tension and promote bubble formation. Thus, high surfactant adsorption leads to a low concentration of surfactant P in the brine solution, affecting foam stability.

The results revealed that the modification of surface wettability of nanoparticles after the adsorption process and the alignment of the adsorbed surfactant molecules once the nanoparticles are located in the gas-liquid interface determine foam stability and low surfactant adsorption onto the nanoparticle surface implies high nanoparticle dosage. Besides, the results showed that negative charges in the SiO_2 surface must be reduced to enhance AOS adsorption by promoting surface wettability and enhanced migration from the bulk phase to the interface. Besides, foam stability depends on the synergy between the surface wettability of the nanoparticles and the ability of the free surfactant to decrease the interfacial tension of the bubbles. For this reason, a comprehensive analysis must be conducted to obtain the most feasible nanoparticle dosage based on the nanoparticle nature, interactions between the nanomaterials and surfactant, and the effect of the nanoparticle-surfactant system on the bubble stability. This work sheds light on the effects of nanoparticle surface wettability and surfactant concentration on foam stability for EOR.

Acknowledgments The authors acknowledge COLCIENCIAS, ANH, and Universidad Nacional de Colombia for their support provided through the agreement 272-2017.

References

1. E.J. Manrique et al., EOR: current status and opportunities, in *SPE Improved Oil Recovery Symposium*, (Society of Petroleum Engineers, 2010)
2. N. Yekeen et al., A comprehensive review of experimental studies of nanoparticles-stabilized foam for enhanced oil recovery. J. Pet. Sci. Eng. **164**, 43–74 (2018)
3. Q.P. Nguyen, A.V. Alexandrov, P.L. Zitha, P.K. Currie, Experimental and modeling studies on foam in porous media: a review. Formation Damage \ldots (2000)
4. J. Yu, C. An, D. Mo, N. Liu, R.L. Lee, Foam mobility control for nanoparticle-stabilized supercritical CO2 foam, in *SPE Improved Oil Recovery Symposium*, (Society of Petroleum Engineers, 2012)

5. Z.F. Zhang, V.L. Freedman, L. Zhong, *Foam Transport in Porous Media-A Review* (Pacific Northwest National Lab (PNNL), Richland, 2009)
6. S.A. Farzaneh, M. Sohrabi, A review of the status of foam application in enhanced oil recovery, in *EAGE Annual Conference & Exhibition Incorporating SPE Europec*, (Society of Petroleum Engineers, 2013)
7. Z. Derikvand, M. Riazi, Experimental investigation of a novel foam formulation to improve foam quality. J. Mol. Liq. **224**, 1311–1318 (2016)
8. A. Cuenca, E. Lacombe, M. Chabert, M. Morvan, E. Delamaide, Enhanced viscosity formulations for steam foam applications: impact on performances in bulk and porous media, in *SPE Canada Heavy Oil Technical Conference*, (Society of Petroleum Engineers, 2015)
9. B.P. Binks, Particles as surfactants—Similarities and differences. Curr. Opin. Colloid Interface Sci. **7**(1–2), 21–41 (2002)
10. B.P. Binks, T.S. Horozov, Aqueous foams stabilized solely by silica nanoparticles. Angew. Chem. Int. Ed. **44**(24), 3722–3725 (2005)
11. Z.-G. Cui, Y.-Z. Cui, C.-F. Cui, Z. Chen, B. Binks, Aqueous foams stabilized by in situ surface activation of CaCO3 nanoparticles via adsorption of anionic surfactant. Langmuir **26**(15), 12567–12574 (2010)
12. D.A. Espinoza, F.M. Caldelas, K.P. Johnston, S.L. Bryant, C. Huh, Nanoparticle-stabilized supercritical CO2 foams for potential mobility control applications, in *SPE Improved Oil Recovery Symposium*, (Society of Petroleum Engineers, 2010)
13. M.F. Fakoya, S.N. Shah, Emergence of nanotechnology in the oil and gas industry: emphasis on the application of silica nanoparticles. Petroleum (2017)
14. F. Guo, S. Aryana, An experimental investigation of nanoparticle-stabilized CO 2 foam used in enhanced oil recovery. Fuel **186**, 430–442 (2016)
15. T.N. Hunter, R.J. Pugh, G.V. Franks, G.J. Jameson, The role of particles in stabilising foams and emulsions. Adv. Colloid Interf. Sci. **137**(2), 57–81 (2008)
16. Y. Hurtado et al., Effects of surface acidity and polarity of SiO2 nanoparticles on the foam stabilization applied to natural gas flooding in tight gas-condensate reservoirs. Energy Fuel **32**(5), 5824–5833 (2018)
17. G. Kaptay, On the equation of the maximum capillary pressure induced by solid particles to stabilize emulsions and foams and on the emulsion stability diagrams. Colloids Surf. A Physicochem. Eng. Asp. **282**, 387–401 (2006)
18. M. Khajehpour, S.R. Etminan, J. Goldman, F. Wassmuth, S. Bryant, Nanoparticles as foam stabilizer for steam-foam process. SPE J. (2018)
19. D. Lee, H. Cho, J. Lee, C. Huh, K. Mohanty, Fly ash nanoparticles as a CO2 foam stabilizer. Powder Technol. **283**, 77–84 (2015)
20. R. Singh, K.K. Mohanty, Nanoparticle-stabilized foams for high-temperature, high-salinity oil reservoirs, in *SPE Annual Technical Conference and Exhibition*, (Society of Petroleum Engineers, 2017)
21. X. Sun, Y. Zhang, G. Chen, Z. Gai, Application of nanoparticles in enhanced oil recovery: a critical review of recent progress. Energies **10**(3), 345 (2017)
22. F.-Q. Tang, Z. Xiao, J.-A. Tang, L. Jiang, The effect of SiO2 particles upon stabilization of foam. J. Colloid Interface Sci. **131**(2), 498–502 (1989)
23. A. Worthen, H. Bagaria, Y. Chen, S.L. Bryant, C. Huh, K.P. Johnston, Nanoparticle stabilized carbon dioxide in water foams for enhanced oil recovery, in *SPE Improved Oil Recovery Symposium*, (Society of Petroleum Engineers, 2012)
24. W. Yang, T. Wang, Z. Fan, Q. Miao, Z. Deng, Y. Zhu, Foams stabilized by in situ-modified nanoparticles and anionic surfactants for enhanced oil recovery. Energy Fuel **31**(5), 4721–4730 (2017)
25. S. Yusuf, M. Manan, M. Jaafar, Aqueous foams stabilized by hydrophilic silica nanoparticles via in-situ physisorption of nonionic TX100 surfactant. Iran J. Energy Environ. (Special Issue on Nanotechnology) **4**(1), 08–16 (2013)

26. M. Zargartalebi, N. Barati, R. Kharrat, Influences of hydrophilic and hydrophobic silica nanoparticles on anionic surfactant properties: Interfacial and adsorption behaviors. J. Pet. Sci. Eng. **119**, 36–43 (2014)
27. D. Panahpoori, B. Dehdari, M. Riazi, R. Parsaei, Visualization experiments on the impact of surfactant and nanoparticle on EOR potential of foam injection, in *Saint Petersburg 2018*, (2018)
28. Y. Kazemzadeh, M. Sharifi, M. Riazi, H. Rezvani, M. Tabaei, Potential effects of metal oxide/SiO2 nanocomposites in EOR processes at different pressures. Colloids Surf. A Physicochem. Eng. Asp. **559**, 372–384 (2018)
29. Y. Kazemzadeh, S. Shojaei, M. Riazi, M. Sharifi, Review on application of nanoparticles for EOR purposes; a critical of the opportunities and challenges. Chin. J. Chem. Eng. (2018)
30. D. López et al., A novel design of silica-based completion nanofluids for heavy oil reservoirs. J. Petrol. Sci. Eng., 107483 (2020)
31. Y. Zhu, X. Pei, J. Jiang, Z. Cui, B.P. Binks, Responsive aqueous foams stabilized by silica nanoparticles hydrophobized in situ with a conventional surfactant. Langmuir **31**(47), 12937–12943 (2015)
32. Z. Du, M.P. Bilbao-Montoya, B.P. Binks, E. Dickinson, R. Ettelaie, B.S. Murray, Outstanding stability of particle-stabilized bubbles. Langmuir **19**(8), 3106–3108 (2003)
33. R. Zhang, P. Somasundaran, Advances in adsorption of surfactants and their mixtures at solid/solution interfaces. Adv. Colloid Interf. Sci. **123**, 213–229 (2006)
34. N. Yekeen, M.A. Manan, A.K. Idris, A.M. Samin, A.R. Risal, Experimental investigation of minimization in surfactant adsorption and improvement in surfactant-foam stability in presence of silicon dioxide and aluminum oxide nanoparticles. J. Pet. Sci. Eng. **159**, 115–134 (2017)
35. N. Yekeen, M.A. Manan, A.K. Idris, A.M. Samin, Influence of surfactant and electrolyte concentrations on surfactant adsorption and foaming characteristics. J. Pet. Sci. Eng. **149**, 612–622 (2017)
36. B.P. Binks, M. Kirkland, J.A. Rodrigues, Origin of stabilisation of aqueous foams in nanoparticle–surfactant mixtures. Soft Matter **4**(12), 2373–2382 (2008)
37. Q. Sun et al., Aqueous foam stabilized by partially hydrophobic nanoparticles in the presence of surfactant. Colloids Surf. A Physicochem. Eng. Asp. **471**, 54–64 (2015)
38. S. Zhang, D. Sun, X. Dong, C. Li, J. Xu, Aqueous foams stabilized with particles and nonionic surfactants. Colloids Surf. A Physicochem. Eng. Asp. **324**(1–3), 1–8 (2008)
39. S. Li, Z. Li, P. Wang, Experimental study of the stabilization of CO2 foam by sodium dodecyl sulfate and hydrophobic nanoparticles. Ind. Eng. Chem. Res. **55**(5), 1243–1253 (2016)
40. S. Li, C. Qiao, Z. Li, S. Wanambwa, Properties of carbon dioxide foam stabilized by hydrophilic nanoparticles and hexadecyltrimethylammonium bromide. Energy Fuel **31**(2), 1478–1488 (2017)
41. F. AttarHamed, M. Zoveidavianpoor, M. Jalilavi, The incorporation of silica nanoparticle and alpha olefin sulphonate in aqueous CO2 foam: Investigation of foaming behavior and synergistic effect. Pet. Sci. Technol. **32**(21), 2549–2558 (2014)
42. A. Bashir, A.S. Haddad, R. Rafati, Nanoparticle/polymer-enhanced alpha olefin sulfonate solution for foam generation in the presence of oil phase at high temperature conditions. Colloids Surf. A Physicochem. Eng. Asp. **582**, 123875 (2019)
43. B. Wei et al., Investigation of synergism between surface-grafted nano-cellulose and surfactants in stabilized foam injection process. Fuel **211**, 223–232 (2018)
44. D.C. Boud, O.C. Holbrook, Gas drive oil recovery process. ed: Google Patents, 1958
45. A.T. Turta, A.K. Singhal, Field foam applications in enhanced oil recovery projects: screening and design aspects. J. Can. Petrol. Technol. **41**(10) (2002)
46. T. Zhu, A. Strycker, C. Raible, K. Vineyard, Foams for mobility control and improved sweep efficiency in gas flooding, in *SPE/DOE Improved Oil Recovery Symposium*, (Society of Petroleum Engineers, 1998)
47. R. Farajzadeh, A. Andrianov, P. Zitha, Investigation of immiscible and miscible foam for enhancing oil recovery. Ind. Eng. Chem. Res. **49**(4), 1910–1919 (2010)

48. R. Hahn, K. Spilker, D. Alexis, H. Linnemeyer, T. Malik, V. Dwarakanath, Low tension foam flooding for chemical enhanced oil recovery in heterogeneous systems, in *SPE Annual Technical Conference and Exhibition*, (Society of Petroleum Engineers, 2018)
49. H. Alkan, A. Goktekin, A. Satman, A laboratory study of CO2-foam process for Bati Raman field, Turkey, in *Middle East Oil Show*, (Society of Petroleum Engineers, 1991)
50. A. Nikolov, D. Wasan, D. Huang, The effect of oil on foam stability: mechanisms and implications for oil displacement by foam in porous media. Paper SPE 15443 presented at the 61st SPE Annual Technical Conference and Exhibition, New Orleans, Los Angeles, 5–8 October. ed, 1986
51. S.A. Farzaneh, M. Sohrabi, Experimental investigation of CO2-foam stability improvement by alkaline in the presence of crude oil. Chem. Eng. Res. Des. **94**, 375–389 (2015)
52. H. Wang, J. Chen, A study on the permeability and flow behavior of surfactant foam in unconsolidated media. Environ. Earth Sci. **68**(2), 567–576 (2013)
53. R. Singh, K.K. Mohanty, Synergistic stabilization of foams by a mixture of nanoparticles and surfactants, in *SPE Improved Oil Recovery Symposium*, (Society of Petroleum Engineers, 2014)
54. B.P. Binks, T.S. Horozov, *Colloidal particles at liquid interfaces* (Cambridge University Press, 2006)
55. F. Ravera, E. Santini, G. Loglio, M. Ferrari, L. Liggieri, Effect of nanoparticles on the interfacial properties of liquid/liquid and liquid/air surface layers. J. Phys. Chem. B **110**(39), 19543–19551 (2006)
56. T.S. Horozov, Foams and foam films stabilised by solid particles. Curr. Opin. Colloid Interface Sci. **13**(3), 134–140 (2008)
57. Y. Hurtado, C.A. Franco, M. Riazi, F.B. Cortés, Improving the stability of nitrogen foams using silica nanoparticles coated with polyethylene glycol. J. Mol. Liq. **300**, 112256 (2020)
58. K.Y. Yoon, H.A. Son, S.K. Choi, J.W. Kim, W.M. Sung, H.T. Kim, Core flooding of complex nanoscale colloidal dispersions for enhanced oil recovery by in situ formation of stable oil-in-water pickering emulsions. Energy Fuel **30**(4), 2628–2635 (2016)
59. J. Yu, M. Khalil, N. Liu, R. Lee, Effect of particle hydrophobicity on CO2 foam generation and foam flow behavior in porous media. Fuel **126**, 104–108 (2014)
60. Q. Liu, S. Zhang, D. Sun, J. Xu, Foams stabilized by Laponite nanoparticles and alkylammonium bromides with different alkyl chain lengths. Colloids Surf. A Physicochem. Eng. Asp. **355**(1–3), 151–157 (2010)
61. C.A. Franco, F.B. Cortés, N.N. Nassar, Adsorptive removal of oil spill from oil-in-fresh water emulsions by hydrophobic alumina nanoparticles functionalized with petroleum vacuum residue. J. Colloid Interface Sci. **425**, 168–177 (2014)
62. C.A. Franco-Ariza, J.D. Guzmán-Calle, F.B. Cortés-Correa, Adsorption and catalytic oxidation of asphaltenes in fumed silica nanoparticles: Effect of the surface acidity. Dyna **83**(198), 171–179 (2016)
63. S. Betancur, F. Carrasco-Marín, C.A. Franco, F.B. Cortés, Development of composite materials based on the interaction between nanoparticles and surfactants for application in chemical enhanced oil recovery. Ind. Eng. Chem. Res. **57**(37), 12367–12377 (2018)
64. M.A. Abed, A. Saxena, H. Bohidar, Micellization of alpha-olefin sulfonate in aqueous solutions studied by turbidity, dynamic light scattering and viscosity measurements. Colloids Surf. A Physicochem. Eng. Asp. **233**(1–3), 181–187 (2004)
65. M. Baviere, B. Bazin, C. Noik, Surfactants for EOR: olefin sulfonate behavior at high temperature and hardness. SPE Reserv. Eng. **3**(02), 597–603 (1988)
66. J. Park, Y. Han, H. Kim, Formation of mesoporous materials from silica dissolved in various NaOH concentrations: Effect of pH and ionic strength. J. Nanomater. **2012** (2012)
67. S.-H. Wu, C.-Y. Mou, H.-P. Lin, Synthesis of mesoporous silica nanoparticles. Chem. Soc. Rev. **42**(9), 3862–3875 (2013)
68. R. Lim, P. Jiang, C. Gao, F. Huang, R. Xu, X. Chen, Experimental investigation of silica-based nanofluid enhanced oil recovery: the effect of wettability alteration. Energy Fuel **31**(1), 188–197 (2017)

69. Q. Sun, Z. Li, S. Li, L. Jiang, J. Wang, P. Wang, Utilization of surfactant-stabilized foam for enhanced oil recovery by adding nanoparticles. Energy Fuel **28**(4), 2384–2394 (2014)
70. C. Wang, H.A. Li, Stability and mobility of foam generated by gas-solvent/surfactant mixtures under reservoir conditions. J. Nat. Gas Sci. Eng. **34**, 366–375 (2016)
71. R. Li, P. Jiang, C. Gao, F. Huang, R. Xu, X. Chen, Experimental investigation of silica-based nanofluid enhanced oil recovery: the effect of wettability alteration. Energy Fuels **31**(1), 188–197 (2017)
72. T. Lu, Z. Li, Y. Zhou, Flow behavior and displacement mechanisms of nanoparticle stabilized foam flooding for enhanced heavy oil recovery. Energies **10**(4), 560 (2017)
73. D. Mo, J. Yu, N. Liu, R.L. Lee, Study of the effect of different factors on nanoparticle-stabilized CO2 foam for mobility control, in *SPE Annual Technical Conference and Exhibition*, (Society of Petroleum Engineers, 2012)

Chapter 10
Nanoparticles for Drilling, Cementing, Hydraulic Fracturing, and Well Stimulation Fluids

Farad Sagala and Nashaat N. Nassar

10.1 Introduction

The worldwide decrease in oil recovery from available resources, coupled with the increase in energy consumption, has revitalized the curiosity of the oil industry to investigate additional prospects in both conventional and unconventional hydrocarbon formations. During oil production, drilling is one of the essential stages that involves cutting a hole using a drill bit that creates a wellbore for oil and gas recovery. However, the design of the appropriate choice of drilling fluids for particular drilling requirements is an essential aspect for the attainment of drilling processes, especially in unconventional reservoirs. Drilling fluids help by cooling of the drill bit and drill pipe, preventing the formation fluids from entering the wellbore by providing a hydrostatic pressure, transporting drill cuttings to the surface from the wellbore, and suspending drill cuttings in case drilling is paused or in the event of well shutdown [1–3]. Generally, drilling fluids are categorized into three main groups, namely, water-based mud (WBM), oil-based mud (OBM), and synthetic-based mud (SBM). OBM and SBM normally offer better-operating efficiency compared to the WBM. Nevertheless, using OBM and SBM is normally not recommended due to the environmental concerns that they may create [4, 5]. Due to the severity of

F. Sagala
Department of Chemical and Petroleum Engineering, University of Calgary (UC), 2500 University Drive NW, Calgary, Alberta, Canada

Department of Energy, Minerals and Petroleum Engineering, Mbarara University of Science and Technology, Mbarara, Uganda

N. N. Nassar (✉)
Department of Energy, Minerals and Petroleum Engineering, Mbarara University of Science and Technology, Mbarara, 1410, Uganda
e-mail: nassar@ucalgary.ca

N. N. Nassar et al. (eds.), *Nanoparticles: An Emerging Technology for Oil Production and Processing Applications*, Lecture Notes in Nanoscale Science and Technology, https://doi.org/10.1007/978-3-319-12051-5_10

the wellbore condition especially the harsh reservoir conditions (high pressure and high temperature), normally the rheological properties of these drilling fluids are altered, hence decreasing their efficiency. Moreover, the conventional drilling fluids still face some critical challenges, such as water loss into fractures, drilling fluid leakage into the surrounding formation, and the decrease of fluid density and/or viscosity in the fluid circulation process. This has led to various researchers venturing into the use of different additives that can assist in improving the rheological properties and performance of these drilling fluids. Numerous investigations have been performed on different drilling types over the past years to improve their performance by altering their characteristics with the addition of various agents such as calcium carbonate, soda ashes, and more recently, nanoparticles [6, 7]. Nanoparticles have exceptional behaviors due to their diminutive size and larger surface area-to-volume ratio, hence showing more reactivity with other molecules. Nanoparticles navigate numerous industries, and their type of selection depends on the projected usage. In particular, nanoparticles are increasingly becoming popular in drilling activities, cementing, hydraulic fracturing, well stimulation, etc. [8–11]. Through manipulation of their physical and chemical properties, scientists have generated various nanomaterials with enhanced intrinsic, mechanical, magnetic, thermal, and rheological properties. The impacts of various forms of NPs positively on the characteristics of various types of drilling fluids have been reported by various investigators [12–14]. On the hand cementing is normally performed during the well completion stage where a mixture of cement is used to strengthen and/or stabilize the casing strings and also provide zone isolation between the pipe and the sedimentary formation. Cement consists of organic complex chemical compounds such as calcium silicate, aluminates, and gypsum that are normally added to water generating C-S-H gel as the major hydrate product [15]. The cementing process is essential during oil well construction as the inadequate cementing procedure can result in drastic effects, such as increased costs, well instability, and risks to the environment. During the cement formulation, cement slurry should be designed with the proper materials to resist the temperature, pressure, and depth. Therefore, there is always a gap to create high-performing slurry materials to boost and enhance cementing properties. To improve the mechanical, chemical, and physical properties of cementing slurry downhole, recently different forms of nanoparticles are added to improve its performance, and recent studies will be reviewed in this chapter. Likewise, hydraulic fracturing involves injecting sand, water, and/or other chemicals or other proppants using high pressure into a wellbore to create fractures in the formations through which petroleum and brine can freely flow. Nonetheless, developing new fracturing fluids that can sustain tremendous rheological properties especially at reservoir conditions, as well as reduce the impairment to the reservoir properties, requires more investigation. In recent years, nanotechnology is attracting attention and developing more interest in the aforementioned areas during various stages of oil production [16]. Investigations are in progress, in tackling and improving the challenges of conventional drilling, cementing, and fracking fluids during well stimulation. This chapter, therefore, will highlight some of the recent advances in using nanoparticles during drilling fluid formulation, designing improved well cementing slurries, and hydraulic fracturing and/or well stimulation fluids. Also, future research

suggestions and some recommendations will be given to facilitate the evaluation of nanoparticle in the aforementioned applications.

10.2 Types of Drilling Fluids

Drilling mud, or drilling fluids, refers to a highly viscous heavy fluid blend that is employed in oil and gas drilling processes. When drilling a new well, normally a certain form of fluid is required. The key purposes of drilling fluids incorporate lifting the drilled cuttings, providing hydrostatic pressure that can prevent the entry of formation fluids into the wellbore, maintaining its stability, cooling and cleaning the drill bit during drilling, and holding the drill cuttings while drilling is inactive or stopped when the drilling unit is being removed from the hole. There are mainly three types of drilling fluids normally used in the oil and gas industry, namely, water-based muds (WBM), which is either dispersible and non-dispersible; oil-based muds (OBM) or the nonaqueous mud; and synthetic-based mud (SBM), in which a wide range of gases can be used [17]. The selection of particular drilling fluid to be used for a particular well and the additives used normally depends on the type or composition of the rock being drilled, environmental effect, and the cost implications. A standard WBM contains clay, which is typically bentonite, to provide the mud with the appropriate viscosity to transport the cutting from the wellbore to the surface. Also, it may contain minerals such as barite (barium sulfate) which is normally added to stabilize the borehole by increasing the weight of the column. These types of mud are traditionally based on water, either freshwater, distilled water, seawater, or natural occurring brines. In general, WBM are suitable for drilling conventional vertical wells at medium depths and less challenging wells, whereas oil-based muds are appropriate for deeper wells, in directional or horizontal drilling, which requires much more stress on the drilling apparatus [18]. In the shale formations, however, the WBM has some drawbacks as it causes swelling which makes its application feeble in such formations. Moreover, shale swelling can result in more severe destructive challenges such as pipe sticking, wellbore instability, and lost circulation [19, 20]. In contrast, oil-based muds (OBMs) normally require the use of petroleum-refined products such as mineral oil and diesel oil in the fluid formulation. Their limitations are mainly attributed to the environmental impacts that are not friendly to the ecosystem. On the other hand, synthetic-based mud (SBM) are prepared using refined fluid components that are made to more exacting property specifications than traditional petroleum-based oils. These types of drilling fluids were proposed due to the environmental concerns of the OBMs, even though most of the drilling muds are highly regulated in their composition, and in certain environments, some specific combinations may be prohibited from use. Nevertheless, synthetic-based drilling fluids are proven to have numerous high-tech and environmental benefits compared to the WBM and OBM and can reduce the total well costs in many cases. Figure 10.1 shows samples of drilling fluids for (a) WBM and OBM (b).

Fig. 10.1 Photographs of (**a**) water-based mud and (**b**) oil-based mud. Copyright permission was obtained from Zeal Environmental Ltd. (http://www.zealenvironmental.com/)

10.3 Application of Nanoparticles in Drilling Fluids

Selection of a proper drilling fluid depends on the type of the formation and particular drilling job to be accomplished to avoid formation damage and corrosion. To enhance the rheological and filtration properties of various drilling fluids, a variety of additives are proposed based on their mechanical, chemical, and physical properties. Normally, temperature and pressure are some of the limitations that influence the selection of conventional additives such as type, particle size, etc. As thus, nanoparticles are suggested as prospective additives that can enhance the rheological characteristics of drilling fluids [17, 21–23]. In the next section of this chapter, the applicability of nanomaterials in each type of drilling fluid will be reviewed with the existing challenges and limitations explained.

10.4 Effect of Nanoparticle Types and Concentration on the Enhancement of Drilling Fluids

Nanoparticle types and concentration play a critical role in improving the rheological properties of different types of drilling fluids. Therefore, the proper selection of nanoparticle types and optimizing their concentration is imperative. Among the commonly used nanoparticles in improving the performance of drilling fluids include clay nanoparticles, silicon dioxide (SiO_2), aluminum oxide (Al_2O_3), copper oxide (CuO), carbon nanotubes, titanium dioxide (TiO_2), and less costly nanomaterials including calcium carbonate ($CaCO_3$) and fly ash nanoparticles, in the case of unconventional reservoirs [17, 24]. The addition of nanoparticles to drilling fluids can enhance various rheological properties such as elastic stability, plastic viscosity, mechanical filtration, gel strength, and yield point. Some of these properties in regard to drilling fluids will be explained briefly below.

(a) **Plastic Viscosity**

Plastic viscosity (PV) is a Bingham model factor that represents the mud viscosity when extended to infinite shear rate depending on the mathematical model of Bingham

[25]. Normally, for proper drilling operations, mud with relatively high PV is not easily pumped and is not preferred by operators. Nevertheless, mud should have an appropriate density to maintain the hydrostatic pressure that is directly proportional to the mud viscosity. Using mud with lower viscosity can result in the mud with a lower density and lower hydrostatic pressure that can cause blowouts during drilling operations. Therefore, for safer drilling activities, an optimum PV is desirable which can be obtained by considering the mud characteristics and the operational conditions [26]. There are various mechanisms under which nanoparticles improve these properties which depend on the mud and nanoparticle characteristics. Adding nanoparticles to the base mud can increase the friction between the two fluid layers which can result in viscosity increment. Normally, NP properties such as their geometry, heat capacity, density, etc. assist in the adjustment of the drilling fluid properties. Bentonite-WBM and the added NPS link or bond together across several chemical linkages to boost the mud PV properties [27]. This modification, however, depends on the type of nanoparticle used.

(b) **Yield point**

Yield point in drilling fluids is also a Bingham plastic parameter that refers to the stress required by the fluid to start moving. The forces of attraction between the colloidal particles in the drilling mud prevents it from moving until the required stress has been applied. Therefore, a higher yield point value is desirable for faster transportation of drilling cuttings towards the surface [28]. A high yield point is required for proper drill cutting transportation out of the well; however, it should not be too excessive to increase the pump pressure when mud starts flowing [29]. The effects of NPs on yield point of Bentonite-WBMs are shown from some studies, for example in Fig. 10.2. It can be observed that different nanomaterials have different behavior in terms of yield point modification.

(c) **Gel Strength**

Gel strength is also another important behavior of drilling fluids that refers to the measurement of electrochemical forces of attraction within the mud system under

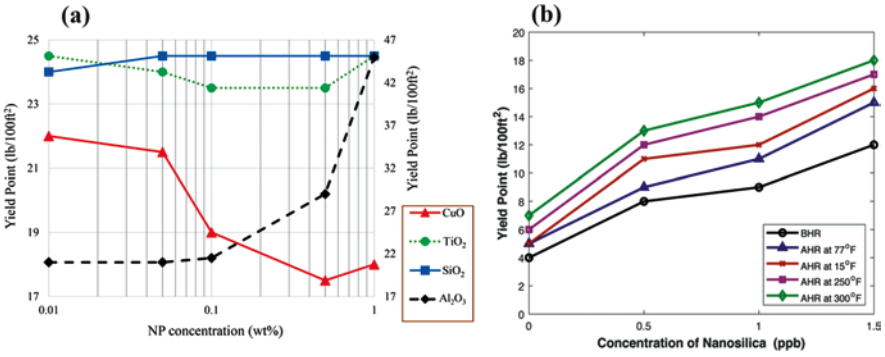

Fig. 10.2 (**a**)Yield point of NPs Bentonite WBM at different concentrations (CuO, TiO2 and SiO2 NPs Bentonite WBM from left Y-axis and Al2O3 NPs Bentonite WBM from right Y-Axis)[30] and (**b**) Yield point of 9 ppg OBM samples at different temperatures [32]. Permissions related to the material excerpted were obtained from Elsevier, and further permission should be directed to Elsevier

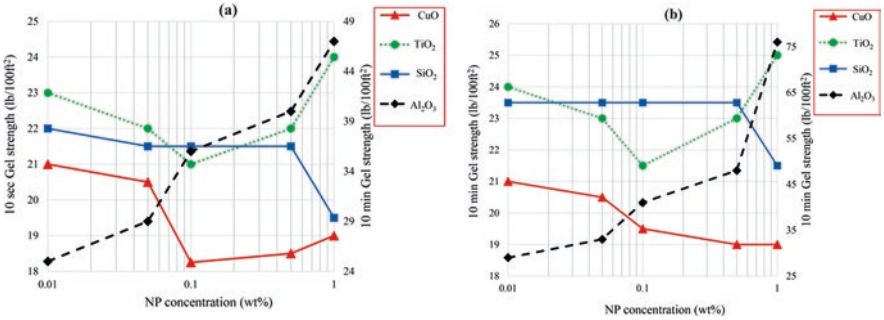

Fig. 10.3 Gel strength of WBM with different NPs quantified in: (**a**) 10 s and (**b**) 10 min [30]. Permissions related to the material excerpted were obtained from Elsevier and further permission should be directed to Elsevier

static conditions. It differs from the yield value because of its time dependence and because it breaks up once the flow is restricted. It also shows the ability of drilling fluids to suspend solids and cuttings. Normally to determine the gel strength, the shear stress is assessed at a lower shear rate after the mud has set. The API procedure for this measurement is normally performed with time frame 10 s to 10 min although measurements between 30 min to 16 h can be performed. It is important to note that a high gel strength is important to prevent several critical drilling challenges. The addition of nanoparticles can therefore improve the gel strength depending on the type, size, concentration, and the measurement time as shown in Fig. 10.3.

(d) **Filtration Loss and Filter Cake Thickness Quality**

The volume of the fluid lost and the thickness of the mud cake are the measurable parameters to quantify this test. High-volume fluid loses during drilling activities are not desirable since they may result in lower hydrostatic pressure and cause formation damage and wellbore instability [31]. Furthermore, filter cake quality assessment and stiffness must be evaluated. The filter mud cake quality is another important parameter that should be addressed during drilling activities. The quality and thickness of the mud cake represent the amount of filter loss that may occur in drilling operations. Therefore, to have proper wellbore stability and prevent fluid loss, it is always appropriate to add some additives to drilling fluids to reduce the filter loss. Adding nanoparticles, depending on the type and concentration, is one of the appropriate ways that has been evidenced to prevent fluid loss by improving the mud cake quality, as seen in Fig. 10.4.

Asaba et al. [33] investigated the impact of nanoparticle concentration and types, namely, aluminum oxide, copper oxide, and magnesium oxide, on the rheological characteristics and the filtration physical properties of WBM fluid at room temperature and higher temperature of 50°C. The authors found out that plastic viscosity of the drilling mud could be decreased by 50% when NPs were used. Also, the yield point for the mud could be enhanced by 84%, 121%, and 231% by adding 0.5%vol

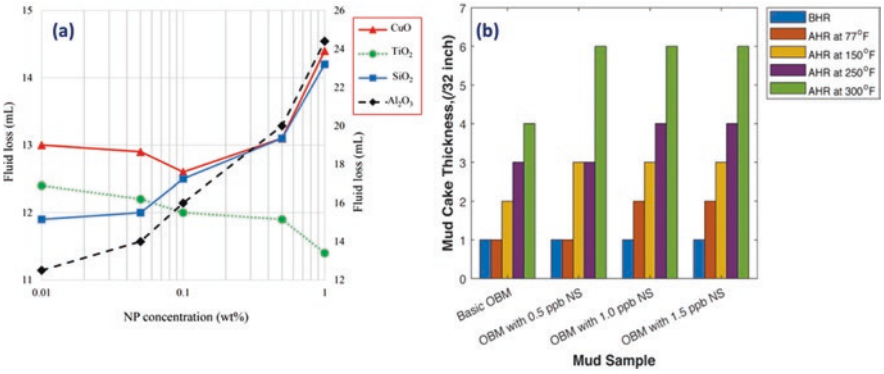

Fig. 10.4 (**a**) WBM fluid loss of different nanoparticles at different concentrations and (**b**) API mud cake thickness in the presence of nanosilica at various concentrations [30, 32]. Permissions related to the material excerpted were obtained from Elsevier, and further permission should be directed to Elsevier

copper oxide, aluminum oxide, and magnesium oxide, respectively. As well, the gel strength improved up to 95% with a fluid loss decrease of 30%. However, they noted that the filtration characteristics were negatively affected by the higher pressure and higher temperature of the formation. The authors noted that increasing the concentration of these nanoparticles had no significant effect on the WBM rheological characteristics. They concluded that the rheological properties, of WBM, can be improved with nanoparticles that can result in proper hole cleaning. In contrast, Yingpei et al. [34] noted a significant increment in the rheological properties and the plugging performance of WBM by increasing the concentration of Fe_3O_4 nanoparticles that were modified with poly(acrylic acid). From their findings, increasing the nanoparticle concentration from 0.05 up to 0.1 wt% resulted in the decrease of the consistency coefficient (K) of the Fe_3O_4/PAA nanoparticles/WBM concentration of the WBM. Using 0.1 wt% nanoparticles was found to perform best as a filtration additive in WBM. Bayat et al. [30] investigated the role of four hydrophilic nanoparticles, aluminum oxide (Al_2O_3), titanium dioxide (TiO_2), silicon dioxide (SiO_2), and copper oxide (CuO). These NPs were added to the formulated bentonite drilling fluids at concentrations of 0.01, 0.05, 0.1, and 1 wt%. Their study showed that the Al_2O_3 NPs could enhance the mud filtration up to 80% but destroy the mud cake quality compared to the based mud. However, the amount of mud filtration had a decreasing trend when SiO_2, TiO_2, and CuO NPs were used especially with mass fractions lower than 0.5 wt%. Moreover, in comparison with the base mud, other properties such as the gel strength and rheological properties were similarly enhanced in the presence of these NPs. Generally, it was deduced that the addition of the NPS at lower concentrations less than 0.5 wt% to the WBM can enhance its rheological and filtration properties. Some of the measured properties using the different nanoparticles (SiO_2, TiO_2 and CuO NPs) are depicted in Fig. 10.5.

The rheological performance of both WBM and OBM at higher temperature was enhanced by adding different nanosilica in the range of 0.5 ppb–1.5 ppb. In their

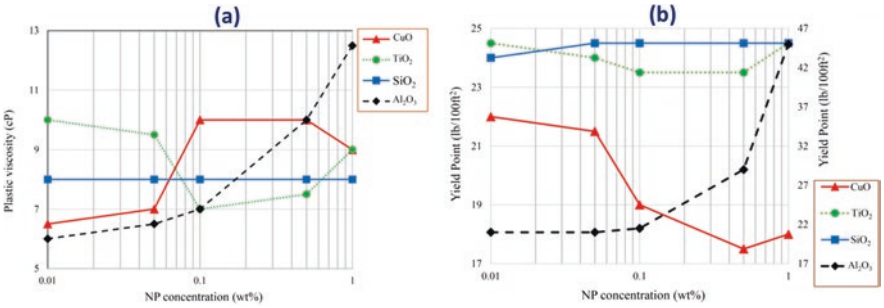

Fig. 10.5 WBM plastic viscosity (**a**) and yield point (**b**) Relative CoF reduction of OBM samples with and without nanosilica [30]. Permissions related to the material excerpted were obtained from Elsevier, and further permission should be directed to Elsevier

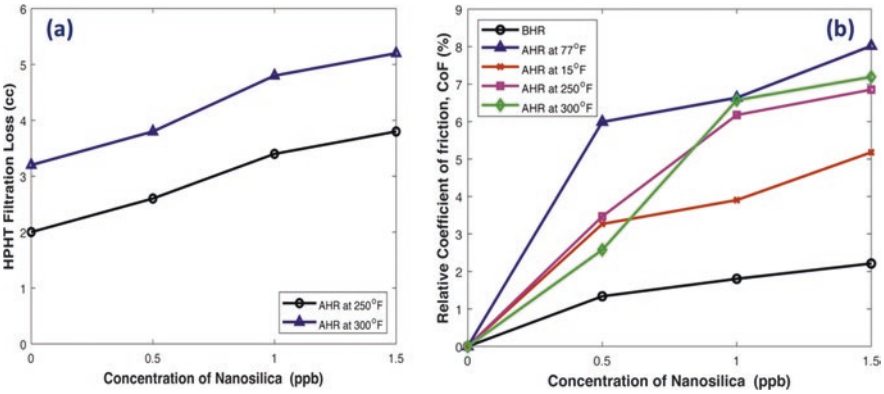

Fig. 10.6 Enhancement of filtration loss properties (**a**) and(**b**) relative coefficient of friction (CoF) reduction of OBM samples with and without nanosilica [32]. Permissions related to the material excerpted were obtained from Elsevier, and further permission should be directed to Elsevier

study, the authors measured various fluid rheological properties, including mud lubricity, electrical stability, and filtration measurements at HPHT, and later rheological models were obtained. Compared to the basic mud, it was found that adding 0.5 ppb nanosilica can improve almost all the tested properties of WBM and OBM [32]. It is always appropriate to optimize the nanoparticles because a higher concentration of nanoparticles used in drilling fluids can increase and alter the friction coefficient of the particles, changing the fluid lubricity which can impact the hole cleaning efficiency [35]. Some of the measured properties in the presence of nanosilica at different temperature are shown in Figs. 10.6, 10.7, and 10.8.

Pitchayut et al. [36] demonstrated that ZnO and copper oxide (CuO) nanoparticles at the concentration in the range of 0.1 to 1 wt% improved the rheological and thermal conductivity of a bentonite-based xanthan gum drilling fluids by up to 38% at elevated temperatures with ZnO therefore improving performance compared to CuO. This improved thermal conductivity can help the drilling fluid to cool more

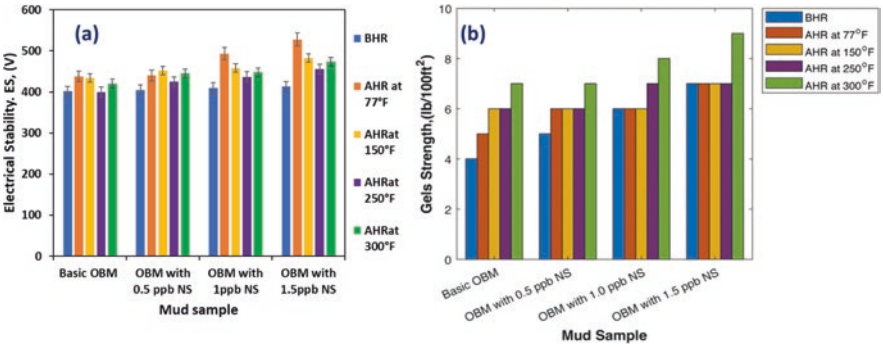

Fig. 10.7 Improving the electrical stability (**a**) and the gel strength (**b**) for oil-based mud using nanoparticles at different concentrations and different temperatures [32]. Permissions related to the material excerpted were obtained from Elsevier, and further permission should be directed to Elsevier

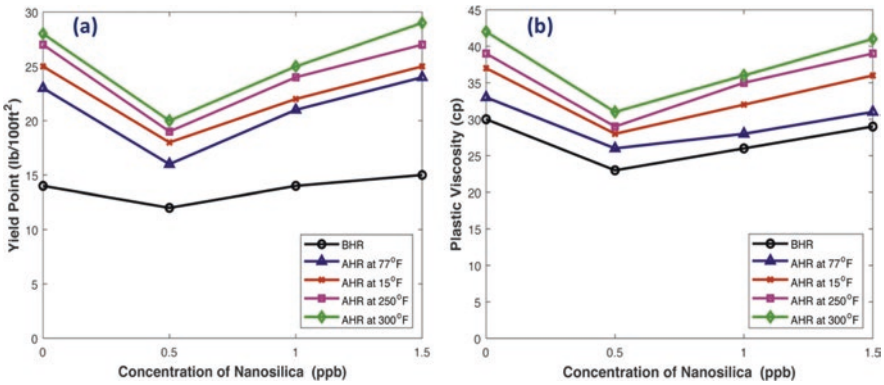

Fig. 10.8 Impact of nanosilica on yield point (**a**) and plastic viscosity (**b**) of drilling mud at different concentrations and temperatures [32]. Permissions related to the material excerpted were obtained from Elsevier, and further permission should be directed to Elsevier

rapidly as it circulates from the wellbore to the surface during the drilling operation. Still, the filtration tests conducted at a higher temperature (100°C and 500 psi) indicated a significant filtration loss reduction (30.2%) with 0.8 wt % CuO in comparison to 18.8% ZnO for the similar concentration. Moreover, there was a significant mud thickness reduction in contrast to the base fluid when these nanoparticles were used. Their findings revealed the capability of using these nanoparticles to improve the properties of WBMs and their possibility to be utilized as filtration loss additives. Another challenge of drilling fluids that have been remediated by the use of nanoparticles is sagging of drilling fluid. Sagging of drilling fluids results in density variation of the mud and, hence, wellbore instability and well control challenges. Wagle et al. [37] showed that nanoparticles can be used to prepare sag-resistant

drilling fluids by stabilizing invert-emulsion drilling fluids. Their results proved that using 6–16 lbm/bbl of nanoparticles in organoclay-free invert-emulsion drilling fluid can minimize the emulsion separation and, hence, reduce sag at temperatures up to 250°F. Nanoparticles have also been utilized as additives to improve the fluid loss from drilling fluids. Vryzas et al. [38] found that using iron oxide (Fe_2O_3) NPs enhanced the fluid loss properties in WBM drilling fluids. Adding 0.5 wt% Fe_2O_3 nanoparticles, the fluid loss could be reduced by 42.5% in comparison with the base mud. Zakaria et al. [39] reported that 70% more improvement in fluid loss could be achieved when 2 wt% of NPs were added to OBM drilling fluids with the similar objective of reducing the fluid loss. Furthermore, in shale formations, wellbore stability is reduced when water from drilling fluids invades shale. In another study, there was a reduction by a factor of 5–50 for the permeability of Atoka shale formation by adding 5–22-nm silica nanoparticles, which are understood to penetrate deep into the shale and prevent water invasion; moreover, the water infiltration into the Atoka formation also decreased by 98% compared to seawater by adding nanoparticles [40]. Additional studies to summarize the role of nanoparticles for drilling fluid properties enhancement are shown in Table 10.1.

Table 10.1 Summary of some recent studies performed using different nanoparticles and different types of drilling fluids

Study properties	Mud type	Type of nanoparticle used	Deduction from the study	Reference
Filtrate volume, lubricity, yield point	WBM	Glass beads, multiwall carbon nanotube (MWCNT), silica nanoparticles	MWCNT were found to be better additives for WBM compared to silica NPs and glass beads. Filtrate volume was reduced; mud cake thickness and yield point were all improved due to the addition of MWCNT.	[41]
Mechanical filtration, fluid loss, and viscosity	WBM	Boron nitride (BN) and iron trioxide (Fe_2O_3)	Addition of 0.0095 wt% BN and Fe_2O_3 reduced the mechanical coefficient by 37%, and 43%, respectively. BN did not show any impact on filter loss. There was viscosity enhancement with both nanoparticles.	[35]
Rheological properties Electrical conductivity Thermal conductivity Shale recovery	WBM	TiO_2	TiO_2 altered the electrical and thermal conductivity of drilling fluids. TiO_2 increased the shale recovery, and thermal resistance was improved by 25% and reduced the filtration volumes up to 27%.	[42]
Plastic viscosity, yield point	WBM	ZnO, montmorillonite, and palygoskite	Addition of 50 nm resulted in more stabilized rheological mud characteristics at HPHT conditions.	[43]

(continued)

Table 10.1 (continued)

Study properties	Mud type	Type of nanoparticle used	Deduction from the study	Reference
Yield point gel strength Plastic viscosity	OBM	Silica and nanoclay	Using 2.0 wt% of nanoclay alone or mixed with 1 wt% silica nanoparticles improved the PV and the gel strength of OBM.	[29]
Plastic viscosity	OBM	SiO_2	Addition of 20 nm nanosilica at 2.0 vol% in OBM increased the PV at room conditions and maintained a stabilized rheological profile at HPHT conditions.	[44]
Yield point Gel strength Plastic viscosity	WBM	Cellulose nanoparticles	Addition of 0.5 wt% cellulose nanoparticles in WBM improved the rheological properties at a higher temperature in the range from 20 to 80°C.	[45]
Viscosity	OBM	Nanographite	Addition of nanographite within OBMs improved the fluid PV at ambient condition.	[46]
Plastic viscosity Yield point Gel strength	WBM	SiO_2	Addition of 1.0 wt% of SiO_2 to WBM at all conditions improved all the tested parameters.	[47]
Yield point Plastic viscosity	WBM	SiO_2 Fe_2O_3	Nanosilica (SiO_2) and ferric oxide (Fe_2O_3) NPs were applied in a WBM. Addition of 0.5 wt% of ferric oxide enhanced the fluid rheological characteristics, while SiO_2 at the same mass fraction showed reverse impacts on the measured rheological properties. Fluid having Fe_2O_3 NPs exhibited more stabilized properties at the measured conditions.	[48]

10.5 Application of Nanoparticles in Cementing Activities

One of the most crucial processes during well completion is cementing whose role is to provide zone seclusion between the pipe and the formation. Oil industries are venturing into materials with higher performance to reduce the costs associated with the repair and reduce losses due to cementing failure. A universal overview of the well cementing procedure is shown in Fig. 10.9. The major causes of cement failure can include cement contraction, partial cement placement, casing centralization, diversion of the cement slurry to the nearby formation, inadequate cement formation, micro-annuli in cement, mechanical or thermal stress, rusting/corrosion of the casing string, etc. As thus, similar to drilling operations, efforts are focused on developing and applying nanomaterials at the nanoscale with superior characteristics to offer ways to acquire significant variations in physical, chemical, and mechanical properties to improve numerous practical issues by enhancing

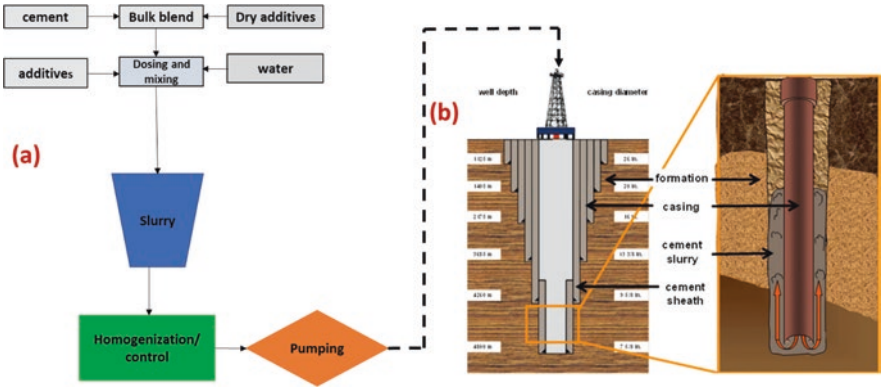

Fig. 10.9 Well cementing process, modified from [54, 55] after permission

mechanical strength and water penetration resistance; accelerating hydration reaction, controlling calcium leaching, density, setting time, heat and electrical conductivity, and filtration; providing self-cleaning properties and viscosity; and reducing the porosity and permeability; etc. Various nanoparticles [15, 49–53] have been evidenced to enhance various cement properties such as impacting toughness, improving the durability, dry shrinkage capacity enhancement and permeability resistance to water, strength, providing self-compacting, etc.

Several researchers have concluded that the addition of nanoparticles to cement can mechanically reinforce cementitious materials because nanoparticles have a high surface area-to-volume ratio that enhances the chemical reactions and are small enough that when dispersed in the slurry, they can occupy the small pores between cement grains, forming thicker concrete and reducing the porosity and permeability. Also, well-distributed nanoparticles act as crystallization centers, quickening cement hydration due to the chemical reactions generated by nanoparticles. Nanoparticles that are highly reactive speed up the pozzolanic reaction (CH + SH-C–S–H) and also react with calcium hydroxide (Ca(OH), forming an additional quantity of C–S–H gel. Similarly, nanoparticles boost the crystallization of small-sized crystals ($Ca(OH)_2$, AF silicate hydrate (C–S–H). Furthermore, adding nanoparticles results in better bonding between aggregates and the cement paste since it enhances the aggregates contact zonal structure [52].

The ability of nanoparticles to enhance the selected cement properties was studied on a laboratory scale, using a colloidal solution of silica (nano-SiO_2), alumina (nano-Al_2O_3) and ternary systems containing calcium oxide, and aluminum (CaO-SiO_2-Al_2O_3). The experiments were conducted through the incorporation of the nanosilica and ternary system in cement slurries. The results indicate the possibility of using nanosilica in cement systems, because the mechanical properties of the systems, such as compressive strength, were improved to almost 90% with concentrations of 0.5 wt% nanosilica. On the other hand, the ternary system introduced qualitative cementitious properties when reacting with water at atmospheric conditions [15]. In another study, multiwalled carbon nanotubes (MWCNTs) were found to enhance the cement properties that included toughness and durability, dry shrinkage capacity, and permeability resistance. Moreover, adding a lower concentration of

Table 10.2 A summary of nanoparticle application during cementing activities

References	Nanoparticle type	Experimental conditions	Deductions
[59]	0.5–1 wt% aluminum oxide	Ambient conditions 25°C	Improved the compressive strength Improved electrical resistivity up to 30%
[60]	Iron oxide	Temperature 25–85°C, pressure 345–465Pa	Improved the compressive strength Improved the setting properties
[61]	MWCNT	Ambient conditions	Improved the setting time
[62]	Silicon dioxide	Low-temperature 15°C and ambient pressure	Enhanced the compressive strength Accelerated the setting time
[63]	Silicon dioxide	Ambient conditions	Improved the mechanical properties
[64]	Iron oxide (0.5 wt%) Silicon dioxide (0.25 wt%)	Ambient conditions	Improved mechanical properties Improved sensing properties
[65]	Nano-synthetic graphite (0.5 wt%)	Ambient conditions	Improving the early compressive strength development
[66]	2 wt% magnesium oxide	Temperature and 40°C and ambient pressure	Improved the setting time Reduced chemical shrinkage
[67]	Aluminum oxide 1.5 wt %	Temperature and 40°F and ambient pressure	Increased tensile strength by 141% Improved mechanical properties
[68]	Graphene nanoplatelets (GNP)	Ambient conditions	Improved mechanical properties up to 30% Reduced chemical shrinkage
[69]	1–2 wt% aluminum oxide	90°C 200 MPa (30,000 psi)	Improving mechanical properties Improved rapid setting with high strength

carbon fibers and carbon nanotubes (CNT) in ultra-range of 0.025–0.05 wt% was found to enhance the electromechanical properties of cement [56, 57]. It has been evidenced that through enhancement of these cement electromechanical and physical properties, it is suitable to apply such cement to offshore oil and gas formations where the cement operations are performed in deeper water bodies. Other applications of nanoparticles in cementing operations have been extensively reported elsewhere [52, 58]. In summary, nanotechnology application for the oil and gas production mainly in upstream processes is expected to result in more advanced materials to enhance the cement properties. This can help to lower the cost and also prevent disastrous wellbore failure. The use of nanomaterials ranging from metal, metal oxides, and carbon nanomaterials can be part of the future additive formulation for cement slurries. Table 10.2 shows a summary of some other studies for enhancing cement properties with nanoparticles and the deductions from such findings.

10.6 Application of Nanoparticles in Well Stimulation and Hydraulic Fracturing

Hydraulic fracturing also known as hydrofracking is a wellbore stimulation technique that involves creating fractures in geological formations using pressurized fluids. During this process, fracking fluids, typically water containing sands and ceramic particles or other suspended proppants with the support of thickening additives, are injected using higher pressure into a wellbore, creating cracks in the deep-rock formations through which natural hydrocarbons and brine flow easily from the reservoir to the wellbore. Hydraulic fracturing stimulation is normally necessary to produce oil from tight reservoir formations with the permeability less than 1 mD; a typical hydrofracking structure is shown in Fig. 10.10.

Before pumping proppant fluids, pad fluids with no proppants are pumped to the formation to open the fractures [70]. Normally, hydrofracturing fluids are used to break down underground formations where oil and gas are trapped. Also, these fracking fluids act as carriers for proppant in the fractures. When the pressure is released, the fracture is kept open due to the pressure, and once released, the proppants are packed inside the fracs to maintain a highly conductive flow of hydrocarbons and prevent the closing of the fractures [71]. Synthetic polymers, biopolymers, foams, viscoelastic surfactant (VES) fluids, and slick water are some of the applied fracturing fluids, with each having different properties that are beneficial under certain conditions [72]. Nowadays, their preparations are well-designed, and of recent, small-sized particles may be added in the nanometer size range. Factors such as reservoir temperature, permeability, and mineralogy define the fluid selection process. For example, temperatures more than 177°C generally warrant synthetic polymers over biopolymers [16]. Water-based fluids are regularly substituted with

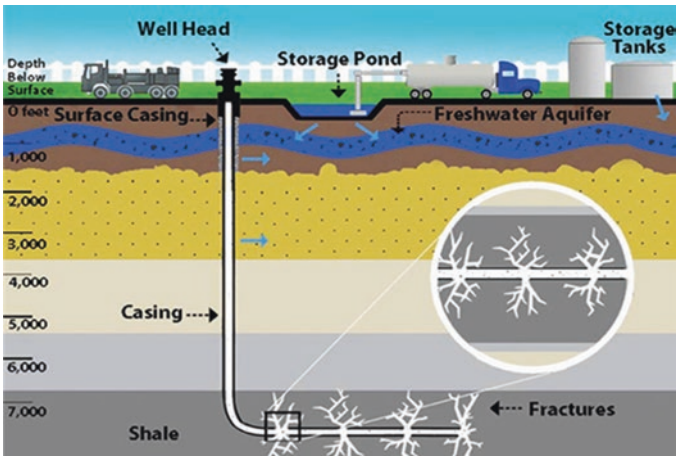

Fig. 10.10 A graphic representation of formation showing hydraulic fracturing operation for the conventional and unconventional formation. Copyright permission was obtained from Oklahoma State University Extension (https://extension.okstate.edu/)

foams, hydrocarbon-based fluids, or alcohol-based fluids in water-responsive formations. In the formations with high leak-off rates, VES-based fluids are normally applied to reduce the damage that could occur if polymer-based fluids are used [16]. Over time, hydraulic fracturing chemicals have been proposed to provide significant performance, improved cleaning of the created fractures, and good control over the hydraulic fracturing operations. Notwithstanding their ability, however, VES-based fluids were found to experience high leak-off rates in moderate-permeability reservoirs less than 200 mD. Because their viscosity at temperature higher than 104°C diminishes significantly, these types of fluids were found ineffective for formations with higher temperatures [73]. Pressure-dependency behavior of borate-crosslinked gels is another problem, where the viscosity was found to decrease significantly under high pressures. Additionally, it is difficult to formulate a fluid that can maintain the fluid viscosity for a given period in high-temperature reservoirs (>176°C). Synthetic polymers (such as acrylamide-based polymers) are frequently employed and have been reported to be used at high concentrations. The high-concentration constraints are necessitated by the need to design a stable viscosity that can withstand high-temperature conditions. Moreover, high polymer loading raises the potential of formation damage caused by the fluid residue. These challenges, which can be addressed by nanotechnology, have a major impact on hydraulic fracturing applications. Nanoparticles have addressed certain technological limitations of fracturing fluids. Low-cost tunable nanoparticles such as nanosilica, carbon nanotubes, nano-sensor, nano-proppants, and polyelectrolyte complex nanoparticles have been used as additives for fracking fluids [16]. For instance, the operating temperature threshold of VES-based fluids was enhanced by adding zinc oxide (ZnO) and magnesium oxide (MgO) nanoparticles from 93 to 121°C [73]. The borate-crosslinked gels were found to maintain their viscosity at higher pressures up to 20,000 psi when boronic acid-functionalized nanolatex silica particles were used as crosslinkers. Moreover, under these high pressures, conventional borate crosslinkers indicated more than 80% reduction in viscosity. Furthermore, the rheological properties of VES combined with polymer fluids were improved by using nanoparticles. Nanoparticles have also been used in the well stimulation of carbonate reservoirs. Nickel nanoparticles were investigated for their ability to generate carbonic acid in situ to improve the performance of hydrochloric acid (HCl)-based acidizing fluids. The nanoparticles were first dispersed in water and then dispersed to formulate the solution. After that, HCl was injected into the carbonate reservoir, generating CO_2 as a result of the HCl reacting with the carbonate reservoir. The generated gas reacted with nickel nanoparticles forming carbonic acid, which enhanced the dissolution of carbonate rocks [74, 75]. For deep sensing of petroleum reservoirs, silver nanowires and tin and bismuth nanoparticles were applied at reservoir temperature and pressure data; this probably is the first phase towards deeper reservoir sensing in the oil field [76]. According to Reza [77], silica and polyelectrolyte complex (PEC) nanoparticles can prevent fluid loss during hydraulic fracturing in low-permeability cores in the range of 10^{-5}–10^{-4} mD, 0.01–0.1 mD, and 1–40 mD. The authors found out that these nanoparticles, when mixed with 2% KCl, can significantly reduce the fluid loss volume for the cores with lower

Table 10.3 Some of the selected nanoparticles used to improve the rheological properties of hydraulic fracturing fluids

References	Nanoparticle type	Improved characteristics
[79]	Silicon dioxide	Reduced permeability damage Reduced adsorption capacity
[80]	Silicon dioxide-hydrophobic NPs (0.5–1.5 wt%)	Improved the permeability of the fractures Formation of microencapsulated acid
[81]	Magnesium oxide Zinc oxide	Improved the rheological properties of fracturing fluid
[82]	Silicon dioxide	Improved the performance of CO_2 foam as hydrofracking fluid at 121°C

permeabilities below 0.1 mD. It was later evidenced that PEC nanoparticles could reduce the fluid loss to zero when utilized with 2% KCl on tight cores, whereas silica nanoparticles revealed slight fluid loss volumes. Generally, both nanoparticle solutions indicated a significant fluid loss control capacity when low permeability and tight cores were used. Furthermore, fluid loss control capability coupled with nanoparticles of specific characteristics of the nanoparticles improved the fracture conductivity by reducing the fluid loss volume caused through formation of thinner filter cakes on the rock surface. This is ascribed to the formation of 3-D network super-micellar structures which supported the development of a low-permeability continuous and integrated reinforced filter cake that obstructed fluid flow [78]. This resulted in the formation of clear fractures with higher fracture conductivity that could produce higher hydrocarbon volumes (Table 10.3).

10.7 Field Applications of Nanoparticles in Drilling, Cementing, and Hydraulic Fracking

Based on the reviewed studies, no major field trials have been reported for nanoparticle application for drilling, cementing, or hydraulic fracturing. Most of the reported studies show nanoparticle applications in these operations at laboratory and development scales. However, some commercial products available from nanomaterials for hydraulic fracturing application were discussed elsewhere [83], as shown in Table 10.4.

10.8 Conclusion

This book chapter focused on highlighting the application of nanoparticles in the areas such as drilling fluids, cementing, hydraulic fracturing, and/or well stimulation. Based on the published literature, nanoparticles are showing promising results based on their performance and efficiency. The obtained findings can be ascribed to

Table 10.4 Commercial products designed from nanomaterials and the reported field applications

Materials	Type of applications	Commercialization	Field	Applications	Reference
OIL perm TM FMMs	Fluid mobility modifier (FMMs)	Halliburton incorporated	Wood ford shale play in Oklahoma	Oil production increased after 30 days for treatment	[83]
Controlled electrolytic metallics (CEM) material(IN-Tallic disintegrating frac balls)	Downhole completion tools	Baker Hughes Incorporated	USA tight formations (Bakken, Niobrara, Marcellus, Utica, Haynesville, Granite Wash, Woodford, Wolfberry, Bone Springs, and Eagle Ford)	Ball-activated sleeve system for multi-stage fracturing of shale gas reservoirs.	[83]
ConFINE fixing agent	Formation fines control additives and clay stabilizers	Baker Hughes Incorporated	The deep-water Gulf of Mexico	For controlling sand and fine migration	[83]
Nano-proppants FracBlack HT™	Nano-proppants	Sun Drilling Technologies	China, South America, and Europe	Applied in traditional and coal bed methane projects (China) Applied as gravel pack material (South America) Applied for recovery of hydrocarbons in both shale and coal bed methane projects (Europe)	[83]

the idiosyncratic properties of nanoparticles. Despite their higher potential, nanoparticles still have challenges such as scale-up for field application due to their economics feasibility and the HSE aspects. This chapter further confirms a number of points. Silica-based nanoparticles continue to be the most investigated nanoparticles used in the improvement of different applications in the oil and gas industry, specifically for the reviewed segments. Generally, most of the nanoparticles that have been used previously depending on their concentrations, sizes and types, for the

various applications, have improved the rheological, filtration and mechanical, thermal stability properties for drilling, cement, and hydraulic fracturing fluids. Specifically, for cementing, the setting time and the mechanical properties were significantly improved using different nanoparticles. Improving the fluid properties may depend on the size, nanoparticle type, shape, nanoparticle concentration, and the operating pressure and temperature of the reservoir. For hydraulic fracturing/well stimulation, given their small particle size and surface area-to-volume ratio, higher hardness and elasticity, and high closure stress resistance, nanoparticles such as fly ash, nanosilica, and carbon nanotubes have been successfully used as effective nano-proppants and have been used to enhance the fracture conductivity and oil recovery. Lastly, it is paramount to investigate the impact of various factors such as nanoparticle type, nanoparticle surface wettability, size reservoir pH properties, salinity on stability, and agglomeration at downhole conditions for better optimization and improved effectiveness.

References

1. J. Abdo, M. Haneef, Nano-enhanced drilling fluids: Pioneering approach to overcome uncompromising drilling problems. J. Energy Resour. Technol. **134**(1) (2012)
2. M. Dardir et al., Preparation and evaluation of some esteramides as synthetic based drilling fluids. Egypt. J. Pet. **23**(1), 35–43 (2014)
3. N.A. Sami, Effect of magnesium salt contamination on the behavior of drilling fluids. Egypt. J. Pet. **25**(4), 453–458 (2016)
4. M. Riley et al., Wellbore stability in unconventional shales-the design of a nano-particle fluid, in *SPE oil and gas India conference and exhibition*, (Society of Petroleum Engineers, 2012)
5. M.K. Al-Arfaj et al., Chemical and mechanical aspects of wellbore stability in shale formations: A literature review, in *Abu Dhabi International Petroleum Exhibition and Conference*, (Society of Petroleum Engineers, 2014)
6. A. Ettehadi, G. Altun, Extending thermal stability of calcium carbonate pills using sepiolite drilling fluid. Pet. Explor. Dev. **44**(3), 477–486 (2017)
7. A.S. Mohammed, Effect of temperature on the rheological properties with shear stress limit of iron oxide nanoparticle modified bentonite drilling muds. Egypt. J. Pet. **26**(3), 791–802 (2017)
8. N.N. Nassar, A. Hassan, P. Pereira-Almao, Application of nanotechnology for heavy oil upgrading: Catalytic steam gasification/cracking of asphaltenes. Energy Fuel **25**(4), 1566–1570 (2011)
9. R. Nazari Moghaddam et al., Comparative study of using nanoparticles for enhanced oil recovery: Wettability alteration of carbonate rocks. Energy Fuel **29**(4), 2111–2119 (2015)
10. F. Sagala et al., Nanopyroxene-based nanofluids for enhanced oil recovery in sandstone cores at reservoir temperature. Energy Fuel **33**(2), 877–890 (2019)
11. M. Amanullah, A.M. Al-Tahini, Nano-technology-its significance in smart fluid development for oil and gas field application, in *SPE Saudi Arabia Section Technical Symposium*, (Society of Petroleum Engineers, 2009)
12. M. Amanullah, M.K. AlArfaj, Z.A. Al-abdullatif, Preliminary test results of nano-based drilling fluids for oil and gas field application, in *SPE/IADC drilling conference and exhibition*, (Society of Petroleum Engineers, 2011)
13. D. Hou et al., Micromechanical properties of nanostructured clay-oxide multilayers synthesized by layer-by-layer self-assembly. Nano **6**(11), 204 (2016)

14. Z. Wang et al., Poly (sodium p-styrene sulfonate) modified Fe3O4 nanoparticles as effective additives in water-based drilling fluids. J. Pet. Sci. Eng. **165**, 786–797 (2018)
15. A. Balza et al., Nanoparticles usage tendencies in cementing systems for hydrocarbon wells, in *Cementing a sustainable future-XIII International Congress on The Chemistry of Cement*, (Madrid, 2011)
16. N. Yekeen et al., Nanoparticles applications for hydraulic fracturing of unconventional reservoirs: A comprehensive review of recent advances and prospects. J. Pet. Sci. Eng., 41–73 (2019)
17. G. Cheraghian et al., Effect of a novel clay/silica nanocomposite on water-based drilling fluids: Improvements in rheological and filtration properties. Colloids Surf. A Physicochem. Eng. Asp. **555**, 339–350 (2018)
18. H. Hakim et al., Performance of polyethylene and polypropylene beads towards drill cuttings transportation in horizontal wellbore. J. Pet. Sci. Eng. **165**, 962–969 (2018)
19. R.T. Ewy, E.K. Morton, Wellbore-stability performance of water-based mud additives. SPE Drill. Complet. **24**(03), 390–397 (2009)
20. S. He et al., The influence of water-based drilling fluid on mechanical property of shale and the wellbore stability. Petroleum **2**(1), 61–66 (2016)
21. K.P. Hoelscher et al., Application of nanotechnology in drilling fluids, in *SPE international oilfield nanotechnology conference and exhibition*, (Society of Petroleum Engineers, 2012)
22. R. Rafati et al., Effect of nanoparticles on the modifications of drilling fluids properties: A review of recent advances. J. Pet. Sci. Eng. **161**, 61–76 (2018)
23. J. Abdo, M. Haneef, Clay nanoparticles modified drilling fluids for drilling of deep hydrocarbon wells. Appl. Clay Sci. **86**, 76–82 (2013)
24. M.T. Alsaba, M.F. Al Dushaishi, A.K. Abbas, A comprehensive review of nanoparticles applications in the oil and gas industry. J. Pet. Explor. Prod. Technol., 1–11 (2020)
25. E. Güneyisi et al., Rheological and fresh properties of self-compacting concretes containing coarse and fine recycled concrete aggregates. Constr. Build. Mater. **113**, 622–630 (2016)
26. A. Piroozian et al., Impact of drilling fluid viscosity, velocity and hole inclination on cuttings transport in horizontal and highly deviated wells. J. Pet. Explor. Prod. Technol. **2**(3), 149–156 (2012)
27. Y. Kang et al., Strengthening shale wellbore with silica nanoparticles drilling fluid. Petroleum **2**(2), 189–195 (2016)
28. A. Noah et al., Enhancement of yield point at high pressure high temperature wells by using polymer nanocomposites based on ZnO & CaCO3 nanoparticles. Egypt. J. Pet. **26**(1), 33–40 (2017)
29. S. Agarwal et al., Flow behavior of nanoparticle stabilized drilling fluids and effect of high temperature aging, in *AADE National Technical Conference and Exhibition*, (2011)
30. A.E. Bayat et al., Experimental investigation of rheological and filtration properties of water-based drilling fluids in presence of various nanoparticles. Colloids Surf. A Physicochem. Eng. Asp. **555**, 256–263 (2018)
31. Z. Deng, P.W. Livanec, J.P. Deville, Novel water-based fluids for Oil-Sands drilling, in *SPE Canada Heavy Oil Technical Conference*, (Society of Petroleum Engineers, 2015)
32. A. Katende et al., Improving the performance of oil based mud and water based mud in a high temperature hole using Nanosilica nanoparticles. Colloids Surf. A Physicochem. Eng. Asp. **577**, 645–673 (2019)
33. M. Al-saba et al., Application of nanoparticles in improving rheological properties of water based drilling fluids, in *SPE Kingdom of Saudi Arabia Annual technical symposium and exhibition*, (Society of Petroleum Engineers, 2018)
34. Y. Tian et al., Fe3O4/poly (acrylic acid) nanoparticles as modifiers for improving rheological and filtration properties of water-based drilling fluids. J. Macromol. Sci. A **56**(5), 393–402 (2019)
35. M.A.A. Alvi et al., The effect of micro-sized boron nitride BN and Iron trioxide Fe 2 O 3 nanoparticles on the properties of laboratory bentonite drilling fluid, in *SPE Norway one day seminar*, (Society of Petroleum Engineers, 2018)

36. P. Dejtaradon et al., Impact of ZnO and CuO nanoparticles on the rheological and filtration properties of water-based drilling fluid. Colloids Surf. A Physicochem. Eng. Asp. **570**, 354–367 (2019)
37. V. Wagle, A.S. Al-Yami, Z. AlAbdullatif, Using nanoparticles to formulate sag-resistant invert emulsion drilling fluids, in *SPE/IADC Drilling Conference and Exhibition*, (Society of Petroleum Engineers, 2015)
38. Z. Vryzas et al., Utilization of iron oxide nanoparticles in drilling fluids improves fluid loss and formation damage characteristics, in *First EAGE Workshop on Well Injectivity and Productivity in Carbonates*, (European Association of Geoscientists & Engineers, 2015)
39. M. Zakaria, M.M. Husein, G. Harland, Novel nanoparticle-based drilling fluid with improved characteristics, in *SPE international oilfield nanotechnology conference and exhibition*, (Society of Petroleum Engineers, 2012)
40. T. Sensoy, M.E. Chenevert, M.M. Sharma, Minimizing water invasion in shales using nanoparticles, in *SPE Annual Technical Conference and Exhibition*, (Society of Petroleum Engineers, 2009)
41. A. Ismail et al., The novel approach for the enhancement of rheological properties of water-based drilling fluids by using multi-walled carbon nanotube, nanosilica and glass beads. J. Pet. Sci. Eng. **139**, 264–275 (2016)
42. A. Parizad, K. Shahbazi, A.A. Tanha, Enhancement of polymeric water-based drilling fluid properties using nanoparticles. J. Pet. Sci. Eng. **170**, 813–828 (2018)
43. J. Abdo et al., ZnO–clay nanocomposites for enhance drilling at HTHP conditions. Surf. Interface Anal. **46**(10–11), 970–974 (2014)
44. K. Anoop et al., Rheology of mineral oil-SiO2 nanofluids at high pressure and high temperatures. Int. J. Therm. Sci. **77**, 108–115 (2014)
45. M.-C. Li et al., Cellulose nanoparticles as modifiers for rheology and fluid loss in bentonite water-based fluids. ACS Appl. Mater. Interfaces **7**(8), 5006–5016 (2015)
46. J. Nasser et al., Experimental investigation of drilling fluid performance as nanoparticles. World J. Nano Sci. Eng. **2013** (2013)
47. S. Taraghikhah, M. Kalhor Mohammadi, K. Tahmasbi Nowtaraki, Multifunctional nanoadditive in water based drilling fluid for improving shale stability, in *International Petroleum Technology Conference*, (International Petroleum Technology Conference, 2015)
48. O. Mahmoud et al., Nanoparticle-based drilling fluids for minimizing formation damage in HP/HT applications, in *SPE international conference and exhibition on formation damage control*, (Society of Petroleum Engineers, 2016)
49. N.A. Yazdi et al., To study the effect of adding Fe2O3 nanoparticles on the morphology properties and microstructure of cement mortar. Life Sci. J. **8**(4), 550–554 (2011)
50. C. Vipulanandan, A. Mohammed, Smart cement modified with iron oxide nanoparticles to enhance the piezoresistive behavior and compressive strength for oil well applications. Smart Mater. Struct. **24**(12), 125020 (2015)
51. S. Kawashima et al., Modification of cement-based materials with nanoparticles. Cem. Concr. Compos. **36**, 8–15 (2013)
52. J.D. Mangadlao, P. Cao, R.C. Advincula, Smart cements and cement additives for oil and gas operations. J. Pet. Sci. Eng. **129**, 63–76 (2015)
53. L. Raki, J. Beaudoin, R. Alizadeh, Nanotechnology applications for sustainable cement-based products, in *Nanotechnology in Construction 3*, (Springer, 2009), pp. 119–124
54. B. Piot, *Cement and Cementing: An Old Technique with a Future?* (SPE Distinguished Lecturer Program, Society of Petroleum Engineers, Richardson, 2009)
55. J. Fink, *Petroleum engineer's guide to oil field chemicals and fluids* (Gulf Professional Publishing, 2015)
56. I. Wong et al., Effects of ultra-low concentrations of carbon nanotubes on the electromechanical properties of cement paste, in *Nanotechnology in Construction*, (Springer, 2015), pp. 371–376

57. Y. Gao et al., Dispersion of multi-walled carbon nanotubes stabilized by humic acid in sustainable cement composites. Nano **8**(10), 858 (2018)
58. F. Sanchez, K. Sobolev, Nanotechnology in concrete–a review. Constr. Build. Mater. **24**(11), 2060–2071 (2010)
59. C. Vipulanandan, A. Mohammed, A. Ganpatye, Smart cement performance enhancement with nanoal 2 o 3 for real time monitoring applications using Vipulanandan models, in *Offshore technology conference*, (Offshore Technology Conference, 2018)
60. C. Vipulanandan et al., Iron nanoparticle modified smart cement for real time monitoring of ultra deepwater oil well cementing applications, in *Offshore technology conference*, (Offshore Technology Conference, 2015)
61. A.K. Santra, P. Boul, X. Pang, Influence of nanomaterials in oilwell cement hydration and mechanical properties, in *SPE international oilfield nanotechnology conference and exhibition*, (Society of Petroleum Engineers, 2012)
62. X. Pang, P.J. Boul, W. Cuello Jimenez, Nanosilicas as accelerators in oilwell cementing at low temperatures. SPE Drill. Complet. **29**(01), 98–105 (2014)
63. M. Jalal et al., Mechanical, rheological, durability and microstructural properties of high performance self-compacting concrete containing SiO2 micro and nanoparticles. Mater. Des. **34**, 389–400 (2012)
64. H. Li, H.-g. Xiao, J.-p. Ou, A study on mechanical and pressure-sensitive properties of cement mortar with nanophase materials. Cem. Concr. Res. **34**(3), 435–438 (2004)
65. S. Ahmed, C.P. Ezeakacha, S. Salehi, Improvement in cement sealing properties and integrity using conductive carbon nano materials: From strength to thickening time, in *SPE annual technical conference and exhibition*, (Society of Petroleum Engineers, 2018)
66. N. Jafariesfad et al., Nano-sized mgo with engineered expansive property for oil well cement systems, in *SPE Bergen one day seminar*, (Society of Petroleum Engineers, 2016)
67. A. Deshpande, R. Patil, Applications of nanotechnology in oilwell cementing, in *SPE Middle East oil & gas show and conference*, (Society of Petroleum Engineers, 2017)
68. M. Alkhamis, A. Imqam, New cement formulations utilizing graphene nano platelets to improve cement properties and long-term reliability in oil wells, in *SPE Kingdom of Saudi Arabia annual technical symposium and exhibition*, (Society of Petroleum Engineers, 2018)
69. A. Nazari, S. Riahi, The effects of Cr2O3 nanoparticles on strength assessments and water permeability of concrete in different curing media. Mater. Sci. Eng. A **528**(3), 1173–1182 (2011)
70. A. Das et al., Rheological and breaking studies of a novel single-phase surfactant-polymeric gel system for hydraulic fracturing application. J. Pet. Sci. Eng. **167**, 559–567 (2018)
71. F. Nath, C. Xiao, Characterizing foam-based Frac fluid using Carreau rheological model to investigate the fracture propagation and proppant transport in eagle ford shale formation, in *SPE Eastern Regional Meeting*, (Society of Petroleum Engineers, 2017)
72. N. Yekeen, E. Padmanabhan, A.K. Idris, A review of recent advances in foam-based fracturing fluid application in unconventional reservoirs. J. Ind. Eng. Chem. **66**, 45–71 (2018)
73. G.A. Al-Muntasheri, F. Liang, K.L. Hull, Nanoparticle-enhanced hydraulic-fracturing fluids: A review. SPE Prod. Operations **32**(02), 186–195 (2017)
74. G. Selvaraj et al., Experimental study of nanoparticles as catalyst in enhancing matrix acidizing for carbonate reservoir. J. Pet. Explor. Prod. Technol., 1–9 (2019)
75. N. Raj, T.V. Pal, Enhancing efficiency of HCl based stimulating fluids by creating in-situ carbonic acid using nickel nanoparticles, in *International Petroleum Technology Conference*, (International Petroleum Technology Conference, 2014)
76. M.N. Alaskar et al., Nanoparticle and microparticle flow in porous and fractured media--an experimental study. SPE J. **17**(04), 1,160–1,171 (2012)
77. R. Barati, Application of nanoparticles as fluid loss control additives for hydraulic fracturing of tight and ultra-tight hydrocarbon-bearing formations. J. Nat. Gas Sci. Eng. **27**, 1321–1327 (2015)

78. M. Fakoya, S. Shah, Enhancement of filtration properties in surfactant-based and polymeric fluids by nanoparticles, in *SPE Eastern Regional Meeting*, (Society of Petroleum Engineers, 2014)
79. Y. Li et al., Reducing hydroxypropyl guar gum adsorption on rock by silica nanoparticles for tight reservoir damage remediation, in *International petroleum technology conference*, (International Petroleum Technology Conference, 2019)
80. R. Singh et al., *Nanoparticle-encapsulated acids for stimulation of calcite-rich shales* (Unconventional Resources Technology Conference (URTEC), 2018)
81. H.A. Nasr-El-Din, M.R. Gurluk, J.B. Crews, Enhancing the performance of viscoelastic surfactant fluids using nanoparticles, in *EAGE Annual Conference & Exhibition incorporating SPE Europec*, (Society of Petroleum Engineers, 2013)
82. A.S. Emrani, A.F. Ibrahim, H.A. Nasr-El-Din, Mobility control using nanoparticle-stabilized CO 2 foam as a hydraulic fracturing fluid, in *SPE Europec featured at 79th EAGE Conference and Exhibition*, (Society of Petroleum Engineers, 2017)
83. S. Gottardo et al., *Use of Nanomaterials in Fluids, Proppants, and Downhole Tools for Hydraulic Fracturing of Unconventional Hydrocarbon Reservoirs* (Publications Office of the European Union, Luxembourg, 2016)

Chapter 11
Double Purpose Drilling Fluid Based on Nanotechnology: Drilling-Induced Formation Damage Reduction and Improvement in Mud Filtrate Quality

Johanna V. Clavijo, Leidy J. Roldán, Diego A. Castellanos, German A. Cotes, Ángela M. Forero, Camilo A. Franco, Juan D. Guzmán, Sergio H. Lopera, and Farid B. Cortés

11.1 Introduction

The production in the Ocelote field is mainly in C7 sand, which corresponds to sand from the Carbonera formation. The well logs recorded during the life cycle of this field show drilling-induced formation damage associated with the drilling process where water-based drilling fluids have been used. Therefore, the production from the new wells was low based on the values estimated from the petrophysical properties. Although this problem has been alleviated by modifying the type and design of the bridging material used in the conventional fluids, there is scope to further reduce the damage and achieve an early stimulation of the formation from other types of mechanisms. Moreover, during the production life of the wells, the productivity decreases because of fines migration (presence of migratory clays) and wettability changes due to organic deposits (crude oil with colloidal instability).

J. V. Clavijo · S. H. Lopera
Grupo de Investigación en Yacimientos de Hidrocarburos, Facultad de Minas, Universidad Nacional de Colombia – Sede Medellín, Medellín, Colombia
e-mail: jovargascl@unal.edu.co; shlopera@unal.edu.co

L. J. Roldán · C. A. Franco (✉) · J. D. Guzmán · F. B. Cortés (✉)
Química Grupo de Investigación en Fenómenos de Superficie—Michael Polanyi, Departamento de Procesos y Energía, Facultad de Minas, Universidad Nacional de Colombia, Sede Medellín, Medellín, Colombia
e-mail: lejroldanva@unal.edu.co; caafrancoar@unal.edu.co; dguzmanc@unal.edu.co; fbcortes@unal.edu.co

D. A. Castellanos · G. A. Cotes · Á. M. Forero
Hocol S.A., Bogotá, Colombia
e-mail: diego.castellanos@hocol.com.co; german.cotes@hocol.com.co; Angela.forero@hocol.com.co

N. N. Nassar et al. (eds.), *Nanoparticles: An Emerging Technology for Oil Production and Processing Applications*, Lecture Notes in Nanoscale Science and Technology, https://doi.org/10.1007/978-3-319-12051-5_11

Mud filtrate and solid particle invasion near the wellbore during the drilling process and the consequent formation damage induced are the main problems in the oil and gas industry [1–3]. The different damage mechanisms due to the mud filtrate are associated with polymer adsorption onto the rock and plugging [1], ionic incompatibility between the filtrate and the formation water [4], aqueous filtrate trapping [5], wettability [6, 7], and pore-blocking effects [8] resulting from changes in the saturation of water [9, 10]. The solid and fine particles inherent to the formation block the pore throats and reduce the effective flow space [11, 12]. Furthermore, an accurate interpretation of the well logs depends strongly on the depth of the mud filtrate and fine mobilization extent.

It is difficult to reduce the near-wellbore invasion of the mud filtrate and mitigate the fines migration given the design of the drilling fluids in terms of the selection of suitably sized bridging material [13–16] and filtration control additives [17] for an appropriate filter cake development [18]. Moreover, the properties of the reservoir and formation fluids, particularly the viscosity, interfacial tension (IFT), and wettability, vary because of the interactions between the reservoir fluid, mud filtrate, and fine particles [10]. Therefore, in the drilling fluid design, reducing the drilling-induced formation damage due to the invasion of the mud filtrate and controlling the fines migration are essential. The solution designed in this study aims to mitigate the formation damage while drilling a well in a field located in the Llanos Basin of Colombia (Ocelote field).

Recently, nanoparticles (NPs) have been employed in NP-based drilling fluids, where the NPs influence the viscosity, filtration control, and thermal and electrical conductivities, among the other properties of the drilling fluid simultaneously [19]. For instance, authors have evaluated the chemical characteristics of NPs [20–23], intercalated clay hybrid [24, 25], and nano-polymer material [26–28] to improve the rheological behavior and filtration properties of the drilling fluids. Others have studied carbon nanotubes, SiO_2, ZnO, and CuO NPs to enhance the thermal and electrical conductivities [19, 29–31]. Some studies have demonstrated that NPs could improve shale inhibition and wellbore stability [32–34]. However, these studies did not consider the inhibition of the formation damage due to the drilling fluids. Moreover, these NP-based drilling fluids neglect the effects of the mud filtrate and fine invasion into the porous media. Most studies focused on bentonite-based drilling fluids, which are associated with a high formation damage degree [35, 36].

More recently, our research group examined the effects of the nanoparticle size and surface acidity on the formation damage due to bentonite-free water-based drilling fluids. Additionally, the authors found that the invaded mud filtrate remained in contact with the heavy oil during the displacement and reduced the viscosity [37]. Therefore, nanofluids should be designed such that they not only reduce the formation damage but also ensure that the mud filtrate invaded allows inhibiting the damage mechanism such as in terms of the fine migration, wettability alteration, and viscosity reduction, while additionally acting as a drilling fluid for stimulation treatment. The NPs could favor the stimulation of the reservoir and reduce the use of additional chemical stimulation treatments for improving the oil and gas production in the early stages. Recently, Al-Yasiri et al. [19] developed a multifunctional

drilling fluid by incorporating NPs. This nanofluid improved the rheology, filtration, and thermal properties of the drilling fluid, overcoming many of the difficulties encountered in drilling operations [19]. To the best of our knowledge, there is no report that addresses both the reduction in drilling-induced formation damage and enhancement in the mud filtrate quality that could improve the oil mobility and help control fines migration with the use of a mud filtrate invaded with NPs.

Therefore, in this study, we designed a double purpose nanofluid to reduce the drilling-induced formation damage while the mud filtrate invaded allows for improving the oil mobility and controlling the migration fines through core flooding tests under reservoir conditions. Our double purpose drilling fluid is a new concept for NP-based drilling fluids to reduce the drilling-induced formation damage while improving the quality of the mud filtrate invaded, allowing for the interaction between the rock and the formation fluids. Improvement in oil mobility and better fines migration control can be expected. This paper is organized into five main sections: (i) NP characterization, (ii) evaluation of rheological and filtration properties, (iii) evaluation of the mud filtrate quality, (iv) core flooding experiments, and (v) field application. Our experimental study on the drilling fluids could help enhance the drilling fluid properties, reduce the drilling-induced formation damage, and employ the mud filtrate as an early stimulation treatment to improve the oil mobility by reducing the wettability change and IFT. Field applications were carried out on the drilling of two horizontal wells, in which a high mud filtration invasion has been historically reported. The results are validated by comparing the behavior of the pilot with a base drilling fluid well whose drilling is carried out using the same drilling fluid but without the nanomaterials. The wells are evaluated in terms of the invasion diameter, well stabilization time, productivity index, and solid production, in order to verify the effectiveness of the NPs in the drilling fluid.

11.2 Materials and Methods

11.2.1 Nanoparticle Characterization

Fumed silica NPs (Si, 99%, Sigma Aldrich, United States) and β-alumina NPs (Al, Petroraza, Colombia) were used. The NPs were characterized using the hydrodynamic diameter (dh = 9.7 ± 4 nm Si and 61.4 ± 6 nm Al) and zeta potential at pH of work (ζ-potential @ pH 10 = −31.54 ± 3 mV Si and − 56.66 ± 2 mV Al) based on the dynamic light scattering technique (DLS) using a Nanoplus-3 from Micrometrics (Norcross, GA, United States). The surface area (SBET = 380 m^2/g Si and 247 m^2/g Al) was determined through N_2 physisorption using the Brunauer–Emmett–Teller method (BET) with a Gemini VII 2390 Surface Area Analyzer (Autosorb-1 from, Quantachrome, United State). Finally, the Fourier transform infrared spectroscopy (FTIR) using an IRAffininty-1 s (Shimadzu, Kyoto, Japan) was applied to determine the functional groups on the NP surface.

11.2.2 Drilling Fluid Preparation and Characterization

The drilling fluid was prepared to blend each component in a mixer (Hamilton Beach, United State) as follows: 300 mL of water, pH was adjusted with caustic soda to reach a value of 10 (NaOH >98%, Sigma Aldrich, United State), 1 g of xanthan gum (Sigma Aldrich, United State), 5 g of starch (Sigma Aldrich, United State), 22 g of diesel, 3.4 g of 600 mesh calcium carbonate ($CaCO_3$, Procomin, Colombia), 15.0 g of 325 mesh $CaCO_3$, and 4.1 g of 200 mesh $CaCO_3$. The Al and Si NPs were added after xanthan gum with a concentration varying from 0 to 0.3 wt.%.

11.2.3 Methods

11.2.3.1 Aging Process

Each of the prepared drilling fluid samples was aged in a hot roller oven (Fann, United States) in a hermetic cylinder at 76 °C for 16 h by adhering to the American Petroleum Institute (API) recommended test procedures [38]. The objective was to evaluate the rheology and filtration control in the worst scenario of the drilling fluid, that is, after thermal and dynamic degradation during the drilling operation under the bottom hole conditions.

11.2.3.2 Rheological and Filtration Test

A rotational viscometer (Ofite, United States) was used to determine the rheological properties of the drilling fluid. The plastic viscosity (PV) was obtained by subtracting the Fann values at θ_{600} and θ_{300}. Yield point (YP) was obtained by subtracting at the PV value the Fann lecture at θ_{300}. Gel strength was measured at 10 s and 10 min (Gel 10s/10 m) reading the maximum dial at θ_3 after at the respective time of not circulation. Finally, the HPHT filtration test (Fann, United States) was conducted to quantify the filtration volume under the static condition with a differential pressure of 500 psi and a temperature of 76 °C, respectively. Additionally, the mudcake thickness was measured using a digital caliper (700–113 MyCal Lite, Mitutoyo America Corp, United State) with several repetitions. These procedures adhered to the standard protocols of the API [38].

Based on the results of the rheological and filtration experiments, the optimal concentration of the NPs was selected to evaluate the performance of the mud filtrate obtained in their respective filtration test for improving the oil mobility and fines migration control.

11.2.3.3 Contact Angle, Spontaneous Imbibition Test, and Interfacial Tension Measurements

The oil-wet rock samples, representative of the formation mineralogy, were immersed into the mud filtrates with and without the NPs for 24 h at 25 °C. The rock samples were oil-wet induced by asphaltene precipitation from an intermediate heavy crude (23° API and asphaltene content of 10.54% by weight) produced from the Ocelote field. Subsequently, the contact angle was measured through the sessile drop method using an Attention Theta optical tensiometer (Biolin Scientific, Finland). Moreover, we conducted a spontaneous test on the imbibition of water into the oil-wet rock impregnated previously with the mud filtrate, before drying at 70 °C overnight, at room temperature to monitor the weight changes in the system after being submerged. The imbibed water mass was recorded for 3.5 h [39, 40]. The wettability changes were analyzed on the basis of the liquid/air/rock contact angles formed in the surface samples treated with the filtrate mud with and without the NPs and in the differences between the imbibed mass. Finally, the IFT between the crude oil/water formation and the crude oil/mud filtrate with and without the NPs was evaluated at 25 °C using a force tensiometer - K11 (Krüss, Germany). The same crude oil used for the oil-wet induction was employed for the IFT measurements and the displacement test.

11.2.3.4 Fines Retention Experimental Test

Fines retention experimental tests were performed in synthetic porous media previously impregnated with the mud filtrate with and without the NPs under atmospheric conditions. The porous media were prepared with 70 g of Ottawa sand (Minercol S.A, Colombia) (12–20 and 25–40 mesh) in a fraction mass of 50% ratio of each mesh. The solution of the fines was composed of a mass fraction of 0.2% kaolinite, because it is considered the most problematic clay and the main reason for the plugging of porous spaces due to its migration [41–43], as seen in the Ocelote field. Hence, fines suspension was injected from the top and flowed through the sand packed through gravity forces. The effluent was collected and passed through the filter paper to measure the quantity or concentration of the fines retained. Before the test, the sand bed was soaked for 24 h with the mud filtrate with the NPs to impregnate the porous media. The filter paper was weighted each time the fines suspension passed through the porous media, thus determining the fines retained using an analytical balance (A & D company, United States) and obtaining the concentration of the resultant fines. The test was completed once the initial concentration was equal to the effluent concentration [42, 44].

11.2.3.5 Displacement Test

Sandstone core samples from the Carbonera C7 formation of the Ocelote field were used to compare the formation damage by the solid particle and mud filtrate invasion from the drilling fluids with and without the NPs and to evaluate the migratory clay control through the invaded mud filtrate. The mineralogical composition of the rock samples consists of quartz (86%), feldspar (2%), illite/smectic (1%), illite/mica (1%), kaolinite (9%), and chlorite (1%). The core flooding experiments were carried out under reservoir and dynamic conditions such as a reservoir pressure of 1627 psi, a confining pressure of 2293 psi, an injection rate of 0.3 mL/min, and a temperature of 76 °C. Table 11.1 lists the basic properties of the core samples from the Ocelote field.

The drilling-induced formation damage due to the drilling fluid was evaluated by comparing the permeability values before and after the injection of the drilling fluid with respect to the protocol by Van der Zwaag [45]. The NP performance was examined considering three scenarios: (1) baseline, (2) drilling fluid injection without NPs, and (3) drilling fluid with NPs, in other words the double purpose drilling fluid. First, a synthetic brine was injected, and the absolute permeability was measured (Kabs). Subsequently, the Ko and relative permeability curves (Kr) were obtained through the injection of the crude oil and synthetic brine, respectively. The crude oil was injected to reach the residual water saturation state. Thereafter, the drilling fluid was circulated in the transverse direction to the production core face with an overbalance pressure of 500 psi, simulating the drilling operative times and appropriate rates of the field. Additionally, while drilling with fluid circulation, the dynamic filtration was measured. Later, the oil effective permeability (Ko) was evaluated by injecting the crude oil. The Kro, Krw, and oil recovery factors after the drilling mud circulation were measured during the injection of the synthetic brine until the residual oil saturation (Sor). Finally, the crude oil was injected, and the return permeability was measured.

To evaluate the fines migration control by the mud filtrate invaded into the core, the drilling fluid with and without the NPs was once again circulated over the core face. The experimental protocol to determine the critical injection rate was based on a study conducted by Cespedes et al. [42]. Crude oil was injected at injection rates of 0.1, 0.3, 0.5, 1.0, 2.0, 3.0, 5.0, and 7.0 mL/min to obtain the injection rate in which Ko is reduced by 10% compared with the previous Ko value.

Table 11.1 Permeability and porosity core samples of the core samples from Carbonera C7 formation of Ocelote field

Core number	Permeability (mD)	Pore volume (mL)	Porosity (%)
1	453	9.7	20.2
2	445	11.1	22.0

11.3 Results

11.3.1 Nanoparticle Characterization

Figure 11.1 shows the transmission electron microscopy (TEM) images. The NPs presented an irregular form, and it was possible to corroborate the nanometric size obtained by the DLS. Figure 11.2 presents the FTIR spectrum and vibrational absorption bands for the Al and Si NPs. The representative bands of the vibration of the silica (Si–OH, Si–O–Si), alumina (Al–OH, Al–O–Al), and hydroxyl (–OH) groups can be observed. The wide peak in the range of 3000–3550 cm^{-1} is associated with Al–OH and Si–OH bonds and adsorbed water molecules on the surface in the case of both the NPs [46]. The peak at approximately 808 cm^{-1} can be attributed to siloxane (Si–O–Si) symmetric vibrations. The peak in the range of 980–1220 cm^{-1} corresponds to Al–O–Al and Si–O–Si linkages. Additionally, the band Si–O–Si groups are responsible for the peak in the range of 1970–1840 cm^{-1} [47]. The FTIR of the NPs is similar, except for the dissimilarities in the intensity of the peaks for the −OH groups. The surface area of the Si NPs is larger than that of the Al NPs, so

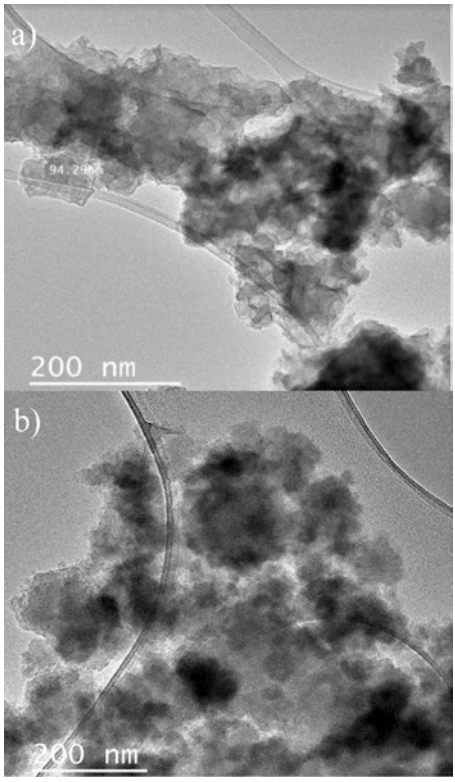

Fig. 11.1 Transmission electron microscopy images (TEM) of (**a**) Al and (**b**) Si NPs at a magnification of 200 nm

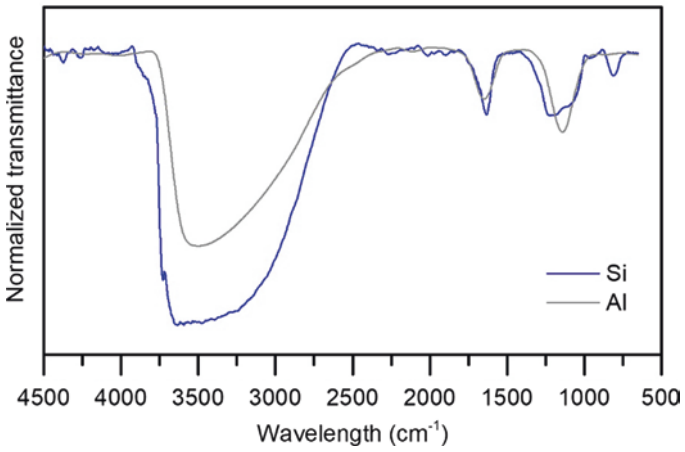

Fig. 11.2 FTIR spectra of Al and Si nanoparticles

the presence of −OH groups could be more representative; even water is adsorbed onto the surface in the case of the Si NPs.

11.3.2 Rheological and Filtration Behaviors

Figure 11.3a–c show the NP concentration effect on the PV, YP, and gel strength at 70 °C, respectively, of the drilling fluid samples after the hot rolling process, representing the critical scenario of the drilling fluids during the operation due to the thermal degradation. As expected, the PV increases with the increase in the NP concentration in the system. However, for Al NP concentrations in the range of 0.03–0.05 wt.%, the PV did not increase. In fact, at a concentration of 0.1 wt.% and higher, the PV increased. The Si NPs presented a higher PV increment than Al NPs. This increment in the PV values is a result of the adsorption of the hydrophilic group of the NPs with the polymer through hydrogen bonding with the –OH groups on the NP surface [48, 49]. However, the Si NPs had a stronger interaction with the polymer. The Al NPs had a lower adsorption capacity than silica [50]. The high PV can be attributed to the viscous base fluid; it means that there is an alteration of the cross-linking effect [51]. The addition of solid particles and the increment in the viscosity did not represent changes in the density of the drilling fluids, conserving the value of 8.9 lb/gal in all the samples. The addition of solid particles did not change the hydrostatic pressure of the fluid, thus ensuring a safe drilling operation. The YP presents a similar behavior as the PV values. The YP values increase with the increase in the NP concentration. However, the effect was stronger in the case of YP than in the case of PV after the addition of the NPs. The average increments for the PV were 5% and 13% for the Al and Si NPs, respectively, whereas for the YP, the increments were 16% and 20%. The YP is considered the flow resistance as a

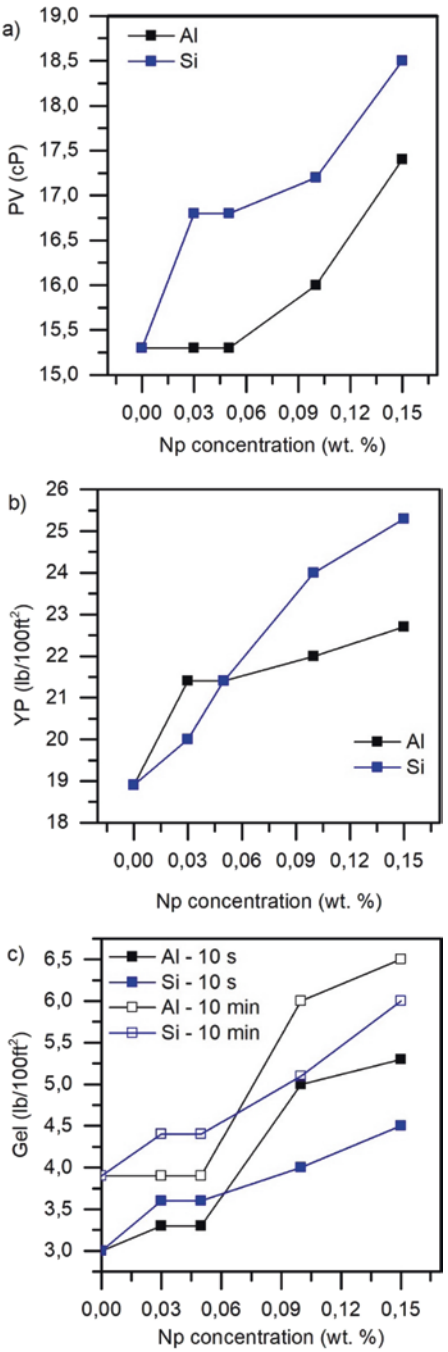

Fig. 11.3 Rheological properties of the drilling fluid samples as a function of the NP concentration: (**a**) plastic viscosity (PV), (**b**) yield point (YP), and (**c**) gel strength at 10 s and 10 min after the hot rolling process

consequence of the electrochemical forces inside the fluid under dynamic conditions [22]. These electrochemical forces were improved because of the electrical charges of the nanoparticles under a pH of 10 (pH of work), and deprotonation of H+ of the Si–OH and Al–OH occurs, resulting in a negative charge in the ζ-potential values, −31.54 and −56.66 mV, for the Si and Al NPs, respectively. The ζ-potential value is related to the colloidal stability due to the repulsion forces between the particles; for ζ-potential lower than −30 mV, a higher stability is obtained because the repulsion forces acts between the particles [24, 37, 52]. With regard to the samples presented herein, the Si NPs presented a lower ζ-potential than the Al nanoparticles, so the repulsion forces weakly favored the aggregation, allowing a higher resistance to flow and generating high PV values.

Otherwise, the gel strength, for the concentration range of 0.03–0.05 wt.%, presented a slight increase. However, at higher concentrations, the properties improve by approximately 60% and 80% with respect to the drilling fluid sample without NPs. Additionally, the gel structure of Al NPs was better than that of the Si NPs for concentrations greater than 0.1 wt.%. The gel strength is one of the major rheological properties indicating the capacity to build a gel structure during static conditions allowing the solid particles and cuttings suspension [22, 53]. This means that Al NPs present better electrostatic forces under static conditions, whereas the Si NPs exhibit the highest performance while the drilling fluid is in circulation. This could be because during the circulation of the drilling fluid, there are more interactions between the polymer chains and the Si NPs than in the case of the Al NPs. The ζ-potential value is quite high for the Al NPs, so in theory, the repulsion forces govern the system; however, under static conditions, the aggregation is predominant. This suggests that the conditions of the dynamic circulation of the fluids favor the Si NP–drilling fluid interactions, whereas the static conditions favor the Al NP–drilling fluid interaction. The NPs could improve the rheological parameter of the drilling fluids through different mechanisms that depend on the continuous phase, water, of the mud system, and characteristics of the NPs, as shown in previous studies [23–25, 27, 54–56]. The Si NPs could improve the viscosity and YP of the drilling fluids and consequently the transport of the solids and cutting to the surface during the drilling operation, whereas the Al NPs are better for the suspension or solids under static conditions. The NPs dispersed in the drilling fluid have a possibility of increasing the friction between the layers, which increases the viscosity [48, 49, 54]. The NPs and polymer may be linked through certain chemical linkages, thereby increasing the PV, YP, and gel strength. These results are in good agreement with the previous findings obtained by our group.

Figure 11.4a, b show the effects of NP concentration on the filtration volume and mudcake thickness at 500 psi and 70 °C of the drilling fluid samples after the hot rolling process. The filtration volume and mudcake thickness decrease until a concentration of 0.05 wt.% and then start to increase with an increase in the NP concentration. The Si and Al NPs presented a higher reduction of 17% in the filtration volume at an optimum concentration of 0.05 wt.%. The Si NPs reduced the mudcake thickness by 18% compared with the base mud, whereas the Al NPs did not present any significant changes. However, above an NP concentration of 0.1 wt.%,

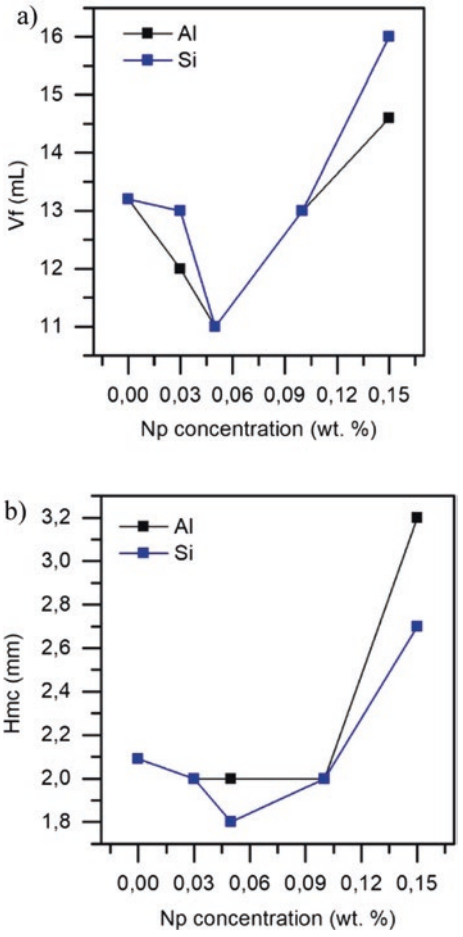

Fig. 11.4 Volume filtration (V_f) and mudcake thickness (h_{mc}) as a function of the NP concentration after the hot rolling process

a heavy filter cake thickness with a low quality was obtained, resulting in a high filtration volume. This behavior could be explained by the aggregation between the particles due to the reduction in the distance between them with the increase in the concentration. This was evident in the fact that the increments in the PV, YP, and gel strength were less at low concentrations; however, above 0.1 wt.%, the resistance to flow increases due to the aggregation. This suggests that the van der Waals and electrostatic attraction forces are predominant at high NP concentration [57]. When the Al and Si NPs are in the region of stability, that is, at ζ-potentials lower than −30 mV, we can expect a higher stability state to occupy the space between the bridging materials, and they can even act as dispersing agents [37, 58]. Some authors have reported that NPs could enhance the rheological and filtration parameters of the drilling fluids [23, 24, 26, 29, 54, 55, 59–62]. The NPs could interact with the polymer additives and strength of the viscoelastic structure [21, 23, 24, 61], while they act in the mudcake occupying the space and reducing the permeability and

porosity [24, 37, 55, 63]. Thus, the effluents from the HPHT filtration test with a concentration of 0.05 wt.%, which presented the highest filtration reduction, were selected to evaluate the possible wettability alteration, reduction in IFT, and migration fines control capacity.

11.3.3 Effluent Evaluations

Generally, the mud filtrate invaded is considered a contamination of the rock, altering the oil saturation, wettability, capillary pressure, among other properties near the wellbore [12, 18]. However, this could change with mud filtrate reduction and enhancement in the quality. This means while drilling, the mud filtrate invaded with the NPs could improve oil mobility and migration fines control because of NP retention in the porous media. Therefore, in this section, the effluents obtained in the HPHT test with an optimal NP concentration of 0.05 wt.% were selected as they showed the highest filtration reduction and improvement in the mudcake thickness to soak the sandstone core and Ottawa sands. The processes of mud filtrate invasion through the rock and wettability alteration were emulated. The results showed reduction in the IFT, improved oil mobility, and migration fines control. Figure 11.5 shows the drops of water (Fig. 11.5a–c) and oil (Fig. 11.5d–f) placed onto the rock surface, before and after mud filtrate soaking. As shown, the rock sample treated with the mud filtrate in the absence of NPs showed an average contact angle of 66.6°. This condition indicates a low oil-wet condition [64, 65]. The same behavior was observed for the rock treatment with the mud filtrate with Si NPs, 69.0°. However, the rock soaked with a mud filtrate with Al NPs presented a reduction of 37% compared with the base scenario (mud filtrate without the NPs), reaching an average contact angle of 41.4°. The presence of Al NPs favored the water-wettability, whereas the rock samples treated with the mud filtrate with the Si NPs did not

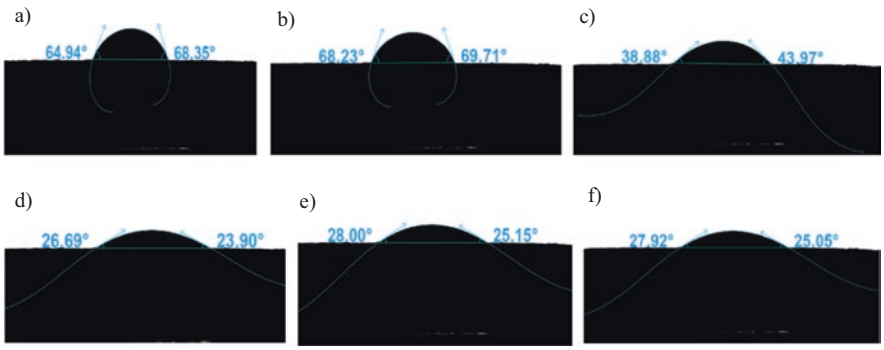

Fig. 11.5 Contact angles for the water/air/rock system treated with the mud filtrate: (**a**) without NPs, (**b**) with 0.05 wt.% Si, and (**c**) with 0.05 wt.% Al. Contact angles for the oil/air/rock system treated with the mud filtrate: (**d**) without NPs, (**e**) with 0.05 wt.% Si, and (**f**) with 0.05 wt.% Al

change the oil wettability to water. For the oil droplets, the contact angles after the mud filtrate treatment with and without the NPs did not change. Thus, the mud filtrate alters the wettability of the water but not of the oil. Subsequently, spontaneous imbibition tests were performed with the rock samples treated with the mud filtrate with and without the NPs. The difference between the former test is the available surface area in contact with the liquid. In the following test, the water could enter the rock and interact with the porous interconnected. Figure 11.6 compares the spontaneous imbibition of the rock samples treated with the mud filtrate in the absence of NPs, with 0.05 wt.% of Si and Al NPs, respectively. A fast-spontaneous imbibition was observed for the rock with the mud filtrate with Al NPs, consistent with the water-wet condition obtained in the contact angle test. This could be due to the capillary pressure, which is the main factor driving the spontaneous imbibition and is greater as the system is more water-wet, whereas the rock samples treated with the mud filtrate without the NPs presented the slowest imbibition process. These results are in good agreement with those obtained from the contact angle test. The mud filtrate that invaded the formation can improve the wettability of the rock. The NPs that have an affinity for the oil phase could be more easily adsorbed onto the surface and can extend, making a thin film between the water drop and the solid surface, as reported in literature [40, 66–68]. This means that the NPs decorate the surfaces with induced oil wettability change into water preferences [40, 69]. Regarding the IFT, the Al nanoparticles in the mud filtrate generated a reduction in the IFT measurement from 31.4 ± 0.5 mN/m to 24.1 ± 0.3 mN/m, which represents a reduction of 24% compared with the crude oil/formation brine, whereas the mud filtrate without the NPs did not represent a significative change, with IFT values of 31.9 ± 0.2 mN/m and 40 ± 0.5 mN/m, respectively. The NPs created a layer at the crude oil and brine interface, thus reducing the friction between them, improving the mobilization of the oil, and decreasing the work required to move the oil droplets [70]. The trapped oil can be recovered if the ratio between the viscous and capillary forces, expressed in literature as the capillary number $Nc = \mu V/\sigma\cos(\theta)$ [71], can

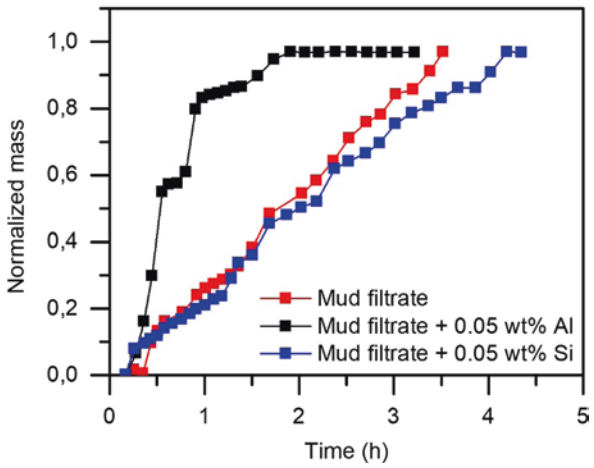

Fig. 11.6 Spontaneous imbibition curves for sandstone cores soaked with a mud filtrate in the absence and presence of Al and Si NPs with a concentration of 0.05 wt.%

be increased when the system exhibits the least flow restriction due to the reduced interfacial and wettability. Wettability alteration and IFT reduction are two important mechanisms for enhanced oil recovery, playing a dominant role in the possible oil mobility mechanisms. The mud filtrate not only works as a conventional stimulation treatment but also helps change the wettability and reduce the IFT.

Figure 11.7 shows the breakthrough curves for the sand samples treated with the mud filtrate with and without the Al and Si NPs at 0.05 wt.%. For the mud filtrate of the base drilling fluid, the breakthrough curve shows an inherent retentive capacity to sand, which is considerably lower than that when it is impregnated with the NPs, as these provide a greater fixate capacity of the fines on the sand. Therefore, the sand sample impregnated with the mud filtrate with the Si NPs presented a greater fines retention. This could be attributed to the better affinity of the Si NPs to clay fines in attaching to the sand grains. The attractive bonds between these particles and the rock matrix are strengthened by the presence of the NPs that had been previously adsorbed onto the surface. In other words, the presence of certain NPs inhibits the fines migration by fixing them to the formation [43, 72]. These results are consistent with the report by Mora et al. [44].

Based on the obtained results, the drilling fluid with Al and Si NPs reported a filtration volume reduction and improvement in rheological properties. Additionally, the mud filtrate that invaded the formation could improve the water-wettability tendency and reduce the IFT, for the case of the mud filtrate with Al NPs, and achieve a greater retention of the fine particles that could be released from the porous media or invaded from the drilling fluid, in the case of the mud filtrate with the Si NPs. The IFT and wettability influence the capillary pressure [73]. In this sense, the reduction in the IFT and water-wet tendency enhances the mobilization of the oil and improves the oil recovery by decreasing the work required to move the oil droplets through

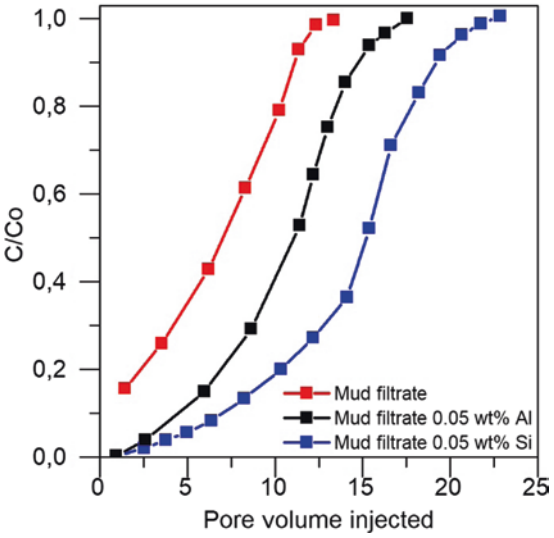

Fig. 11.7 Breakthrough curves for the sand samples treated with the mud filtrate in the absence and presence of 0.05 wt.% Al and Si NPs

the pore throat [70]. Therefore, the mud filtrate invaded will not represent other mechanisms of formation damage during drilling operation; otherwise, this mud filtrate could improve the properties of the rock and the formation fluids such as the conventional stimulation treatment. Finally, a dual purpose drilling fluid based on nanotechnology could be obtained through the enhancement of the drilling fluid properties and improvement of the rock properties through the enhancement of the mud filtrate quality. To corroborate the effect of these NPs under the reservoir and dynamic conditions through displacement tests, the Al NPs at 0.05 wt.% was selected owing to the filtration volume reduction, wettability alteration, IFT reduction, and fine migration control, although to a lower extent, given that the Si NPs only presented fines migration control effect and not wettability or IFT improvement.

11.3.4 Displacement Test

The best NP and its concentration obtained in the static test, Al 0.05 wt.%, were evaluated by conducting a dynamic filtration test through core flooding under reservoir and dynamic conditions. Table 11.2 lists the oil effective permeability for the three scenarios reported. The reduction in the oil effective permeability owing to the double purpose drilling fluid was lower than the mud unless the NPs. Finally, the return permeability of the drilling fluid without the NPs presented a good return, reaching its initial oil effective permeability. However, the drilling fluid with the NPs allowed not only the return of the permeability but also a stimulation of the permeability by 12% compared with the initial permeability value. The difference in the oil effective permeability reductions after injecting the drilling fluid with and without the NPs can be explained by the aggregation effect of the particles achieved in the presence of NPs, allowing a lower invasion of the fines particles and mud filtrate due to a less impermeable mudcake and therefore less formation damage, which can be corroborated by the reduction in the filtration volume shown in Fig 11.8.

The dynamic filtration behavior was reduced by 52% after the addition of the Al NPs to the double purpose drilling fluid, as shown in Fig. 11.8. During the first minutes, the highest filtration volume was obtained. In this scenario, the internal mudcake is in motion. However, for the drilling fluid with the NPs, the change in the

Table 11.2 Comparison of oil effective permeability reduction due to the drilling fluids with and without 0.05 wt.% Al NPs

Mud type	Drilling fluid	Drilling fluid +0.05 wt.% Al NPs
Initial permeability (mD)	393	393
Damage permeability (mD)	202	282
Permeability reduction (%)	48.6	28.2
Return permeability (mD)	390	442
Permeability reduction (%)	0.7	12.5

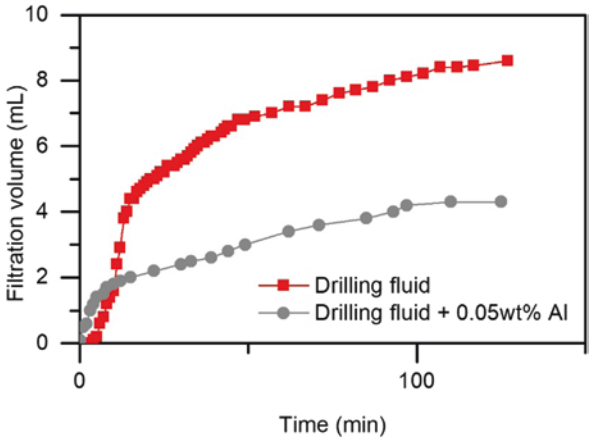

Fig. 11.8 Dynamic filtration curves for the drilling fluid with 0.05 wt.% Al nanoparticles

slope is faster, indicating the development of the mudcake with low permeability and porosity. For the drilling fluid without the NPs, it required more time to reach a low-permeability mudcake to allow for the reduction in the mud filtrate invasion and buildup of the external mudcake. At this time, a high filtration volume was reached. In the second stage, the external mudcake was evaluated, where a seal was developed on the wall of the wellbore. Regarding the drilling fluid with the NPs, the filtration volume tends to stop, whereas for the drilling fluid without the NPs, the external mudcake is not yet consistent, so the filtration volume increases over time. The NPs plug the pores and prevent the solid particles and mud filtrate invasion. Based on the studies carried out by our research group, the NPs improve the filter cake properties and solid packing, thus reducing the filtration volume and the growth time for a stable and low-permeability filter cake formation [37, 55, 58].

Figure 11.9 shows the relative permeability curves for the baseline, drilling fluid with and without Al NPs. Once again, the cores used in the study presented the same petrophysical properties that ensure the reproductivity of the study, meaning that it could represent the C7 formation. The Kro value at residual water saturation, endpoint, for the scenario without the NPs presented the highest reduction as a result of the highest solid particles and mud filtrate induced while circulating the drilling fluid, as reported in Fig. 11.8. However, the NP addition allowed the lowest reduction in the endpoint value. Therefore, the formation damage or the permeability reduction was the lowest. After drilling fluid without the NP circulation, the residual oil increased, and the water saturation decreased, compared with the baseline scenario. The opposite was obtained for the drilling fluid in the presence of the NPs, achieving a reduction in the Sor. This could be explained by the change in the wettability; the porous media retained water and produced crude oil. These results are consistent with the evaluation of the effluents in the static test and the reduction of the Krw curves. Finally, the NPs in the drilling fluid improved the oil mobility based on the conservation of the Kro slope. The NPs could inhibit the formation damage and improve the wettability through the decoration of the porous media and reduction in the IFT, which does not occur in a conventional drilling fluid.

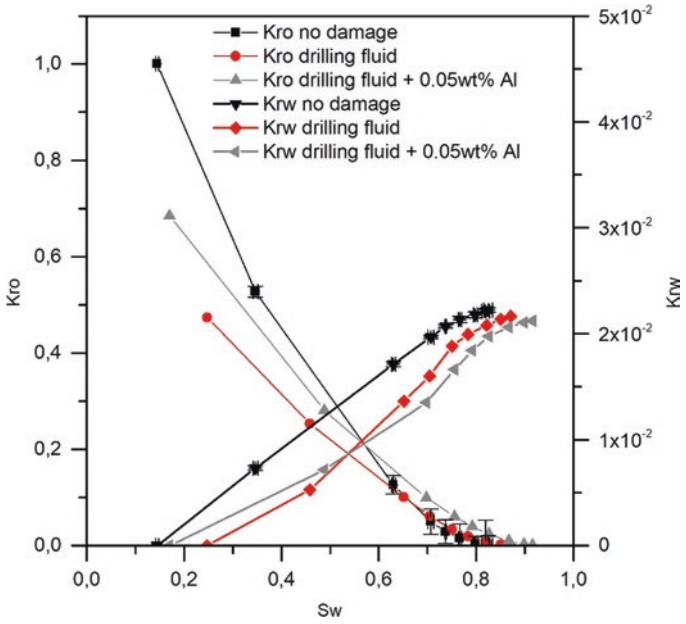

Fig. 11.9 Relative permeability curves for the scenario without damage, after the injection of the base drilling fluid and with 0.05 wt.% alumina nanoparticles (Al)

Fig. 11.10 Oil recovery factor curves for the drilling fluid with and without 0.05 wt.% Al nanoparticles

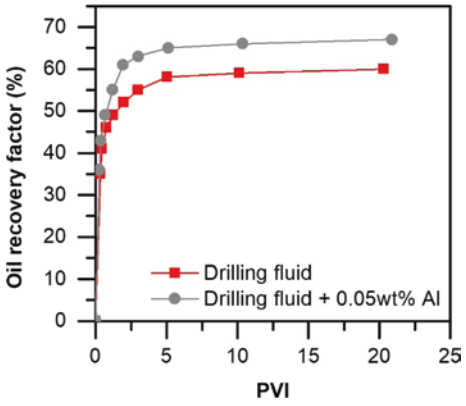

Figure 11.10 shows the oil recovery factor for the drilling fluid with and without the NPs. The drilling fluid system without the NPs showed an oil recovery of 59%. The drilling fluid with a 0.05 wt.% Al NPs provided an oil recovery of 66%, compared with the drilling fluid system without the NPs. According to this result, the NPs in the drilling fluids reduced the formation damage by the mud filtrate and solid particle invasion. Moreover, the NPs could change the wettability of the porous medium that favored the permeability return, obtaining 7% more crude oil than the conventional drilling fluid. Additionally, as mentioned before, the mud filtrate from

the double purpose drilling fluid helped reduce the IFT, indicating that the trapping oil can be recovered.

Figure 11.11 shows the behavior of Ko by varying the injection rate after the mud filtrate circulation with and without the NPs. The objective was to determine the rate at which the fines particles detach from the porous media and flow through blocking the pore spaces and reduce the permeability mudcake. The addition of the NPs to the drilling fluid and subsequent invasion of these through the mud filtrate increased

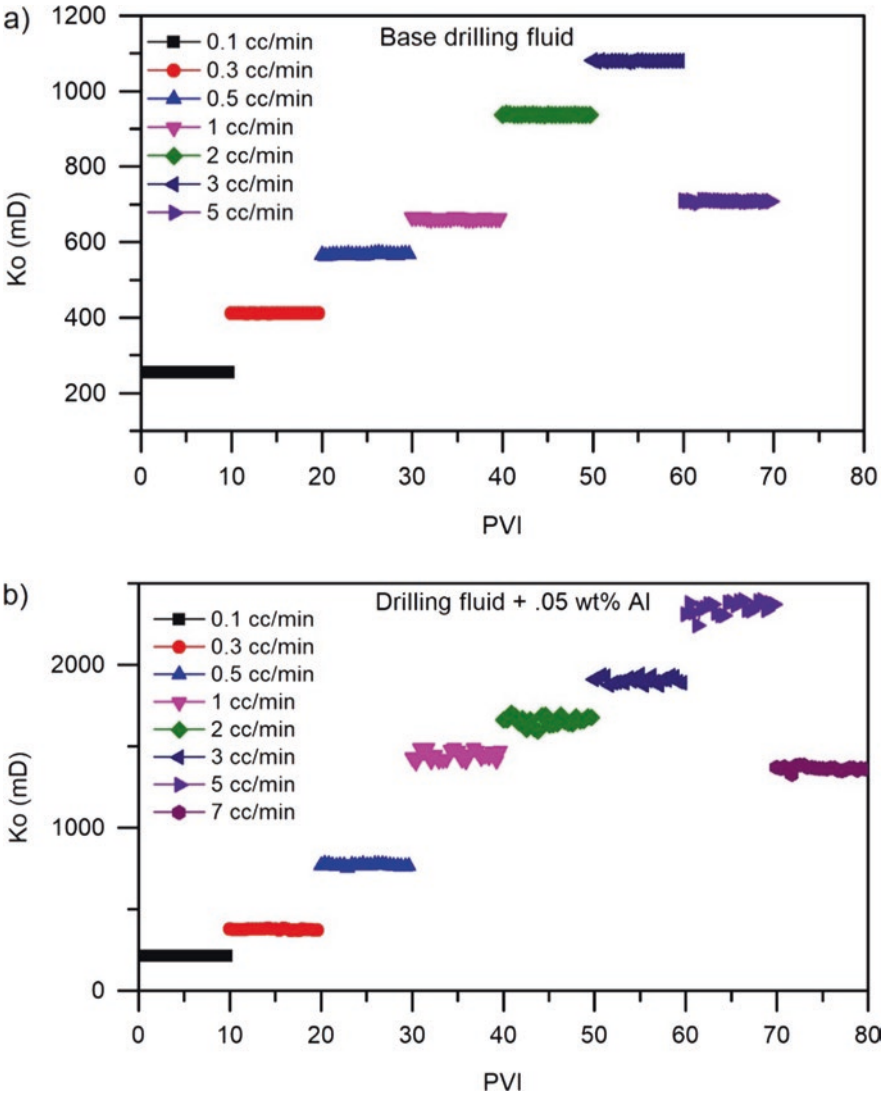

Fig. 11.11 Critical injection rate to crude oil after mud filtrate injection from (**a**) base drilling fluid and (**b**) drilling fluid with 0.05 wt.% alumina nanoparticles (Al)

the injection rate from 5 mL/min (base drilling fluid) to 7 mL/min, an increase of 25%. The NPs decorate the porous medium, and once the fines particles start migrating, they are trapped by the NPs with no possibility of migrating or plugging the throats.

11.3.5 Field Application

The main damage mechanisms of the Ocelot field have been identified, that is, drilling-induced formation damage associated with the drilling process where water-based muds are dominant. During the production life of the wells, the productivity decreases because of the migration of fines (presence of migratory clays) and wettability changes due to organic deposits (crude oil with colloidal instability). During the drilling operation of new wells, the drilling fluid allows the formation of an efficient seal that helps reduce the filtration volume and solid invasion. Additionally, the mud filtrate acts as a carrier fluid for the entry of NPs and helps improve the properties of the rock by changing the tendency of the wettability to water and controlling the fines and clay migration. Therefore, this damage mechanism is the most important during the production stage.

A pilot was carried out in July 2020 in two wells in the Ocelote field whose target formation is C7A. To evaluate the behavior in the two types of wells, the study was initially carried out in a deviated well where the risks of differential sticking are less. Subsequently, based on the results obtained, the second pilot will be run in a horizontal well in the same production unit. From the above, a more effective result is expected in the horizontal well where historically a greater invasion of mud filtration has been reported given the drilling conditions.

The validation of the results will be carried out by comparing the behavior of the pilot with a base well whose drilling will be carried out using the same drilling fluid without nanomaterials. These wells will be considered as twins and will be characterized by their similarity in terms of the structural location, target formation, mineralogy, deviation, extent of completion, types of fluids produced, and expected productivity indexes. The last parameter is directly associated with the petrophysical properties and well pressure conditions. The described comparison could help evaluate the variation in the following parameters between the twin wells in order to verify less fluid invasion, higher productivity associated with less drilling-induced formation damage, and early fine stabilization.

11.3.5.1 Invasion Diameter Calculation by Well Logging

Given the different research depths of resistivity tools and the difference between the formation water salinity and the drilling mud salinity, it is possible to define an invasion profile both in wells without the nanofluids and in wells where the technology is tested and thus compare the values in the formation of interest and quantify

the percentage of decrease. This is achieved through a statistical distribution of the resistivity curves in each of the wells.

11.3.5.2 Stabilization Time of Production Fluids

During the development of the Ocelote field, it has been found that there are wells that take longer to produce the completion fluids. These cases from a petrophysical viewpoint have been associated with poor filtration control. Given the above, the time it takes to produce the formation fluids and the volumes obtained before producing the formation fluids will be calculated, discounting for the pipeline capacities. The reservoir fluids are expected to be obtained more quickly in the pilot with the nanomaterials.

11.3.5.3 Productivity Index

The initial productivity index will be compared by normalizing per feet of open formation between the pilot wells and the comparison wells in the area. For the pilot well, a lower deviation in the real productivity index is expected due to petrophysical properties, which translates into less formation damage. Less formation damage may be associated with less invasion of the mud filtrate and restoration of the formation wettability.

11.3.5.4 Solid Production

Wellhead monitoring of the solid content produced during a month will be carried out at equal time intervals so that a low solid content can be expected in the pilot due to the stabilization of the NPs. The solids will be characterized by DRX and PSD to confirm that they correspond to fines from the reservoir.

11.4 Conclusion

Alumina and silica NPs presented enhancement in the rheological and filtration properties of a drilling fluid. The Si NPs at 0.05 wt.% presented an increase in PV of over 9% compared with the drilling fluid without the NPs. However, the Al NPs required a concentration of 0.1 wt.% to realize the same performance. The Al and Si NPs could improve the YP and gel strength of the drilling fluids, but a concentration of 0.1 wt.% was required to have significant changes. The filtration volume under HPHT conditions after the aging process was reduced by 17% when adding 0.05 wt.% of Si and Al NPs. The Si NPs reduced the mudcake thickness by 18%.

The Al NPs exhibited the highest performance in terms of the contact angle reduction, 37%, IFT reduction 44%, and fine migration control, 66%. This indicates that the NPs invaded through the mud filtrate could generate a water-wettability tendency and retain the fines during the production time. Thus, the Al NPs were selected for evaluation in displacement tests, not only owing to better filtration reduction but also in terms of improving the oil mobility.

The Al NPs at 0.05 wt% in the drilling fluid reduce the filtration volume under dynamic conditions by 52.1%, and the decrease in the oil effective permeability due to the double purpose drilling fluid was lower than that of the mud without the NPs by 20.2%. The NPs inhibited the formation damage owing to the reduction in the invasion of filtrate and solid particles. The system allowed a high water retention by increasing the saturation window, thus improving the mobility of the oil. These characteristics provided an additional recovery of 10% crude compared with the baseline scenario.

The Al NPs serve two objectives in the drilling fluid. After the drilling fluid circulation, an increase in the critical injection rate of 66% was observed, indicating a greater stability of the fines in the porous media. Thus, the treatment shows a potential not only to reduce the damage by the drilling fluids but also as an agent for fine migration.

The results (field application) are in the process of execution, starting from the selection of drilling fluids and wells that meet the requirements, wells with percentage of damage induced during drilling, fines migration, deposition of organics, and subsequent changes in the wettability during the production life. Additionally, we expect that the results will help compare the invasion diameter, well stabilization time, productivity index, and solid production in the two wells called twin wells, one of which will be drilled without the NPs and the other using the mud with NPs based on its formulation.

Acknowledgments The authors want to thank HOCOL S.A for granting permission to present and publish this paper and Engineers Oscar Medina and Johanna Roldán for their help in the experimental tests. We would also like to recognize the Universidad Nacional de Colombia and Colciencias for logistical and financing assistance in the doctoral studies of Johanna Vargas Clavijo through the announcement of 785/2018.

References

1. B. Peng, S. Peng, B. Long, Y. Miao, W.Y. Guo, Properties of high-temperature-resistant drilling fluids incorporating acrylamide/(acrylic acid)/(2-acrylamido-2-methyl-1-propane sulfonic acid) terpolymer and aluminum citrate as filtration control agents. J. Vinyl Addit. Technol. **16**, 84–89 (2010)
2. M. Aston, P. Mihalik, J. Tunbridge, S. Clarke, Towards zero fluid loss oil based muds, in *SPE Annual Technical Conference and Exhibition* (2002)
3. D. Jiao, M.M. Sharma, Dynamic filtration of invert-emulsion muds. SPE Drill. Complet. **8**, 165–169 (1993)

4. S. Gharat, J. Azar, D. Teeters, Effect of incompatibilities caused by fluids filtrates on formation properties, in *SPE Formation Damage Control Symposium* (1994)
5. D.B. Bennion, R.F. Bietz, F.B. Thomas, M.P. Cimolai, Reductions in the productivity of oil and low permeability gas reservoirs due to aqueous phase trapping. J. Can. Pet. Technol. **33**, 45–54 (1994)
6. D. Jia, J. Buckley, and N. Morrow, Alteration of wettability by drilling mud filtrates, in SCA Symposium, Norway, September (1994)
7. G. Phelps, G. Stewart, J. Peden, The effect of filtrate invasion and formation wettability on repeat formation tester measurements, in *European Petroleum Conference* (1984)
8. A. Wojtanowicz, Z. Krilov, J. Langlinais, Experimental determination of formation damage pore blocking mechanisms. J. Energy Resour. Technol. **110**, 34–42 (1988)
9. R. Caenn, H. Darley, G. Gray, Chapter 10—Completion, reservoir drilling, workover, and packer fluids, in *Composition and Properties of Drilling and Completion Fluids*, 6h edn., (Gulf Professional Publishing, Boston, 2011), pp. 477–533
10. J. Argillier, A. Audibert, D. Longeron, Performance evaluation and formation damage potential of new water-based drilling formulas. SPE Drill. Complet. **14**, 266–273 (1999)
11. R. Caenn, H.C.H. Darley, G.R. Gray, Chapter 7 – The filtration properties of drilling fluids11a glossary of notation used in this chapter will be found immediately following this chapter's text, in *Composition and Properties of Drilling and Completion Fluids*, ed. by R. Caenn, H. C. H. Darley, G. R. Gray, 7th edn., (Gulf Professional Publishing, Boston, 2017), pp. 245–283
12. R. Caenn, H.C.H. Darley, G.R. Gray, Chapter 10 – Drilling problems related to drilling fluids, in *Composition and Properties of Drilling and Completion Fluids*, ed. by R. Caenn, H. C. H. Darley, G. R. Gray, 7th edn., (Gulf Professional Publishing, Boston, 2017), pp. 367–460
13. A. Suri, M.M. Sharma, Strategies for sizing particles in drilling and completion fluids. SPE J. **9**, 13–23 (2004)
14. M. Dick, T. Heinz, C. Svoboda, M. Aston, Optimizing the selection of bridging particles for reservoir drilling fluids, in *SPE International Symposium on Formation Damage Control* (2000)
15. W. He, M. P. Stephens, Bridging particle size distribution in drilling fluid and formation damage, in *SPE European Formation Damage Conference* (2011)
16. S. Vickers, M. Cowie, T. Jones, A.J. Twynam, A new methodology that surpasses current bridging theories to efficiently seal a varied pore throat distribution as found in natural reservoir formations. Wiertnictwo, Nafta, Gaz **23**, 501–515 (2006)
17. H.C. Darley, G.R. Gray, *Composition and Properties of Drilling and Completion Fluids* (Gulf Professional Publishing, Boston, 1988)
18. F. Civan, Chapter 18-Drilling mud filtrate and solids invasion and mudcake formation, in *Reservoir Formation Damage*, (Gulf Professional Publishing, Burlington, 2007)
19. M. Al-Yasiri, D. Wen, Gr-Al2O3 nanoparticles based multi-functional drilling fluid. Ind. Eng. Chem. Res. **58**, 23 (2019)
20. S. M. Javeri, Z. M. W. Haindade, C. B. Jere, Mitigating loss circulation and differential sticking problems using silicon nanoparticles, in *SPE/IADC Middle East Drilling Technology Conference and Exhibition* (2011)
21. A. Salih, T. Elshehabi, H. Bilgesu, Impact of nanomaterials on the rheological and filtration properties of water-based drilling fluids, in *SPE Eastern Regional Meeting* (2016)
22. A.E. Bayat, P.J. Moghanloo, A. Piroozian, R. Rafati, Experimental investigation of rheological and filtration properties of water-based drilling fluids in presence of various nanoparticles. Colloids Surf. A Physicochem. Eng. Asp. **555**, 256–263 (2018)
23. S.R. Smith, R. Rafati, A. Sharifi Haddad, A. Cooper, H. Hamidi, Application of aluminium oxide nanoparticles to enhance rheological and filtration properties of water based muds at HPHT conditions. Colloids Surf. A Physicochem. Eng. Asp. **537**, 361–371 (2018)

24. M.M. Barry, Y. Jung, J.-K. Lee, T.X. Phuoc, M.K. Chyu, Fluid filtration and rheological properties of nanoparticle additive and intercalated clay hybrid bentonite drilling fluids. J. Pet. Sci. Eng. **127**, 338–346 (2015)
25. Y. Jung, Y.-H. Son, J.-K. Lee, T.X. Phuoc, Y. Soong, M.K. Chyu, Rheological behavior of clay–nanoparticle hybrid-added bentonite suspensions: Specific role of hybrid additives on the gelation of clay-based fluids. ACS Appl. Mater. Interfaces **3**, 3515–3522 (2011)
26. M.-C. Li, Q. Wu, K. Song, C.F. De Hoop, S. Lee, Y. Qing, et al., Cellulose nanocrystals and polyanionic cellulose as additives in bentonite water-based drilling fluids: Rheological modeling and filtration mechanisms. Ind. Eng. Chem. Res. **55**, 133–143 (2015)
27. M.-C. Li, Q. Wu, K. Song, Y. Qing, Y. Wu, Cellulose nanoparticles as modifiers for rheology and fluid loss in bentonite water-based fluids. ACS Appl. Mater. Interfaces **7**, 5006–5016 (2015)
28. L. Liu, X. Pu, K. Rong, Y. Yang, Comb-shaped copolymer as filtrate loss reducer for water-based drilling fluid. J. Appl. Polym. Sci. **135**, 45989 (2018)
29. J.K.M. William, S. Ponmani, R. Samuel, R. Nagarajan, J.S. Sangwai, Effect of CuO and ZnO nanofluids in xanthan gum on thermal, electrical and high pressure rheology of water-based drilling fluids. J. Pet. Sci. Eng. **117**, 15–27 (2014)
30. S.S. Hassani, A. Amrollahi, A. Rashidi, M. Soleymani, S. Rayatdoost, The effect of nanoparticles on the heat transfer properties of drilling fluids. J. Pet. Sci. Eng. **146**, 183–190 (2016)
31. M. Sedaghatzadeh, A. Khodadadi, An improvement in thermal and rheological properties of water-based drilling fluids using multiwall carbon nanotube (MWCNT). Iran. J. Oil Gas Sci. Technol. **1**, 55–65 (2012)
32. J. Cai, M.E. Chenevert, M.M. Sharma, J.E. Friedheim, Decreasing water invasion into Atoka shale using nonmodified silica nanoparticles. SPE Drill. Complet. **27**, 103–112 (2012)
33. P.J. Boul, B. Reddy, J. Zhang, C. Thaemlitz, Functionalized nanosilicas as shale inhibitors in water-based drilling fluids. SPE Drill. Complet. **32**, 121–130 (2017)
34. Y. Kang, J. She, H. Zhang, L. You, M. Song, Strengthening shale wellbore with silica nanoparticles drilling fluid. Petroleum **2**, 189–195 (2016)
35. M. Amanullah, An environment friendly and economically attractive thermal degradation inhibitor for bentonite mud, in *SPE Europec/EAGE Annual Conference and Exhibition* (2006)
36. D. Longeron, J. Argillier, A. Audibert, An integrated experimental approach for evaluating formation damage due to drilling and completion fluids, in *SPE European Formation Damage Conference* (1995)
37. J.V. Clavijo, L.J. Roldán, L. Valencia, S.H. Lopera, R.D. Zabala, J.C. Cárdenas, et al., Influence of size and surface acidity of silica nanoparticles on inhibition of the formation damage by bentonite-free water-based drilling fluids. Part I: Nanofluid design based on fluid-nanoparticle interaction. Adv. Nat. Sci. Nanosci. Nanotechnol. **10**, 045020 (2019)
38. R. API, *13B-1: Recommended Practice for Field Testing Water-Based Drilling Fluids, and ISO 10414-1* (American Petroleum Institute, Washinton, DC, 2003)
39. M. Franco-Aguirre, R.D. Zabala, S.H. Lopera, C.A. Franco, F.B. Cortés, Interaction of anionic surfactant-nanoparticles for gas-wettability alteration of sandstone in tight gas-condensate reservoirs. J. Nat. Gas Sci. Eng. **51**, 53–64 (2018)
40. J. Giraldo, P. Benjumea, S. Lopera, F.B. Cortés, M.A. Ruiz, Wettability alteration of sandstone cores by alumina-based nanofluids. Energy Fuel **27**, 3659–3665 (2013)
41. X. Liu, F. Civan, Formation damage and skin factor due to filter cake formation and fines migration in the near-wellbore region," in *SPE Formation Damage Control Symposium* (1994)
42. C. Céspedes Chávarro, *Desarrollo de un nanofluido para la estabilización de finos de la formación barco del campo Cupiagua* (Universidad Nacional de Colombia-Sede Medellín, Medellín)
43. C. Franco Ariza, F. Cortés, D. Arias-Madrid, E. Taborda, N. Ospina, R. Zabala*, et al.*, "Inhibition of the formation damge due to fine migration on low-permeability reservoirs of sandstone using silica-based nanfluids: from laboratory to a successful field trial.," 2018, p. 231 New York : Nova Science Publishers

44. C.M. Mera, C.A.F. Ariza, F.B. Cortés, Uso de nanopartículas de sílice para la estabilización de finos en lechos empacados de arena Ottawa. Informador Técnico **77**, 27–34 (2013)
45. C.H. van der Zwaag, Benchmarking the formation damage of drilling fluids, in *SPE International Symposium and Exhibition on Formation Damage Control* (2004)
46. L.F. Isernia, FTIR study of the relation, between extra-framework aluminum species and the adsorbed molecular water, and its effect on the acidity in ZSM-5 steamed zeolite. Mater. Res. **16**, 792–802 (2013)
47. B. Gohari, N. Abu-Zahra, Polyethersulfone membranes prepared with 3-aminopropyltriethoxysilane modified alumina nanoparticles for Cu (II) removal from water. ACS Omega **3**, 10154–10162 (2018)
48. J.R. Kennedy, K.E. Kent, J.R. Brown, Rheology of dispersions of xanthan gum, locust bean gum and mixed biopolymer gel with silicon dioxide nanoparticles. Mater. Sci. Eng. C **48**, 347–353 (2015)
49. L.J. Giraldo, M.A. Giraldo, S. Llanos, G. Maya, R.D. Zabala, N.N. Nassar, et al., The effects of SiO2 nanoparticles on the thermal stability and rheological behavior of hydrolyzed polyacrylamide based polymeric solutions. J. Pet. Sci. Eng. **159**, 841–852 (2017)
50. J.J. Adams, Asphaltene adsorption, a literature review. Energy Fuel **28**, 2831–2856 (2014)
51. N.K. Maurya, A. Mandal, Studies on behavior of suspension of silica nanoparticle in aqueous polyacrylamide solution for application in enhanced oil recovery. Pet. Sci. Technol. **34**, 429–436 (2016)
52. A.L. Lorenzen, T.S. Rossi, I.C. Riegel-Vidotti, M. Vidotti, Influence of cationic and anionic micelles in the (sono) chemical synthesis of stable Ni (OH) 2 nanoparticles: "In situ" zeta-potential measurements and electrochemical properties. Appl. Surf. Sci. **455**, 357–366 (2018)
53. R. Caenn, H.C.H. Darley, G.R. Gray, Chapter 6 – The rheology of drilling fluids, in *Composition and Properties of Drilling and Completion Fluids*, ed. by R. Caenn, H. C. H. Darley, G. R. Gray, 7th edn., (Gulf Professional Publishing, Boston, 2017), pp. 151–244
54. A.R. Ismail, N.M. Rashid, M.Z. Jaafar, W.R.W. Sulaiman, N.A. Buang, Effect of nanomaterial on the rheology of drilling fluids. J. Appl. Sci. **14**, 1192 (2014)
55. J. Vargas, L. J. Roldán, S. H. Lopera, J. C. Cardenas, R. D. Zabala, C. A. Franco*, et al.*, Effect of silica nanoparticles on thermal stability in bentonite free water-based drilling fluids to improve its rheological and filtration properties after aging process, in *Offshore Technology Conference Brasil* (2019)
56. Z. Vryzas, L. Nalbandian, V.T. Zaspalis, V.C. Kelessidis, How different nanoparticles affect the rheological properties of aqueous Wyoming sodium bentonite suspensions. J. Pet. Sci. Eng. **173**, 941–954 (2019)
57. J. Jiang, G. Oberdörster, P. Biswas, Characterization of size, surface charge, and agglomeration state of nanoparticle dispersions for toxicological studies. J. Nanopart. Res. **11**, 77–89 (2009)
58. S. Bentacur, F.B. Cortés, G.A.A. Espinosa, Mejoramiento de los fluidos de perforación usando nanopartículas funcionalizadas: Reducción de las pérdidas de filtrado y del espesor de la retorta. Boletín de Ciencias de la Tierra, 5–14 (2014)
59. M. Zakaria, M.M. Husein, G. Harland, Novel nanoparticle-based drilling fluid with improved characteristics, in *SPE International Oilfield Nanotechnology Conference and Exhibition* (2012)
60. L. Whatley, R. Barati, Z. Kessler, J.-S. Tsau, Water-based drill-in fluid optimization using polyelectrolyte complex nanoparticles as a fluid loss additive, in *SPE International Conference on Oilfield Chemistry* (2019)
61. Z. Vryzas, V.C. Kelessidis, M.B.J. Bowman, L. Nalbantian, V. Zaspalis, O. Mahmoud, et al., Smart magnetic drilling fluid with in-situ rheological controllability using Fe3O4 nanoparticles, in *SPE Middle East Oil and Gas Show and Conference, MEOS, Proceedings* (2017), pp. 2558–2569
62. J.T. Srivatsa, M.B. Ziaja, An experimental investigation on use of nanoparticles as fluid loss additives in a surfactant – Polymer based drilling fluid, in *Society of Petroleum Engineers – International petroleum technology conference 2012, IPTC 2012* (2012), pp. 2436–2454

63. N.C. Mahajan, B.M. Barron, Bridging particle size distribution: A key factor in the designing of non-damaging completion fluids, in *SPE Formation Damage Symposium* (1980)
64. W. Anderson, Wettability literature survey-part 2: Wettability measurement. J. Pet. Technol. **38**, 1246–1262 (1986)
65. A. Cassie, S. Baxter, Wettability of porous surfaces. Trans. Faraday Soc. **40**, 546–551 (1944)
66. K. Kondiparty, A.D. Nikolov, D. Wasan, K.-L. Liu, Dynamic spreading of nanofluids on solids. Part I: Experimental. Langmuir **28**, 14618–14623 (2012)
67. S. Al-Anssari, S. Wang, A. Barifcani, M. Lebedev, S. Iglauer, Effect of temperature and SiO2 nanoparticle size on wettability alteration of oil-wet calcite. Fuel **206**, 34–42 (2017)
68. H. Jang, W. Lee, J. Lee, Nanoparticle dispersion with surface-modified silica nanoparticles and its effect on the wettability alteration of carbonate rocks. Colloids Surf. A Physicochem. Eng. Asp. **554**, 261–271 (2018)
69. C. Franco, E. Patiño, P. Benjumea, M.A. Ruiz, F.B. Cortés, Kinetic and thermodynamic equilibrium of asphaltenes sorption onto nanoparticles of nickel oxide supported on nanoparticulated alumina. Fuel **105**, 408–414 (2013)
70. A. Roustaei, S. Saffarzadeh, M. Mohammadi, An evaluation of modified silica nanoparticles' efficiency in enhancing oil recovery of light and intermediate oil reservoirs. Egypt. J. Pet. **22**, 427–433 (2013)
71. L.J. Giraldo, J. Gallego, J.P. Villegas, C.A. Franco, F.B. Cortés, Enhanced waterflooding with NiO/SiO2 0-D Janus nanoparticles at low concentration. J. Pet. Sci. Eng. **174**, 40–48 (2019)
72. N.C. Ogolo, O.A. Olafuyi, M. Onyekonwu, Effect of nanoparticles on migrating fines in formations, in *SPE International Oilfield Nanotechnology Conference and Exhibition* (2012)
73. W.G. Anderson, Wettability literature survey-part 4: Effects of wettability on capillary pressure. J. Pet. Technol. **39**, 1283–1300 (1987)

Chapter 12
Evaluation from Laboratory to Field Trial of Nanofluids for $CaCO_3$ Scale Inhibition in Oil Wells

Richard D. Zabala, Carlos A. Franco, Oscar E. Medina, Leidy J. Roldan, C. Candela, José Reyes, German Lucuara, Sergio H. Lopera, Farid B. Cortés, and Camilo A. Franco

12.1 Introduction

Inorganic scale precipitation is a common and recurring problem in the oil and gas industry [1]. Primarily, calcium carbonate ($CaCO_3$) scales are the most common source of formation damage from precipitation/deposition of mineral scales [1, 2]. The precipitation of inorganic compounds can be developed due to the incompatibility of two fluids [3] or due to the ion concentration that exceeds the solubility under reservoir conditions [4]. Hydrochloric acid (HCl) is frequently used for the remediation of calcium carbonate scales as it offers good short-term performance and low costs [5]. However, these kinds of acid treatments have a short life, and a further decline in production is frequently observed due to scales re-precipitation [6]. Additionally, due to the corrosive nature of HCl, the use of expensive corrosion

R. D. Zabala · C. A. Franco · C. Candela · J. Reyes · G. Lucuara
Departamento de Tecnologías de Producción, Gerencia Técnica, Vicepresidencia Técnica de Desarrollo, Ecopetrol S.A, Bogotá, Colombia
e-mail: richard.zabala@ecopetrol.com.co; carlosal.franco@ecopetrol.com.co; carlos.candela@ecopetrol.com.co; jose.reyesho@ecopetrol.com.co; german.lucuara@ecopetrol.com.co

O. E. Medina · L. J. Roldan · F. B. Cortés (✉) · C. A. Franco (✉)
Química Grupo de Investigación en Fenómenos de Superficie—Michael Polanyi, Departamento de Procesos y Energía, Facultad de Minas, Universidad Nacional de Colombia – Sede Medellín, Medellín, Colombia
e-mail: oemedinae@unal.edu.co; lejroldanva@unal.edu.co; fbcortes@unal.edu.co; caafrancoar@unal.edu.co

S. H. Lopera
Grupo de Investigación en Yacimientos de Hidrocarburos, Facultad de Minas, Universidad Nacional de Colombia – Sede Medellín, Medellín, Colombia
e-mail: shlopera@unal.edu.co

N. N. Nassar et al. (eds.), *Nanoparticles: An Emerging Technology for Oil Production and Processing Applications*, Lecture Notes in Nanoscale Science and Technology, https://doi.org/10.1007/978-3-319-12051-5_12

inhibitors is necessary to protect the injection and pipelines only for a short period [5]. For high-temperature applications, the use of organic acids is preferred because of corrosion problems [1]. The dissolution of calcium carbonate by chelating agents such as ethylenediaminetetraacetic (EDTA) is also well known [7]. These kinds of treatments are less aggressive than acid treatments. However, dissolution rates are slower, and its use in stoichiometric proportions increases costs [8, 9].

The inhibition methods are based on the use of initiation inhibitors, which interact with the nucleation sites of the crystals, limiting their size. Since a little amount of treatment is required, it is an effective way to avoid the deposition of mineral scales [8, 9]. The different inhibitors correspond to one (or more) of the following inhibition mechanisms [10, 11]: (1) crystal distortion, where the inhibitor interferes with the growth of the crystal producing an irregular structure; (2) dispersion, where charges are induced on the surface of the crystal in such a way that the crystals repel each other; (3) chelation, where bonds are formed with certain metal ions forming soluble complexes [12]; and (4) threshold effect, where the inhibitor acts by retarding the precipitation of salts. Phosphonates through the threshold effect prevent nucleation and growth of inorganic scale crystals because they have a high tolerance to Ca^{2+} ions [4, 13]. Additionally, phosphonate-based treatments are stable in a wide range of temperature and pressure at reservoir conditions [14]. These compounds, when used in the formulation of nanofluids, have shown promising results, since, in synergy with nanoparticles (NPs) of different chemical natures, they act on the surface of inorganic scale crystals, affecting their size and morphology [13].

In this sense, nanomaterials and nanofluids are presented as an alternative for the inhibition and/or remediation of formation damage caused by the precipitation of inorganic scales. Due to their small size (1–100 nm) [15, 16], their high surface area [17, 18], their high dispersibility, and their adjustable physicochemical properties, nanomaterials are suitable for injection to reservoir conditions without the risk of blockage and promoting better dispersion throughout the reservoir, including reaching inaccessible places for other types of treatments [19, 20]. The nanoparticles, due to their high reactivity, block the nucleation sites in the inorganic scale crystals, preventing their subsequent growth and precipitation [21, 22]. In this sense, some studies have been focused on the evaluation of different nanoparticles and nanofluids for the $CaCO_3$ scaling inhibition. Shen et al. [23] found that Ca-diethylenetriamine Penta methylene phosphonic acid (Ca-DTPMP) nanoparticles present good diffusion and retention into the porous media, inhibiting the $CaCO_3$ precipitation. On the other hand, Zhang et al. [24] found the same results using metal phosphonate-based nanoparticles surrounded by surfactants. Moreover, Haghtalab et al. [25] demonstrated that at 25 °C, the efficiency of Ca-DTPMP nanoparticles for the inhibition and deleting of crystal growth of $CaCO_3$ increases as the concentration of the inhibitor increases, as well particle size decreases. Other studies include core flooding evaluation at reservoir conditions such as Franco et al. [22], who evaluated Ca-DTIPMP-based nanofluids to inhibit and remediate the $CaCO_3$ scaling in tight reservoirs. The authors classified the treatment as a threshold inhibitor and founded excellent performance for the inhibition and removal of the formation damage.

Although several researchers have reported on the study of $CaCO_3$ crystal growth inhibition using nanoparticles as reported above [22, 26, 27], there are few studies focused on the formation damage by inorganic scales under high pH values [26, 27]. This evaluation is important since there are some applications within the chemical enhanced oil recovery (CEOR) such as the injection of alkalis or the alkali-surfactant-polymer (ASP) technique that improve the hydrocarbon sweep efficiency in the reservoir and increase the crude oil recovery factor [28]. However, these applications can produce a collateral effect of raising the pH of the formation water to values that can range between 9 and 11 [19, 28]. This deviation from normal conditions (pH between 6 and 8) cause problems of precipitation of mineral scales due to the incompatibility between formation and injection water [28]. Also, it is worth to mention that, to the best of our knowledge, there is no report about the application of nanofluids for the inhibition from laboratory up to field test in crude oil reservoirs at high pH.

Therefore, the main objective of this work is to evaluate the inhibition efficiency of a homemade nanofluid in the inhibition of the formation damage by precipitation/deposition of $CaCO_3$ scales at high pH through static and dynamic experiments and its subsequent application in a field test in a Colombian field with previous $CaCO_3$ scaling due to ASP implementation. The chapter is divided into three sections, including (*i*) static experiments, where the nanoparticle and nanoparticle/carrier fluid ratio are selected; (*ii*) dynamic experiments, where the treatment efficiency to inhibit and remediate $CaCO_3$ scaling damage at reservoir conditions is evaluated; and (*iii*) field test.

This work, for the first time, reports the execution of a test at field level to inhibit the precipitation of inorganic scales through nanotechnology. In this way, a new landscape is opened, for future applications due to the success of this implementation.

12.2 Materials and Methods

12.2.1 Materials

Commercial TiO_2, CeO_2, and SiO_2 nanoparticles were provided from Sigma Aldrich (St. Louis, MO, USA). The γ-Al_2O_3, nanoparticles were supplied by Petroraza S.A.S. (Sabaneta, Colombia). Sodium hydroxide (NaOH) and $MgNO_3{\cdot}6H_2O$ (Merck KGaA, Darmstadt, Germany) were used for MgO nanoparticle synthesis. Diethylenetriamine pentamethylene phosphonic acid (DTPMP, 50 wt%) and HCl 37% were provided by Sigma Aldrich (St. Louis, MO, USA). *n*-Hexadecyl-trimethyl ammonium bromide (CTAB) and $CaCl_2{\cdot}2H_2O$ were purchased for Merck KGaA (Darmstadt, Germany). All these reagents were used for Ca-DTPMP nanoparticle synthesis. For batch experiments, sodium bicarbonate ($NaHCO_3$, $\geq$99.7%, Merck KGaA, Darmstadt, Germany) was used. Methanol (99.8% purity) and toluene

(99.8% purity) were employed for porous media cleaning and were obtained from Merck KGaA (Darmstadt, Germany). Sodium chloride (NaCl, 99.5%, Merck KGaA, Darmstadt, Germany) was employed for nanofluid preparation. A commercial EDTA-based treatment "B200" supplied by Petroraza S.A.S. (Sabaneta, Colombia) was employed as carrier fluid (CF) for nanofluid formulation.

Moreover, for the dynamic tests, it has employed a Colombian light crude oil with a 29.9 °API gravity, a viscosity of 40.3 cP at 25 °C, and saturates, aromatics, resins and asphaltenes content of 50.74%, 29.85%, 14.55%, and 4.86% in mass fraction, respectively.

12.2.2 Methods

12.2.2.1 Synthesis of Ca-DTPMP Nanoparticles

The synthesis method of Ca-DTPMP nanoparticles begins by mixing 0.75 M of $CaCl_2{\cdot}2H_2O$ and 3.8% in mass fraction of CTAB in an aqueous solution. The solution is stirred at 300 rpm until a pH of 6.0 is reached. Then, a phosphonate solution of 0.1 M is prepared, and using NaOH the pH is adjusted to 9.0. The phosphonate solution is added dropwise to the $CaCl_2{\cdot}2H_2O$ and stirred for 1 h until a milky white precipitate is observed. The mixture is placed in a water bath for 12 h at 80 °C, filtered, and dried at 100 °C for 12 h. Details of the protocol are reported in a previous study [22].

12.2.2.2 Synthesis of MgO Nanoparticles

MgO nanoparticles were synthesized by the sol-gel technique. The protocol in detail is described in previous work [29]. First, a mixture of 0.2 M of magnesium nitrate and 0.5 M of sodium hydroxide in an aqueous solution was done. The sodium hydroxide was added dropwise to the $MgNO_3{\cdot}6H_2O$ solution until a pH of 12.5 is obtained. The mixture is continuously stirred until a white precipitate is observed. At this point, the mixture is filtered and washed with methanol several times. The remaining solution is centrifugated for 30 min at 4500 rpm and dried at room temperature. Finally, nanoparticles are calcinated at 300 °C for 2 h.

12.2.2.3 Characterization of Nanoparticles

The hydrodynamic size of the nanoparticles was determined through dynamic light scattering (DLS) measurements using a nanoplus-3 (Micromeritics, Norcross, GA, USA). The same equipment was used to obtain the point of zero charge (pH_{pzc}) of the synthesized and commercial nanoparticles in 20 cm^3 of deionized water at different pH (from 2 to 10). The surface area (S_{BET}) of the nanoparticles was estimated

following the Brunauer-Emmett-Teller (BET) method by nitrogen adsorption/desorption at −196 °C in a Gemini VII 2390 from Micromeritics (GA, United States).

12.2.2.4 Nanofluid Preparation

A commercial fluid (CF) named B200 was employed as a carrier fluid for nanoparticle suspension. The properties for the aqueous phase such as density, conductivity, surface tension, and pH were 1.16 $g \cdot mL^{-1}$, 83.24 $\mu S \cdot cm^{-1}$, 27.2 $mN \cdot m^{-1}$, and 5.52, respectively. CF also was characterized by FTIR to determine chemical composition following protocols described in previous works [16, 22, 30]. The nanofluids were prepared by adding 50 $mg \bullet L^{-1}$ of nanoparticles to the carrier fluid based on the static results and based on a previous study [22]. The solution is stirred during 2 h at 300 rpm and then sonicated by 1 h to achieve complete distribution of the nanoparticles in the aqueous fluid for being used in the core flooding test. In this order, the nanofluid is composed of Ca-DTPMP nanoparticles and the EDTA-based carrier fluid, without free DTPMP. The stability of the prepared nanofluid was evaluated though zeta potential measurements and ultraviolet-visible technique using a wavelength of 400 nm, following the protocols described in a previous work [16].

12.2.2.5 Batch Experiments for Inhibition of $CaCO_3$ Scaling

The inorganic scale precipitation/inhibition experiments were performed using synthetic supersaturated calcium carbonate solutions in 100 cm^3 glass vessels at 54.4 °C. Following the protocol described in previous work [25], 50 cm^3 of $CaCl_2 \cdot 2H_2O$ (0.08 M) were added to the container, then the required amount of nanoparticles was added, and the mixture was subjected to an ultrasound bath for 40 min to guarantee a complete dispersion of the particles in the brine. Subsequently, 50 cm^3 of a $NaHCO_3$ solution (0.08 M) were added, and the aliquot was taken immediately for the first measurement. The inhibition capacity of $CaCO_3$ was obtained by measuring Ca^{2+} in solution in the previous mixture. The latter was measured indirectly using an EDTA titration (0.01 M). All experiments were carried out for 140 min. At the end of the titration, the samples were left for 8 h at 54.4 °C, and a final aliquot was taken. pH was adjusted to 10 for scaling evaluation and was monitored during the test. Equation 12.1 was used to calculate the inhibition efficiency (%Inh) of nanofluids:

$$\%\mathrm{Inh} = \frac{C_a - C_b}{C_c - C_b} \cdot 100 \tag{12.1}$$

where C_a, C_b, and C_c are the concentration of Ca^{2+} in the treated sample after precipitation, in the blank after precipitation (system without nanoparticles), and in blank before precipitation, respectively. Additionally, the size of the $CaCO_3$ crystals formed in the presence and absence of the nanofluid was evaluated by DLS. Batch experiments were carried out for different nanoparticles. Then, the nanoparticle

with the best yield was selected for nanofluid formulation using the commercial carrier fluid.

12.2.2.6 Core Flooding Tests

To evaluate the efficiency of the nanofluid for inhibiting and remediating $CaCO_3$ scaling at high pH, core flooding experiments were developed. A Colombian sandstone core of a hydrocarbon was employed, and its petrophysical properties are shown in Table 12.1. The sandstone core is composed of 99.0% in a mass fraction of quartz and 1.0% in a mass fraction of a mixture of clays, including kaolinite, chlorite, and illite. The evaluation of the nanofluid in the inhibition and remediation of the formation damage caused by mineral scales was carried out mainly in three stages: (*i*) evaluation of the base permeabilities, (*ii*) damage inhibition, and (*iii*) damage remediation.

Initially, 10 pore volumes (PV) of reservoir brine composed by 2.0% in mass fraction of KCl were injected at a fixed flow rate of 0.3 $cm^3 \bullet min^{-1}$ for measuring the absolute permeability of the system. Then, 10 PV of oil are injected, and the effective oil permeability is measured at residual water saturation (*Swr*). Subsequently, 10 PV of the reservoir brine is injected again, and the effective permeability to water at residual oil (*Sor*) is determined. For the inhibition experiment, 3 PV of the Ca-DTPMP-based nanofluid are injected and left for a soaking time of 8 h. Next, the damage is generated by the injection of incompatible brines. Oil and brine are injected again to obtain *Ko, Kw, Kro,* and *Krw.* Then, if the inhibition is effective, the durability of the treatment is evaluated by injecting 10 PV of two problematic brines, composed of 0.08 M of $NaHCO_3$ solution (B1) and 0.08 M of $CaCl_2 \cdot 2H_2O$ solution (B2) two more times and evaluating *Kro, Krw,* and *Kw* with the injection of 10 PV of crude oil and 10 PV of KCl-based brine. The experimental conditions were kept constant during each perdurability test.

In the next stage, remediation damage efficiency is evaluated. At this point, the damage is generated from the injection of 10 PV of B1 and B2 brines. The mixture of these incompatible brines provides the $CaCO_3$ scale formation. Subsequently, the reduction in *Kro, Krw*, and *Kw* is quantified by saturating the medium with crude oil and 2% in mass fraction of KCl synthetic brine. At this point, the injection of 3 PV of the nanofluid is performed. The system is then soaked for 8 h. The effect will be evaluated by changing the permeabilities of the system by injecting oil and synthetic brine.

Table 12.1 Properties of porous media employed for the core flooding experiments

Property	Value
Length	7.05 cm
Diameter	3.80 cm
Porosity	16%

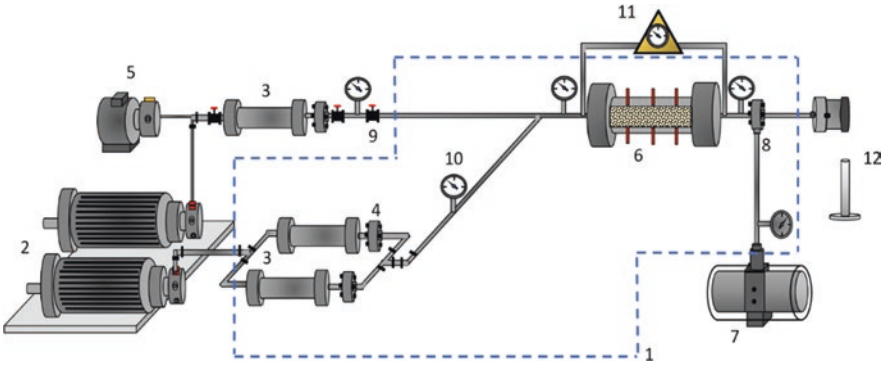

Fig. 12.1 Experimental setup for the displacement test. Legend: (*1*) oven (framed in dotted blue line), (*2*) the positive displacement pump, (*3*) displacement cylinders, (*4*) filters, (*5*) electric hydraulic pump, (*6*) the core holder, (*7*) the pressure multiplier, (*8*) the backpressure system, (*9*) valve, (*10*) manometer, (*11*) pressure transducer, and (*12*) the graduated cylinder

After the removal and quantification stage of the damage remediation, the encrusting brines B1 and B2 are injected again to try to induce damage by calcium carbonate scales to evaluate the effectiveness of a single treatment injection for removing the mineral scale formation damage. In this sense, the inorganic scale precipitation is induced, and the pressure differential is recorded during the injection of each one of the fluids, reservoir brine, and crude oil.

The core flooding tests were done at 54.4 °C (130 °F) and confining and pore pressures of 1800 and 300 psi, respectively. Figure 12.1 shows a representative diagram of the experimental setup used, consisting of three displacement cylinders (Max Servicios S.A.S., Colombia) that contain the synthetic brains, nanofluid and crude oil, positive displacement pumps (DB Robinson Group, Edmonton, AB, Canada), an electric hydraulic pump (Enercap, Actuant Corporation, WI, USA), a core holder along with the sand pack, manometers (Rosemount, Emerson, MO, USA), and valves (Swagelok, OH, USA).

12.3 Results

12.3.1 Carrier Fluid and Nanoparticles Characterization

Figure 12.2 shows the FTIR spectra obtained. Results show a predominant band between 3450 and 3500 cm^{-1} assigned to N–H stretching or free –OH groups. The IR bands located between 769 and 1100 cm^{-1} are related to N–H stretching or overlapping to C–C groups. Also, the band at 1641 cm^{-1} is due to the stretching vibrations of C=O bonds. Hence, the results confirm that the CF is EDTA based.

Table 12.2 shows the mean hydrodynamic diameter of the nanoparticles. For commercial fumed silica (SiO_2) nanoparticles, aluminum oxide (Al_2O_3), and ceria

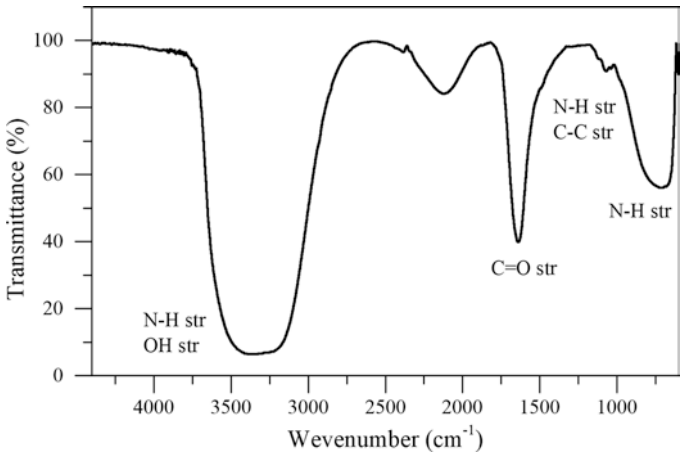

Fig. 12.2 FTIR spectra of carrier fluid

Table 12.2 Mean particle size (d_{50}), BET surface area (S_{BET}), and point of zero charge (pH_{pzc}) of nanoparticles

Nanoparticle	d_{50} (nm)	S_{BET}	pH_{pzc}
Ca-DTPMP	66.0	46.0	9.0
SiO_2	11.0	382.0	3.0
Al_2O_3	35.0	277.0	9.0
CeO_2	22.0	64.0	7.5
MgO	80.0	230.0	11.0

(CeO_2), a hydrodynamic diameter median of 11, 35 and 22 nm, respectively, was obtained. In the case of the synthesized magnesium oxides (MgO) and Ca-DTPMP nanoparticles, the mean hydrodynamic diameters are 80 and 66 nm, respectively. Besides, the surface area increases in the order Ca-DTPMP < CeO_2 < MgO < Al_2O_3 < SiO_2. It is important to mention that the nanoparticles are nonporous. These results are according to the report in the literature [15, 22, 29]. As for the pH_{pzc} values, above pH = 7, Al_2O_3, CeO_2, MgO, and Ca-DTPMP nanoparticles acquire a positive surface charge, and SiO_2-nanoparticles acquire a negative charge [31]. In the presence of the carrier fluid, for the pH of scaling evaluation close to 10, nanoparticles Ca-DTPMP, Al_2O_3, CeO_2, MgO, and SiO_2 acquire a Zeta potential value around −60 mV, −30 mV, −5 mV, − 8 mV, and 14 mV, respectively. Therefore, it is expected that Ca-DTPMP nanoparticles are more dispersed in the carrier fluid than the other systems, leading to high stability during the injection process.

12.3.2 Selection of Nanoparticle by Batch Experiments for $CaCO_3$ Scaling Inhibition

Table 12.3 summarizes the inhibition efficiency for $CaCO_3$ precipitation of the different nanoparticles after 2 and 8 h. As a first instance, the efficiencies are greater during the first 2 h, and a considerable decrease is observed after 8 h. This behavior can be explained since nanoparticles get attached to the active growth sites of calcium carbonate, changing the pattern of growth and slowing down the crystal formation process. After 8 h, a decrease in the efficiency of each nanoparticle is observed. These substantial differences can be mainly associated with the fact that during the first 2 h of the experiment, the growth of inorganic scale crystals occurs. At this point, the nanoparticles, through different interactions, are adsorbed on the crystals, changing the growth pattern and slowing down the crystal formation process [22, 23]. However, a balance in crystal growth has not yet been achieved; hence, there is desorption of the calcium carbonate crystal inhibitor, allowing it to grow easier. This implies that an adsorption/desorption equilibrium occurs for a higher time. Probably, for 8 h, the system gets the equilibrium, and it was corroborated by Ca^{2+} ion concentration, which remains constant after 140 min.

As for the nanoparticle chemical nature effect, the inhibition efficiency increases in the order $MgO < CeO_2 < Al_2O_3 < SiO_2 <$ Ca-DTPMP for both times. In general, the presence of nanoparticulated materials inhibits the precipitation of Ca^{2+} ions. Following the theory of the electric double layer, positively charged ions on the surface of the nanoparticle attract the most negatively charged (CO_3^{2-}), which will form a layer around the surface. This agrees with our previous results [22]. These ions can interact with Mg^{2+}, Ce^{3+}, and Al^{3+} ions present in MgO, CeO_2, and Al_2O_3 nanoparticle surface, respectively. This, in turn, CO_3^{2-} will attract the most positively charged ions (Ca^{2+}), formatting an outer layer rich in cations around the carbonate ion layer. The presence of dipole moments in the solution could promote multiple layer formation within the double layer and thus aid in arranging the ions in a favorable pattern for crystallization [32].

Moreover, due to the threshold inhibitor mechanism, the Ca-DTPMP nanoparticles control and prevent the growth of $CaCO_3$ scales to a higher degree than the rest

Table 12.3 Inhibition efficiencies for $CaCO_3$ precipitation at 54.4 °C using 50 mg•L^{-1} of different nanoparticles

	Inhibition efficiency	
Nanoparticle	2 h	8 h
Ca-DTPMP	63.0	25.0
SiO_2	57.1	20.2
Al_2O_3	55.0	18.3
CeO_2	54.3	18.2
MgO	48.3	17.4

of nanoparticles, mainly by the interactions with the functional groups P–OH and P–O–Ca on the crystal structure. The nano-Ca-DTPMP allows retaining the Ca^{2+} concentrations in the bulk solutions [22]. These results are in agreement with the report by [22], where it was demonstrated that the $CaCO_3$ crystals obtained by using of Ca-DTPMP nanoparticles as an inhibitor present softer textures, amorphous structures, less amount of adherents, and, therefore, less restriction to be transported through the porous media and production lines.

12.3.3 Nanofluid Selection by Batch Experiments for Inhibition of $CaCO_3$ Scaling

In this section, the Ca-DTPMP/CF ratio was evaluated by varying the concentration of the nanoparticles in the carrier fluid. The concentrations evaluated were 50, 250, 1000, and 2000 mg•L^{-1}, obtaining Ca-DTPMP/CF ratio of 10, 50, 200, and 400, respectively.

Both the inhibitor (Ca-DTPMP nanoparticles-aqueous solution) and the carrier fluid were evaluated in the absence of nanoparticles, at a fixed Ca-DTPMP/CF ratio. Efficiencies less than 15% were obtained at 2 h, due to the chelating effect of EDTA. As CF is composed by EDTA, good performance can be obtained under a correct stoichiometric ratio, where the scaling process can be inhibited by chelating/sequestering the scaling cation. Table 12.4 shows the efficiencies of calcium carbonate precipitation inhibition, obtained with the Ca-DTPMP-based nanofluid, for different Ca-DTPMP/CF ratios and the effect of CF without nanofluids. In this test, the mixture of the calcium chloride and sodium bicarbonate brines was carried out to promote the calcium carbonate precipitate, and the addition of the nanofluid was done to inhibit this precipitation. The efficiencies were determined through the concentration of calcium in the solution for the periods of 2 and 8 h, based on a blank sample, which consisted of the brine mixture, without adding treatment for inhibition. From Table 12.4 it is observed that the carrier fluid has the lowest inhibition efficiency. However, the inhibition efficiency achieved is due to the chemical nature of the phosphonate-based fluid. These chemical inhibitors require a low number of

Table 12.4 Inhibition efficiencies for $CaCO_3$ precipitation at 54.4 °C at different Ca-DTPMP/CF ratios

	Inhibition efficiency	
Ca-DTPMP/CF ratio	2 h	8 h
CF without nanoparticles	35.0	13.0
10	100.0	87.0
50	87.0	80.0
200	78.0	48.0
400	60.0	38.0

growth inhibitory molecules to prevent the growth of mineral scales, blocking nucleation, through interaction with crystal nucleation sites, and avoiding contact between ions. Phosphonates act under a chelation effect either by inhibition of nucleation or retardation of crystal growth. Besides, the inhibition efficiencies obtained with nanofluids are higher than those obtained by evaluating only nanoparticles. The interaction of the nanoparticles with the synthesis fluid allows having a system where the nanoparticles are adsorbed on the active growth sites of calcium carbonate, delaying their growth [13, 23]. The carrier fluid helps to dissolve the precipitate because the action of the nanoparticles on the crystal makes it softer, more unstable, and less adherent, so that the amount of precipitate generated decreases considerably, as well as the difference between the efficiencies of the two periods evaluated, achieving a more efficient treatment in the inhibition of $CaCO_3$ precipitation due to its chemical nature. Moreover, the acidic character of the CF may lead to the dissolution of $CaCO_3$ crystals, and hence higher inhibition efficiency is obtained.

In addition, according to the zeta potential at scaling evaluation conditions, low agglomeration of the Ca-DTPMP nanoparticles is achieved due to its high dispersion, leading to higher coverage of the $CaCO_3$ crystals. Furthermore, the analysis ensured the low agglomeration of nanoparticles since no significant change in light absorption was detected.

The highest inhibition efficiency at 2 and 8 h was obtained with the nanofluid prepared with a Ca-DTPMP/CF ratio of 10. This is due to the negative charge that the nanoparticles acquire in the CF for the working pH, added to the colloidal stability of the system for low Ca-DTPMP/CF reactions. For a ratio of 10, the nanoparticles are more dispersed in the nanofluid, with a zeta potential value of −22. Less agglomeration allows a greater coverage of the $CaCO_3$ crystals and therefore a greater inhibition efficiency. The systems with ratios of 200 and 500, despite having a higher content of the scale inhibitor, their Z potential values for the working pH, are around −10. Despite being negatively charged, their tendency to agglomerate is much greater, and therefore their efficiency decreases. It can be concluded that nanoparticles have a synergistic effect with the carrier fluid, improving or adding inhibition mechanisms according to their stability. The formation of soluble complexes was not observed, as it is common in the presence of ferrous oxides [33, 34].

12.3.4 Core Flooding Test

12.3.4.1 Inhibition of $CaCO_3$ Scaling

Figure 12.3a, b shows the relative permeability and oil recovery curves for nanoparticles and carrier fluid, independently evaluated. According to the results, the injection of the nanoparticles and the carrier fluid generate a reduction in the residual oil saturation, obtaining better results for the Ca-DTPMP nanoparticles than for the carrier fluid. In addition, the slopes of both curves change slightly compared to the

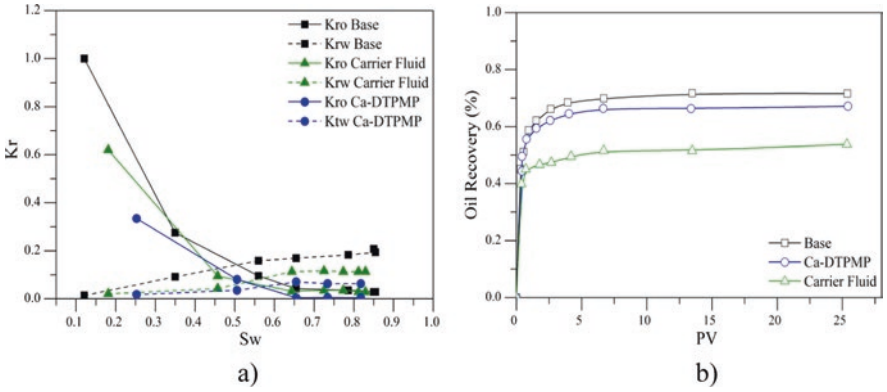

Fig. 12.3 (**a**) Relative permeability curves and (**b**) oil recovery curves for the inhibition of $CaCO_3$ precipitation using 50 mg•L^{-1} of Ca-DTPMP and carrier fluid. Temperature at 54.4 °C (130 °F) and confining and pore pressures of 1800 and 300 psi

Table 12.5 Values of oil and water effective permeabilities for the inhibition of $CaCO_3$ precipitation using 50 mg•L^{-1} of Ca-DTPMP-based nanofluid. Temperature at 54.4 °C (130 °F) and confining and pore pressures of 1800 psi and 300 psi

Phase	*Kw* (mD)	*Ko* (mD)
Base	25.0	43.0
Perdurability 1	24.0	42.0
Perdurability 2	24.0	41.5
Perdurability 3	19.0	39.0

baseline, keeping the *Kro* slope greater than *Krw.* Similarly, the curves move to the right, to a greater degree for nanoparticles, showing their ability to keep the system highly wettable to water. On the other hand, panel b of the same Fig. 12.3b shows that the amount of recovered oil is greater for the Ca-DTPMP nanoparticles than for the carrier fluid. However, both show high efficiencies due to the chelating effect of the CF and the ability of the nanoparticles to prevent the growth of $CaCO_3$ crystals.

Besides, the obtained permeability values are presented after the injection of the nanofluid and after the induction of damage by injecting 10 pore volumes of incompatible brines. Also, the durability of the treatment was evaluated. It should be noted that the injected nanofluid had a soaking time of 8 h. Then, $CaCO_3$ scaling damage was produced three times to evaluate the perdurability of the treatment. Each stage was referred as *perdurability 1 (P1)*, *perdurability 2 (P2)*, and *perdurability 3 (P3)*. Table 12.5 shows the behavior of the oil and water effective permeabilities in the damage inhibition phase. For water, during the three injections of B1 and B2, the permeability slightly falls from 25 mD to 24 mD, 24 mD, and 19 mD, respectively. For the *perdurability 3* stage, the system decreases its effectiveness at a low extent. The results indicate that the nanofluid has a high ability to maintain effective water

permeability close to its initial even though several pore volumes were injected. Analogous to the effective water permeability data, the oil permeability showed similar behavior, with reductions from 43 mD to 42, 41, and 39 mD for the first, second, and third evaluation of the permeability, respectively. However, in the third evaluation, the *Ko* only decreased by 10%, showing better results than the *Kw* reduction. It is important to mention that the measurements for the base system were taken before the flooding of the incompatible brines.

Figure 12.4a shows the base relative permeability curves and the respective curves for the three durability evaluations. The base curve indicates a water-wet porous medium due to the high value of *Kro* at residual water saturation, a slightly higher slope of the *Kro* curve compared to that of *Krw,* and finally, a high value of the residual saturation of water concerning that of oil. In each durability evaluation phase, both the water and oil relative permeability curves are reduced. Analogous to the reduction of the effective permeability curves, the system does not undergo substantial changes in the first two evaluations of durability. In the third evaluation, the *Kro* and *Krw* fall sharply, and the residual saturations increase. In the case of *perdurability 2*, it can be noted that the curves shift to the right, indicating that the system

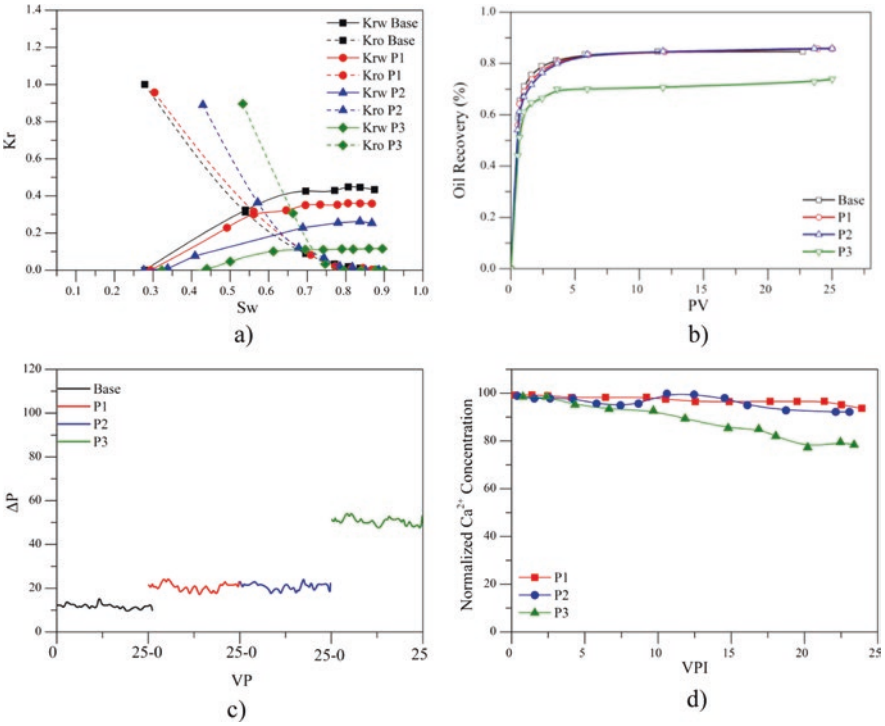

Fig. 12.4 (**a**) Relative permeability curves, (**b**) oil recovery curves, (**c**) pressure drop and (**d**) normalized Ca^{2+} concentration profiles in effluents for the inhibition of $CaCO_3$ precipitation using 50 mg•L^{-1} of Ca-DTPMP-based nanofluid. Temperature at 54.4 °C (130 °F) and confining and pore pressures of 1800 and 300 psi

is changing to a strong water-wet condition. On the other hand, the residual oil saturation was reduced. Also, the mobility to water is reduced. In the case of *perdurability 3*, there is no significant decrease in residual oil saturation. However, there is a higher irreducible water saturation compared to the previous cases, implying an increase in water wettability. There is also a decrease in the mobility of water concerning the base. Besides, the oil recovery curves and the behavior of the nanofluid as an inhibitor are presented in Fig. 12.4b. The first two perdurability evaluations do not undergo major changes, while for the third durability evaluation, the system does not inhibit efficiently, and scale deposition occurs, leading to an oil recovery reduction of 9%.

Figure 12.4c shows the pressure drop profiles for each stage. For the base curve, the pressure drop stabilizes near 10 psi. Then, during the inhibition processes, the pressure drops increase by 55%, and the value is maintained until the *perdurability* 2 stage. Finally, during *perdurability 3*, pressure drop increases to approximately 60 psi, which is in accordance with the oil and water permeabilities. On the other hand, Fig. 12.4d shows the profiles for the Ca^{2+} concentration in the recovered effluents that were analyzed following the same procedure of batch experiments. Results show that during each inhibition stage, there is a correct performance of the nanofluids, avoiding the scaling of inorganic scales in porous media. Finally, the pH was monitored in the collected water effluents, obtaining insignificant variations.

12.3.4.2 Remediation of $CaCO_3$ Scaling

Remediation of mineral scaling formation damage was evaluated in two main stages. Initially, the damage was caused by the deposition of inorganic calcium carbonate scales by the injection B1 and B2 in the porous medium. Then, the effectiveness of Ca-DTPMP nanoparticles, CF, and nanofluid was analyzed. Figure 12.5a

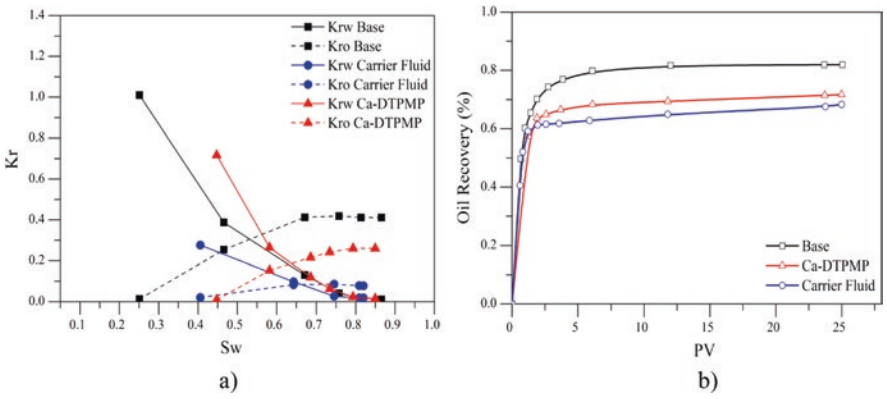

Fig. 12.5 (**a**) Relative permeability curves and (**b**) oil recovery curves for the remediation of $CaCO_3$ precipitation using 50 mg•L^{-1} of Ca-DTPMP and carrier fluid. Temperature at 54.4 °C (130 °F) and confining and pore pressures of 1800 psi and 300 psi

shows relative permeability curves for Ca-DTPMP nanoparticles and CF. In the first instance, it is observed that both the CF and the nanoparticles dissipate the *Sor* after the remediation of the formation damage. In addition, the system in both cases maintains its preference to be wet by the water, reflected in the displacement of the *Kr* to the right. As for the recovery of the OOIP, shown in Fig. 12.5b, this was greater for the nanoparticles than for the CF. Like the inhibition process, both systems present good results when evaluated individually.

For nanofluid evaluation, the changes in the permeability of both the oil and water phase are summarized in Table 12.6. From the results, it is observed that by depositing inorganic scales, formation damage of 57% is generated according to the reduction of the *Kw* values. When injecting the nanofluid for permeability restauration, a *Kw above* the base water permeability was obtained. This suggests that the treatment removes the deposited inorganic scales and improves the flow conditions of the system.

Regarding the oil effective permeabilities (*Ko*), it is observed that after the treatment injection, there is an increase of 13% compared to the base permeability. Hence, it can be said that the treatment not only removes mineral scaling formation damage but also favors the flow conditions of water and oil in the porous medium.

Figure 12.6 shows the relative permeability curves and the oil recovery curves for the systems after damage caused by inorganic scales deposition and after the damage removal with the nanofluid. From panel a of Fig. 12.6, it can be identified that when damage is generated, the residual saturation of both the water and oil increase; therefore, the mobility of both phases is strongly affected. After the treatment injection, the medium becomes more wettable to the water and recovers the mobility of oil and water phases; however, it should be noted that the mobility of the water remains slightly below to the base, while that of the oil tends to overcome the basic mobility conditions.

Figure 12.6b shows the results of the oil recovery curves during the damage removal stage. Once the damage caused by scale deposition is generated, only a recovery of 37% of the original oil in place is obtained. After treatment injection, a recovery 3% higher to the base scenario is achieved. It is validated again that the treatment not only removes the damage but also improves the rock and fluid conditions, allowing recovery values to be reached above the base conditions (scenario without damage).

Table 12.6 Values of oil and water effective permeabilities for the remediation of $CaCO_3$ precipitation using 50 mg•L^{-1} of Ca-DTPMP-based nanofluid. Temperature at 54.4 °C (130 °F) and confining and pore pressures of 1800 psi and 300 psi

Phase	*Kw* (mD)	*Ko* (mD)
Base	28.0	45.0
Damage	16.0	25.0
Nanofluid injection	29.0	61.0

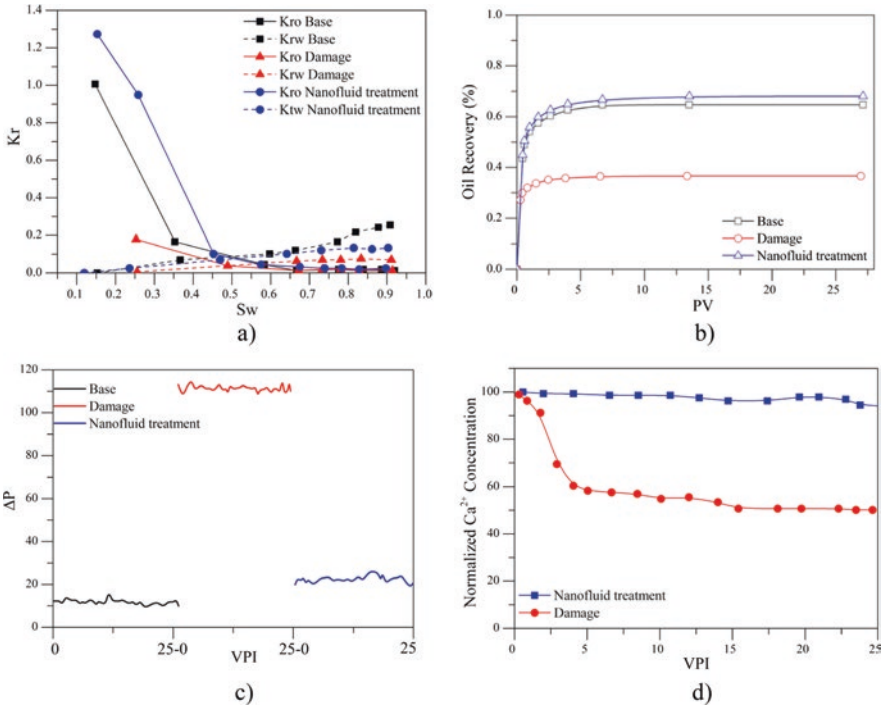

Fig. 12.6 (**a**) Relative permeability curves, (**b**) oil recovery curves, (**c**) pressure drop, and (**d**) normalized Ca^{2+} concentration profiles in effluents for the remediation of $CaCO_3$ precipitation using 50 mg•L^{-1} of Ca-DTPMP-based nanofluid. Temperature at 54.4 °C (130 °F) and confining and pore pressures of 1800 and 300 psi

On the other hand, the pressure drop profiles are presented in Fig. 12.6c. For the baseline, the pressure drop is adjusted to 11 psi. The fall is associated with the movement of fluids during oil recovery. After damage induction, the values increase to 116 psi, and, finally, after the injection of nanofluids, the value stabilizes at around 20 psi. Finally, the effluents recovered in both stages were analyzed by Ca^{2+} concentration and are showed in Fig. 12.6d. The results indicate that after the removal of formation damage, a negligible concentration of Ca^{2+} ions is observed in the recovered effluents, which corroborates the high efficiency of nanofluids to remedy damage due to mineral scaling. Finally, the pH was monitored in the collected water effluents, in which no variation was observed in its value, that is, the high pH was maintained during the experiment.

12.3.5 Field Trial

Based on the static and dynamic results on the evaluation of the inhibition of the precipitation of inorganic scales, a pilot test was designed in an oil field in Southern Colombia. The brine was composed by 13,500 mg•L^{-1} of Na^+, 185 mg•L^{-1} of K^+, 394 mg•L^{-1} of Mg^{++}, 7600 mg•L^{-1} of Ca^{++}, 390 mg•L^{-1} of Sr^{++}, 31 mg•L^{-1} of Fe^{++}, 35,454 mg•L^{-1} of Cl^-, 80 mg•L^{-1} of SO_4, and 128 mg•L^{-1} of HCO_3, indicating that the experimental conditions evaluated represented a more drastic scenario for the $CaCO_3$ scaling.

The chosen well was completely closed, and its production was zero barrels per day due to the conditions obtained after the alkali-surfactant polymer (ASP) flooding process to which it was exposed during years. The results obtained with the EOR process were not successful, leading to high pH values in the reservoir water, which favored the precipitation of the calcium carbonate in the near-wellbore area. The CO_2 content, in this case, was negligible, which indicates that the main damage mechanism is related to brines incompatibility and high pH values. In this sense, the nanofluid with the best results for the remediation and inhibition of the formation damage by inorganic scale was injected in the field trial. As the selected well had an electric submersible pump (ESP) for artificial lift, the nanofluid was injected through the annular and left to soak during 12 h. Figure 12.7 shows the results of the pilot test carried out in a field in Southern Colombia. The porosity of this field is between 15% and 20% with an average permeability of 2500 mD.

The blue shaded box coincides with an ASP stimulation treatment carried out between January 2014 and January 2015 that resulted in a complete cessation of production attributed to formation damage due to precipitation/deposition of calcite

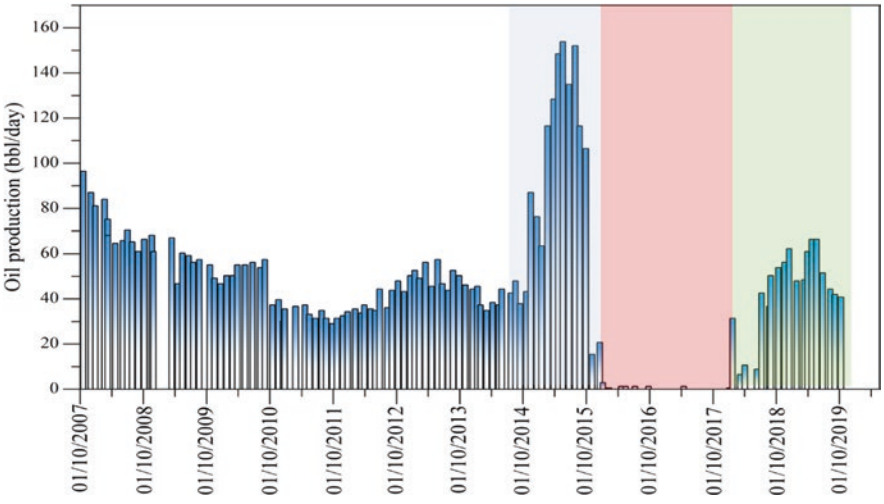

Fig. 12.7 Pilot test: Evaluation of the efficiency of the nanofluid in the removal and inhibition of damage by precipitation/deposition of mineral scales

scales for the alteration of the pH of the formation water, which leads to formation damage for inorganic scales.

In January 2017, it started with the injection of the nanofluid (green box). The implementation was successful showing an increase in oil production of 66 barrels per day during the first year of production after a total cessation of approximately 1 year. After 24 months of monitoring, oil production remains above the baseline. This result showed the ability of the nanofluid for remediating and inhibiting calcium carbonate precipitation/deposition formation damage under high pH conditions. It is worth mentioning that this phenomenological approach is based on fluid-fluid and fluid-surface interactions that lead to the successful formulation of a nanotechnology-based chemical treatment that can remediate and inhibit this formation damage.

The nanoparticle concentration was monitored after the well is open for production, as shown in Fig. 12.8. It is observed that, after the job, concentrations of nanoparticles lower than 20 mg•L^{-1} are obtained, indicating a high interaction with the porous medium and leading to high perdurability of the treatment. It is worth mentioning that, as an additional benefit of the treatment, the lifting costs were reduced. Before nanofluid, the ESP constantly failed due to the $CaCO_3$ scaling and the well-needed intervention every 40 days. After the nanofluid injection, the production was constant for more than 1 year without the need for well intervention.

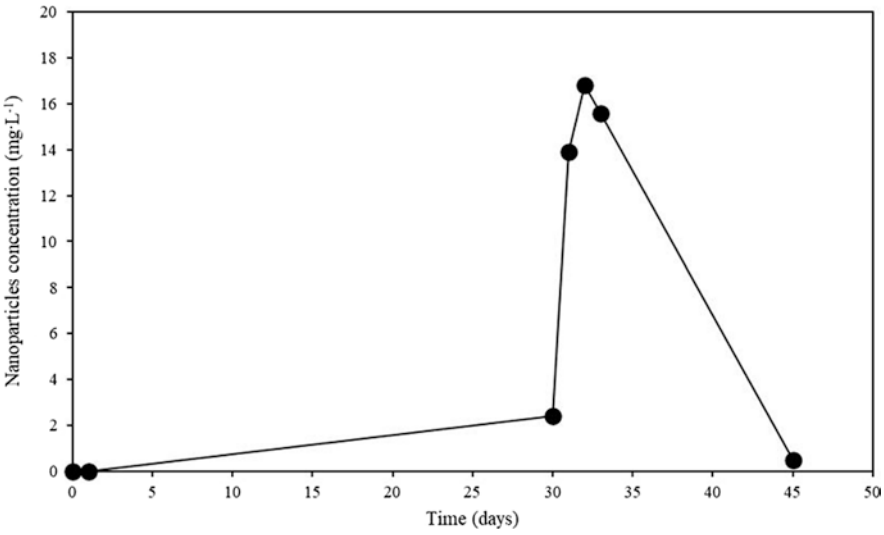

Fig. 12.8 Nanoparticles tracking after the stimulation process

12.4 Conclusion

Static tests at high pH show a 100% inhibition percentage of the damage caused by inorganic scales in the presence of the Ca-DTPMP-based nanofluid. The nanofluid evaluated can be identified as a double effect inhibitor that acts on the calcite crystals limiting their growth. The synergistic effect between the nanoparticles and the transport fluid is evident, which shows an excellent performance both in the elimination and in the inhibition of the formation damage of mineral scales at high pH and reservoir conditions. Dynamic inhibition tests also show the excellent durability of the treatment. Finally, the implementation of the technology in the field was successful showing an increase in oil production of 66 barrels per day during the first year of production. After 24 months of monitoring, oil production remains above the baseline. Due to these field results, the technology was implemented in other wells in the field and expanded to other fields. The economy of the project is greatly improved because in the stimulation/inhibition work strategy, it was reduced from 2 to 1 stage because the wells are stimulated and inhibited in a single program and not in two stages, as is normally done.

Acknowledgments The authors would like to acknowledge to ECOPETROL S.A and Universidad Nacional de Colombia for their logistical, technical, and financial support. At the same time, the authors also acknowledge Grupo de Investigación en Fenómenos de Superficie-Michael Polanyi.

References

1. P. Smith, C. Clement Jr, A.M. Rojas, Combined scale removal and scale inhibition treatments, in *International Symposium on Oilfield Scale* (2000)
2. T. Østvold, P. Randhol, Kinetics of CaCO3 scale formation. The influence of temperature, supersaturation and ionic composition, in *International Symposium on Oilfield Scale* (2001)
3. A. Khormali, D.G. Petrakov, Laboratory investigation of a new scale inhibitor for preventing calcium carbonate precipitation in oil reservoirs and production equipment. Pet. Sci. **13**, 320–327 (2016)
4. A.B. Merdhah, A. Yassin, Formation damage due to scale formation in porous media resulting water injection. System **14**, 15 (2008)
5. F.F. Chang, H.A. Nasr-El-Din, T. Lindvig, X. Qui, Matrix acidizing of carbonate reservoirs using organic acids and mixture of HCl and organic acids, in *SPE Annual Technical Conference and Exhibition* (2008)
6. C. Wang, S.-P. Li, T.-D. Li, Calcium carbonate inhibition by a phosphonate-terminated poly (maleic-co-sulfonate) polymeric inhibitor. Desalination **249**, 1–4 (2009)
7. A. Tariq, N. Jun Hong, H. Nasr-El-Din, Chelating agents in productivity enhancement: A review, in *SPE Oklahoma City Oil and Gas Symposium* (2017)
8. K. Malave Tomala, A.E. Larrea Idiarte, Estudio de problemas de incrustaciones y evaluación de quimicos anti-incrustanes en nucleos seleccionados para diseños de tratamientos tipo "squeeze"a las areniscas uyt del campo shushufindi, Thesis, Escuela Superior Politécnica del Litoral (ESPOL), Guayaquil, Ecuador (2009)
9. M.S. Kamal, I. Hussein, M. Mahmoud, A.S. Sultan, M.A. Saad, Oilfield scale formation and chemical removal: A review. J. Pet. Sci. Eng. **171**, 127–139 (2018)

10. P.G. Koutsoukos, P. Klepetsanis, N. Spanos, D. Kanellopoulou, Calcium carbonate crystal growth and dissolution inhibitors, in *CORROSION 2007* (2007)
11. K. Sawada, The mechanisms of crystallization and transformation of calcium carbonates. Pure Appl. Chem. **69**, 921–928 (1997)
12. M. Finšgar, J. Jackson, Application of corrosion inhibitors for steels in acidic media for the oil and gas industry: A review. Corros. Sci. **86**, 17–41 (2014)
13. B. Zhang, L. Zhang, F. Li, W. Hu, P.M. Hannam, Testing the formation of Ca–phosphonate precipitates and evaluating the anionic polymers as Ca–phosphonate precipitates and CaCO 3 scale inhibitor in simulated cooling water. Corros. Sci. **52**, 3883–3890 (2010)
14. F.H. Browning, H.S. Fogler, Effect of precipitating conditions on the formation of calcium – HEDP precipitates. Langmuir **12**, 5231–5238 (1996)
15. O.E. Medina, J. Gallego, D. Arias-Madrid, F.B. Cortés, C.A. Franco, Optimization of the load of transition metal oxides (Fe2O3, Co3O4, NiO and/or PdO) onto CeO2 nanoparticles in catalytic steam decomposition of n-C7 asphaltenes at low temperatures. Nano **9**, 401 (2019)
16. O.E. Medina, Y. Hurtado, C. Caro-Velez, F.B. Cortés, M. Riazi, S.H. Lopera, et al., Improvement of steam injection processes through nanotechnology: An approach through in situ upgrading and foam injection. Energies **12**, 4633 (2019)
17. O.E. Medina, C. Olmos, S.H. Lopera, F.B. Cortés, C.A. Franco, Nanotechnology applied to thermal enhanced oil recovery processes: A review. Energies **12**, 4671 (2019)
18. O.E. Medina, J. Gallego, L.G. Restrepo, F.B. Cortés, C.A. Franco, Influence of the Ce4+/Ce3+ redox-couple on the cyclic regeneration for adsorptive and catalytic performance of NiO-PdO/CeO2±δ nanoparticles for n-C7 asphaltene steam gasification. Nano **9**, 734 (2019)
19. S.B. Márquez, F.B. Cortés, F.C. Marín, Desarrollo de Nanopartículas Basadas en Sílice para la Inhibición de la Precipitación/Depositación de Asfaltenos. MSc Investigación, Ingenieria de Petróleos, Universidad Nacional de Medellin (2015)
20. O.E. Medina, C. Caro-Vélez, J. Gallego, F.B. Cortés, S.H. Lopera, C.A. Franco, Upgrading of extra-heavy crude oils by dispersed injection of NiO–PdO/CeO2±δ nanocatalyst-based nanofluids in the steam. Nano **9**, 1755 (2019)
21. C.A. Franco, N.N. Nassar, M.A. Ruiz, P. Pereira-Almao, F.B. Cortés, Nanoparticles for inhibition of asphaltenes damage: Adsorption study and displacement test on porous media. Energy Fuel **27**, 2899–2907 (2013)
22. M. Franco-Aguirre, R.D. Zabala, S.H. Lopera, C.A. Franco, F.B. Cortés, Ca-DTPMP nanoparticles-based nanofluids for the inhibition and remediation of formation damage due to CaCO3 scaling in tight gas-condensate reservoirs. J. Pet. Sci. Eng. **169**, 636–645 (2018)
23. D. Shen, P. Zhang, A.T. Kan, G. Fu, H.A. Alsaiari, M.B. Tomson, Control placement of scale inhibitors in the formation with stable Ca-DTPMP nanoparticle suspension and its transport in porous medium, in *SPE International Oilfield Scale Conference* (2008)
24. P. Zhang, D. Shen, C. Fan, A. Kan, M. Tomson, Surfactant-assisted synthesis of metal-phosphonate inhibitor nanoparticles and transport in porous media. SPE J. **15**, 610–617 (2010)
25. A. Haghtalab, Z. Kiaei, Evaluation of the effective parameters in synthesis of the nano-structured scaling inhibitors applicable in oil fields with sea water injection process. J. Nanopart. Res. **14**, 1210 (2012)
26. J. Guo, S.J. Severtson, Inhibition of calcium carbonate nucleation with aminophosphonates at high temperature, pH and ionic strength. Ind. Eng. Chem. Res. **43**, 5411–5417 (2004)
27. J. Guo, S.J. Severtson, Application of classical nucleation theory to characterize the influence of carboxylate-containing additives on CaCO3 nucleation at high temperature, pH, and ionic strength. Ind. Eng. Chem. Res. **42**, 3480–3486 (2003)
28. A.A. Olajire, Review of ASP EOR (alkaline surfactant polymer enhanced oil recovery) technology in the petroleum industry: Prospects and challenges. Energy **77**, 963–982 (2014)
29. J. Villegas, I. Moncayo-Riascos, D. Galeano-Caro, M. Riazi, C.A. Franco, F.B. Cortés, Functionalization of γ-alumina and magnesia nanoparticles with a fluorocarbon surfactant to promote ultra gas-wet surfaces: Experimental and theoretical approach. ACS Appl. Mater. Interfaces (2020)

30. Y. Hurtado, C. Beltrán, R.D. Zabala, S.H. Lopera, C.A. Franco, N.N. Nassar, et al., Effects of surface acidity and polarity of SiO2 nanoparticles on the foam stabilization applied to natural gas flooding in tight gas-condensate reservoirs. Energy Fuel **32**, 5824–5833 (2018)
31. S. Pérez-Robles, C.A. Matute, J.R. Lara, S.H. Lopera, F.B. Cortés, C.A. Franco, Effect of nanoparticles with different chemical nature on the stability and rheology of acrylamide sodium acrylate copolymer/chromium (III) acetate gel for conformance control operations. Nano **10**, 74 (2020)
32. H.S. Frank, W.-Y. Wen, Ion-solvent interaction. Structural aspects of ion-solvent interaction in aqueous solutions: A suggested picture of water structure. Discuss. Faraday Soc. **24**, 133–140 (1957)
33. Z. Amjad, Influence of iron oxide (rust) on the performance of phosphonates as calcium carbonate inhibitors, in *CORROSION 2016* (2016)
34. G. Graham, R. Stalker, R. McIntosh, The impact of dissolved iron on the performance of scale inhibitors under carbonate scaling conditions, in *International Symposium on Oilfield Chemistry* (2003)

Chapter 13
Removal of Uranium from Flowback Water of Hydraulic Fracturing Processes in Unconventional Reservoirs Using Phosphorus- and Nitrogen-Functionalized Activated Carbons

Karol Z. Acosta, Mauricio Holguín, Mónica M. Lozano, Francisco Carrasco-Marín, Raúl Ocampo, Agustín F. Pérez-Cadenas, Camilo A. Franco, and Farid B. Cortés

13.1 Introduction

Gas unconventional reservoirs are currently considered as viable sources of energy for different countries to ensure their requirements and increase the reserves to consolidate energy self-sufficiency [1, 2]. Thus, the production of unconventional oil and gas has increased continuously. For example, in 2015, the annual production of unconventional oil and gas amounted to 30 billion BOPD and 9.273×10^8 Nm^3 [3], respectively, mainly due to the hydraulic fracturing (HF). Hydraulic fracturing is a technique commonly used for the oil and gas exploitation in reservoirs of ultralow permeability rocks such as tight, shale, and coal beds. This technique uses water-based fluids composed of surfactants, polymer, clay stabilizers, biocide, and sand that are injected at high pressures into the formation [4]. This process creates new

K. Z. Acosta · M. Holguín · M. M. Lozano · C. A. Franco (✉) · F. B. Cortés (✉)
Grupo de Investigación en Fenómenos de Superficie–Michael Polanyi, Facultad de Minas, Universidad Nacional de Colombia – Sede Medellín, Medellín, Colombia
e-mail: kzapata@unal.edu.co; jmholguinas@unal.edu.co; caafrancoar@unal.edu.co; fbcortes@unal.edu.co

F. Carrasco-Marín · A. F. Pérez-Cadenas
Grupo de Investigación en Materiales del Carbón, Facultad de Ciencias, Universidad de Granada, Granada, Spain
e-mail: fmarin@ugr.es; afperez@ugr.es

R. Ocampo
Centro de Investigaciones y Estudios de Posgrado, Facultad de Ciencias Químicas, Universidad Autónoma de San Luis de Potosí, San Luis de Potosí, Mexico
e-mail: raul.ocampo@uaslp.mx

N. N. Nassar et al. (eds.), *Nanoparticles: An Emerging Technology for Oil Production and Processing Applications*, Lecture Notes in Nanoscale Science and Technology, https://doi.org/10.1007/978-3-319-12051-5_13

fractures in the formation, favoring the well productivity due to the increased connectivity of existing pores and fractures, and hence increases the permeability to conduct the fluids into the well [5]. Nevertheless, the rock associated to these reservoirs has different radioactive elements such as thorium (Th) and uranium (U) [6], which are known as naturally occurring radioactive materials (NORM) [7]. Terrestrial NORM typically found in geological formations consists of isotopes from the uranium-238 decay series, thorium-232 decay series, and potassium-40. In many cases it is the decay products of the uranium and thorium decay chain that present a larger problem to the environment (e.g., Radon-228). Accordingly, significant amounts of produced waters are generated during the exploitation and fracturing processes named production water flowback, which carry with it sand, chemical, organic compounds, radioactive elements (depending on the geochemical of the formation), among others [4, 7]. The NORM are well-documented contaminants of oil and gas wastes [7]. However, to the best of our knowledge, there are no studies reported in the scientific literature about NORM removal from the water production in HF process in unconventional reservoirs. Some authors report the adsorption of uranyl (VI) ions in aqueous solutions by magnetic polyethyleneimine-modified activated coal [8], NORM adsorption by a batch of insolubilized humic acid [9], biosorption removal of Th(IV) by *Aspergillus niger* [10], and others that include adsorption with other materials like zeolite, two-dimensional MXene material, and resins [11, 12]. Therefore, the main objective of this work is to develop activated carbons (AC) from olive stones with unique chemical surface characteristics for uranium (U) removal. For this proposal, carbon surfaces have been modified by doping with different heteroatoms of nitrogen, phosphorus, and phosphorus/nitrogen. The adsorption studies have been focused on uranyl acetate aqueous solutions. Moreover, the effects of the chemical nature of the adsorbent, adsorbent/adsorbate ratio, and salinity were evaluated based on the fluid-surface interactions. Besides, the obtained isotherms were fitted with a mathematical model for explaining the phenomenological behavior. Finally, a reuse test was designed based on the desorption/adsorption data for understanding the perdurability of the synthesized materials.

13.2 Materials and Methods

13.2.1 Materials

Olive stones (agro-industrial waste) were selected as raw material for activated carbon production. These were crushed and sieved to 1.0–2.0 mm size and subsequently dried at 90 °C until constant weight. Phosphoric acid (reagent grade ≥ 80%, Sigma-Aldrich, St. Louis, MO, USA) was employed for the chemical activation of the raw material before carbonization. Melamine (99%, Sigma Aldrich, St. Louis, MO, USA), phosphoric acid, and ammonium phosphate (reagent grade ≥ 98%, Sigma Aldrich, St. Louis, MO, USA) were used for the functionalization of the

material surface. Distilled water was used for the washing protocol. On the other hand, a uranyl acetate was used as a precursor of the uranyl ion (reagent grade ≥ 98%, Sigma Aldrich, St. Louis, MO, USA).

13.2.2 Methods

13.2.2.1 Preparation of Activated Carbons

Activated carbons (ACs) were produced by chemical activation of olive stones with the phosphoric acid solution following the process before described by Moreno-Castilla et al. [13]. Thus, 100 g of olive stones were mixed with the phosphoric acid solution in a mass ratio of 1:2. The mixture was macerated and dried using an IR lamp for 20 h. It was then carbonized in a tubular furnace (Heraeus, Hanau, Germany) by heating at 10 °C/min up to 840 °C. A soaking time of 2 h under a nitrogen flow of 300 cm^3/min was used. The material obtained was treated with distilled water until pH = 7.

13.2.2.2 Modification of Activated Carbons

After the AC material was dried at 100 °C for 24 h, an incipient impregnation process was used for surface modifications [14]. In this sense, an appropriate quantity of functionalizing agents such as melamine, phosphoric acid, and ammonium phosphate was used to dope the carbon surface with heteroatoms such as N (AC-N), P (AC-P), or N and P (AC-NP) in the AC sample, respectively. For this proposal, the solutions with the heteroatoms (P, N, and N and P) were prepared based on the solubility limit in water and/or ethanol [15]. Then, these solutions were gradually dropped on AC material. After the impregnation, the materials were dried using an IR lamp for 20 h, and finally, they were heated at 700 °C under a nitrogen.

13.2.2.3 Characterization of Activated Carbons

Scanning electron microscopy (SEM) analysis was used for studying the morphology of the materials using a GEMINI-1530 microscope (Berlin, Germany). Textural properties were calculated from sorption isotherms of N_2 using a Quadrasorb SI instrument (Florida, USA). Previously, the carbons were degassed overnight at 110 °C. The Brunauer–Emmett–Teller (BET) equation was fitted to isotherms to estimate the surface area (S_{BET}), while the Dubinin–Radushkevich (DR) model was used to calculate the micropore properties (micropore volume, V_{mic}, and micropore mean size, L_{mic}) [16]. Mercury porosimetry was developed to obtain the macropore volume V_{macro} (pore size from 50 to 10,000 nm) and mesopore, L_{meso}, and macropore width (L_{macro}) by using an AutoPore IV 9510 instrument up to a pressure of

2000 kg cm^{-2} (Georgia, USA). Pore size distributions (PSD) were calculated by the application of QSDFT to N_2 adsorption isotherms and mercury porosimetry results. Total pore volume, V_T, was calculated from the whole PSD, and mesopore volume, V_{meso}, was calculated by the integration between 2 and 50 nm. The carbon chemical properties were obtained by X-ray photoelectron spectroscopy analysis (XPS) and by determining the pH_{IEP} [17].

13.2.2.4 Material Selection

In order to determine the most efficient materials during U removal, adsorption tests were carried out according to the method previously reported by Khalili et al. [12]. Adsorption assays were carried out in aqueous solutions, in the absence of salts and using a ratio of 10:1 adsorbent/adsorbate and 500 mg/L of uranyl in solution. The adsorptive couple is contacted during 24 h at 300 rpm later, they are separated by centrifugation (4000 rpm), and the residual uranyl content in the supernatant was determined by using a spectrofluorometer with $\lambda_{Exc.}$=369 nm, $\lambda_{Emi.}$=510, Slit exc. = 10 nm, and Slit emi. = 10 nm (Thermo Scientific, Waltham, MA, USA).

13.2.2.5 Adsorption Isotherms

Uranyl adsorption isotherms were developed on the materials that turned out to be more efficient. For this, a solution containing 1000 mg/L of uranyl acetate (U) in deionized water was prepared and subsequently diluted at concentrations between 10 and 500 mg/L in the different systems (varying the amount of ACs materials and varying salinity) at pH 6.3. The residual concentration of U during the adsorption was determined by using spectrofluorometer (Thermo Scientific, Waltham, MA, USA) to the conditions previously described. The time for reaching the adsorption equilibrium was around 4 hours. The amounts adsorbed in units of milligram of uranyl per gram mass of materials were estimated according to Eq. (13.1) according to the method described by Franco et al. [18]:

$$N_{ads} = \frac{(C_0 - Ce)V}{W} \tag{13.1}$$

Where C_0 (mg/L) is the initial uranyl concentration while Ce (mg/L) is the uranyl equilibrium concentrations; V (L) is the volume of the uranyl solution, and W (g) is the mass of carbons used to essay. The concentration of uranyl residual in the supernatant was determined by fluorescence as described above.

13.2.2.6 Effect of Adsorbent/Adsorbate Ratio on Adsorption Efficiency of Uranyl

For this, different amounts of ACs materials were employed (100 mg per 20 ml of uranyl solution (a ratio of 5:1), 200 mg per 20 mL of solution (10:1), and 400 mg per 20 ml of solution (20:1)), and the other conditions for the adsorption were maintained constant. The isotherms were estimated as explained above.

13.2.2.7 Effect of Salinity on Adsorption Efficiency of Uranyl

For this, three salt concentrations using KCl were prepared (1% w/v, 3% w/v, and 5% w/v; the salinities were chosen considering the average hardness of the flowback water), and the other conditions were maintained constant (adsorbent/adsorbate ratio 10:1 and pH 6.3). Then, isotherms were estimated, as explained above.

13.2.2.8 Reuse Process

The desorption test of using basic solutions was carried out in order to evaluate the capacity of the material in reuse processes. For this, the composites AC material-uranyl were left in a NaOH solution at pH of 12.0. After 24 h, the content of uranyl in the medium was monitored by fluorescence using a new calibration curve. Subsequently, the materials were used in resorption tests. For this, 200 mg of desorbed materials were added to 10 ml of an aqueous solution of uranyl to 500 mg/L (pH = 6.3), then the mixture was stirred at 300 rpm during 4 h, and the content of uranyl in the solutions was again measured; a total of 30 adsorption-re-adsorption cycles were carried out.

13.2.2.9 Solid-Liquid Equilibrium (BET) Model

The BET model has been extensively used to fit sorption isotherm experimental data [19]. This model describes mainly the multilayer adsorption phenomena for liquid-solid systems [20–23]. The model is presented below:

$$q = q_{\max} \frac{K_S C_E}{\left(1 - K_L C_E\right)\left(1 - K_L C_E + K_S C_E\right)}$$

where q is the amount of uranyl (mg/g) adsorbed at equilibrium, $q_{\max}$ is the maximum adsorption capacity (mg/g), C_E is the equilibrium concentration of uranyl in the aqueous phase (mg/L), and K_S (L/mg) and K_L (L/mg) are the equilibrium constants of adsorption for the first layer and the upper layers, respectively.

13.3 Results

13.3.1 Material Characterization

AC morphologies were analyzed by SEM; illustrative images are shown in Fig. 13.1. AC samples are three-dimensional networks of amorphous particles in a micrometric regime, arranged randomly, and with spaces between the primary particles, which define their porosity, which is essential for physisorption phenomena. Other studies have described this type of arrangement [24, 25].

The N_2 sorption isotherms of AC materials are presented in Fig. 13.2. Carbons show type I–IV hybrid isotherms with a H4 hysteresis loop according to UIPAC (International Union of Pure and Applied Chemistry) [26], and these results are characteristic of microporous-mesoporous hybrid materials with narrow slit-like pores. The slight slope at low relative pressures less than 0.1 is evidence of the development of the monolayer. After that, the curve is pronounced indicating the beginning of the multilayer fission, which corresponds to the filling of mesopores. Other studies have revealed the ability of phosphoric acid to increase the micro- and mesoporous space, causing the collapse of macropores [25, 27, 28].

The textural properties of materials derived from the isotherms are summarized in Table 13.1. All samples (AC materials) were microporous-mesoporous hybrid; V_{micro} and V_{meso} represented, each one, the 40% of VT. Functionalized materials exhibited VT slightly lower than the AC sample (control), which is expected, considering that the heteroatoms block the pore by deposition in the micro- and mesoporous spaces [27]. However, the modification with phosphoric acid (P) had a dual activating consequence, increasing total porous volume.

The pore size distributions (PSD) of the AC materials are shown in Fig. 13.3. The results attained by the coupling of nitrogen isotherms and mercury porosimetry confirm that carbon materials are microporous–mesoporous materials; V_{macro} represents less than 20% of V_T in all cases. All distributions showed bimodal behaviors;

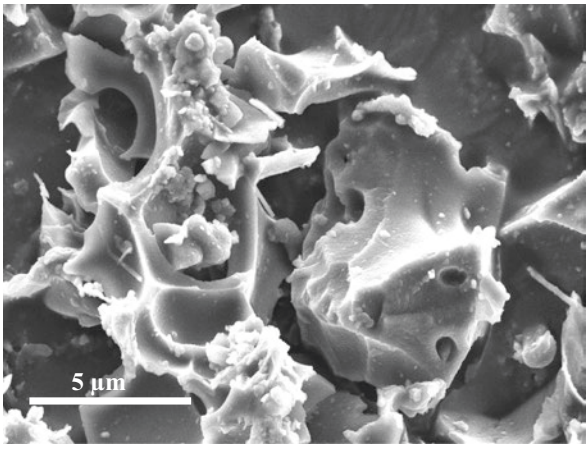

Fig. 13.1 The microstructure of the activated carbon without functionalization (AC) sample obtained by SEM analysis

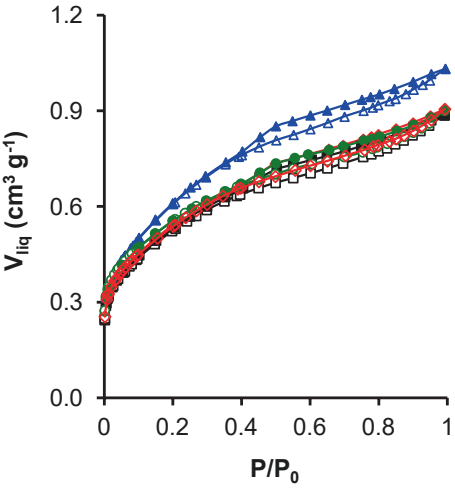

Fig. 13.2 N2-Isotherms at −196 °C for ●, activated carbon without functionalization (AC); ◆, activated carbon functionalized with melamine (AC-N); ▲, activated carbon functionalized with phosphoric acid (AC-P); and ■, activated carbon functionalized with ammonium phosphate (AC-NP). Adsorption (open symbols); desorption (closed symbols)

Table 13.1 Textural properties of activated carbon without functionalization (AC), activated carbon functionalized with melamine (AC-N), activated carbon functionalized with phosphoric acid (AC-P), and activated carbon functionalized with ammonium phosphate (AC-NP)

Sample	S_{BET} m^2/g	V_{micro} cm^3/g	L_{micro} nm	V_{meso} cm^3/g	L_{meso} nm	V_{macro} cm^3/g	V_T cm^3/g
AC	1224	0.442	1.33	0.375	2.46	0.145	0.962
AC-N	1169	0.420	1.36	0.404	2.44	0.125	0.951
AC-P	1296	0.450	1.37	0.484	2.38	0.123	1.071
AC-NP	1139	0.409	1.34	0.403	2.18	0.041	0.848

micropore mean width was centered on L_0 (N_2) 1.34 ± 0.03 nm, and mesopore mean width was centered on d, 2.36 ± 0.28 nm for AC materials, and this region represents the 80% of total area. These results agree with those reported by Moreno-Castilla et al. [13].

In addition to the available porous space, the surface chemistry of the material is essential for the stabilization of the adsorptive couple. The chemical compositions of the carbons are summarized in Table 13.2. In general, the surface of the materials was constituted mainly of C atoms (≈ 80%) and presented residual nitrogen in AC-N and AC-NP for the functionalization method and phosphorus atoms either by the process of functionalization or activation. The pH_{IEP} becomes an important parameter to characterize the chemistry of carbons [29, 30]. It is defined as the pH value at which the total charge on the surface of the adsorbent is neutral [30] and determines the charge density of materials under different pH. Furthermore, it is strongly dependent on the chemical groups that possess the materials on their surfaces. The pH_{IEP} for all materials is acidic.

The use of the activating agent (H_3PO_4) promoted the formation of cross-links with phosphoryl groups; these chemical groups are proton-active and generate a negatively charged surface with low pH_{IEP}. Comparable results have been found by

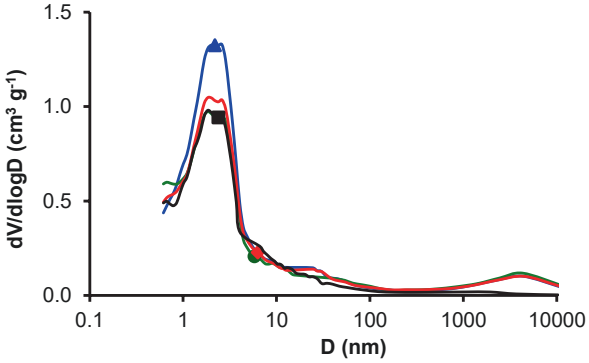

Fig. 13.3 Pore size distribution for: ●, activated carbon without functionalization (AC); ◆, activated carbon functionalized with melamine (AC-N); ▲, activated carbon functionalized with phosphoric acid (AC-P); and ■, activated carbon functionalized with ammonium phosphate (AC-NP). Obtained by the application of QSDFT to N_2 adsorption isotherms and mercury porosimetry

Table 13.2 Atomic concentration on the surface of activated carbon series. Assessed by XPS analysis

	Surface atomic concentrations (%)					
Sample	C1s	O1s	N1s	P2p	Heteroatoms (O + P)	pH_{IEP}
AC	85.5	7.7	–	6.7	14.4	2.44
AC-N	84.6	7.6	1.1	6.7	14.3	2.96
AC-P	83.4	7.7	–	8.9	16.6	1.92
AC-NP	82.3	7.7	0.6	7.3	15.0	2.03

other researchers [30]. The addition of heteroatoms such as nitrogen, free (N), or combined (NP), slightly increased the value of pH_{IEP}. However, for all AC materials, the surface chemistry is determined to a greater extent by the activating agent (H_3PO_4) [13, 31, 32]. In brief, the AC-N and AC-NP samples display a higher pH_{IEP} value than the other materials for the presence of amino groups on its surface (groups positively charged – Lewis bases). In contrast, AC and AC-P materials show the lowest value for pH_{IEP} due to the presence of phosphoryl groups, also called acid groups or proton-active that gives a negative charge density to the materials and, consequently, a lower value of pH_{IEP} [33].

13.3.2 Material Selection

The capacity of activated carbons with different chemical natures to remove uranyl was evaluated. Explicitly, the carbons evaluated reached removals of uranyl between 50% and 100% after 4 h. The adsorption efficiencies are given in the following order (97%) AC-N > (96%) AC > (81%) AC-NP > (56%) AC-P for the uranyl

concentration evaluated at temperature of 25 °C and adsorbent/adsorbate ratio of 10:1. Figure 13.4 shows the correlation between the porous and chemical properties of the materials and the ability to remove uranyl ions. According to the results, the mesoporous volume and the surface chemistry of the materials, measured through the pH_{IEP} and the heteroatoms (HETAM) content, are fundamental during the adsorption phenomenon (a high Pearson correlation coefficient (PCC) > 0.80), The macro- and microporous properties seem to have no relation with (PCC < 0.50) the adsorptive capacity of the materials on the uranyl ions.

In the present study, the correlation between the microporous volume and the adsorptive capacity of the materials seems not to be clear. However, the mesoporous carbons with the lowest number of heteroatoms (P + O), represented by a higher value for pH_{IEP}, were more efficient in the adsorption of uranyl. According to previous reports, uranyl chemical species at pH 6.3 are solvated with hydroxyl groups

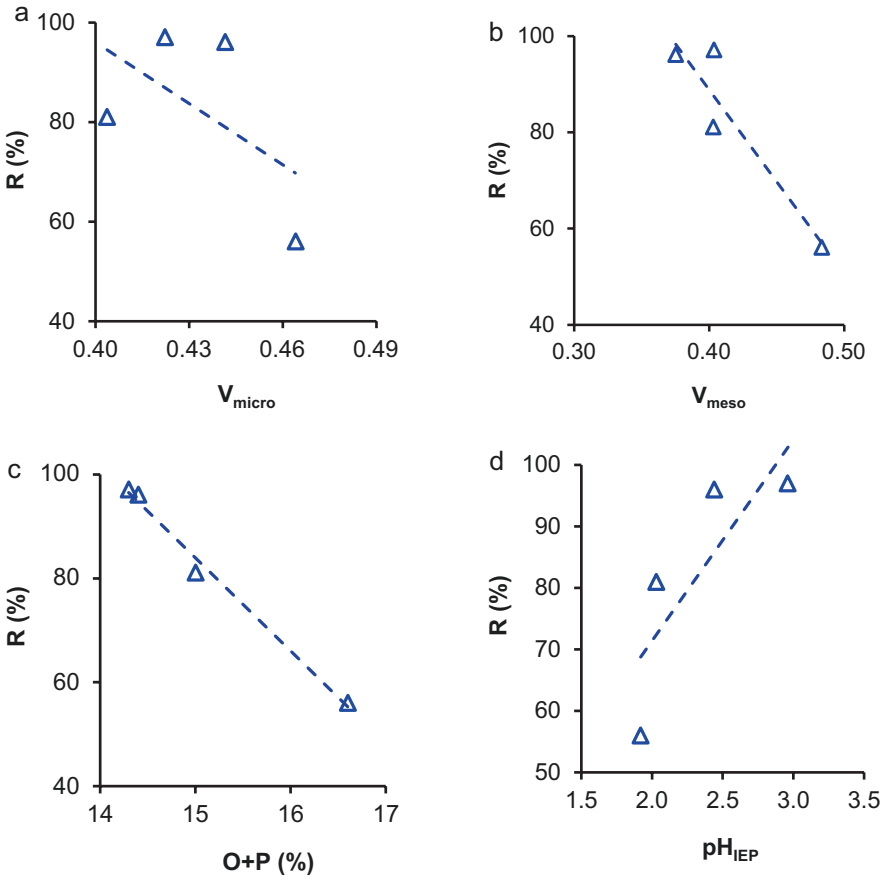

Fig. 13.4 Correlation between porous texture and chemical properties of materials and the ability to remove uranyl ions (R%)

associated with water molecules through ion-ion and ion-dipole interactions forming species like $UO_2(OH)^+$, $(UO_2)_2(OH)_2^{2+}$, and $(UO_2)^3(OH)^{5+}$ [34]; when the size and shape of a uranyl solvated with a single layer of water molecules are considered, as can be seen in Fig. 13.5, the inability of the complex to deposit correctly in the micropores (size <2 nm) is highlighted, unlike the narrow mesopores (slightly higher than 2 nm) that allow a better spatial accommodation of the hydrated uranyl.

On the other hand, less acidic surfaces, with higher pH_{IEP}, benefited to a greater extent the uranyl – surface interaction. The high affinity between the adsorptive couple, Uranyl – AC, and Uranyl-AC-N, compared to the others materials it is due to a lower repulsive force between the highly electronegative zones of the complex attributed to the presence of oxygen atoms and the surface of the carbons AC and AC-N, less negative (higher pH_{IEP}). Materials such as AC-P and AC-NP are characterized by a more significant number of phosphoryl and phosphate groups (heteroatoms (P + O), as can be seen in Table 13.2) that will eventually establish higher repulsive interactions with the uranyl group oxygen and decrease the adsorptive capacity of acid materials. Therefore, the most promising materials, AC and AC-N, were used for the adsorption efficiency tests.

13.3.3 Effect of Adsorbent/Adsorbate Ratio on the Adsorption Efficiency of Uranyl

Figure 13.6 shows the experimental isotherms for uranyl adsorption onto AC and AC-N materials with the BET model fit at 298 K using different absorbent/adsorbate ratios. The adsorption isotherms for all scenarios have type III behavior according to the IUPAC classification [26]; in this type of isotherm, the adsorbate has a similar affinity for the adsorbent as for itself. The monolayer acts as a free site for another molecule to adsorb, and so on [25]; this leads to an uneven coating, with

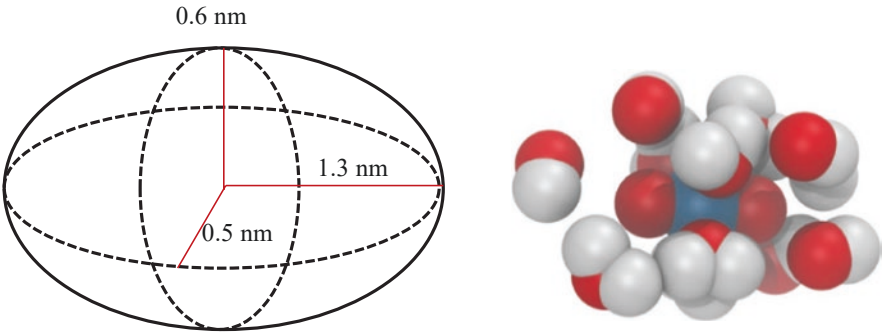

Fig. 13.5 Ellipsoid shape and mean size of a hydrated uranyl cation molecule with a single layer of water (five molecules) using dynamic

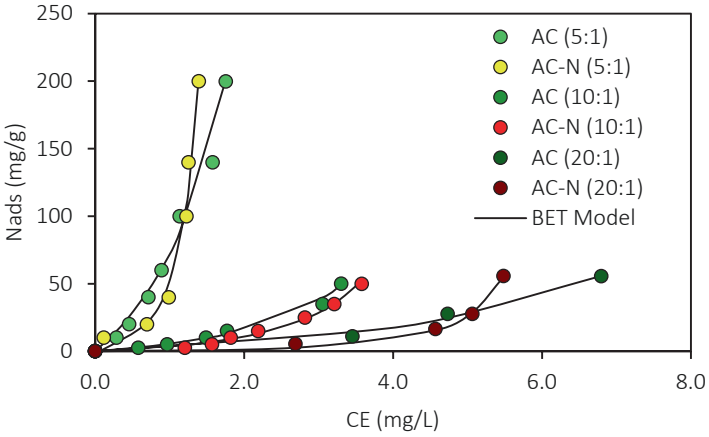

Fig. 13.6 Uranium-isotherms at 25 °C and different adsorbent/adsorbate ratio using activated carbon without functionalization (AC) ● 5:1, ● 10:1, ● 20:1 and activated carbon functionalized with melamine (AC-N) ● 5:1, ● 10:1, and ● 20:1

Table 13.3 Estimated BET model parameters for uranyl adsorption isotherms over activated carbon without functionalization (AC) and activated carbon functionalized with melamine (AC-N) using different adsorbent/adsorbate ratio

AC					AC-N				
R	K_L L/mg	K_s L/mg	q_{max} mg/g	R^2	*R*	K_L L/mg	K_s L/mg	q_{max} mg/g	R^2
5:1	0.35	0.14	200.8	0.97	**5:1**	0.53	0.06	200.58	0.98
10:1	0.18	0.07	58.2	0.99	**10:1**	0.18	0.05	55.64	0.99
20:1	0.09	0.04	54.9	0.99	**20:1**	0.15	0.02	51.14	0.99

free zones, other covered with monolayer, and parts covered with multilayer. These results agree with the report by other authors [15, 35].

There are no statistical differences between AC and AC-N during the uranyl adsorption. Moreover, as can be seen in Fig. 13.6, the isotherms showed a different amount of adsorbed according to the ratio adsorbate/adsorbent employed. The upper isotherm corresponds to 5:1, the middle isotherm to 10:1, and the lower isotherm to 20:1 adsorbent/adsorbate ratio, and the adsorbed amount decreases in the order 5:1 ratio > 10:1 ratio > 20:1 ratio in the entire range of equilibrium concentration (CE). These findings are supported by the values of BET model parameters listed in Table 13.3, where q_{max} decreases as the value of the ratio increases. Besides, K_L y K_S values followed a similar tendency of q_{max}, indicating that the adsorption affinity increases, and the multilayer adsorption greatly affected as the ratio adsorbate/adsorbent decreases for the two samples evaluated. As shown in Table 3, the BET model described well the experimental results of the adsorption isotherms according to the values of R2. Lower K_S values related with increased ratio

adsorbate/adsorbent also indicate that adsorption is less stable and the uranyl molecules may be adsorbed perpendicularly to the carbon surface [22, 35, 36].

In this instance, the results can be attributed to the decrease of the available active sites for adsorption by mass units caused by increasing the carbon dosage, which consequently influences the interactions between the materials and uranyl. This condition improves carbon-carbon interaction and hence the diminution of the accessible active sites for adsorption. Therefore, this decreases the possibility of uranyl contacting the carbon surface. Similar results were published by Garcia et al. [35]. They assessed the adsorption of azo-dye Orange II over iron-benzene-tricarboxylate and observed a reduction in the amount adsorbed with the increase of the quantity of the adsorbent. Also, some authors like Guzman et al. [15] also found similar results when determining that the rise in the concentration of nanoparticles decreased the adsorbed amount of asphaltenes of them. In both studies, the results are attributed to the particle aggregation of adsorbent as a result of high adsorbent mass and the reduction of available porous sites. Finally, is important to remark that q_{max} is mainly determined by the availability of sites on the materials, which decreases as amount of material increases.

13.3.4 Effect of Salinity on Adsorption Efficiency of Uranyl

When evaluating the impact of salinity on adsorption efficiency using AC and AC-N, 100% removal was evidenced at concentrations of uranyl between 50 and 1000 mg/L using saline concentrations of 1%, 3%, and 5% w/v, showing a higher performance in comparison with the non-saline system (uranyl removals between 56% and 97%). It appears that the presence of 1–5% w/v of saline concentration is enough to promote the total removal of uranyl, even when it is found at levels as diverse as 50 mg/L and 1000 mg/L. When AC and AC-N are at higher pHs than their pHIEP, negative sites on the material surfaces are favored. Thus, the probability of adsorbate-adsorbent encounter is reduced due to the high electronegativity of the uranyl molecules. The presence of ions in solution from the salt, especially the cations (M+), forms a bridge between the adsorptive pair establishing material (anion) – salt (cation) – uranyl (- dipole) interactions [37, 38].

13.3.5 Reuse Process of Activated Carbons

Reuse tests are useful to define the half-life time of absorbent materials. In the present study, 30 cycles of desorption-re-adsorption of uranyl on AC and AC-N materials were performed. The asequible sites of the carbons were restored by washing with 0.1 M NaOH, followed by de-ionized water and the subsequent sorption cycle. Thirty adsorption-desorption cycles were completed, and the adsorption power of AC and AC-N was found to be closely analogous during the 25th cycles. For the

AC-N, there is a decline by 15% in the 30th cycle, which can be due to the degradation of functionalizing agent. Meanwhile, the AC sample keeps constant during the 30 cycles evaluated. In addition, the results showed that desorption at basic pH is desirable for AC and AC-N recovery. These outcomes indicate that the activated carbons have a small affinity, rapidly saturable for some or all NaOH-modified uranyl species including uranyl hydroxide in the monomeric form $UO_2(OH)_2$ and in the dimeric $(UO_2)_2(OH)_4$ [34]. At pH 13, the AC and AC-N have a negative surface charge, and uranyl also tends to occur as an anionic species, for example, $UO_2(OH)_2$ and $(UO_2)_2(OH)_4$. This is an electrostatically unfavorable condition for the adsorption, which also can explain the decrease in the uranium adsorption on AC-N at pH 13 after 25 cycles. Currently, there is no knowledge of studies that report on the removal of uranyl species in fracturing waters; close research was done by Dutta et al. [34]; however, the assays were limited to interpreting the adsorptive phenomena in an aqueous medium; in that case, 93% or 186 mg/g removals of uranyl ions in the absence of salts at pH 6.0 were achieved. In comparison, in the present work, removals of 100% or 500 mg/g of uranyl ions at pH 6.3 and ranges of salinities between 0% and 5% were reached, which is one of the greatest adsorption efficacies described so far.

13.4 Conclusion

A new adsorbent made of activated carbon has been developed for fast and efficient adsorptive removal of uranyl ions at pH 6.3 as a proposal for water treatment in hydraulic fracturing processes. The results advised that the carbons with narrow mesoporosity and the highest value of pH_{IEP} were most efficient in the adsorption of uranyl, specifically AC and AC-N. The strong affinity is due to a lower repulsive force between the adsorptive couple added to the presence of narrow mesoporosity that allows the accommodation of hydrated uranyl species. On the other hand, the parameters of the BET model showed that the amount adsorbed decreases as the adsorbent/adsorbate ratio increases as a consequence of the reduction of available active sites for adsorption by mass unit, caused by increasing the carbon dosage and the aggregation of the primary particles of the material as previously reported. The BET adsorption isotherm suggested a maximum adsorption capacity (removal of %100) of 500 mg/g in 4 h, using a 5:1 of adsorbent/adsorbate ration and saline concentrations between 0% and 5% w/v which is a result not previously achieved since there is no knowledge of the removal of uranyl species from water used in hydraulic fracturing processes.

The sustainability of AC and AC-N has been demonstrated by showing the regeneration and reusability for 30 cycles. It is essential to highlight that the water used in hydraulic fracturing processes reports salinities and pHs in the ranges selected for the current investigation so that it can be concluded that AC and AC-N materials have tremendous potential for efficient uranium de-contamination of these waters. In future work, slight variations in pH could be considered on the removal capacity

of the investigated materials. Finally, it is presumed that the majority of NORM is found in anionic form, product of the combined action between the salts of the formation and the pH; therefore it would be correct to predict that the developed materials will be effective for the removal of other radioactive such as thorium and potassium.

Acknowledgments The authors would like to acknowledge Fondo Nacional de Financiamiento para la Ciencia, la Tecnología y la Innovación "Francisco José de Caldas," Agencia Nacional de Hidrocarburos, Colciencias and Universidad Nacional de Colombia for their support provided in Agreement 064 of 2018 and Spanish Ministry of Science, Innovation and Universities - State Research Agency-_Project ref. RTI2018-099224-B-I00. The authors also acknowledge Research Groups *Fenómenos de Superficie Michael Polanyi, Adsorción y Catálisis*, and especially to *Daniel Lopez Suarez* and *Ivan Moncayo* for their theoretical support in the research. Finally, authors thank Colciencias for the financing of the doctoral student Karol Zapata Acosta through the announcement 617/2014.

References

1. S. Zendehboudi, N. Rezaei, A. Lohi, Applications of hybrid models in chemical, petroleum, and energy systems: A systematic review. Appl. Energy **228**, 2539–2566 (2018)
2. Q. Wu, Y. Xu, X. Wang, T. Wang, S. Zhang, Volume fracturing technology of unconventional reservoirs: Connotation, design optimization and implementation. Pet. Explor. Dev. **39**, 377–384 (2012)
3. H. Wang, F. Ma, X. Tong, Z. Liu, X. Zhang, Z. Wu, D. Li, B. Wang, Y. Xie, L. Yang, Assessment of global unconventional oil and gas resources. Pet. Explor. Dev. **43**, 925–940 (2016)
4. J.D. Guzmán, D. Pineda, C.A. Franco, Ó.F. Botero, S.H. Lopera, F.B. Cortés, Effect of nanoparticle inclusion in fracturing fluids applied to tight gas-condensate reservoirs: Reduction of methanol loading and the associated formation damage. J. Nat. Gas Sci. Eng. **40**, 347–355 (2017)
5. M. Guo, X. Lu, C.P. Nielsen, M.B. McElroy, W. Shi, Y. Chen, Y. Xu, Prospects for shale gas production in China: Implications for water demand. Renew. Sust. Energ. Rev. **66**, 742–750 (2016)
6. G.V. Åkerblom, C. Wilson, Radon gas—A radiation hazard from radioactive bedrock and building materials. Bull. Int. Assoc. Eng. Geol./Bull. l'Association Int. Géologie l'Ingénieur **23**, 51–61 (1981)
7. A.W. Nelson, A.W. Knight, D. May, E.S. Eitrheim, M.K. Schultz, Naturally-occurring radioactive materials (NORM) associated with unconventional drilling for shale gas, in *Hydraulic Fracturing: Environmental Issues*, ACS Symposium Series, vol. 1216, (American Chemical Society, Washington, DC, 2015), pp. 4–89. ISBN 9780841231221
8. T.A. Saleh, Naeemullah, M. Tuzen, A. Sarı, Polyethylenimine modified activated carbon as novel magnetic adsorbent for the removal of uranium from aqueous solution. Chem. Eng. Res. Des. **117**, 218–227 (2017)
9. F. Khalili, G. Al-Banna, Adsorption of uranium(VI) and thorium(IV) by insolubilized humic acid from Ajloun soil – Jordan. J. Environ. Radioact. **146**, 16–26 (2015)
10. H. Ding, X. Luo, X. Zhang, H. Yang, Alginate-immobilized Aspergillus niger: Characterization and biosorption removal of thorium ions from radioactive wastewater. Colloids Surf. A Physicochem. Eng. Asp. **562**, 186–195 (2019)
11. S. Li, L. Wang, J. Peng, M. Zhai, W. Shi, Efficient thorium(IV) removal by two-dimensional Ti2CTx MXene from aqueous solution. Chem. Eng. J. **366**, 192–199 (2019)

12. F.I. Khalili, N.H. Salameh, M.M. Shaybe, Sorption of uranium(VI) and thorium(IV) by Jordanian bentonite. J. Chem. **2013**, 586136 (2013)
13. C. Moreno-Castilla, F. Carrasco-Marín, M.V. López-Ramón, M.A. Alvarez-Merino, Chemical and physical activation of olive-mill waste water to produce activated carbons. Carbon N. Y. **39**, 1415–1420 (2001)
14. S. Eskandari, G. Tate, N.R. Leaphart, J.R. Regalbuto, Nanoparticle synthesis via electrostatic adsorption using incipient wetness impregnation. ACS Catal. **8**, 10383–10391 (2018)
15. J.D. Guzmán, S. Betancur, F. Carrasco-Marín, C.A. Franco, N.N. Nassar, F.B. Cortés, Importance of the adsorption method used for obtaining the nanoparticle dosage for Asphaltene-related treatments. Energy Fuel **2052–2059**, 30 (2016)
16. E. Bailón-García, F. Carrasco-Marín, A.F. Pérez-Cadenas, F.J. Maldonado-Hódar, Development of carbon xerogels as alternative Pt-supports for the selective hydrogenation of citral. Catal. Commun. **58**, 64–69 (2015)
17. A.F. Pérez-Cadenas, F.J. Maldonado-Hódar, C. Moreno-Castilla, On the nature of surface acid sites of chlorinated activated carbons. Carbon N. Y. **41**, 473–478 (2003)
18. C.A. Franco, N.N. Nassar, F.B. Cortés, Removal of oil from oil-in-saltwater emulsions by adsorption onto nano-alumina functionalized with petroleum vacuum residue. J. Colloid Interface Sci. **433**, 58–67 (2014)
19. S. Brunauer, P.H. Emmet, E. Teller. Adsoprtion of Gases in Multimolecular Layers. J. Am. Chem. Soc. 60, 309–319 (1938)
20. A. Ebadi, J.S. Soltan Mohammadzadeh, A. Khudiev, What is the correct form of BET isotherm for modeling liquid phase adsorption? Adsorption **15**, 65–73 (2009)
21. A. Al-Futaisi, A. Jamrah, R. Al-Hanai, Aspects of cationic dye molecule adsorption to palygorskite. Desalination **214**, 327–342 (2007)
22. C.-H. Weng, Y.-F. Pan, Adsorption of a cationic dye (methylene blue) onto spent activated clay. J. Hazard. Mater. **144**, 355–362 (2007)
23. C.-H. Weng, Y.-F. Pan, Adsorption characteristics of methylene blue from aqueous solution by sludge ash. Colloids Surf. A Physicochem. Eng. Asp. **274**, 154–162 (2006)
24. K. Zapata Acosta, F. Carrasco-Marin, F. Cortés, C. Franco, S. Lopera, B. Rojano, Immobilization of P. stutzeri on activated carbons for degradation of hydrocarbons from oil-in-saltwater emulsions. Nano **9**, 500 (2019)
25. A. Elmouwahidi, Z. Zapata-Benabithe, F. Carrasco-Marín, C. Moreno-Castilla, Activated carbons from KOH-activation of argan (Argania spinosa) seed shells as supercapacitor electrodes. Bioresour. Technol. **111**, 185–190 (2012)
26. M. Thommes, K. Kaneko, A.V. Neimark, J.P. Olivier, F. Rodriguez-Reinoso, J. Rouquerol, K.S.W. Sing, Physisorption of gases, with special reference to the evaluation of surface area and pore size distribution (IUPAC technical report). Pure Appl. Chem. **87**, 1051–1069 (2015)
27. K. Zapata, F. Carrasco-Marín, J.P. Arias, J. Castelo-Quibén, C.A. Franco, B. Rojano, F.B. Cortés, Novel biomaterial design based on Pseudomonas stutzeri–carbon xerogel microspheres for hydrocarbon removal from oil-in-saltwater emulsions: A new proposed treatment of produced water in oilfields. J. Water Process Eng. **35**, 101222 (2020)
28. K. Zapata Acosta, F. Carrasco-Marin, F.B. Cortes, C.A. Franco, S.H. Lopera, B.A. Rojano, Immobilization of P. stutzeri on activated carbons for degradation of hydrocarbons from oil-in-saltwater emulsions. Nanomater (Basel) **9**, 500 (2019)
29. P. Trivedi, L. Axe, Ni and Zn sorption to amorphous versus crystalline iron oxides: Macroscopic studies. J. Colloid Interface Sci. **244**, 221–229 (2001)
30. A. Lazaro, K. Sato, H.J.H. Brouwers, J.W. Geus, Pore structure development of silica particles below the isoelectric point. Microporous Mesoporous Mater. **267**, 257–264 (2018)
31. M. Tschapek, L. Tcheichvili, C. Wasowski, The point of zero charge (pzc) of kaolinite and SiO2+AI2O3 mixtures. Clay Miner. **10**, 219–229 (1974)
32. M. Kosmulski, The pH-dependent surface charging and the points of zero charge. J. Colloid Interface Sci. **253**, 77–87 (2002)

33. M. Kosmulski, C. Saneluta, Point of zero charge/isoelectric point of exotic oxides: Tl2O3. J. Colloid Interface Sci. **280**, 544–545 (2004)
34. R.K. Dutta, M.A. Shaida, K. Singla, D. Das, Highly efficient adsorptive removal of uranyl ions by a novel graphene oxide reduced by adenosine 5′-monophosphate (RGO-AMP). J. Mater. Chem. A **7**, 664–678 (2019)
35. E.R. García, R.L. Medina, M.M. Lozano, I. Hernández Pérez, M.J. Valero, A.M.M. Franco, Adsorption of azo-dye orange II from aqueous solutions using a metal-organic framework material: Iron-benzenetricarboxylate. Materials (Basel) **7**, 8037–8057 (2014)
36. J. Wang, C.P. Huang, H.E. Allen, D.K. Cha, D.-W. Kim, Adsorption characteristics of dye onto sludge particulates. J. Colloid Interface Sci. **208**, 518–528 (1998)
37. B. Biswas, B. Sarkar, R. Rusmin, R. Naidu, Bioremediation of PAHs and VOCs: Advances in clay mineral-microbial interaction. Environ. Int. **85**, 168–181 (2015)
38. U.C. Ugochukwu, M.D. Jones, I.M. Head, D.A.C. Manning, C.I. Fialips, Biodegradation and adsorption of crude oil hydrocarbons supported on “homoionic” montmorillonite clay minerals. Appl. Clay Sci. **87**, 81–86 (2014)

Chapter 14
Nanoparticles for Cleaning up Oil Sands Process-Affected Water

Afif Hethnawi, Adle Mosleh, and Nashaat N. Nassar

14.1 Introduction

With industrial development, energy demand from conventional and renewable energy sources increases and becomes crucial concern [1]. Renewable sources of energy, despite their general awareness, are contributed only about 19.1 % of the global energy demand in 2013 [2]. Up to date, this trend has been growing steadily [3]. Thus, fossil fuel obtained by conventional crude oil stands out to remain the predominant energy source worldwide for the upcoming decades [4]. This demand, as reported by the International Energy Agency (IEA), is expected to rise from 84.7 million barrel/day in 2008 to 105 barrel/day in 2030 [5, 6]. However, the conventional reserves of oil are depleting [6, 7]. Thus, more efforts are needed to shift the oil production from conventional to the development of nonconventional resources, including oil sands [6]. The conventional oil reserves are more economically feasible to recover and process compared with that for the unconventional oil reserves [4, 7, 8]. Canada, for instance, is ranked as third globally (along with Saudi Arabia and Venezuela) in terms of domestic oil reserves [9]. The reserves in northern Alberta, Canada, are estimated to contain more than 1.7 trillion barrels of bitumen, as a largest oil deposits in the world [3]. For that reason, oil industry is considered and an energy intensive industry and a major consumer for the fresh water. This led such industry to be subjected to strict environment regulations, and hence, the oil industry is considering improving the efficiency and reducing the environment footprint of current oil recovery, storage, and pipeline transportation methods.. In terms of recovery, the deposited oil or bitumen, depending on how deep the oil sands reserves,

A. Hethnawi · A. Mosleh · N. N. Nassar (✉)
Department of Chemical and Petroleum Engineering, University of Calgary, Calgary, Alberta, Canada
e-mail: nassar@ucalgary.ca

N. N. Nassar et al. (eds.), *Nanoparticles: An Emerging Technology for Oil Production and Processing Applications*, Lecture Notes in Nanoscale Science and Technology, https://doi.org/10.1007/978-3-319-12051-5_14

is essentially recovered by employment of two main methods: open-pit mining or in situ extraction methods that are schematically shown in Fig. 14.1.

Less than 20 % of Alberta's bitumen reserves are close to the surface to be mined (less than 50 m) [3]. Anything deeper cannot be economically mined because huge amount of waste material needs to be removed before accessing to the bitumen-rich oil sands [9]. For about 80 % of Alberta's oil sands (deeper than 50 m), in situ thermal method can be used with substantial consumption of energy and water [9].

Unlike surface mining, in situ technology offers the benefit of removing the bitumen from the ground while leaving the sand in place [9]. Typically, an average of 0.4 barrels of fresh water is needed to recover each barrel of bitumen by SAGD process, while oil sands surface mining process uses three to four barrels of high-quality water for each barrel of oil produced [10, 11]. In Alberta, most of the high-quality water (around 90%) used for mining operations is typically recycled from the production process, while the rest is withdrawn from the Athabasca river [10,

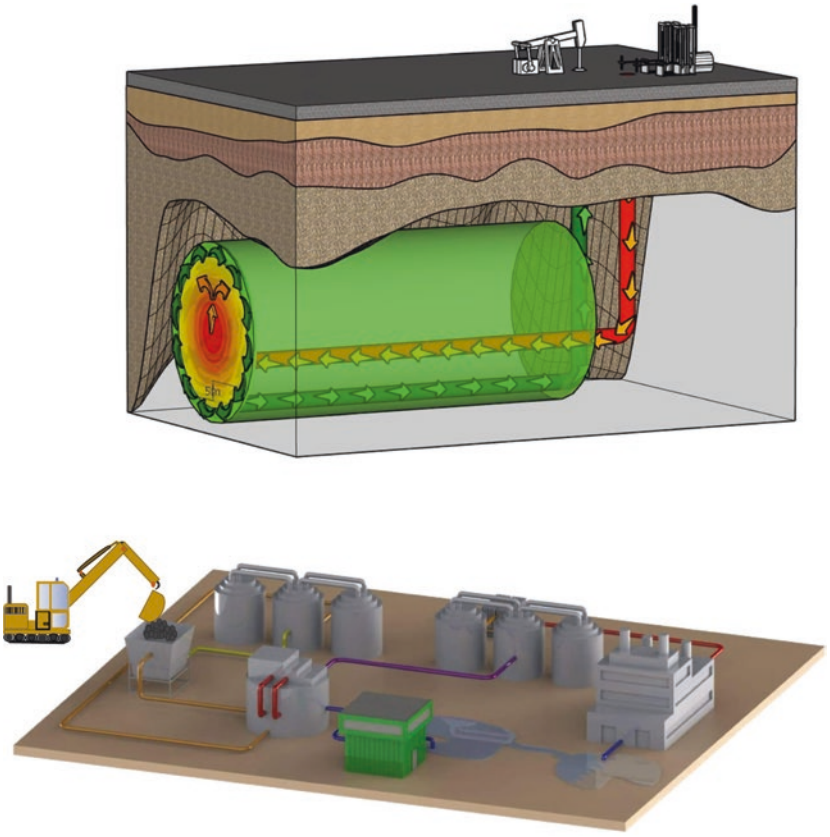

Fig. 14.1 Schematic representation for the extraction of bitumen from oil sand through (**a**) steam-assisted gravity drainage (SAGD) and (**b**)open-pit surface mining processes. Copyright permission was obtained from Vista Projects (https://www.vistaprojects.com/)

11]. The most well-known in situ process is SAGD which is currently considered as the most widely practiced one for bitumen extraction from oil sands in Alberta, Canada, due to its lower cost and higher efficiency. In Alberta alone, 80% (or 135 billion barrels) of the oil sands are located in these underground deposits and would be difficult to access without applying SAGD process [12]. In principle, SAGD process requires drilling of two horizontal wells [13–15]. The upper well is utilized to inject the heated steam inside the oil well deposit [13–15]. This steam builds up heat, which delivers its latent heat to the adjacent area, reducing the viscosity of the bitumen and subsequently mobilizing it [13–15]. Thus, the mobilized bitumen, along with the condensate steam, is drained downward by gravity to the second horizontal well, from which it pumps to the surface [13–15]. The recovered bitumen on the surface is separated via subsequent cooling units, generating huge amounts of wastewater in the form of produced water (PW). Then, the bitumen is transferred to surface-upgrading facilities in order to convert the low-quality oil to synthetic crude oil. The PW, on the other hand, is transferred to sequential de-oiling and treatment train to improve the water quality to be reused for boiler feedwater (BFW) in a once-through steam generator (OTSG) that produces steam from a high-quality water [9, 12, 16]. Constrains on water quality are produced by once-through steam generator (OTSG). OTSG is specifically developed heat recovery steam generator for thermal recovery applications [17]. In OTSG design, a single pass of water through the generator coil and no separator drum are available, generating 80 % quality steam with water-to-steam ratio of 1:4 [3]. PW is generally characterized by having high concentrations (from 1000 to 10,000 mg/L) of brine, silica, alkalines, and total dissolved solids (TDS) [18–20]. Exceeding the "threshold requirement concentrations" is undesirable for the reuse of PW as boiler feedwater (in oil field steam generator), unless it can be effectively treated through selective water treatment technologies [21]. Thus, the generated SAGD produced water must meet the strict requirements in the employed boiler for steam generation [17, 22–25]; otherwise, boiler drum and tubes can be damaged or corroded.

On the other hand, open-pit mining, like traditional mineral mining operations, is largely employed where oil sands reserves are closer to the surface [26]. Practically, large shovels scoop the oil sand into trucks which then move it to crushers where the large clumps of earth are processed [26, 27]. Then, the crushed oil is mixed with warm water, oil sand lumps and rocks, air, and caustics, forming slurry mixture that mainly composed of about sand with minimal composition of bitumen [26, 27]. After that, the slurry mixture undergoes to a simple water-based gravity separation process to extract the bitumen fraction [26–28]. In the gravity separation vessel, flotation cells are used to liberate the bitumen deposited in the sand grains by injecting free air bubbles to slurry mixture, generating a froth product that is formed on the top of the vessel [26–28]. This froth composes of about 60% by weight bitumen, 30% water, and 10% solids [26–28]. The unrecyclable effluent is discharged to tailing ponds [26–28]. The bitumen froth is further treated with organic solvents to remove water and residual solids from the bitumen, before sending it to upgrading plants [26–28]. The bottom product is mostly composed of solids and water in the form of tailings and is pumped to tailing ponds. In those tailing ponds, the mixture, based on the sand

particle size and compositions, is separated into two main layers: a layer of coarse solids with characteristic size greater than 44μm and other layer enriched with smaller fine solid particles [29]. The heavier layer tends to be settled down at high rate and precipitate quickly to be used to construct contaminant dikes, while the other layer remains at the top of the pond as fluid fine tailings [26–29]. From the fluid fine tailings, great portion of fine sand particles and clay stay suspended and eventually form a mud-like slurry (30–45% solids by weight) called mature fine tailings (MFT) [26–29]. Around 86% of the volume of MFT contains water that cannot be easily recycled, because of the presence of stable sand particles (very fine, negatively charged clays that cannot be separated from water by gravity); these sand particles form a vastly disproportional amount of slurries that constantly repel each other, inhibiting Brownian agglomeration and making it difficult for settling to take place [26–29]. To address this challenging issue, tremendous efforts, with varying levels of success and feasibility, have been proposed to speed up the settling rate of the fine particles in MFT and maximize the water recovery rate [29].

With respect to storage and transportation of the recovered oil, pipelines are a critical part of Canada's oil transportation infrastructure [30, 31]. Pipeline transport is the safest and most efficient way to move large volumes of oil from development areas to refineries, petrochemical plants, and even to homes or businesses [30, 31]. Although pipelines are convenient and appear to be better options compared to other means of transportations, there are issues to be concerned like crude oil spills. For instance, the TransCanada pipeline that transports oil to the US Midwest has experienced 14 spills, with the latest spill at North Dakota pipeline pumping station in May 2011[30, 31]. A campaigner with Greenpeace Canada considers this as an act of aggression toward plants, wildlife, and people who live in the path of pipelines. In fact, these oil spills, without an effective removal method, showed adverse impacts to ecosystems and the long-term effects of environmental pollution that calls for an urgent need to develop a wide range of materials for cleaning up oil from oil-impacted areas [32].

In conclusion, bitumen recovery operations (i.e., open-pit mining or SAGD) and oil pipelines generate a considerable amount of oil sands process-affected water (OSPW) and oil spills. These OSPWs, without any treatment, can cause low bitumen recovery, fouling, corrosion, and scaling problems at the extraction and transportation facilities. As a result, a series of OSPW treatments is necessary before recycling or environmental release of this water. Therefore, oil sands companies in Canada are eagerly seeking novel technologies in order to modify the technologies they currently implement for recycling the generated OSPW. In this regard, this chapter aims to provide an overview about the main conventional treatment technologies applied in treating SAGD produced water, mature fine tailings (MFT), and oil spills. Thus, the chapter critically highlights and deeply describes the conventional treatment technologies along with their suggested modification methods and some emerging techniques that have been recently reported from fundamentals to process optimization and eventually the parameters that affect the process efficiency. The chapter comprehensively describes tailoring designs of some eco-friendly nanoparticles developed by Nassar's group at the University of Calgary to

be effectively combined or integrated with the many physical and/or chemical processes utilized for remediation of OSPW.

14.2 Treatment of SAGD Produced Water

During the SAGD operations, the strict water quality requirements for steam generation can be met by reducing the levels of suspended and dissolved organic matters, hardness, and silica [33]. For example, the level of TOC, which reflects soluble, emulsified, and suspended organics, in produced water varies from 100 to 700 ppm [21, 24, 33]. Also, silica levels can reach up to 400 ppm. These levels should be maintained below 50 ppm TOC and 30 ppm silica in the feedwater to OTSG [21, 24, 33]. Thus, sequential primary, secondary, and tertiary stages are conventionally applied. In the primary stage, the oil content is reduced from 2000 to 500 ppm from the PW by applying three-phase separators followed by skimming [15]. These separator units maintain high retention times (i.e., 3h), which allows for oil/water separation. In the primary stage, the suspended solid presented in the PW is removed by induced gas flotation (IGF) process that uses air or, low density gas, typically methane [15]. However, introducing gasses in IGF in some occasions cannot effectively remove the suspended solid and requires high retention times [15]. Therefore, ionic polyacrylamide is added to flocculate the suspended solids in the IGF, which are able to destabilize the suspended solids via surface neutralization and facilitate floc formation by interparticle bridging mechanism[15]. The outlet from IGF is fed to a sand filter, which contributes to lowering the suspended solid concentration between 30 and 40 ppm. The tertiary stage consists of chemical treatment train that is aimed at reducing the residual concentrations of silica, TOC, and total hardness from the PW to meet water specification for the OTSG [15, 21, 24, 33]. The chemical treatment train combines three successive processes of warm lime softening unit (WLS), followed by walnut shell filtration (WSF), and weak acid cationic exchanging unites (WAC).

14.2.1 Warm Lime Softening (WLS) Unit

In the WLS, the hardness (calcium and magnesium ions) and total alkalinity are removed by adding chemicals like lime ($Ca(OH)_2$), soda ash (Na_2CO_3), and caustic soda (NaOH). As a result, the concentrations of silica and hardness are diminished to values less than 50 mg/L and 50 mg/L as $CaCO_3$ at high temperature (65−85 °C), respectively [15, 21, 24, 33]. Fundamentally, the silica, under the aqueous conditions, exists in crystalline or amorphous forms [34]. There are various forms of crystalline silica, but the most abundant one is quartz, having a very low solubility in water, around 6 mg/L (as SiO_2) at 25 °C [34]. However, amorphous silica is more soluble in water with maximum solubility of 100–140 mg/L (as SiO_2) at 25 °C [34].

The amorphous silica can be essentially classified as dissolved, colloidal, and particulate silica [34]. Dissolved silica includes various silica species: monomers (Q^0), dimers (Q^1), trimers (Q^2), and polymeric silicic acid (Q^3) as shown in Fig. 14.2 [34]. As reported previously, the silica species are in transition among each other according to the medium pH and the presence of other ions [34–36]. With polymerization of silicic acid by condensation, a three-dimensional gel network of insoluble or colloidal silica (amorphous silica) is generated [34–36]. Hence, the presence of diverse forms of silica is considered to be "anomalous," indicating that the stability in terms of pH does not follow a certain trend [35, 36]. Hence, the formed silica at various medium pH can be presented on two domain states of silica: colloidal domain, which is insoluble and amorphous (polymerization), and mono-clear silicate. At medium's pH above 9 (pH of SAGD produced water), the concentration of mono-clear domain silica and other species is dominant in an aqueous condition [34–36].

The removal of hardness and silica in WLS is carried out by introducing lime ($Ca(OH)_2$), soda ash (Na_2CO_3), magnesium oxide (MgO), and sodium hydroxide (NaOH) to the generated PW, in which the soluble calcium and magnesium hardness convert to insoluble calcium carbonate and magnesium hydroxide that contribute in simultaneous precipitation of silica [15, 17, 21, 24, 33]. Firstly, the removal of carbonate hardness by lime is accomplished by one of the following reactions [15, 17, 21, 24, 33]:

$$Ca(HCO_3)_2 + Ca(OH)_2 \Rightarrow 2CaCO_3 \downarrow + 2H_2O \tag{14.1}$$

$$Mg(HCO_3)_2 + Ca(OH)_2 \Rightarrow CaCO_3 \downarrow + MgCO_3 + 2H_2O \tag{14.2}$$

$$MgCO_3 + Ca(OH)_2 \Rightarrow CaCO_3 \downarrow + Mg(OH)_2 \downarrow \tag{14.3}$$

$$Ca(HCO_3)_2 + 2NaOH + Ca^{2+} \Rightarrow 2CaCO_3 \downarrow + 2H_2O + 2Na^+ \tag{14.4}$$

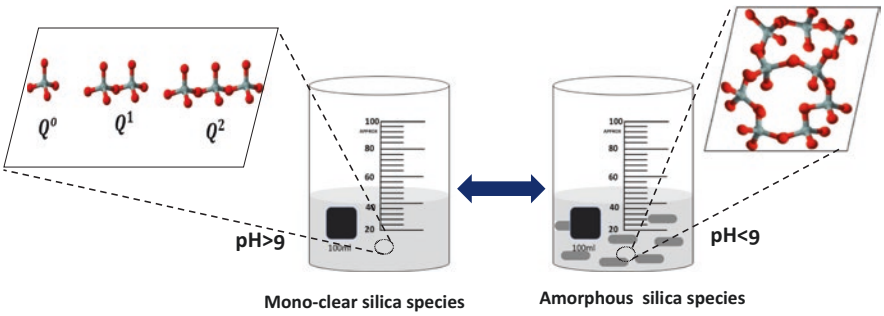

Fig. 14.2 Model of silica species and their polymerization path into amorphous structure under aqueous conditions. Color code: O: red; Si: light gray

Also, the removal of calcium non-carbonate hardness by soda ash is carried out by [15, 17, 21, 24, 33]:

$$CaSO_4 + Na_2CO_3 \Rightarrow CaCO_3 \downarrow + Na_2SO_4 \tag{14.5}$$

$$CaCl_2 + Na_2CO_3 \Rightarrow CaCO_3 \downarrow + 2NaCl \tag{14.6}$$

On the other hand, the removal of magnesium non-carbonate hardness by lime and soda ash can be done by one of the following chemical reactions [15, 17, 21, 24, 33]:

$$MgCl_2 + Ca(OH)_2 \Rightarrow Mg(OH)_2 \downarrow + CaCl_2 \tag{14.7}$$

$$CaCl_2 + Na_2CO_3 \Rightarrow CaCO_3 \downarrow + 2NaCl \tag{14.8}$$

$$MgSO_4 + Ca(OH)_2 \Rightarrow Mg(OH)_2 \downarrow + CaSO_4 \tag{14.9}$$

$$CaSO_4 + Na_2CO_3 \Rightarrow CaCO_3 \downarrow + Na_2SO_4 \tag{14.10}$$

With lime softening process, the silica presented in the PW can be significantly reduced via forming precipitated metal ions, such that the silica removal by magnesium oxide can be carried out in the same softening unit simultaneously with the removal of hardness from the PW by lime and soda ash [15, 17, 21, 24, 33]. Thus, the purpose of MgO addition is to interact with silica and precipitate silica compounds from the produced water. However, the mechanism at which the silica is removed by MgO has not been fully described [37–40]. Several studies based on physiochemical processes have investigated the removal of silica with the use of many metal oxide compounds [37–40]. Table 14.1 lists some attempts that have been reported to study the removal of silica by using different metal oxides/hydroxides from synthetic PW. The table includes the process involved in removing of silica in each study, materials used, summary of the main results, and references [37–40].

All the tabulated studies showed effective removal of silica through precipitation along with adsorption mechanisms using diverse metal oxides/hydroxides. It can be also noticed that the presence of MgO results in highly efficient silica removal, especially at high temperature (i.e., WLS conditions) [37–40]. In fact, using MgO after hydration at WLS conditions has shown faster and more efficient removal of silica. However, the MgO without sufficient hydration, which occurs in a separate slurry mixing tank, may exist in non-slaked form after reaching to the WLS unit, which contributes in attaining unpredictable performance in the real application. In fact, existence of non-slaked MgO at WLS conditions resulted in obtaining high removal of silica, compared with the slaked form, due to adsorption of silica on the surface of the formed $Mg(OH_{)2}$ [40]. Unfortunately, introducing great amount of magnesium compounds increases the conductivity in the treated waters, which can

Table 14.1 Most recent studies that have reported the removal of silica from synthetic produced water with the use of different metal oxides/hydroxides [37–41]

Process	Material and methods	Main results	References
Coagulation/ precipitation	Metal hydroxide (ferry, aluminum, and calcium)	The content of 35 mg/L SiO_2 in synthetic PW can be completely removed by aluminum compounds at ambient conditions.	[37]
		Aluminum compound as catalyzer reacts with colloid silica in the form of pure amorphism.	
		The soluble silica can be adsorbed by ferric hydroxide, which enhances the speed of colloid silica coagulation and settling at ambient conditions.	
		The concentration of soluble silica in treated wastewater is reduced to 3–5 mg/L when ferric coagulant is added.	
Coagulation/ flocculation	Combination of magnesium compound, sodium hydroxide precipitation, and zinc sulfate	The silica was removed at room conditions through magnesium compound, pH regulator, and zinc sulfate.	[38]
		The concentration of silica (calculated with SiO_2) was reduced to less than 50 mg/L in the optimal condition: 500–600 mg/L of NaOH, 700–800 mg/L of $MgCl_2 \cdot 6H_2O$, and 100–150 mg/L of zinc sulfate.	
		The removal efficiency of silica by zinc sulfate was higher than that by general coagulants such as aluminum and ferric salts.	
		High temperature (70–90EC) and long settle time (> 1.0 h) in a mixing jar were advantageous to the silica removal.	
Electroco agulation (EC)/ adsorption	EC by corrode Fe^0 or Al^0 anodes to release Fe(II) (or Al(III)) ions into the solution	Formation of Fe(II) or Al(III) allowed to react with solutes in the solution to form Fe-containing (or Al-containing) precipitates that can adsorb a wide variety of contaminants.	[39]
		In Fe^0-EC, the precipitation of FeS minerals resulted in a rapid removal of sulfide and adsorption of silica onto FeS.	
		In Al^0-EC, silica was removed via adsorption onto aluminum hydroxides, compared with sulfide that was poorly removed.	

(continued)

Table 14.1 (continued)

Process	Material and methods	Main results	References
Adsorption/ precipitation	Slaked and non-slaked MgO	Silica removal by slaked and non-slaked MgO has been investigated at different pH values (8.0−11.3) with different dosages (100−1000 ppm) and contact time (15−120 min) at WLS operating temperatures (65−85 °C).	[40]
		Silica removal takes place through two possible competing mechanisms: adsorption on the formed $Mg(OH)_2$ or precipitation by forming magnesium silicate precipitates.	
		Slaked MgO achieves lower silica removal percentage than non-slaked MgO at WLS conditions because MgO slaking makes silica adsorption on the formed $Mg(OH_)_2$ more predominant.	
Adsorption/ precipitation	Sparingly soluble magnesium compounds (MgO,$Mg(OH)_2$ and $(MgCO_3)_4{\cdot}Mg(OH)_2{\cdot}5H_2O$)	The use of three sparingly soluble magnesium compounds (MgO, $Mg(OH)_2$ and$(MgCO_3)_4{\cdot}Mg(OH)_2{\cdot}5H_2O$) has been investigated at three pHs (10.5, 11.0, and 11.5) and five dosages (250–1500 mg/L) at ambient temperature (~20 °C).	[41]
		The results showed that only 40% silica removal was obtained.	
		To increase silica removal, the slurries of sparingly soluble compounds were pre-acidified with concentrated sulfuric acid and tested at the same conditions. In this case, high removal rates were obtained (80–86%) at high pH (11.5), even at ambient temperature.	

be avoided by applying sparingly soluble magnesium compounds, such as (MgO,$Mg(OH)_2$ and $(MgCO_3)_4{\cdot}Mg(OH)_2{\cdot}5H_2O$)) that might be considered as promising alternative [41]. As a matter of fact, significant reduction in the conductivity was obtained by applying the sparingly soluble magnesium compounds, with low removal efficiency of silica (i.e., 40 %) at pH 10.5, dosages of 250 mg/L, and at ambient temperature (~20 °C) [41]. The same study showed that the removal efficiency of silica was then improved up to 80% by pre-acidifying the sparingly magnesium compounds with concentrated sulfuric acid, which is not industrially favorable [41].

From the listed studies in Table 14.1, it can be also noticed that all the suggested metal oxides/hydroxides applied to remove silica from organic-free synthetic produced water under conditions mimicking the WLS operations [37–41]. These results cannot be representative for the real performance of MgO in removing of silica from the authentic water, likely due to the influence of organic species. In addition, using massive amounts of lime, ash, and metal oxides/hydroxides for simultaneous removal of hardness and silica is costly ineffective, such that WLS contributes in 80% of the operation cost and 30% of the capital investment of the tertiary treatment train for the PW generated from SAGD process. In fact, introducing lime, ash, and slaked and non-slaked magnesium might enhance the concentration of divalent ions (i.e., Ca^{+2} and Mg^{+2}), which increase the need for another unit to be eliminated (i.e., WAC). Installation of WAC unit adds extra operational and capital costs for the whole chemical treatment process [17].

14.2.2 Walnut Shell Filter (WSF) Unit

In WSF, a deep bed-filter media, commonly termed walnut shell filters, are traditionally utilized due to their oil and solid filtration performance combined with ease of backwashing. WSF is applied to reduce the free oil content in SAGD produced water below 50 mg/L [17]. Practically, the walnut shell filter media, compared with other minerals and polymers, have several unique characteristics (e.g., hard, lightweight, chemically inert, nontoxic, and biodegradable) [42–45]. These characteristics, in addition to its high affinity to uptake many mineral oils and heavy metals, have motivated many industries to use them as effective filtration media or even active sorbents [42–45]. However, the walnut shell particles (WS-VR) have amorphous and compact structure due to high contents of cellulose and hemicellulose inert layers. Presence of such inert layer on the WS-VR, without surface modification, does not allow for enhancing the surface activity, thereby creating active sorbent that is able to capture many contaminants [42–45]. Table 14.2 displays some recent studies that have focused on removing several dissolved heavy metals and organic pollutants with the use of surface-modified walnut shell particles [46–50]. As noticed, all the tabulated works focused on producing active sorbents from the walnut shell particles after surface modification, through activation at high temperature or/and with the use of strong acid/bases or/and different agents. Also, the modified walnut shell particles were used to treat heavy metals, pharmaceuticals, and toxic organic molecules only in batch adsorption experiments, without continuous investigation inside fixed bed column that operates under various hydrodynamic conditions [46–50].

14.2.3 Weak Acid Cationic Exchange (WAC) Unit

In WAC, alkalization of water is carried out by using WAC resins (i.e., carboxylic type acids), in order to remove the divalent ions of Ca^{2+} and Mg^{2+} generated from WLS unit [17]. The WAC resins are spherical beads of a network of cross-linked polymers [34]. The cross-linked polymers are composed of functional groups with fixed co-ions that are negative charge located on each functional group along with the polymer matrix [34]. These co-ions are pre-saturated with cations that are mobile and free to move on the pores of the polymer matrix [34]. With adding these resins to the PW phase, the cations tend to diffuse in the bulk phase at high rate, yielding negatively charged resins [34]. Consequently, the counterions presented in the wastewater solution can migrate into the negatively charged resin phase and replace the cations stoichiometrically till attaining the equilibrium [34]. At equilibrium, the concentration differences of the ions are balanced that maintain the electroneutrality between the bulk solution and resin phase [34]. The WAC resins are generally described by formula of R-COOH that are able to remove the alkalinity from the carbonate hardness by the following equation [17]:

$$2\mathrm{RCOOH} + \mathrm{Ca}\left(\mathrm{HCO_3}\right)_2 \Rightarrow \left(\mathrm{RCOO}\right)_2 \mathrm{Ca} + 2\mathrm{CO_2} + 2\mathrm{H_2O} \tag{14.11}$$

$$2\mathrm{RCOOH} + \mathrm{Mg}\left(\mathrm{HCO_3}\right)_2 \Rightarrow \left(\mathrm{RCOO}\right)_2 \mathrm{Mg} + 2\mathrm{CO_2} + 2\mathrm{H_2O} \tag{14.12}$$

Also, the removal of divalent ions by WAC resin can be done as follows [17]:

$$2\mathrm{RCOOH} + \mathrm{M^{2+}} \Rightarrow \left(\mathrm{RCOO}\right)_2 \mathrm{Ca} + 2\mathrm{H^+} \tag{14.13}$$

$$\mathrm{H^+} + \mathrm{HCO_3^-} \Rightarrow \mathrm{H_2O} + \mathrm{CO_2} \tag{14.14}$$

$$2\mathrm{H^+} + \mathrm{CO_3^{2-}} \Rightarrow \mathrm{H_2O} + \mathrm{CO_2} \tag{14.15}$$

The carboxylate resins require alkaline species in the water to react with the more tightly bound hydrogen ions[17]. Thus, the resins are able to remove Ca, Mg, and heavy metals (i.e., Pb) from sulfates after conversion to sodium resins as shown below [17, 34]:

$$\mathrm{RCOOH} + \mathrm{NaOH} \Rightarrow \mathrm{RCOONa} + \mathrm{H_2O} \tag{14.16}$$

$$2\mathrm{RCOONa} + \mathrm{CaSO_4} \Rightarrow \left(\mathrm{RCOO}\right)_2 \mathrm{Ca} + \mathrm{Na_2SO_4} \tag{14.17}$$

$$2\mathrm{RCOONa} + \mathrm{MgSO_4} \Rightarrow \left(\mathrm{RCOO}\right)_2 \mathrm{Mg} + \mathrm{Na_2SO_4} \tag{14.18}$$

$$2\mathrm{RCOONa} + \mathrm{PbSO_4} \Rightarrow \left(\mathrm{RCOO}\right)_2 \mathrm{Pb} + \mathrm{Na_2SO_4} \tag{14.19}$$

Table 14.2 Most recent studies that have reported the using of surface modified walnut shell filter particles to treat several types of heavy metals, pharmaceuticals, and toxic organic molecules [46–50]

Number	Title	Methods	References
1	Removal of Cr(VI) from aqueous solutions by modified walnut shells	The nutshell particle surfaces were only treated by acids at high temperature (>200 °C).	[46]
		The modified nutshell particles were used to remove the chromium.	
2	Selective removal of cesium from aqueous solutions with nickel (II) hexacyanoferrate (III) functionalized agricultural residue–walnut shell	The nutshell surface modification was chemically done by $NiCl_2$ and the treatment of $K_3[Fe(CN)_6]\cdot 3H_2O$.	[47]
		The modified nutshell was used to remove cesium ion (Cs^+) from aqueous solutions.	
3	Adsorption of naphthalene from aqueous solution onto fatty acid modified walnut shells	The surface of the nutshell was modified by fatty acid.	
		The removal was tested for naphthalene.	
4	Highly synergistic effects on ammonium removal by the co-system of *Pseudomonas stutzeri* XL-2 and modified walnut shell biochar	The walnut shell particles were modified by pyrolysis at 300 C and impregnated by 1.0 M NaOH. Then the material was washed, dried at 60 °C, pyrolyzed at 450 °C, and impregnated by 0.5 M $MgCl_2$ for 4 h.	[48]
		The modified material was used as sorbent for ammonia.	
5	Adsorption of lead ion from aqueous solution by modified walnut shell: kinetics and thermodynamics	The walnut shell particles were treated by acid and maleic anhydride to be used as adsorbent for lead.	[49]
		The modified walnut shell particles were used to remove lead from water.	
6	Characterization of metal oxide-modified walnut-shell-activated carbon and its application for phosphine adsorption: equilibrium, regeneration, and mechanism studies	The walnut shell particles were first activated at elevated temperature. Then they were modified by metal oxide.	[50]
		The modified nutshell particles were used to remove phosphine (PH_3) from water.	

Considering the previous reaction sets, WAC resins exhibit marked degree of volume expansion after conversion from hydrogen to sodium form, which is considered as one of their major disadvantages [17, 34]. Their permeance is also sensitive to the medium's pH, such that the apparent capacity increases to the maximum at pH higher than 11 (above pK_a) [17, 34]. Applying organic resins in cationic exchanger significantly contributes in increasing the total dissolved solids, causing numerous operational problems like fouling of pipelines and equipment and clogging of injection wells [17, 34].

Hence, replacement of the current scheme with a process which can separate almost all silica and reject more than 90% of the dissolved organic matters will considerably reduce the capital and operating costs due to the reduction of size and number of steam generators. Accordingly, many authors have made considerable efforts to come up with emerging technologies in order to modify or replace the current treatment train with more effective and economical solutions [17, 34].

14.2.4 Emerging Techniques for SAGD Produced Water Treatment

In the last decade, many studies have reported some emerging techniques for treatment of SAGD produced water that depends on either chemical or membrane filtration processes (Table 14.3) [51–56]. As shown from Table 14.3, most of the recent studies focused on fabrication of effective and inherently fouling-resistant membranes with better performance than some commonly used membranes (i.e., ceramic membranes) that showed some serious challenges [52–56]. These challenges have led the researchers to develop various fouling remediation techniques to break up surface deposits, backflushing with permeate and the use of many different chemical cleaning agents [52–56] . These modified membranes showed great potential in treating SAGD produced water, under well-controlled temperatures and pH [52–56].

Basically, the surface of the commercial ceramic membranes is highly hydrophobic because of the charged hydroxyl groups that occupy the selective layer [52–56]. Thus, the predominant surface charge of a ceramic membrane is pH-dependent given the isoelectric point of the selective layer's constituent metal oxide [52–56]. In many cases, controlling the pH of the feed solution so that the membrane surface charge leads to the electrostatic repulsion of charged foulants is an adequate method of fouling alleviation [52–56]. However, bituminous foulants like asphaltenes possess amphoteric functional groups, meaning that they can exhibit both positive and negative surface charges at any given feed pH [52–56]. To mitigate the interaction between amphoteric bitumen and the hydroxyl groups, the membrane surface can be chemically modified by a highly hydrophilic polymer (i.e., charge-neutral polyethylene oxide (PEO) functional silanes) in a way that reduces its electrostatic charge. On the other hand, implementing single-layer cellulose-based membranes toward thin-film composite (TFC) polyamide (PA)-based membranes showed superior permeation properties with better flux and selectivity, compared with commercially available membranes of TFC [52–56].

Implementing these surface modifications for the membranes provided successful forming of hydrophilic layers on the membrane surface that subsequently improves membrane flux and mitigated any irreversible effects [52–56]. However, the application of these modified membranes requires well-tuned and strict environment (i.e., temperature and pH), such that high pH and temperatures resulted in better separation performance, which enlarge the operational costs. Additionally,

Table 14.3 Most recent emerging techniques that have been reported for treatment of SAGD produced water [51–56]

Number	Topic	Material and methods	Main results	References
1	Treatment of oil sands produced water using combined electrocoagulation and chemical coagulation technique	Hybrid electrocoagulation-chemical coagulation (EC-CC) process has been used as an alternative to conventional chemical processes for the treatment of steam-assisted gravity drainage (SAGD) produced water under influence of various electrode material, cell configuration, pH and temperature of the solution, chemical coagulant dosage, intensity of the electrical current, mixing rate, and treatment time.	Parameters except the electrode arrangement had a significant effect on the removal of silica and TOC.	[52]
			The chemical coagulant and the treatment time had the most significant contribution to the efficiency by 40% and 26%, respectively.	
			The optimum condition for the highest TOC removal efficiency (39.8%) was obtained by applying 0.34 A to Al electrode in a bipolar (BP) configuration when the pH, temperature, coagulant concentration, mixing rate, and reaction time were set to 8, 60 °C, 200 mg/L, 700 rpm, and 90 min, respectively.	
2	Developing high-throughput thin-film composite polyamide membranes for forward osmosis treatment of SAGD produced water	High-performance thin-film composite TFC membranes by an innovative adjustment of interfacial polymerization (IP) reaction between m-phenylenediamine (MPD) and trimesoyl chloride (TMC) at the surface of a polyethersulfone (PES) microporous support.	Reducing the temperature of the organic solution down to −20 °C effectively reduced the thickness of the PA selective layer and thus significantly enhanced water permeation through the membranes.	[53]
			The water flux increased more than double for membranes prepared at 25 °C to 38.5 and LMH at −20 °C, when 3 M NaCl solution and de-ionized water were used as draw and feed solutions, respectively.	
			The performance of lab-synthesized TFC membranes was also evaluated for the treatment of boiler feedwater (BFW) of steam-assisted gravity drainage (SAGD) process.	

Number	Topic	Material and methods	Main results	References
3	Silane surface-modified ceramic membranes for the treatment and recycling of SAGD produced water	Membranes were synthesized from ceramic modified by highly hydrophilic and neutral organosilane.	The modification was successful in mitigating the irreversible fouling caused by bituminous ultrafines.	[54]
			The permeate flux of the 150 and 300 kDa membranes more than doubled after modification in a 20% silane solution.	
			The filtered water obtained from the modified membranes was of superior quality to that of the untreated membrane, as evidenced by total organic carbon analysis.	
4	Surface-modified multi-lumen tubular membranes for SAGD produced water treatment	Membranes were made from multi-lumen tubular ceramic membranes chemically modified using several charge-neutral polyethylene oxide (PEO)-based organosilanes. Membranes with a pore size of 10 nm and selective layers of either γ-Al_2O_3 or TiO_2 were modified based on protocols previously used on small-scale ceramic membrane disks.	Modification of γ-Al_2O_3 membranes by a 30% solution of straight-chain PEO-silane increased permeate flux by factors as high as 2.9.	[55]
			Modification of TiO_2 membranes also improved permeate flux.	
			Flux recovery factors upon backflushing increased from 1.3 to 1.6.	
			The decline in performance when switching to a SAGD feed, with a higher pH, total organic carbon, and alkalinity, was significantly less severe for modified TiO_2 membranes compared to unmodified counterparts.	
			Surface modification of tubular ceramic membranes with PEO-based silanes was successful in improving the rejection of bituminous foulants from the membrane surface.	

(continued)

Table 14.3 (continued)

Number	Topic	Material and methods	Main results	References
5	Development of antifouling membranes using agro-industrial waste lignin for the treatment of Canada's oil sands produced water	Antifouling polyethersulfone (PES) membranes were prepared from industrial waste derivative of lignin, sulfonated Kraft lignin (SKL), containing highly hydrophilic and negatively charged functional groups, as a bulk modifier for the fabrication.	The modified membrane containing the highest amount of SKL additive (3 wt.%) exhibited profound enhancement in the flux recovery ratio from 52.2% to 98.2% compared to the pristine PES membrane against the complex mixture of organic pollutants in SAGD produced water.	[56]
			The rejection of the organics decreased only slightly from 61.7% for the pristine membrane to 56.1% for the 3 wt.% SKL-embedded membrane, while the permeability and molecular weight cutoff (MWCO) increased by 43.3 LMH/psi and 144 kDa, respectively.	
6	An integrated oxy-cracking, nano-adsorption, and steam gasification processes for treatment of SAGD produced water	In treatment of SAGD produced water samples, the oxy-cracking technique is used as a pre-treatment step in order to generate solubilized organic intermediates under basic conditions at temperatures (473–253 K) and at a pressure of 1000 psi. The oxy-cracked organics from SAGD effluents were adsorbed onto silica-embedded NiO extrudates inside a packed-bed column under various operational parameters (i.e., flow rate, inlet concentration, and bed height. The catalytic steam gasification reaction was performed on the adsorbed species to produce syngas from the adsorbed organic matters and to regenerate the extrudates in order to use them sustainably for further cycles.	The integrated method was successfully implemented to reduce the total organic carbon from SAGD produced water.	[57]
			The oxy-cracking reaction involved a deep oxidation process flowed by a partial oxidation reaction with formation of oxy-cracked intermediates solubilized in the liquid phase.	
			The results showed that the column was able to remove greater amounts of TOC molecules at low flow rates, low inlet concentrations, and high bed heights.	
			The extrudates were regenerated and reused for two cycles of adsorption via the catalytic steam gasification process.	

Number	Topic	Material and methods	Main results	References
7	TOC removal by nanoparticles embedded into the diatomite at industrial level field test rotary drum filter tests	Iron oxide nanoparticles were prepared by coprecipitation method and embedded into a 22.7 kg of diatomite at mass ratios of 0.5, 1, and 2 wt.%, by preparing them separately in a pre-coat slurry mix tank over a period of 65 min. The slurry mixture of embedded nanoparticles in diatomite was used to coat the rotary drum filter (RDF). The RDF applied vacuum that sucked the TOC molecules onto the drum pre-coated surface and the effluent wastewater was pumped out to the discharge tank. The effluent samples were periodically collected, and their TOC concentrations were measured as the time proceeding during the test. Each experiment was conducted at constant feed flow rate, amount of diatomite.	The results showed that the breakthrough time and TOC removal efficiency were increased by increasing the concentration of nanoparticles embedded onto the diatomite. Enhancing the employed amount of diatomite whether its embedded with nanoparticles or not significantly influenced enhanced the TOC removal efficiency.	[58]
8	Iron hydroxide nanoparticles anchored on the walnut shell filtration media for simultaneous removal of silica and TOC from SAGD produced water.	Simultaneous remediation of silica and TOC was achieved by modifying the surface of the walnut shell with anchoring low mass percentages (e.g., < 5wt%) of iron (hydroxide) nanoparticles under moderate hydrolysis conditions (e.g., temperature, hydrolysis time, and concentration of nanoparticle precursor). The nanoparticles anchored on walnut shell particles (WS-NPs) were fully characterized, and their effectiveness toward the removal of TOC and silica was examined using batch and column experiments. Regeneration and recyclability of the spent materials were successfully investigated following direct backwashing and blade stirring methods.	The WS-NPs due to the presence of the nanomaterials showed an outstanding ability to remove TOC and silica, such that the modified material performed well in removing up to 85% of silica and TOC compared with the non-modified nutshell filter particles that showed <5% removal efficiency in the batch sorption tests. The packed column with WS-NPs and similar to the industrial operation showed an improved breakthrough behavior, without having channeling or pressure drop limitations. Regeneration cycles of the spent column were successfully done following direct backwashing and blade stirring methods.	[51]

(continued)

the synthesis methodologies followed in fabrication or surface modifying these membranes are not simple and need too many steps, which had significant environmental and cost downsides [52–56]. On the other hand, using combined electrocoagulation and chemical coagulation technique (study number 1) resulted in great performance in removing of silica and TOC [52]. However, attaining successful removal of silica and TOC required changing the medium pH and temperature, which is not industrially recommended. The table also includes another integrated technique that has been lately done for effective removal of TOC from SAGD produced water samples through sequential oxy-cracking, nano-adsorption, and steam gasification processes, which schematically described in Fig. 14.2 [57]**.**

14.2.4.1 Nanoparticle as an Emerging Technique for Treatment of SAGD Produced Water

An Integrated Oxy-Cracking, Nano-Adsorption, and Steam Gasification Processes for Treatment of SAGD Produced Water

The oxy-cracking process (e.g., a combination of consecutive oxidation and cracking reactions) has been developed as a modification to the Zimpro process for sewage-sludge oxidation and as an alternative and efficient approach for converting residual feedstocks into value-added products [59, 60]. Ashtari et al. (2016) first employed the oxy-cracking process for converting n-C_7 asphaltenes into light hydrocarbons, thus making them more accessible to subsequent hydrocracking reactions [60]. Recently our research group has utilized the oxy-cracking process for converting residual feedstock like petroleum coke into various commodity products [61]. We also advanced the process selectivity and conversion by introducing the copper silicate catalysts[62]. The oxy-cracking reaction mechanism was inspired by the generalized lumped kinetics model for wet air oxidation, which assumes that not all the organic compounds present in wastewater are directly oxidized to CO_2 and H_2O, and instead, the rest of the hydrocarbons are converted to intermediate products which might be further oxidized [63]. However, during the oxy-cracking reaction, in an alkaline aqueous medium, regardless of the type of feedstock, it was stated that the reaction conversion was insignificantly influenced by oxygen pressure beyond 5.2 MPa [64]. Hence, working at this pressure range (3.4–5.2 MPa) and temperature (150–250°C) keeps the water under subcritical conditions. At subcritical conditions, the dielectric constant of water dramatically changes with the temperature, and thus the reaction media changes from ionic to radical reaction. For instance, the solid petroleum coke, under well-monitored oxidation and alkaline conditions, can be oxy-cracked to light organic compounds (i.e., carboxylic, naphthenic acids, and their corresponding organic compounds) [64]. In contrast to the oxidation reaction, the oxy-cracking reaction is able to convert the insoluble hydrocarbon to a more soluble form at moderate temperatures and pressure [64]. Enhancing the solubility of the organic species can reduce the selectivity of the oxidation reaction toward formation of carbon dioxide. Thus, involving the

oxy-cracking reaction into one process can create an eco-friendly and green technology. In treatment of SAGD produced water, as tabulated, the oxy-cracking technique has been employed for converting the existent inactive organic pollutants into active ones through oxygen incorporation with minimal emission of CO_2 [57, 65]. After that, the oxy-cracked organics from SAGD effluents were adsorbed onto silica-embedded NiO extrudates inside a packed-bed column that operated under various operational conditions (i.e., flow rate, inlet concentration, and bed height) [65]. Finally, the catalytic steam gasification reaction has been performed on the adsorbed species to produce syngas from the adsorbed oxy-cracked organic matter and to regenerate the extrudates to use them sustainably for further cycles of adsorption-gasification processes. The results have shown that this combined technique has been successfully implemented in reducing the high concentration levels of TOC from SAGD produced water samples to acceptable levels. In fact, the oxy-cracking reaction kinetics obeyed the lumped kinetic model involving two basic reactions [57]. The first reaction implied a deep oxidation process at which the organic species were completely oxidized to CO_2 and H_2O, while the second reaction involved a partial oxidation reaction with formation of oxy-cracked intermediates solubilized in the liquid phase [57]. Additionally, the in-house prepared SiO_2-NiO extrudates showed high adsorption affinity and TOC removal efficiency for the oxy-cracked hydrocarbons at low feed flow rate, low initial concentration, and high bed depth, then, great tendency for regeneration via gasification-adsorption processes. The photographs of the vials shown in Fig. 14 are for the virgin SAGD produced water (dark color), oxy-cracked SAGD produced water (yellowish color), and oxy-cracked SAGD produced water after adsorption in the packed-bed column (colorless). As seen by naked eye, a high degree of treatment was obtained for SAGD produced water, which can be indicated by converting their color from blackish to almost colorless. Thus, the treatment method performed well in removing the total organic carbon and silica from SAGD wastewater. This can be considered as a proof of concept for integrating oxy-cracking, adsorption, and catalytic steam gasification for cleaning up OSPW. Indeed, this approach is considered the first of its kind in the field of sustainable wastewater treatment. Even so, this combined technique was not fully efficient in removing silica and TOC simultaneously. Besides, applying this technique involved harsh conditions (i.e., high temperature, pressure, and pH), in order to optimize the solubility and selectivity of the oxy-cracked product, which could add extra operational costs and hamper the application at large scale. Indeed, weak monitoring of the oxy-cracking reaction allows to form undesirable by-products.

TOC Removal by Nanoparticles Embedded into the Diatomite at Industrial Level Field Test Rotary Drum Filter Tests

From Table 14.3, an industrial level field tests in a rotary drum filter (RDF) are included, which are commercially used to remove plenty of suspended and dissolved contaminants generated from different industrial effluents [58]. Figure 14.4

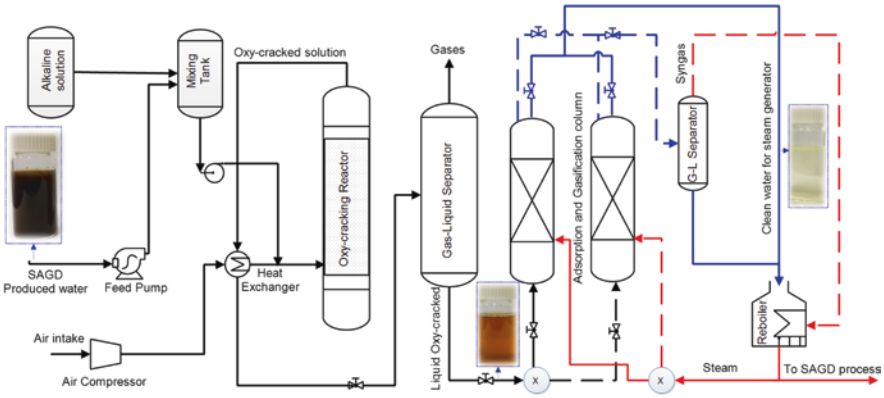

Fig. 14.3 A schematic representation of the proposed configurations for SAGD produced water using the oxy-cracking process. The vial images represent the SAGD wastewater before and after treatment by oxy-cracking at temperature 200 ºC and pressure 3.4 MPa and after 2 h adsorbed in the packed-bed column [66]. Permission related to the material excerpted were obtained from Elsevier, and further permission should be directed to Elsevier

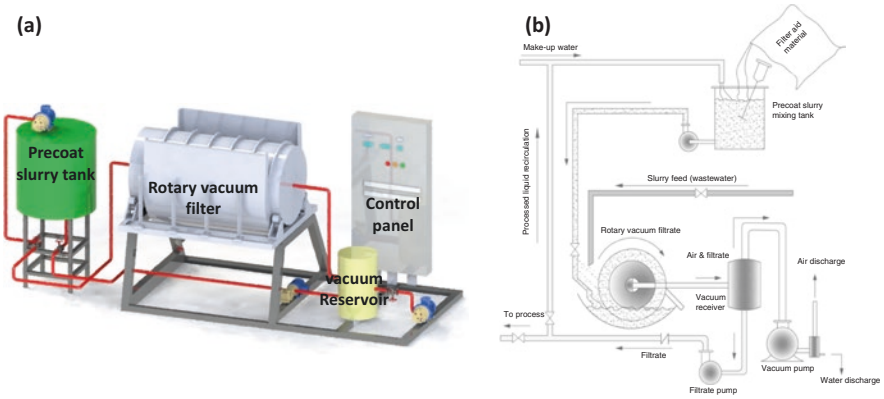

Fig. 14.4 (**a**) Three-dimensional and (**b**) two-dimensional schematic representations for a commercial rotary drum vacuum filtration unit (RDF) [58]. Copyright permission was obtained from the author

represents a schematic representation for the RDF, which mainly contains a drum rotating in a tub that accumulates the influent water. Before running the RDF, the drum is pre-coated with a filter aid material of diatomite [58]. The influent water is typically injected to the tub below the drum, which rotates through the influent water. Then a vacuum is applied that allows the wastewater to be sucked onto the drum's pre-coated surface, leading to the adherence of the suspended solid pollutants to the filter while it is rotating. The vacuum sucks the liquid portion through the filter media to the internal part of the drum, resulting in a filtrated liquid that is pumped away. Solids on the other hand adhere to the pre-coated surface. The drum then automatically passes a knife through the adhered solid and part of diatomite, revealing a fresh surface media. The RDF can work effectively in removing many

suspended pollutants. However, it has low efficiency in removing the dissolved TOC. Thus, the filter aid material was modified with anchoring low mass fraction (i.e., < 5 wt.%) of iron oxide nanoparticles, which were in-house prepared by coprecipitation method. As shown from the table, increasing the concentration of nanoparticles from 0.5 to 2 wt.% allowed to create capturing site that can effectively enhance the adsorption of the TOC molecules, which led to increasing the breakthrough time and TOC removal efficiency. Furthermore, it was also obtained that with increasing the feed flow rate, the breakpoint time and the adsorbed TOC molecules decreased [58]. The reason behind this is that when the flow rate increased, the residence time of TOC molecules was not enough for adsorption equilibrium to be reached at that flow rate, and the adsorption zone quickly saturates the precoated layer. Therefore, the contact time of TOC is very short at a high flow rate [58]. That subsequently reduced the TOC removal efficiency. On the other hand, when the feed flow rate is low, the TOC had more time to contact the sorption sites of adsorbent that led to achieving a higher removal of TOC molecules [67]. However, increasing the concentration of the nanoparticles embedded in the diatomite and the feed flow rate led to attaining channeling effect on the pre-coated filter aid layers. This channeling affect resulted from accumulation of more TOC molecules that tend to block the porous media and enhancing the pressure drop. Hence, it is highly recommended to operate under well-controlled operational parameters to avoid the pressure drop limitations that might occur due to embedding of nanoparticles.

Iron Hydroxide Nanoparticles Anchored on the Walnut Shell Filtration Media for Simultaneous Removal of Silica and TOC from SAGD Produced Water

As explained before, effectiveness of the walnut shell filter toward removal of many pollutants can be also enhanced via following some surface modification methods similar to those listed in Table 14.2. However, none of these studies have been continuously implemented via the column tests or to improve the depth filtration of the WSF unit toward removing of silica and TOC simultaneously [51]. In Table 14.3, study number 8 describes an innovative technique used to improve the removal of silica and TOC by anchoring low mass percentages of iron hydroxide nanoparticles on the walnut shell filtration. Presence of these nanoparticles enhanced the surface activity of the walnut shell filter particles, which create the potential to capture both silica and TOC [51]. The anchorage of iron hydroxide nanoparticles can be done chemically by two main steps: acid activation and formation of iron hydroxide nanoparticles under moderate hydrolysis conditions (e.g., temperature, hydrolysis time, and concentration of nanoparticle precursor). The purpose of the first step is permitting to generate open macropores and cavities that contribute in rendering diffusion sites that tend to accommodate the nanoparticles [51]. In the second step, iron hydroxide agglomerates in nanoscale are formed from thermal hydrolysis of ferric ions that originate from dissociation of ferric salt. Under aqueous conditions, the dissociative ferric ions are coordinately bonded with water molecules in the nature of aqueous complexes [68]. These complexes progressively go through

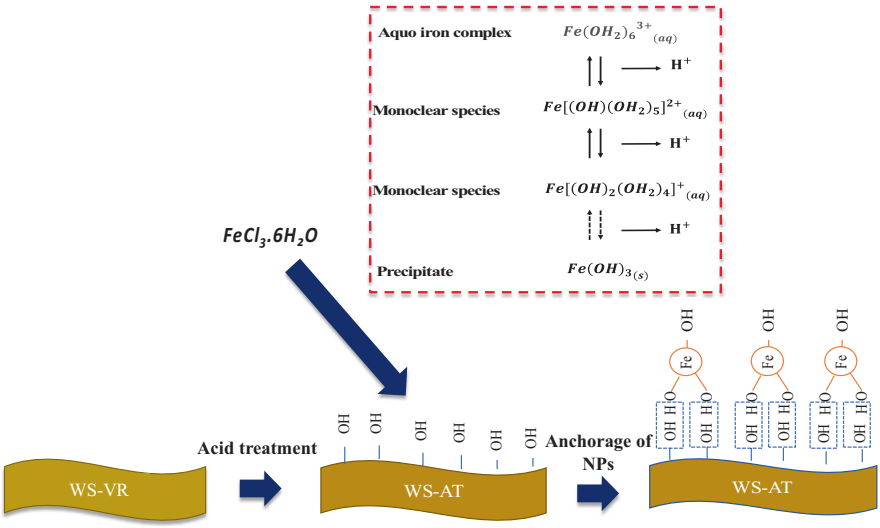

Fig. 14.5 Surface modification of the walnut shell surface (WS-VR) through acid treatment anchorage of iron hydroxide nanoparticles. Copy right permission was obtained from reference [51]

arrays of hydrolytic reactions as described in Fig. 14.5. During the hydrolytic reactions, deprotonation of the complexes is carried out yielding groups of soluble mono-clear and non-soluble species. Then, the generated species are able to be anchored on the hydroxylated filtration particles by:

1- Forming oxygenated bridges: The hydroxylated and acid treated particles interacted with one of the mono-clear species by forming oxygenated bridges through a nucleophilic substitution mechanism [69].
2- Bidentate adsorption: The hydroxylated species are adsorbed on the precipitate species of iron hydroxide by bidentate adsorption mechanism [68].

It can be concluded from the table that the filter aid particles due to the presence of iron hydroxide nanomaterials outperform in remediation of TOC and silica molecules in comparison with that achieved by applying the non-modified nutshell filter particles in the batch and column sorption tests [51]. The TFD calculations based on the theoretical adsorption energies have also proven that silica and TOC molecules adsorb more strongly to the surface of nanoparticle-functionalized walnut shell compared with the bare walnut shell [70–82]. Under continuous operations, the WS-NPs resulted in improved breakthrough behavior in the absence of any pressure drop limitations.

This clearly proves that applying the anchored walnut shell particles with nanoparticles can potentially form a high-quality water with low levels of both silica (<30mg/L) and TOC (<50mg/), meeting the strict requirements in the employed

boiler for steam generation. According to that, altering the non-modified walnut shell particles (WS-VR) with our modified once (WS-NPs) in the WSF should provide a replacement for the conventional treatment train, in which the conventional WLS, WSF, and WAC can be substituted with one single unit. Interestingly, to evaluate the regeneration option, three consecutive regeneration studies were successfully done on the spent column following direct backwashing and blade stirring methods. Evidence to date suggests that WS-NPs is a stable sorption/filtration medium, in that relatively small amount of iron hydroxide nanoparticles that have low tendency to be lost over time during treatment, regeneration, and backwashing steps. However, additional long-term testing is required to confirm these finding and to quantify the effective lifetime of the media.

14.3 Enhancing Settling and Dewatering of Mature Fine Tailings (MFT)

Various treatment processes, with varying levels of success and feasibility, have been used to speed up the settling rate of the fine particles in MFT and maximize the water recovery rate for reuse in the industry [83–86]. These treatment methods can be classified as natural, biological, physical/mechanical, and chemical techniques [25, 87]. With natural processes, the solid contents in the MFT are increased up to 45% by freeze-thaw technology, such that the tailings are allowed to be frozen during the wintertime and then thawed in the summer [25, 87]. At sub-zero temperatures, ice crystals are continuously growing to form segregated reticulated ice fine-grained structure, which converts the dispersed MFT slurry layers to more face-to-face compact layers [25, 87]. With thawing, the MFT compact layers tend to agglomerate into irregular four-sided polygons, causing a significant reduction in the moisture content. Additionally, some researchers have suggested the use of concentrated sulfuric acid before the freeze-thaw cycle for more reduction in the moisture contents [25, 87]. Implementing freeze-thaw technology, as a natural process, is labor intensive and time-consuming process [25, 87]. In biological process, on the other hand, active species are planted and grown up on a high-water content area by photosynthesis [83–86]. Afterward, the natural plants tend to consume the water by the respiration processes through the leaves and roots, which leads to dewatering of the tailings. However, creating the suitable environments for the plants is not possible all the time [83–86]. In fact, this method highly depends on the local climate conditions, and plants cannot grow in high saline and sodic environments. In the case of the physical/mechanical processes (i.e., filtration and centrifuge treatment), the most traditional one is filtration, which has low environmental impacts. Furthermore, centrifuging of the MFT requires a small storage area to generate tailings with 60% solid contents [83–86]. Filtration and centrifugation, however, are costly physical separation methods. Thus, the chemical treatment has remained as

the most adapted technology to enhance the flocculation and consolidation of MFT. Commercially, traditional consolidated tailings (CT) followed by paste tailing processes are consequently practiced to enhance the consolidation and water recovery rates of the MFTs [83–86].

14.3.1 Composite Tailing (CT) Treatment

In CT, massive quantities of coagulant aids such as gypsum, lime, acids, and acid-lime combinations are extensively introduced to generate unstable and non-segregating deposits with less water contents [88–90]. Both lime and gypsum are the mostly applied coagulant aids in CT due to their great tendency in forming residual calcium ions. These ions strongly eliminates the organic layer presented on surfaces of the stable MFT clay particles [88–90]. This subsequently enhances the aggregation of the clay particles in the form of non-segregating tailing slurry [88–90]. However, the recovered water due to the presence of high residual concentrations of calcium and sulfate might negatively impact the oil recovery process and the environment [88–90]. In fact, the presence of residual amounts of calcium ions has a deleterious effect on the bitumen recovery process and imparts hardness to water [88–90]. While rich water with high amount of sulfate ions often undergoes anaerobic reduction, releasing harmful gasses such as H_2S, which is highly toxic to the environment and living organisms [88–90]. Here in Alberta, some local companies developed the CT by injecting $Ca(OH)_2$ together with CO_2 into the freshly produced tailings, which precipitate the dissolved $Ca(OH)_2$ as $CaCO_3$, which can be removed by a further thickening process. Such modification allows to form crystals of $CaCO_3$ that tend to uptake the fine particles presented in the MFT as sediments.

14.3.2 Paste Tailing Processes

Paste tailing is defined as tailings that have been significantly dewatered using polymeric flocculants to a point where they do not have a critical flow velocity when pumped, do not segregate as they deposit, and produce minimal (if any) [88–90]. Thus, the paste tailing process relies heavily on the flocculation performance of the applied commercial flocculants, such as the polyacrylamide-based polymeric flocculants (PAM)-based polymeric flocculants, to enhance the water solid separation in the MFTs [84–86, 91–94]. In the presence of polymeric flocculants, the destabilized particles presented in the MFT are flocculated into two main stages, namely, perikinetic (microscale) and orthokinetic (macroscale) flocculation [34]. The perikinetic flocculation occurred after destabilizing the molecules on the wastewater solution randomly or immediately during their Brownian motion via thermal agitation. This stage of flocculation can produce flocs that have poor or strong settling

characteristics [34]. Orthokinetic flocs, on the other hand, generate developed particles that can be promoted by mechanical agitation. The mechanical agitation (by Jar test) induces a velocity gradient in the liquid, improving the contact between the particles. The previously mentioned stages have a significant value in optimizing the flocculation/consolidation period upon selecting the proper conditions [34].

Unfortunately, PAM-induced floccules are loosely packed and settled slowly, since they are not able to reasonably flocculate the fine tailing particles [84–86, 91–94]. More precisely, the backbone of PAM contains amide groups, which contribute in generating strongly bonded gel-like polymeric networks that retain large volumes of water, with poorly consolidating sediments [91–93]. To alleviate these issues, many studies focused their efforts on structurally modifying the PAM to dewater MFT more effectively than the commercial PAM. These structurally modified PAM can potentially destabilize the solid particles presented in the MFTs by several mechanism as explained in the next section.

14.3.3 Destabilization Mechanisms

Fundamentally, stability of the solid particles presented in the MFTs is governed by the intermolecular force between the clay particles, electrical double layer among the charged particles, which is observed by the DLVO theory [34].

In the MFT colloidal suspension, counterions in addition to negatively charged clay particles are presented. The clay particles due to their negative charges tend to have intrinsic electrical repulsion force, which is responsible for existing of steric stabilization [34]. In principle, major fraction from the counterions tends to migrate and electrostatically neutralize the negatively charged clay particles [34], while minor fractions from the counterions diffuse away from the clay surface. Hence, an equilibrium distribution is established from both competing actions, in which the concentration of the counterions is gradually reduced with increasing the distance from the clay surface. The ionic distribution of the diffused counterions is referred as Gouy layer [34]. According to Gouy definition, two layers (double layer) can be presented in the clay suspension. The first layer is made from the positively charged counterions next to the clay surface "diffusion zone," and the second layer is formed from the negatively charged clay surface itself. The thickness of the diffusion layer (κ^{-1}) in Å can be calculated in by using the following expression [34]:

$$\kappa^{-1} = 10^{10}\left[\frac{(2)(1000)e^2 N_A I}{\varepsilon\varepsilon_o kT}\right]^{-1/2} \tag{14.20}$$

where 10^{10} is the length conversion $\left(\frac{\text{Å}}{\text{m}}\right)$, 1000 volume conversion (L/m^3) , e is the electron charge ($1.6022\times10^{-19}C$), N_A Avogadro's number (6.022×10^{22} /mol), I is the ionic strength, $\frac{1}{2}\sum Z^2 M\left(\frac{mole}{L}\right)$, Z is the magnitude of positive or negative charge on the ion, M is the molar concentration of cationic or anionic species *(mole/L)*, ε is

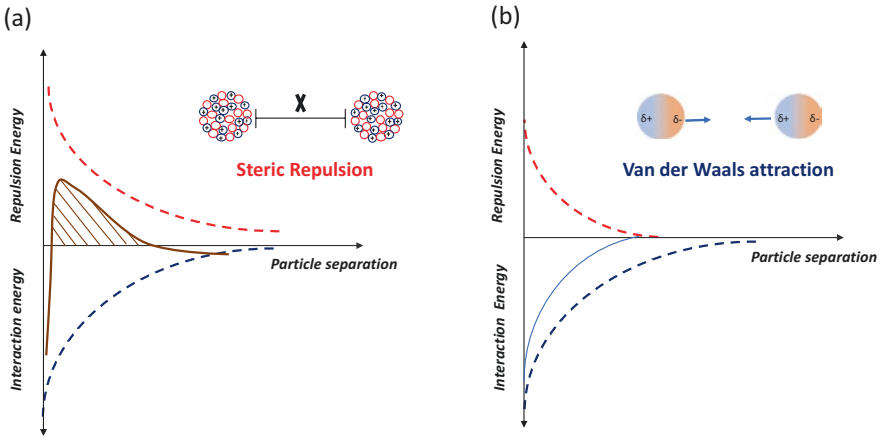

Fig. 14.6 Graphical representation of the stability mechanism according to DLVO theory with (**a**) and (**b**)without energy barrier. The graphical representation was drawn based on the concept available in reference [34]

the permissibility relative to vacuum ((*ε for water is* 78.54), ε_o is the permissibility in vacuum ($8.85\times\frac{10^{-12}C^2}{J.m}$), k is Boltzmann constant ($1.38\times10^{-23}J/K$), and T is the absolute temperature (K). Thickness of the formed double layer is strongly influenced by the physical properties of suspension, such as the temperature, bulk fluid concentration, and counterionic valence. For instance, at high ionic concentration and valance of counterions, counterions are diffused away from the Gouy's layer, resulting in double layer reduction [34]. However, Gouy's definition has limitations in accurately presenting the characteristic of the formed electrical double layer [34] . In fact, the ionic size and interaction between the clay surface, counterions, and medium are not accounted. Alternatively, Stern's theory came up with more practical model, such that it showed that the distance of the closest approach of a counterion to the charged surface is limited by the size of these ions [34]. Nevertheless, both Gouy's and Stern's theories cannot explain the stability of the solid particles presented in the tailings based on clay surface charged properties, interactions, and the balance between the repulsion and interaction forces in the suspension [34]. For better achieving of this, DLVO theory preciously describes the stability of the colloidal suspension by quantitatively consideration of (1) agglomeration and aggregation of the clay particles, (2) the force between charged particle interaction in the aqueous medium, and (3) the balance between the attractive van der Waals (vdW) force and the repulsive force caused by the overlap of electrical double layers surrounding the clay particles. In details, with using DLVO theory [65] (Derjaguin, Landua, Verwery, and Overbeek), the stability mechanism of the colloids can be quantitatively explained in terms of energy barrier. This energy barrier represents the difference between the repulsion and the attraction energy as presented in Fig. 14.6. The figure includes two possible cases with respect to the forces of repulsion. In the first case (Fig. 14.6a), the repulsion force is extended far in the

suspension, while in the second case (Fig. 14.6b), it was considerably decreased. In each figure, the net total energy is presented by the solid line [65].

For the first case, the net energy curve contains significant repulsion force that must be overcame when the particles are grouped together by van der Waals attraction, such that exceeding the energy barrier (the area under the solid line) by rupturing the net force that holds the particles far away from each other, which allows them to get attracted by van der Waals force [65]. In the second case, energy barrier exists to overcome, and the colloidal particles can be easily and rapidly flocculated by micro-flocculation. In the flocculation/consolidation process, the determination of the stability mechanism depends on the selected flocculant, its dosage, water/wastewater system solution, and mixing tools. Most importantly, the use of affordable and appropriate flocculant, depending on their action in destabilizing the colloidal particles, is consider the driving force for using flocculation/consolidation method in simultaneous removal of various polluting substances. Therefore, the use of vast categories of additives has been repeatedly reported, which fall into either hydrolyzing metal coagulants or polymeric flocculants [65].

Changing the ionic strength around the colloidal particles has significant effect on the stability mechanism. Double-layer compression, for instance, requires a reduction in the double layer around the colloidal particles, which causes changing on the ionic strength induced from addition of indifferent electrolyte, resulting in destabilizing of colloids under unstable conditions [65]. Consequently, colloids get close to each other with the presence of thin electric double layers. To more reduction of double layer, salts of counterion can be added, exceeding double layer repulsion that leads to coagulation of particles. However, this mechanism is industrially infeasible because it involves providing massive amounts of salts to achieve a practical destabilization of the particles [65]. Therefore, double-layer compression using salts was replaced by a destabilizing method of charge neutralization. Charge neutralization is often carried out by adsorbing the hydrolyzed metals or polymeric species on the clay surface [65].

Furthermore, high dosage of charge-neutralizing coagulants may lead to fast aggregation of the solids presenting on the colloidal suspension [65]. Interparticle bridging [65], other mechanism, can be achieved by chemical bonding or physical attachment of water-soluble polymer to the particle surface. In this mechanism, very small part of the polymer can adhere to the particle surface, while the bulk groups of the polymer chain cannot. These chains extend toward the solution, helping in adherence of the neighbor particles, forming bridged particles [65]. Then, the bridged particles during mixing are able to interact effectively with each other to form and develop flocs that are destabilized as a next step to induce aggregation and settling of large agglomerates. With the use of various cationic PAM-based copolymer, charge neutralization and interparticle bridging are considered as the most popular mechanisms responsible for enhancing the settling and dewatering of MFT. The aforementioned cationic PAM-based copolymers have been synthesized by bonding organic or inorganic agents to the PAM chain by grafting or copolymerization, in order to create organic-inorganic hydride flocculant, thermosensitive polymeric flocculants, and cationic copolymers with hydrophobic moieties [84–86, 91–94].

14.3.4 Flocculation Behavior with Inorganic-Organic PAM-Based Hybrid Copolymers

The enhancement of the flocculation efficiency of many polymeric flocculants was traditionally achieved by mixing them with inorganic microparticles [95–98]. However, controlling the dispersion of the microparticles in the presence of organic flocculants limited their applications [95–98]. To avoid such technical issue, many reviewers proposed combining inorganic agents (i.e., hydroxides of aluminum, calcium, magnesium, and iron) to the organic structure of PAM allowing to form inorganic-organic hydride copolymeric flocculants (Table 14.4) [95–98]. The studies listed in Table 14.4 show great potential of the organic-inorganic hybrid flocculants, in comparison with the commercial PAM, toward enhancing settling and consolidation of solid particles presented in MFT (study number 1) and kaolinite suspensions (studies number 2–4), via bridging and charge neutralization mechanisms [95]. Al-PAM, for instance, allowed to densify and destabilize the diluted MFT suspension through two stage processes: flocculation/sedimentation and filtration to reduce the dewatering time, indicating that the presence of positively charged $Al(OH)_3$ particles created strong affinity between aluminum and oxygen was responsible for Al-O linkage, which led to the adsorption of $Al(OH)_3$ on the silica surface [95]. Although applying both stages showed shortening in the filtration time of the diluted MFT sample (10–30 wt.% solid) from 25 min to 10, such process required high dosages of Al-PAM and generates a filtration cake with high moisture content (>23wt.%) [95]. The formed cake will require another separation process to recover the trapped moisture, adding extra cost for the process. The other studies reported the synthesis of other hybrid flocculants that depend on complex free-radical polymerization that is carried out under well-controlled temperature and drying conditions. The flocculation/consolidation performance of these inorganic-organic flocculants has been only investigated with kaolinite suspension not a real MFT. In fact, the optimal operating condition with the use of kaolinite suspension was reported between pH 2 and 2.5, which cannot be achieved with the real MFT suspension that has pH value around 9.

14.3.5 Flocculation Behavior with Stimuli-Responsive Polymers

In the last 10 years, using of stimuli-responsive polymeric flocculants to accelerate settling and consolidation rates has gained great attention by some authors. The stimuli-responsive polymers are defined as polymers that are able to change their conformation and solubility under certain conditions (i.e., temperature, pH, electromagnetic field, and ionic strength) [91, 99]. Among them, thermo-responsive polymers have been extensively utilized as flocculants for faster solid-liquid separation. Poly(N-isopropylacrylamide) (PolyNIPAm) has been reported as the most

Table 14.4 Most recent inorganic-organic hybrid flocculants used to enhance settling and dewatering of MFT and kaolinite suspension

Number	Title	Materials and methods	Main results	References
1	Al-PAM assisted filtration system for abatement of mature fine tailings	Al-PAM was synthesized in-house by polymerization of acrylamide monomer in an aluminum hydroxide colloidal suspension with $(NH_4)2S_2O_8/NaHSO_3$ as initiator at 40 °C. Al-PAMs of different molecular weights and aluminum contents were used. The Al-PAM of intrinsic viscosity of 750 cm/g, equivalent to an average molecular weight of two million Daltons, was identified to perform the best. In the current study, this selected Al-PAM was used exclusively to flocculate MFT after proper dilution from 30 wt.% to 10 wt.% solid.	Effective flocculation of ultrafine particles was confirmed by lower turbidity of supernatant after settling of diluted MFT with Al-PAM addition. When MFT diluted to 10 wt.% solids was filtered with 75 ppm Al-PAM addition, a filtration cake of 23 wt.% moisture content was produced after 25 min of filtration. To shorten the filtration time, a two-stage dewatering process was introduced: flocculation and thickening of diluted MFT, followed by filtration of sediments. With such an approach, filtration time could be further shortened considerably from 25 min to 10 min to produce a filter cake of 23 wt% moisture.	[80]
2	A novel flocculant of $Al(OH)_3$–polyacrylamide ionic hybrid	The hybrid $Al(OH)_3$–polyacrylamide (HAPAM) has been synthesized using a redox initiation system ($(NH_4)_2S_2O_8$–$NaHSO_3$) at 40 °C in aqueous medium. The flocculation behavior for 0.25 wt.% kaolin suspension was evaluated by spectrophotometry and phase contrast microscopy.	It was found that an ionic bond exists between $Al(OH)_3$ colloid and polyacrylamide (PAM) chains in the HAPAM and the flocculation efficiency of HAPAM is much better than that of commercial polyacrylamide (PAM) and PAM/$AlCl_3$ blend. The synergism between $Al(OH_{)3}$ and PAM in ionic HAPAM exists in the kaolin flocculating process. It can be attributed to electrostatic interaction between the positive $Al(OH)_3$ core and the negative particle of kaolin as well as the adsorption-bridging effect of polyacrylamide chains in the HAPAM.	[81]

(continued)

Table 14.4 (continued)

Number	Title	Materials and methods	Main results	References
3	Polyacrylamide-based inorganic hybrid flocculants with self-degradable property	Inorganic-organic hybrid flocculant was produced from inorganic soil-TiO_2-PAM hybrid materials by coating of titanium dioxide (TiO_2) nanoparticles on the surface of inorganic soils and subsequent polymerization of acrylamide (AM) on these nanoparticles under visible light. Inorganic soils including kaolin, bentonite, montmorillonite, and diatomaceous earth were used to control the volume and to reduce the cost, and the TiO_2 nanoparticles accelerated PAM degradation. To further investigate the flocculation performance of kaolinTiO_2-PAM hybrid materials, we prepared a 5 g/L kaolin suspension as the wastewater model with 1 ml, 2 ml and 4 ml of 5 g/L kaolin suspensions, respectively. Another 5 g/L kaolin suspension was used as the blank control. The solutions were stirred identically (i.e., in a "jar test" apparatus) at 150 rpm for 30 s and 60 rpm for 5 min, followed by 15 min of settling.	This hybrid material holds great promise in dewatering technologies and environmental protection for the reserves of oil sand. In the first 5 min, flocculation was obvious due to the adsorption and bridging effect of PAM, as evidenced by floccules at the bottom. With extended time, the transmittance increased gradually, indicating that the content gradually became clear. When 2 ml flocculant was added, the flocculating effect reached optimum. Excess flocculant affected the transmittance of the solution. Compared to traditional PAM-based hybrid flocculantskaolin-TiO_2-PAM hybrid material allowed "degradation by itself".	[82]
4	Flocculation of kaolin in water using novel calcium chloride-polyacrylamide ($CaCl_2$-PAM) hybrid polymer	A novel calcium chloride-polyacrylamide hybrid polymer has been synthesized by a redox initiation system by using $(NH_4)_2S_2O_8$ and $NaHSO_3$ to initiate free-radical solution polymerization of one molar acrylamide solution at 50 °C. One mole of calcium chloride was blended with polymerized acrylamide solution to synthesis a novel inorganic–organic composite polymer ($CaCl_2$-PAM hybrid polymer). Flocculation performance of kaolinite suspension was tested at various dosage and pH.	The kaolin suspension flocculation was found to be pH and dosage dependent. Response surface methodology was done using central composite design and showed that the $CaCl_2$-PAM hybrid polymer was able to reduce >98.0% of turbidity. The optimal operating condition was reported between pH 2 and 2.5 and dosage between 2 and 3 mg/L.	[83]

commonly applied thermosensitive polymeric flocculant [91, 99]. This polymer can be adsorbed on the surface of the clay particles by hydrogen bonding at temperature below the lower critical solution temperature (LCST) that is about 32 °C [91, 99]. With enhancing temperature above the LCST, significant phase transition can occur, at which the coil size is reduced by one third of the original size, leading to convert the polymer from hydrophilic to hydrophobic [91, 99]. The hydrophobic interaction is essentially controlled by the isopropyl groups that tend to be limited with formation of intra-chain interactions below the LCST [91, 99]. Thus, primary aggregation step is carried out by heating the wastewater thermosensitive polymer suspension above LCST, and once the big flocs are formed, the sediments are cooled down by secondary consolidation step, so the polymer becomes hydrophilic again and detaches from the particles; thus, the small particles can fill the gap between flocs to further enhance the consolidation [91, 99]. However, the thermosensitive polymer of PolyNIPAm is non-ionic and cannot neutralize the negatively charged clay particles, which limits its application in flocculation of fine clay particles. Thus, many researchers have done many attempts on introducing cationic groups with hydrophobic moiety to polyNIPAm in order to achieve higher flocculation ability [91, 99]. Table 14.5 displays some recent studies focused on applying diverse thermosensitive copolymers that are synthesized by copolymerization of N-isopropylacrylamide (NIPAm) with some hydrophobic moieties such as 2-aminoethyl methacrylamide hydrochloride (AEMA), 5-methacrylamido-1,2-benzoboroxole (MAAmBo), 2-aminoethyl methacrylamide hydrochloride, and poly(acrylamidest-diallyldimethylammonium chloride) (poly(AAm-st-DADMAC)), to create thermosensitive copolymers that are able to effectively flocculate and consolidate the fine solid in kaolinite suspension [91, 99]. As shown, significant enhancement in settling and dewatering has been achieved by flocculating the MFT and kaolinite suspensions with application of these thermosensitive copolymers in comparison with commercial anionic PAM. However, using thermosensitive polymers for large-scale application as flocculant for MFT has some downsides, related to the energy needed to heat up the slurry above the LCST and utilizing excess dosage of polymers to ensure good coverage of particle surfaces to induce aggregation above LCST [91, 99].

14.3.6 Flocculation Behavior with Hydrophobically Modified Polymeric Flocculants

Copolymerization of acrylamide (AC) with other hydrophobic monomers such as polypropylene oxide (PPO), hyperbranched functional polyethylene (HB*f*PE), and diallyl dimethylammonium (DADMAC) is one of the most commonly used approaches to enhance the dewaterability of the MFT aggregates (Table 14.6) [83, 92, 100]. In all the cases displayed in Table 14.6, the copolymer composition and average molecular weight were the most important factors affecting the settling and dewatering performance of MFT [83, 92, 100].

Table 14.5 Most recent studies that have used thermosensitive copolymers in enhancing settling and consolidation of kaolinite suspension and MFT [76, 84]

Number	Title	Materials and methods	Main results	References
1	Temperature- and pH-responsive benzoboroxole-based polymers for flocculation and enhanced dewatering of fine particle suspensions	Random copolymers based on N-isopropylacrylamide (NIPAAm) containing 2-aminoethyl methacrylamide hydrochloride (AEMA) and 5-methacrylamido-1,2-benzoboroxole (MAAmBo) were synthesized by conventional free-radical polymerization at70 °C in oil bath. The polymerization was carried out in the inert atmosphere for 24 h. The polymers were purified by dialysis against double distilled deionized water for 4 days. The fine kaolinite suspension flocculation performance was evaluated in solid–liquid separation at various pH and temperatures.	The strong interactions between benzoboroxole residues and kaolin hydroxyl groups were evaluated for the first time in the flocculation of fine particle suspensions. The lower critical solution temperatures (LCSTs) of PAMN decrease because of the hydrophobic nature of the benzoboroxole moieties, resulting in strong hydrophobic interaction at temperatures higher than the LCSTs. Temperature- and pH-responsive polymer, P(AEMA51-st-MAAmBo76-st-NIPAM381) (denoted as PAMN) shows the ability to induce fastest settling at a low dosage of 25 ppm and under the condition of pH 9 and 50 °C. The accelerated settling rate is considered to be due to the strong adhesion of benzoboroxole residues to the kaolin hydroxyl groups, the electrical double layer force, and the hydrophobic force. During condensation phase, increasing the pH of sediment to pH 11 could attain the most compact sediments.	[84]

2	Flocculation and dewatering of mature fine tailings using temperature-responsive cationic polymers	Temperature-responsive copolymer with cationic charge was prepared with N-isopropylacrylamide (NIPAm) and 2-aminoethyl methacrylamide hydrochloride (AEMA) by conventional free-radical polymerization. The flocculation performance of the copolymer, poly(AEMA-st-NIPAm), was compared to five different mixture ratios of polyNIPAm and cationic poly(acrylamidest-diallyldimethylammonium chloride) (poly(AAm-st-DADMAC)). The effects of polymer mixture ratios, polymer dosages, and temperature on solid–liquid separation as a function of initial settling rates (ISR), supernatant turbidity, sediment solid content, and water recovery were investigated.	Poly(NIPAm) can facilitate particle aggregation by bridging and hydrogen bonding under lower critical solution temperature (LCST), whereas at temperature above LCST, the adsorption of poly(NIPAm) chains on particles can be enhanced by hydrophobic interaction. A two-step (25 °C → 50 °C → 25 °C) consolidation can further enhance the sediment solid content by polyNIPAm. The neutral property of polyNIPAm resulted in high turbidity of supernatant, mixing with poly(AAm-stDADMAC) increases the clarity of supernatant by neutralization of fine particles. The copolymer poly(AEMA-st-NIPAm) functions as a polyelectrolyte to enhance the polymer adsorption onto particles via electrostatic interactions, thus further improving ISR and supernatant clarity.	[76]

Table 14.6 Most recent studied focused on synthesis of hydrophobically modified polymers and their applications in enhancing settling and dewatering of MFT [68, 77, 85]

Number	Title	Materials and methods	Main results	References
1	Using acrylamide/propylene oxide copolymers to dewater and densify mature fine tailings	Acrylamide (AC) was copolymerized by micellar polymerization with different amounts of polypropylene oxide macromonomers (PPO) to produce PAM-PPO graft copolymers with different hydrophobicities and molecular weights at 65 °C. Flocculation and dewatering performance was evaluated by determination of initial settling rate (ISR), turbidity, capillary suction time (CST), and solids content after centrifugation of mature fine tailings.	The PAM-PPO copolymers dewatered and densified MFT more efficiently than a reference commercial anionic PAM supposedly because the PPO hydrophobic groups reduced the amount of water trapped inside the polymer floccules. The PAM-PPO copolymers had molecular weights ten times smaller than the reference anionic PAM flocculant, which reduced their viscosities and shear sensitivities. As a result, it is easier to mix these copolymers with tailings under a wider window of operating conditions. The aged MFT (stored for approximately 10 months) were more easily dewatered, especially at high solids content (20 wt.%).	[77]
2	Flocculation of oil sands tailings by hyperbranched functionalized polyethylenes (HB*f*PE)	A series of hyperbranched functional polyethylene (HB*f*PE) flocculants with functional group contents ranging from 30 to 50 mol% were synthesized at 35 °C. The synthesized copolymers were used to flocculate oil sands mature fine tailings diluted to a concentration of 20 wt.%.	MFTs (diluted to a concentration of 20 wt.%) treated with the novel HB*f*PE had higher settling rates, lower capillary suction time (CST), and lower turbidity than when treated with a reference polyacrylamide (PAM). Within the HB*f*PE series, the settling performance improved when the functional group content in the copolymer increased. When combined with centrifugation, the HB*f*PE flocculants generated sediments with higher solid contents than PAM within a shorter centrifugation time.	[85]

Copolymerizing different average molecular weights of AC and PPO (poly(AAm)-g-PPO) significantly influenced the flocculation of the MFT [83, 92, 100]. At low solid content MFT (2 wt.% solids), the flocculation performance of poly(AAm)-g-PPO was not similar to the anionic polyacrylamide (A-PAM) as indicated from the obtained values of ISR and CST [83, 92, 100]. In fact, the used dosages for the copolymer were much lower than that for the commercial PAM (optimum performance achieved at about 2000 ppm for A-PAM versus 10 000 ppm for poly(AAm)-gPPO) [83, 92, 100]. The reason behind this referred to the large average molecular weight of the A-PAM (around 17 million Daltons) compared with that of poly(AAm)-gPPO). It has been also obtained that the addition of calcium prior to flocculation with A-poly(AAm) may help in reducing the PAM dosage, since it increased the degree of pre-aggregation of the suspended solids [83, 92, 100].

At high solid content MFT (20 wt.%), on the other hand, the authors observed that poly(AAm)-g-PPO gave much better dewatering than A-PAM at their respective optimum dosages, as indicated by about ten times difference in the CST values measured after flocculation [83, 92, 100]. The authors have claimed that the reason for this was due to the presence of more hydrophobic segments in the in poly(AAm)-g-PPO in comparison with A-PAM, not to the molecular weight difference [92]. To verify this, the author compared the flocculation performance of equal molecular weights of neutral PAM (N-PAM) and poly(AAm)-g-PPO, and the results have proven that the copolymer could still dewater MFT much better than the neutral poly(AAm) (CST of about 40 s versus CST of about 400 s) [92]. Likewise, flocculating low solid contents MFT (5 wt.% solid) with A-PAM led to much higher ISR compared to that of hyperbranched functional polyethylene (HBfPE) flocculants, but the HB*f*PE outperformed when it was flocculated with 20 wt.% solids [92]. These results were attributed to the extremely larger molecular weight of the A-PAM (100 times higher than HBfPE) [100]. The authors have hypothesized that the high molecular weight plays limited role in flocculation performance when the distance between the solid particles presented in the MFT are shorter at high solid content [100]. These results are not in agreement with that obtained by using poly(acrylamide-codiallyldimethylammonium chloride) poly(AAm-co-DADMAC). In fact, the average molecular weight does not play a considerable role (within the relatively wide range examined from 90 to 1450 kg mol−1[83], it is conceivable that it will become a factor for much lower molecular weights) in determining the performance of the copolymer based on the CST and SRF analyses [83]. The authors showed that the cationic copolymeric composition statistically influenced the settling and dewaterability performance, such that the flocculation and dewatering performance was better in the presence of more cationic segments, suggesting that charge neutralization is the dominant mechanism in dewatering MFT [83]. It has been also reported from the same study that addition of more AC to the system of AAm-co-DADMAC enhanced the rate polymerization. However, presence of more AC lowered the dewatering performance of the copolymer. Therefore, presence of low mass fraction of AC might save some polymer for dewatering MFTs but sacrifices kinetics of the polymerization reaction, and polymerizations at lower rates are, in general, economically less favorable than at higher rates.

According to that, the flocculation/consolidation performance is highly influenced by the molecular weight of the hydrophobically modified polymeric flocculant, such that better dewatering performance can be achieved by the polymeric flocculants grafted with more segments of hydrophobic agents (i.e., high molecular weight) for the MFT samples with high solid contents. However, in industrial applications when dealing with thick MFTs (i.e., 30 wt. % solids), there should be a desired range of polymer molecular weights.

14.3.7 Emerging Techniques for Treatment of Tailings

In addition to their high stability, MFTs might contain plenty of toxic and nonbiodegradable organic compounds that cannot be discharged to the environment such as naphthenic acids (NAs) [65, 101]. Thus, some emerging technologies have been recently proposed to remove the highly toxic NA compounds and enhance the settling and dewaterability of the MFTs. Nafie et al. (2017), for instance, have reported using β-Cyclodextrin-grafted nanopyroxene as eco-friendly platform for selective removal of NAs [101]. Nafie et al. (2018) also have suggested using oxy-cracking technique to destabilize the solid particles presented in the MFTs in order to enhance their flocculation consolidation behavior without applying any polymeric flocculants [65].

14.3.7.1 Oxy-Cracking Technique for Settling and Dewaterability of Oil Sands Mature Fine Tailings (MFT)

With employment of the oxy-cracking technique, the solid particles presented in the MFTs can be destabilized without adding polymeric flocculants by simultaneous oxidation and cracking reactions at which the residual bitumen presented on the MFT particles are cracked and solubilized in the liquid phase. This subsequently allowed for agglomeration and fast settling of the solid particles presented in the MFT, as schematically described in Fig. 14.7. The oxy-cracking procedure was experimentally done by placing well-mixed MFT sample inside one Parr reactor along with a strong basic material (i.e., KOH), which acts as a solubilizing agent [65]. The strong alkaline material is added to the mixture to ensure that the oxy-cracked products are completely solubilized in the aqueous phases and not converted to CO_2. After that, the Parr reactor was tightly closed, allowing to the oxy-cracking reaction to carry out under the flow of oxygen at temperature range of 423–498 K and pressure of 1000 psi over time ranging from 0.25 to 2h [65]. After completion of the reaction, the reactor is opened to release the excess of oxygen and undesirable product (i.e., CO_2) [65]. Then, the oxy-cracked product was directly transferred to a graduated cylinder to record the initial settling rates (ISRs) and

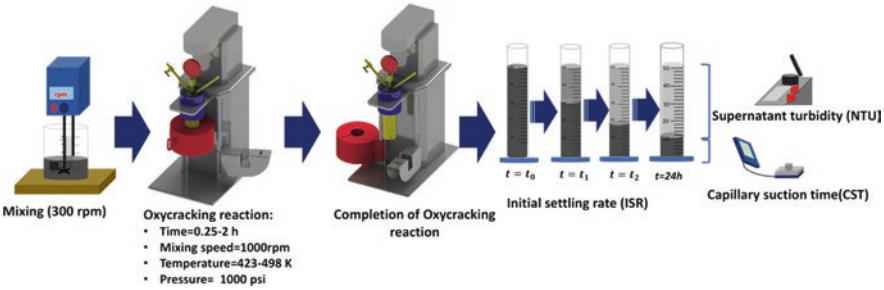

Fig. 14.7 Schematic representation for oxy-cracking of the diluted sample of MFT and testing its initial settling rate (ISR), supernatant turbidity, and capillary suction time (CST)

capillary suction times (CSTs) at different time interval [65]. The mechanism at which the oxy-cracking reaction was carried out for of the stable particle existed in MFT can be described by using a complex model [65]. In such model, the hydrocarbon species presented on MFT fine particles were initially decomposed in the presence of the free ·OH radicals into a variety of oxygenated intermediates, which tend to be cracked into different group of organic compounds, such as carboxylic and phenolic acids. Some of those intermediates were further oxidized to form carbonate or emitted as CO_2 in the gas phase [65]. Thus, the oxy-cracking reaction is able to break down these hydrocarbons and increase their solubility in the water phase, and thereby they detach from the fine solids. The fine solids will then agglomerate and settle faster [65]. The results showed that the mudline was diminished by 65% over 24 h for all the MFT samples after oxy-cracking in comparison with the non-oxy-cracked MFT. On the other hand, the consolidation (CSTs) tests arose fast and easy dewatering for the oxy-cracked MFT samples [65]. Furthermore, it has been obtained that both the temperature and residence time had no significant effect on settling rate. According to the CST measurements, it was also found that oxy-cracked MFT sample at 423 K, compared with the other samples, was easier to dewatered [65]. Although the oxy-cracking technique is an effective process for enhanced particle settling in oil sands tailings, it is not practical for massive quantity of MFT and non-economically feasible. In fact, oxy-cracking of great quantity of MFT requires larger size Parr reactor or running the reaction for longer time, which elevates the capital and operational costs. In addition, weak monitoring of the oxy-cracking reaction might cause releasing of extra amount of CO_2 that is harmful to the environment.

14.3.7.2 Using β-Cyclodextrin-Grafted Nanopyroxene for Naphthenic Acids (NAs) Removal

In the removal of NAs, β-cyclodextrin-grafted nanopyroxene has been used, combining the multifunctionality of B-cyclodextrins (BDN) and superficial ion exchange property of the nanopyroxene [102]. β-Cyclodextrin consists of hydrocarbon chains branched with large numbers of primary and secondary hydroxyl groups, creating lipophilic cavities [102]. Due to their biocompatibility and high affinity toward adsorbing several macromolecules, β-cyclodextrin has been commonly used to for wastewater treatment fields [102]. Thus, successful grafting of β-cyclodextrin on the surface of nanopyroxene allowed to create a novel adsorbent with excellent characteristics, which have a strong ability to capture complex organic pollutants, such as NAs. However, the nanopyroxene, without primarily functionalizing it with a dual affinity agent, cannot be grafted by the β-cyclodextrin [101, 103]. Thus, the nanoparticle surface was firstly coated with an organic-inorganic hybrid bridge of 3-glycidyloxypropyl trimethoxysilane (TG3), as shown in Fig. 14.8. In fact, the TG3, in the presence of toluene, is covalently bonded to the surface of the nanopyroxene by creating methoxy oxygenated sites [101, 103]. As a second step, the hydroxyls on the surface of BDN are activated by dissolving the dried monomer in an organic solvent of N,N-dimethylformamide (DMF) in the presence of a basic catalyst of sodium hydride, and then the mixture is dried, and its slurry product is added to a reflux system [102]. The slurry product in addition to the previously prepared solution of nanoparticles is mixed together for two hours at high temperature (i.e., 423 K). Such conditions allow for opening the epoxy ring for the

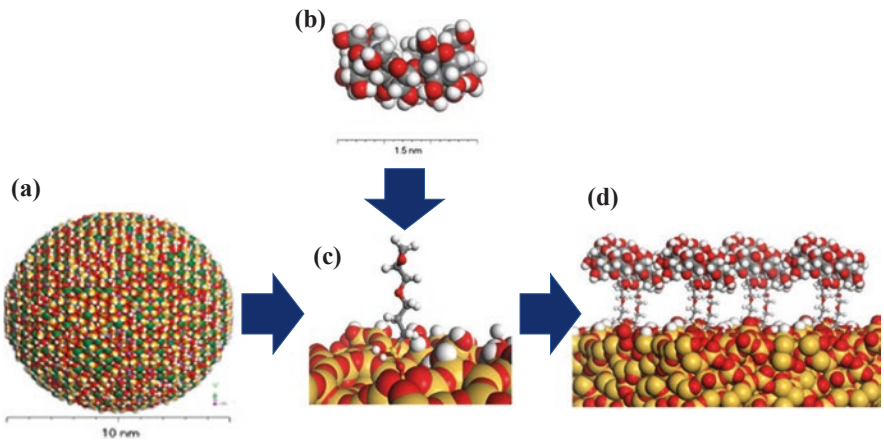

Fig. 14.8 CPK representation for the (**a**)10 nm of nanopyroxene (PNPs), (**b**) side view of β-cyclodextrin (BCN) molecule, (**c**) 45 ° perspective view presenting the primary coating PNPs with 3-glycidyloxypropyl tri-methoxy-silane (TG3), and (**d**) side view for the grafted nanoparticles of PNPs with BCN (PNPs-BCN) interacted with two hydrolyzed TG3 molecules. Red atoms represent oxygen, gray atoms represent carbon, white atoms represent hydrogen, and yellow atoms represent silicon [101]. Permissions related to the material excerpted were obtained from the American Chemical Society (ACS) and further permission should be directed to ACS

interaction by nucleophilic substitution with the activated O^- from the hydroxyls presented on the monomer [102]. The cavities presented on the structure BDN allows the accommodation of large and complex organic molecules such as naphthenic acids via adsorption [101]. These cavities are generated due to the distribution of the oriented units of the glucose molecules that is in the form of circular cones on the structure of BDN [101]. These trapping cones on the BDN are composed of seven methyl alcohol groups that are held together in a unique structure by intermolecular forces other than those of full covenant bonds (host-guest interaction) [102]. The results have shown successful adsorption of NAs on the grafted nanoparticles after performing batch adsorption test for synthetic wastewater containing NAs. Nevertheless, these types of grafted nanoparticles are not easy to prepare and required following complex procedure which depends on sever conditions.

14.4 Oil Spill Removal

The oil spills, without an effective removal method, showed adverse impacts to ecosystems and the long-term effects of environmental pollution that calls for an urgent need to develop a wide range of materials for cleaning up oil from oil-impacted areas [104, 105]. Additionally, the oil spills generate oil-water emulsions with produced water, hampering their treatment and disposal processes through physical separation, chemical processes, or biological degradation [104, 106]. Thus, a wide range of materials for oil spill removal has been successfully implemented including dispersants, absorbents, solidifiers, booms, and skimmers [105–108]. Recently, many scientists argue that applying most of these materials for oil remediation can be toxic—some at least as toxic as dishwashing liquid—and could be more harmful to the environment than the oil itself [104]. Also, there is potential for dispersants to bioaccumulate in seafood. Alternatively, many less harmful porous absorbents with some attractive characteristics (i.e., hydrophobicity or oleophilicity and high uptake capacity) have been used due to their high performance toward removal of the oil spill at high capacity and the possibility of recovery from the oil spill site [108]. Adding these porous sorbents facilitates a change from liquid to semisolid phase, and once this change is achieved, the removal of the oil, by removal of the absorbent structure, then becomes much easier. Also, many porous materials can, in some cases, be regenerated [109]. However, these materials have limited recyclability, due to the need for an effective oil/water separation process after each sorption step. The sorbed oil also requires mechanical handling, filtration, or high-rate centrifugation procedures that cannot be obtained under continuous operations. Traditionally, the oil/water separation occurred following standards like ASTM F716 and ASTM F726 [110]. These standards have shown inaccurate gravimetric measurements for the removed oil. Accordingly, applying these standards is inappropriate in describing the phenomena responsible for oil spill removal [111]. Recently, nanoparticle technology appeared to provide a practical and interesting alternative. As sorbents, nanoparticles have some unique properties, such as large

specific surface area per unit volume, high and fast equilibrium uptake, and great dispersibility for in situ treatment [112]. These properties have attracted many researchers to study their potential in the removal of oil spills via magnetite nanoparticles. Magnetite nanoparticles are economically favorable and easy to use as adsorbents in large-scale application. Also, they allow easy separation and recovery by applying an external magnetic field [8]. For the purpose of magnetic separation, magnetic nanoparticles can be synthesized into two forms: direct sorbent or in form of nanocomposite feature. Direct sorbent is formed when the magnetic nanomaterial occupies the whole structure of every single part of the nanoparticle [113]. Nanocomposite structure, on the other hand, is obtained when the magnetite is presented in nanoscale within the structure of the material to provide the desired function for the nanoparticles [103, 109].

14.4.1 Modified ASTM Protocol for Oil Removal Quantification

Under well-controlled conditions, the modified protocol for ASTM standard for oil spill absorption performance can be employed as shown in Fig. 4.9. The protocol allows for gravimetric evaluation of oil spills, which interact with the magnetic nanoparticles, without the employment of filtration or any other physical separation. Before testing the oil removal performance, a noncontact experiment should be initially performed to eliminate the real effect of the particle dispersion and their response toward the magnetic separation. During the experiment, a pre-weighted oil spill is simulated into a 500-mL beaker filled with deionized water at room temperature (Fig. 14.9a). After that, a certain amount of magnetic nanomaterial is added and distributed evenly on the oil under magnetic stirring for 2 min. Then, magnetic separation is used to withdraw the oil spill by placing a magnet 2 mm away from the water surface. Oil spill uptake is estimated by calculating the difference between the weight of simulated and magnetically separated oil spills (Fig. 14.9b-d). If there was a significant effect on self-magnetism of the particles, it should be subtracted from the uptaken oil spill.

14.4.2 Magnetic Oil Sorbent-based Nanoparticles

Due to the lack of stability, the naked iron oxide nanoparticles are either easily oxidized in air or tend to aggregate under aqueous conditions, which limits their application in remediation of oil spills. Thus, protection or functionalization procedures during or after the synthesis have recently been performed to apply the iron oxide nanoparticles more wisely [114–120]. These methods include coating or functionalization with organic or inorganic chemical agents, embedding the iron oxide

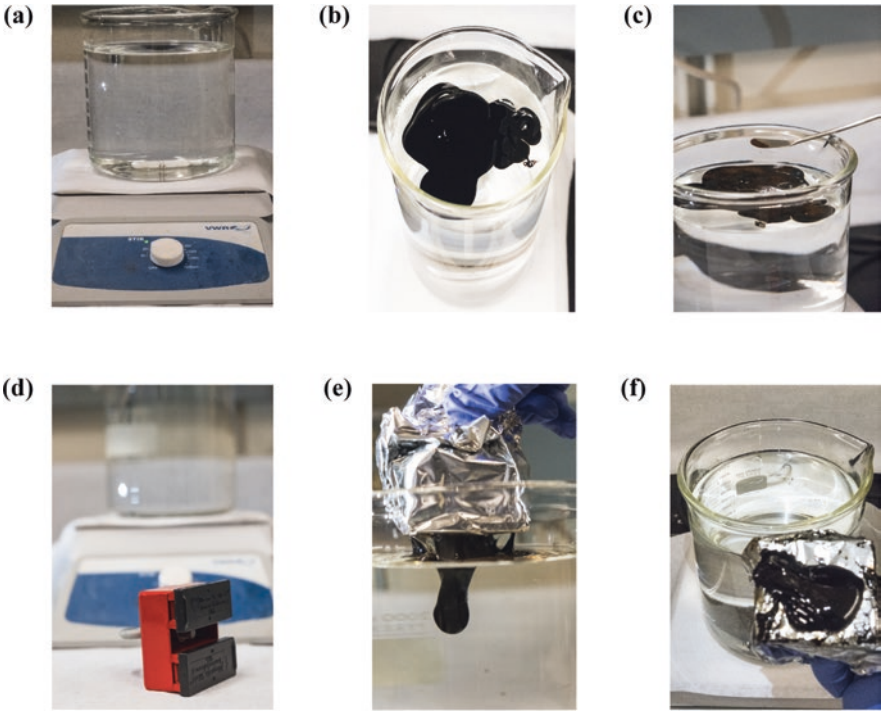

Fig. 14.9 Oil sorption test using a magnet, modification to ASTM F726-12. Photographs taken by the first author of this chapter

nanoparticles in polymer composites, and combining the iron oxide nanoparticles with activated carbon by physical and chemical methods [114–120]. Table 14.7 illustrates the most recent magnetic sorbents used for oil removal in addition to their functional materials, synthesis method, application, and their maximum oil uptake [114–120]. The table presents many magnetic oil sorbents that have been synthesized by combining the magnetic sorbents with organic compounds, macromolecules, biomolecules, polymers, inorganic materials, and activated carbon. These magnetic oil sorbents are characterized by having some favorable properties, including high sorption uptake, high hydrophobicity, high unsinkable properties to contact with oil (low density are easier to collect after sorption), ferromagnetism, and reusability [114–120]. The table shows that the magnetic structure of these magnetic sorbents mainly consists of iron oxide, which can be directly added in forms of powder or synthesized by several methods [114–120]. As shown from the table, the iron oxide has been directly added to the hydrothermally treated melamine di-borate (M_2B) to obtain magnetic hexagonal boron nitride [119]. On the other hand, the iron oxide can be synthesized by co-precipitation method, thermal decomposition, hydrothermal synthesis, and microemulsion. In co-precipitation, a chemical reaction is carried out between Fe^{3+} and Fe^{2+} salts in a highly basic solution and the absence of oxygen [68, 114–120]. For surface functionalization or coating, the

Table 14.7 Recently reported magnetic sorbents used for synthetic and real oil spill removal along with their synthesis methods, application, and maximum uptakes [99–105]

Number	Magnetic sorbents	Synthesis method	Application	Maximum oil removal	References
1	Magnetite functionalized with oleic acid	• The surfactant of oleic acid was used to modify ferrite nanoparticles by chemical precipitation • The -COOH groups of oleic acid have a high affinity with the Fe atoms of iron oxide	Crude oil	95 wt.%	[99]
2	Quaternized chitosan-coated magnetite	• Chitosan-coated iron oxide nanoparticles produced by grafting chitosan onto Fe_3O_4 coated with silica and 3-aminopropyltriethoxysilane (APTES)	Diesel-in-water emulsion	90 wt.%	[100]
4	Functionalized styrene (St) and sodium dodecyl sulfonate (SDS) with magnetite	• Synthesis was done by a two-step procedure • Magnetic Fe_3O_4 was prepared, and then, the silanization of Fe_3O_4 was performed by adding sodium dodecyl benzene sulfonate (SDBS) or sodium dodecyl sulfonate (SDS) followed by grafting of styrene	Diesel oil/lubricating oil	3g/g	[101]
5	Magnetic carbon nanotube sponges	• Fabrication was done by using ferrocene and dichlorobenzene as precursors by chemical vapor deposition	Diesel oil and gasoline	56 g/g	[102]

7	Magnetic coconut/palm shell-based carbon	• The sorbent prepared by pyrolyzing coconut shells. Then, activated carbon/Fe_3O_4 composites were obtained by in situ coprecipitation • An ammonia solution was added to the solution containing Fe^{3+}, Fe^{2+}, and activated carbon, and the mixture was heated to facilitate the binding of iron oxide nanoparticles to surface functionalities of the activated carbon	Premium oil	9.33 g/g	[103]
6	Hexagonal Magnetic boron nitride	• Magnetic boron nitride (MBN) by adding a stoichiometric ratio of 2:1 boric acid/melamine, melamine diborate (M_2B) precursor of boron nitride together with and powdered steel filings in proportion of 5% by mass. Precipitation of M_2B on the surface of the suspended steel filing particles. It is suggested that the use of a smaller volume of water and abrupt quenching are responsible for accelerating the precipitation of the precursor of boron nitride and facilitating the gathering of the iron particles from the steel filing within the M_2B.	Crude oil	53 g/g	[104]
7	Yeast-based magnetic bio-nanocomposite	Yeast-based magnetic bio-nanocomposite (Y-MG) can be prepared by mixing the yeast biomass with a heated suspension of magnetite nanoparticles that can be formed by the classical co-precipitation method under acidic conditions.	Of motor oil (NMO), mixed used motor oil (MUMO) and petroleum 28 °API (P28API)	3.5 gNmO/g, 0.2 gMUMO/g, and 2.8gP28API/g	[105]

coprecipitation method has been developed by adding functional materials or surface-active agents in the reaction media to reduce the aggregation and oxidation of naked iron oxide nanoparticles [114–120]. It has been reported that the size, shape, structure, and magnetic properties of iron oxide nanoparticles could be affected by the conditions of preparation, such as the type of Fe^{3+} or Fe^{2+} salt, the Fe^{3+}/Fe^{2+} ratio, the pH value, the reaction temperature, and the ionic strength of the media [121]. One disadvantage of the method is that during both the synthesis and purification process, the pH value has to remain high, which adversely affects the formation of uniform and monodispersed nanoparticles. Instead, high-quality monodispersed magnetic iron oxide nanoparticles can be formed by thermal decomposition method. In such method, the raw materials used frequently are organometallic compounds primarily including $Fe(cup)_3$ (cup = N-nitrosophenylhydroxylamine), $Fe(acac)_3$ (acac = acetylacetonate), or $Fe(CO)_5$ in an organic solution phase containing stabilizing surfactants under relatively high temperatures (200–300 °C) [68]. Unfortunately, the iron oxide generated by this method have a narrow size distribution and are highly monodispersed while only dissolvable in nonpolar solvents. With hydrothermal method, on the other hand, a chemical reaction occurred in aqueous solution containing iron salts under hydrothermal conditions, namely, a high-temperature aqueous solution (130–250 °C) and high vapor pressure (0.3–4 MPa) [68]. Through a hydrothermal process, the iron-based precursors could influence the size and shape of the magnetic products, and an appropriate hydrothermal temperature could cause an increase in the saturation magnetization.

Microemulsion, other synthesis process, is a thermodynamically stable method that generate magnetic sorbents from two immiscible phases in form water-in-oil micro-emulsion in the presence of surfactant [68]. The generated microemulsion consists of aqueous droplets stabilized by surfactant molecules in continuous phase [68]. The droplets, then, exist as reaction media to monitor the shape and size distribution of particles prepared by precipitating iron salts. Compared with the previously mentioned methods, many authors have proven that the formed nanoparticles by microemulsion method had a smaller size and higher saturation magnetization [68]. However, it is not simple and requires extra efforts for separating the nanoparticles and controlling their synthesis conditions. As shown in the table, the tabulated magnetic sorbents showed great potential in removing different types of synthetic and crude oils, especially the magnetic carbon nanotubes (study number 5), that outperformed with maximum uptake of 56g gasoline/g [118]. Nevertheless, these magnetic carbon nanotubes showed high bio-persistence. Hence, short- or long-term exposure of them might lead to harmful effect to the living organisms and human being (i.e., induced sustained inflammation, lung cancer, and gene damage in the lung). From the studies listed in the table, it is also worth to note that none from the first five studies have clearly described the mechanism at which the oil has been removed with the use of magnetic sorbents [114–120]. In most of the cases, it is not clear whether the removal of oil was due to surface effect (adsorption) or capillary effect (pore filling) of crude oil molecules on a hydrophobic magnetic sorbent, especially after surface modification [119]. Accordingly, sorption as general term is used to encompassing both “adsorption” and “absorption” phenomena,

such that both phenomena normally have been used interchangeably [119]. The last two studies, in contrary, had better observation for the mechanism involved in removing of oil by testing the magnetic sorbent in the removal of other dyes with opposite charges as model molecules, such that methylene blue (MB) and amaranth acid red (AR) [119]. By attaining the adsorptive removal isotherms from both model molecules, the involved mechanism in removal of the crude oil has been identified [119].

14.5 Conclusion

This book chapter examined the sources, characteristics, and water quality constrains for oil sands process affect water (OSPW) generated during the extraction or transportation of the bitumen and the different methods available for their treatment and disposal. Accordingly, this chapter comprehensively discusses the conventional physical/chemical treatment methods for the OSPW generated during oil extraction processes such as steam-assisted gravity drainage (SAGD) and surface mining. The chapter also provided an overview about the materials and methods that are traditionally utilized to remove the oil spills produced during oil transportation. In treatment of SAGD produced water, we critically reviewed the primary, secondary, tertiary, and emerging treatment technologies used to reduce the high concentration levels of silica, total organic carbon, and total hardness. We deeply reviewed some classical technologies implemented to enhance settling and consolidation of oil sand tailings, such as freeze-thawing, centrifugation, consolidated tailings (CT), and paste technologies (i.e., polymeric flocculation). Furthermore, we highlighted the advantaged and challenges of some recent magnetic sorbents used for oil spill remediation. As a result, we conclude that:

1- In the chemical treatment of SAGD produced water, introducing lime, ash, and slaked and non-slaked magnesium might enhance the concentration of divalent ions (i.e., Ca^{+2} and Mg^{+2}), which increases the need for another unit to be eliminated (i.e., WAC). This unfortunately adds additional disadvantages and extra operational and capital costs for the whole chemical treatment process. In the walnut shell filter unit, surface modification can be done for the filter aid material to enhance the removal efficiency of silica and TOC.
2- For enhancing settling and consolidation of fine tailings, the conventional technologies such as filtration and centrifugation are costly material or/and energy intensive physical separation methods. Thus, the chemical treatment has remained as the most adapted technology to enhance the flocculation and consolidation of MFT. Nevertheless, the chemical treatment requires adding of massive amount of coagulant aid (i.e., gypsum) and high molecular weight of polymeric flocculants (i.e., polyacrylamide-based copolymers).
3- Traditional remediation methods for the oil spills are either energy or material intensive. Additionally, many international scientists argue that most of the

applied materials for oil remediation can be toxic and could be more harmful to the environment than the oil itself. Many researchers have alternatively used magnetic sorbents that showed better performance and less environmental impact.

4- A family of eco-friendly nanoparticles, as part of emerging techniques, developed by Nassar's group at the University of Calgary has been effectively combined or integrated with the many physical and /or chemical processes utilized for remediation of OSPW.

References

1. S. Mekhilef, R. Saidur, A. Safari, A review on solar energy use in industries. Renew. Sust. Energ. Rev. **15**, 1777–1790 (2011). https://doi.org/10.1016/j.rser.2010.12.018
2. M. Bhattacharya, S.R. Paramati, I. Ozturk, S. Bhattacharya, The effect of renewable energy consumption on economic growth: evidence from top 38 countries. Appl. Energy **162**, 733–741 (2016). https://doi.org/10.1016/j.apenergy.2015.10.104
3. E.W. Allen, Process water treatment in Canada's oil sands industry: I. Target pollutants and treatment objectives. J. Environ. Eng. Sci. **7**, 123–138 (2008). https://doi.org/10.1139/S07-038
4. R.D. Schlosberg, R. Jordan, A more sustainable way to win oil from oil sands-part II. Characterization. J. Sustain. Energy Eng **5**, 13–28 (2017) https://www.energytoday.net/conventional-energy/sustainable-way-win-oil-oil-sands/
5. L. Pérez-Lombard, J. Ortiz, C. Pout, A review on buildings energy consumption information. Energy Build. **40**, 394–398 (2008). https://doi.org/10.1016/j.enbuild.2007.03.007
6. R.A. Frank, J.W. Roy, G. Bickerton, S.J. Rowland, J.V. Headley, A.G. Scarlett, C.E. West, K.M. Peru, J.L. Parrott, F.M. Conly, L.M. Hewitt, Profiling oil sands mixtures from industrial developments and natural groundwaters for source identification. Environ. Sci. Technol. **48**, 2660–2670 (2014). https://doi.org/10.1021/es500131k
7. S. Sorrell, J. Speirs, R. Bentley, A. Brandt, R. Miller, Global oil depletion: a review of the evidence. Energy Policy **38**, 5290–5295 (2010). https://doi.org/10.1016/j.enpol.2010.04.046
8. W. Pu, B. Wei, F. Jin, Y. Li, H. Jia, P. Liu, Z. Tang, Experimental investigation of CO2huff-n-puff process for enhancing oil recovery in tight reservoirs. Chem. Eng. Res. Des. **111**, 269–276 (2016). https://doi.org/10.1016/j.cherd.2016.05.012
9. G. Giacchetta, M. Leporini, B. Marchetti, Economic and environmental analysis of a Steam Assisted Gravity Drainage (SAGD) facility for oil recovery from Canadian oil sands. Appl. Energy **142**, 1–9 (2015). https://doi.org/10.1016/j.apenergy.2014.12.057
10. S. Canada, Oil Sands. Tailings Mine Waste **2010**, 339–339 (2010). https://doi.org/10.1201/b10569-42
11. Cenovus Energy, *Oil Sands, Water Management*, (2016) 2014–2015. http://www.cenovus.com/operations/oilsands.html.
12. A. Energy, Steam Assisted Gravity Drainage Facts and Stats Steam Assisted Gravity Drainage Process, (2017) 2017. https://open.alberta.ca/dataset/f7c779ea-9776-4d59-a1b3-178d533f0ebc/resource/aac73d46-3ae0-478e-9b19-e64afa41b1f2/download/FSSAGD.pdf.
13. M. Rashedi, O. Xu, S. Kwak, S. Sedghi, J. Liu, B. Huang, An integrated first principle modeling to steam assisted gravity drainage (SAGD). J. Pet. Sci. Eng. **163**, 501–510 (2018). https://doi.org/10.1016/j.petrol.2018.01.005
14. L. Guangyue, L. Shangqi, S. Pingping, L. Yang, L. Yanyan, A new optimization method for steam-liquid level intelligent control model in oil sands Steam-assisted Gravity

Drainage (SAGD) process. Pet. Explor. Dev. **43**, 301–307 (2016). https://doi.org/10.1016/S1876-3804(16)30034-9
15. A. Al-As'ad, *Treatment of SAGD Water Using Low Coagulant Dose And Fenton Oxidation*, MCs Thesis, Univeristy of Calgary, (2013).
16. X. Dong, H. Liu, Z. Zhang, L. Wang, Z. Chen, Performance of multiple thermal fluids assisted gravity drainage process in Post SAGD Reservoirs. J. Pet. Sci. Eng. **154**, 528–536 (2017). https://doi.org/10.1016/j.petrol.2016.12.032
17. J. Hajinasiri, *Treatment of Steam Assisted Gravity Drainage Produced Water Using Polymeric Membranes*, MSc Thesis, University of Alberta, (2015).
18. M.A. Petersen, H. Grade, Analysis of steam assisted gravity drainage produced water using two-dimensional gas chromatography with time-of-flight mass spectrometry. Ind. Eng. Chem. Res. **50**, 12217–12224 (2011). https://doi.org/10.1021/ie200531h
19. N.A. Abdelwahab, N. Shukry, S.F. El-kalyoubi, Separation of Emulsified Oil from Wastewater Using Polystyrene and Surfactant Modified Sugarcane Bagasse Wastes Blend. Clean Techn. Environ. Policy **23**, 235–249 (2020). https://doi.org/10.1016/j.seppur.2008.06.002
20. Y. Gang, C. Shuo, Q. Xie, W. Gaoliang, F. Xinfei, Y. Hongtao, Enhanced separation performance of carbon nanotube–polyvinyl alcohol composite membranes for emulsified oily wastewater treatment under electrical assistance. Sep. Purif. Technol. **197**, 107–115 (2018). https://doi.org/10.1016/j.seppur.2008.12.015
21. S.S. Atallah, C. Tremblay, A.Y. Mortazavi, Silane surface modified ceramic membranes for the treatment and recycling of SAGD produced water. J. Pet. Sci. Eng. **157**, 349–358 (2017). https://doi.org/10.2118/04-08-01
22. T. Kar, A. Mukhametshina, Y. Unal, B. Hascakir, The effect of clay type on steam-assisted-gravity-drainage performance. J. Can. Pet. Technol. **54**, 412–423 (2015). https://doi.org/10.2118/173795-PA%0A
23. K. Zhang, D. Pernitsky, M. Jafari, Q. Lu, Effect of MgO slaking on silica removal during warm lime softening of sagd produced water. Ind. Eng. Chem. Res. **60**, 1839–1849 (2021). https://doi.org/10.2118/97686-MS
24. H. Kawaguchi, Z. Li, Y. Masuda, K. Sato, H. Nakagawa, Dissolved organic compounds in reused process water for steam-assisted gravity drainage oil sands extraction. Water Res. **46**, 5566–5574 (2012). https://doi.org/10.1016/j.watres.2012.07.036
25. E.W. Allen, Process water treatment in canada's oil sands industry: II. A review of emerging technologies. J. Environ. Eng. Sci. **7**, 499–524 (2008)
26. A.T. Lima, K. Mitchell, D.W.O. Connell, J. Verhoeven, P. Van Cappellen, Environmental science & policy the legacy of surface mining : remediation , restoration , reclamation and rehabilitation. Environ Sci Policy **66**, 227–233 (2016). https://doi.org/10.1016/j.envsci.2016.07.011
27. J.Z. Zhou, H. Li, R.S. Chow, Q. Liu, Z. Xu, J. Masliyah, Role of mineral flotation technology in improving bitumen extraction from mined Athabasca oil sands—II. Flotation hydrodynamics of water-based oil sand extraction. Can. J. Chem. Eng. **98**, 330–352 (2020). https://doi.org/10.1002/cjce.23598
28. C.E. Willis, V.L.S. Louis, J.L. Kirk, K.A.S. Pierre, C. Dodge, Tailings ponds of the Athabasca Oil Sands Region, Alberta, Canada, are likely not significant sources of total mercury and methylmercury to nearby ground and surface waters. Sci. Total Environ. **647**, 1604–1610 (2019). https://doi.org/10.1016/j.scitotenv.2018.08.083
29. S. Shamim, Novel Mature Fine Tailings Treatment Using Colloidal Silica Particles, (2018).
30. M.E. Hansen, E. Dursteler, Pipeline, rail & trucks: economic, environmental, and safety impacts of transporting oil and gas in the U.S, Strata. (2017) 1–6. https://www.strata.org/pdf/2017/pipelines.pdf.
31. https://www.capp.ca/energy/transportation/, (n.d.).
32. J. Beyer, H.C. Trannum, T. Bakke, P.V. Hodson, T.K. Collier, Environmental effects of the deepwater horizon oil spill: a review. Mar. Pollut. Bull. **110**, 28–51 (2016). https://doi.org/10.1016/j.marpolbul.2016.06.027

33. A.Y. Ku, C.S. Henderson, M.A. Petersen, D.J. Pernitsky, A.Q. Sun, Aging of water from Steam-Assisted Gravity Drainage (SAGD) operations due to air exposure and effects on ceramic membrane filtration. Ind. Eng. Chem. Res. **51**, 7170–7176 (2012). https://doi.org/10.1021/ie3005513
34. G.T. John, C. Crittenden, R. Rhodes Trussell, D.W. Hand, K.J. Howe, *Water Treatment Princible and Design*, 2nd edn. (Willy, 2005)
35. M. Drahansky, M. Paridah, A. Moradbak, A. Mohamed, F.A. Owolabi, M. Asniza, S.H. Abdul Khalid, Aqueous Silica and Silica Polymerisation. INTECH **3**, 13 (2016). https://doi.org/10.5772/57353
36. D.B. van den Heuvel, E. Gunnlaugsson, I. Gunnarsson, T.M. Stawski, C.L. Peacock, L.G. Benning, Understanding amorphous silica scaling under well-constrained conditions inside geothermal pipelines. Geothermics **76**, 231–241 (2018)
37. Z. Yubin, Z. AXuelu, Removal of silica from heavy oil wastewater to be reused in a boiler by combining magnesium and zinc compounds with coagulation. Desalination **216**, 147–159 (2007)
38. Z. Yubin, Y. Changzhu, P. Wenhong, Z. Xuelu, Removal of silica from heavy oil wastewater to be reused in a boiler by combining magnesium and zinc compounds with coagulation. Desalination **216**, 147–159 (2007)
39. C. Héline, L.-T. Anh, Effective removal of silica and sulfide from oil sands thermal in-situ produced water by electrocoagulation. J. Hazard. Mater. **380**, 120880 (2019)
40. K. Zhang, D. Pernitsky, M. Jafari, Q. Lu, Effect of MgO slaking on silica removal during warm lime softening of SAGD produced water. Ind. Eng. Chem. Res. (2021). https://doi.org/10.1021/acs.iecr.0c05484
41. I. Latour, R. Miranda, A. Blanco, Silica removal with sparingly soluble magnesium compounds. Part I. Sep. Purif. Technol. **138**, 210–218 (2014). https://doi.org/10.1016/j.seppur.2014.10.016
42. A. Charbel, S.Y. Tremblaya, A. Mortazavi, Silane surface modified ceramic membranes for the treatment and recycling of SAGD produced water. J. Pet. Sci. Eng. **157**, 349–358 (2017)
43. B. Khorshidi, I. Biswas, T. Ghosh, T. Thundat, M. Sadrzadeh, Robust fabrication of thin film polyamide-TiO2 nanocomposite membranes with enhanced thermal stability and anti-biofouling propensity. Sci. Rep. **8**, 1–10 (2018). https://doi.org/10.1038/s41598-017-18724-w
44. A. Karkooti, A.Z. Yazdi, P. Chen, M. McGregor, N. Nazemifard, M. Sadrzadeh, Development of advanced nanocomposite membranes using graphene nanoribbons and nanosheets for water treatment. J. Membr. Sci. **560**, 97–107 (2018). https://doi.org/10.1016/j.memsci.2018.04.034
45. C.H. Rawlins, F. Sadeghi, N.O. Varco, Experimental study on oil removal in nutshell filters for produced-water treatment. SPE Prod. Oper. **33**, 145–153 (2017)
46. T. Altun, E. Pehlivan, Removal of Cr(VI) from aqueous aolutions by modified walnut shells. Food Chem. **132**, 693–700 (2012). https://doi.org/10.1016/j.foodchem.2011.10.099
47. D. Ding, Z. Lei, Y. Yang, C. Feng, Z. Zhang, Selective removal of cesium from aqueous solutions with Nickel (II) Hexacyanoferrate (III) functionalized agricultural residue-walnut shell. J. Hazard. Mater. **270**, 187–195 (2014). https://doi.org/10.1016/j.jhazmat.2014.01.056
48. M. Zhu, J. Yao, L. Dong, J. Sun, Adsorption of Naphthalene from aqueous solution onto fatty acid modified walnut shells. Chemosphere **144**, 1639–1645 (2016). https://doi.org/10.1016/j.chemosphere.2015.10.050
49. S. Li, Z. Zeng, W. Xue, Adsorption of lead ion from aqueous solution by modified walnut shell: kinetics and thermodynamics. Environ. Technol. (United Kingdom). **40**, 1810–1820 (2019). https://doi.org/10.1080/09593330.2018.1430172
50. Q. Yu, M. Li, P. Ning, H. Yi, X. Tang, Characterization of metal oxide-modified walnut-shell activated carbon and its application for phosphine adsorption: equilibrium, regeneration, and mechanism studies. J. Wuhan Univ. Technol. Mater. Sci. Ed. **34**, 487–495 (2019). https://doi.org/10.1007/s11595-019-2078-y
51. A. Hethnawi, K. Hashlamoun, S. Sessarego, M. Chehelamirani, N.N. Nassar, Simultaneous removal of Silica and TOC from Steam Assisted Gravity Drainage (SAGD) produced

water using iron-hydroxide-coated walnut shell filter media. J. Water Process Eng. JWPE-D-20 (2021)
52. L. Shamaei, B. Khorshidi, B. Perdicakis, M. Sadrzadeh, Treatment of oil sands produced water using combined electrocoagulation and chemical coagulation techniques. Sci. Total Environ. **645**, 560–572 (2018). https://doi.org/10.1016/j.scitotenv.2018.06.387
53. B. Khorshidi, A. Bhinder, T. Thundat, D. Pernitsky, M. Sadrzadeh, Developing high throughput thin film composite polyamide membranes for forward osmosis treatment of SAGD produced water. J. Membr. Sci. **511**, 29–39 (2016). https://doi.org/10.1016/j.memsci.2016.03.052
54. A. Charbel, S.Y. Tremblaya, A. Mortazavi, Silane surface modified ceramic membranes for the treatment and recycling of SAGD produced water. J. Pet. Sci. Eng. **157**, 349–358 (2017). https://doi.org/10.1016/j.petrol.2017.07.007
55. C. Atallah, S. Mortazavi, A.Y. Tremblay, A. Doiron, Surface-modified multi-lumen tubular membranes for SAGD-produced water treatment. Energy Fuel **33**, 5766–5776 (2019). https://doi.org/10.1021/acs.energyfuels.9b00585
56. L. Shamaei, B. Khorshidi, M.A. Islam, M. Sadrzadeh, Development of antifouling membranes using agro-industrial waste lignin for the treatment of Canada's oil sands produced water. J. Membr. Sci. **611**, 118326 (2020). https://doi.org/10.1016/j.memsci.2020.118326
57. A. El-Qanni, *Development of Sustainable Nanosorbcats Based Technology for Hydrocarbons and Organic Pollutants Recovery from Industrial Wastewater*, (2017)
58. A. Hethnawi, *Poly(ethylenimine)-Functionalized Pyroxene Nanoparticles Embedded on Diatomite for Removal of Total Organic Carbon from Industrial Wastewater: Batch and Fixed-bed studies* (University of Calgary, 2017)
59. R. Thummar, N. Limbasiya, A. Upadhyay, *Wet Air Oxidation Process for Sludge Treatment* (Zimpro Process), Semant. Sch. Corpus ID: (2015).
60. P. Haghighat, L.C. Ortega, P. Pereira-Almao, Experimental study on catalytic hydroprocessing of solubilized asphaltene in water: A proof of concept to upgrade asphaltene in the aqueous phase. Energy Fuel **30**, 2904–2918 (2016). https://doi.org/10.1021/acs.energyfuels.6b00275
61. A.D. Manasrah, N.N. Nassar, L.C. Ortega, Conversion of petroleum coke into valuable products using oxy-cracking technique. Fuel **215**, 865–878 (2018). https://doi.org/10.1016/j.fuel.2017.11.103
62. A.D. Manasrah, G. Vitale, N.N. Nassar, Catalytic oxy-cracking of petroleum coke on copper silicate for production of humic acids. Appl. Catal. B Environ. **264**, 118472 (2020). https://doi.org/10.1016/j.apcatb.2019.118472
63. L. Li, P. Chen, E.F. Gloyna, Generalized kinetic model for wet oxidation of organic compounds. AICHE J. **37**, 1687–1697 (1991). https://doi.org/10.1002/aic.690371112
64. A.D. Manasrah, N.N. Nassar, L.C. Ortega, Conversion of petroleum coke into valuable products using oxy-cracking technique. Fuel **215**, 865–878 (2018)
65. G. Nafie, A. D. Manasrah, B. Mackay, I. Badran, N. N. Nassar (eds.), Oxy-cracking reaction for enhanced settling and dewaterability of oil sands tailings. Ind. Eng. Chem. Res. **58**, 4988–4996 (2019)
66. A.D. Manasrah, N.N. Nassar, Oxy-cracking technique for producing non-combustion products from residual feedstocks and cleaning up wastewater. Appl. Energy **280**, 115890 (2020). https://doi.org/10.1016/j.apenergy.2020.115890
67. A. Hethnawi, N.N. Nassar, A.D. Manasrah, G. Vitale, Polyethylenimine-functionalized pyroxene nanoparticles embedded on diatomite for adsorptive removal of dye from textile wastewater in a fixed-bed column. Chem. Eng. J. **320**, 389–404 (2017). https://doi.org/10.1016/j.cej.2017.03.057
68. R.M. Cornell, U. Schwertmann, the Iron Oxides: Structure, Properties, Reactions, Occurrences and Uses, 2nd ed., Copyright © 2003 Wiley-VCH Verlag GmbH & Co. KGaA, (2003). doi:https://doi.org/10.1002/3527602097.
69. C. Nieto-Delgado, J.R. Rangel-Mendez, Anchorage of Iron Hydro (oxide) Nanoparticles onto Activated Carbon to Remove As (V) from Water. Water Res. **46**, 2973–2982 (2012)

70. J. Zhao, Z. Lu, X. He, X. Zhang, Q. Li, T. Xia, W. Zhang, C. Lu, Y. Deng, One-Step Fabrication of Fe(OH)3@Cellulose Hollow Nanofibers with Superior Capability for Water Purification. ACS Appl. Mater. Interfaces **9**, 25339–25349 (2017). https://doi.org/10.1021/acsami.7b07038
71. X. Zhu, L. Yiming, H. Yang, Z. Yangge, S. Changxing, W. Weiqing, Adsorption of Ferric Ions on the Surface of Bastnaesite and Its Significance in Flotation. Miner. Eng. **158**, 106588 (2020)
72. S. Grimme, S. Ehrlich, L. Goerigk, Effect of the damping function in dispersion corrected density functional theory. J. Comput. Chem. **32**, 1456–1465 (2011)
73. S. Grimme, J. Antony, S. Ehrlich, H. Krieg, A consistent and accurate ab initio parametrization of density functional dispersion correction (DFT-D) for The 94 Elements H-Pu. J. Chem. Phys. **132**, 154104 (2010)
74. P.E. Blöchl, Projector Augmented-wave method. Phys. Rev. B **50**, 17953 (1994)
75. R.G. Pillai, N. Yang, S. Thi, J. Fatema, M. Sadrzadeh, D. Pernitsky, Characterization and comparison of dissolved organic matter signatures in steam-assisted gravity drainage process water samples from athabasca oil sands. Energy Fuel **31**, 8363–8373 (2017)
76. S. Guha Thakurta, A. Maiti, D.J. Pernitsky, S. Bhattacharjee, Dissolved organic matter in steam assisted gravity drainage boiler blow-down water. Energy Fuel **27**, 3883–3890 (2013)
77. Y. Nishiyama, P. Langan, H. Chanzy, Crystal structure and hydrogen-bonding system in cellulose Iβ from SYNCHROTRON X-ray and neutron fiber diffraction. J. Am. Chem. Soc. **124**, 9074–9082 (2002)
78. C. Zhu, I. Dobryden, J. Rydén, S. Öberg, A. Holmgren, A.P. Mathew, Adsorption behavior of cellulose and its derivatives toward Ag (I) in aqueous medium: an AFM, spectroscopic, and DFT study. Langmuir **31**, 12390–12400 (2015)
79. D. Zheng, Y. Zhang, Y. Guo, J. Yue, Isolation and characterization of Nanocellulose with a Novel Shape from Walnut (Juglans regia L.) Shell agricultural waste. Polymers (Basel) **11**, 1130 (2019)
80. S. Zhao, J. Niu, L. Yun, K. Liu, S. Wang, J. Wen, Z. Zhang, The relationship among the structural, cellular, and physical properties of walnut shells. HortScience **54**, 275–281 (2019)
81. K. Momma, F. Izumi, VESTA 3 for three-dimensional visualization of crystal, volumetric and morphology data. J. Appl. Crystallogr. **44**, 1272–1276 (2011)
82. T. Tsuneda, *Density Functional Theory in Quantum Chemistry*, 3rd edn. (2014)
83. V. Vajihinejad, R. Guillermo, J.B.P. Soares, Dewatering Oil Sands Mature Fine Tailings (MFTs) with Poly(acrylamide-co-diallyldimethylammonium chloride): Effect of Average Molecular Weight and Copolymer Composition. Ind. Eng. Chem. Res. **56**, 1256–1266 (2017). https://doi.org/10.1021/acs.iecr.6b04348
84. R. Hripko, V. Vajihinejad, F. LopesMotta, J.B.P. Soares, Enhanced flocculation of oil sands mature fine tailings using hydrophobically modified polyacrylamide copolymers. Glob. Challenges. **2**, 1700135 (2018). https://doi.org/10.1002/gch2.201700135
85. S.P. Gumfekar, T.R. Rooney, R.A. Hutchinson, J.B.P. Soares, Dewatering oil sands tailings with degradable polymer flocculants. ACS Appl. Mater. Interfaces **9**, 36290–36300 (2017). https://doi.org/10.1021/acsami.7b10302
86. D.K. Thompson, F.L. Motta, J.B.P. Soares, Investigation on the flocculation of oil sands mature fine tailings with alkoxysilanes. Miner. Eng. **111**, 90–99 (2017). https://doi.org/10.1016/j.mineng.2017.06.008
87. C. Wang, D. Harbottle, Q. Liu, Z. Xu, Current state of fine mineral tailings treatment: a critical review on theory and practice. Miner. Eng. **58**, 113–131 (2014). https://doi.org/10.1016/j.mineng.2014.01.018
88. S. Renault, C. Lait, J.J. Zwiazek, M. MacKinnon, Effect of high salinity tailings waters produced from gypsum treatment of oil sands tailings on plants of the boreal forest. Environ. Pollut. **102**, 177–184 (1998). https://doi.org/10.1016/s0269-7491(98)00099-2

89. M.J. Salloum, M.J. Dudas, P.M. Fedorak, Microbial reduction of amended sulfate in anaerobic mature fine tailings from oil sand. Waste Manag. Res. **20**, 162–171 (2002). https://doi.org/10.1177/0734242X0202000208
90. J.G. Matthews, W.H. Shaw, M.D. Mackinnon, R.G. Cuddy, Development of composite tailings technology at Syncrude. Int. J. Surf. Min. Reclam. Environ. **16**, 24–39 (2002). https://doi.org/10.1076/ijsm.16.1.24.3407
91. D. Zhang, T. Thundat, R. Narain, Flocculation and dewatering of mature fine tailings using temperature-responsive cationic polymers. Langmuir **33**, 5900–5909 (2017). https://doi.org/10.1021/acs.langmuir.7b01160
92. L.G. Reis, R.S. Oliveira, T.N. Palhares, L.S. Spinelli, E.F. Lucas, D.R.L. Vedoy, E. Asare, J.B.P. Soares, Using acrylamide/propylene oxide copolymers to dewater and densify mature fine tailings. Miner. Eng. **95**, 29–39 (2016). https://doi.org/10.1016/j.mineng.2016.06.005
93. K.C. Lister, H. Kaminsky, R.A. Hutchinson, Evaluation of a novel polymeric flocculant for enhanced water recovery of mature fine tailings. Processes. **8**, 735 (2020). https://doi.org/10.3390/pr8060735
94. D.R. Vedoy, J.B. Soares, Water-soluble polymers for oil sands tailing treatment: A Review. Can. J. Chem. Eng. **93**, 888–904 (2015)
95. A. Alamgir, D. Harbottle, J. Masliyah, Z. Xu, Al-PAM assisted filtration system for abatement of mature fine tailings. Chem. Eng. Sci. **80**, 91–99 (2012). https://doi.org/10.1016/j.ces.2012.06.010
96. W.Y. Yang, J.W. Qian, Z.Q. Shen, A novel flocculant of Al(OH)3-polyacrylamide ionic hybrid. J. Colloid Interface Sci. **273**, 400–405 (2004). https://doi.org/10.1016/j.jcis.2004.02.002
97. X. Wei, J. Tao, M. Li, B. Zhu, X. Li, Z. Ma, T. Zhao, B. Wang, B. Suo, H. Wang, J. Yang, L. Ye, X. Qi, Polyacrylamide-based inorganic hybrid flocculants with self-degradable property. Mater. Chem. Phys. **192**, 72–77 (2017). https://doi.org/10.1016/j.matchemphys.2017.01.064
98. K.E. Lee, T.T. Teng, N. Morad, B.T. Poh, Y.F. Hong, Flocculation of kaolin in water using novel calcium chloride-polyacrylamide (CaCl2-PAM) hybrid polymer. Sep. Purif. Technol. **75**, 346–351 (2010). https://doi.org/10.1016/j.seppur.2010.09.003
99. H. Lu, Y. Wang, L. Li, Y. Kotsuchibashi, R. Narain, H. Zeng, Temperature- and pH-responsive benzoboroxole-based polymers for flocculation and enhanced dewatering of fine particle suspensions. ACS Appl. Mater. Interfaces **7**, 27176–27187 (2015). https://doi.org/10.1021/acsami.5b09874
100. L. Botha, S. Davey, B. Nguyen, A.K. Swarnakar, E. Rivard, J.B.P. Soares, Flocculation of oil sands tailings by hyperbranched functionalized polyethylenes (HBfPE). Miner. Eng. **108**, 71–82 (2017). https://doi.org/10.1016/j.mineng.2017.02.004
101. G. Nafie, G. Vitale, L. Carbognani Ortega, N.N. Nassar, Nanopyroxene grafting with β-Cyclodextrin monomer for wastewater applications. ACS Appl. Mater. Interfaces **9**, 42393–42407 (2017). https://doi.org/10.1021/acsami.7b13677
102. J. Roberts, M. Caserio, *Basic Principles of Organic Chemistry*, 2nd edn. (Benjamin, 1977)
103. A. Kumar, G. Sharma, M. Naushad, S. Thakur, SPION/β-cyclodextrin core-shell nanostructures for oil spill remediation and organic pollutant removal from waste water. Chem. Eng. J. **280**, 175–187 (2015). https://doi.org/10.1016/j.cej.2015.05.126
104. B. Doshi, M. Sillanpää, S. Kalliola, A review of bio-based materials for oil spill treatment. Water Res. **135**, 262–277 (2018). https://doi.org/10.1016/j.watres.2018.02.034
105. J. Ge, H.Y. Zhao, H.W. Zhu, J. Huang, L.A. Shi, S.H. Yu, Advanced sorbents for oil-spill cleanup: recent advances and future perspectives. Adv. Mater. **28**, 10459–10490 (2016). https://doi.org/10.1002/adma.201601812
106. M. Husseien, A.A. Amer, A. El-Maghraby, N. Hamedallah, Oil spill removal from water by using corn stalk: factors affecting sorption process. Int. J. Environ. Waste Manag. **16**, 281–292 (2015). https://doi.org/10.1504/IJEWM.2015.074907
107. M.O. Adebajo, R.L. Frost, J.T. Kloprogge, O. Carmody, S. Kokot, Porous materials for oil spill cleanup: a review of synthesis and absorbing properties. J. Porous. Mater. **10**, 159–170 (2003). https://doi.org/10.1023/A:1027484117065

108. M.F. Fingas, *Handbook of Oil Spill Science and Technology* (Wiley, 2015)
109. K.B. Debs, D.S. Cardona, H.D. da Silva, N.N. Nassar, E.N. Carrilho, P.S. Haddad, G. Labuto, Oil spill cleanup employing magnetite nanoparticles and yeast-based magnetic bionanocomposite. J. Environ. Manag. **230**, 405–412 (2019)
110. A. Bazargan, J. Tan, G. McKay, Standardization of oil sorbent performance testing. J. Test. Eval. **6**, 1271–1278 (2015)
111. J.H. Ramirez Leyva, A. Hethnawi, G. Vitale, N.N. Nassar, Magnetic nanostructured white graphene for oil spill and water cleaning. Ind. Eng. Chem. Res. **57**, 13065–13076 (2018). https://doi.org/10.1021/acs.iecr.8b02785
112. A. El-qanni, N.N. Nassar, G. Vitale, A. Hassan, Maghemite nanosorbcats for methylene blue adsorption and subsequent catalytic thermo-oxidative decomposition: computational modeling and thermodynamics studies. J. Colloid Interface Sci. **461**, 396–408 (2016). https://doi.org/10.1016/j.jcis.2015.09.041
113. O. Saber, N.H. Mohamed, A. Alijaafari, Synthesis of magnetic nanoparticles and nanosheets for oil spill removal. Nanosci. Nanotechnol-Asia **5**, 32–43 (2015)
114. A.A.S. Osama, H.M. Nermen, Synthesis of magnetic nanoparticles and nanosheets for oil spill removal. Nanosci Nanotechnol Asia **5**, 32–43 (2015)
115. T. Lü, Y. Chen, D. Qi, Z. Cao, D. Zhang, H. Zhao, Treatment of emulsified oil wastewaters by using chitosan grafted magnetic nanoparticles. J. Alloys Compd. **696**, 1205–1212 (2017). https://doi.org/10.1016/j.jallcom.2016.12.118
116. L. Yu, G. Hao, J. Gu, S. Zhou, N. Zhang, W. Jiang, Fe3O4/PS magnetic nanoparticles: Synthesis, characterization and their application as sorbents of oil from waste water. J. Magn. Magn. Mater. **394**, 14–21 (2015). https://doi.org/10.1016/j.jmmm.2015.06.045
117. X. Gui, Z. Zeng, Z. Lin, Q. Gan, R. Xiang, Y. Zhu, A. Cao, Z. Tang, Magnetic and highly recyclable macroporous carbon nanotubes for spilled oil sorption and separation. ACS Appl. Mater. Interfaces **5**, 5845–5850 (2013). https://doi.org/10.1021/am4015007
118. W. Ngarmkam, C. Sirisathitkul, C. Phalakornkule, Magnetic composite prepared from palm shell-based carbon and application for recovery of residual oil from POME. J. Environ. Manag. **92**, 472–479 (2011). https://doi.org/10.1016/j.jenvman.2010.08.031
119. J.H. Ramirez Leyva, A. Hethnawi, G. Vitale, N.N. Nassar, Magnetic nanostructured white graphene for oil spill and water cleaning. Ind. Eng. Chem. Res. **57**, 13065–13076 (2018). https://doi.org/10.1021/acs.iecr.8b02785
120. K.B. Debs, D.S. Cardona, H.D.T. da Silva, N.N. Nassar, E.N.V.M. Carrilho, P.S. Haddad, G. Labuto, Oil spill cleanup employing magnetite nanoparticles and yeast-based magnetic bionanocomposite. J. Environ. Manag. **230**, 405–412 (2019). https://doi.org/10.1016/j.jenvman.2018.09.094
121. P. Xu, G. Ming, D. Lian, C. Ling, S. Hu, M. Hua, Use of iron oxide nanomaterials in wastewater treatment : a review. Sci. Total Environ. **424**, 1–10 (2012). https://doi.org/10.1016/j.scitotenv.2012.02.023

Chapter 15
Challenges and Uncertainties of Using Nanoparticles in Oil and Gas Applications

Farad Sagala, Afif Hethnawi, and Nashaat N. Nassar

15.1 Introduction

In recent years, nanoparticle application in the field of oil and gas has attained momentous attention, and several researchers are continuing to report tremendous promising results [1–4]. Nanotechnology can be defined as a field of applied sciences that focuses on the design, manipulation, detection, and employing of nano-sized materials, structures, components, devices, and systems at the nanoscale. There are several inimitable properties that nanoparticles possess that make them suitable for oil and gas application. Based on their small sizes, nanoparticles can be transported into a porous medium that could not be accessed by the larger particles. Moreover, based on their large surface-area-to-volume ratio, at the nanoscale, nanoparticles can be modified to contain specific interfacial, magnetic, or chemical properties to perform certain functions [5–7]. Utilization of nanoparticle technology can accelerate the production of oil and gas by providing a platform that makes their separation in the reservoir more acquiescent in the coming years [8, 9]. Nanomaterials have a great potential to introduce tremendous and revolutionary changes in various areas of oil and gas such as drilling, exploration, production, imaging, tight

F. Sagala
Department of Chemical and Petroleum Engineering, University of Calgary (UC), University Drive NW, Calgary, AB, Canada

Department of Energy, Minerals and Petroleum Engineering, Mbarara University of Science and Technology, Mbarara, Uganda

A. Hethnawi · N. N. Nassar (✉)
Department of Chemical and Petroleum Engineering, University of Calgary (UC), University Drive NW, Calgary, AB, Canada
e-mail: nassar@ucalgary.ca

N. N. Nassar et al. (eds.), *Nanoparticles: An Emerging Technology for Oil Production and Processing Applications*, Lecture Notes in Nanoscale Science and Technology, https://doi.org/10.1007/978-3-319-12051-5_15

reservoirs, and EOR [10–13]. For example, using nanoparticle can help to improve the stability and rheological properties of drilling fluids hence providing safe drilling in unstable zones by increasing the rate of penetration, reduce the drilling costs, and lessen the environmental footprints. Additionally, using properly designed nanoparticles in imaging can facilitate the creation of naturally occurring fractures in tight reservoirs [13]. This is due to their sizes and high surface-area-to-volume ratio, as well as their high mobility in the porous medium, enhanced heat and mass transfer that makes them appropriate for harsh-reservoir conditions [9, 14]. Nanoparticles can also be synergized with other conventional materials such as alkaline, surfactants, polymers, and recently low salinity water flooding [15–17] to recover trapped oil from the reservoir. Various types of nanoparticles such as metals and metal oxides have currently been proven to recover additional oil after water flooding, through several mechanisms such as alteration of wettability, IFT reduction, disjoining pressure, viscosity reduction and improvement of mobility ratio, inhibition of wax and asphaltene deposition, etc. [11, 14, 18]. Furthermore, different parameters such as nanoparticle concentration, size, temperature, wettability, injection sequence, rock permeability, and salinity have been evidenced to affect the nanofluid flooding performance in nano-EOR [19, 20]. Notwithstanding the substantially increasing interests of nanoparticle applications in the oil and gas industry, however, there still exist some challenges that limit their full adoption to field scale. The focus of this chapter, therefore, is to address some of the current challenges limiting nanoparticle application for field scale. Also, some concerns, environment impacts, and uncertainties of using nanoparticle in oil and gas are explored.

15.2 Challenges of Nanoparticles in Oil Recovery Applications

Despite the increasing research in the application of nanomaterials in the oil and gas industry, there are still some challenges limiting nanoparticles to laboratory scale. These will be discussed in this chapter. Figure 15.1 shows an overview of common impediments of nanofluids application in the oil and gas industry.

15.2.1 Cost of the Materials and Synthesis Pathways

Cost of the materials involved in synthesizing nanoparticles tends to limit their scalability for further pilot and field applications. When scaling-up, technical and economic problems always arise; thus, only a fraction of the laboratory nanomaterials can be saved. Also, currently most of the used nanomaterials require harsh conditions to be synthesized. For example, silica nanoparticles that are commonly used in EOR require calcination and freeze-drying under nitrogen during the synthesis process [21, 22]. This makes the material costly, impacting the scalability of the

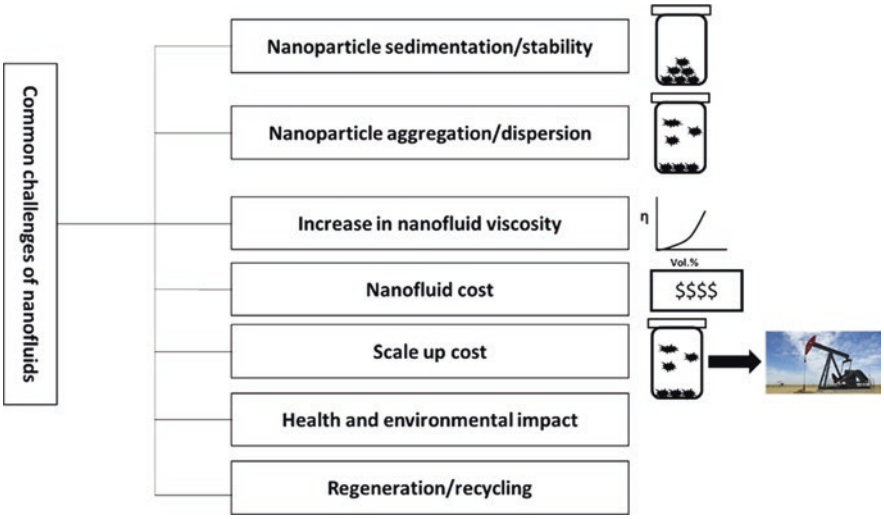

Fig. 15.1 Summary of common challenges of nanofluids application in the oil and gas industry

material for field applications. There is therefore a need to formulate clear and simple synthesis protocols that offer pathways for scalability at low costs. Also, the proposed nanomaterials must be better somehow than the existing conventional methods used in EOR or at least provide better advantages than the competitor or introduce a new necessity or technique. It needs to be a process not covered by any previously developed materials, most importantly at low cost while minimizing the risks. Besides, most of the researchers that have been successful in developing these new promising nanomaterials lack industrial patterners, have no business plans, and lack scale-up expertise which limits the application process. It is important to note that not all newly developed and promising materials end up being scaled up and commercialized. Successful scale-up and commercialization of developed materials are always associated with their ability to deliver a huge benefit to a company, corporation, or government. Early detection of industrial partners is of key importance for the development of material for commercial scale. Lastly, cost analysis of nanoparticles to back up the experimental findings is further needed. The analysis of costs involved should be based on the crude oil prices in the world markets and compared with the cost of the conventional EOR agents commonly used, such as surfactants, polymers, alkaline, or a combination. This will guarantee the economic viability of nanoparticles as EOR alternatives now or later.

15.2.2 Stability and Control over the Particle Size

Among the serious technical challenges that affect the applicability of nanoparticles in EOR is the preparation of a homogeneous suspension of nanofluids. Nanoparticles tend to agglomerate resulting in the formation of clusters, due to molecular

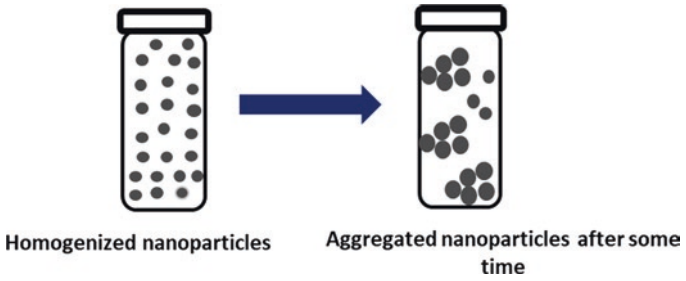

Fig. 15.2 Nanoparticles in suspension

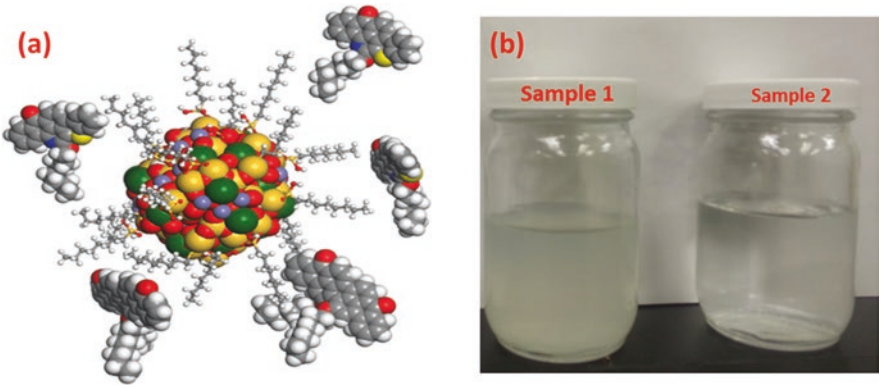

Fig. 15.3 (**a**) Nanoparticle surface modified with various silanol groups and (**b**) nanofluid before and after the surface modification. Permissions related to the material excerpted were obtained from the American Chemical Society (ACS) and further permission should be directed to ACS *Energy Fuels* 2019, 33(2), 877–890

interactions, between the forces such as van der Waals forces [23]. An illustration of the nanoparticle before and after agglomeration is shown in Fig. 15.2. Nanoparticle agglomeration increases as filler fraction increases, due to the closeness of the particles and higher van der Waals forces of attraction or weaker electrostatic repulsive forces. This may generate other problems such as viscosity increments. Agglomeration of nanoparticles results in a reduction of the effective surface area-to-volume ratio, which impacts the overall performance of the nanofluids [24]. Normally, due to harsh reservoir conditions such as salinity and temperature, nanoparticles tend to aggregate and form clusters due to the force imbalance between the attractive and repulsive forces [25, 26]. This greatly affects their performance in such harsh environments. Therefore, future findings need to focus more on discovering proper functionalities in the form of silanes, polymers, or surfactants that can provide stable nanofluids. A typical example of modifying agents that can be used in nanoparticle stability is depicted in Fig. 15.3. However, the modifying agent attached to the surface of the nanoparticles in the process of stabilizing them should not change the particle morphology and topology which may alter their performance. Additionally, the selected stabilizing agent for the nanoparticles should

ease their propagation through a reservoir under harsh conditions of temperature and salinity. A proper stabilizing agent should be able to stabilize the nanoparticle in both static and dynamic conditions. Furthermore, the attached functional groups should also minimize the adsorption of nanoparticles on the rock surface. The long-term chemical stability of functional groups along with low production cost is another challenge which should be considered.

15.2.3 Screening Criteria for Reservoir

As research in the application of nanomaterials in oil and gas continues to emerge, methods of screening relevant to nanoparticle application in EOR need to be established, similar to the conventional EOR methods such as alkaline flooding, surfactant flooding, polymer flooding, etc. that have various screening criteria before their application. Initial findings based on the charge composition of the nanoparticles recommend negatively charged nanomaterials for sandstone reservoirs and positively charged materials for carbonates rocks. However, other parameters such as oil properties, rock properties, reservoir temperature, etc. need to be screened before using nanoparticles. Also, other properties of the nanomaterials such as the nanoparticle hydrophilicity or hydrophobicity may affect their performance during EOR.

15.2.4 Regeneration and Recovery of the Nanoparticles

Nanoparticles that can be recycled offer better options for applications. Some nanoparticles offer easy regeneration pathways compared to others. Weiwei et al. [27] reported that boron nitride can be reused easily by washing, burning, or heating in air because the material is resistant to oxidation. The authors concluded that the withstanding routes of such materials can enhance their great potential in various applications. However, there some other proposed regeneration techniques for other nanomaterials that can be used to recover the materials such as backwashing by adjusting the pH. Therefore, before their application, the proposed nanomaterials require some regeneration protocol that may offer prolonged use to minimize the costs.

15.2.5 Transportation and Deposition

Deposition of the nanoparticle can be defined as the process of particles at nanoscale attaching to the solid surfaces in the form of aggregates or deposits. These coatings are deposited on the surface as a monolayer or a multilayer depending on the

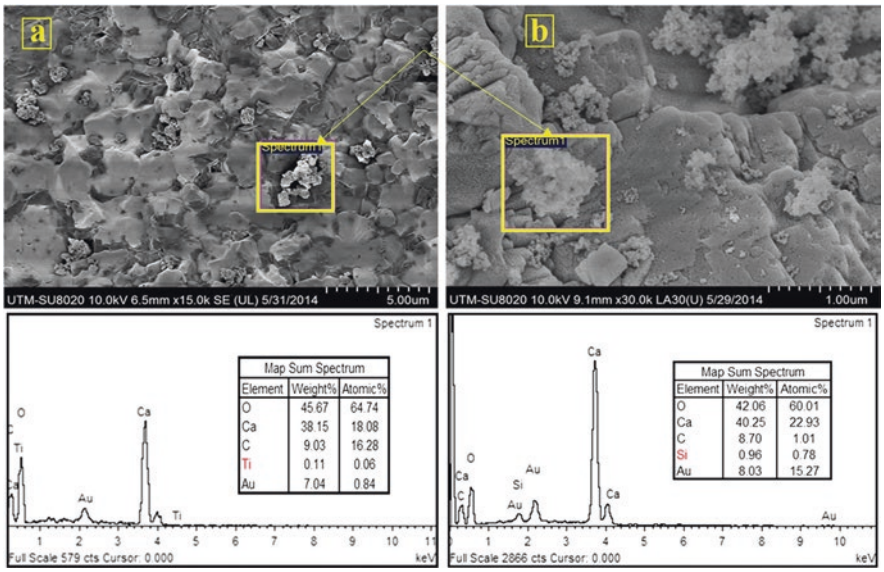

Fig. 15.4 Nanoparticle deposition (Obtained from Ref. [30]. Permissions related to the material excerpted were obtained from Elsevier and further permission should be directed to Elsevier)

deposition method. However, nanoparticles are usually difficult to deposit due to their physical properties such as size and particle morphology. Several mechanisms for improving oil recovery during nano-EOR have been proposed. However, the interactions between NPs and rock surfaces require further investigation. Figure 15.4 shows the deposition tread of nanoparticles as they propagate inside the porous medium. As nanoparticles propagate in the porous medium, they tend to adsorb on the rock surface depending on their ionic interaction and the rock surface [28]. Retention of nanoparticles in the porous medium can also be caused by the increase in ionic strength and grain size of the nanoparticles [29]. This may result in pore blockage and impairment of rock properties such as porosity and permeability [14]. However, there is a lack of experimental and numerical studies that perfectly describes the NP behavior in the porous medium. The existing models are mainly limited to the physical interactions of NPs, and chemical interactions have not yet been considered. Also, a synergistic effect of using a mixture of more than one type of nanoparticle has not been reported with the existing models. Better performance may be obtained from such combinations. Several parameters impact the transportation and deposition of nanoparticles in the porous medium, such as nanoparticle size, flow rate, formation type, petrophysical properties such as porosity and permeability, nanoparticle concentration used during the injection, injection sequence, etc. Optimization of these aforementioned parameters is paramount to control and limit the nanoparticle deposition.

15.3 Concerns and Uncertainties of Using Nanotechnology in Oil and Gas

Similar to any new technology, nanotechnology is expected to introduce both advantages in terms of applications and hazards or implications for human society and the ecosystem. The unique properties of nanomaterials have given rise to many amazing potential applications such as the generation of energy and storage, medical applications, speeding up chemical reactions, and now oil and gas-related activities. For any new technology that comes along, we have to consider how we can use the technology responsibly for society's benefit while minimizing the health-related hazards that the new technology may poses.

Although nanotechnology contributes tremendously to technological advancement in many applications and is attracting attention for possible applications in medicine, health, agriculture, and energy industries, there are still some unresolved critical uncertainties [32]. It has been conceptualized as an environmentally friendly technique over the last decade, and many indirect and direct applications of nanomaterials are being used in the marketplace. However, there is minimal data on the nanometric effect of nanoparticles on human health and the environment due to limited field applications [32]. Some primary findings reported no health-related issues and concerns of nanomaterials [33]. For instance, the UK Royal Society (London, UK) and the Royal Academy of Engineering (London, UK) released a report which concluded that nanomaterials in several applications pose no new health risks [34]. However, the associated benefits of nanoparticles from the environmental perspective are combined with challenges that may be difficult to predict. Also, there is little information about the disposal, manufacturing, reactivation usage, regeneration, disposal, and any associated risk in the exposure to nanomaterials [35]. Karin et al. [36] demonstrated that plastic nanoparticles have an effect on the survival of aquatic zooplankton and can penetrate the blood-to-brain barrier in fish and cause behavioral disorders; however, more finding while using other nanoparticles requires investigations. Nanomaterials based on their dimensions, shapes, and surface energy may match with some of the biological body molecules such as proteins or nucleic acids. Hence, when they come in contact with the fluids of the body, they can be absorbed easily. These adsorbed materials may spread to the target sites such as the heart, liver, or blood cells and cause damage [37]. However, studies have shown that remediation management and control of nanomaterials can reduce their environmental and health hazards [37]. Less exposure to nanomaterials and using respirators has been suggested as a possible measure of preventing nanoparticle inhalation that may result in respiratory irritation and damage to body organs [33]. For example, titanium, nickel, CNTs, cobalt, and polystyrene have been postulated as examples of nanoparticles responsible for respiratory toxicity compared to quartz nanomaterials [37]. There is a need to examine ethically related issues and create test protocols and procedures that will guarantee safe

handling of nanomaterials for EOR laboratory, pilot, and field applications. Currently, several agencies have started health access and environmental safety inspection of nanoparticles and have developed precautions. For example, in the United States, agencies such as National Toxicology Program (NTP), National Center for Environmental Research of the Environmental Protection Agency (EPA), National Institute of Occupational Safety and Health (NIOSH), National Institute of Environmental Health have all been commissioned for application and risk assessment of nanomaterials [33, 38]. Oil and gas industries need to consider the findings from various researchers, institutes, and other industries that use nanotechnology. This will facilitate rapid understanding of occupational safety and environmental and health implications of using nanotechnology.

In summary, as a recommendation to nanoparticle users, less exposure to nanomaterials and using respirators has been suggested as a way of diminishing nanoparticle inhalation that may result in respiratory irritation and damage to other body organs [33].

15.4 Conclusion

Nanoparticles have promising potential for oil and gas applications owing to their unique behavior and exceptional properties that differ from their bulk counterparts, but the employment of nanoparticle technology in the oil and gas industry is also limited by several challenges which affect their field applications. Various fascinating properties exhibited by different nanoparticles have been reported by many researchers. EOR has received much consideration, but many researchers have recently initiated studies in other areas of research related to oil and gas application such as exploration, drilling, production, refinery, etc. The application of these materials is very promising as evidenced by the trend in the published literature in recent years. However, field applications are still limited due to lack of consensus of the reported findings regarding the mechanism of NANO-EOR possibly due to human artifacts. Furthermore, nanoparticles are currently expensive, as a result of inefficient synthesis pathways. However, mass production of nanomaterials can help to reduce the overall cost enabling the applicability of nanomaterials for various applications. Furthermore, it would be helpful for scientists and engineers in the oil field to conjoin with other researchers in academia and other industries where nanotechnology has made a substantial breakthrough. Since nanotechnology has made a significant impact in various industrial sectors, it is plausible that solutions in the oil field can be found. This integration can yield successful outcomes for oil and gas applications. Nevertheless, through an integrated partnership between oil companies and academic institutions, piloting nanotechnology and performing field trials can conceivably offer inexpensive and quick solutions before their full implementation to the industry. Also, efforts should be made to find cheaper sources of nanoparticles since their applicability to the oil field requires large quantities. Lastly, priority should be given to investigating the safe applicability and recovery

opportunities of nanoparticles in the oil and gas field to give nominal effect on HSE. In the absence of government regulations, the establishment of industry best practices will be highly useful.

References

1. L.J. Giraldo et al., The effects of SiO2 nanoparticles on the thermal stability and rheological behavior of hydrolyzed polyacrylamide based polymeric solutions. J. Pet. Sci. Eng. **159**, 841–852 (2017)
2. X. Kong, M. Ohadi, Applications of micro and nano technologies in the oil and gas industry-overview of the recent progress, in *Abu Dhabi International Petroleum Exhibition and Conference*, (Society of Petroleum Engineers, 2010)
3. N.N. Nassar, A. Hassan, P. Pereira-Almao, Application of nanotechnology for heavy oil upgrading: Catalytic steam gasification/cracking of asphaltenes. Energy Fuel **25**(4), 1566–1570 (2011)
4. M.F. Fakoya, S.N. Shah, Emergence of nanotechnology in the oil and gas industry: Emphasis on the application of silica nanoparticles. Petroleum **3**(4), 391–405 (2017)
5. K. Zhou et al., Application of magnetic nanoparticles in petroleum industry: a review. J. Pet. Sci. Eng., 106943 (2020)
6. F. Sagala, A. Hethnawi, N.N. Nassar, Hydroxyl-functionalized silicate-based nanofluids for enhanced oil recovery. Fuel **269**, 117462 (2020)
7. A. Bera et al., Mechanistic study on silica nanoparticles-assisted guar gum polymer flooding for enhanced oil recovery in sandstone reservoirs. Colloids Surf. A Physicochem. Eng. Asp., 124833 (2020)
8. A.I. El-Diasty, A.M.S. Ragab, Applications of nanotechnology in the oil & gas industry: Latest trends worldwide & future challenges in Egypt, in *North Africa Technical Conference and Exhibition*, (Society of Petroleum Engineers, 2013)
9. M. Khalil et al., Advanced nanomaterials in oil and gas industry: design, application and challenges. Appl. Energy **191**, 287–310 (2017)
10. S. Li, L. Hendraningrat, O. Torsaeter, Improved oil recovery by hydrophilic silica nanoparticles suspension: 2 phase flow experimental studies, in *IPTC 2013: International Petroleum Technology Conference*, (2013)
11. A. Esfandyari Bayat et al., Impact of metal oxide nanoparticles on enhanced oil recovery from limestone media at several temperatures. Energy Fuel **28**(10), 6255–6266 (2014)
12. H. Zhang, A. Nikolov, D. Wasan, Enhanced oil recovery (EOR) using nanoparticle dispersions: Underlying mechanism and imbibition experiments. Energy Fuel **28**(5), 3002–3009 (2014)
13. H.C. Lau, M. Yu, Q.P. Nguyen, Nanotechnology for oilfield applications: Challenges and impact. J. Pet. Sci. Eng. **157**, 1160–1169 (2017)
14. R. Hashemi, N.N. Nassar, P.P. Almao, Nanoparticle technology for heavy oil in-situ upgrading and recovery enhancement: Opportunities and challenges. Appl. Energy **133**, 374–387 (2014)
15. H. ShamsiJazeyi et al., J. Appl. Polym. Sci. **131**(15) (2014)
16. M. Zargartalebi, R. Kharrat, N. Barati, Enhancement of surfactant flooding performance by the use of silica nanoparticles. Fuel **143**, 21–27 (2015)
17. F. Sagala, A. Hethnawi, N.N. Nassar, Integrating silicate-based nanoparticles with low salinity water flooding for enhanced oil recovery in sandstone reservoirs. Ind. Eng. Chem. Res. (2020)
18. O. Torsater et al., Improved oil recovery by nanofluids flooding: an experimental study, in *SPE Kuwait International Petroleum Conference and Exhibition*, (Society of Petroleum Engineers, 2012)
19. L. Hendraningrat, S. Li, O. Torsæter, A coreflood investigation of nanofluid enhanced oil recovery. J. Pet. Sci. Eng. **111**, 128–138 (2013)

20. L. Hendraningrat, S. Li, O. Torsater, Effect of some parameters influencing enhanced oil recovery process using silica nanoparticles: an experimental investigation, in *SPE Reservoir Characterization and Simulation Conference and Exhibition*, (Society of Petroleum Engineers, 2013)
21. R. Dubey, Y. Rajesh, M. More, Synthesis and characterization of SiO2 nanoparticles via sol-gel method for industrial applications. Mater. Today Proc. **2**(4–5), 3575–3579 (2015)
22. L.P. Singh et al., Sol-gel processing of silica nanoparticles and their applications. Adv. Colloid Interf. Sci. **214**, 17–37 (2014)
23. A. Nasiri et al., Effect of dispersion method on thermal conductivity and stability of nanofluid. Exp. Thermal Fluid Sci. **35**(4), 717–723 (2011)
24. E.V. Timofeeva et al., Thermal conductivity and particle agglomeration in alumina nanofluids: experiment and theory. Phys. Rev. E **76**(6), 061203 (2007)
25. Y. Min et al., The role of interparticle and external forces in nanoparticle assembly, in *Nanoscience And Technology: A Collection of Reviews from Nature Journals*, (World Scientific, 2010), pp. 38–49
26. R.P. Bagwe, L.R. Hilliard, W. Tan, Surface modification of silica nanoparticles to reduce aggregation and nonspecific binding. Langmuir **22**(9), 4357–4362 (2006)
27. W. Lei et al., Porous boron nitride nanosheets for effective water cleaning. Nat. Commun. **4**, 1777 (2013)
28. A.E. Bayat et al., TiO2 nanoparticle transport and retention through saturated limestone porous media under various ionic strength conditions. Chemosphere **134**, 7–15 (2015)
29. X. Lv et al., Effects of grain size and structural heterogeneity on the transport and retention of nano-TiO2 in saturated porous media. Sci. Total Environ. **563**, 987–995 (2016)
30. A.E. Bayat et al., Transport and retention of engineered Al2O3, TiO2, and SiO2 nanoparticles through various sedimentary rocks. Sci. Rep. **5**, 14264 (2015)
31. K. Mattsson et al., Brain damage and behavioural disorders in fish induced by plastic nanoparticles delivered through the food chain. Sci. Rep. **7**(1), 1–7 (2017)
32. Kahan, D.M. and D. Rejeski, Project on Emerging Nanotechnologies. 2009
33. A. Nel et al., Toxic potential of materials at the nanolevel. Science **311**(5761), 622–627 (2006)
34. R. Society, *Nanoscience and Nanotechnologies: Opportunities and Uncertainties* (Royal Society, 2004)
35. K.W. Powers et al., Research strategies for safety evaluation of nanomaterials. Part VI. Characterization of nanoscale particles for toxicological evaluation. Toxicol. Sci. **90**(2), 296–303 (2006)
36. K. Mattsson et al., Brain damage and behavioural disorders in fish induced by plastic nanoparticles delivered through the food chain. Sci. Rep. **7**(1), 11452 (2017)
37. R. Purohit et al., Social, environmental and ethical impacts of nanotechnology. Mater. Today Proc. **4**(4), 5461–5467 (2017)
38. N. Yekeen et al., A comprehensive review of experimental studies of nanoparticles-stabilized foam for enhanced oil recovery. J. Pet. Sci. Eng. **164**, 43–74 (2018)

Index

N. N. Nassar et al. (eds.), *Nanoparticles: An Emerging Technology for Oil Production and Processing Applications*, Lecture Notes in Nanoscale Science and Technology, https://doi.org/10.1007/978-3-319-12051-5